

Dumitru Luca
Lucel Sirghi
Claudiu Costin *Editors*

Recent Advances in Technology Research and Education

Proceedings of the 16th International
Conference on Global Research and
Education Inter-Academia 2017



Advances in Intelligent Systems and Computing

Volume 660

Series editor

Janusz Kacprzyk, Polish Academy of Sciences, Warsaw, Poland
e-mail: kacprzyk@ibspan.waw.pl

About this Series

The series “Advances in Intelligent Systems and Computing” contains publications on theory, applications, and design methods of Intelligent Systems and Intelligent Computing. Virtually all disciplines such as engineering, natural sciences, computer and information science, ICT, economics, business, e-commerce, environment, healthcare, life science are covered. The list of topics spans all the areas of modern intelligent systems and computing.

The publications within “Advances in Intelligent Systems and Computing” are primarily textbooks and proceedings of important conferences, symposia and congresses. They cover significant recent developments in the field, both of a foundational and applicable character. An important characteristic feature of the series is the short publication time and world-wide distribution. This permits a rapid and broad dissemination of research results.

Advisory Board

Chairman

Nikhil R. Pal, Indian Statistical Institute, Kolkata, India

e-mail: nikhil@isical.ac.in

Members

Rafael Bello Perez, Universidad Central “Marta Abreu” de Las Villas, Santa Clara, Cuba

e-mail: rbellop@uclv.edu.cu

Emilio S. Corchado, University of Salamanca, Salamanca, Spain

e-mail: escorchado@usal.es

Hani Hagrass, University of Essex, Colchester, UK

e-mail: hani@essex.ac.uk

László T. Kóczy, Széchenyi István University, Győr, Hungary

e-mail: koczy@sze.hu

Vladik Kreinovich, University of Texas at El Paso, El Paso, USA

e-mail: vladik@utep.edu

Chin-Teng Lin, National Chiao Tung University, Hsinchu, Taiwan

e-mail: ctlin@mail.nctu.edu.tw

Jie Lu, University of Technology, Sydney, Australia

e-mail: Jie.Lu@uts.edu.au

Patricia Melin, Tijuana Institute of Technology, Tijuana, Mexico

e-mail: epmelin@hafsamx.org

Nadia Nedjah, State University of Rio de Janeiro, Rio de Janeiro, Brazil

e-mail: nadia@eng.uerj.br

Ngoc Thanh Nguyen, Wroclaw University of Technology, Wroclaw, Poland

e-mail: Ngoc-Thanh.Nguyen@pwr.edu.pl

Jun Wang, The Chinese University of Hong Kong, Shatin, Hong Kong

e-mail: jwang@mae.cuhk.edu.hk

More information about this series at <http://www.springer.com/series/11156>

Dumitru Luca · Lucel Sirghi
Claudiu Costin
Editors

Recent Advances in Technology Research and Education

Proceedings of the 16th International
Conference on Global Research
and Education Inter-Academia 2017

 Springer

Editors

Dumitru Luca
Faculty of Physics, Iasi Plasma
Advanced Research Center
Alexandru Ioan Cuza University of Iasi
Iasi
Romania

Claudiu Costin
Faculty of Physics, Iasi Plasma
Advanced Research Center
Alexandru Ioan Cuza University of Iasi
Iasi
Romania

Lucel Sirghi
Faculty of Physics, Iasi Plasma
Advanced Research Center
Alexandru Ioan Cuza University of Iasi
Iasi
Romania

ISSN 2194-5357

ISSN 2194-5365 (electronic)

Advances in Intelligent Systems and Computing

ISBN 978-3-319-67458-2

ISBN 978-3-319-67459-9 (eBook)

DOI 10.1007/978-3-319-67459-9

Library of Congress Control Number: 2017952850

© Springer International Publishing AG 2018

This work is subject to copyright. All rights are reserved by the Publisher, whether the whole or part of the material is concerned, specifically the rights of translation, reprinting, reuse of illustrations, recitation, broadcasting, reproduction on microfilms or in any other physical way, and transmission or information storage and retrieval, electronic adaptation, computer software, or by similar or dissimilar methodology now known or hereafter developed.

The use of general descriptive names, registered names, trademarks, service marks, etc. in this publication does not imply, even in the absence of a specific statement, that such names are exempt from the relevant protective laws and regulations and therefore free for general use.

The publisher, the authors and the editors are safe to assume that the advice and information in this book are believed to be true and accurate at the date of publication. Neither the publisher nor the authors or the editors give a warranty, express or implied, with respect to the material contained herein or for any errors or omissions that may have been made. The publisher remains neutral with regard to jurisdictional claims in published maps and institutional affiliations.

Printed on acid-free paper

This Springer imprint is published by Springer Nature

The registered company is Springer International Publishing AG

The registered company address is: Gewerbestrasse 11, 6330 Cham, Switzerland

Preface

The progress in science during the last century is of a paramount importance, not only for the enrichment of human knowledge, but also for the spectacular increase in the quality of life. Basic research and applied research have driven crucial developments in communications and information technologies, which became key factors for the onset and the rapid evolution of the fourth industrial revolution that we are facing now. This revolution is based on the involvement of the information technology in industry management, research and innovation, global communications, education and, to a larger extent, in the everyday life.

The higher education institutions, where advanced scientific research is a *modus vivendi*, could not remain outside the global process of creation and transferring of knowledge. A couple of universities from Japan and Central and Eastern European countries decided, in 2002, to constitute an academic community, named Inter-Academia, and to align their education and research programs with the mainstream of several cutting-edge topics, such as materials sciences, plasma and solid-state physics, nanotechnology, metrology, photonics, biotechnology, e-learning, intelligent and soft computing. One of the outcomes of the cooperation within the Inter-Academia community, comprising nowadays 14 universities and research institutes, is the organization of an international conference, hosted at a time by each of its members, on yearly basis.

The current book *Recent Advances in Technology Research and Education. Proceedings of the 16th International Conference on Global Research and Education Inter-Academia 2017* is dedicated to recent developments in scientific research and technology education. It is intended to be a middle- and long-term scientific reference source for the global scientific community. The book contains 42 selected contributions submitted to the 16th International Conference on Global Research and Education Inter-Academia 2017, organized by the Faculty of Physics of Alexandru Ioan Cuza University of Iași, Romania. This third volume in series, following the editions in 2015 and 2016, is an expression of the expertise of 119 individual authors, leading researchers from 14 countries, several of them affiliated to universities and research institutes not belonging to the Inter-Academia yet.

We express our gratitude to the authors for their hard work to submit adequate standard papers for the Conference. The work of the Scientific Committee members for coordination in organizing the review process and designing the Conference Program is greatly acknowledged.

Dumitru Luca

Contents

Material Science and Technology, Smart Materials

Hydrothermal Synthesis and Characterization of Mixed Fluoride Based Nanophosphors	3
Anastasiya M. Dorokhina, Vadim V. Bakhmetyev, and Maxim M. Sychov	
Transfer of Light Energy from UV to Visible Domain in Coordination Compounds of Europium(III)	11
V.I. Verlan, O.T. Bordian, M.S. Iovu, I.P. Culeac, and V.E. Zubareva	
Phase Composition, Structure and Mechanical Properties of Carbon Coatings Doped by Carbide-Forming Metals	18
Alexandr V. Rogachev, Alexander S. Rudenkov, Dmitry G. Piliptsov, Xiaohong Jiang, and Nikolay N. Fedosenko	
Ellipsometric Control of Laser Welded Materials	26
Maryana M. Negrub, David Hélie, Iryna V. Yurgelevych, and Leonid V. Poperenko	
Comparison of Euler-Bernoulli and Timoshenko Beam Equations for Railway System Dynamics	32
Amir Mosavi, Rami Benkreif, and Annamária R. Varkonyi-Koczy	
Interaction of Hydrogen Isotopes with Radiation Damaged Tungsten	41
Yasuhisa Oya, Keisuke Azuma, Akihiro Togari, Qilai Zhou, Yuji Hatano, Masashi Shimada, Robert Kolasinski, and Dean Buchenauer	
Reviewing the Novel Machine Learning Tools for Materials Design	50
Amir Mosavi, Timon Rabczuk, and Annamária R. Varkonyi-Koczy	
Sol-gel Preparation and Luminescent Properties of Transparent Thin Films and Ceramics of $ZrO_2:Ti^{3+}$	59
Dmitry Kovalenko, Dumitru Luca, Vladimir Gaishun, Larisa Sudnik, Vasily Vaskevich, and Alexey Rusikin	

Development of Functional Coatings by Electron-Beam Sputtering of Sol-Gel Targets	65
Dmitry Kovalenko, Dumitru Luca, Vladimir Gaishun, Larisa Sudnik, Alexandr V. Rogachev, Vasily Vaskevich, Yanina Kosenok, and Alexey Rusykin	
Omega-Structured Substrate-Supported Metamaterial for the Transformation of Wave Polarization in THz Frequency Range	72
Igor Semchenko, Sergei Khakhomov, Andrey Samofalov, Maksim Podalov, Vitaliy Solodukha, Alyaxandr Pyatlitski, and Natalya Kovalchuk	
Core-Shell Powders with Titanium Coating	81
Sergey Bogdanov and Maxim Sychov	
Temperature Fields in the In/CdTe Structure Under Laser-Induced Doping in Liquid	87
V.A. Gnatyuk, V.L. Dubov, D.V. Fomin, A.Yu. Seteikin, and T. Aoki	
Nanotechnology	
Photon-Coupled, Photoswitchable Protein-Based OR, NOR Logic Gates	99
Balázs Rakos	
Plasma-Chemical Synthesis of Plasmon Metal-Polymer Coatings, Their Structure and Properties	104
Alexandr V. Rogachev, Maxim A. Yarmolenko, and Alexandr A. Rogachev	
Automatic Evaluation of Surface Nanostructuring Using Image Processing	110
Mihaela Luca, Adrian Ciobanu, Silviu-Ioan Bejinariu, Anca Ignat, Claudia Teodora Teodorescu-Soare, George Stoian, and Dumitru Luca	
Friction and Adhesion Forces at a Nanoscopic Contact Between Titanium Dioxide Thin Film Surfaces	120
Lucel Sirghi	
Photoluminescence Properties of the Nanocomposites PEPC/Eu(o-MBA)₃Phen and PEPC/Eu(TTA)₃(Ph₃PO)₂	128
O.T. Bordian	
Surface Forces Between Hydrophobic Surfaces Obtained by Self-assembled Monolayers Deposition of Octadecyltrichlorosilane	135
Alexandra Besleaga, Florentina Samoila, and Lucel Sirghi	

Nanostructure and Ferroelectric Properties of Sol-Gel SBTN-Films for Electronic Devices 144
 Sergei A. Khakhomov, Alina V. Semchenko, Vitaliy V. Sidsky, Vladimir E. Gaishun, Dumitru Luca, Vladimir V. Kolos, Vitaliy A. Solodukha, Alyaxandr N. Pyatlitski, and Natalya S. Kovalchuk

Sol-Gel Synthesis of ZnO Nanorods for MEMS 151
 Alexandr V. Rogachev, Alina V. Semchenko, Dmitry L. Kovalenko, Vitaliy V. Sidsky, Olga I. Tyulenkova, Nina I. Tyulenkova, Dumitru Luca, Vitaliy A. Solodukha, Alyaxandr N. Pyatlitski, and Natalya S. Kovalchuk

Plasma Physics

Pharmacokinetics of Cyclosporine A of Transdermal Delivery Using Microplasma and Oral Administration 161
 Jaroslav Kristof, Hideto Miyamoto, Marius Blajan, and Kazuo Shimizu

Flow Control by Dielectric Barrier Discharge Microplasma 169
 Marius Blajan, Akihiko Ito, Jaroslav Kristof, and Kazuo Shimizu

Investigations on Crystallinity and Surface Oxidation States of Nb:TiO₂ DC-Sputtered Films 176
 Marius Dobromir, Radu Paul Apetrei, Claudia Teodora Teodorescu-Soare, Alina Semchenko, Dmitry Kovalenko, and Dumitru Luca

Pulsed Magnetron Sputtering: The Role of the Applied Power on W Coatings Properties 183
 Ioana-Laura Velicu, Vasile Tiron, Ilarion Mihaila, and Claudiu Costin

Preparation of Nb-Doped TiO₂ Nanotubes Using Magnetron Sputtering 191
 Claudia Teodora Teodorescu-Soare, Marius Dobromir, George Stoian, and Dumitru Luca

Electric and Electronic Engineering. Manufacturing Technology

Generation and Evaluation of Surrogate to Design Fuel Supply System 203
 Keisuke Fujii, Shun Egawa, and Kazuhiro Takeda

Optimal Design of Electrical Machines: State of the Art Survey 209
 Marcell Baranyai, Amir Mosavi, Istvan Vajda, and Annamária R. Varkonyi-Koczy

Review on the Usage of the Multiobjective Optimization Package of modeFrontier in the Energy Sector 217
 Amir Mosavi, Rituraj Rituraj, and Annamária R. Varkonyi-Koczy

Industrial Applications of Big Data: State of the Art Survey	225
Amir Mosavi, Alvaro Lopez, and Annamária R. Varkonyi-Koczy	
Robotics, Measurement, Identification and Control	
Calculation Method of Chemical Kinetics to Search the Optimal Experimental Conditions in a Micro Flow Reactor	235
Keisuke Nonaka, Masato Abe, and Kazuhiro Takeda	
Robot Control in iSpace by Applying Weighted Likelihood Function	243
Adrienn Dineva, Balázs Tusor, Péter Csiba, and Annamária Várkonyi-Kóczy	
Dissipation and Thermal Time Constants in Graphite of an Ultra-Small Bead Thermistor	249
Daniel Radu, Iordana Astefanoaei, and Catalin Agheorghiesei	
Monitoring Hand Gesture and Effort Using a Low-Cost Open-Source Microcontroller System Coupled with Force Sensitive Resistors and Electromyography Sensors	261
Andrei Vasile Nastuta and Catalin Agheorghiesei	
Soft Computing Techniques and Modeling	
Firmware Enhancements for BYOD-Aware Network Security	273
Massimiliano Pedone, Kamen Kanev, Paolo Bottoni, Domenico Vitali, and Alessandro Mei	
Ontology Extension for Personalized Accessible Indoor Navigation	281
Gabriella Simon-Nagy and Rita Fleiner	
A Load Balancing Algorithm for Resource Allocation in Cloud Computing	289
Seyedmajid Mousavi, Amir Mosavi, and Annamária R. Varkonyi-Koczy	
A Fuzzy Data Structure for Variable Length Data and Missing Value Classification	297
Balazs Tusor, Annamária R. Várkonyi-Kóczy, and János T. Tóth	
Multimedia, Internet-Based Education and e-Learning	
A Multifaceted Approach Towards Education in Data Analytics	307
Reneta P. Barneva, Isabelle Bichindaritz, Valentin E. Brimkov, Joaquin Carbonara, Sanjeena Dang, Federico Gelsomini, Kamen Kanev, Jeanette Sperhac, and Lisa Walters	

BYOD Collaborative Kanji Learning in Tangible Augmented Reality Settings 315
Federico Gelsomini, Kamen Kanev, Patrick Hung, Bill Kapralos, Michael Jenkin, Reneta P. Barneva, and Mariagioia Vienna

Flipping Out in Japan: Engineering the Academic English Classroom for Innovation. 326
Valerie Anne Wilkinson and Damon Michael Chandler

An Exercise in First and Second-Order Cybernetics: The 18th Year of General Systems Theory (GST) Communication Project. 334
Valerie Anne Wilkinson

Predicting the Future Using Web Knowledge: State of the Art Survey 341
Amir Mosavi, Yatish Bathla, and Annamária Varkonyi-Koczy

Author Index. 351

**Material Science and Technology,
Smart Materials**

Hydrothermal Synthesis and Characterization of Mixed Fluoride Based Nanophosphors

Anastasiya M. Dorokhina, Vadim V. Bakhmetyev,
and Maxim M. Sychov^(✉)

Saint-Petersburg State Institute of Technology,
Moskovsky Prospect, 26, St.-Petersburg, Russia
{nastya.dorokhina, vadim_bakhmetyev, msychov}@mail.ru

Abstract. Finely dispersed (particle size less than 200 nm) NaGdF₄:Eu³⁺ and BaGdF₅:Eu³⁺ phosphors providing efficient luminescence at $\lambda_{em} = 616$ nm and 592 nm respectively are synthesized and the effect of hydrothermal treatment on their phase composition, dispersity and luminescent performances is studied. NaGdF₄:Eu³⁺ phosphor synthesized using a hydrothermal method in ethylene glycol medium allows the preparation of stable colloid solutions and can be used for photodynamic therapy of malignant tumors.

Keywords: Photodynamic therapy · Nanophosphors · Mixed fluorides · Hydrothermal synthesis

1 Introduction

Photodynamic therapy (PDT) is a modern promising approach to malignant tumor therapy based on the introduction of a photosensitizer capable of selective accumulation in the tumor tissue and generation of action of active oxygen under lighting to destroy tumor cells. However, strong absorption of light by body tissues limits the use of this method. To expand the use of PDT, it is proposed to create a pharmaceutical composition combining a photosensitizer and nanophosphor converting X-ray or gamma radiation into light with a wavelength necessary for the photosensitizer activation. The most important goal in this field is the development of nanophosphors as radiation converters for commonly used photosensitizers. Such nanophosphors should meet the following requirements: non-toxicity and biocompatibility for the human body, efficient generation of necessary light upon excitation by X-ray or γ -radiation that easily penetrates into the tissues of the body, and have particle size of the order of hundreds of nanometers allowing to prepare a colloidal solution suitable for incorporation into human's organism [1].

In our previous studies [2–5], phosphors Zn₃(PO₄)₂:Mn²⁺, NaBaPO₄:Eu²⁺, Y₂O₃:Eu³⁺, Y₃Al₅O₁₂:Eu³⁺ were proposed for this purpose. The main complication in this way is determined by the fact that convenient high temperature (more than 800 °C) synthesis of these phosphors leads to agglomeration of the phosphor nanoparticles into large associates. To address this problem, hydrothermal method for the synthesis of phosphors was proposed, involving heat treatment of a liquid medium in an autoclave at moderate temperatures below 210 °C. Particularly, this approach is applicable to the

synthesis of lanthanide fluorides advantageous in respect of effective X-ray induced luminescence in combination with high density and non-toxicity [6].

Since X-ray scattering in tissues is negligible, lanthanides are effective dopants for such phosphors, as they have high atomic number and specific electronic energy states providing emission in the UV-vis region. Incorporation of elements with high atomic numbers into the matrix provides generation of electrons with sufficient energy for down-conversion upon appropriate choice of lanthanide sensitizers and luminescent centers [7]. Fluoride materials offer advantages in terms of high density, mechanical hardness and radiation hardness [8, 9].

Fluoride-based phosphors $ALnF_4$ (A = alkali metal; Ln = lanthanide) are preferable matrices for optically emitting lanthanide phosphors (since they have low phonon energy states [10–12]) and for down-conversion due a wide band gap (9–10 eV) [13]. Rare-earth dopants provide the host material contraction resulting in unit cell densities as high as 8.44 g/cm³ and increased X-ray absorption [14].

Particularly, gadolinium serves as an excellent photosensitizer for UV-excited down-converting lanthanide emitters [15, 16]. The $Gd^{3+}(\text{host})-Eu^{3+}(\text{dopant})$ combination is the best-studied down-converting system.

This study is aimed at hydrothermal synthesis of $NaGdF_4:Eu^{3+}$ and $BaGdF_5:Eu^{3+}$ nanophosphors and study of their properties.

2 Experimental

Synthesis of $NaGdF_4:15\%Eu^{3+}$ (Aqueous Medium). Nanoparticles of $NaGdF_4$ -doped with Eu^{3+} were synthesized by the citrate method [17]. A transparent aqueous solution containing 4 mL of 0.2 M Gd and 0,2 M Eu chlorides and 8 mL of 0.2 M sodium citrate was heated to 90 °C. Sodium fluoride (16 mL of 1 M) solution was added to the solution, upon which the solution turned whitish. The nanoparticles were heated for 2 h. The nanoparticles were centrifuged and washed twice before further measurements were carried out. As-synthesized particles were heated in a Teflon-lined autoclave at 210 °C for 1 h in phosphate buffer. To study the effect of pH upon the of phosphor properties two samples were synthesized in a weakly acidic (pH 6.05) and weakly basic medium (pH 7.20).

Synthesis of $BaGdF_5:15\%Eu^{3+}$ and $NaGdF_4:15\%Eu^{3+}$ (Organic Medium). Water-soluble and polyethylene glycol (PEG)-coated $BaGdF_5:15\%Eu^{3+}$ and $NaGdF_4:15\%Eu^{3+}$ nanoparticles were synthesized by method [18]. 8.5 ml of 0.2 M solution of $GdCl_3$ (1.7 mmol $GdCl_3$) and 1.5 ml of a 0.2 M solution of $EuCl_3$ (0.3 mmol $EuCl_3$) were added to 44 mL ethylene glycol (EG). Then add to the solution 2 mmol NaCl (2 mmol $BaCl_2$) was added to above solution and stirred for 30 min. PEG (2 g) (Mw = 2000) was added and sonicated the solution for 15 min. After that, 16 mL of EG containing NH_4F was added to above mixture. The mixture solutions were stirred and sonicated for another 30 min and then transferred into a 100 mL stainless Teflon-lined autoclave and kept at 200 °C for 24 h. The reaction mixture was washed and centrifuged several times with ethanol and bidistilled water to remove other residual solvents and then suspended in bidistilled water for further use.

XRD characterization of the phosphors was carried out on a Rigaku SmartLab 3 X-ray diffractometer. The investigation of the particle size of phosphors by laser light scattering was performed on a Shimadzu SALD-7500 nano laser analyzer. The electron micrographs were made using a scanning electron microscope Tescan Vega 3 SBH. The luminescence spectra were measured with an AvaSpec-3648 spectrofluorimeter.

3 Results and Discussion

XRD results of the synthesized phosphors are shown in Fig. 1. The location of all the peaks in X-ray pattern of $\text{BaGdF}_5:\text{Eu}^{3+}$ corresponds the cubical BaGdF_5 (PDF card 24-98) without any admixture phases. The peaks relating to initial $\text{NaGdF}_4:\text{Eu}^{3+}$

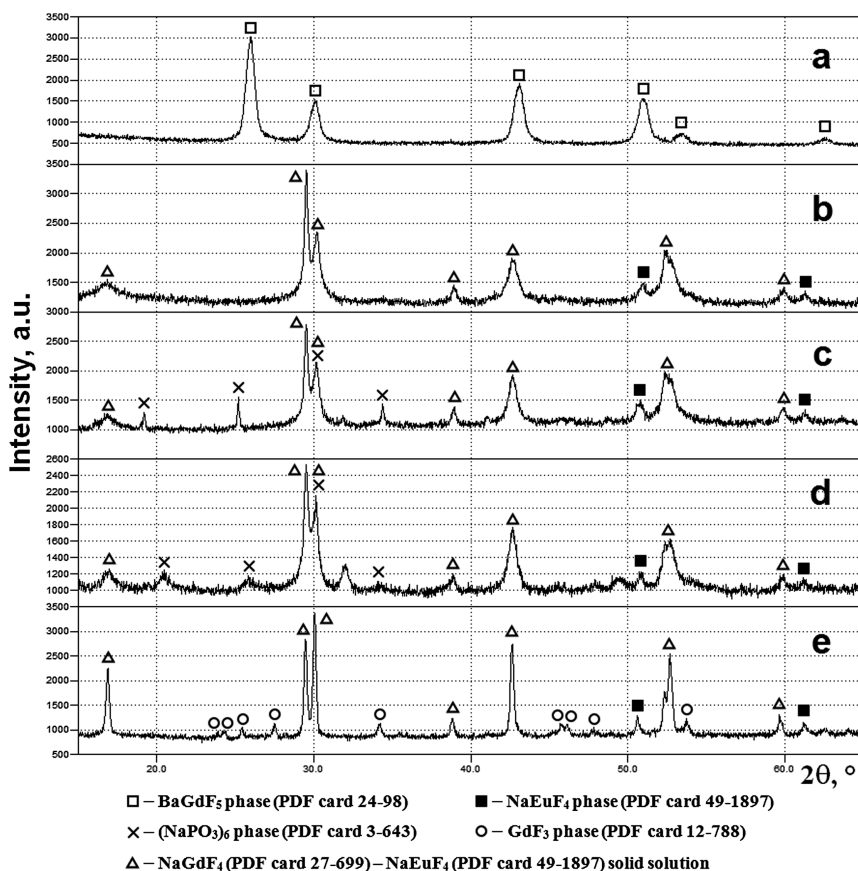


Fig. 1. XRD patterns of the synthesized phosphors: a – $\text{BaGdF}_5:\text{Eu}^{3+}$ synthesized in ethylene glycol medium; b – $\text{NaGdF}_4:\text{Eu}^{3+}$ synthesized in aqueous medium, initial; c – $\text{NaGdF}_4:\text{Eu}^{3+}$ synthesized in aqueous medium and hydrothermal treated at pH = 6.05; d – $\text{NaGdF}_4:\text{Eu}^{3+}$ synthesized in aqueous medium and hydrothermal treated at pH = 7.20; e – $\text{NaGdF}_4:\text{Eu}^{3+}$ synthesized in ethylene glycol medium.

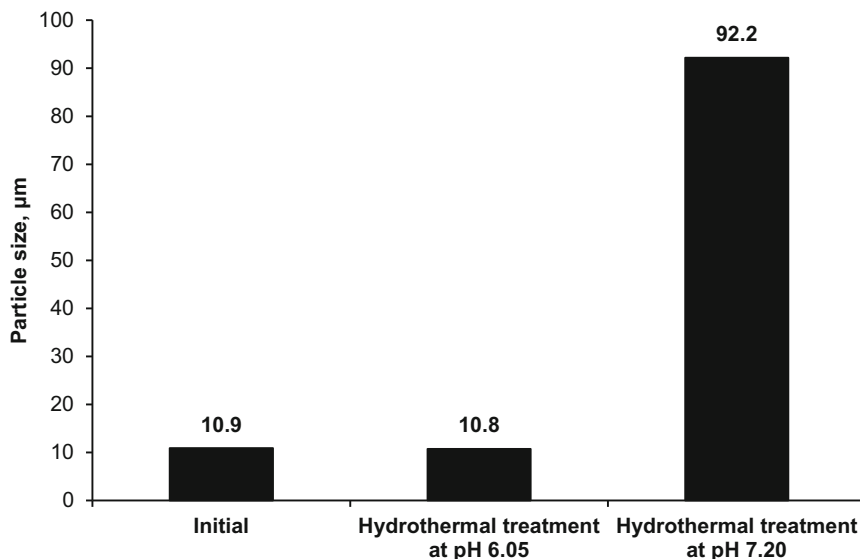


Fig. 2. Particle size of $\text{NaGdF}_4:\text{Eu}^{3+}$ phosphors synthesized in an aqueous medium measured by laser light scattering.

synthesized in aqueous medium are located between the peaks corresponding to hexagonal NaGdF_4 (PDF card 27-699) and hexagonal NaEuF_4 (PDF card 49-1897). Thus, it may be concluded that the synthesized $\text{NaGdF}_4:\text{Eu}^{3+}$ phosphor is a substitutional solid solution, in which Eu atoms replace gadolinium. Hydrothermal processing of $\text{NaGdF}_4:\text{Eu}^{3+}$ phosphors in phosphate buffer solution results in the appearance of peaks corresponding the sodium hexametaphosphate (NaPO_3)₆ (PDF card 3-643) likely formed from disodium phosphate in the course of processing. XRD pattern of $\text{NaGdF}_4:\text{Eu}^{3+}$ synthesized in ethylene glycol also corresponds to substitutional solid solution $\text{NaGdF}_4\text{-NaEuF}_4$. In addition, weak peaks related to gadolinium fluoride (PDF card 12-788) are also present in the X-ray spectrum of this sample, which is obviously an impurity phase formed in the course of hydrothermal synthesis. XRD of $\text{NaGdF}_4:\text{Eu}^{3+}$ synthesized in ethylene glycol are much narrower compared with those for samples synthesized in an aqueous medium. This indicates that ethylene glycol hydrothermal synthesis provides samples with higher crystallinity. According to calculations using Scherrer equation, the crystallite size of $\text{NaGdF}_4:\text{Eu}^{3+}$ phosphors synthesized in the aqueous medium and ethylene glycol are 14–16 nm and 43 nm, respectively.

The results of particle size measurement for $\text{NaGdF}_4:\text{Eu}^{3+}$ phosphors synthesized in an aqueous medium by laser light scattering are shown in Fig. 2. According to these data, obtained, the initial phosphor particle size is about 10.9 μm and remains almost unchanged (10.8 μm) after hydrothermal treatment in a slightly acidic medium (pH = 6.05). On the contrary, hydrothermal treatment in weakly basic medium (pH = 7.20) leads to a sharp enlargement of the particles to 92.2 μm as a result the colloidal solution destabilization and sedimentation. Probably, weakly basic medium promotes the destruction of sodium citrate shell on the surface of the phosphor

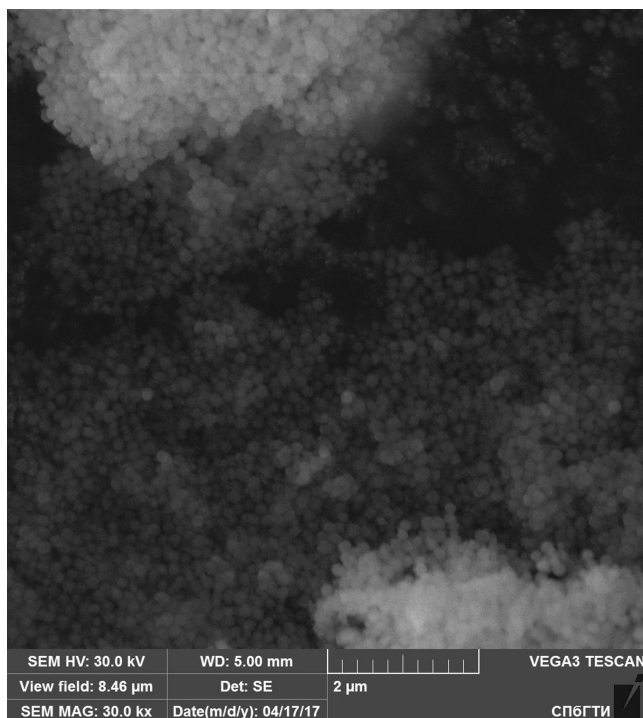


Fig. 3. SEM micrograph of $\text{NaGdF}_4:\text{Eu}^{3+}$, phosphor synthesized in an ethylene glycol medium.

particles, resulting in their aggregation. Therefore, in this case, the laser light scattering indicates the size of agglomerates instead of individual particles.

To further confirm the determined particle size, SEM characterization was also performed. As an example, Fig. 3 shows a SEM micrograph of $\text{NaGdF}_4:\text{Eu}^{3+}$, phosphor synthesized in an ethylene glycol medium. It can be seen that the size of the phosphor particles does not exceed 200 nm, that affords preparation of a stable colloid solution suitable for the application in photodynamic therapy.

The luminescence spectra of synthesized phosphors measured at ambient temperature (20 °C) are shown in Figs. 4 and 5. For $\text{BaGdF}_5:\text{Eu}^{3+}$, the most intensive band with the peak at 592 nm relates to ${}^5\text{D}_0 \rightarrow {}^7\text{F}_1$ electronic transition [3]. This band is quite far from the absorption band of commercial photosensitizers [1]. Consequently, this phosphor is not suitable for PDT application. In the case of $\text{NaGdF}_4:\text{Eu}^{3+}$ the most intensive band corresponds to ${}^5\text{D}_0 \rightarrow {}^7\text{F}_2$, transition with the peak at 616 nm more convenient for luminescence energy transfer to photosensitizers.

The luminescence spectra were used to calculate the corresponding intensities (total luminescence intensity and intensity of the band with the maximum of 616 nm). The results presented in Fig. 6 indicate that $\text{NaGdF}_4:\text{Eu}^{3+}$, synthesized in an aqueous medium without hydrothermal treatment provides the intensity (both overall and at

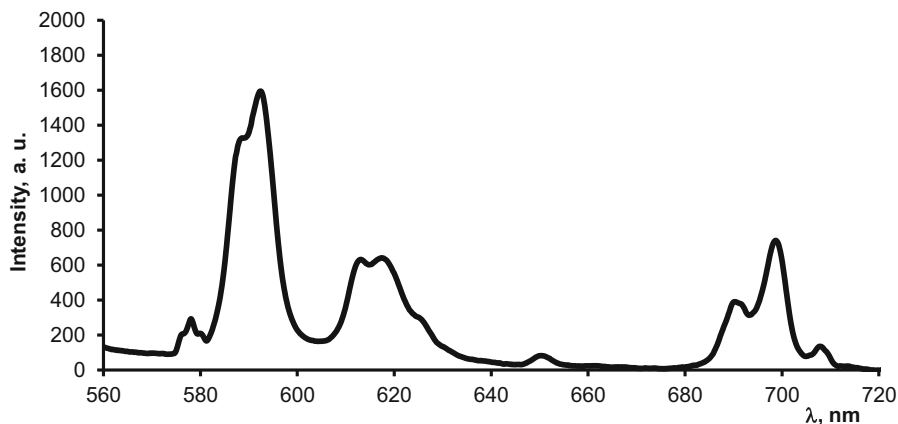


Fig. 4. Luminescence spectra of $\text{BaGdF}_5:\text{Eu}^{3+}$ phosphor.

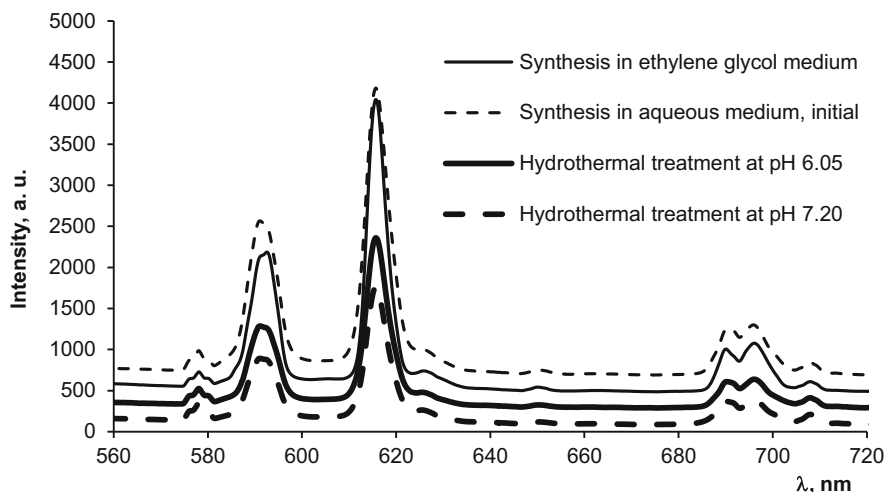


Fig. 5. Luminescence spectra of $\text{NaGdF}_4:\text{Eu}^{3+}$ phosphors.

616 nm. Hydrothermal treatment in an autoclave leads to a decrease in the luminescence intensity (probably due to the appearance of $(\text{NaPO}_3)_6$ admixture phase). $\text{NaGdF}_4:\text{Eu}^{3+}$ phosphor synthesized in an ethylene glycol medium has a 15% lower luminescence intensity than the sample synthesized in an aqueous medium, despite the larger crystallite size. This is probably also determined by the presence of GdF_3 impurity phase in the phosphor. However, in terms of particle size, this phosphor is much more suitable for PDT application.

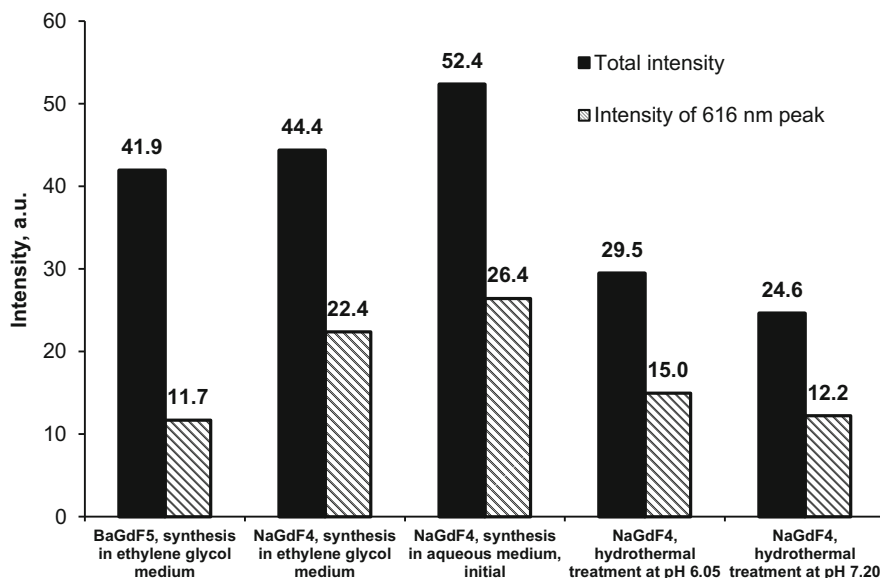


Fig. 6. Luminescence intensities of the synthesized phosphors (total and for the band at 616 nm).

4 Conclusion

Hydrothermal method is applied for the synthesis of BaGdF₅:Eu³⁺ and NaGdF₄:Eu³⁺ in aqueous and ethylene glycol medium. The obtained data indicate that NaGdF₄:Eu³⁺ phosphor precipitation directly affords the admixture-free hexagonal NaGdF₄ phase, while the subsequent hydrothermal processing in a phosphate buffer solution leads to the appearance of admixture phases and consequent decrease of the luminescence intensity. Furthermore, processing in a weakly basic medium also results in the agglomeration of the phosphor particles (probably due to the sodium citrate shell destruction) and destabilization of the phosphor colloid solution.

It is found that, in contrast to preparation in aqueous medium, hydrothermal synthesis in ethylene glycol allows phosphors with smaller particles (less than 200 nm) with better crystallinity and more suitable for use in PDT.

Acknowledgment. The reported study was funded by RFBR according to the research project No. 16-33-00998 МОЛ_а.

References

1. Bakhmetyev, V., Sychov, M., Orlova, A., Potanina, E., Sovestnov, A., Kulvelis, Y.: Nanophosphors for photodynamic therapy of oncological diseases. *Nanoindustry* **8**, 46–50 (2013)

2. Minakova, T.S., Sychoy, M.M., Bakhmetyev, V.V., Eremina, N.S., Bogdanov, S.P., Zyatikov, I.A., Minakova, L.Y.: The influence of $Zn_3(PO_4)_2$: Mn – luminophores synthesis conditions on their surface and luminescent features. *Adv. Mater. Res.* **872**, 106–111 (2014)
3. Malygin, V.V., Lebedev, L.A., Bakhmetyev, V.V., Keskinova, M.V., Sychoy, M.M., Mjakin, S.V., Nakanishi, Y.: Synthesis and study of luminescent materials on the basis of mixed phosphates. *Adv. Intell. Syst. Comput.* **519**, 47–54 (2016)
4. Bakhmetyev, V.V., Lebedev, L.A., Vlasenko, A.B., Bogdanov, S.P., Sovestnov, A.E., Minakova, T.S., Minakova, L., Sychoy, M.M.: Luminescent materials on the basis of yttrium oxide and yttrium aluminum garnet used for photodynamic therapy. *Key Eng. Mater.* **670**, 232–238 (2016)
5. Bakhmetyev, V.V., Minakova, T.S., Mjakin, S.V., Lebedev, L.A., Vlasenko, A.B., Nikandrova, A.A., Ekimova, I.A., Eremina, N.S., Sychoy, M.M., Ringuede, A.: Synthesis and surface characterization of nanosized $Y_2O_3:Eu$ and $YAG:Eu$ luminescent phosphors which are useful for photodynamic therapy of cancer. *Eur. J. Nanomed.* **8**(4), 173–184 (2016)
6. Peng, J., Sun, Y., Liu, Q., Yang, Y., Zhou, J., Feng, W.: Upconversion nanoparticles dramatically promote plant growth without toxicity. *Nano Res.* **5**(11), 770–782 (2012)
7. Sudheendra, L., Das, G.K., Li, C., Stark, D., Cena, J., Cherry, S., Kennedy, I.M.: $NaGdF_4:Eu^{3+}$ nanoparticles for enhanced x-ray excited optical imaging. *Chem. Mater.* **26**(5), 1881–1888 (2014)
8. Vasilchenko, V.G., Kobayashi, M.: Multicomponent Crystals based on Heavy Metal Fluorides for Radiation Detectors. In: Sobolev, B.P. (ed.) *Institute d'Estudis Catalans, Barcelona, Spain* (1994)
9. Sobolev, B.P., Krivandina, E.A., Derenzo, S.E., Moses, W.W., West, A.C.: *MRS Online Proc. Library*, 348, 277 – 283 (1994)
10. Guggenheim, H.J., Johnson, L.F.: *Appl. Phys. Lett.* **15**(2), 51–52 (1969)
11. Sommerdijk, J.L.: *J. Lumin.* **4**(4), 441–449 (1971)
12. Auzel, F.: *Chem. Rev.* **104**(1), 139–174 (2003)
13. Wegh, R.T., Donker, H., Oskam, K.D., Meijerink, A.: *Science* **283**(5402), 663–666 (1999)
14. Thoma, R.E., Insley, H., Hebert, G.M.: *Inorg. Chem.* **5**(7), 1222–1229 (1966)
15. Wegh, R.T., Donker, H., Oskam, K.D., Meijerink, A.: *J. Lumin.* **82**(2), 93–104 (1999)
16. Ye, S., Zhu, B., Chen, J., Luo, J., Qiu, J.R.: *Appl. Phys. Lett.* **92**(14), 141112–141113 (2008)
17. Sudheendra, L., Ortalan, V., Dey, S., Browning, N.D., Kennedy, I.M.: *Chem. Mater.* **23**(11), 2987–2993 (2011)
18. Zeng, S., Tsang, M.-K., Chan, C.-F., Wong, K.-L., Hao, J.: *Biomaterials* **33**(36), 9232–9238 (2012)

Transfer of Light Energy from UV to Visible Domain in Coordination Compounds of Europium(III)

V.I. Verlan¹(✉), O.T. Bordian¹, M.S. Iovu¹, I.P. Culeac¹,
and V.E. Zubareva²

¹ Institute of Applied Physics of the Academy of Sciences of Moldova,
No. 5 Academy Str., 2028 Chisinau, Republic of Moldova
vverlan@gmail.com

² Institute of Chemistry of the Academy of Sciences of Moldova,
No. 3 Academy Str., 2028 Chisinau, Republic of Moldova

Abstract. We propose a new technology for preparation of luminescent coordination organic compounds (COC) with Eu^{3+} ions with down-conversion of light and extended absorption spectral response to UV. The optimal ionic and neutral ligands for coordination of rare-earth ions were selected for each specific organic compound $Eu(TTA)_3H_2O$, $Eu(TTA)_3Phen$, $Eu(TTA)_3(Ph_3PO)_2NO_3$, $Eu(TTA)_3(Ph_3PO)_2$, $Eu(DBM)_3Phen$ and $Eu(o-MBA)_3Phen$. Selection of different COC was aimed at obtaining the compatibility with polymer and improving the efficiency of the luminescence through energy transfer. Characterization of Eu coordinating compounds was carried out by UV-Vis absorption and PL spectroscopy. The mechanism of energy transfer to rare-earth ions has been discussed.

Keywords: Europium coordination compound · Photoluminescence · Energy transfer

1 Introduction

Europium(III) complex compounds with organic ligands are widely used in bio-medical diagnostics as well as in photonic devices and solar energy conversion [1–3]. Fluorescence probes based on Europium(III) binary and ternary complexes have extensive applications in immunofluorescence assays for determination of biologically active substances, including drugs, in the study of biochemical properties of systems, etc. [4, 5].

All these practical applications, especially biomedical and analysis, are based on the characteristic luminescence determined by the Eu^{3+} ion $4f$ shell, sensitized by the intramolecular transfer of excitation energy from the singlet and triplet levels of the ligand to Eu^{3+} radiation levels. For $Eu(III)$ coordination organic compounds with characteristic narrowband emission spectra, high Stokes shift, long lifetime, which allows signal detection with a time resolution, and elimination of non-radiant transitions.

The main purpose of this work was to study the optical properties of the ligands applied for obtaining coordination compounds with Eu^{3+} ion with the important electronic transitions of level $^5D_0 \rightarrow ^7F_j$ in the $4f$ shield.

2 Optical Properties of Ligands

Physical properties of coordination compounds with rare-earth ions (absorption, luminescence, etc.), their compatibility with various solvents and polymers, depend in a great extent on the underlying ligands compounds. We have analyzed available literature data in order to choose the optimal ligands applicable for the accomplishment. From different types of ligands we have investigated optical properties and solubility of the following materials: *1,3-diphenylpropane-1,3-dione (DBM)*, *triphenylphosphineoxide (TPPO)*, *4,4,4-trifluoro-1-(2-thienyl)-1,3-butanedione (TTA)*, *1,10-phenanthroline (Phen)*, *2-methylbenzoic acid (o-MBA)*.

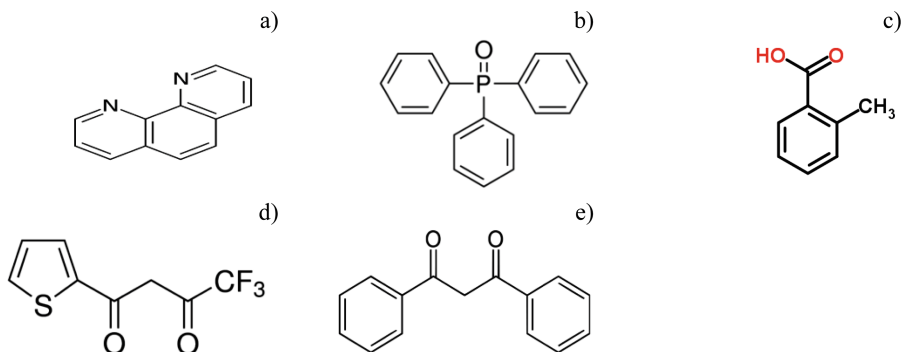


Fig. 1. Illustration of chemical structure of the ligands used in preparation of organic rare-earth coordination compounds: (a) Phen; (b) TPPO; (c) o-MBA; (d) TTA; (e) DBM.

Optical transmission measurements were carried out in the range 300–800 nm on the spectrometer *Specord UV VIS (Carl Zeiss, Jena)*. Optical transmission spectra of the ligands in methanol saturated solutions were registered by use of standard UV fused quartz cuvettes with two polished sides with 10 mm path length. All the measurements of PL spectra were carried out in the same conditions of excitation with a nitrogen laser 337 nm at room temperature.

The chemical structures of investigated ligands are illustrated in Fig. 1. Figure 2 shows the plot of the absorption spectrum of ligands and methanol (the solvent using for dissolving of the ligands was methanol). The absorption threshold of the ligands was determined from the Tauc plot [6] $(\alpha h\nu)^{1/n} = f(h\nu)$, where the value of the exponent n is determined by the nature of the transition of amorphous – crystalline material: for allowed direct transitions $n = 1/2$. Consequently, the absorption threshold was estimated from experimental data, plotted according to the Tauc equation in the

coordinates $(\alpha h\nu)^{1/n}$ vs. $h\nu$. From linear interpolation of the experimental plot we obtained the energy values for the absorption threshold, $E_g = LOMO - HOMO$. In this way, from experimental data we estimated for each ligand the energy values E_g : *TTA* – 3.06; *DBM* – 3.11; *Phen* – 3.56; *TPPO* – 3.72; *o-MBA* – 4.15; H_2O – 4.25 eV.

For optical measurements the ligands were divided into two groups: (a) ligands with valence anionic–cationic bonds - *TTA*, *DBM* and *o-MBA*; and (b) ligands with coordinating bonds to Eu^{3+} ion - *Phen*, *TPPO* and H_2O . These ligands are used for obtaining the organic coordination compounds of rare-earths. They are responsible for the energy transition to the central lanthanide ion (E_g is comparable to the energy of transitions ${}^5D_0 \rightarrow {}^7F_j$ for the ion Eu^{3+} within the $4f$ shell) and for compatibility with a particular group of solvents.

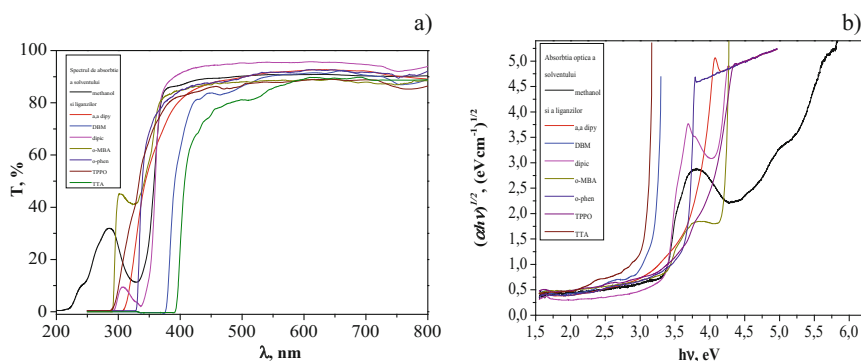


Fig. 2. Optical transmission spectra of the solvent and solutions of ligands in methanol (a) and their corresponding absorption spectra plotted in Tauc coordinates (b).

3 Synthesis of Europium(III) Coordination Compounds

All reagents used for preparation of the Europium(III) coordination compounds were of analytical grade and were used without further purification.

$Eu(TTA)_3H_2O$. The compound *tris(2-thenoyltrifluoroacetate) (aqua) Europium(III)* was prepared using the method described in [3, 7] with some modifications and in the presence of sodium hydroxide. The purification was carried out by dissolution in benzene with the subsequent precipitation in hexane.

$Eu(TTA)_3Phen$. *Tris(2-thenoyltrifluoroacetato) (monophenanthroline) Europium (III)* was obtained similar to [3, 7] with some modifications. In 10 ml of hot ethanol 3 mmol of *thenoyltrifluoroacetone* and 1 mmol of *o-phenanthroline* were dissolved and 3 mmol of 1 N *sodium hydroxide* was added. The mixture was stirred while 1 mmol of *Europium nitrate hexahydrate* in 5 ml of water was added dropwise. A dense white microcrystalline precipitate separated immediately. After cooling the mixture, the solid

was collected and purified by dissolution in benzene (30 ml) and precipitation in hexane. Anal. calcd. for $C_{36}H_{20}EuF_9N_2S_3O_6$: $C - 43.42$; $H - 2.02$; $N - 2.81$. Found: $C - 43.19$; $H - 2.44$, $N - 2.63$.

Eu(DBM)₃Phen. *Tridibenzoyl methane o-phenanthroline Europium(III)*: 0.67 g of DBM was dissolved in 10 ml of *ethanol*. To this solution add 0.2 g of *phenanthroline* - light yellow transparent solution. 3 ml of 1 N *NaOH* solution was added to the received solution. Instant color becomes intense yellow. 0.26 g of $EuCl_3$ salt were added 5 ml of *ethanol*. Incomplete dissolution was observed and turbidity remains. And upon addition of 1 ml H_2O the material was completely dissolved but the turbidity remained. To the fertile solution add a few drops of $EuCl_3$ solution, and it immediately precipitates. The yellow viscous compound was formed, which was subsequently dissolved, filtered and washed with ethanol and chloroform. As a result, after filtration and drying, 0.55 g of the material was dissolved in acetone. Anal. calcd. for $C_{57}H_{41}EuN_2O_6$, %: $C - 6.33$; $H - 4.13$; $N - 2.80$. Found: $C - 6.843$; $H - 4.28$; $N - 2.29$.

Eu(o-MBA)₃Phen. A warmed *ethanol* solution (96%) containing 0.4 g (3 mmol) of *o-methylbenzoic acid* and 0.2 g (1 mmol) of *1,10-phenanthroline* was adjusted to pH 6.0–7.0 with 1 M *NaOH* solution. Further, *Europium chloride* (1 mmol) dissolved in 5 ml of water was added dropwise to the organic mixture and stirred. A light pink precipitate was formed immediately. The precipitate was filtered, washed with small portions of ethanol, dried thoroughly in air. The synthesis yield was 0.56 g (37.6%). For $C_{36}H_{29}O_6N_2$ it was calculated, %: $Eu - 20.61$; $C - 58.63$; $H - 3.97$; $N - 3.80$; Found, %: $Eu - 20.88$; $C - 59.23$; $H - 4.17$; $N - 3.75$.

Eu(TTA)₂(Ph₃PO)₂NO₃. The synthesis of organic coordinated compound of *bis(thenoyltrifluoroacetato) bis(triphenyl-phosphine oxide)(mononitrate) Europium(III)* was carried out after the scheme described in for analogue compounds with some modifications. An amount of 4 mmoles (0.44 g) of β -diketone and 2 mmoles (0.56 g) of neutral ligand were dissolved in 10 ml. of hot 96% *ethanol*, and 2 ml. of 1 N *sodium hydroxide* were added. The mixture was stirred, while 1 mol of *Europium nitrate* in 5 ml of water was added dropwise. A type of light cream precipitate formed immediately. The precipitate was filtered off, washed with *ethanol*, dried thoroughly in air, and the solid complex was obtained. Yield was (0.85 g). For $C_{52}H_{38}F_6EuNO_9P_2S_2$ anal. calcd, %: $C = 51.49$; $H = 3.16$; $N = 1.15$; $S = 5.28$. Found, %: $C = 51.49$; $H = 3.48$; $N = 0.95$; $S = 5.14$.

Eu(TTA)₃(Ph₃PO)₂. The synthesis of *bis(thenoyltrifluoroacetato) bis(triphenylphosphine oxide)(mononitrate) Europium(III)*. 0.66 g (3 mol) of *thenoyltrifluoroacetone (TTA)* and 0.56 g (2 mol) of *triphenylphosphine oxide (TPPO)* were dissolved in 10 ml of warm 96% *ethanol* and 3 ml of a 1 N *sodium hydroxide* solution was added. The mixture was stirred, while 1 mol of *Europium chloride* in 5 ml of water was added dropwise. A light pink precipitate was immediately formed. The precipitate was filtered off, washed with small portions of *ethanol* and *diethyl ether*, dried thoroughly in air, and the solid of the complex was obtained. The yield was

0.68 g. For $C_{60}H_{42}F_9EuO_8P_2S_3$ calcd, %: $C = 52.53$; $H = 3.09$. Found, %: $C = 52.37$; 52.28 ; $H = 3.18$; 2.98 .

Figure 3 illustrates the chemical structure formulas synthesized as described above. The photoluminescence spectra of all coordinating compounds with the Eu^{3+} ions are of the same shape and with the same emission peaks. The only difference between them is the maximum magnitude of the PL intensity that determines the efficacy. Radiative transitions can be observed in PL spectra of *Europium* ions centered at 580, 590, 612–615, 651, and 700 nm (Fig. 4). These transitions are attributed to internal $4f$ electron transitions of Eu^{3+} ion ${}^5D_0 \rightarrow {}^7F_i$ ($i = 0, 1, 2, 3$ and 4), respectively, with a strong emission band in 612–615 nm domain (${}^5D_0 \rightarrow {}^7F_2$). From comparison of the photoluminescence spectra of investigated organic compounds one can observe a larger enhancement of the luminescence intensity in the case of $Eu(TTA)_3(Ph_3PO)_2$ compound.

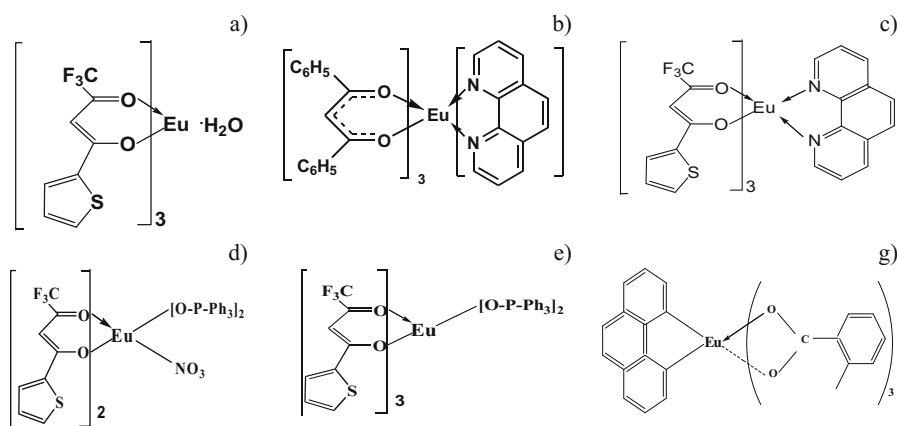


Fig. 3. Illustration of structural formulas of synthesized coordination compounds with Eu^{3+} ion: (a) $Eu(TTA)_3H_2O$; (b) $Eu(DBM)_3Phen$; (c) $Eu(TTA)_3Phen$; (d) $Eu(TTA)_2(Ph_3PO)_2NO_3$; (e) $Eu(TTA)_3(Ph_3PO)_2$; (g) $Eu(o-MBA)_3Phen$.

PL high efficiency in coordinating compounds with Eu^{3+} ions can be explained by the mechanism of energy transfer through the excited electrons from the S and T levels of the ligands to the Eu^{3+} central ion (Fig. 4). The observed photoluminescent emission bands are associated with the radiative transitions ${}^5D_0 \rightarrow {}^7F_i$ from the excited state in the Eu^{3+} $4f$ shell. Experimental results indicate that among our investigated compounds $Eu(TTA)_3(Ph_3PO)_2$ exhibits the most efficient transfer of energy from ligands to Eu^{3+} (Fig. 4a).

From analysis of experimental results on photoluminescence and absorption spectra we can identify the cascade of the energy transfer from $LUMO$ energy levels of ligands to the energetic levels of the $4f$ electronic shell of the Eu^{3+} ion (Fig. 4d). It should be noted that the energy of singlet (S) and triplet (T) levels of ligands in COC are higher than the energies of corresponding PL of Eu^{3+} ion ${}^5D_0 \rightarrow {}^7F_i$.

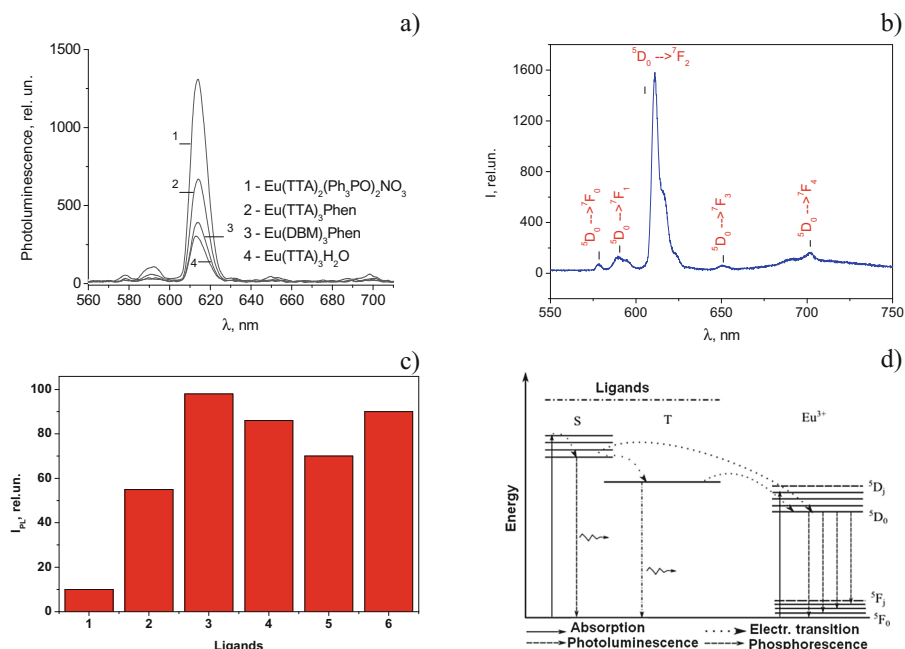


Fig. 4. Illustration of PL spectra: (a) PL spectra of the COC powders; (b) PL spectrum of $\text{Eu}(\text{TTA})_2(\text{Ph}_3\text{PO})_2\text{NO}_3$ powder at 6 wt. % of concentration COC in solution; (c) shows the maximum values of PL intensity in $\text{Eu}(\text{III})$ COC with different ligands: 1 – $\text{Eu}(\text{TTA})_3\text{H}_2\text{O}$; 2 - $\text{Eu}(\text{TTA})_3\text{Phen}$; 3 - $\text{Eu}(\text{TTA})_3(\text{Ph}_3\text{PO})_2$; 4 - $\text{Eu}(\text{TTA})_3(\text{Ph}_3\text{PO})_2\text{NO}_3$; 5 - $\text{Eu}(\text{DBM})_3\text{Phen}$; 6 - $\text{Eu}(\text{o-MBA})_3\text{Phen}$. (d) illustrates the diagram of possible Dexter and Foerster transfer of excitation energy to Eu^{3+} ion (antenna effect).

4 Conclusions

A series of new photoluminescent coordination organic compounds based on the Eu^{3+} ion were synthesized and their optical properties were investigated by UV-V is and PL spectroscopy. It was established that the energy of the absorption threshold E_g for all investigated ligands is greater than the energy required for excitation of the transitions ${}^7\text{F}_0 \rightarrow {}^5\text{D}_0$ within the Eu^{3+} ion shell $4f$. The PL emission spectra of investigated coordinating compounds are associated with the internal transitions of Eu^{3+} ion, ${}^5\text{D}_0 \rightarrow {}^7\text{F}_i$ ($i = 0, 1, 2, 3$ and 4), which peak positions are centered at 537, 580, 612–615, 650 and 702 nm. The half-width of the PL band at 612–615 nm is less than 10 nm, which indicates that COC exhibits an atom-like fluorescence emission with high intensity and color purity. The mechanism of energy transfer in COC to rare-earth ions has been discussed.

Acknowledgements. This work was supported by the Supreme Council for Science and Technological Development of the Academy of Sciences of Moldova (Project No. 11.817.05.03A and No. 11.836.05.04A), as well as by the Science and Technology Center in Ukraine (Project No. 6117).

References

1. Poluektov, N.S., Kononenko, L.I., Efryushina, N.P., Beltyukova, S.V.: Spectrophotometric and Luminescent Methods for Determination of Lanthanides, 256 p. Naukova Dumka, Kiev (1989)
2. Katkova, M.A., Vitukhnovsky, A.G., Bogkarev, M.N.: Coordination compounds of rare earth metals with organic ligands for electroluminescent diodes. *Usp. Khim.* **74**(12), 1193–1215 (2005)
3. Kuzmina, N.P., Eliseeva, S.V.: Photo- and electroluminescence of the coordination compounds of rare-earth elements(III). *J. Inorg. Chem.* **51**(1), 80–96 (2006)
4. Rieutord, A., Prognon, P., Brion, F., Mahuzier, G.: Liquid chromato-graphic determination using lanthanides as time-resolved luminescence probes for drugs and xenobiotics: advantages and limitations. *Analyst* **122**, 59R–66R (1997)
5. Motson, G., Fleming, J., Brooker, S.: Potential applications for the use of lanthanide complexes as luminescent biolabels. *Adv. Inorg. Chem.* **55**, 361–431 (2004)
6. Tauc, J.: Optical properties and electronic structure of amorphous Ge and Si. *Mater. Res. Bull.* **3**, 37–46 (1968). doi:[10.1016/0025-5408\(68\)90023-8](https://doi.org/10.1016/0025-5408(68)90023-8)
7. Melby, L.R., Rose, N.J., Abramson, E., Caris, J.C.: Synthesis and fluorescence of some trivalent lanthanide complexes. *J. Am. Chem. Soc.* **86**(23), 5117–5125 (1964)

Phase Composition, Structure and Mechanical Properties of Carbon Coatings Doped by Carbide-Forming Metals

Alexandr V. Rogachev¹, Alexander S. Rudenkov¹(✉),
Dmitry G. Piliptsov¹, Xiaohong Jiang², and Nikolay N. Fedosenko¹

¹ International Chinese-Belarusian Scientific Laboratory by Vacuum-Plasma Technologies, Francisk Skorina Gomel State University, 246019 Gomel, Belarus
{rogachevav, pdg_}@mail.ru, arudenkov05@gmail.com,
fedosenko@gsu.by

² International Chinese-Belarusian Scientific Laboratory by Vacuum-Plasma Technologies, Nanjing University of Science and Technology,
210094 Nanjing, China
jiangxh24@mail.njust.edu.cn

Abstract. The regularities of the influence of the nature of carbide-forming metals (titanium, chromium) used as alloying elements, the substrate material, on the phase composition, the structure of carbon coatings deposited from the impulse cathode plasma are determined. It is shown that alloyed coatings are an amorphous matrix in which metal-containing clusters with a size of 40–90 nm are formed. The introduction of chromium into the carbon matrix leads to the increase in the content of carbon atoms in the sp^3 state, alloying the same coating with titanium causes the decrease in the number of atoms with sp^3 hybridization, the increase in the size and order of Csp^2 clusters. Microhardness, elasticity modulus, internal mechanical stresses, tribotechnical properties of chromium and titanium-alloyed carbon coating deposited from impulse cathode plasma on various substrates are determined. It has been established that metal alloying of carbon coatings leads to the decrease in the level of internal stresses by 1.2–3.2 times, especially when deposited on a sublayer of chromium.

Keywords: Carbon coatings · Phase · Microhardness · Internal stress · Friction

1 Introduction

Carbon diamond-like coatings alloyed by metals are characterized by peculiarities of phase and structural conditions: depending on the nature of the metal, sp^3 hybridized carbon atoms increase or decrease, the order of sp^2 clusters changes [1, 2]. When introducing carbide-forming metals into the volume of the carbon layer, in addition to carbides, it is possible to form single-phase systems - solid solutions, and at high metal concentrations – their nanoparticles [2–5]. These phase changes affect the properties of the coatings. More complex processes occur at the friction of the alloyed carbon layers. During the friction process of carbon-based alloyed film systems, the produced thermally stable solid carbide nanophases, metal nanoparticles influence the processes of contact interaction. On certain conditions and at certain regimes these nanophases and

nanoparticles can produce transferred films on the surface of friction which influence the contact interaction processes. It does not exclude the catalytic or inhibitory influence of filler atoms on the tribochemical processes in the contact zone [6, 7].

The aim of the research is to determine the features of the nature influence of car-bide-forming metals (titanium, chromium) used as alloying elements, the substrate material on the phase composition, structure and mechanical properties of carbon coatings.

2 Experimental

The deposition of the carbon component of the coating was carried out from the plasma formed by the method of pulsed sputtering of a graphite cathode (purity of 99.9%) by a spark discharge with the voltage of 350 V, a pulse repetition rate of 15 Hz, the pulse current of about 3500 A. The alloying of carbon coatings by metals was carried out by electric arc evaporation (arc current 60–100 A, voltage 40 V) during the deposition of a carbon layer. The silicon monocrystal plates with a previously deposited titanium or chromium sublayer and without it were used as substrates for coatings. The phase composition, dispersity, and relative content of sp^3 and sp^2 clusters were evaluated by Raman spectroscopy. Raman spectra were stimulated by 532 nm radiation and 10 mW power (Senterra, Bruker).

The chemical composition and binding energy in the coatings was determined by X-ray photoelectron spectroscopy (XPS) using PHI Quanta (Japan). The produced spectrum was calibrated along the C1s line with the binding energy of 284.6 eV. The mathematical treatment of the spectra was carried out by Origin 7.0 software. The spectra were decomposed using Gaussian functions.

The microhardness was determined by the Knupp method (AFFRI DM-8) with an indenter load of 50 g (491 mN) for 10 s. Due to the fact that the thickness of the coatings does not exceed 500 μm , the measured microhardness is considered as the parameter characterizing the “film-substrate” system.

The internal stresses in the coatings were determined from the change in the radius of curvature of the silicon substrate before and after the deposition of the coatings in accordance with the procedure given in [8–10].

The elasticity modulus of the coatings was determined by the nanoindentation method (G200, Agilent) with a probe of TB22192ISO at a load of 0.3 mN. The measurement result was estimated on the basis of ten independent tests.

Tribotechnical tests were carried out according to the “sphere-plane” scheme (UMT 2-EC, Bruker). A ball of Si_3N_4 was used as a counterbody. The friction was carried out at the load of 0.5 N and a sliding speed of 0.1 m/s in the air at a relative humidity of 42–45% and the temperature of 22 °C. After carrying out tribotechnical tests, the profile of the friction track was estimated by profilometry methods.

3 Results and Discussion

The average size of these particles is 10–100 nm, depending on the current of the electric arc evaporator which agrees with the data given in [11]. The average size of structural formations containing in a-C:Cr coatings is somewhat larger in comparison

with the size of clusters a-C:Ti coatings. As the arc current increases from 60 to 90 A, the particle size increases from 10 to 100 nm (for Ti/a-C:Ti coatings) and from 40 to 100 nm (for Cr/a-C:Cr coatings) (Fig. 1).

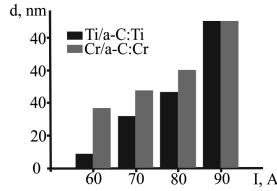


Fig. 1. The average size of structural inhomogeneities at different values of the current of the electric arc evaporator.

The dependence of the size of the nanoparticles on the arc current suggests that their formation is mainly related to the generation features of metallic plasma during electric arc evaporation, the presence of metal nanoparticles in the flow. We note that as the arc current increases, the evaporation rate increases and, correspondingly, the concentration of the metal in the coating as well, which, in its turn, can also affect the size of the formations.

The analysis results of the surface distribution of grains show that on the surface of coatings alloyed by titanium, the number of grains is higher than on the surface of chromium-containing coatings. It should be noted that the roughness of the alloyed coatings is practically independent on the substrate material and 1.4–2.0 times higher than the roughness of single-component a-C layers (17.7 nm) (Table 1). The highest roughness is recorded when the carbon coatings are alloyed by titanium.

Table 1. Roughness and internal stresses of the coating.

Coatings	Thickness	R_{MS} , nm	Internal stress, GPa
Si/a-C	305	17.7	0.73
Cr/a-C	312	21.7	0.32
Si/a-C:Cr	302	28.7	0.48
Cr/a-C:Cr	315	27.1	0.23
Si/a-C:Ti	322	38.4	0.61
Ti/a-C:Ti	303	33.5	0.28

The features of the phase condition of metal-containing carbon coatings are determined by Raman spectroscopy. The Raman spectra of all types of coatings are characterized by the presence of a broad peak with a center near 1520 cm^{-1} . Based on the representation of this peak as superpositions of D- and G-peaks with centers at 1370 cm^{-1} and 1580 cm^{-1} , respectively, the ratio of the intensity of the I_D/I_G peaks are determined, characterizing the relative number of carbon atoms in conditions with sp^2 and sp^3 configuration, and the coordinates G-peak, depending on the concentration of

carbon atoms Csp^3 phase [12]. Figure 2 shows that the ratio of I_D/I_G integrated intensities for carbon coatings containing chromium decreases from 0.63 to 0.19, and the position of the G-peak shifts to smaller wave numbers, indicating the increase in the number of carbon atoms in the condition with sp^3 hybridization. In this case, the presence of a chromium sublayer does not have a significant effect on the change in the phase composition of the carbon coating (Fig. 2).

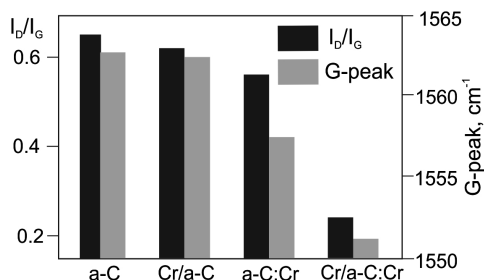


Fig. 2. I_D/I_G ratio and position G-peak for Si/a-C, Cr/a-C, Si/a-C:Cr, Cr/a-C:Cr coatings

In contrast to chromium-containing carbon coatings, for a-C:Ti coatings (Fig. 3), in comparison with a-C layers, the I_D/I_G ratio increases and the G-peak shifts to higher wavenumber, which indicates a decrease in the number of atoms with sp^3 hybridization, an increase in the size and order of Csp^2 clusters [10].

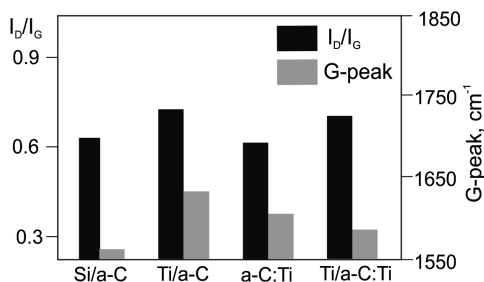


Fig. 3. I_D/I_G ratio and position G-peak for Si/a-C, Ti/a-C, Si/a-C:Ti, Cr/a-C:Ti coatings

The presented conclusions are in full agreement with the results of X-ray photoelectron spectroscopy.

The spectra of C1s conditions of carbon coatings containing chromium can be introduced as the sum of peaks at 283.3, 284.3, 285.1, 286.1 and 287.0 eV which correspond to the chemical bonds of C-Cr, Csp^2 , Csp^3 , C-O, C=O. In C1s spectrum of the not alloyed a-C and Cr/a-C coatings the peaks which are typical for Csp^2 , Csp^3 , C-O, C=O bonds are found. At this X-ray photoelectronic spectroscopy of chromium alloyed coatings is identical to the spectrum of a-C:Cr coatings deposited onto the

sublayer of chromium. For power spectrum Cr2p of chromium atoms, which determine $2p_{3/2}$ condition, the presence of two peaks is typical located at 574.4 eV and 575.6 eV corresponding to Cr-C (Cr-Cr), Cr-O bonds. But, the data analysis of X-ray photoelectron spectroscopy for Cr2p peak does not allow unambiguously differentiate the difference in the chemical bonds between metallic chromium (Cr-Cr) and chromium carbide (C-Cr). That is why the presence of peaks both in C1s and Cr2p spectra should be estimated in complex for the analysis of chemical interaction which occurs into the coating.

On the basis of the gathered data it is possible to conclude that the chemical interaction of chromium takes place with carbon which mainly possesses sp^2 configuration.

X-ray photoelectron spectra of C1s typical for Ti/a-C:Ti coatings can be presented as a sum of four spectral bands the maximums of which are located at 284.4 eV (Csp^2), 285.3 eV (Csp^3), 286.6 eV (C-O), 283.2 eV (C-Ti). The analysis of the sum shows that for Ti/a-C:Ti coatings a slight displacement of C1s peak to a lower energy of the bond is observed in comparison with C1s peak for a-C coating what is determined by the presence of Ti-sublayer and can be explained by the change of relative part of interatomic bonds of carbon-carbon and carbon-titanium. These results are the notion of the fact that Ti sublayers limit the binding of titanium atom with carbon of sp^3 -hybridization, what can be the consequence of regrouping of atoms in a-C:Ti-coating due to the diffusion and the reaction between Ti и a-C:Ti layers.

As a consequence of the phase and structural changes associated with the introduction of chromium and titanium in the carbon layer, we should also consider the data given in Table 1 for determining the roughness of the coatings and their internal stresses. As it can be seen from the table, the alloying of the coatings by metals is accompanied by the increase in roughness for some of the layers, but internal mechanical stresses decrease significantly, 1.2–3.2 times. The highest level of stress still presents when the coating is alloyed by titanium. In this case, for the layers with ~ 300 nm thickness, a determined dependence of the stresses on the nature of the substrate material is manifested. The highest stresses are formed when the coating is deposited on a silicon surface possessing a crystallographic structure which is significantly different from the coating structure.

It was shown in [13–15] that in single-component carbon coatings, the increase in the concentration of Csp^3 bonds promotes the increase in the level of internal stresses. In the case of alloyed layers, this effect, as shown in Table 1, is not dominant. Chromium and titanium produce a different effect on the phase composition of the coating: the introduction of chromium into the carbon matrix leads to the increase in the content of carbon atoms with sp^3 hybridization, alloying by titanium helps reduce the number of carbon atoms in the sp^3 phase, increase the size and order of Csp^2 clusters. At the same time, when introducing these metals, especially when alloyed by chromium, the internal stresses decrease. Apparently, the processes of defect formation in the carbon matrix and, accordingly, internal stresses are influenced by highly dispersed phases of metal carbide.

Figure 4 shows the values of the microhardness (H, GPa) and the modulus of elasticity (E, GPa) of the alloyed layers.

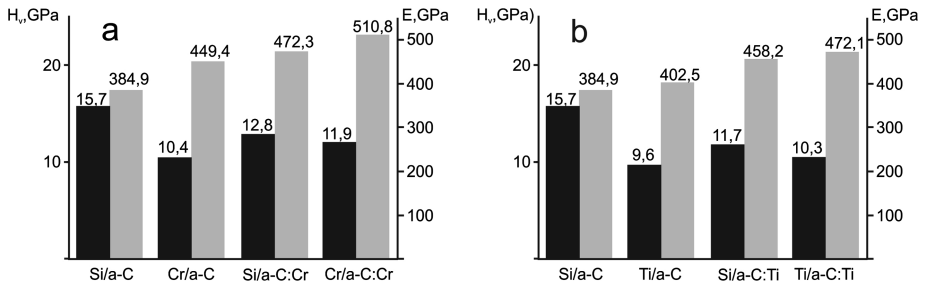


Fig. 4. Microhardness and modulus of elasticity of carbon coatings alloyed by chromium (a) and titanium (b)

It has been established that the microhardness for Cr/a-C:Cr and Si/a-C:Cr coatings is higher than for Cr/a-C and for similar coatings containing titanium in its composition, which agrees with the results of [16], where a higher content of the sp^3 phase is observed when chromium is alloyed. Some decrease in the hardness of the coating when deposited on a soft sublayer of chromium or titanium is consistent with the data of [17].

To analyze the elastic properties of thin coatings, the so-called plasticity index is often used, defined as the ratio of hardness and modulus (H/E) values [18]. The value of the ratio H/E to some extent characterizes the wear resistance of the coating. We note that the plasticity index H/E for all coatings under research lies in the range of values typical for elastic coatings [19].

The tribotechnical tests show that the kinetic dependences of the friction coefficient of alloyed coatings are monotonic and their character is practically independent of their composition (Fig. 5).

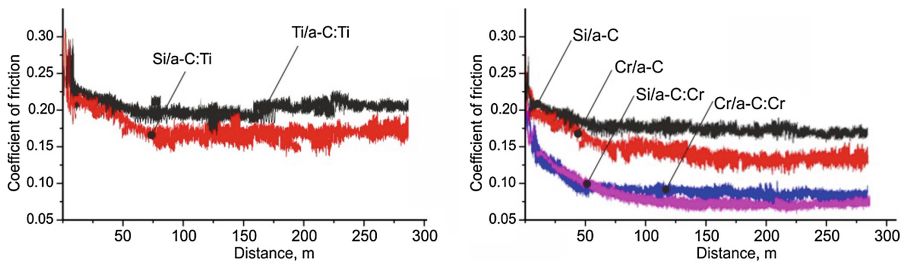


Fig. 5. The kinetic dependences of the friction of a-C coatings containing chromium, titanium

Figure 5 shows that in the course of friction, at its initial stage, a significant decrease in the coefficient of friction is registered, which, as pointed in [2, 3], is due to the course of graphitization of the surface layer, the accumulation of graphite particles that act as a lubricant. The presence of chromium and titanium sublayers influences the value of the friction coefficient: Cr/a-C:Cr and Ti/a-C:Ti coatings show the lowest coefficient of friction.

4 Conclusion

The regularities of the influence of the nature of carbide-forming metals (titanium, chromium) used as alloying elements, the substrate material, on the phase composition, the structure of carbon coatings deposited from the impulse cathode plasma are determined. It is shown that alloyed coatings are an amorphous structural matrix in which metal-containing formations with a size of 40–90 nm are formed, the value of which increases with increasing arc current of the electric arc evaporator. The introduction of chromium into the carbon matrix leads to the increase in the content of carbon atoms in the sp^3 state, alloying the same coating with titanium causes the decrease in the number of atoms with sp^3 hybridization, the increase in the size and order of Csp^2 clusters. Microhardness, elasticity modulus, internal mechanical stresses, tribotechnical properties of chromium and titanium-alloyed carbon coating deposited from impulse cathode plasma on various substrates are determined. It has been established that metal alloying of carbon coatings leads to the decrease in stresses by 1.2–3.2 times, especially when deposited on a layer of chromium. On the basis of the obtained results and data on the change in the phase composition of the carbon layers during the alloying process, the conclusion is made on the determining influence on the internal stresses of the highly disperse phase of metal carbide.

References

1. Rogachev, A.V.: The tribotechnical properties of composite coatings deposited by the vacuo-um-plasma methods. *Frict. Wear* **29**(3), 285–592 (2008)
2. Donnet, C.: Recent progress on the tribology of doped diamond-like and carbon alloy coatings: a review. *Surf. Coat. Technol.* **100–101**, 180–186 (1998)
3. Grill, A.: Tribology of diamond-like carbon and related materials: an updated review. *Surf. Coat. Technol.* **95**, 507–513 (1995). Elsevier Science
4. Donnet, C., Erdemir, A.: *Tribology of Diamond-like Carbon Films: Fundamentals and Applications*. Springer Science & Business Media, Berlin (2007)
5. Bauer, C.: Mechanical properties and performance of magnetron-sputtered graded diamond-like carbon films with and without metal additions. *Diam. Relat. Mater.* **11**, 1139–1142 (2002)
6. Sayn, N.I.: Influence of substrate nature and heat treatment of diamond-like coatings on their tribotechnical properties. *Frict. Wear* **26**(2), 182–186 (2005)
7. Wang, M.: Characterization of metal-containing amorphous hydrogenated carbon films. *J. Mater. Res.* **7**, 667–675 (1992)
8. Zhang, S.: Toughening of hard nanostructural thin films: a critical review. *Surf. Coat. Technol.* **198**, 2–8 (2005)
9. Robertson, J.: Hard amorphous (diamond-like) carbons. *Prog. Solid State Chem.* **21**, 199–333 (1991)
10. Bull, S.: Failure modes in scratch adhesion testing. *Surf. Coat. Technol.* **50**, 25–32 (1991)
11. Cheng, Y.-T.: Relationships between hardness, elastic modulus, and the work of indentation. *Appl. Phys. Lett.* **73**, 614–616 (1998)
12. Wang, A.Y.: Structure and mechanical properties of W incorporated diamond-like carbon films prepared by a hybrid ion beam deposition technique. *Carbon* **44**, 1826–1832 (2006)

13. Zhang, Y.B.: Study of mechanical properties and stress of tetrahedral amorphous carbon films prepared by pulse biasing. *Surf. Coat. Technol.* **195**, 338–343 (2005)
14. Grill, A.: Diamond-like carbon: state of the art. *Diam. Relat. Mater.* **8**, 428–434 (1999)
15. Anders, S.: Effect of vacuum arc deposition parameters on the properties of amorphous carbon thin films. *Surf. Coat. Technol.* **68–69**, 388–393 (1994)
16. Dai, W.: Microstructure and property evolution of Cr-DLC films with different Cr content deposited by a hybrid beam technique. *Vacuum* **85**, 792–797 (2011)
17. Gayathri, S.: Influence of Cr content on the micro-structural and tribological properties of PLD grown nanocomposite DLC-Cr thin film. *Mater. Chem. Phys.* **167**, 194–200 (2015)
18. Dwivedi, N.: Nanoindentation testing on copper/diamond-like carbon bi-layer films. *Curr. Appl. Phys.* **12**, 247–253 (2011)
19. Zou, C.: Effects of Cr concentrations on the microstructure, hardness, and temperature-dependent tribological properties of Cr-DLC coatings. *Appl. Surf. Sci.* **286**, 137–141 (2013)

Ellipsometric Control of Laser Welded Materials

Maryana M. Negrub¹(✉), David Hélié², Iryna V. Yurgelevych¹,
and Leonid V. Poperenko¹

¹ Faculty of Physics, Taras Shevchenko National University of Kyiv,
Academician Glushkov Avenue 2, Building 1, Kyiv 03680, Ukraine
{manyunya1423, vladira_19}@ukr.net, plv@univ.kiev.ua

² Center for Optics, Photonics and Laser, Université Laval,
2375, rue de la Terrasse, Quebec City, QC G1V 0A6, Canada
david.helie.l@gmail.com

Abstract. The results of ellipsometric diagnostic of femtosecond laser welded fused silica-silica, fused silica-copper and fused silica-silicon samples are presented. The bonded interface of each sample is composed of numerous laser weld seams at their periphery in a closed shape pattern so as to seal the inner part due to optical contact of two species. The angular dependencies of ellipsometric parameters Δ and Ψ were obtained for the several areas of bonded interface of each sample, namely: laser weld seam at the periphery and laser sealing inner part. The parameter Δ abrupt changes in the vicinity of the Brewster's angle φ_B for the weld seam of the fused silica-silica sample while the dependence $\Delta(\varphi)$ (φ is an angle of light incidence) for optical transmission window is characterized by smoother curve. The value of φ_B for the weld seam is slightly less than the value φ_B of optical transmission window for this sample by 0.2° . Such behavior of ellipsometric parameter Δ may be explained by the material modification inside glass due to femtosecond laser irradiation. This change is typically characterized by densification and caused by variation in the refractive index, and it may be also characterized by a strong birefringence inside the welded area.

Keywords: Optical materials · Laser welding · Ellipsometry · Brewster's angle

1 Introduction

Today, providing of a strong and resistant to the influence of external factors contact between two glasses or glass and nontransparent material is an important technological issue [1–3]. This problem can be decided by different methods. There are following: direct bonding, anodic bonding, thermocompression bonding, anodic thermocompression bonding, ultrahigh vacuum bonding [4]. The simplest method of bonding is direct bonding of two materials. There are some problems with this method [1]. Firstly, both surfaces must be very well polished and cleaned. Secondary, air gap, which can appear because of not close bonding of materials and defects of the surface, changes the optical properties of such joints (because of interference), and lift-off of optical contact

can occurred. Nowadays, many technologies which can reinforce the optical contact are known. One of them is using of femtosecond laser welding of the materials after the direct bonding procedure [4–6]. This welding yields resistance to mechanical and temperature factors. It should be also noted that inside the perimeter of weld seam optical transmission properties of the joint are not changed.

There are optical methods which are applicable for the investigation of the optical properties of joints inside the welding perimeter and on the weld seam. One of them it is ellipsometry, which has such benefit as an ability to investigate the optical properties of the weld seam both on the external surface of the sample and the interface inside the joint.

So the main aim of this research is ellipsometrical investigation of the optical properties of the femtosecond laser welded optical materials.

2 Experiment

Assemblies that were inspected include fused silica-silica (sample 1), fused silica-copper (sample 2) and fused silica-silicon (sample 3) (Fig. 1). The bonded interface of each sample is composed of numerous laser weld seams at their periphery in a closed shape pattern so as to seal the inner part (optical transmission window) due to optical contact of two species.

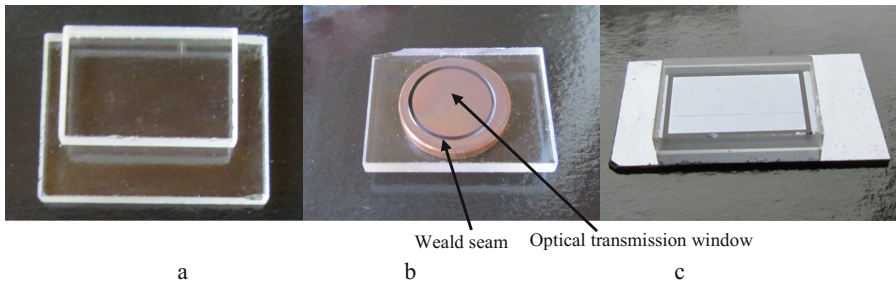


Fig. 1. Photographs of femtosecond laser welded optical materials: (a) fused silica-silica (sample 1), (b) fused silica-copper (sample 2), (c) fused silica-silicon (sample 3).

It is seen (Fig. 1) that there are no interference fringes for samples 1 and 3 unlike the sample 2.

The UV grade fused silica samples used for the experiment were rectangular $10 \times 15 \text{ mm}^2$ windows of 2 mm thickness. The fused silica samples were direct-bonded to silica, copper and silicon substrates prior to welding experiments. All samples and substrates were polished to achieve a required flatness and cleaned to remove any leftover dust on the surfaces prior to direct bonding. A Coherent REGA 9050 Titanium-sapphire femtosecond laser system with wavelength 790 nm and pulse width 70 ps was used for laser welding of the samples. The sample preparation and welding setup are described in [4] in details. The illustration of experimental setup used for welding is presented in [4] too.

Polarization measurements were carried out by multiple-angle-of-incidence single-wavelength ellipsometry [7]. The measurements were performed within the several areas of bonded interface of each sample, namely: laser weld seam at the periphery and laser sealing inner part due to optical contact of two species. The ellipsometric parameters, such as the phase shift Δ between the p- and s-components of the polarization vector and the azimuth Ψ of the restored linear polarization, were obtained as dependencies on the light incidence angle φ using a laser ellipsometer LEF-3M-1 with $\lambda = 632.8$ nm.

3 Results and Discussion

The angular dependencies $\Delta(\varphi)$ and $\Psi(\varphi)$ of the fused silica-silica sample are plotted in Fig. 2 for a set of angular values including the Brewster's angle φ_B as defined at $\Delta = 90^\circ$. The value of φ_B for the weld seam is slightly less than the value φ_B of optical transmission window. The dependence $\Delta(\varphi)$ for optical transmission window of the fused silica-silica sample is characterized by smoother curve. However, there is an abrupt change of ellipsometric parameter Δ in the vicinity of the Brewster's angle for the weld seam of the fused silica-silica sample. The minimum of the parameter Ψ shifts towards smaller angles of incidence φ too. There is some decrease of minimal value of the azimuth Ψ_{\min} for the weld seam of the fused silica-silica sample by 0.18° .

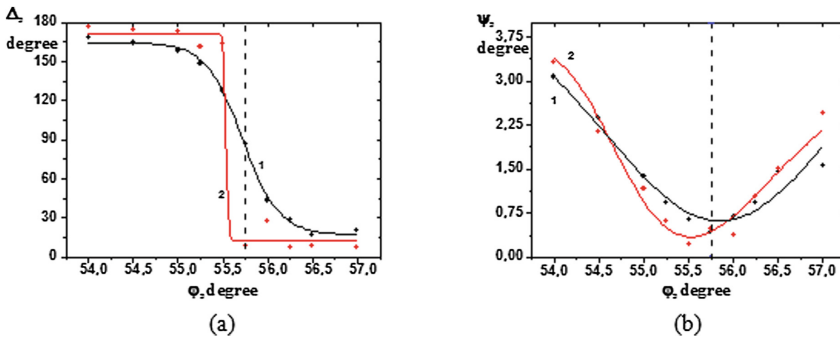


Fig. 2. Angular dependence of the ellipsometric parameters Δ (a) and Ψ (b) for the central area (optical transmission window) (curve 1) and the weld seam (curve 2) of the fused silica-silica sample.

Such behavior of ellipsometric parameters may be explained by the material modification inside fused silica due to femtosecond laser irradiation. The density and refractive index of the laser exposed regions could change. The similar data were earlier obtained for other dielectric materials, namely, laser volumetric marking plastic objects for recording of digital information in [8, 9].

These dependences don't demonstrate any significant differences for optical transmission window without interference fringes and the weld seam of the sample 2 (Fig. 3).

The behavior of $\Delta(\varphi)$ and $\Psi(\varphi)$ dependences for this sample is different from one for dielectrics. The presence of metal (copper) in bonded samples leads to increase in a principle angle of incidence φ_p as also defined at $\Delta = 90^\circ$ by several degrees in comparison to the φ_B for the fused silica-silica sample 1.

Unfortunately, conclusive measurements of $\Delta(\varphi)$ and $\Psi(\varphi)$ were not obtained for the 3 samples. It was impossible to measure in similar manner ellipsometric parameters Δ and Ψ for a set of angular values including the Brewster's angle φ_B of this sample because of experimental restriction connected with selection of the range of the φ changes. Nevertheless as an example, in Fig. 4(a) its partial angular dependence of $\Psi(\varphi)$ is presented. For comparison with our data obtained such dependence for chemically pure silicon is also shown in Fig. 4(b). It is seen that such ellipsometric parameter as Ψ of the weld seam is essentially different from ones for pure Si because this ellipsometric parameter doesn't demonstrate the typical deep minimum $\Psi(\varphi)$ just within the selected incidence angles.

The ellipsometric diagnostic of the bonded interface of each sample was carried out in several areas of optical transmission window too. The ellipsometric parameters Δ and Ψ were measured for certain angle of incidence. The results of measurements are shown in Table 1.

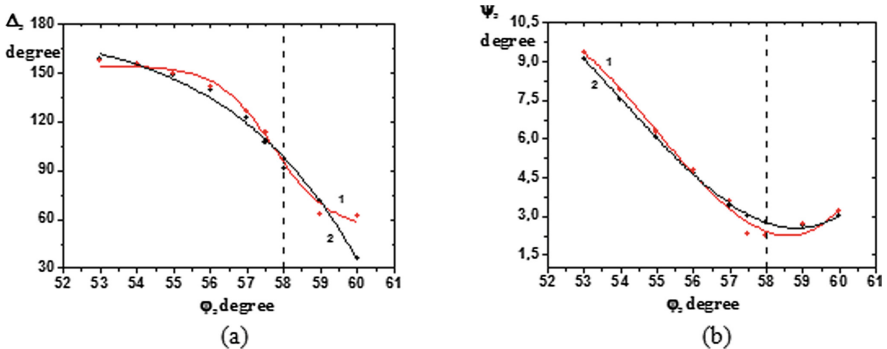


Fig. 3. Angular dependence of the ellipsometric parameters Δ (a) and Ψ (b) for the central area (optical transmission window) without interference fringes (curve 1) and the weld seam (curve 2) of the fused silica-copper sample.

The small changes of the parameters Δ and Ψ are observed in different three areas of optical transmission window only for sample 3. Hence its interface is characterized by qualitative bond between two optical materials. The sample 2 is characterized by significant changes of the ellipsometric parameters measured within different areas of optical transmission window, in particular within interferential fringes of various color. Such changes of the ellipsometric parameters and the presence of the interferential fringes in some part of optical transmission window are related to numerous surface reflection due to a pending air gap between the surfaces.

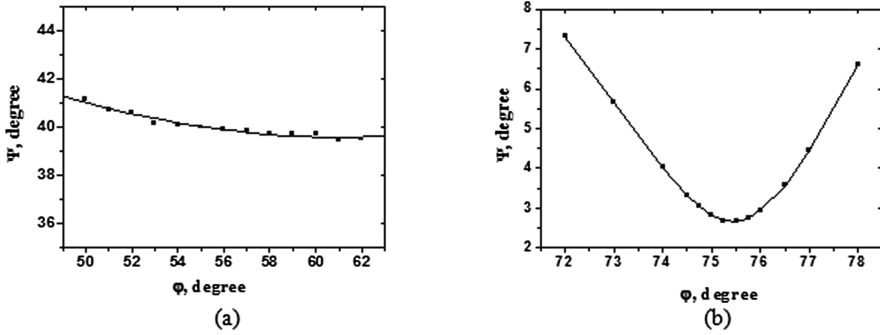


Fig. 4. Angular dependence of the ellipsometric parameters Ψ for the weld seam of the fused silica-silicon sample (a) and chemically pure silicon sample (b).

Table 1. The ellipsometric parameters Δ and Ψ measured in different areas No 1–3 of optical transmission window for samples. The errors of the determination of the ellipsometric parameters were of $\delta\Delta = \pm 0.35\text{--}0.75^\circ$ and $\delta\Psi = \pm 0.01\text{--}0.10^\circ$.

Number of area	Sample 1 fused silica-silica ($\varphi = 56^\circ$)		Sample 2 fused silica-copper ($\varphi = 57^\circ$)		Sample 3 fused silica-silicon ($\varphi = 56^\circ$)	
	Δ , deg	Ψ , deg	Δ , deg	Ψ , deg	Δ , deg	Ψ , deg
1	47.84	0.71	145.02	43.76	177.19	40.42
2	50.36	0.70	100.64	16.78	176.22	40.59
3	32.88	0.77	97.49	7.22	179.00	40.56

4 Conclusion

The ellipsometric diagnostic of femtosecond laser welded optical materials, namely: fused silica-silica, fused silica-copper and fused silica-silicon samples was performed. Specific changes of ellipsometric parameters Δ and Ψ within angles of light incidence in the vicinity of the Brewster's angle as well as principal angle ($\Delta = 90^\circ$) of the samples based on silica, copper or silicon were observed. There is an abrupt change of ellipsometric parameter Δ around the Brewster's angle for the weld seam of the fused silica-silica sample. The value of the Brewster's angle φ_B for the weld seam is slightly less than the value φ_B of optical transmission window of fused silica-silica sample by 0.2° . The dependence $\Delta(\varphi)$ for optical transmission window of the fused silica-silica sample is characterized by smoother curve. The presence of metal (copper) in bonded samples leads to increase in a principle angle of incidence φ_P by 2.25° in comparison to the φ_B for the fused silica-silica sample. The observed behavior of the ellipsometric parameters may be explained by appropriate changes in the material density and the refractive index of the fused silica within the contact range after femtosecond laser irradiation.

References

1. Pobl, A., Krauter, G.: Wafer direct bonding: tailoring adhesion between brittle materials. *Mater. Sci. Eng. R* **25**, 1–88 (1999)
2. Krauter, G., Schumacher, A., Gosele, U.: Low temperature silicon direct bonding for application in micromechanics: bonding energies for different combination of oxides. *Sens. Actuators A* **70**, 271–275 (1998)
3. Hunt, C.E., Desmond, C.A., Ciarlo, D.R., Bennett, W.J.: Direct bonding of micromachined silicon wafers for laser diode heat exchanger applications. *J. Micromech. Microeng.* **1**(3), 152–156 (1991)
4. Hélie, D., Lacroix, F., Vallée, R.: Reinforced direct bonding of optical materials by femtosecond laser welding. *Appl. Opt.* **51**(12), 2098–2106 (2012)
5. Hélie, D., Lacroix, F., Vallée, R.: Reinforcing a direct bond between optical materials by filamentation based femtosecond laser welding. *JLMN-J. Laser Micro/Nanoeng.* **7**(3), 163–169 (2012)
6. Tamaki, T., Watanabe, W., Itoh, K.: Laser micro-welding of transparent materials by a localized heat accumulation effect using a femtosecond fiber laser at 1558 nm. *Opt. Express* **14**(22), 10460–10468 (2006)
7. Azzam, R.M.A., Bashara, N.M.: *Ellipsometry and Polarized Light*. Elsevier Science Ltd, Amsterdam (1987)
8. Gnatyuk, V.A., Kanev, K.D., Mizeikis, V., Aoki, T., Gagarsky, S.V., Poperenko, L.V.: Laser volumetric marking and recording of digital information. In: *Proceedings of the 11th International Conference on Global Research and Education in Engineers for Better Life “INTER-ACADEMIA 2012”*, pp. 189–200, Budapest, Hungary (2012)
9. Gnatyuk, V.A., Vlasenko, O.I., Levytskyi, S.N., Gagarsky, S.V., Zelenska, K.S., Poperenko, L.V., Aoki, T.: Laser marking in transparent materials and mechanisms of laser-induced defect formation laser-induced marks as information carriers in digital encoding. In: *Proceedings of the 2014 Fotonica AEIT Italian Conference on Photonics Technologies*, p. 6843885, Naples, Italy (2014)

Comparison of Euler-Bernoulli and Timoshenko Beam Equations for Railway System Dynamics

Amir Mosavi¹(✉), Rami Benkreif²,
and Annamária R. Varkonyi-Koczy^{1,2}

¹ Kalman Kando Faculty of Electrical Engineering, Institute of Automation,
Obuda University, Becsi Way 94-96, Budapest 1034, Hungary
amir.mosavi@kvk.uni-obuda.hu

² Department of Mathematics and Informatics, J. Selye University,
Elektrarenska cesta 2, 945 01 Komarno, Slovakia

Abstract. In railway system dynamics the dynamic stability problem has significant role particularly when it comes to dealing with the motion of the vertically deformable joints on damped Winkler foundation. Timoshenko and Euler-Bernoulli beam equations are the two widely used methods for dynamics analysis of this problem. This paper describes a comparison between Euler-Bernoulli and Timoshenko beam equations to investigate the track motion dynamic stability via solving the fourth order partial differential of the both models on an Elastic Foundation. This article aims at identifying an efficient model for future investigation on the track motion dynamics stability for the advanced railway systems.

Keywords: Railway system dynamics · Euler-Bernoulli beam · Timoshenko beam

1 Introduction

There are numerous theories and modeling systems applied to the structural analysis and design of the beam for studying the railway system dynamics [1]. Among them the Euler-Bernoulli beam [2] is the most popular and widely used in the research community. Very recently, Wang [3], described the drawbacks with this theory in dealing with the deep beams. He further proposed the Timoshenko beam theory which is an advanced yet a simplified version of Euler-Bernoulli [4]. Today, the Timoshenko and Euler-Bernoulli beam model equations are the two widely used models for analyzing of the railway system dynamics. However in the novel model of Timoshenko the shear deformation forces have come into account, which were missing in Euler-Bernoulli model. In addition the cross section in Euler-Bernoulli theory stays stationary while in the Timoshenko's it rotates due to the shear forces [5]. Nevertheless in the both theories the reciprocal contact of the beam and the soil is generally the clue for solving the analysis modelling of the railway system dynamics. The spring elements are often the optimum replacement for the elastic foundation [6]. Further, the applied loads act in a

transverse relation to the longitudinal axis as described in [7]. The deflection and internal forces of the beam are defined by the general theory of the beam [8].

1.1 Railway System Dynamics

The railway system dynamics includes two longitudinal parallel rails. They are fixed to the sleepers with a certain distance among them. The sleepers are fixed in the ground by a layer of ballast that is distributed all over the ground with a certain thickness [5]. The rail performance is about transferring the wheel load of the train to the sleepers while maintaining the rails in the suitable positions [6]. The load goes through the sleeper from the rail and it is transmitted to the ballast [6]. Yet the transformation of the load depends on a lot of factors such as shape, size, and depth of ballast [9]. Figure 1 demonstrates the railway system dynamics, loads, and the stress distributions on the ballast. In Fig. 1, adopted from [10], F_{ziR} , F_{ziL} , F_{yiL} , and F_{yiR} are the forces between the sleeper i and the left and right rails. In addition, the F_{ysbi} is the equivalent support force due to the ballast in the lateral direction. The d_r is the half distance between the left and right rails, d_b is the half distance between the centers of the left and right ballast bodies.

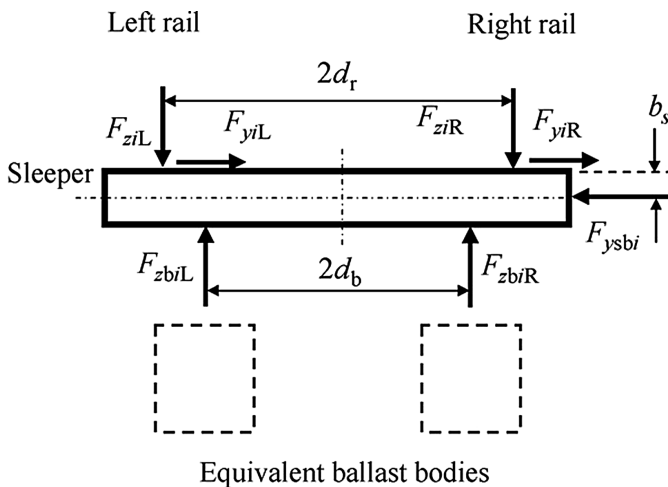


Fig. 1. Illustration of the railway system dynamics, loads, and the stress distributions on the ballast [10]

As Jin [10] states, by increasing the number of the wheels less bending moment is produced and the negative bending moment under neighboring wheel provides a relief of stress. According to Ling [16] the main factors effecting the value of the relief stress are the distance among the wheels and the range of the point of contraflexure of the rail. To design novel locomotives the railway system dynamics is to be carefully figured accordingly to well calculate the stress.

2 Timoshenko and Euler-Bernoulli Beam Equations

In solid mechanics there have been numerous theories introduced for structural modeling and analysis of beam [17–19]. Timoshenko beam [4, 9] has been well studied and used for modeling the railway system dynamics and analysis [20–22]. Mosavi [23] describes that the main hypothesis for Timoshenko beam theory is that the unloaded beam of the longitudinal axis must be straight [8]. In addition the deformations and strains are considered to be small, and the stresses and strains can be modeled by Hook's law. Further to model the deformation [8], the plane of cross section will stay normal to the longitudinal axis and all applied loads act transversally. In 1921 the theory has been further advanced [10], then it was refined in 1922 by Timoshenko [4]. Since then it has been widely used for applications in vibration analysis of beam applied to railway system dynamics. Later, the nonlocal theory for vibration analysis of micro and Nano-structure [3, 23] has been the adjustment in Timoshenko theory. According to Kahrobaian [5] there has been another effort to study beam vibration by utilizing the wave mechanics and it is not necessary if the beam material is isotropic and homogenous [9, 24]. The beam on elastic foundation model considered the spine of a lot of development over the years that made to track design [7, 21, 25]. In 1867 Winkler [8, 13, 26] introduced this model and it is still up until now in use for easy and quick deflection calculation of tracks. The mathematical formulation in the model is correct with a simple physical interpretation. Yet one can consider the rail modelled as an unlimited Euler-Bernoulli beam with an infinite longitudinal Winkler foundation [11], which considered as a boundless longitudinal support, separated by elastic vertical springs. The beam gets support by a distributed force that it is proportional with the beam deflection. The rail deflection $z(x)$ could be obtained from the differential equation by only using two track parameters [11].

$$EI \frac{\partial^4 z(x)}{\partial x^4} + kz(x) = q(x) \quad (1)$$

where, the real parameters $z(x)$, x , $q(x)$, EI and k are respectively, the rail deflection, the length coordinate, the distributed load on the rail, the beam bending stiffness EI (N/m^2) and the foundation stiffness ($\frac{N}{m^2}$, i.e. $\frac{N}{m}$ per Meter of rail).

3 Equation of Motion

Since 1921 the Timoshenko beam theory has been witnessed a great deal of development, and it has been used in modeling different scenarios [10]. Further, in 1948, the spread of waves in the transverse vibrations of bars and plates have determined by this theory. To obtain the solution for Timoshenko [10], the beam equation [8], and the Laplace transform was used. The operator of Timoshenko is the key to the system (1–4) that we aim at solving it.

$$a \cdot b + c^2 \partial_t^2 = (\partial_x^2 - a^2 \partial_t^2) (\partial_x^2 - b^2 \partial_t^2) + c^2 \partial_t^2 \quad (2)$$

Figure 2 illustrates the Winkler foundation using spring and damp for moving load in the railway road track showing the deformation of the beam [6]. The model is a moving loaded wheel on elastic foundation where a parallel connects linear Hertzian spring and damp the contact between the wheels and the rails [13]. This model is selected due to its relative simplicity, ease of calibration, and acceptance in engineering practice. As illustrated in Fig. 2, the soil-foundation interface is assumed to be an assembly of discrete, nonlinear elements composed of springs, dashpots and gap elements. It is intended to capture forces behavior of the ballast with a minimal number of parameters.

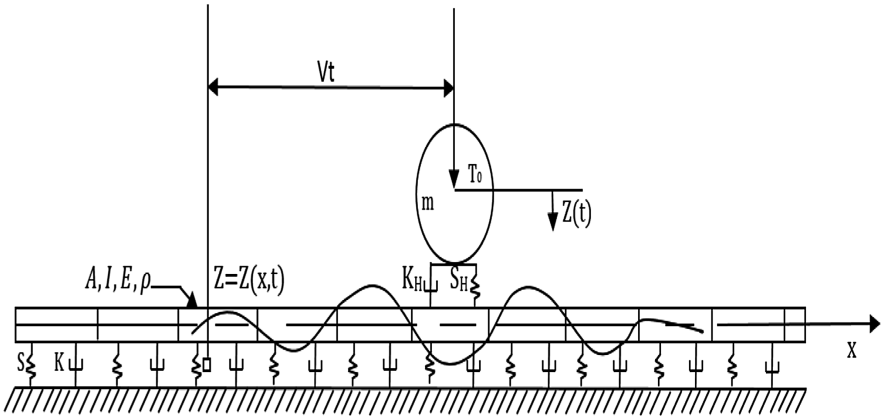


Fig. 2. Winkler foundation using spring and damp for moving load in the railway road track showing the deformation of the beam [6]

From Fig. 2 the model shows that $z(x, t)$ is the vertical displacement of the rail [3, 12]. We want to get a solution for the model in the form:

$$z(x, t) = B(\xi)e^{wt} \tag{3}$$

where

$$\xi = x - yt, \text{ and } e^{wt} = e^{(a+bi)t} = e^{at}(\cos(bt) + i \sin(bt)) \tag{4}$$

Using the derivatives of z with respect of x and t , Eq. (5) simplifies to ODE and with substitution [14]. we get

$$EI [B^{IV} - (a^2 + b^2)(w^2B - 2vwB''' + v^2B^{IV}) + a^2b^2(w^2B - 2vwB' + v^2B)] + \rho A(w^2B - 2vwB' + v^2B'') + k(wB - vB') + sB = \delta \tag{5}$$

We are looking for the characteristic polynomial of the Timoshenko model.

$$P_t(\lambda) = EI\lambda^4 + \rho A(w - v\lambda)^2 + k(w - v\lambda) + s - (w - \lambda v)^2(\alpha\lambda^2 - \beta)$$

$$\underbrace{\hspace{15em}}_{P_{BE}(\lambda)} \tag{6}$$

Where

$$\alpha := EI(a^2b^2) \quad \text{and} \quad \beta := EIa^2b^2$$

The characteristic polynomial of E-B in the form:

$$P_{BE}(\mu) = \frac{4\rho AP_{BE}(\lambda)}{4\rho As - k^2} \tag{7}$$

We consider the roots of the polynomial above as functions hold with two parameters, namely v and w following the same method in [12]. As Zoller and Zobory [7] describe if we are looking for moderately damped, if and only if our relation:

$$4s(\rho A - \alpha + \beta) - k^2 \tag{8}$$

Using non-dimensional variables which introduced in [3], we get

$$P(\mu) = \mu^4 + (c\mu - a - bi)^2(1 + \varepsilon_1 - \varepsilon_2\mu^2) + 1 \tag{9}$$

From the polynomial above we should use polynomial in the form

$$iP(i\mu) = 2ac\mu^2\varepsilon_2 - 2ab\varepsilon_2\mu^2 + 2ac\mu\varepsilon_1 - 2ab\varepsilon_1 + 2ac\mu - 2ab + i[-c^2\mu^4\varepsilon_2 + 2bc\mu^3\varepsilon_2 + a^2\mu^2\varepsilon_2 - b^2\mu^2\varepsilon_2 - c^2\mu^2\varepsilon_1 + 2c\mu b\varepsilon_1 - c^2\mu^2 + \mu^4 + a^2\varepsilon_1 - b^2\varepsilon_1 + 2c\mu b + a^2 - b^2 + 1] \tag{10}$$

By Routh-Hurwitz theorem [15].

$$f(z) = a_0z^n + b_0z^{n+1} + a_1z^{n-2} + b_1z^{n-3} + \dots (a_0 \neq 0) \tag{11}$$

$$\left\| \begin{array}{cccccc} b_0 & b_1 & b_2 & \dots & b_{n-1} \\ a_0 & a_1 & a_2 & \dots & a_{n-1} \\ 0 & b_0 & b_1 & \dots & b_{n-2} \\ 0 & a_0 & a_1 & \dots & a_{n-2} \\ 0 & 0 & b_0 & \dots & b_{n-3} \\ \dots & \dots & \dots & \dots & \dots \\ \dots & \dots & \dots & \dots & \dots \end{array} \right\| \left(a_k = 0 \text{ for } k > \left\lfloor \frac{n}{2} \right\rfloor, b_k = 0 \text{ for } k > \left\lfloor \frac{n-1}{2} \right\rfloor \right) \tag{12}$$

Using the matrix of Hurwitz [15], which is the matrix of square of order n and apply it in the polynomial (17).

The statement of theorem $\text{Det}A_8 \neq 0$ is proved.

The condition from the determinant of $A = 0$, $a \neq 0$ and $b = c = 0$, then

$$\mu^2 = -\frac{1}{2}a^2\varepsilon_2 \pm i\frac{1}{2}\sqrt{a^4\varepsilon_2^2 - 4a^2\varepsilon_1 - 4a^2 - 4} \tag{13}$$

So, if our condition satisfied, then we have two roots in the left-hand and right-hand as well in the half plane.

Proof. If our polynomial (16) has no imaginary root, $\mu = ri$ and $v = bi$, then we have new polynomial in the form

$$q(r) = r^4 + (cr - b)^2(r^2\varepsilon_2 + \varepsilon_1 + 1) + 1 \tag{14}$$

From our polynomial above we can get the possible values of b [14]. In our case the discriminant of b is 0, that imply the real roots (r) are in the range of the smooth real functions. The values of b it can write in the form [12].

$$b \pm (r) = \frac{cr^3\varepsilon_2 + cr\varepsilon_1 + cr \mp \sqrt{r^6\varepsilon_2 + r^4\varepsilon_1 + r^4 + r^2\varepsilon_2 + \varepsilon_1 + 1}}{r^2\varepsilon_2 + \varepsilon_1 + 1} \tag{15}$$

In the case if

$$c \geq \frac{\sqrt{2}\sqrt{(\varepsilon_1^2 + 2\varepsilon_1 + 1)}(-\varepsilon - 2 + \sqrt{\varepsilon_1^2 + \varepsilon_2^2 + 2\varepsilon_1 + 1})}{\varepsilon_1^2 + 2\varepsilon_1 + 1} \tag{16}$$

then, the functions b_{\pm} have zeroes and we always have real roots For the Eq. (15), the positive branch in the form

$$\lim_{n \rightarrow \infty} b_+(r) = +\infty \tag{17}$$

The negative branch in the form

$$\lim_{n \rightarrow \infty} b_{(-)}(r) = -\infty \tag{18}$$

is satisfied.

Now if the derivative

$$b' \pm (r) = (3c\varepsilon_2r^2 + c\varepsilon_1 + c + 1 + \frac{1}{2\frac{6r^5\varepsilon_2 + 4r^3\varepsilon_1 + 4r^3 + 2r\varepsilon_2}{\sqrt{r^6\varepsilon_2 + r^4\varepsilon_1 + r^4 + r^2\varepsilon_2 + \varepsilon_1 + 1}}})(r^2\varepsilon_2 + \varepsilon_1 + 1)^{-1} - 2\frac{(c\varepsilon_2r^2 + c\varepsilon_1r + cr + \sqrt{r^6\varepsilon_2 + r^4\varepsilon_1 + r^4 + r^2\varepsilon_2 + \varepsilon_1 + 1})r\varepsilon_2}{(r^2\varepsilon_2 + \varepsilon_1 + 1)^2} \tag{19}$$

is vanishing, then the extrema can be found. From this we obtain equation with respect to r . Using maple, we obtained solution for r . $\text{Min } b_+ = b_+(\sqrt{-r})$ and $\text{max } b_- = b_-(\sqrt{r})$. If $c = 0$ and $b \geq 1$, then the polynomial q can have imaginary roots, so b is in the range of the functions b_{\pm} . Where the roots of $\mu = ri$ of p , two of them in the right-hand half plane and two of in the left-hand also, then q has two conjugate noimaginary root pairs. So, b is out of the range of functions b_{\pm} .

Remark 1. The situation as to that of the un-damped classical case, so we can ignore the damping out if $\text{Re}(w) = \frac{-k}{2\rho A + \beta}$ where w is complex frequencies [13].

4 The Solution of the System

Making the similar analysis adapted from [13], and implementing the method given by, Zobory and Zoller [12]. Then, any non-dimensional speed c appears as critical speed [8], for some non-dimensional critical frequencies n [14].

$$\begin{aligned} \text{If } c &= \frac{\sqrt{2}\sqrt{(\varepsilon_1^2 + 2\varepsilon_1 + 1)(-\varepsilon - 2 + \sqrt{\varepsilon_1^2 + \varepsilon_2^2 + 2\varepsilon_1 + 1})}}{\varepsilon_1^2 + 2\varepsilon_1 + 1} \\ \text{Nor } c &= 0 \end{aligned} \tag{20}$$

Using the method introduced in [13]. From that we found the same result of the complex frequencies given by [16].

$$w_{1,2} = \frac{-k_H \pm i\sqrt{4ms_H - k_H^2}}{2m} \tag{21}$$

5 Conclusions

This article presents a comparison between Euler-Bernoulli and Timoshenko beam equations to investigate the track motion dynamic stability via solving the fourth order partial differential of the both models on an Elastic Foundation. It is described that the Timoshenko model, unlike the Euler-Bernoulli model, represents a deformable model. Further, it is concluded that the Timoshenko model has the supremacy in the beams with a low aspect ratio. Considering the restraints analysis of the models, the beam vibration of the Euler-Bernoulli produces the instability caused by the inadvertent excitation of un-modelled modes. In conclude, in Euler-Bernoulli beam theory the shear deformation is neglected and at longitudinal axis the plane section will stay normal. However, for Timoshenko model, the plane section will not be normal but it stays plane. Therefore, the shear deformation presents a variation among the plane section rotation and the normal to the longitudinal axis. As the result the Euler-Bernoulli beams theory is not able to consider the transverse shear stresses, while Timoshenko beams theory is capable of doing so. This research recognizes the

Timoshenko model as an efficient way to investigate the track motion dynamics stability for the advanced railway system dynamics studies.

Acknowledgement. This work has partially been sponsored by the Research & Development Operational Program for the project “Modernization and Improvement of Technical Infrastructure for Research and Development of J. Selye University in the Fields of Nanotechnology and Intelligent Space”, ITMS 26210120042, co-funded by the European Regional Development Fund.

References

1. Zobory, I., Zoller, V.: Track-vehicle dynamical model consisting of a beam and lumped parameter component. *Prídica Polytech.* **25**, 3–8 (1997)
2. Mosavi, A., Vaezipour, A.: Reactive search optimization; application to multiobjective optimization problems. *Appl. Math.* **3**, 1572–1582 (2012)
3. Wang, X.: Timoshenko beam theory: a perspective based on the wave-mechanics approach. *Wave Motion* **57**, 64–87 (2015)
4. Roux, A.: Elastic waves in a Timoshenko beam with boundary damping. *Wave Motion* **57**, 194–206 (2015)
5. Kahrobaiyan, M.: A Timoshenko beam element based on the modified couple stress theory. *Mech. Sci.* **79**, 75–83 (2014)
6. Andersen, L., Nielsen, S.: Vibrations of a track caused by variation of the foundation stiffness. *Probab. Eng. Mech.* **18**, 171–184 (2003)
7. Zobory, I., Zoller, V.: Dynamic behaviour of a railway track. *Prog. Ind. Math.* **67**, 405–409 (2002)
8. Yankelevsky, D.: Analysis of beam on nonlinear Winkler foundation. *Comput. Struct.* **31**, 287–292 (1989)
9. Dinev, D.: Analytical solution of beam on elastic foundation by singularity functions. *Eng. Mech.* **19**, 381–392 (2012)
10. Jin, X.: Effect of sleeper pitch on rail corrugation at a tangent track in vehicle hunting. *Wear* **265**, 1163–1175 (2008)
11. Garg, V.: *Dynamics of Railway Vehicle Systems*. Elsevier Canada, Toronto (2012)
12. Zobory, I., Zoller, V.: On dynamics of the track rail supporting parameters. *Transp. Eng.* **39**, 83–85 (2011)
13. Ding, Z.: A general solution to vibrations of beams on variable Winkler elastic foundation. *Comput. Struct.* **47**, 83–90 (1993)
14. Deng, H., Chen, K., Cheng, W., Zhao, S.: Vibration and buckling analysis of double-functionally graded Timoshenko beam system on Winkler-Pasternak elastic foundation. *Compos. Struct.* **160**, 152–168 (2017)
15. Esveld, C.: *Modern Railway Track*, vol. 45, pp. 575–588. MRT-Productions, Zaltbommel (2001)
16. Ling, L.: A 3D model for coupling dynamics analysis of high-speed train/track system. *Dyn. Anal.* **15**, 964–983 (2014)
17. Mosavi, A.: Decision-making models for optimal engineering design and their applications. Doctoral Dissertation, University of Debrecen, Hungary (2013)
18. Mosavi, A.: Optimal engineering design. Technical report, University of Debrecen (2013)
19. Baeza, L.: Railway train-track dynamics for wheel flats with improved contact models. *Nonlinear Dyn.* **45**, 385–397 (2006)

20. Mosavi, A.: A multicriteria decision making environment for engineering design and production decision-making. *Int. J. Comput. Appl.* **69**, 26–38 (2013)
21. Dahlberg, T.: *Railway track dynamics-a survey*. Linköping University (2003)
22. Mosavi, A.: Decision-making in complicated geometrical problems. *Int. J. Comput. Appl.* **87**, 22–25 (2014)
23. Mosavi, A.: On engineering optimization the splined profiles. In: *Proceedings of International modeFRONTIER* (2010)
24. Bogacz, D.: Response of beam on visco-elastic foundation to moving distributed load. *J. Theoret. Appl. Mech.* **46**, 763–775 (2008)
25. Mosavi, A., et al.: Multiple criteria decision making integrated with mechanical modeling. In: *Composite Materials* (2012)
26. Koh, C.: Moving element method for train-track dynamics. *J. Numer. Methods Eng.* **56**, 1549–1567 (2003)

Interaction of Hydrogen Isotopes with Radiation Damaged Tungsten

Yasuhisa Oya¹(✉), Keisuke Azuma¹, Akihiro Togari¹, Qilai Zhou¹,
Yuji Hatano², Masashi Shimada³, Robert Kolasinski⁴,
and Dean Buchenauer⁴

¹ Shizuoka University, 836 Ohya, Suruga-ku, Shizuoka 422-8529, Japan
{oya.yasuhisa, azuma.keisuke.16, togari.akihiro.17,
zhou.qilai}@shizuoka.ac.jp

² Hydrogen Isotope Research Center, Organization of Promotion of Research,
University of Toyama, Gofuku, Toyama 930-8555, Japan
hatano@ctg.u-toyama.ac.jp

³ Fusion Safety Program, Idaho National Laboratory,
Idaho Falls, ID 83415, USA
masashi.shimada@inl.gov

⁴ Chemistry, Combustion and Materials Center, Sandia National Laboratory,
Livermore, CA 94550, USA
{rkolasi, dabuche}@sandia.gov

Abstract. This paper reviews recent achievement of hydrogen isotope behavior for damaged tungsten. To demonstrate neutron irradiation, the irradiation damages were introduced into W by energetic Fe²⁺ irradiation and D retention behavior was examined by thermal desorption spectroscopy (TDS). The D trapping behavior was evaluated using Hydrogen Isotope Diffusion and Trapping (HIDT) code. It was found that D trapping states consisted of two-four stages with the trapping energy of 0.60 eV, 0.85 eV, 1.15-1.25 eV and 1.55 eV depending on the damage concentration and distribution. Based on these experimental results, the hydrogen isotope retention behavior in actual fusion condition was demonstrated. It was found that most of hydrogen isotope was retained in tungsten wall even if the wall temperature was kept at operation temperature.

Keywords: First keyword · Second keyword · Third keyword

1 Introduction

Elucidation of hydrogen isotope dynamics including tritium is one of the key issues for sustainable D-T reaction in the fusion reactor. Accumulation of fundamental knowledge related to tritium dynamics, namely retention, permeation and diffusion, in fusion materials is required. Especially, plasma facing material (PFM) will be directly exposed to D-T plasma and receive large heat load with energetic particle implantation, leading to the complicated tritium behavior in PFM. Therefore, the retention and diffusion behaviors of tritium in tungsten should be accumulated with the wide range of damage concentration and heating temperature. Recently, many studies were devoted for

demonstrating the tritium dynamics using various experimental techniques, namely neutron irradiation using research reactor or heavy ion implantations under the framework of JA-US collation, TITAN & PHENIX projects and so on [1–3]. After D plasma exposure at 573 K, the D retention in W beforehand irradiated with neutrons to the damage concentration of 0.025 displacements per atom (dpa) was significantly larger than that in unirradiated W. Deuterium thermal desorption for the n-irradiated W was characterized by a minor peak at ~ 500 K and major peak at ~ 750 K and relatively gentle slope at temperature above 800 K, whereas for unirradiated W major TDS peak was located at ~ 550 K. It can be said that the D retention in damaged W was clearly enhanced. However, the hydrogen trapping mechanism for damage W is not sufficiently cleared yet. Therefore, this paper reviews the progress of hydrogen isotope trapping studies for damaged W.

2 Experimental

Disk type samples (ϕ 10 mm \times t 0.5 mm) purchased by A.L.M.T. Corp. Ltd. with stress relieve condition were used. These samples were annealed at 1173 K for 30 min. to remove residual impurities and intrinsic damages. Thereafter, 6.0 MeV Fe^{2+} irradiation was performed onto these samples with the damage concentrations up to 1.0 displacement per atom (dpa) at room temperature using Takasaki Ion Accelerators for Advanced Radiation Application (TIARA) at National Institutes for Quantum and Radiological Science and Technology (QST). After irradiation samples were transferred to Shizuoka University and each sample was irradiated at 300 K with 1 KeV D_2^+ with a flux of 1.0×10^{18} $\text{D m}^{-2} \text{ s}^{-1}$ up to a fluence of 5.0×10^{21} D m^{-2} . The D desorption behavior was evaluated by thermal desorption spectroscopy (TDS) with the heating rate of 0.5 K s^{-1} from room temperature to 1173 K using a quadruple mass spectrometer (SPECTRA Microvision) which was calibrated by D_2 standard leak.

To evaluate the damage distribution behavior, combination of 0.8 MeV and 6.0 MeV Fe^{2+} irradiation was also done using same facility at room temperature as mentioned above. Thereafter, 1.0 KeV D_2^+ implantation was performed up to the fluence of 1.0×10^{22} D m^{-2} . TDS was also applied to these samples and evaluated the D retention.

The microstructure of the damaged W was evaluated using 3 mm disc with back thinned by electrolytic polishing process at Institute of Applied Mechanics at Kyushu University (JEM 2000EX, JASCO Inc.).

Based on these experimental results, simulation of the TDS spectra can be performed using the recently developed Hydrogen Isotope Diffusion and Trapping (HIDT) simulation code [4]. The parameters used in this simulation could be found in our previous papers [4–6].

3 Results and Discussion

Figure 1 shows D_2 TDS spectra for Fe^{2+} damaged W with the damage concentration up to 1.0 dpa. It was found that the D_2 desorption for undamaged W was located at lower temperature region less than 600 K. By introducing the damages, the shape of TDS was

clearly changed and additional desorption stages were found at higher temperature side. In lower damage concentration, the desorption stage at ~ 600 K (Stage 2) was found and the damage concentration above 0.03 dpa, large desorption stage located around 800 K (Stage 3) was observed. At higher damage concentration, Stage 3 was a major D trapping state. Both of Stages 2 and 3 were shifted toward higher temperature side as the damage concentration was increased. Figure 2 shows HIDT simulation results to elucidate D behavior in W. Using three trapping sites (0.65 eV, 1.25 eV and 1.55 eV), which corresponds to the desorption of D trapped by dislocation loops, vacancies and voids, it was found that the simulation well demonstrated the experimental results [4]. D distribution was also evaluated using the present HIDT simulation as shown in Fig. 3.

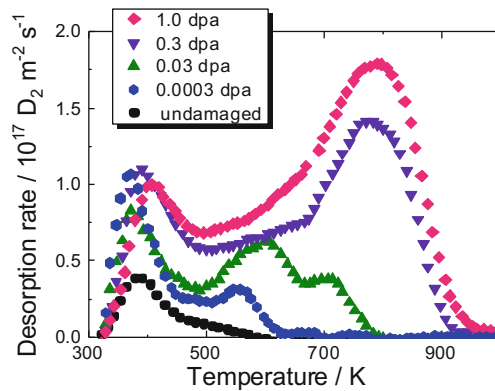


Fig. 1. D₂ TDS spectra for Fe²⁺ damaged W with various damage concentration up to 1.0 dpa. That for undamaged W was also shown [4].

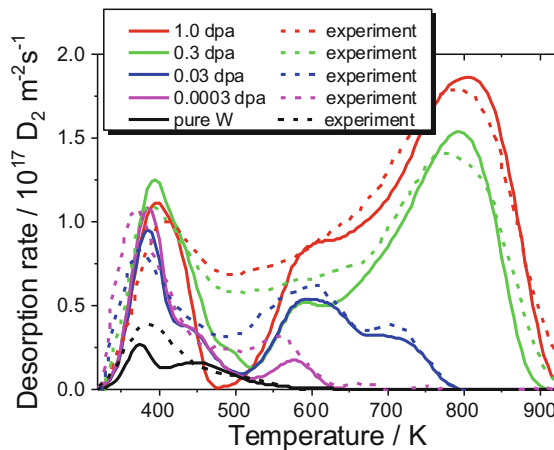


Fig. 2. Comparison of D₂ TDS spectra derived by experiment and HIDT simulation [5].

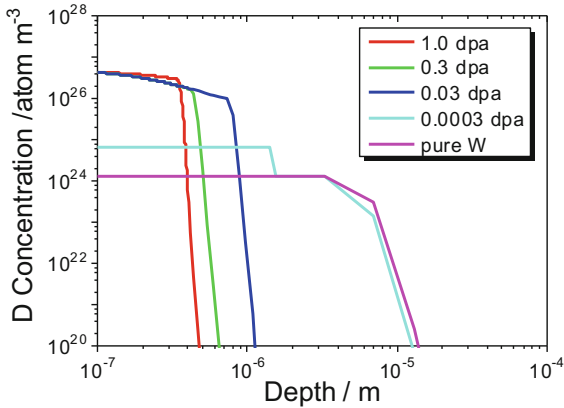


Fig. 3. D depth profiles for Fe^{2+} damaged W with various damage concentration up to 1.0 dpa.

It was clear that dense damage accumulated D trapping and refrained from D diffusion toward bulk. These results indicated that the introduction of irradiation damages would control the D retention behavior in W.

To evaluate the effect of damage distribution on D retention in damaged W, combination of 0.8 MeV and 6 MeV Fe^{2+} irradiation was applied. Figure 4 shows the simulation of damage distribution in W using The Stopping and Range of Ions in Matter (SRIM) code [7]. Major irradiation damages were introduced in the depth of 0.5 μm by 0.8 MeV and 1.5 μm by 6.0 MeV Fe^{2+} . For sets of irradiation damaged W were prepared, namely 0.1 dpa by 0.8 MeV and 0.03 dpa by 6.0 MeV Fe^{2+} , 0.1 dpa by 0.8 MeV and 0.1 dpa by 6.0 MeV Fe^{2+} , only 0.1 dpa by 6.0 MeV Fe^{2+} and only 0.01 dpa by 6.0 MeV Fe^{2+} . D_2 TDS spectra for these three samples were shown in Fig. 5. In this experiment, four major D desorption stages were assumed to be the desorption temperatures of 400 K, 550 K, 650 K and 850 K, which were assumed to be the desorption of D adsorbed on the sample surface or trapped by dislocation loops, the desorption of D trapped by vacancies, vacancy clusters and voids, respectively. The D desorption at lowest temperature of 400 K was almost the same, which indicates the D adsorbed near the surface or trapped by dislocation loops would be almost saturated despite of more dislocation loops were introduced by 0.8 MeV + 6.0 MeV Fe^{2+} irradiation as shown in Fig. 6. It was also found that large D desorption at lower temperature at 550 K was found for 0.8 MeV + 6.0 MeV Fe^{2+} irradiated W compared to that for only 6.0 MeV Fe^{2+} irradiated W. However, the D desorption at 650 K was opposite behavior and total D retention for 0.8 MeV + 6.0 MeV Fe^{2+} irradiated W was lower than that for only 6.0 MeV Fe^{2+} irradiated W in spite of damage accumulation near surface region as summarized in Table 1. These facts indicated that D detrapping would be enhanced by multiple 0.8 MeV + 6.0 MeV Fe^{2+} irradiation due to the formation of dense D trapping sites by heavy irradiation damages, which led to enhance the D recombination and quick re-emission from the surface. It can be said that hydrogen isotope recycling would be proceeded by dense damage formation near surface shallow region.

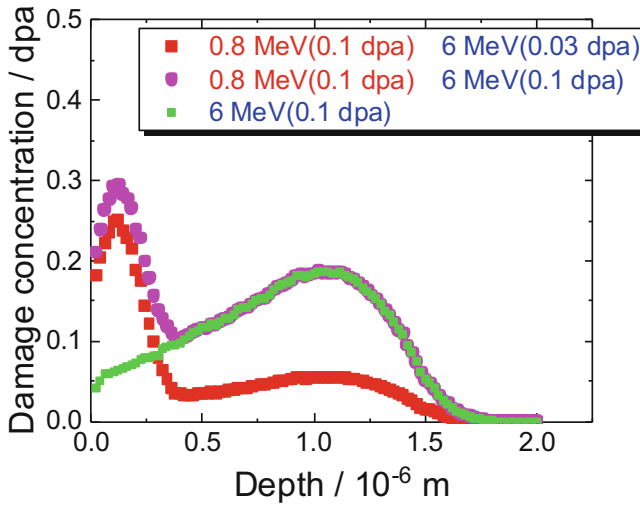


Fig. 4. Damage distribution by 0.8 MeV and 6 MeV Fe^{2+} irradiation [7].

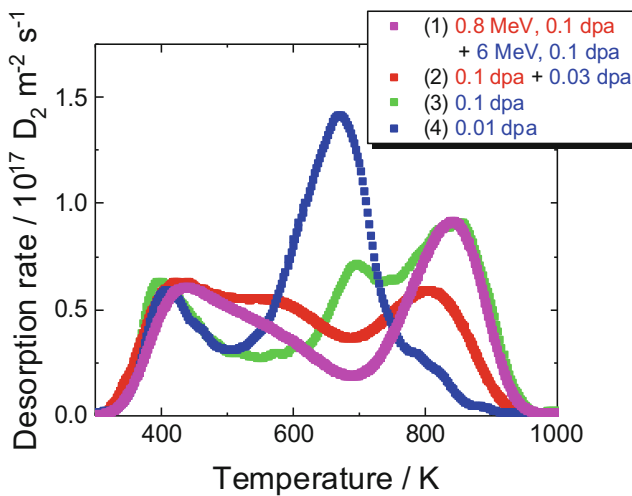


Fig. 5. D_2 TDS spectra for 0.8 MeV and 6.0 MeV Fe^{2+} implanted W with various damage concentrations. TDS results for only 6.0 MeV Fe^{2+} implanted W with 0.1 dpa and 0.01 dpa were also shown for comparison [8].

The HIDT simulation was also applied for 0.8 MeV + 6.0 MeV Fe^{2+} irradiated W as shown in Fig. 6. By assuming the trapping energies of 0.65, 0.85, 1.15–1.25 and 1.50 eV, respectively, it can be said that the simulation represents the experimental results well (Fig. 7).

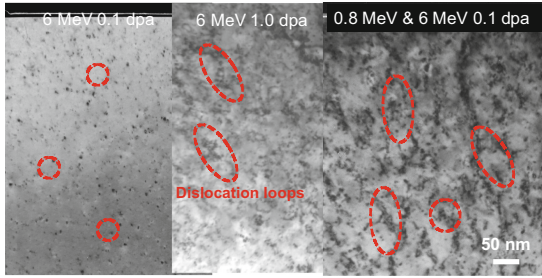


Fig. 6. TEM images for 6.0 MeV (0.1 dpa) and 6.0 MeV (1.0 dpa) and 0.8 MeV (0.1 dpa) + 6 MeV (0.1 dpa) Fe²⁺ irradiated W focused on dislocation loops at the room temperature [8].

Table 1. Total D retention for 0.8 MeV and 6.0 MeV Fe²⁺ implanted W with various damage concentrations [8].

Ion energy (MeV) and damage concentration (dpa)	D retention ($D^+ m^{-2}$)
0.8 (0.1) + 6.0 (0.1)	1.1×10^{20}
0.8 (0.1) + 6.0 (0.03)	1.1×10^{20}
6 (0.1)	1.3×10^{20}
6 (0.01)	1.2×10^{20}

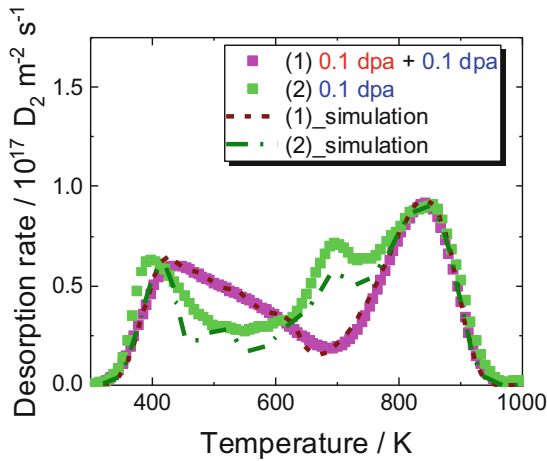


Fig. 7. Comparison of D₂ TDS spectra for 0.8 MeV + 6.0 MeV Fe²⁺ damaged W derived by experiment and HIFT simulation. That for only 6.0 MeV Fe²⁺ damaged W was also shown for comparison [8].

Based on these experimental results, hydrogen isotope behavior for fusion relevant condition was simulated. It is reported that the present first wall conditions were assumed as follow [9]. The operation wall temperature will be around 423–473 K with

the hydrogen isotope energy less than 300 eV with the flux range of 10^{19} – 10^{21} $\text{m}^{-2} \text{s}^{-1}$. The maximum damage concentration by 14 MeV neutron irradiation will be 0.7 dpa at the end of ITER operation. Based on these assumption, HIDT simulation was applied and hydrogen isotope distribution in W was evaluated. Figure 8 shows the comparison of D depth profiles at room temperature and 473 K as a function of implantation (operation) time. It was found that D migration by room temperature irradiation was reached more than 10 nm after 10 s and the D concentration was almost saturated at the time of 500 s. Thereafter, D was migrated toward the bulk. For 473 K case, D was migrated toward bulk without D saturation at the surface. This simulation also showed that total D retention at 473 K would be almost half to that at room temperature. After the operation, D evacuation was also simulated as shown in Fig. 9. This simulation results showed that quick reduction of retained D through the surface was observed, but this reduction was limited for surface region and most of deuterium would be retained in W bulk. Therefore, it can be concluded higher temperature above 473 K will be required if more tritium should be removed after fusion plasma operation for safety.

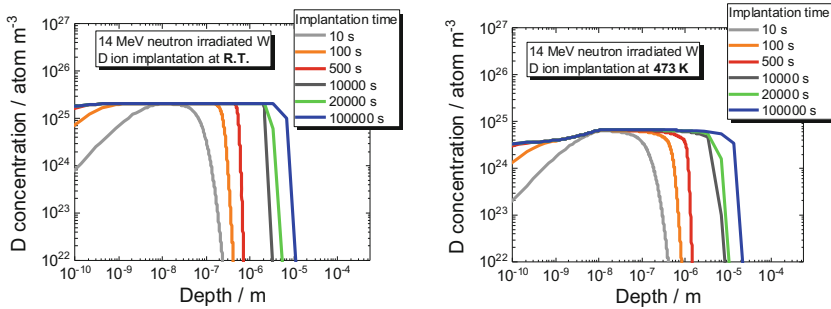


Fig. 8. Comparison of D depth profiles at room temperature and 473 K as a function of im-plantation (operation) time.

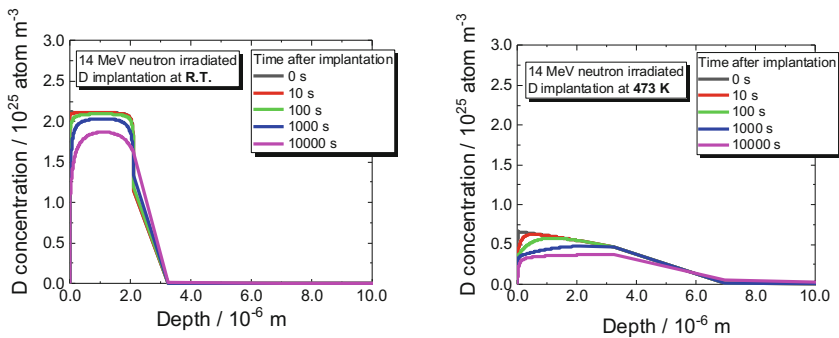


Fig. 9. D depth profiles after 10000 s D implantation (operation) at room temperature and 473 K. The temperature was kept after the implantation (operation).

4 Summary

Recent results related to hydrogen isotope behavior for damaged W, which will be used for plasma facing wall, were summarized. Energetic Fe^{2+} was irradiated onto W to simulate 14 MeV neutron irradiation and D retention behavior was studied by TDS. It was found that D trapping behavior was clearly controlled by damage concentration. In addition, accumulation of damages near surface region led to form dense D retention region, which enhanced to recombination and desorption. HIRT simulation code was applied to simulate the experimental results by applying the trapping energies of 0.60, 0.85, 1.15–1.25 and 1.55 eV, the simulation clearly demonstrated the experimental results. Based on these experimental results, the hydrogen isotope retention behavior in actual fusion condition was demonstrated. It was found that most of hydrogen isotope was retained in tungsten wall even if the wall temperature was kept at operation temperature.

Acknowledgement. The Fe^{2+} irradiation was done at QST in the framework of Inter-University Laboratory for the Common Use of Nuclear Facilities program (Kaihoken). This study was performed under Japan-US collaboration program, PHENIX and supported by University of Toyama (NIFS16KUHR035). This material is based upon work supported by the U.S. Department of Energy Office of Science, Office of Fusion Energy Sciences, under the DOE Idaho Operations Office contract number DE-AC07-05ID14517. Sandia National Laboratories is a multimission laboratory managed and operated by National Technology and Engineering Solutions of Sandia, LLC., a wholly owned subsidiary of Honeywell International, Inc., for the U.S. Department of Energy's National Nuclear Security Administration under contract DE-NA-0003525.

References

1. Shimada, M., Hatano, Y., Oya, Y., Oda, T., Hara, M., Cao, G., Kobayashi, M., Sokolov, M., Watanabe, H., Tyburska-Puschel, B., Ueda, Y., Calderoni, P., Okuno, K.: Overview of the US-Japan collaborative investigation on hydrogen isotope retention in neutron-irradiated and ion-damaged tungsten. *Fusion Eng. Des.* **87**, 1166–1170 (2012)
2. Hatano, Y., Shimada, M., Oya, Y., Cao, G., Kobayashi, M., Hara, M., Merrill, B.J., Okuno, K., Sokolov, M.A., Katoh, Y.: Retention of hydrogen isotopes in neutron irradiated tungsten. *Mater. Trans.* **54**, 437–441 (2013)
3. Oya, Y., Shimada, M., Kobayashi, M., Oda, T., Hara, M., Watanabe, H., Hatano, Y., Calderoni, P., Okuno, K.: Comparison of deuterium retention for ion-irradiated and neutron-irradiated tungsten. *Phys. Scr.* **T145**, 014050 (2011)
4. Oya, Y., Li, X., Sato, M., Yuyama, K., Hang, L., Kondo, S., Hinoki, T., Hatano, Y., Watanabe, H., Yoshida, N., Chikada, T.: Thermal desorption behavior of deuterium for 6 MeV Fe ion irradiated W with various damage concentrations. *J. Nucl. Mater.* **461**, 336–340 (2015)
5. Oya, Y., Hatano, Y., Shimada, M., Buchenauer, D., Kolasinski, R., Merrill, B., Kondo, S., Hinoki, T., Alimov, V.: Recent progress of hydrogen isotope behavior studies for neutron or heavy ion damaged W. *Fusion Eng. Des.* **113**, 211–215 (2016)

6. Fujita, H., Yuyama, K., Li, X., Hatano, Y., Toyama, T., Ohta, M., Ochiai, K., Yoshida, N., Chikada, T., Oya, Y.: Effect of neutron energy and fluence on deuterium retention behaviour in neutron irradiated tungsten. *Phys. Scr.* **T167**, 014068 (2016)
7. Ziegler, J.F., Biersack, J.P.: SRIM - The Stopping and Range of Ions in Solids. <http://www.srim.org/>
8. Fujita, H., Uemura, Y., Sakurada, S., Azuma, K., Zhou, Q., Toyama, T., Yoshida, N., Hatano Y., Chikada, T., Oya, Y.: The damage depth profile effect on hydrogen isotope retention behavior in heavy ion irradiated tungsten. *Fusion Eng. Des.* (in press)
9. Roth, J., Tsitrone, E., Loarte, A., et al.: Recent analysis of key plasma wall interactions issues for ITER. *J. Nucl. Mater.* **390–391**, 1–9 (2009)

Reviewing the Novel Machine Learning Tools for Materials Design

Amir Mosavi^{1,2(✉)}, Timon Rabczuk¹,
and Annamária R. Varkonyi-Koczy^{2,3}

¹ Institute of Structural Mechanics, Bauhaus University Weimar,
Weimar, Germany

amir.mosavi@kvk.uni-obuda.hu,
timon.rabczuk@uni-weimar.de

² Institute of Automation, Obuda University,
Becsí Way 94-96, Budapest 1034, Hungary

³ Department of Mathematics and Informatics, J. Selye University,
945 01 Komarno, Slovakia

Abstract. Computational materials design is a rapidly evolving field of challenges and opportunities aiming at development and application of multi-scale methods to simulate, predict and select innovative materials with high accuracy. Today the latest advancements in machine learning, deep learning, internet of things (IoT), big data, and intelligent optimization have highly revolutionized the computational methodologies used for materials design innovation. Such novelties in computation enable the development of problem-specific solvers with vast potential applications in industry and business. This paper reviews the state of the art of technological advancements that machine learning tools, in particular, have brought for materials design innovation. Further via presenting a case study the potential of such novel computational tools are discussed for the virtual design and simulation of innovative materials in modeling the fundamental properties and behavior of a wide range of multi-scale materials design problems.

Keywords: Machine learning · Optimization · Materials design

1 Introduction

Any technology based upon complex devices or hardware relies on innovative materials design to progress and stay competitive [1]. Although the demand for materials is endlessly growing, the experimental materials design is attached to high costs and time-consuming procedures of synthesis. Consequently simulation technologies have become completely essential for material design innovation [1]. Computational materials design aims at development and application of multi-scale methods to simulate advanced materials with high accuracy [2]. The interdisciplinary realm of computational materials design is under pressure to develop advanced tools for materials design innovation [3, 4]. The key to meet the ever-ongoing demand on increasing performance, quality, specialization, and price reduction of materials is the availability of

simulation tools which are accurate enough to predict and optimize novel materials on a low computation cost [5]. A major challenge however would be the hierarchical nature inherent to all materials [6]. Accordingly to understand a material property on a given length and time scale it is crucial to optimize and predict the mechanisms on shorter length and time scales all the way down to the most fundamental mechanisms describing the chemical bond. Consequently the materials systems are to be simultaneously studied under consideration of underlying nano-structures and mesomanufacturing Scales. Such design process is highly nonlinear and requires advanced multiobjective optimization (MOO) [7] and decision-support tools [8]. In addition the performance and behavior of new materials must be predicted in different design scenarios and conditions [9]. Consequently material design innovation is facing the ever-growing need to provide a computational toolbox that allows the development of tailor-made molecules and materials through the optimization of materials behavior [10]. However extensive potential of machine learning and big data technologies in generating knowledge reported to be highly relevant and promising in the development of multi-scale methods to predict innovative materials properties for specific applications [2, 7, 9, 11]. The ultimate goal is to develop a novel platform for material design innovation: a data-driven computational toolbox for the virtual design and simulation of innovative materials. In fact the computational material design innovation requires an adaptive solver that can be modeled according to the problem at hand for the target materials and applications.

2 Research Background

The framework of a predictive simulation-based optimization of advanced materials which has not been realized yet represents a central challenge within simulation technology [12]. The goal of such toolbox within the context of computational materials science is to provide new insights and understanding of the properties of materials and phenomena associated with their design, synthesis, processing, characterization, and utilization [13]. A major challenge one faces when developing such tools is the hierarchical nature inherent to all materials. In order to understand a property on a given length and time scale it is crucial to understand/simulate the properties and mechanisms on all shorter length and time scales all the way down to the most fundamental mechanisms describing the chemical bond. A number of pioneer research e.g. [13, 14], have already taken firm steps toward developing open-source toolboxes to help the scientific community collaborate, share information, simulate and predict the fundamental properties and behavior of nanoscale and mesoscale materials [15]. This challenging task is accomplished through a variety of scale bridging methods which requires artificial intelligence [16].

2.1 Interdisciplinary Research: The Role of Artificial Intelligence

Developing a toolbox for materials design requires a great deal of understanding about big database technologies, prediction and optimization algorithms to work with. In fact thermodynamic and electronic structure calculations of materials [17], systematic

storage of the information in database repositories [18] and materials characterization and selection and gaining new physical insights [19], account for big database technologies. Huge databases cannot be produced or analyzed by the researcher's direct intervention, and must therefore be performed with the aid of artificial intelligence tools for an automatic flow of the investigations. In addition making decision on the optimal materials design needs optimization tools as well as an efficient decision support system for post processing [17, 20, 21]. This is considered as a design optimization process of the microstructure of materials with respect to desired properties and functionalities [18, 22]. Such process requires a smart agent which learn from dataset and make optimal decisions. The solution of this inverse problem with the support of the virtual test laboratories [19, 23] and knowledge-based design [20, 24], would be the foundation of tailor-made molecules and materials toolbox [21, 25]. With the integrated toolbox at hand the virtual testing concept and application is realized. To do so predicting the overall behavior of existing materials from their microstructure is desired which leads to virtually modify the materials properties [26]. This further allows virtual experiments with entirely new materials and molecules [6, 27]. Advanced functional materials with unprecedented properties can then be identified by a systematic exploration of microstructure modifications [28]. Basic machine learning technologies such as simple artificial neural networks, and standard genetic algorithms are used for this purpose [29].

3 Machine Learning for Materials Design: State of the Art

From the development of concrete for civil constructions [30, 31], to the latest innovations in lithium-ion batteries [32–36], machine learning has brought promising advancements in revolutionizing the simulation technologies and materials prediction. Takahashi and Tanaka [37] well clarify how machine learning is enhancing human capabilities in predicting the properties of materials. Machine learning and big data applications can perfectly use big datasets of materials and their properties to “Learn” and “Predict” new materials with desirable traits [37]. In fact, Khan [38] pioneered the potential of machine learning by identifying non-linear correlations between temperature and composition and mechanical properties in nanocomposites. In Solar Energy and photovoltaic sector [39], we can expect extraordinary with the exceptional prediction power of the data-driven modeling capability of machine learning [40]. In medicine big data and machine learning have shown great potential in diagnostics [41]. Thank to machine learning and the novel big data technologies: microstructural image data has been highly improved, where image-driven machine learning used for microstructure prediction [42–44]. As the beneficial of machine learning and data-driven modeling in materials design and computational mechanics are increasingly reported, the new frontier in materials prediction, has become also of particular interest of Panchal et al. [40] for innovative custom-made materials. Recently, Nanthakumar et al. [43], and Hamdia [45], initiated utilization of machine learning in order to predict the fracture toughness and also to optimally design sandwich structures. They see a great potential in big data and machine learning in materials design as a new paradigm for designing materials according to their target applications. Kirchdoerfer and Ortiz [36], use big data

technologies and machine learning as a powerful computing tool for two case studies in computational mechanics which shows promising results. This article aims to advance the work of Kirchdoerfer and Ortiz's work [36] via targeting general application to materials design. This goal will be realized with our novel implementation of machine learning and intelligent optimization earlier demonstrated in [13].

3.1 Research Gap

Computational material design innovation to perfect and achieve great success needs to dramatically improve and put crucial components in place. To be precise data science, data mining tools, efficient codes, big data technologies, advanced machine learning techniques, latest optimization algorithms for intelligent and interactive optimization, open and distributed networks of repositories, fast and effective descriptors, and strategies to transfer knowledge to practical implementations are the research gaps to be addressed [22]. However most of the current toolboxes rely only on a single algorithm and/or address a limited ranges/scales of the design problems [23]. Considering the current research on developing open-source toolboxes: absence of the optimization tool for making optimal decision, absence of robust design systems, absence of the post processing tool for multicriteria decision-making, lack of big data tools for an effective consideration of huge material databases are further gap in the research [24]. To conclude, the process of computational materials design innovation requires a set of up-to-date solvers to be used to deal with a wide ranges/scales of problems. Furthermore an advanced database would require cloud computing, big data technologies, learning from data capabilities and a powerful set of intelligent optimization tools which are currently missing [25]. To reach this goal our proposed toolbox would include machine learning and big database technologies to address general applications.

4 Case Study

The case study in this section aims at shaping the future of materials design innovation with machine learning strategy. A toolbox is proposed for predictive simulation-based optimization of advanced materials to model, simulate, and predict the fundamental properties and behavior of multi-scale materials. In this case study novel data-driven computing platform for materials design innovation is developed and implemented where calculations are carried out directly from experimental material datasets. The proposed computing platform presents an innovative implementation of advanced machine learning and intelligent optimization technique. In this case several prominent streams of research and development have emerged regarding integrated design of materials to satisfy the application-dependent performance requirements. With the involvement of advanced machine learning and big data technologies, the artificial systems would learn and generate knowledge from large databases of material properties to provide predictive analysis capability for unmodeled materials [2, 44, 47]. As the result the data-driven computation models can enhance human capability in predicting the properties of materials. To do so large amounts of material data are analyzed to accelerate the discovery and design of new materials based on their applications.

Here a machine learning application is proposed as an adaptive solver toolbox for the virtual optimal design and simulation of innovative materials to model the fundamental properties and behavior of a wide range of multi-scale materials design problems. Here machine learning and intelligent optimization techniques [3] enable problem-specific solvers with vast potential applications in industry and business where solver provides the ability of learning from data [4].

4.1 Methodology

Here machine learning integrated optimization is used for predicting the three-dimensional structure multi-scale material to effectively solve such sub-tasks and combine their outputs into a reliable 3D structure predictor. In the proposed method every individual design process, according to the problem at hand, can be modeled on the basis of the solvers available in the toolbox. The methodology is based on transferring data to knowledge to optimal decisions through machine learning and intelligent optimization [4]. In addition, and efficient big data technology [45, 46], is used to build models and extract knowledge. Consequently the large database containing the calculated thermodynamic and electronic properties of existing and hypothetical materials is interrogated intelligently in the search of materials with the desired properties. The proposed machine learning and intelligent optimization toolbox fosters research and development in intelligent optimization and reactive search [3]. A variety of solvers integrated within the toolbox include data mining, predictive analytics, machine learning, business intelligence, data analytics, learning and intelligent optimization approach. These solvers provide the ability of learning from data, empowered reactive search optimization [13], to obtain better solutions. To come up with the optimal material design an advanced optimization tool is integrated into the toolbox so called "Reactive Search" [3]. The methodologies of interest for Reactive Search include machine learning, predictive analytics and statistics, in particular reinforcement learning, active or query learning, neural networks, and meta-heuristics. Previously such implementation has been proposed for material selection of composite material [13, 14, 18], dealing with complicated geometrical problem [11], construction workers (civil engineering problems) [32], welded bean design (structural engineering) [13], and Robotics [29]. The two tasks of learning models and determining optimal configurations are proceeded hand in hand to solve challenging material design problems. The toolbox software components implementing several machine learning methods e.g. MLP, SVM [13] from many sources, and they are applied and tuned by cross-validating them on a given dataset. For the optimization purposes the local search which manages the locally optimal configurations is an effective building block for solving complex discrete and continuous optimization problems, and the local minima traps can be cured by Reactive Search. To denote a framework based on solving continuous optimization problem a cooperating collection of self-adaptive local searchers form Cooperating Reactive Search [4] for creating individual solvers for a problem at hand.

4.2 Implementation: Textile Composites Design

To evaluate the effectiveness of the method the case study of the textile composites design with MOO, adapted from [12, 18], is implemented. This implementation describes a novel application dealing with decision conflicts often seen among design criteria in composites materials design [30]. The aim is to represent the potential of machine learning applications in solving large-scale materials design problems. Figure 1 represents the optimization and the post-processing for screening the mesomanufacturing trade-offs using the machine learning and optimization code of Lionsolver and Grapheur [48]. The optimal design options are explored through simultaneously analyzing materials properties in a multitude of disciplines, design objectives, and scales. The complexity increases with considering the fact that the design objective functions are not mathematically available and the designer must be in the loop of optimization to evaluate the mesomanufacturing scales of the draping behavior of textile composites.

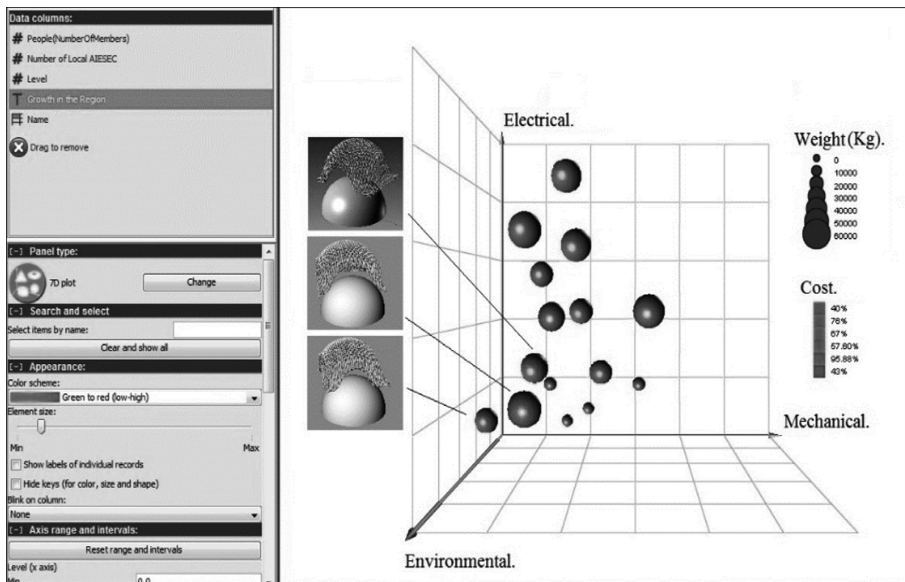


Fig. 1. Design optimization and post-processing: screening the mesomanufacturing trade-offs

As it is illustrated in Fig. 1, the problem has a relatively large-scale decision space of electrical, mechanical, weight, cost, and environmental attributes. To solve the problem an interactive MOO model is created. Further with the aid of the multidimensional visualization, illustrated in Fig. 1, the designer in the loop formulates and systematically compares different alternatives against the large sets of design criteria to tackle complex decision-making task of exploring trade-offs and also designing break-even points. With the designer in the loop, interactive schemes are developed for screening the trade-offs to identify the most suitable candidates.

5 Conclusions

This article presents the state of the art of machine learning applications utilized in materials design innovation. To perform the survey, the latest technological advancements that machine learning have brought to computational materials design realm are reviewed. Further, a machine learning and intelligent optimization application, as an effective platform for developing a novel data-driven computational toolbox for materials design is proposed. The proposed platform is a simple yet powerful concept leading to value-added technology that reduces computation time to design application-based tailored materials. The novel toolbox is particularly designed for the virtual design and simulation of advanced materials to model, simulate, and predict the fundamental properties and behavior of multi-scale materials. In addition, the effectiveness of the computation methodology for the optimal design and simulation of the innovative materials properties and behavior is presented in the context of a case study.

Acknowledgement. This work has been sponsored by the Research & Development Program for the project “Modernization and Improvement of Technical Infrastructure for Research and Development of J. Selye University in the Fields of Nanotechnology and Intelligent Space”, ITMS 26210120042, co-funded by the European Regional Development Fund.

References

1. Artrith, N., Urban, A.: An implementation of artificial neural-network potentials for atomistic materials simulations. *Comput. Mater. Sci.* **114**, 135–150 (2016)
2. Bayer, F.: Robust economic model predictive control using stochastic information. *Autom.* **74**, 151–161 (2016)
3. Battiti, R., Brunato, M.: *The LION Way: Machine Learning*, Lionlab (2015)
4. Brunato, M., Battiti, R.: Learning and intelligent optimization: one ring to rule them all. *Proc. VLDB Endow.* **6**, 1176–1177 (2013)
5. Mosavi, A.: Predictive decision model (2015). <https://doi.org/10.13140/RG.2.2.21094.63047>
6. Ceder, G.: Challenges for materials design. *Mater. Res.* **35**, 693–701 (2010)
7. Fischer, C.: Predicting crystal structure by merging data mining. *Nature* **5**, 641–646 (2006)
8. Jain, A.: A high-throughput infrastructure for density functional theory calculations. *Comp. Mater. Sci.* **50**, 2295–2310 (2011)
9. Nanthakumar, S., Zhuang, X., Park, H., Rabczuk, T.: Topology optimization of flexoelectric structures. *J. Mech. Phys. Solids* **105**, 217–234 (2017)
10. Lencer, D.: A map for phase-change materials. *Nat. Mater.* **7**, 972–977 (2008)
11. Mosavi, A.: Decision-making software architecture; the visualization and data mining assisted approach. *Inf. Comput. Sci.* **3**, 12–26 (2014)
12. Milani, A.: Multiple criteria decision making with life cycle assessment for material selection of composites. *Express Polym. Lett.* **5**, 1062–1074 (2011)
13. Mosavi, A., Vaezipour, A.: Reactive search optimization; application to multiobjective optimization problems. *Appl. Math.* **3**, 1572–1582 (2012)
14. Mosavi, A.: A multicriteria decision making environment for engineering design and production decision-making. *Int. J. Comput. Appl.* **69**, 26–38 (2013)

15. Mosavi, A.: Decision-making in complicated geometrical problems. *Int. J. Comput. Appl.* **87**, 22–25 (2014)
16. Mosavi, A., Varkonyi, A.: Learning in robotics. *Int. J. Comput. Appl.* **157**, 8–11 (2017)
17. McDowell, D.: Simulation-assisted design of materials. *Microstruct.* **65**, 617–647 (2010)
18. Mosavi, A., et al.: Multiple criteria decision making integrated with mechanical modeling of draping for material selection of textile composites. In: *Composite Materials 18* (2012)
19. Saito, T.: *Computational materials design*, vol. 34. Springer Science & Business Media, Heidelberg (2013)
20. Stucke, D.: Predictions of new crystalline states. *Nano Lett.* **3**, 1183–1186 (2003)
21. Mosavi, A.: Optimal engineering design. Technical report, University of Debrecen (2013)
22. Curtarolo, S.: High-throughput computational materials design. *Nature* **12**, 191–201 (2013)
23. Setyawan, W., Curtarolo, S.: High-throughput electronic band structure calculations: challenges and tools. *Comp. Mater. Sci.* **49**, 299–312 (2010)
24. Kolmogorov, A.: Prediction of new crystal structure phases. *Phys. Rev.* **73**, 180–195 (2006)
25. Rajan, K.: Materials informatics. *Mater. Today* **8**, 38–45 (2005)
26. Levy, O.: Uncovering compounds by synergy of cluster expansion and high-throughput methods. *J. Am. Chem. Soc.* **132**, 4830–4833 (2010)
27. Bhadeshia, H.: Neural networks in materials science. *Mater. Sci.* **25**, 504–510 (2009)
28. Mosavi, A.: Computational modeling of the multi-field problems in engineering: a data-driven approach. In: *Frontiers of Structural and Civil Engineering*. Springer (2017)
29. Mosavi, A., Varkonyi-Koczy, A.R.: Integration of machine learning and optimization for robot learning. *Adv. Intell. Syst. Comput.* **519**, 349–355 (2017)
30. Mosavi, A., Rabczuk, T.: Learning and intelligent optimization for computational materials design innovation. In: *Learning and Intelligent Optimization*. Springer (2017)
31. Mosavi, A.: Decision-making in complicated geometrical problems. *Int. J. Comput. Appl.* **87**, 22–25 (2014)
32. Mosavi, A.: Reconsidering the multiple criteria decision making problems of construction workers with the aid of Grapheur. In: *ANSYS and EnginSoft* (2011)
33. Xiong, W.: Design and accelerated insertion of materials. *Comp. Mater.* **2**, 150–159 (2016)
34. Chou, J.: Machine learning in concrete strength simulations: multi-nation data analytics. *Constr. Build. Mater.* **73**, 771–780 (2014)
35. Shandiz, M., Gauvin, R.: Application of machine learning methods for the prediction of crystal system of cathode materials. *Comput. Mater. Sci.* **117**, 270–278 (2016)
36. Kirchdoerfer, T., Ortiz, M.: Data-driven computational mechanics. *Comput. Methods Appl. Mech. Eng.* **304**, 81–101 (2016)
37. Takahashi, K., Tanaka, Y.: Material synthesis and design from first principle calculations and machine learning. *Comput. Mater. Sci.* **112**, 364–367 (2016)
38. Khan, A.: Correlating dynamical mechanical properties with temperature. *Comput. Mater. Sci.* **45**, 257–265 (2009)
39. Pierro, M.: Multi-model ensemble for day ahead prediction of photovoltaic power generation. *Sol. Energy* **134**, 132–146 (2016)
40. Panchal, J.: Computational modeling in materials engineering. *Design* **45**, 4–25 (2013)
41. Wang, X.: Human breath-print identification by E-nose, using information-theoretic feature selection prior to classification. *Sens. Actuators* **217**, 165–174 (2015)
42. DeCost, B., Holm, E.: A computer vision approach for automated analysis and classification of microstructural image data. *Comput. Mater. Sci.* **110**, 126–133 (2015)
43. Nanthakumar, S., Valizadeh, N., Park, H., Rabczuk, T.: Surface effects on shape and topology optimization of nanostructures. *Comput. Mech.* **56**, 97–112 (2015)

44. McKinsey, G.I.: Big Data: The Next Frontier for Innovation, Competition and Productivity. McKinsey Global Institute (2011)
45. Hamdia, K.: Predicting the fracture toughness of PNCs. *MatScience* **102**, 304–313 (2015)
46. Mosavi, A., Vaezipour, A.: Developing effective tools for predictive analytics and informed decisions. Technical report (2013). <https://doi.org/10.13140/RG.2.2.23902.84800>
47. Kotthaus, H.: Machine learning R programs. *Comput. Simul.* **85**, 14–29 (2015)
48. Brunato, M., Battiti, R.: Grapheur: a software architecture for reactive and interactive optimization. In: *Learning and Intelligent Optimization*, pp. 232–246 (2010)

Sol-gel Preparation and Luminescent Properties of Transparent Thin Films and Ceramics of $\text{ZrO}_2\text{:Ti}^{3+}$

Dmitry Kovalenko¹(✉), Dumitru Luca², Vladimir Gaishun¹,
Larisa Sudnik³, Vasily Vaskevich¹, and Alexey Rusikin¹

¹ Francisk Skorina Gomel State University,
Sovetskaya str. 104, 246019 Gomel, Belarus
{dkov, vgaishun, vaskevich, rusykin}@gsu.by

² Alexandru Ioan Cuza University of Iasi,
11, Carol I Blvd., 700506 Iasi, Romania
dumitru.luca@uaic.ro

³ Institute of Powder Metallurgy, NAS of Belarus,
Platonova str. 41, 220005 Minsk, Belarus
lsudnik@tut.by

Abstract. We developed a sol-gel method for the preparation of luminescent materials (powders and films) based on zirconium dioxide doped with titanium. The films were prepared from organometallic compounds of zirconium and titanium. The film-forming solution was covered on the substrates by spin-coating method, then annealing at temperatures of 300–500 °C. The powder was obtained by gelation of film-forming solution, dried at 120 °C, then annealed at 1000 °C in air. The luminescence spectra of developed $\text{ZrO}_2\text{:Ti}^{3+}$ sol-gel coatings have two broad band peaks with maxima at 490 nm and 670 nm ($\lambda_{\text{exc}} = 325$ nm). The powder luminescence spectrum features a broadband peak with a maximum at 510 nm with excitation at a wavelength of $\lambda_{\text{exc}} = 325$ nm. The bright white-blue broad band emission at the region 490–510 nm was assigned to the $\text{Ti}^{3+} 3d^1(\text{eg}) \rightarrow 3d^1(\text{t}_2\text{g})$ transition.

Keywords: Sol-gel method · Luminescence · Zirconium dioxide · Titanium dioxide

1 Introduction

The search for and development of new effective luminescent materials are important for improving the quality of traditional electronic devices and for newly developed instruments, as well as for new non-traditional applications. The persistent luminescence materials are inserted in this context with a wide variety of applications, such as fabrication of new light panels for work in aggressive environments and luminescent-contact temperature sensors. The most studied persistent luminescence materials are doped with rare-earth (RE) ions, but the RE elements are currently having high prices, therefore new alternatives are needed to comply with this problem. One such promising material is zirconium dioxide doped with titanium, lutetium or

phosphorus, and a lot of publications have been devoted to the investigation of their luminescence properties recently. The additives used can enhance the luminescent properties and produce phosphors with fairly wide operating temperature ranges and a long afterglow.

The urgency on the development of new photonic materials has increased in the last three decades, due to the need of efficient light converting and energy storage, and to their respective applications in solar cells and sustainable energy [1, 2]. Thus, the luminescence arising from refractive materials is of particularly interest, due to the unique mechanical properties and good chemical and thermal stability of these materials [3]. They have been widely studied, since their optical properties are strongly correlated to the structural effects and could be related to a variety of photo-physical phenomena [4, 5]. The persistent luminescence materials occur in this context with a wide variety of applications, such as emergency lighting [6] and even medical diagnostics [7, 8].

ZrO₂ shows versatile polymorphism with three different crystal structures: cubic (c-ZrO₂), tetragonal (t-ZrO₂) and monoclinic (m-ZrO₂) [9, 10]. The point symmetry of the Zr site is C_{2h} and D_{4h} for the monoclinic and tetragonal form, respectively, indicating that the local monoclinic structure is less symmetric than tetragonal, as well. Although m-ZrO₂ is stable at room temperature, it is transformed to the tetragonal phase at 1150 °C, and then to cubic at 2370 °C [11]. Similar phase transitions are obtained by doping zirconia with e.g. rare earths (R³⁺); a few per cent of the R³⁺ dopant yields the tetragonal phase, whilst for ca. 10%, the cubic one is obtained.

Regarding the luminescence arising from the non-doped zirconia, several explanations have been offered in the literature, such as: emission from defects [12], self-activated emission [13, 14] and metal impurities [15]. With a more profound investigation, the titanium present as an impurity in zirconia provides an unambiguous explanation for the serendipitous spectroscopic behaviour.

In this work the zirconia nanomaterials doped Ti were synthesized using a simple one-step sol-gel method. Their structural characterization was carried out with the X-ray powder diffraction technique. The luminescence was studied with conventional UV-excited spectroscopy, and discussed in relation with the X-ray data and mechanical properties.

2 Synthesis of Materials

Synthesis of coatings can be divided into the following stages:

1. Preparation of the film-forming solution (mixing of the initial components);
2. Maturation of the film-forming solution (hydrolysis and polycondensation reactions);
3. Film deposition on the substrate;
4. Final film formation (drying and heat treatment).

In the hydrolysis of zirconium and titanium compounds (alkoxides and non-organic salts, mainly ethoxides and propoxides) in aqueous and anhydrous solutions, the primary products, at low pH values, are basic salts of variable composition. At higher pH

values, hydrated forms of zirconia are formed, which is attributed to the formula $Zr(OH)_2$ or $ZrO_2 \cdot nH_2O$, where “n” depends on the aging and drying conditions. Hydrated zirconia has a high adsorption capacity to both cations and anions. The content and nature of the dopants in ZrO_2 depend on the pH of the medium upon covering and the initial titanium compound.

In this paper, titanium ethoxide was chosen as the initial alkoxy compound for the preparation of film-forming solutions, since the hydrolysis of titanium ethoxide in a solvent with the addition of a defined amount of ultrapure water at mild conditions leads to the formation of a stable solution. Film-forming solutions were prepared as follows: The required amount of zirconium (IV) propoxide was mixed with titanium (IV) ethoxide in a proportion of 100 to 1. After stirring, an aqueous acid solution was added to the resulting sol and mixed. The as-prepared film-forming solutions were deposited on the substrates by the spin-coating method.

After application, the obtained samples were placed in a muffle furnace for step-by-step heat treatment in air from 100 °C to 800 °C. Drying corresponds to a state where dust particles do not glue to the surface of film. The drying process starts on the surface of the coating. The solid layer formed on top of film does not allow free removal of solvent vapors located in the underlying. Thus, drying is carried out step-by-step: in the initial period, i.e. with intensive evaporation of the solvent, at a low temperature, then at increasing temperatures.

The rate of curing of coatings depends on the type of film-forming solution, coating thickness, temperature, drying method and other factors. The degree of drying depends on the hardness of the coating and is characterized by three stages. Firstly, in air at temperature of 18–23 °C, then at 60–100 °C and higher, in a muffle furnace, at 400–900 °C.

According to the results of the study of the mechanical properties, the ZrO_2 - TiO_2 films the obtained coatings have a high mechanical resistance to abrasion and can be used in the optical industry.

For the obtained ZrO_2 - TiO_2 powder, film-forming solution (gel) was gelled by drying and calcination at 1000 °C in air, resulting in the ceramics material. For investigation of luminescence properties and structure of this material, the ceramics was grinded.

3 Results and Discussion

3.1 Phase Formation

The X-ray powder diffraction measurements were carried out on multifunctional X-ray diffractometer DRON-7 with $CuK\alpha_1$ radiation (1.5406 Å) in the 2θ range of 20–70°. Whilst the sol-gel method could lead to different products, due to the complexity of the process, the ZrO_2 nanomaterials were promptly synthesized when the crude gel was annealed above 1000 °C. The phase formation of zirconia sol-gel derived materials depends on the initial parameters of the synthesis, such as the W ratio, solvent polarity, relative concentrations of the species in the reactional medium, etc.

The same synthetic conditions were applied for the preparation of the non-doped as well as Ti-doped materials, and the XRD diffraction patterns show significant similarity

for all the products (Fig. 1). Since the monoclinic phase is thermodynamically stable at room temperature, it is the major component of all crystalline phases, as indicated by the 28.3° and 31.5° (in 2θ) diffraction peaks related to the (111) peaks [16].

The patterns of the non-doped and Ti doped material correspond exclusively to the monoclinic phase (space group P21/c; Z: 4).

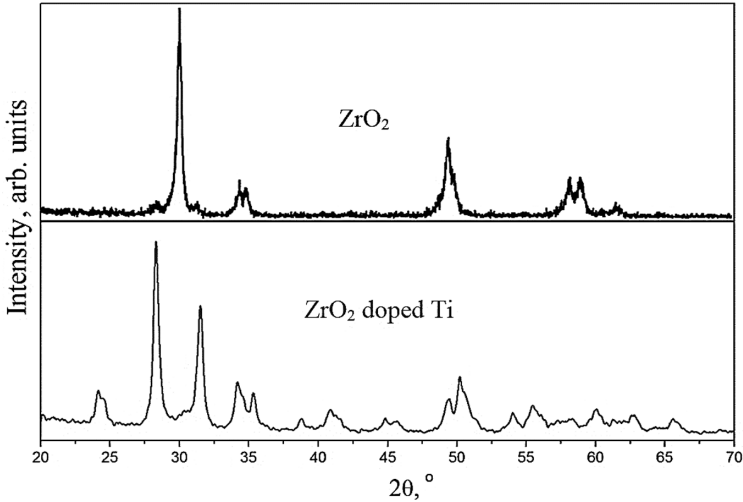


Fig. 1. X-Ray diffraction patterns of ZrO_2 and $\text{ZrO}_2\text{-Ti}$ powder

The tetragonal phase of the ZrO_2 is thermodynamically unstable at room temperature, though it can be stabilized when doping with some trivalent ions, such as the rare earths. The crystallite size seems to play a key role in the stabilization of this metastable tetragonal phase, due to the excess of surface energy of the nanosized crystals.

3.2 Luminescence $\text{ZrO}_2\text{:Ti}^{3+}$ Materials

The photoluminescence of non-doped zirconia has been reported widely in the literature but, basically, it remains an open question. Diverse explanations for the luminescence arising from non-doped zirconia materials have been given, however, the most recurrent one is related to the defects acting as luminescence centers [12]. Other works have suggested that titanium, present as an impurity, could activate the zirconia luminescence due to an asymmetrical coordination of oxygens [13, 14].

Among the known different impurities in zirconia, Ti is the best and natural candidate to show luminescence since the Ti^{3+} ($3d^1$) ion can be easily photoexcited and, with radiative relaxation to the ground level, it emits light.

The non-negligible persistent luminescence of non-doped ZrO_2 has been reported previously in a rather qualitative manner, however. There exist no works in the literature reporting the mechanism of persistent luminescence considering the energetics in the system (e.g. band gap, defect structure, etc.) and thus the knowledge of the mechanism becomes important when designing new zirconia materials.

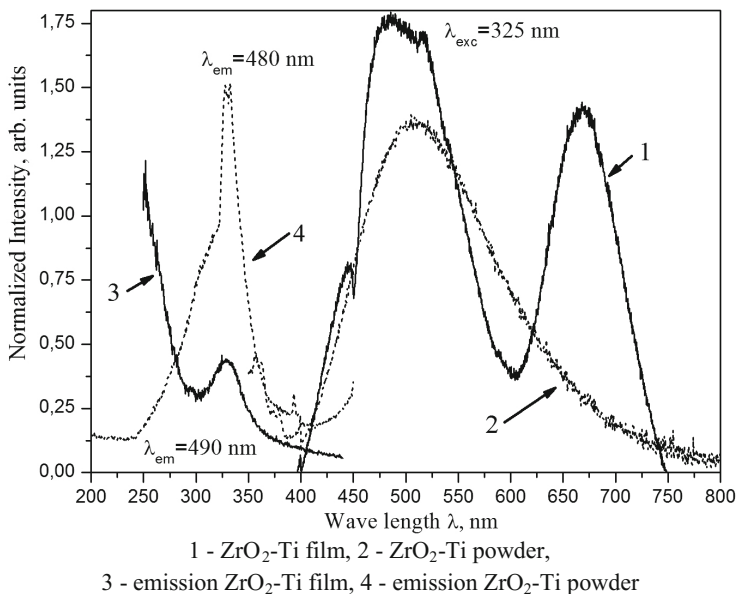


Fig. 2. Luminescence and emission spectra of ZrO₂-TiO₂ sol-gel films and powder.

In order to probe the origin of the luminescence in the Zr materials doped with Ti, the UV excited emission (Fig. 2) and the luminescence spectra were studied. The samples shows a broad band emission centered at 490 nm, upon excitation at 325 nm. The normalized spectra for the different materials showed similarity, indicating that the emission center is the same in all cases.

4 Conclusions

A sol-gel-based synthesis method was developed to prepare photo-luminescent materials (powders and films) based on Ti-doped zirconia. The films were prepared from organometallic compounds of zirconium and titanium. The film-forming solution was deposited on the substrates by spin-coating method, then heat treatment at temperatures of 300–500 °C was applied. The powder was obtained by gelation of the film-forming solution, upon drying at 120 °C, followed by annealing at 1000 °C in air.

The luminescence spectra of developed ZrO₂:Ti³⁺ sol-gel coatings have two broad band peaks with maxima at 490 nm and 670 nm ($\lambda_{exc} = 325$ nm). The powder luminescence spectrum has a broadband peak with a maximum at 510 nm with excitation at a wavelength of $\lambda_{exc} = 325$ nm.

The bright white-blue broad band emission at the region 490-510 nm was assigned to the Ti³⁺ 3d¹(eg) → 3d¹(t_{2g}) transition.

Acknowledgments. The work was supported by Belarusian Foundation for Fundamental Research (Project T16-RA005) and by the Romanian Academy.

References

1. de Wild, J., Meijerink, A., Rath, J.K., Van Sark, W.G.J.H.M., Schropp, R.E.I.: *Sol. Energy Mater. Sol. Cells* **94**(11), 1919–1922 (2010)
2. Granqvist, C.G., Wittwer, V.: *Sol. Energy Mater. Sol. Cells* **54**(1–4), 39–48 (1998)
3. Jeon, T.S., White, J.M., Kwong, D.L.: *Appl. Phys. Lett.* **78**(3), 368–370 (2001)
4. Rodrigues, L.C.V., Stefani, P., Brito, H.F., Felinto, M.C.F., Hölsä, J., Lastusaari, M., Laamanen, T., Malkamäki, M.: *Solid State Chem.* **183**(10), 2365–2371 (2010)
5. Xing, Y.J., Xi, Z.H., Xue, Z.Q., Zhang, X.D., Song, J.H., Wang, R.M., Xu, J., Song, Y., Zhang, S.L., Yu, D.P.: *Appl. Phys. Lett.* **83**(9), 1689–1691 (2003)
6. Aitasalo, T., Dereń, P., Hölsä, J., Jungner, H., Krupa, J.-C., Lastusaari, M., Legendzie-wicz, J., Niittykoski, J., Stręć, W.: *Solid State Chem.* **171**(1–2), 114–122 (2003)
7. Escribano, P., Juliano-Lopez, B., Planelles-Arago, J., Cordoncillo, E., Viana, B., Sanchez, C.: *Mater. Chem.* **18**(1), 23–40 (2007)
8. Bunzli, J.-C.G., Comby, S., Chauvin, A.-S.: *Rare Earths* **25**(3), 257–274 (2007)
9. Shukla, S., Seal, S., Vij, R.: *Nano Lett.* **3**(3), 397–401 (2003)
10. Shukla, S., Seal, S.: *Phys. Chem. B* **108**(11), 3395–3399 (2004)
11. Foster, A.S., Sulimov, V.B., Gejo, F.L., Shluger, A.L., Nieminen, R.M.: *Phys. Rev. B* **64**(22), 224108 (2001)
12. Sarver, J.F.: *Electrochem. Soc.* **113**(2), 124–128 (1966)
13. Phatak, G.M., Gangadharan, K., Pal, H.: *Bull. Mater. Sci.* **17**(2), 163–169 (1994)
14. Cong, Y., Li, B., Lei, B., Li, W.: *Lumin.* **126**(2), 822–826 (2007)
15. Hench, L.L., West, J.K.: *Chem. Rev.* **90**(1), 33–72 (1990)
16. Carvalho, J.M., Rodrigues, L.C.V., Hölsä, J., Lastusaari, M., Nunes, L.A.O., Felinto, M.C.F. C., Malta, O.L., Brito, H.F.: *Opt. Mater. Express* **3**(2), 331–340 (2012)
17. Malashkevich, G.E., Mel'nichenko, I.M., Poddenezhnyi, E.N., Semchenko, A.V.: *Phys. Solid State* **40**, 420–426 (1998)

Development of Functional Coatings by Electron-Beam Sputtering of Sol-Gel Targets

Dmitry Kovalenko¹(✉), Dumitru Luca², Vladimir Gaishun¹,
Larisa Sudnik³, Alexandr V. Rogachev¹, Vasily Vaskevich¹,
Yanina Kosenok¹, and Alexey Rusykin¹

¹ Francisk Skorina Gomel State University,
Sovetskaya Str. 104, 246019 Gomel, Belarus
{dkov, vgaishun, rogachevav, vaskevich, ykosenok,
rusykin}@gsu.by

² Institute of Powder Metallurgy of NAS of Belarus,
Platonova Str. 41, 220005 Minsk, Belarus
dumitru.luca@uaic.ro

³ Alexandru Ioan Cuza University of Iasi,
Bulevardul Carol I, Nr.11, 700506 Iasi, Romania
lsudnik@tut.by

Abstract. To obtain coatings by electron-beam sputtering have been developed and synthesized by a sol-gel method based on a target of SiO_2 , TiO_2 , ZrO_2 , $\text{ZrO}_2/\text{In}_2\text{O}_3$, Al_2O_3 . Spectroscopic studies conducted for formed coatings and identified their main optical characteristics such as refractive index, reflectance, transmission and absorption. Researches morphology layers formed by atomic force.

Keywords: Sol-gel target · Electron-beam sputtering · PVD/sol-gel method · Target of SiO_2 · TiO_2 · ZrO_2 · $\text{ZrO}_2/\text{In}_2\text{O}_3$ · Al_2O_3

1 Introduction

At present, the method of vacuum formation of coatings from the active gas phase and sol-gel method widely used for the synthesis of composite materials having practical application in various fields of modern industry (electronic, optical, metallurgical) [1]. When creating functional coatings by electron beam dispersion in a vacuum, the important target parameters are: optical properties (the dependence of the complex refractive index on the wavelength and the transparency region of the material); quality of the target (presence of inhomogeneities and impurities); mechanical properties (hardness, brittleness); cost and availability and some other specific properties. Currently, the targets are obtained by standard methods of pressing oxides of the necessary substances, which makes it difficult to create targets of complex composition. The targets in this paper were obtained using the sol-gel method. This method allows to obtain targets of complex composition on the basis of several compounds and to alloy

them with various metal particles and rare earth elements. The obtained targets are not inferior in price and quality to standard targets. A hybrid PVD/sol-gel method for the synthesis of coatings is that at the first stage xerogels are formed, which are subsequently subjected to sputtering by electron beam dispersion. In the vacuum-plasma deposition of nanocomposite systems, there are practically no processes of passivation of nanoparticles. They retain high catalytic properties and are active nuclei of matrix structure.

2 Materials and Methods

The scheme of formation of sol-gel targets are presented on Fig. 1. In a first step was forming initial sol on the base of reaction of hydrolysis and policondensation of metal-organics compounds of Si, Ti, Zr. This solution also used for forming xerogelas and like a binding components for obtained targets with powder of TiO_2 , ZrO_2 , $\text{ZrO}_2/\text{In}_2\text{O}_3$, Al_2O_3 . Some targets were doped with rare earth elements. This common used materials for formation antirefractive, protective coatings and luminescence materials. The optimum organic basic compound for forming a stable sol was found, along with the optimal mode of gelation, drying, heat treatment for forming a homogeneous target thickness of 5–7 mm and a diameter of 35 mm, with a mean surface area of $500 \text{ m}^2/\text{g}$ (Fig. 1).

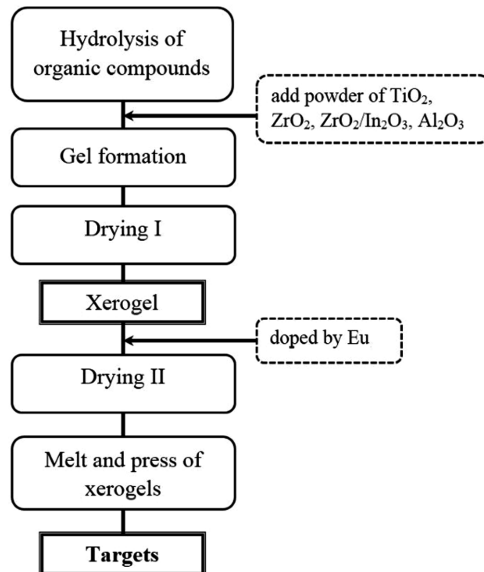


Fig. 1. Synthesis scheme of doped sol-gel targets

Formation of single-layer coatings was carried out using vacuum coaters VU-1A (Smorgon, Belarus), equipped with a source of electron-beam evaporation UELI-I and complex photometric thickness control Iris 0211 (Essent Optics Ltd, Belarus). Source electron beam evaporation UELI-I is specifically designed for vacuum evaporation of refractory oxides, semiconductors and metals with a maximum accelerating voltage of 12 kV and a maximum load current of 500 mA. The coatings were formed on silicon substrates, quartz, optical glass M4 (2 mm, $R = 0.9$) [2, 3].

3 Results and Discussion

3.1 AFM Results

To study the features of the formation of coatings of various nature, the surface of coatings was investigated by atomic force microscopy.

The obtained coatings, to a greater or lesser extent, have a grain structure with an average grain diameter at the base of 20 to 95 nm. The largest values of the grain diameter are SiO_2 coatings formed from targets made by the sol-gel method. However, the grains of these coatings have the smallest values of the ratio of the height of the grain to its grain diameter $h_{\text{grains}}/D_{\text{grains}} = 0.010\text{--}0.015$, which indicates the formation of fairly “flat” grains (Fig. 2).

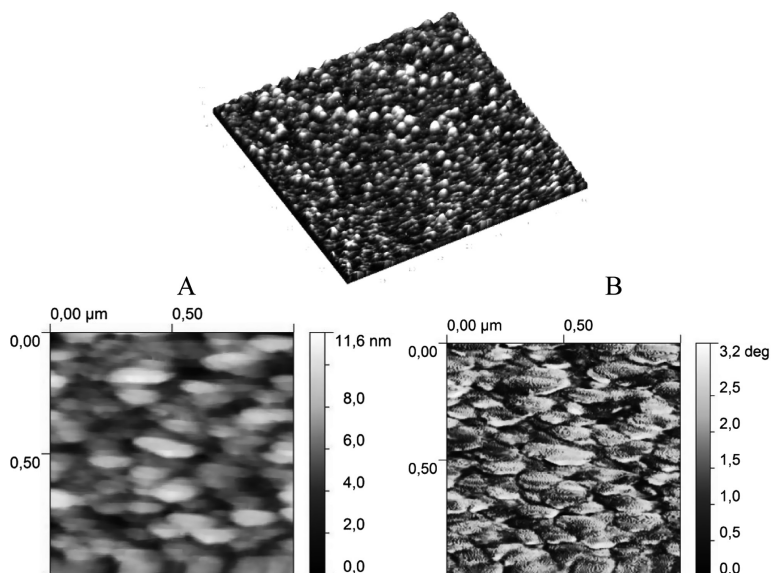


Fig. 2. AFM images of the coating surface from the SiO_2 sol-gel target: A - topography; B - phase contrast

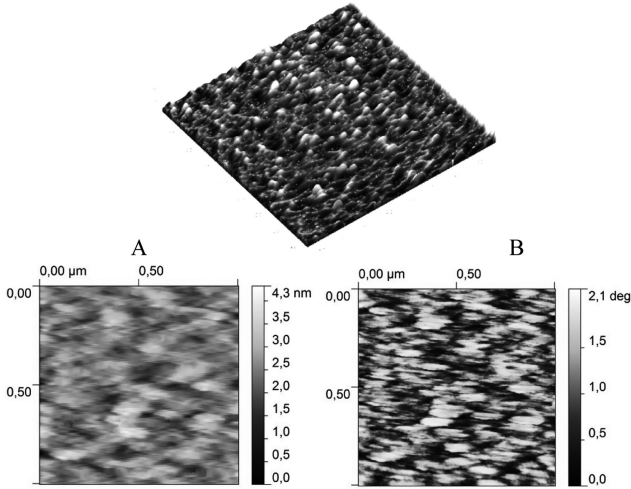


Fig. 3. AFM images of the coating surface from the TiO₂ sol-gel target: A - topography; B - phase contrast

TiO₂ coatings have the highest values of the ratio of the height of the grain to its diameter of $h_{\text{grains}}/D_{\text{grains}} = 0.083$ (Fig. 3).

Numerical results of the investigation of the topology of coatings by atomic force microscopy are presented in Table 1.

Table 1. Topological parameters of the surface of coatings

Coating type	Average value in height, Z (nm)	Average diameter of grains at the base, D (nm)	Sub-roughness, Ra (nm)	The average ratio of the height of the grain to its diameter, h/D
SiO ₂ (commercial target)	5.79	50	0.97	0.040
SiO ₂ (sol-gel)	5.37	95	1.21	0.015
TiO ₂ (commercial target)	3.76	30	0.79	0.083
TiO ₂ (sol-gel)	2.86	75	0.64	0.010
ZrO ₂ (commercial target)	3.62	20	0.69	0.100
ZrO ₂ (sol-gel)	13.12	77	2.75	0.110

3.2 Mechanical Properties

The strength of the coatings obtained during the work was determined by the abrasion method with a rubber tip made from medium density food grade rubber (P-C), through a cambric gasket with the following parameters:

- Rotation frequency – from 30 to 100 min⁻¹;
- A number of turnovers (speed) – 3000;
- Tip load – 200 g;
- Distance from the axis of rotation – 5 mm.

The results of the study of mechanical abrasion resistance are presented in Table 2.

Table 2. Mechanical resistance of coatings.

Coating type	Mechanical stability, wear cycles
TiO ₂	>5000
ZrO ₂ /In ₂ O ₃	>5000
Al ₂ O ₃ :Eu (1 wt.%)	>5000
ZrO ₂ :Eu (1 wt.%)	>4700
TiO ₂ :Eu (1 wt.%)	>5000

According to the results of the study of mechanical strength, it can be concluded that the coatings obtained have a high mechanical resistance to abrasion and can be used in optics.

3.3 Optics

To study the optical characteristics, measurements were made of transmission and reflection spectra of coatings based on TiO₂:Eu (1 wt.%), Al₂O₃:Eu (1 wt.%), ZrO₂/In₂O₃, ZrO₂:Eu (1 wt.%). The spectra were recorded with a PHOTON RT spectrophotometer, the transmission of coatings on 2 mm thick glasses was measured in the wavelength range from 350 to 1000 nm, reflection of coatings on silicon substrates was measured in the wavelength range from 200 to 1000 nm. Figure 4 shows the transmission spectrum of the obtained coatings.

The main optical properties of thin coatings, such as: refractive index $n(\lambda)$ and thickness d , can be determined from the transmission spectra and was measured the refractive index and the thickness of the synthesized coatings. Optical characteristics were studied using a laser ellipsometer LEF-757 (operating wavelength 635 nm). Table 3 shows the refractive index and the thickness of the coatings.

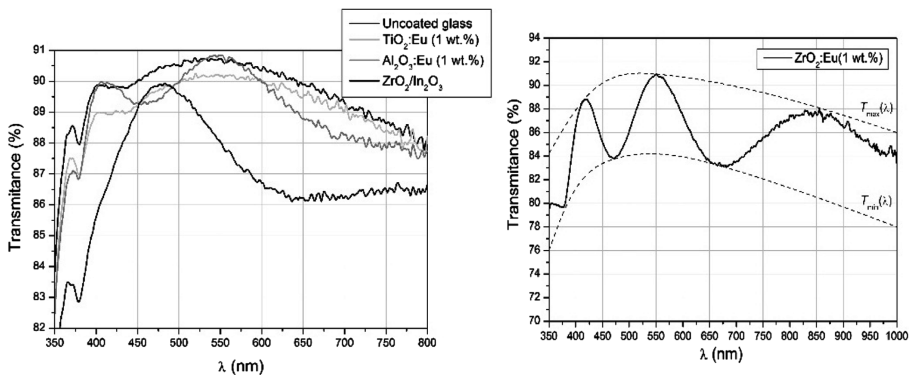


Fig. 4. Transmission spectra of coatings based on TiO₂:Eu (1 wt.%), Al₂O₃:Eu (1 wt.%), ZrO₂/In₂O₃, ZrO₂:Eu (1 wt.%)

Table 3. Refractive index and thickness of coatings

Coating type	Tabular value of the refractive index	The experimental mean value of the refractive index	Coating thickness, nm
TiO ₂	1.95	1.87	270.7
ZrO ₂ /In ₂ O ₃	–	1.72	237.5
Al ₂ O ₃ :Eu (1 wt.%)	1.75 for Al ₂ O ₃	1.49	191.0
ZrO ₂ :Eu (1 wt.%)	1.97 for ZrO ₂	1.85	379.4
TiO ₂ :Eu (1 wt.%)	1.95 for TiO ₂	2.13	242.4

The reflection spectra of the coatings obtained are shown in Fig. 5.

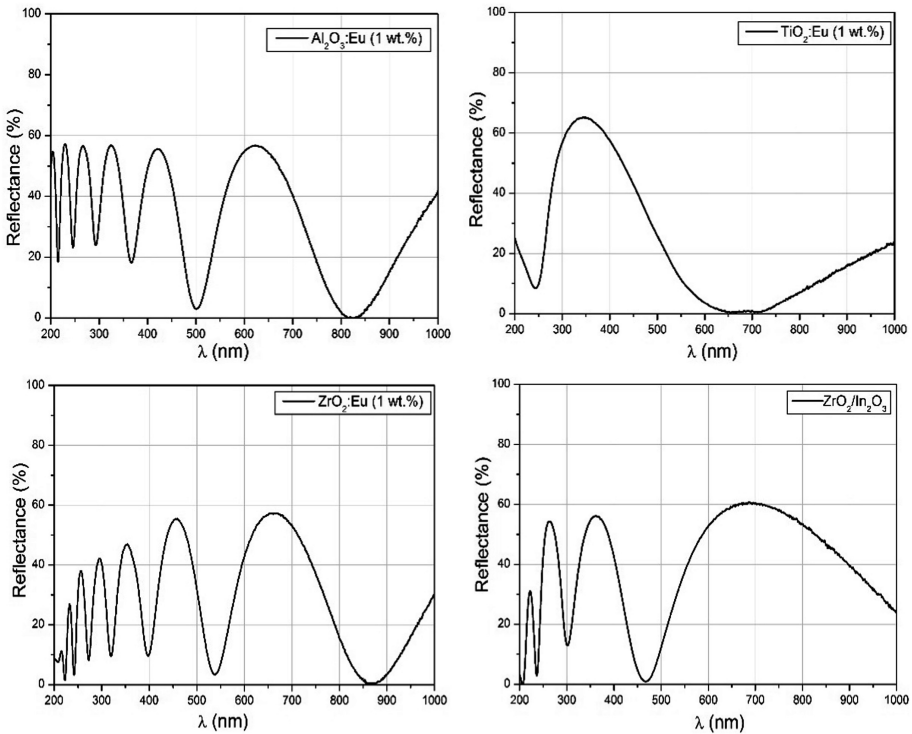


Fig. 5. Spectra of reflection of coatings obtained by spraying sol-gel targets

From the reflection spectrum of the TiO₂:Eu (1 wt.%) coating, it can be seen that in the region 640–720 nm the intensity of the reflected radiation is reduced to 0%, which is caused by the phenomenon of total internal reflection for radiation of a given wavelength. Coatings based ZrO₂/In₂O₃, Al₂O₃:Eu (1 wt.%), ZrO₂:Eu (1 wt.%) obtained by sputtering the sol-gel targets have the same reflection pattern in the ultraviolet region. The alternation of the maxima and minima of the reflection

coefficient indicates the interference of the incident and reflected waves. When a light wave passes through the refractive surface of the coating and the substrate, reflection occurs from their surfaces, the reflected waves are superimposed, forming alternation of maxima and minima on the reflection spectrum. This indicates the structural perfection of the thin coatings obtained. Coatings based on $\text{ZrO}_2/\text{In}_2\text{O}_3$, Al_2O_3 , ZrO_2 also have regions in which the reflected radiation intensity fails to 0%, which is associated with the phenomenon of total internal reflection. A comparative analysis of the reflectance spectra of coatings obtained from sol-gel targets based on $\text{ZrO}_2/\text{In}_2\text{O}_3$, $\text{Al}_2\text{O}_3:\text{Eu}$ (1 wt. %), $\text{ZrO}_2:\text{Eu}$ (1 wt. %), $\text{TiO}_2:\text{Eu}$ (1 wt. %) revealed that the optical properties of the coatings obtained are substantially. Depend on the component composition of the targets.

4 Conclusions

In this work shown that sol-gel methods can be used for obtain targets of complex composition based on several compounds and doped with rare-earth elements, which are subsequently sputtering by electron-beam dispersion. This method is simple and allows varying in wide range properties of obtained materials, to achieve significant interaction of components and the required dispersion. In the result coatings have high homogeneity, are transparent in the visible range and have a high adhesion to the surface of the substrate.

Acknowledgments. The work was supported by Belarusian Foundation for Fundamental Research (Project T16-RA005) and by Academy of Sciences of Romania.

References

1. Antonenko, S.V.: Technology of Thin Films, Textbook, p. 104. MEPI, Moscow (2008)
2. Rogachev, A.V., Zhou, B., Jiang, X., Liu, Z., Shen, R.: Mater. Sci. Semicond. Process. **16**, 513–519 (2013)
3. Rogachev, A.V., Kovalenko, D.L., Luca, D., Gaishun, V.E., Gorbachev, D.L., Vaskevich, V.V., Dobromir, M., Chirtsov, A.S.: Adv. Mater. Res. **1117**, 156–158 (2015)

Omega-Structured Substrate-Supported Metamaterial for the Transformation of Wave Polarization in THz Frequency Range

Igor Semchenko¹(✉), Sergei Khakhomov¹, Andrey Samofalov¹,
Maksim Podalov¹, Vitaliy Solodukha², Alyaxandr Pyatlitski²,
and Natalya Kovalchuk²

¹ Department of General Physics and Department of Optics,
Francisk Skorina Gomel State University,
Sovyetskaya Str. 104, 246019 Gomel, Belarus

{isemchenko, khakh, samofalov, podalov}@gsu.by

² JSC “INTEGRAL”, Korjnevsky Str. 12, Minsk, Belarus

{vsolodukha, nkovalchuk}@integral.by, petan@tut.by

Abstract. The objective of the paper is creating wide-band polarization transformers consisting of two-dimensional regular array of omega-elements on the substrate, which show resonance-frequency behavior in THz frequency range.

1 Introduction

The idea of creating a broadband polarization converter based on spiral or omega elements in the terahertz spectral range has not been implemented yet, therefore it is new and very important from the practical viewpoint. Recent studies show that a wideband filter for circularly polarized waves based on an array of particles can be realized in the terahertz spectral range. Selected topics are new and promising. This is due to the recent rapid development of metamaterial technologies [1–4], as well as the improvement of bulk laser lithography technologies, which is one of the most modern and promising for obtaining volume periodic dielectric microstructures. New methods of metallization of micrometer dielectric arrays have appeared, which makes it possible to vary its electrodynamic properties. A wide-band converter of a linearly polarized wave into a circularly polarized one (and vice versa) on the basis of chiral elements is still not realized in THz spectral range (but realized in microwave) [5].

In papers [6–11] the arrays on the base of helical elements were considered. Earlier, in papers [12–14] we calculated and experimentally studied the omega elements with the optimum ratio of the electric dipole moment and the magnetic moment in the microwave range (2.55–3.8 GHz). Parameters of a metamaterial consisting of omega elements effectively transforming the incident linearly polarized wave into a reflected wave with circular polarization were obtained.

In this paper, we studied an omega-structured metamaterial on a substrate the parameters of which are optimized for the terahertz radiation range. The interference of terahertz waves in a substrate is considered and the thickness of the substrate is

determined, which makes it possible to obtain the best transformation of the polarization of the wave reflected from the metamaterial. It is shown that a metamaterial based on an array of omega elements on a substrate can perform the functions of an effective polarization transformer of an electromagnetic wave when it is reflected.

2 The Study of the Polarization Properties of a Single Omega Element

The design of the optimal omega element for the THz band gives the change in the parameters of the element in accordance with the change in the wavelength of the incident radiation. Under the condition of the main frequency resonance, the length of the optimal omega element in the rectified state is equal to half the wavelength of the incident radiation, respectively, the wavelength of the radiation with a frequency of 1 THz will be 0.3 mm, and the length of the metalized strip, forming the omega element, will be 0.15 mm.

The optimality condition for the omega element is that the element induces equally significant electric dipole and magnetic moments [12]. The calculation performed within the framework of the quasi-stationary current model showed the following dependence of the radius of the omega element on the wavelength:

$$r = \frac{\lambda(\sqrt{2} - 1)}{2\pi}. \quad (1)$$

Based on this condition, the geometric parameters of the omega element, shown in Fig. 1, were obtained. Copper was chosen as the material of the conductive stripe of the omega element.

In the program of electrodynamic modeling, the polarization properties of a single omega element with optimal parameters (Fig. 2) in the frequency range

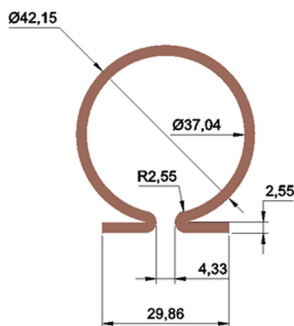


Fig. 1. Geometric parameters of the omega element for the THz band (dimensions are in micrometers)

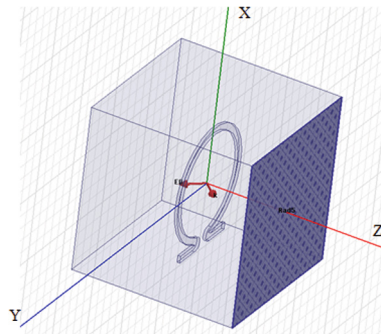


Fig. 2. The omega element model for the THz band

from 0.1 to 1.7 THz for different orientations of the vector \vec{E} and the vector \vec{k} of the incident wave were studied. When solving the problem, we used a normally incident plane linearly polarized wave.

The analysis of the simulation results allows us to conclude that under normal direction of the wave vector \vec{k} of the incident electromagnetic wave, relative to the plane of the omega element turn, the ellipticity coefficient of the radiated wave is maximum, i.e. 0.97, with the direction of the vector \vec{E} of the incident electromagnetic wave along the axis oy, i.e. along the arms of the omega element. When the vector \vec{E} of the electromagnetic wave is directed at an angle of 45° and 90° , relative to the axis oy, the value of the ellipticity coefficient of the radiated wave decreases. When the direction of the vector \vec{E} is at an angle of 90° with respect to the axis oy, the ellipticity coefficient of the radiated wave reaches the value 0.82. The maximum of the frequency resonance is close to the calculated resonant frequency in 1 THz, in the range from 0.9 to 1.2 THz.

With oblique direction of the wave vector \vec{k} of the incident electromagnetic wave relative to the plane of the omega element turn, the ellipticity coefficient of the radiated wave is equal to 0.96, with the direction of the vector \vec{E} in the yoz plane. In this case, the ellipticity coefficient reaches the maximum at a resonance frequency of 1 THz in all cases of the study.

The best excitation of the omega element can be achieved by activating two modes: electric and magnetic. The first mode is most strongly activated when the vector \vec{E} oscillates along the arms of the omega element or, as in our case, along the axis oy. The second one is activated when the vector \vec{B} oscillates through the omega-element turn. The contributions equality of the electric dipole moment and the magnetic moment to the intensity of the radiated wave indicates the optimality condition of the omega element as a polarizer of electromagnetic waves. This was confirmed by the result of the simulation. The greatest ellipticity coefficient, practically equal to 1, was observed when the vector \vec{E} of the incident wave was directed at an angle of 135° relative to the axis oy in the xoy plane. When the vector \vec{E} is directed along the axis oy, a wide resonance peak at a frequency of 1 THz was observed, with an ellipticity coefficient of 0.98. With the direction of the vector \vec{E} along the axis ox, a sufficiently high ellipticity coefficient of 0.94 for the radiated wave at a frequency of 0.9 THz was observed as well.

Thus, based on the results of the simulation of a single omega element, we can conclude that an omega element calculated for the terahertz range is an effective polarizer of electromagnetic waves, in particular, at a frequency of 1 THz. The omega element transforms the polarization of the incident electromagnetic wave most effectively at the resonance frequency with the direction of the vector \vec{E} along the axis oy, i.e. along the arms of the omega element, and the vector \vec{B} along the axis oz, i.e. orthogonally to the loop of the omega element. As for the direction of the wave radiation with transformed polarization, its wave vector should not be parallel to the arms of the omega element or the normal vector to the omega-element loop. It is necessary that both the electric dipole moment and the magnetic moment of the omega element should make equally significant contributions to the radiated wave, in this case it acquires a polarization close to the circular one.

3 The Study of the Polarization Properties of the Omega Elements Array Without a Substrate

In order to find the optimal parameters for the location of omega elements in the structural array, the electromagnetic properties of the metasurface were simulated for various distances between the omega elements (L) ranging from 40 to 120 μm at an interval of 5 μm , while the array is in the air (Fig. 3).

Theoretical analysis showed that the transformation of a linearly polarized wave (with an ellipticity coefficient close to 1) is possible on such a structure only if the wave falls at an angle of 45° . The oscillations of the incident wave \vec{E} vector must be in a plane which is perpendicular to the metasurface plane and should pass through omega elements arms. And one of the tasks at this stage of the research is to test this hypothesis.

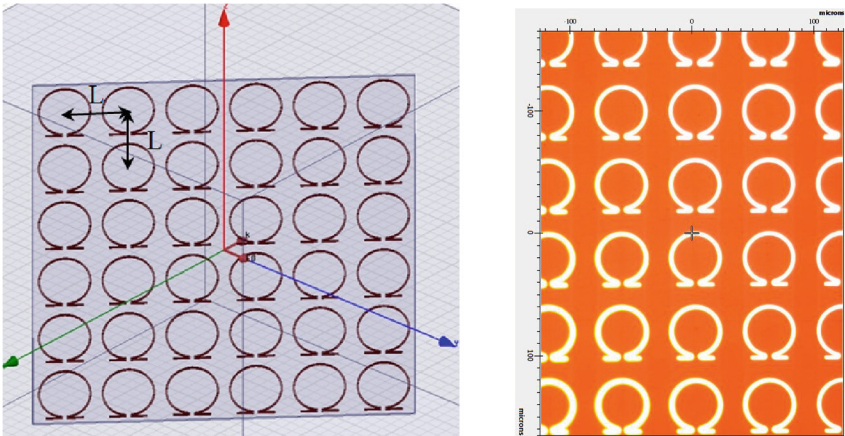


Fig. 3. The direction of vectors \vec{E} and \vec{k} of the incident wave with respect to the metasurface formed by omega elements (a), photo of manufactured omega array (b)

The study of the frequency dependence (in the range of 0.5 to 2 THz) of the ellipticity coefficient (K) of the wave, reflected from a metasurface consisting of omega elements, for different distances between omega elements (L) and for different directions of the vectors \vec{E} and \vec{k} of the incident wave has been carried out.

Based on the simulation results of the metasurface consisting of omega elements, we can conclude that a two-dimensional array with a distance between elements $L = 60 \pm 10 \mu\text{m}$, calculated for the terahertz range, is an effective polarizer of electromagnetic waves, in particular, at frequencies close to 1 THz. The metasurface based on omega elements transforms the polarization of the incident electromagnetic wave most effectively at the resonance frequency with the direction of the vector \vec{E} parallel to the omega-element arms, and the vector \vec{k} at an angle of 45° to the metasurface (Fig. 4).

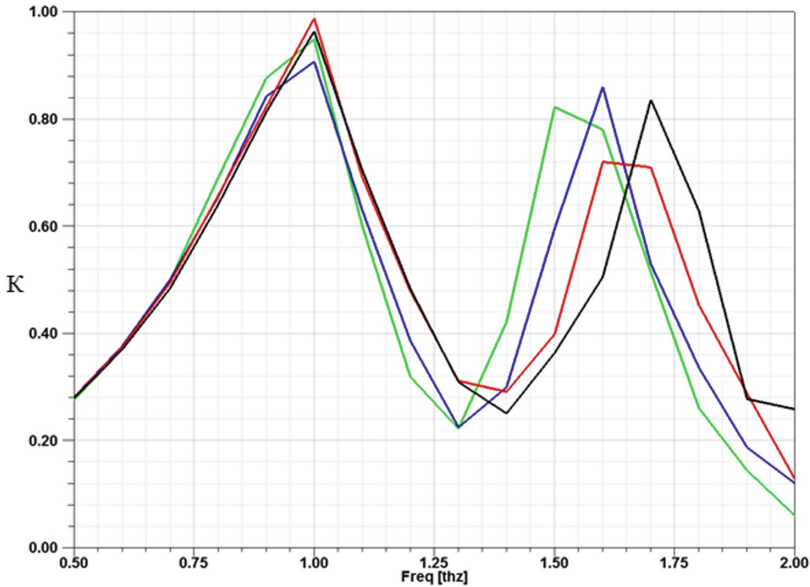


Fig. 4. The graphs of the frequency dependence of the ellipticity coefficient of the wave reflected from the metasurface at an angle of 45° for different values of L (50, 55, 60, 65 μm) (the vector \vec{E} is directed along the axis oy , and the vector \vec{k} is at an angle of 45° to the metasurface ($K_{\text{max}} = 0.987$ at a frequency of 1 THz at $L = 55 \mu\text{m}$ (red line))

The occurrence of the second maximum on the graphs in the range of higher frequencies can be explained by the fulfillment of resonance conditions not for the entire length of the omega element, but only for the length of its loop.

4 The Study of the Polarization Properties of the Metasurface Formed by Omega Elements on a Substrate Made of Various Materials

To make the experimental samples it is necessary to choose a polymer substrate on which an array of omega elements with micro-dimensions and resonance properties will be applied, thus creating a metasurface. Possible variants of the substrate material are fluoroplastic, polyethylene, polypropylene and polyamide (nylon). These polymers have a low value of the dielectric permeability, therefore, they have a small absorption of electromagnetic waves in the range under study and make a small contribution to the effective dielectric permeability of the whole sample. The problem is that the presence of a substrate must not disturb the balance of the electric dipole moments and the magnetic moments of the omega elements, i.e. the previously calculated optimal parameters of these elements should not change much.

The frequency dependence of the ellipticity coefficient (K) of the wave reflected from the metasurface on polymer substrates at different substrate thicknesses was simulated (in the range of 0.5 to 2 THz).

Three values of distance, which had been most well-established at the previous stage of simulation, between omega elements were used: 50, 55 and 60 μm . The wave vector \vec{k} of the incident wave for all models was directed at an angle of 45° to the metasurface on the substrate (Fig. 5).

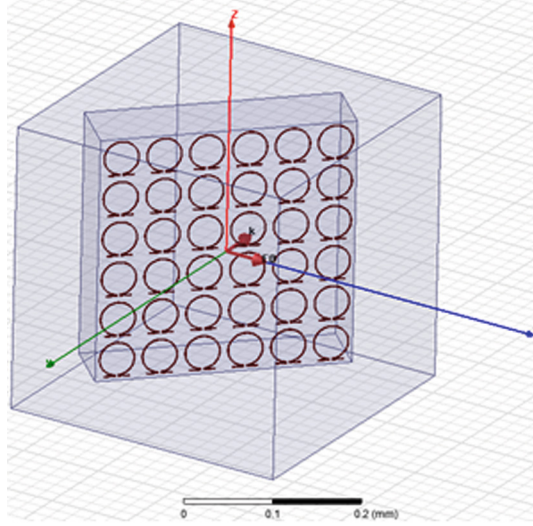


Fig. 5. The direction of the vector \vec{E} with respect to the omega element arms for the metasurface on a substrate

To take into account the interference of terahertz waves in the metamaterial substrate, we calculated the thickness values of the polymer films at which the interference maximum of the reflected wave is observed [15].

$$d_{max} = \frac{(m - \frac{1}{2})\lambda}{2\sqrt{n^2 - \sin^2\alpha}}, \quad (2)$$

where $m = 1$ is interference order, n is a refractive index of a polymeric substrate material, λ is a wavelength, α is the angle of incidence ($\alpha = 45^\circ$).

The value d_{max} for fluoroplastic, polyethylene, polypropylene and polyamide is equal to 60.34 μm , 56.21 μm , 57.18 μm and 53.50 μm , respectively. As a result of the simulation a clear correlation was set between the thickness of the dielectric substrate necessary for the efficient polarization conversion, with the d_{max} value. The maximum of the ellipticity coefficient of the wave reflected from the metasurface is observed at a substrate thickness d_{max} . For further verification of this correlation the thickness of the substrate was chosen in the range of $d_{max} \pm 10 \mu\text{m}$.

The graphs of the frequency dependence of the ellipticity coefficient of the reflected electromagnetic wave at various distances between the omega elements (L) and the thickness of the polymer substrate, equal to d_{max} for the fluoroplastic, are shown in Fig. 6.

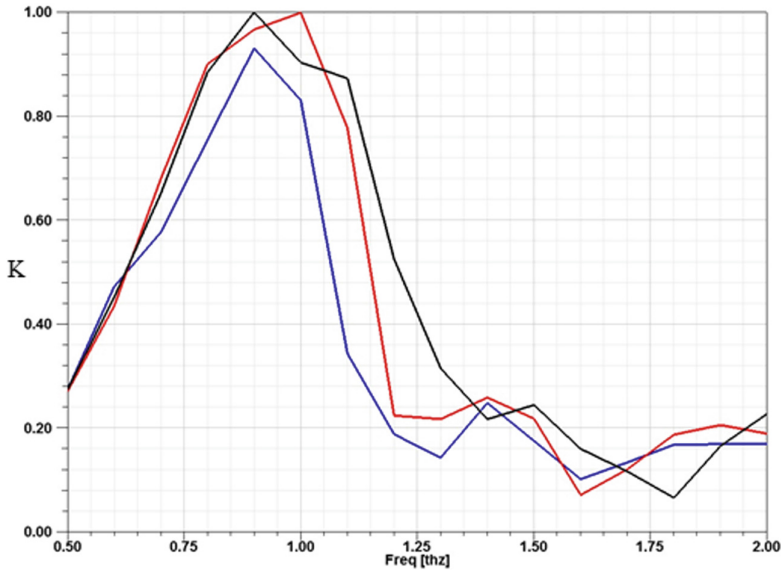


Fig. 6. The graphs of the frequency dependence of the ellipticity coefficient of the wave reflected from the metasurface formed by omega elements on a fluoroplastic substrate with a thickness of $60.34 \mu\text{m}$ for different values of L (the vector \vec{E} is directed along the axis oy). The black line is plotted for $L = 50 \mu\text{m}$, the red line corresponds to $L = 55 \mu\text{m}$, the blue line is plotted for $L = 60 \mu\text{m}$.

The analysis of the simulation results allows us to draw a conclusion about the possibility of using fluoroplastic, polyethylene and polypropylene as a substrate of the metasurface formed by omega elements to create a polarization transducer for electromagnetic waves in the THz range. But the ellipticity coefficient (K) of the reflected wave depends essentially on the direction of the vector \vec{E} of the incident wave. The ellipticity coefficient assumes the greatest value when the vector \vec{E} is directed along the axis oy (i.e. along the arms of the omega elements), which corresponds to the theoretical analysis. When the vector \vec{E} of the incident wave rotates by 90° (perpendicular to the arms of the omega elements), the value of the ellipticity coefficient decreases almost in two times.

The maximum value of the ellipticity coefficient, equal to unity, is observed at a thickness of the fluoroplastic substrate equal to $60.34 \mu\text{m}$, with distances between

omega elements of 50 and 55 μm (Fig. 6). The metasurface with a distance between the elements $L = 50 \mu\text{m}$ showed relatively high values of the ellipticity coefficient at any thicknesses and substrate materials.

Hence, all of the materials mentioned above can be used for the manufacture of a prototype metamaterial sample on a substrate for the THz range.

5 Conclusion

The simulation has been carried out using the finite elements method for the resonant electromagnetic properties of a single omega element and a metasurface consisting of omega particles in the THz range. Considering the results of this simulation we can conclude that the metasurface based on omega elements and calculated to convert the polarization of electromagnetic waves of the terahertz range, is an effective polarizer, near the 1 THz frequency in particular.

The resonant electromagnetic properties of a metasurface based on omega elements on a substrate made of various polymer materials of different thicknesses in the THz range have been simulated. The analysis of the simulation results allows us to conclude that it is possible to use fluoroplastic, polyethylene and polypropylene as a substrate of a metasurface formed by omega elements to create a polarization transformer in the THz range. The ellipticity coefficient of the reflected wave depends essentially on the direction of the vector \vec{E} and \vec{k} of the incident wave. The ellipticity coefficient assumes the greatest value when the vector \vec{E} is directed along the arms of the omega elements, and the wave vector \vec{k} of the incident wave is directed at an angle of 45° to the metasurface. The maximum value of the ellipticity coefficient, which is close to unity, is observed at a thickness of the polymer substrate calculated considering the interference maximum of the reflected wave from the boundaries of the film, when electromagnetic radiation falls on this film at an angle of 45° to the metasurface.

Acknowledgment. The research has been conducted according to the task of the State programme of scientific research of Belarus for 2016–2020 «Photonics, opto- and microelectronics» of the sub-programme «Photonics».

References

1. Landy, N.I., Sajuyigbe, S., Mock, J.J., Smith, D.R., Padilla, W.J.: Perfect metamaterial absorber. *Phys. Rev. Lett.* **100**, 207402 (2008)
2. Gansel, J.K., Thiel, M., Rill, M.S., Decker, M., Bade, K., Saile, V., Freymann, G., Linden, S., Wegener, M.: Gold helix photonic metamaterial as broadband circular polarizer. *Science* **325**, 1513 (2009)
3. Zhao, Y., Belkin, M.A., Alù, A.: Twisted optical metamaterials for planarized ultrathin broadband circular polarizers. *Nat. Commun.* **3**, 870 (2012)
4. Niemi, T., Karilainen, A.O., Tretyakov, S.A.: Synthesis of polarization transformers. *IEEE Trans. Antennas Propag.* **61**, 3102 (2013)

5. Asadchy, V.S., Faniayeu, I.A., Ra'di, Y., Khakhomov, S.A., Semchenko, I.V., Tretyakov, S. A.: Broadband reflectionless metasheets: frequency-selective transmission and perfect absorption. *Phys. Rev. X* **5**(3), 031005-1–031005-10 (2015)
6. Semchenko, I.V., Khakhomov, S.A., Naumova, E.V., Prinz, V.Ya., Golod, S.V., Kubarev, V.V.: Study of the properties of artificial anisotropic structures with high chirality. *Crystallogr. Rep.* **56**(3), 366–373 (2011)
7. Semchenko, I.V., Khakhomov, S.A., Tretyakov, S.A., Sihvola, A.H.: Electromagnetic waves in artificial chiral structures with dielectric and magnetic properties. *Electromagnetics* **21**, 401–414 (2001)
8. Semchenko, I.V., Samofalov, A.L., Khakhomov, S.A.: Radiation of circularly polarized electromagnetic waves by the artificial flat lattice with two-turn helical elements. In: 10th International Conference on Complex Media and Metamaterials Bianisotropics' 2004. Het Pand, Chent, Belgium, pp. 236–239 (2004)
9. Semchenko, I.V., Khakhomov, S.A., Tretyakov, S.A., Sihvola, A.H.: Microwave analogy of optical properties of cholesteric liquid crystals with local chirality under normal incidence of waves. *J. Phys. D Appl. Phys.* **32**, 3222–3226 (1999)
10. Asadchy, V.S., Faniayeu, I.A., Ra'di, Y., Semchenko, I.V., Khakhomov, S.A.: Optimal arrangement of smooth helices in uniaxial 2D-arrays. In: Proceedings of the 7th International Congress on Advanced Electromagnetic Materials in Microwaves and Optics. IEEE, New York, p. 244 (2013)
11. Semchenko, I.V., Khakhomov, S.A., Asadchy, V.S., Golod, S.V., Naumova, E.V., Prinz, V. Ya., Goncharenko, A.M., Sinityn, G.V., Lyakhnovich, A.V., Malevich, V.L.: Investigation of electromagnetic properties of a high absorptive, weakly reflective metamaterial-substrate system with compensated chirality. *J. Appl. Phys.* **121**, 015108-1–015108-8 (2017)
12. Semchenko, I.V., Khakhomov, S.A., Podalov, M.A., Tretyakov, S.A.: *J. Commun. Technol. Electron.* **52**(09), 1002–1005 (2007)
13. Balmakou, A., Podalov, M., Khakhomov, S., Stavenga, D., Semchenko, I.: *Opt. Lett.* **40**(09), 2084–2087 (2015)
14. Semchenko, I.V., Khakhomov, S.A., Samofalov, A.L., Podalov, M.A., Songsong, Q.: The effective optimal parameters of metamaterial on the base of omega-elements. In: Jabłoński, R., Szewczyk, R. (eds.) *Recent Global Research and Education: Technological Challenges*. AISC, vol. 519, pp. 3–9. Springer, Cham (2017). doi:[10.1007/978-3-319-46490-9_1](https://doi.org/10.1007/978-3-319-46490-9_1)
15. Born, M., Wolf, E.: *Principles of Optics*. Pergamon Press, Oxford (1959)

Core-Shell Powders with Titanium Coating

Sergey Bogdanov¹ and Maxim Sychov^{1,2}(✉)

¹ Saint-Petersburg State Institute of Technology (Technical University),
Moskovsky pr. 26, St. Petersburg 190013, Russia
{bogdanovsp, msychov}@mail.ru

² Institute of Silicate Chemistry of RAS, Saint-Petersburg, Russia

Abstract. In this work core-shell materials are developed for the utilization in additive technologies. Several examples are given of synthesis of refractory powders covered by shells of titanium and its compounds. Peculiarities of gas phase synthesis and structure of fabricated coatings are discussed.

Keywords: Coatings on powders · Composite materials · Iodide transport

1 Introduction

Development of the methods of additive manufacturing of ceramics is of great importance, especially when product should have extremely high properties [1]. However, the use of refractory powders for additive technologies is complicated because of the high temperature necessary for their sintering. One of possible solutions of this problem is the use of core-shell composite powders. At the same time, material of the shell has to not only reduce sintering temperature, but to form a refractory binder. In this work it is suggested to use nano- and micro films of the titanium metal as a coating on particles of refractory powders.

Earlier conducted researches [2] have shown that simple and economical method of fabrication of titanium shells on fine powders is the gas transport. When selecting a heterogeneous system, suitable for the transport of substances, it is important to ensure that the balance of the system in this temperature range is not dramatically shifted to the right or left. Convenient and affordable agent for gas transportation that satisfies this condition is iodine. Already at room temperature titanium metal starts to react with iodine vapors [3], but rapidly the reaction proceeds at a temperature of about 200 °C. The interaction is described:



To a temperature 377 °C iodide TiI_4 is liquid [3]. The rise in temperature above 377 °C leads to the evaporation of the titanium iodide [3]. Titanium iodide vapors reaction with an excess of titanium results in formation of TiI_3 , and then TiI_2 . Formation of titanium film on the powder's surface starts at 400 °C [2]. Transport of titanium to the substrate by means of iodide does not require a temperature or pressure gradient [2].

2 Experimental Part

2.1 Materials and Methods

As core ceramic powders we used different oxides (Al_2O_3 , ZrO_2 , SiO_2 , MgO , $\text{MgO} \cdot \text{Al}_2\text{O}_3$), carbides (WC , SiC , B_4C), nitrides (BN , Ti_2CN , AlN , Si_3N_4) and diamond powders of different grain sizes. Titanium used for coating was a metal powder with a grain size of 5 to 35 μm .

Experiments on coating of powders with titanium by the method of iodide-transport was carried out in a quartz reactor filled with argon. The mixture of the ceramic powder with a powder of titanium metal and iodine was placed in the reactor, vacuumed and then filled with argon. The pressure in a cold reactor was 0.12–0.14 MPa. Then reactor was put in an oven preheated to a predetermined temperature. The reactor was kept in an oven preset time, maintaining the pressure in the range of 0.15–0.18 MPa. Then reactor was removed from the furnace and cooled in air, and the product of the reactions was obtained.

The source and the coated powders were studied by scanning electron microscopy (SEM) using Tescan Vega 3 SBH microscope with X-ray microprobe AZtec X-Act and by X-ray diffraction (XRD) analysis using DRON-3 diffractometer. To decrypt the obtained XRD data we used the ICDD PDF card files.

To measure the thickness of coatings we used two methods. Yakovic-Newbery method is based on comparing the intensity of characteristic radiation signals of the element measured for the coating and volume standard. Since the spatial resolution of x-ray microanalysis for electron microscopes is some 1 μm , for powders of smaller size we used the method of calculation. The method consisted in measurement of specific surface of powder, the mass fraction of coating material in the composition and the determination of its phase composition. Then the average thickness of the coating was calculated. Using X-ray microprobe of electron microscope, it was confirmed that all the metal or its compound are on the surface of the powder substrate.

2.2 Results of the Experiments

As a result of experiments it was established that titanium is capable of forming coating on all of the used powders. The thickness and phase composition of the coatings vary depending on the process conditions. Let us consider the formations of coatings on diamond powders. In the presence of iodine titanium begins to react with the surface of amorphous carbon already at 300 °C [4], but on the surface of monocrystalline grains of diamond the coating starts to form only at temperatures above 500 °C. Until 550 °C the coating is transparent. Yakovic-Newbery measurements showed that coatings formed during 2 h at 600 °C have thickness from 31 to 72 nm for different crystals. For the whole sample, the average coating thickness is 50 nm. X-ray analysis shows the presence of titanium metal phase. Titanium forms fine grained uniform coating, Fig. 1a, in contrast to chromium, Fig. 1b, which under these conditions react with the substrate with the formation of Cr_7C_3 dendrite crystals. The rise of reaction temperature to 700 °C results in interaction of titanium with the substrate with the formation of carbide TiC coating, which has a two-phase composition. Above 900 °C XRD method detects the phase TiC_8 along with the carbide TiC .

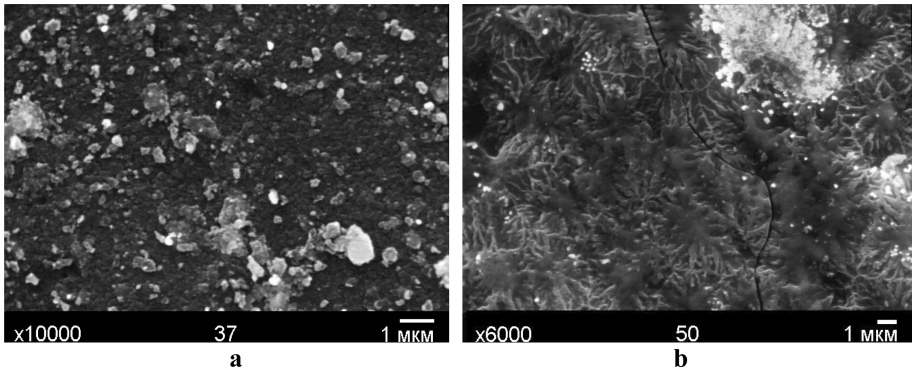


Fig. 1. SEM photo of the surface structure of single crystals of diamond with titanium coating with a thickness of 50 nm (a) and with chromium coating with a thickness of 1000 nm (b).

We also obtained titanium coated powders of the detonation nanodiamonds (DND) (Fig. 2). The source material was a powder in the form of agglomerates with a size of 0.8–1 μm , consisting of plate-like crystals. The diameter of the plates was 100 to 500 nm, thickness less than 50 nm. The size of regions of coherent scattering, calculated according to the Scherrer equation was 6 nm. Scanning electron microscopy confirmed the uniform distribution of titanium in the sample. Depending on the proportion of titanium in the initial charge mixture, the estimated coating thickness was from 0.5 to 3 nm.

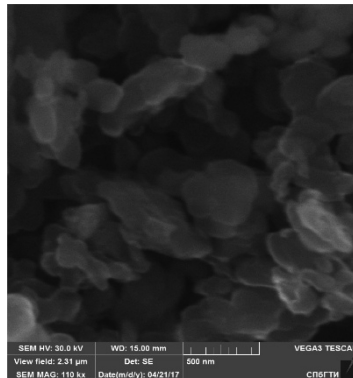


Fig. 2. SEM images of particles of detonation diamond coated with titanium (calculated coating thickness 3 nm).

When getting a film of titanium on other powders ($\alpha\text{-Al}_2\text{O}_3$, ZrO_2 , SiO_2 , MgO , spinel $\text{MgO}\cdot\text{Al}_2\text{O}_3$), carbides (WC , SiC , B_4C), nitrides (cBN , gBN , Ti_2CN , AlN , Si_3N_4), we observed similar processes. Till 700 $^\circ\text{C}$ coating consists of titanium metal, above it products of the interaction of Ti with the substrate are detected. For example,

the boron nitride coating consists of TiN and TiB phases, and at temperatures over 900 °C TiB₂ appears. For carbides above 700 °C in addition to titanium we observed phases: on the tungsten carbide – TiC_{0.59} and Ti_xW_{1-x}, on the silicon carbide – TiC and Ti₅Si₃ on the boron carbide – TiC and TiB₂. The surface structure of titanium films on the micro-powders (from 1 to 40 μm) of all used materials is the same (Fig. 3).

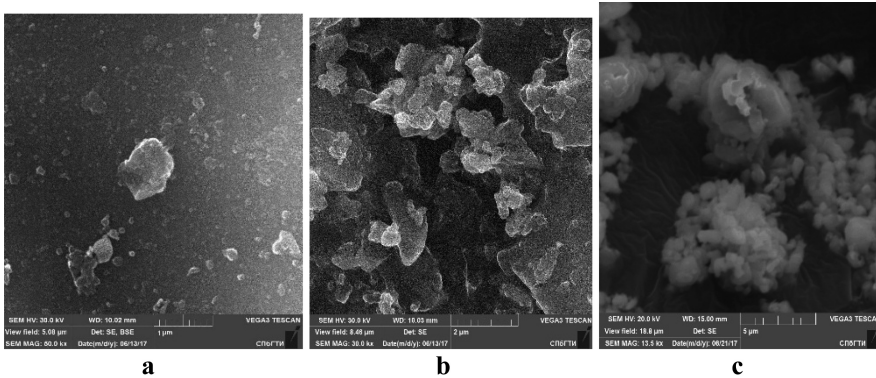


Fig. 3. SEM images of SiC (a), B₄C (b) and Al₂O₃ (c) samples with a titanium coating

The use of titanium as a shell on the refractory ceramic core must activate the sintering of the composition during the formation of the products by methods of additive technologies. After sintering of nanodiamonds at 4–5 GPa pressure and 1300–1700 °C temperature derived materials had open porosity 0–1%, total porosity 3–10%. Compressive strength was 12 GPa which is 3 times higher than tungsten-less ceramics and tungsten carbide materials. Microhardness was 50–90 GPa, that is comparable with hardness of polycrystalline diamonds.

Also suggested here approach allowed us to obtain plates for cutting tools using cBN powders with coating, the particle size of powders was below 3 μm. Plates were successfully tested for cutting quenched steel at 160 m/min. When such small particle size powder are used without coating, it is not possible to obtain good quality instrument.

Using Ti and TiN coated SiC micropowders ceramics plates were fabricated by hot pressing at 3.5–4 GPa pressure and 1600 °C temperature. Due to chemical bonds formed between titanium coating and SiC resulted ceramics has high density (3.4–3.5 g/cm³), hardness (12–20 GPa) and 4...5 increased wear resistance comparing to conventional material.

Coated WC nanopowders were used for the fabrication of protective coatings for titanium alloys. As a result wear resistance increased 2 times and corrosion resistance also improved.

In the next stage of work was studied the chemical properties of titanium films. Earlier [2] it was discovered that freshly prepared powders with nanofilms of titanium are pyrophoric. We compared the ability of oxidation of titanium films and the original metal powder. To do this, one crucible was charged with a mixture of a source powder and titanium powder and the other with the core-shell obtained from the same mixture.

Both crucibles were placed in the oven heated to 700 °C and annealed in air. X-ray spectra of the products of calcination are shown in the Figs. 4 and 5. It is seen that the titanium powder under these conditions mostly remained, there are only traces of TiO₂ oxide. The coating on the corundum (α -Al₂O₃) is almost completely oxidized, and the shell on the periclase (MgO) was oxidized and reacted with the substrate with the formation of geikielite MgTiO₃.

It is established that titanium shell is active not only towards oxidation, but also reacts with nitrogen readily. So in a nitrogen atmosphere all the titanium is converted into nitride at a temperature of 700 °C. Figure 6 shows grains of silicon carbide of 125–160 μ m size coated with titanium in argon atmosphere (Fig. 6a). Then the argon atmosphere was replaced with nitrogen, the photos of this material is shown in the Fig. 6b.

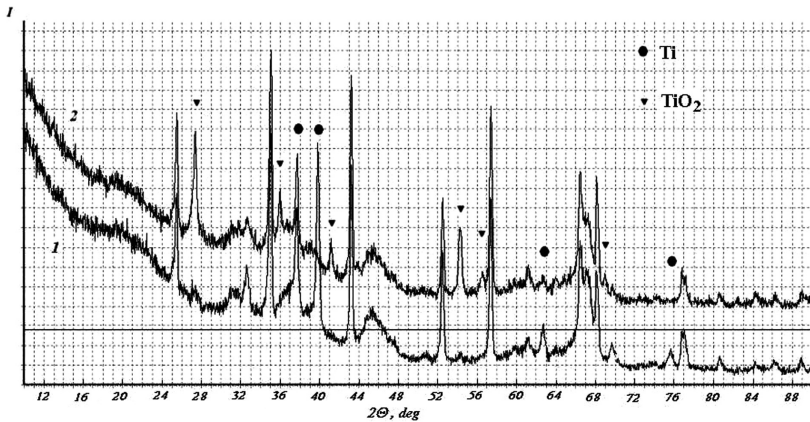


Fig. 4. XRD plots of the samples annealed at 700 °C for 2 h; the mixture of powders of Al₂O₃ and Ti (spectrum 1), Al₂O₃ coated with titanium (spectrum 2).

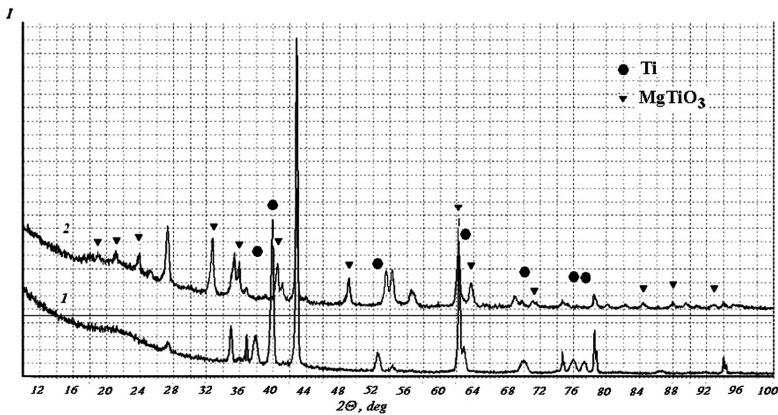


Fig. 5. XRD plots of the samples annealed at 700 °C for 2.5 h; mixture of powders of MgO and Ti (spectrum 1), MgO plated titanium (spectrum 2).

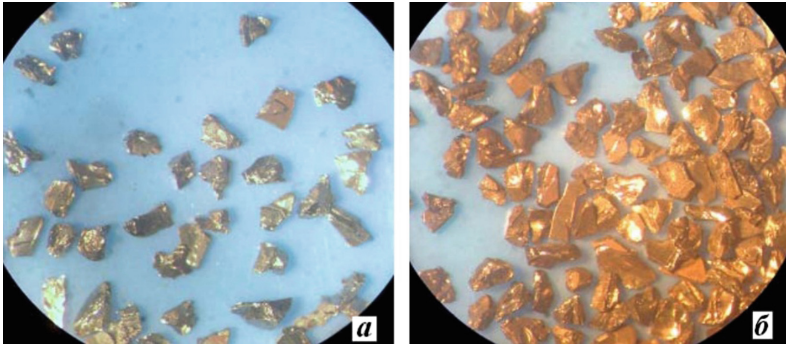


Fig. 6. SiC grains coated with Ti (a, in argon) and TiN (b, in nitrogen)

3 Discussion and Conclusions

In this work titanium shells are synthesized on oxides (Al_2O_3 , ZrO_2 , SiO_2 , MgO , $\text{MgO} \cdot \text{Al}_2\text{O}_3$), carbides (WC , SiC , B_4C), nitrides (BN , Ti_2CN , AlN), diamond. For each material the modes of titanium transport are optimized and the structure and properties of coverings are studied. It is found that a thin titanium film on the surface of ceramic powders may be obtained at temperatures below 700°C .


The coatings have high chemical activity. Reactivity of titanium films is higher than that of metal powders of titanium, from which they were obtained. Film of titanium is easily oxidized and interacts with the substrate with the formation of refractory carbides, nitrides and intermetallic compounds. A number of materials with the core/shell structure with titanium coating were tested in sintering of composites by hot pressing. It is established that titanium shell facilitates the sintering of the refractory material of the core and chemical reactions form a durable refractory binder. Coated titanium powders have increased coefficient of blackness which is advantageous for the technology of selective laser sintering (SLS)/selective laser melting (SLM).

Acknowledgement. The study was performed with the support of Russian Science Foundation (project No. 17-13-01382).

References

1. Bogdanov, S.P., Sychov, M.M., Lebedev, L.A., Mjakin, S.V., Gravit, M.V.: Core-shell powders for additive manufacturing of articles for underground construction. *Proc. Eng.* **165C**, 1579–1586 (2016)
2. Bogdanov, S.P.: Preparation of coatings on powders by the iodide transport method. *Glass Phys. Chem* **37**, 172–178 (2011)
3. Rolsten, R.F.: *Iodide Metals and Metal Iodides*. Wiley, New York (1961)
4. Bogdanov, S.P.: Titanium carbide synthesis in the presence of iodine. *Refract. Ind. Ceram* **56(5)**, 551–556 (2016)

Temperature Fields in the In/CdTe Structure Under Laser-Induced Doping in Liquid

V.A. Gnatyuk¹ , V.L. Dubov², D.V. Fomin², A.Yu. Seteikin²,
and T. Aoki³

¹ V.E. Lashkaryov Institute of Semiconductor Physics of the National Academy of Sciences of Ukraine, Prospekt Nauky 41, Kiev 03028, Ukraine
gnatyuk@ua.fm

² Amur State University, Ignatyevskoye sh. 21,
Blagoveshchensk 675027, Russia

³ Research Institute of Electronics, Shizuoka University,
Hamamatsu 432-8011, Japan

Abstract. In/CdTe barrier structures formed by laser irradiation of CdTe crystals pre-coated with an In dopant film are the subject of study. The computational simulation of thermal processes and calculations of the time-dependent temperature distributions in the structure of water environment (3–5 mm)/In film (400 nm)/CdTe crystal (0.5 mm) under irradiation from the In film side in water with KrF excimer laser pulses ($\lambda = 248$ nm, $\tau = 20$ ns) have been performed. An implicit finite difference method with smoothed coefficients and permissible cooling due to “evaporation” of In atoms from the dopant film surface and boiling of a water layer adjacent to the metal was used. The minimum laser pulse energy density necessary for melting of the whole In film was determined as $E = 1300$ J/m², however the temperature at the In/CdTe interface did not reach the CdTe melting point even at higher $E = 1500$ J/m². It was shown that cooling due to “evaporation” of In atoms and boiling of the surrounding water layer did not significantly effect the laser heating process.

Keywords: In film · CdTe crystal · Pulse laser irradiation · Temperature distribution · Heating · Melting

1 Introduction

Nowadays, laser-assisted techniques, in particular based on short pulse irradiation, have been widely employed for processing of semiconductors for various applications [1, 2]. Recently, great success has been achieved in application of nanosecond pulse laser irradiation for doping of a surface layer of CdTe semiconductor and formation of M-p-n diode structures for high energy radiation detectors [3–7]. A special emphasis was made on development of solid-phase doping of CdTe crystals with an In impurity by laser-induced stress and shock waves generated as a result of rapid thermal expansion of the near-surface In region heated during nanosecond laser radiation action [3]. It has been shown that employing irradiation of p-like CdTe crystals pre-coated with an In dopant film (electrode) by nanosecond laser pulses in water environment, it is possible

to incorporate and activate In atoms (donors) with high concentration in the thin surface region of CdTe and thus, to form a shallow and sharp p - n junction [4–6].

However, highly non-equilibrium and non-stationary processes under nanosecond laser irradiation make impossible experimental measuring the temperatures at the surface of samples, metal-semiconductor interface and in the bulk of CdTe that, thus hinders predicting the doping effect. Therefore, laser-stimulated thermal processes under irradiation of In/CdTe structures need further detailed study.

A certain simulation of laser-induced heating of the In film and calculation of the temperature distributions inside the CdTe/In/water structure were carried out for an interesting case of direct impact of laser pulses on the CdTe/In interface under irradiation of the structure through the CdTe crystal in water using infrared radiation of a YAG:Nd laser ($\lambda = 1064$ nm and $\tau = 8$ ns) [7]. However, the M - p - n structured In/CdTe/Au detectors fabricated by direct action of KrF excimer laser pulses ($\lambda = 248$ nm, $\tau = 20$ ns) on the In dopant film deposited on the CdTe crystal surface, demonstrated higher electrical and spectral characteristics [4]. Therefore, for that case [4–6], the simulation of thermal processes and computational calculations of the time-dependent temperature distributions in the structure of water environment/In film/CdTe crystal have been performed to determine the optimal regimes of laser irradiation for efficient induced doping. The calculation results obtained for different energy densities of KrF excimer laser pulses are presented and discussed.

2 Experimental Details

2.1 Formation of the In/CdTe/Au Structure

Cadmium telluride (CdTe) is the most important material for room temperature semiconductor X/γ -ray detectors because of its optimal physical properties that makes this semiconductor very attractive for compact solid-state high energy radiation sensors with high energy resolution which are widely used in industry, medicine, security, ecology, space astronomy and other application fields [8, 9].

The fabrication of In/CdTe/Au diodes with a p - n junction formed by the developed technique of laser-induced solid phase doping of the thin surface region of high resistivity (111) oriented CdTe single crystals pre-coated with a relatively thick

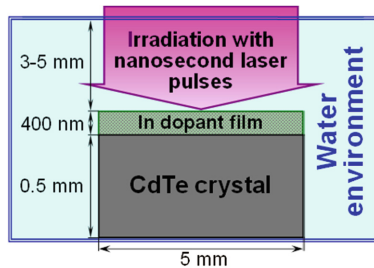


Fig. 1. Schematic illustration of irradiation of the In film/CdTe crystal structure with KrF excimer laser pulses ($\lambda = 248$ nm, $\tau = 20$ ns) in water environment.

($\sim 300\text{--}500$ nm) In dopant/electrode film, has been described in details as the technological procedures of creation of M-*p-n* structured X/ γ -ray radiation detectors [4–6].

Figure 1 shows the procedure of laser irradiation of the In/CdTe structure. A parallelepiped-like ($5 \times 5 \times 0.5$ mm³) CdTe crystal with a deposited In film (400 nm) was subjected to irradiation from the In-coated side with single pulses of a KrF excimer laser ($\lambda = 248$ nm, $\tau = 20$ ns) in water at the depth of $\sim 3\text{--}5$ mm.

2.2 Parameters of Substances of the Structure

For the simulation of laser-induced thermal processes, the following three-region structure was considered: environment (water layer with the depth of 3–5 mm)/metal dopant film (In film with the thickness of 400 nm)/semiconductor substrate (CdTe crystal with the thickness of 0.5 mm) (Fig. 1). The corresponding data characterizing thermal and optical properties CdTe and In were taken from the literature [8–12]. Some physical parameters, used for the calculations of the time-dependent temperature distributions in these media, are shown in Table 1.

Table 1. Parameters of the media used for the temperature calculations [8–10].

Parameters	Water	In solid	In liquid	CdTe
Density, ρ , kg/m ³	983	7310	7020	5850
Heat capacity, c , J/(kg K)	4182	232.9	259.5	$205 + 3.6 \times 10^{-2}$
Thermal conductivity, λ , W/(m K)	0.659	81.8	33.1	$1507/T$
Melting point, K		429.75		1365
Boiling point, K	373.1		2345	

In the present case, the temperature dependences of the thermodynamic parameters of the media have not been taken into account, although for more accurate calculations it is supposed to use temperature dependent values [10].

3 Calculation and Discussion of Results

3.1 Formulation of the Calculation Problem

It was supposed that under irradiation of an In dopant film, deposited on the CdTe crystal surface, with a single laser pulse, a highly doped *n*-type CdTe:In superficial layer was formed and a built-in *p-n* junction was created as a result of implantation of In atoms into the thin CdTe region because of generation and propagation of stress and shock waves [3–6]. Laser-induced point defect formation in the CdTe crystal lattice and significant increase in diffusion and baro-diffusion of an In impurity contributed in creation of a large number of donor centers In_{Cd} [10].

The minimum laser pulse energy density necessary for melting of the 400 nm In film on the CdTe crystal surface, carried out in a water environment, has been determined using an implicit finite difference method with smoothed coefficients and permissible cooling due to “evaporation” of In atoms from the In film surface and boiling of a water layer adjacent to the metal surface [13].

The calculations were carried out using the step of discretization spatial coordinate $h = 10^{-8}$ m and time coordinate $t = 10^{-11}$ s. A KrF excimer laser emitted single pulses with wavelength of 248 nm and duration $\tau = 20$ ns. The laser pulse energy density E varied from 1000 J/m² to 1500 J/m² and it was considered uniformly distributed over the In surface area of the In/CdTe sample and invariant in time. The heat conductivity equations without laser radiation (1) and with volumetric heat sources (2) were used:

$$c\rho \frac{\partial T}{\partial t} = \lambda \frac{\partial^2 T}{\partial x^2}, \quad (1)$$

$$\frac{\partial T}{\partial t} = \lambda \frac{\partial^2 T}{\partial x^2} + Q, \quad (2)$$

where

$$Q = (1 - R) \frac{E}{\tau} \alpha(x, T) \left(\exp\left(-\int_0^x \alpha(x', T) dx'\right) \right), \quad (3)$$

R and $\alpha(x, T)$ are the coefficients of reflection and absorption of indium which were accepted for $\lambda = 248$ nm as 0.8 and 10^8 m⁻¹, respectively [11, 12].

Then, the following boundary conditions were used. The boundary condition of water/external environment:

$$-\lambda_{\text{H}_2\text{O}} \frac{\partial T}{\partial x} = 0. \quad (4)$$

The boundary condition of water/indium before boiling of water:

$$-\lambda_{\text{H}_2\text{O}} \frac{\partial T_{\text{H}_2\text{O}}}{\partial x} = -\lambda_{\text{In}} \frac{\partial T_{\text{In}}}{\partial x}, \quad (5)$$

where $T_{\text{In}} = T_{\text{H}_2\text{O}}$. The boundary condition of water/indium after boiling of water:

$$-\lambda_{\text{In}} \frac{\partial T_{\text{In}}}{\partial x} = -k(T_{\text{In}} - T_{\text{H}_2\text{O}}), \quad (6)$$

where k is the coefficient of boiling heat transfer for water/metal which was assumed in this calculation to be equal to 4000 (average value for a boiling water/metal boundary). The boundary condition of water/indium after melting of indium:

$$-\lambda_{\text{In}} \frac{\partial T_{\text{In}}}{\partial x} = -k(T_{\text{In}} - T_{\text{H}_2\text{O}}) - Q_{\text{evap}}, \quad (7)$$

where Q_{evap} is the heat flux from the indium film surface due to “evaporation” of In atoms. The boundary condition of indium/cadmium telluride:

$$-\lambda_{\text{In}} \frac{\partial T_{\text{In}}}{\partial x} = -\lambda_{\text{CdTe}} \frac{\partial T_{\text{CdTe}}}{\partial x}, \quad (8)$$

where $T_{\text{In}} = T_{\text{CdTe}}$. The boundary condition of cadmium telluride/external boundary:

$$-\lambda_{\text{CdTe}} \frac{\partial T}{\partial x} = 0. \quad (9)$$

3.2 Results and Analysis

The result of the calculation of the temperature distributions in the structure of water (3–5 mm)/In (400 nm)/CdTe (0.5 mm) under laser radiation is shown in Fig. 2. As seen, the temperature increases with increasing laser pulse energy density, while the shape of the temperature distributions does not change.

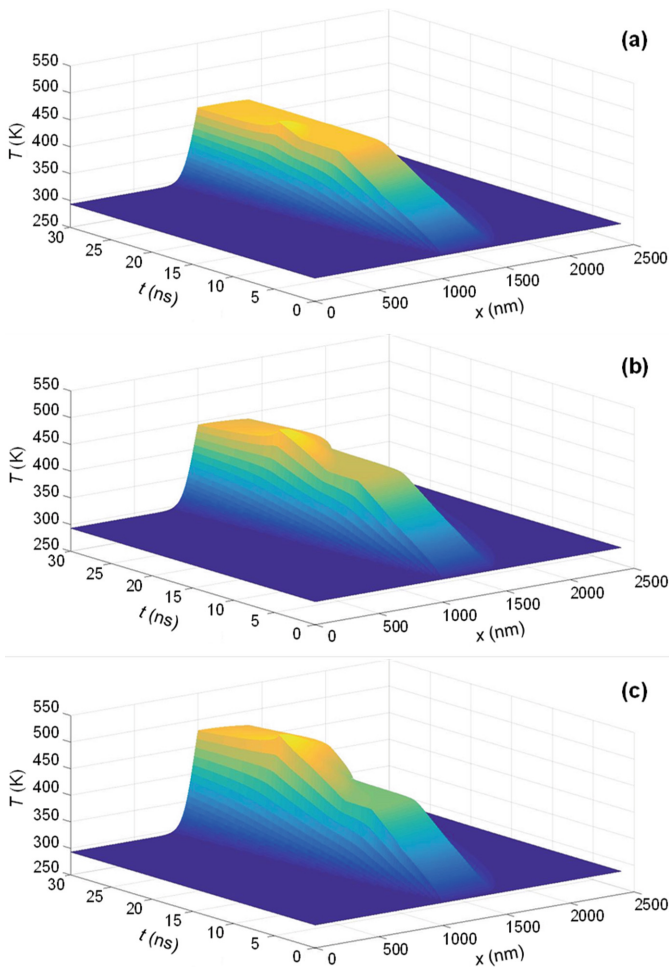


Fig. 2. Temperature distribution in the structure of water environment/In film/CdTe crystal under irradiation from the In film side with laser pulse energy density E (J/m^2): 1100 (a), 1300 (b), 1500 (c).

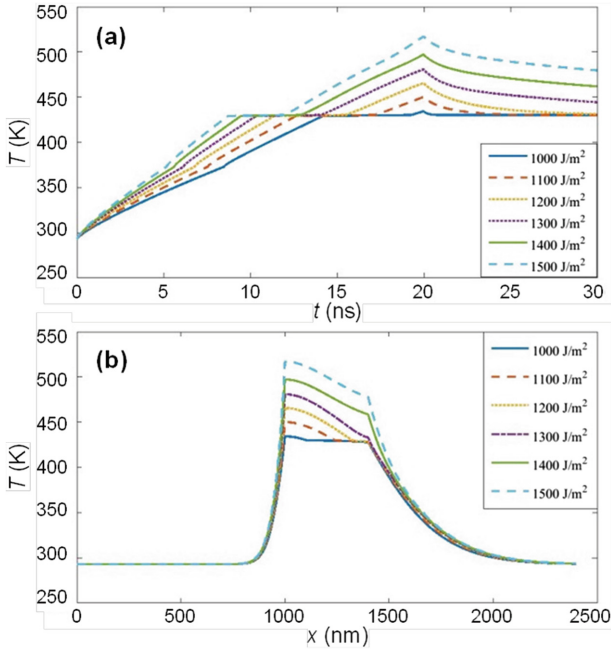


Fig. 3. Temperature distribution in the structure of water environment/In film/CdTe crystal under irradiation from the In film side in dependence on laser pulse energy density vs time for the maximum temperature layer (a) and vs coordinate in 20 ns after irradiation starts (b).

The time (a) and coordinate (b) distribution profiles, depending on the laser energy density, are shown in Fig. 3. According to the calculation results, the temperature increases linearly (not counting the region where the indium melts) that is associated with high laser pulse energy density.

The influence of the cooling water layer and cooling due to “evaporation” of In atoms from the dopant film surface is small and it does not have a noticeable effect during the irradiation of this structure by a short laser pulse. In order to finally verify this, the heating flux of transmitted laser radiation into the In film ($\sim 10^{12}$ W/m²) and fluxes of the cooling indium surface are compared (Fig. 4). As seen, the cooling flows from surfaces film are several orders of magnitude lower than the heating flow of the structure of water (3–5 mm)/In (400 nm)/CdTe (0.5 mm) under pulse laser radiation.

The whole In film (400 nm) was melted at laser pulse energy densities above 1300 J/m². The melting time at $E = 1500$ J/m² was about 13 ns, but the temperature at the boundary of the In film and CdTe substrate did not reach the melting temperature of the semiconductor (Fig. 3(b)). Therefore, there was no melting of a CdTe layer near the In/CdTe interface (Fig. 5). Thus, mixing of these substances (In and CdTe) in liquid (melted) state could not occur.

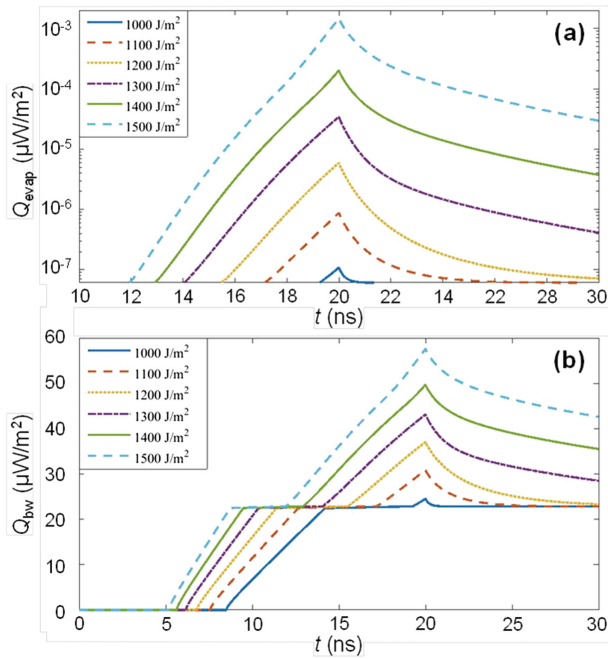


Fig. 4. Cooling flows from the In film surface in the structure of water environment/In film/CdTe crystal due to In evaporation (a) and boiling of water near the In film surface (b) in dependence on laser pulse energy density.

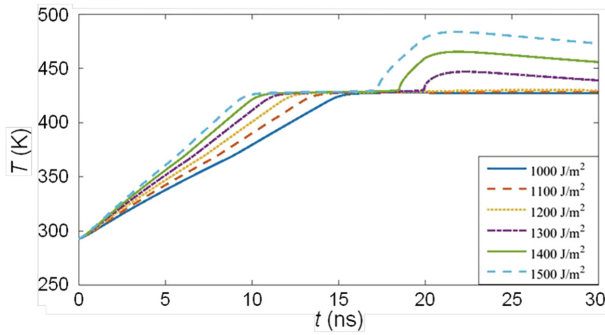


Fig. 5. Temperature distribution at the boundary of the In film/CdTe crystal in the structure of water environment/In film/CdTe crystal under irradiation from the In film side with different laser pulse energy densities.

Thermal, elastic, stress and diffusion processes of laser-stimulated penetration of In atoms into the thin region of CdTe crystal and estimation of the amount of the introduced impurity need additional study.

4 Conclusion

The In film was completely melted at laser pulse energy density $E = 1300\text{--}1500 \text{ J/m}^2$, however the temperature at the In film/CdTe crystal boundary was still much lower the melting point of CdTe. Cooling due to “evaporation” of In atoms and boiling of the surrounding water layer did not significantly effect the laser heating process. As shown, the cooling flows were several orders of magnitude lower than the heating flux of laser radiation. The results can be used for optimization of the laser-induced doping of CdTe and formation of In/CdTe/Au diodes for X/ γ -ray detectors [3–7].

Acknowledgement. This research was partly supported by the NATO Science for Peace and Security Programme (Project SENERA, SfP-984705) and Bilateral Cooperative Program of The State Fund for Fundamental Researches of Ukraine (SFFR) and The Japan Society for the Promotion of Science (JSPS) (Grant No Φ 68/54-2016).

References

1. Misra, N., Xu, L., Rogers, M.S., Ko, S.H., Grigoropoulos, C.P.: Pulsed laser annealing of semiconductor structures for functional devices. *Phys. Status Solidi (c)* **5**(10), 3264–3270 (2008)
2. Phillips, K.C., Gandhi, H.H., Mazur, E., Sundaram, S.K.: Ultrafast laser processing of materials: a review. *Adv. Optics Photonics* **7**(4), 684–712 (2015)
3. Gnatyuk, V.A., Aoki, T., Hatanaka, Y.: Laser-induced shock wave stimulated doping of CdTe crystals. *Appl. Phys. Lett.* **88**(24), 242111-1-3 (2006)
4. Gnatyuk, V.A., Aoki, T., Grushko, E.V., Kosyachenko, L.A., Vlasenko, O.I.: High resolution CdTe X- and gamma-ray detectors with a laser-formed *p-n* junction. In: *Proceedings of SPIE 8142*, p. 81420B-1-7 (2011)
5. Gnatyuk, V.A., Levytskyi, S.N., Vlasenko, O.I., Aoki, T.: Laser-induced doping of CdTe crystals in different environments. *Adv. Mater. Res.* **222**, 32–35 (2011)
6. Gnatyuk, V.A., Levytskyi, S.N., Vlasenko, O.I., Aoki, T.: Formation of doped nano-layers in CdTe semiconductor crystals by nanosecond pulse laser irradiation. *Thai J. Nanosci. Nanotechnol.* **1**(2), 7–16 (2016)
7. Zelenska, K.S., Gnatyuk, D.V., Aoki, T.: Modification of the CdTe-In interface by irradiation with nanosecond laser pulses through the CdTe crystal. *J. Laser Micro/Nanoeng.* **10**(3), 298–303 (2015)
8. Zanio, K.: Cadmium telluride. In: Willardson, R.K., Beer, A.C. (eds.) *Semiconductors and Semimetals*, vol. 13. Academic Press, New York (1978)
9. Triboulet, R., Siffert, P.: *CdTe and related compounds; physics, defects, hetero- and nano-structures, crystal growth, surfaces and applications*, 1st edn. Elsevier, Amsterdam and Oxford (2010)
10. Veleshchuk, V.P., Vlasenko, O.I., Vlasenko, Z.K., Gnatyuk, V.A., Levytskyi, S.N.: Dependence of the CdTe melting threshold on the pulse duration and wavelength of laser radiation and the parameters of non-equilibrium charge carriers. *Ukrainian J. Phys.* **62**(2), 159–165 (2017)

11. Adachi, S.: Optical Constants of Crystalline and Amorphous Semiconductors: Numerical Data and Graphical Information. Springer Science + Business Media, New York (1999)
12. Koyama, R.Y., Smith, N.V., Spicer, W.E.: Optical properties of indium. *Phys. Rev. B* **8**(6), 2426–2432 (1973)
13. Samarskii, A.A., Vabishchevich, P.N.: Computational Heat Transfer. Mathematical Modelling, vol. 1. Wiley, New York (1995)

Nanotechnology

Photon-Coupled, Photoswitchable Protein-Based OR, NOR Logic Gates

Balázs Rakos^{1,2}(✉)

¹ Department of Automation and Applied Informatics,
Budapest University of Technology and Economics, Budapest, Hungary
balazs.rakos@gmail.com

² MTA-BME Control Engineering Research Group, Budapest, Hungary

Abstract. We demonstrate from a theoretical point of view that the OR and NOR logic gates can be implemented with the application of well-arranged, existing fluorescent photoswitchable proteins, driven by well-designed photon pulses. The building blocks of the proposed molecular architectures are the Dronpa, Padron and mTFP0.7 proteins. The experimental realizability is also discussed in this work.

Keywords: Molecular electronics · Organic electronics · Photoswitchable protein · Logic circuits · Photon coupling

1 Introduction

In order to keep up with Moore's law, micro/nanoelectronics-related technology should eventually reach the molecular dimensions regarding the basic electronic components of computing architectures. Much work has been done in order to propose novel operational principles by which molecular structures could be harnessed for such purposes [1–4]. Due to their advantageous properties, proteins may be possible building elements of logic circuits in the future [5–7].

In a recent paper [8], we proposed novel, universal computing structures consisting of photon pulse-driven, photon-coupled, hypothetical photoswitchable proteins, which may enable us to realize terahertz-frequency, low power consuming and dissipating computing processors one day. Our present work shows that the OR and NOR logic gates can be potentially realized with three different, existing fluorescent photoswitchable proteins, the Dronpa [9], Padron [10] and mTFP0.7 [11] molecules.

In Sect. 2, we provide a brief summary of the properties and operation of photoswitchable proteins. The proposed architectures and their operation are introduced in Sect. 3. The results are discussed, and the study is concluded in Sects. 4 and 5, respectively.

2 Photoswitchable Proteins

Fluorescent proteins are a subclass of proteins capable of emitting radiation with a peak emission wavelength, λ_{em} upon irradiation by light with a well-defined peak excitation wavelength, λ_{ex} . In the case of reversible photoswitchable fluorescent proteins, the

molecule can be reversibly switched between its fluorescent and non-fluorescent states with the aid of proper light pulses with λ_{on} and λ_{off} wavelengths (λ_{on} is the wavelength necessary for switching the protein to its fluorescent state, and λ_{off} switches it back to its non-fluorescent state). Based on [12], the following Table 1 gives a summary of the switching properties of the three photoswitchable proteins, which are the building blocks of the logic gates proposed in the present work.

Table 1. Switching properties of Dronpa, Padron, and mTFP0.7.

Protein	λ_{ex}	λ_{em}	λ_{on}	λ_{off}
Dronpa	503 nm	517 nm	405 nm	488 nm
Padron	503 nm	522 nm	488 nm	405 nm
mTFP0.7	453 nm	488 nm	405 nm	458 nm

The switching mechanism in such proteins is related to conformational changes in their molecular structure. In most cases it is the combined result of trans-cis isomerization of the chromophore, and protonation-deprotonation actions, however, other mechanisms are also involved in other types of photoswitchable proteins. A detailed summary of the operational principle of switching can be found in [12, 13].

Fluorescent photoswitchable proteins have a wide variety of applications, such as tracking of the interactions and movements of proteins, and super resolution imaging [13]. Their utilization, however, is not restricted only to biology-related applications, they might be used in information storage systems and computing architectures in the future [5–8, 13].

3 Dronpa-Padron-mTFP0.7-Based OR, NOR Gates

3.1 Structure and Operational Principle of the OR Gate

The proposed two-input OR gate consists of one Padron, and two mTFP0.7 proteins (see Fig. 1). The mTFP0.7 molecules, which are in their fluorescent baseline, resting states serve as the two inputs, and the Padron protein in its dark, non-fluorescent baseline state in the middle of the arrangement functions as the output.

The operation of the gate is described in the following. The output molecule, Padron is continuously irradiated by light with $\lambda = 503$ nm (excitation wavelength for its fluorescent state, see Table 1). Since originally it is in its dark state, it does not display fluorescence in response to the corresponding irradiation. However, if one or both input proteins (mTFP0.7s in their fluorescent states) are irradiated by a $\lambda = 453$ nm wavelength light (excitation wavelength for the fluorescent state of mTFP0.7), it results in an emission of radiation with $\lambda = 488$ nm wavelength. Since this radiation switches Padron to its fluorescent state, it starts to emit radiation with $\lambda = 522$ nm due to the steadily available $\lambda = 503$ nm irradiation. Therefore the output protein emits radiation only if one or both of the input molecules are irradiated by a proper light pulse. If excitation light on the input molecules and fluorescent light emitted from the output correspond to logic ‘1’, and the absence of light is equivalent to

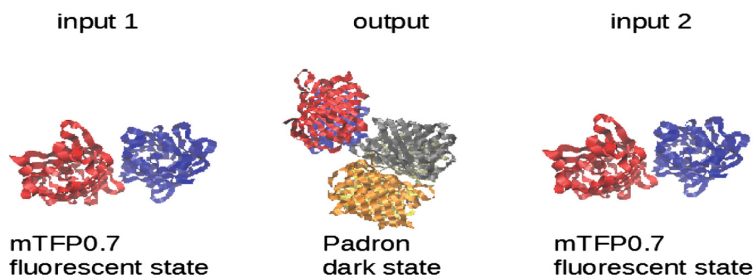


Fig. 1. Arrangement of the mTFP0.7-Padron OR gate. The molecular structures of the proteins were depicted with VMD [14] using their 3D structural data obtained from the Protein Data Bank [15].

logic ‘0’, the operation realizes an OR gate. The gate is ‘reusable’, since Padron eventually relaxes back to its non-fluorescent, dark state, the gate automatically resets itself (it is not even necessary to switch Padron back to its dark state with a proper light pulse, although the relaxation can be hastened with its application).

3.2 Structure and Operational Principle of the NOR Gate

The two-input NOR gate consists of one Dronpa, and two mTFP0.7 proteins (see Fig. 2). The input proteins are identical to those in the OR gate, the output molecule, however, is a Dronpa protein in its fluorescent resting state.

The operational principle of the NOR gate is very similar to that of the OR gate, but in this case the output protein, Dronpa emits radiation with $\lambda = 517$ nm wavelength in its resting, fluorescent state due to the $\lambda = 503$ nm irradiation (excitation wavelength for its fluorescent state, see Table 1). However, if one or both input mTFP0.7 proteins are irradiated by the proper excitation light pulse, radiation from the output will be stopped, since the mTFP0.7 molecules emit radiation with $\lambda = 488$ nm upon excitation, which switches Dronpa to its dark, non-radiative state (the switching behavior of Dronpa is the exact opposite to that of Padron). This gate is also ‘reusable’, since Dronpa also relaxes back to its resting state, which is fluorescent in its case.

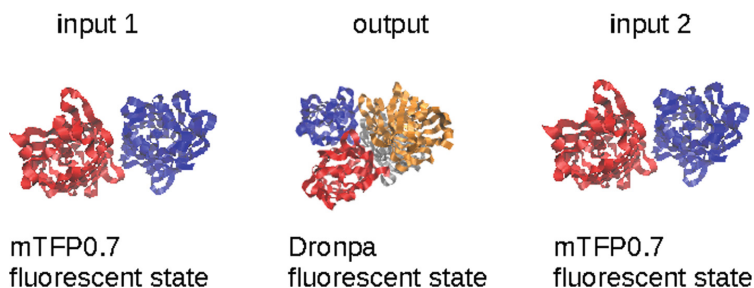


Fig. 2. Arrangement of the mTFP0.7-Dronpa NOR gate. The molecular structures of the proteins were depicted with VMD [14] using their 3D structural data obtained from the Protein Data Bank [15].

3.3 On the Experimental Realization

According to the author's opinion, the proposed structures may be realized and tested with the aid of the current nanofabrication methods and presently available equipment. In the following, we will briefly discuss such possibilities.

Proteins can be fixed on substrates by various procedures (e.g. self-assembled molecular monolayers), just like in the case of Dronpa samples prepared for single-molecule measurements [16]. Furthermore, present day nanofabrication tools and procedures already enable us to arrange molecules next to each other with precision on the order of few nanometers [17]. In this way, mTFP0.7, Dronpa and Padron molecules may be placed on a substrate with the desired arrangements.

The input proteins may be switched individually with the aid of a near-field optical microscope-like setup. Finally, the emitted radiation by the output molecule can be read out in a way similar to [16].

4 Discussion

The significance of the photoswitchable protein-based OR, NOR gates proposed in this work lies in their relatively easy realizability with the currently available tools and methods, since they consist of existing molecules. However, their performance is inferior to the similar, but hypothetical photoswitchable protein-based arrangements proposed in [8]. One of the main drawbacks of the currently introduced structures is their slow response (in the order of milliseconds) [16]. Furthermore, due to our limited choices regarding the already available photoswitchable proteins, the molecules of the proposed gates must be irradiated individually in order to be operational (in [8] we showed that well-designed light pulses acting on an entire logic architecture can operate it if the properties of the individual building blocks are chosen properly). On the other hand, we think that the easier implementability of the proposed architectures far outweighs these drawbacks.

5 Conclusion

In this study, we proposed simple, two-input OR and NOR gate architectures, based on photon-coupled, photon pulse-driven fluorescent photoswitchable proteins. Since the molecular building blocks of the structures are readily available, their experimental realization may be accomplished relatively easily. We hope that the corresponding experiments will be realized in the not too distant future, giving a boost to the related research and development, leading to the potential commercialization of such architectures in the future.

References

1. Körner, H., Mahler, G.: Optically driven quantum networks: applications in molecular electronics. *Phys. Rev. B* **48**(4), 2335–2346 (1993)

2. Lloyd, S.: Programming pulse driven quantum computers. 17 December 1999, [arXiv:quant-ph=9912086](https://arxiv.org/abs/quant-ph/9912086)
3. Csurgay, Á.I., Porod, W., Rakos, B.: Signal processing by pulse-driven molecular arrays. *Int. J. Circuit Theory Appl.* **31**, 55–66 (2003)
4. Rakos, B., Porod, W., Csurgay, Á.I.: Computing by pulse-driven nanodevice arrays. *Semicond. Sci. Technol.* **19**, 472–474 (2004)
5. Rakos, B.: Simulation of Coulomb-coupled, protein-based logic. *J. Autom. Mob. Robot. Intell. Syst.* **3**(4), 46–48 (2009)
6. Rakos, B.: Coulomb-coupled, protein-based computing arrays. *Adv. Mater. Res.* **222**, 181–184 (2011)
7. Rakos, B.: Modeling of dipole-dipole-coupled, electric field-driven, protein-based computing architectures. *Int. J. Circuit Theory Appl.* **43**, 60–72 (2015)
8. Rakos, B.: Pulse-driven, photon-coupled, protein-based logic circuits. *Adv. Intell. Syst. Comput.* **519**, 123–127 (2016)
9. Ando, R., Mizuno, H., Miyawaki, A.: Regulated fast nucleocytoplasmic shuttling observed by reversible protein highlighting. *Science* **306**, 1370–1373 (2004)
10. Stiel, A.C., Trowitzsch, S., Weber, G., Andresen, M., Eggeling, C., et al.: A bright-state structure of the reversibly switchable fluorescent protein Dronpa guides the generation of fast switching variants. *Biochem. J.* **402**, 35–42 (2007)
11. Henderson, J.N., Ai, H.W., Campbell, R.E., Remington, S.J.: Structural basis for reversible photobleaching of a green fluorescent protein homologue. *Proc. Natl. Acad. Sci. U.S.A.* **104**, 6672–6677 (2007)
12. Bourgeois, D., Adam, V.: Reversible photoswitching in fluorescent proteins: a mechanistic view. *IUBMB Life* **64**(6), 482–491 (2012)
13. Zhou, X.X., Lin, M.Z.: Photoswitchable fluorescent proteins: ten years of colorful chemistry and exciting applications. *Curr. Opin. Chem. Biol.* **17**(4), 682–690 (2013)
14. Humphrey, W., Dalke, A., Schulten, K.: VMD - visual molecular dynamics. *J. Molec. Graph.* **14**(1), 33–38 (1996)
15. www.rcsb.org
16. Habuchi, S., Ando, R., Dedecker, P., Verheijen, W., Mizuno, H., Miyawaki, A., Hofkens, J.: Reversible single-molecule photoswitching in the GFP-like fluorescent protein Dronpa. *Proc. Nat. Acad. Sci.* **102**(27), 9511–9516 (2005)
17. Howorka, S., Hesse, J.: Microarrays and single molecules: an exciting combination. *Soft Matter* **10**, 931–942 (2014)

Plasma-Chemical Synthesis of Plasmon Metal-Polymer Coatings, Their Structure and Properties

Alexandr V. Rogachev, Maxim A. Yarmolenko^(✉),
and Alexandr A. Rogachev

F. Skorina Gomel State University, 246019 Gomel, Belarus
{rogachevav, simmak79, rogachev78}@mail.ru

Abstract. The regularities of the formation of plasmon resonant absorption of metal composite polymer coatings from the active gas phase formed by electron-beam dispersion of a mixture of a polymer and a metal salt are examined. The laser ultraviolet assisting action on PMMA additionally activates volatile dispersing products. This leads to an intensification of secondary polymerization processes, the formation of coatings with a lower content of oxygen-containing side groups. Laser action promotes the formation of silver nanoparticles in a coating composition with a narrow size distribution.

Keywords: Polymer coatings · PMMA · Silver nanoparticles

1 Introduction

The method of electron beam formation in a vacuum permits to deposit layers without the use of solution [1–3]. The process of electron beam dispersion can be easily combined with laser assist. This allows the initiation of photochemical reactions in the gas phase generated by the electron beam.

The aim of the work was to study influence treatment of products of electron beam dispersion by laser ultraviolet radiation ($\lambda = 266$ nm) on the molecular structure and morphology of the deposited composite polymer coatings.

2 Experimental

The coatings were deposited from the gas phase formed by the exposure of the target to low-energy electron flow of 800–1600 eV energy and 0.01–0.03 A/cm² density. The coatings deposition process was carried out in a vacuum chamber at the initial residual gases pressure of $\approx 4 \cdot 10^{-3}$ Pa.

Laser assisting of electron beam dispersion of the target was carried out according to the scheme shown in Fig. 1. The source of laser radiation was a laser L-2137U +HG-5. Wavelength of laser radiation $\lambda = 266$ nm. Pulse duration – 6 ns, energy of the laser pulse – 117 mJ, diameter of the laser spot of radiation – 7 mm. The energy of the laser radiation was insufficient to realize the laser dispersion of the material and the notable heating of the target.

The powders of polymethylmethacrylate (PMMA), silver nitrate (AgNO_3 , $\geq 99.0\%$, Aldrich) and their mechanical mixtures in a mass ratio of 1:1 were used as the target material.

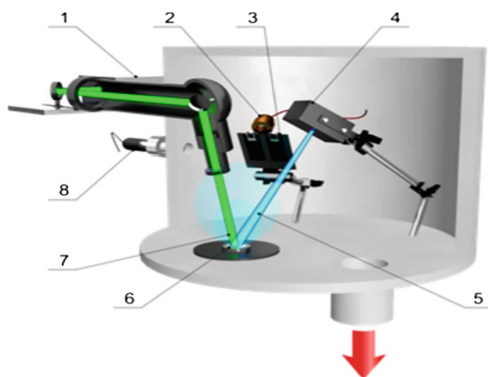


Fig. 1. Scheme of electron beam dispersion of material in vacuum under laser assisting conditions: 1 – laser; 2 – quartz crystal microbalance (QCM); 3 – substrates; 4 – electron beam evaporator; 5 – electron beam; 6 – polymer target; 7 – laser beam; 8 – manometer

Only coatings with the same effective thickness were analyzed.

Substrates during deposition of coatings were quartz plates (for spectroscopic measurements in the visible region), NaCl plates (for registration of IR spectra).

The UV–Vis spectroscopic studies were performed using the Cary-50 (Varian) spectrophotometer. The molecular structure was studied on Vertex-70 (Bruker) IR-Fourier spectrophotometer.

3 Results and Discussion

Initially, the influence of the laser assisting on the structure of the coatings formed by electron beam on the silver salt was investigated. The coating was characterized by a wide plasmon peak (Fig. 2). In the absence of laser assisting there was virtually no absorption in the electronic spectrum of the coating.

The features of the electron beam formation of coatings based on PMMA were considered. It is known that the pyrolysis of polymethylmethacrylate in the temperature range 150–500 °C is accompanied by almost 100% monomer formation. Destruction begins with random break in the polymer chain. The breaking of a polymeric chain leads to the appearance of two free radicals. The radicals subsequently dissociate and form a monomer.

The influence of laser ultraviolet assisting should additionally initiate the processes of breaking according to Norrish type I and II reactions. A consequence of such chemical interactions is the rapid breaking of the polymer chain.

Thus, the formation of PMMA coatings in a vacuum from thermal degradation products of a polymer is possible with the activation treatment of decomposition products. In the process of electron beam influence, this treatment is carried out simultaneously with the process of dispersing the polymer compound. It should be noted that the production of PMMA is usually a result of free radical polymerization of the monomer. The laser assist of the products of the dispersion of a polymer electron beam cannot be an obstacle in the method of depositing a polymer layer.

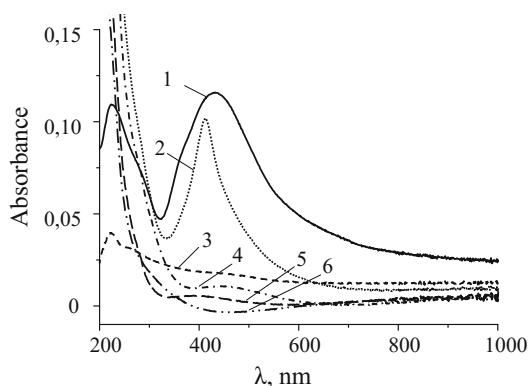


Fig. 2. Electronic spectra of formed coatings: 1 – AgNO_3 coating formed with laser assisting; 2 – PMMA – AgNO_3 coating formed with laser assisting; 3 – AgNO_3 coating formed without laser assisting; 4 – PMMA coating formed without laser assisting; 5 – PMMA coating formed with laser assisting; 6 – PMMA – AgNO_3 coating formed without laser assisting.

In Fig. 3 shows the kinetics of electron-beam polymer dispersion under conditions of absence and laser action on the polymer target. After turning off the power of the electron beam gun, the QCM fixed the process of desorption for a long time. In the conditions of laser assisting, this process was more pronounced and prolonged. The observed phenomenon is due to the presence in the products of electron-beam dispersion of low-molecular compounds that are not capable of polymerization on a substrate.

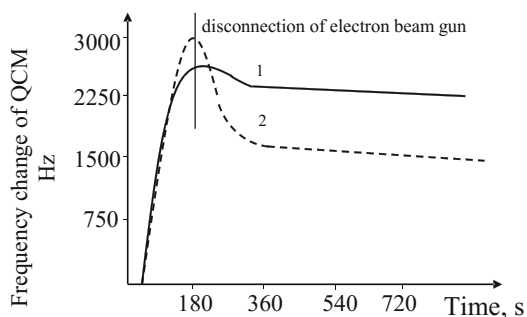


Fig. 3. Kinetics of electron-beam dispersion of PMMA: 1 – without laser assisting; 2 – with laser assisting ($\lambda = 266$ nm).

Figure 4 shows the results of IR spectroscopic studies of the initial polymer and coatings formed from the active gas phase. The most significant differences between the polymer spectra and coatings are:

- The presence for the polymer of absorption in the wavenumber range is $3700\text{--}3400\text{ cm}^{-1}$;
- A significant decrease in the width of the absorption bands of C-H stretching vibrations ($3200\text{--}2700\text{ cm}^{-1}$) in the IR spectrum of coatings in comparison with the IR spectrum of the initial polymer;
- For coatings the shift of the absorption bands at $1900\text{--}1000\text{ cm}^{-1}$ toward lower wavenumber in comparison with the IR spectrum of the polymer is fixed.

Absorption in the wavenumber range $3600\text{--}3000\text{ cm}^{-1}$ indirectly indicates the presence in the initial PMMA of a significant amount of moisture. Confirmation is the presence of absorption at 1640 cm^{-1} (deformation vibrations OH) and at 2130 cm^{-1} .

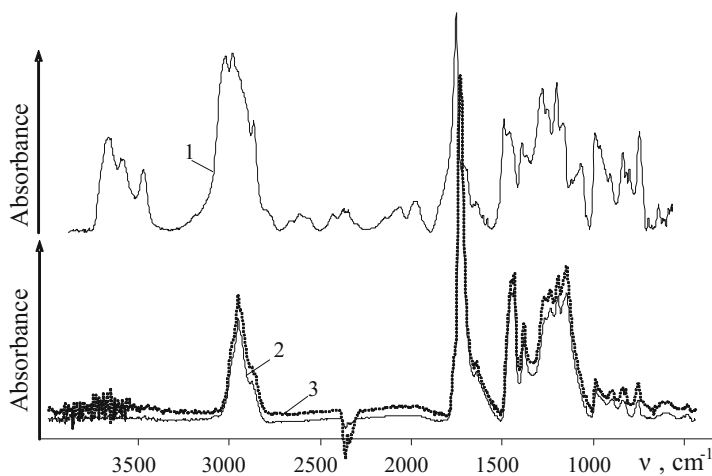


Fig. 4. IR spectra: 1 – initial PMMA polymer; 2 и 3 – PMMA coatings formed without and with using laser assisting ($\lambda = 266\text{ nm}$) respectively.

The observed shift in the absorption bands of oxygen-containing groups toward lower wavenumber is due to intermolecular interaction. Intermolecular interaction is determined by the physical state of the sample. The formation of strong hydrogen bonds leads to a significant decrease in the vibration frequencies of the carbonyl group. So, the molecular structure of coatings is more ordered than the structure of the initial polymer. The decrease in the width of the absorption bands in the valence vibrations region of C-H groups can be a consequence of the formation of a more ordered structure and the processes of detachment of methyl groups under electron beam influence.

Comparative analysis of molecular structures of coatings obtained with and without laser assisting is performed. Attention was paid to the absorption band at 1730 cm^{-1} ,

responsible for the vibrations of the C=O group. This absorption band is composite and can be decomposed into two bands near 1730 and 1705 cm^{-1} . According to the literature, the low-frequency shoulder associate with the absorption of bound carbonyl groups, the high-frequency shoulder associate with the absorption of free carbonyl groups. For coatings formed under conditions of laser assisting and without assistance, D_{1705}/D_{1730} respectively, 0.27 and 0.25. For PMMA powder, there is no absorption at 1705 cm^{-1} . Only the high-frequency shoulder is fixed.

The ratio of the optical densities of the bands at 2950 and 1730 cm^{-1} was analyzed. The absorption at 2950 cm^{-1} is associated with the valence vibrations of C–H in CH_3 . For coatings formed under conditions of laser assisting and without assistance, D_{2950}/D_{1730} respectively, 0.30 and 0.26.

The laser assisting advantage is to reduce the content of carbonyl groups in the molecular structure of the deposited PMMA coating. The cause of this phenomenon can be Norrish reactions initiated by laser radiation. The decrease in the content of oxygen-containing side groups promotes an increase in the mobility of fragments of macromolecules during polymerization. This leads to an increase D_{1705}/D_{1730} .

IR spectra of coatings formed in the process of electron-beam dispersion of a mechanical mixture of polymer and salt are shown in Fig. 5. The spectra contain weakly intense absorption bands (1500–1100 cm^{-1}), characteristic of the initial salt. The laser action promotes the decomposition of the salt.

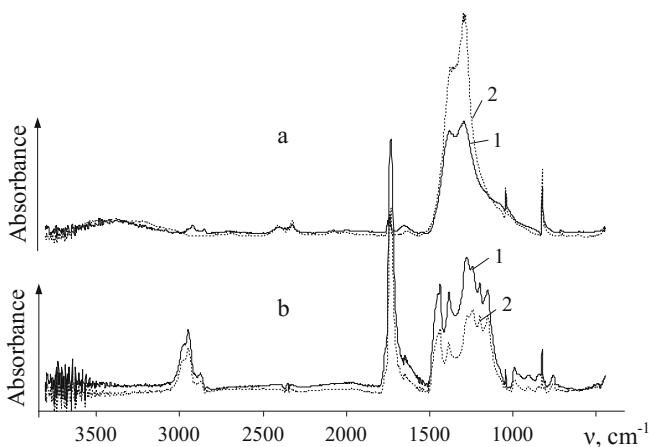


Fig. 5. IR spectra of composite coatings: a – AgNO_3 coating; b – PMMA – AgNO_3 coating; 1 – without laser assisting; 2 – with laser assisting ($\lambda = 266$ nm).

The electronic spectra of coatings are shown in the Fig. 2. Composite coatings formed under laser assisting are characterized by intense plasmon absorption with a maximum near 410 nm. Laser action promotes the formation of silver nanoparticles in a coating composition with a narrow size distribution. In the electronic spectrum of the coating formed without a laser assisting is no evident plasmon absorption.

4 Conclusion

The regularities of the formation of plasmon resonant absorption of metal composite polymer coatings from the active gas phase formed by electron-beam dispersion of a mixture of a polymer and a metal salt are examined. It has been established that the influence of electron beam on a target containing a polymer and a metal salt leads to its decomposition. The laser ultraviolet assisting action on PMMA additionally activates volatile dispersing products. This leads to an intensification of secondary polymerization processes, the formation of smoother coatings with a lower content of oxygen-containing side groups.

References

1. Liu, Z.: Electron-beam deposition of polyethylene composite coatings at various initiators and inhibitors. *Polym. Eng. Sci.* **52**, 2134–2139 (2013)
2. Sun, J.: Nanocomposite coatings based on copper and the products of polyethylene destruction, features of their formation, structure and antibacterial properties. *RSC Adv.* **6**, 29220–29228 (2016)
3. Qi, C.: Nanocomposite coatings for implants protection from microbial colonization: formation features, structure, and properties. *Surf. Coat. Technol.* **315**, 350–358 (2017)

Automatic Evaluation of Surface Nanostructuring Using Image Processing

Mihaela Luca¹✉, Adrian Ciobanu¹, Silviu-Ioan Bejinariu¹,
Anca Ignat², Claudia Teodora Teodorescu-Soare³, George Stoian⁴,
and Dumitru Luca³

¹ Institute of Computer Science, Romanian Academy, Bd. Carol I, Nr. 8,
700505 Iași, Romania

mihaela.luca@iit.academiaromana-is.ro

² Faculty of Computer Science, “Alexandru Ioan Cuza” University,
Str. General Berthelot, Nr. 16, 700483 Iași, Romania

³ Faculty of Physics, “Alexandru Ioan Cuza” University,
Bd. Carol I, Nr. 11, 700506 Iași, Romania

⁴ National Institute of Research and Development for Technical Physics,
Bd. Mangeron 47, 700050 Iași, Romania

Abstract. Automatic assessing of morphological ordering of nanostructured surfaces was performed by employing several techniques of image processing. We used a set of top-view images of pristine TiO₂ nanotube, arrays prepared by anodization in ammonia-based electrolytes of a Ti surface. We have designed procedures to automatically evaluate the overall repeatability of morphological features. Using adaptive thresholds to obtain the contours of the nanostructures (nanotubes), we managed to compute the percentages featuring the nanotubes presence in order to compare the probes. We quantitatively assess the titania nanotube arrays structures in terms of spatial (morphological) ordering using several image processing procedures, trying to alleviate the computing burden related to the characterization of large area samples.

Keywords: Nanotubes · Image processing · Texture features selection · Watershed transform

1 Introduction

Titania materials are, since long, one of the most intensively studied subjects in materials science, due to their unique combination of convenient physical and chemical properties. All of these properties converge towards the development of applications in environment protection, medicine, various industries and energy conversion [1]. Pristine titania materials feature remarkable chemical and thermal stability, mechanical hardness, optical transparency in the visible range, high refractive index, photocatalytic activity and bactericidal ability related to photoinduced oxidation capability [2]. Under UV irradiation, when incident photon energy is larger than the material's band gap, the titania surface earns properties of super-hydrophilicity, self-cleaning, antifogging and self-sterilisation [3].

Modification of TiO₂ materials by doping with various chemical elements further enhances the materials performances and applications. A special interest occurred during the last decades for nanostructured TiO₂ materials as titania nanotube arrays (TNA), prepared by various techniques. Among them, electrochemical corrosion of Ti surface is accompanied, in specific conditions, by a self-organization process in which the oxide develops as highly ordered nanotubes with adjustable geometrical characteristics. By proper choice of electrolyte content, discharge current and duration, TNA with controlled characteristics can be synthesized [4].

For basic and technological reasons, quantitative assessment of TNA geometric repeatability over large surface/volumes is of paramount importance, when materials homogeneity is required. In this respect, computer-aided image processing is expected to bring valuable information in terms of processing large chunks of morphology data acquired from high-resolution scanning microscopy images.

1.1 Image Acquisition of Nanostructures

In the present work we used, as sample test objects, a set of top-view high-resolution field-enhanced secondary electron microscopy (FE-SEM) images of several TNA samples. TNA layers were prepared by the oxidation of metal Ti surface via surface anodization in ammonia-based electrolytes [5]. The system used to acquire images was a Cross Beam System (NEON 40EsB) from Carl Zeiss with electron beam resolution of $1.1 \div 2.5$ nm and magnification ranging between $12\times$ and $2,600,000\times$. The system was equipped with EDS, SE, in-lens and BSE detectors.

The specimens had homogenous content; therefore no compositional contrast was present in the images. The specimens were imaged at normal incidence, to ensure topographic contrast, exclusively, in the acquired images. The angle of incidence of the beam will usually vary locally, due to surface micro-roughness of the sample surface. This is sensed by the SE detector, which gives direct information of surface orientation with respect to the detector. The voltage used was low enough (5 kV) in order to have detailed image of the specimen surface and a good topographic contrast.

2 Nanotubes Detection by Image Processing Procedures

We devised several procedures to automatically identify specific features of the samples, evaluating data about the array morphology and crystallinity in relation with the photocatalytic activity. In the following paragraphs, two different approaches are presented. The first one uses the Watershed Transform (WST) to detect the area occupied by nanotubes, the second one classifies the images using texture features.

2.1 Watershed Transform - Method and Results

Surfaces evaluation is made mainly by evaluating the area occupied by nanotubes. A convenient solution might be to find the nanotubes using the classical threshold based segmentation. Because the nanotubes are touching each other, their number cannot be evaluated. A good detection of nanotubes can be obtained by applying the WST.

We propose a two-step method for nanotubes detection and evaluation in the SEM images. First, the image is segmented using the WST to detect the items suitable to represent the nanotubes. Then, the detected candidates are analyzed using some geometrical criteria, to obtain a more accurate classification.

Image Segmentation Using Watershed Transform

A precise detection of nanotubes can be obtained by applying the WST [6]. Considering the input image as a terrain surface and the pixel values as elevation of a terrain in the corresponding positions, WST simulates the water filling of the relief basins using water sources placed in the local minimum positions. During the filling process, barriers are built to avoid basins merging. The process continues while the water level is lower than the highest position of the terrain (the brightest pixel). When the process stops, the created barriers specify the borders of the segmented regions [6–8].

The quality of watershed segmentation depends on the following strategies applied during processing. The first one is related to the touching objects. As it was mentioned before, some barriers are built during the flooding process. This is done by defining some markers – possible barriers, using the distance transform [9].

Because the flooding starts from local minima values, in case of noisy or highly textured images, the objects in the scene can be segmented in more regions (over-segmentation). This is caused by the fact that the local minima gray level values are not correlated to the existing objects in the scene to be segmented [7]. In [7] it is proposed a strategy for merging the resulted regions by using clustering algorithms.

In other approaches and also in this one, the foreground markers established using the distance transform, are used to define the positions from which the flooding process starts. The complete segmentation procedure is resumed in Fig. 1, [8].

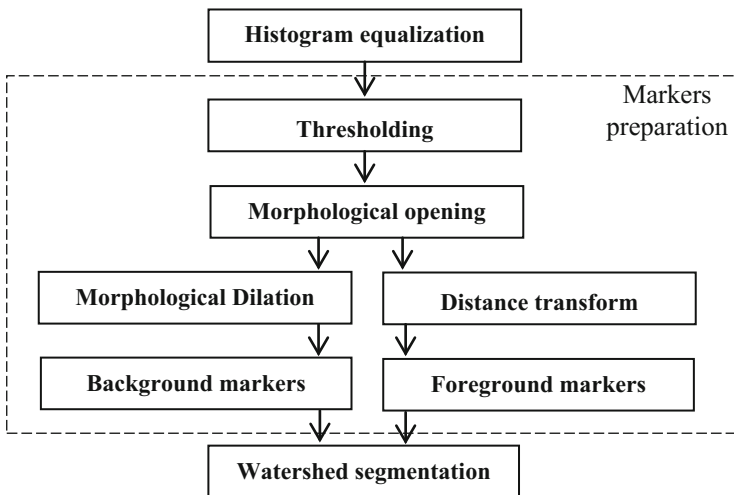


Fig. 1. Structure of the image analysis system [8].

In the first step, enhancement procedures have to be applied: the input nanotube images (Fig. 2) are inverted (obtaining black background and white objects), and a histogram equalization procedure is applied increasing the image contrast (Fig. 3).

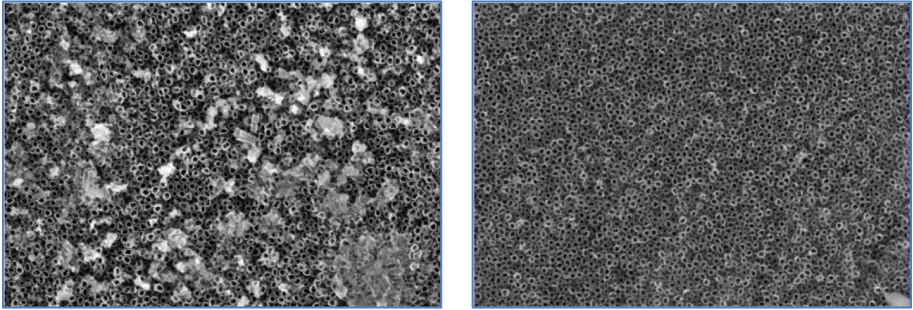


Fig. 2. Original images - obtained at 0.2 kHz, 15 V (left), and 0.4 kHz, 15 V (right).

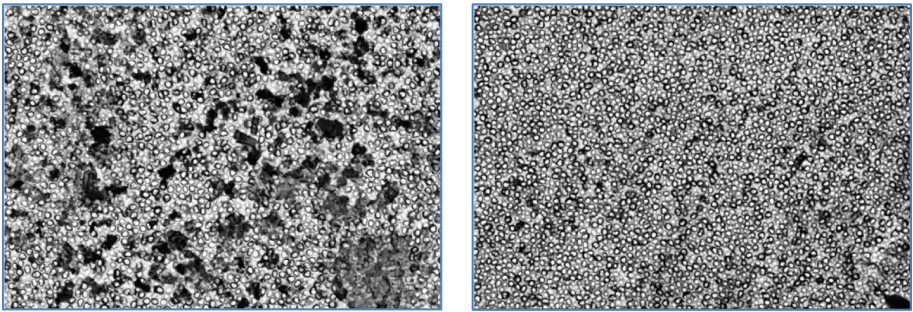


Fig. 3. Histogram equalization on inverted images of the two selected probes (above)

Before applying WTS, the marker image has to be prepared. In the marker image the pixels in image are classified as background and foreground, if possible. The remaining pixels for which the membership to these classes cannot be established are marked as unknown. In order to be able to find the background and foreground markers, the Otsu's binarization method is applied (Fig. 4). It assumes that the image contains two classes of pixels (background and foreground) and the threshold is determined by minimizing the variance within each class [8, 10, 11]. Because the foreground objects are connected and also there is a lot of noise, to remove small objects, morphological opening is applied (Fig. 5).

To detect the background, a morphological dilation which removes the holes is applied (Fig. 6). Black pixels in the resulted image are considered to be the background.

To find the foreground objects and disconnect them, the distance transform is applied to the morphological opening output (Fig. 7) and the distance image is binarized (Fig. 8). The threshold was determined by experiments and usually it is about 5%

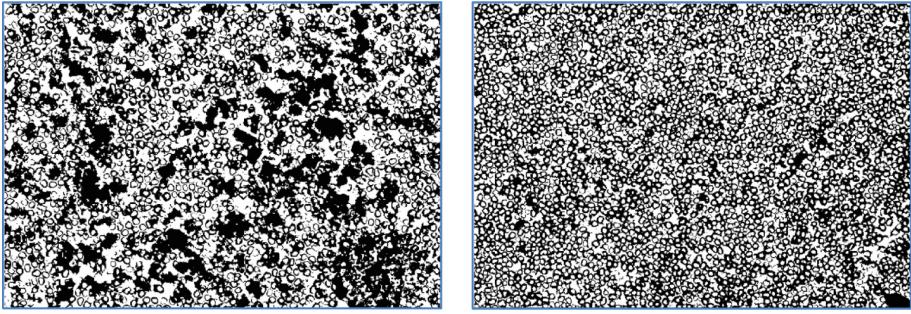


Fig. 4. Otsu segmentation of the two previously selected images

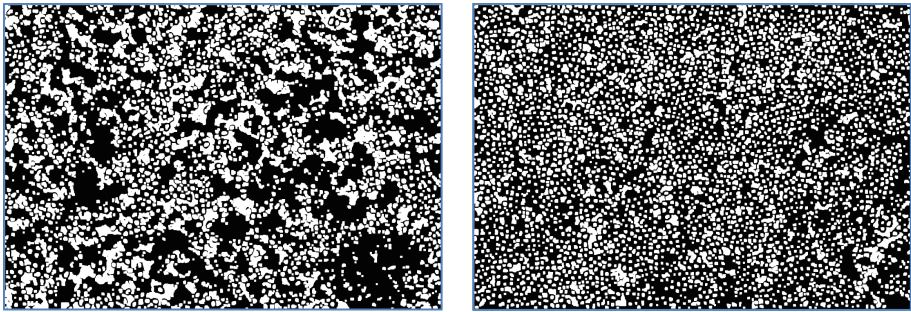


Fig. 5. Opening processed images

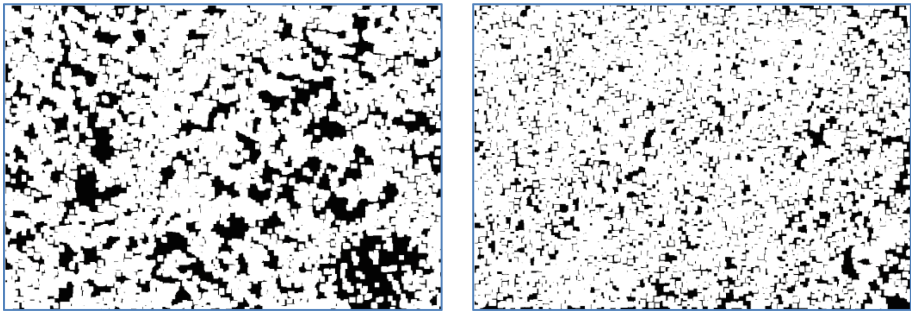


Fig. 6. Background

of the maximum pixel value in the distance image. The image areas that are not classified as background or foreground are denoted as unknown (Fig. 9). The final marker image is depicted in Fig. 10, in which the black pixels are considered background, the white pixels are considered as foreground and the gray pixels are subject of watershed segmentation, to determine the objects limits.

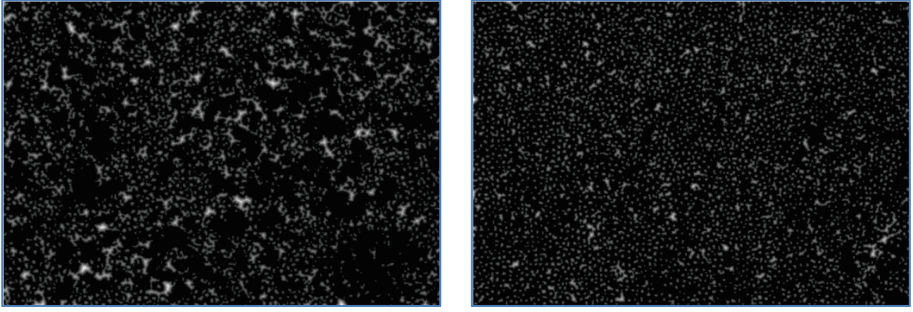


Fig. 7. Distance transform

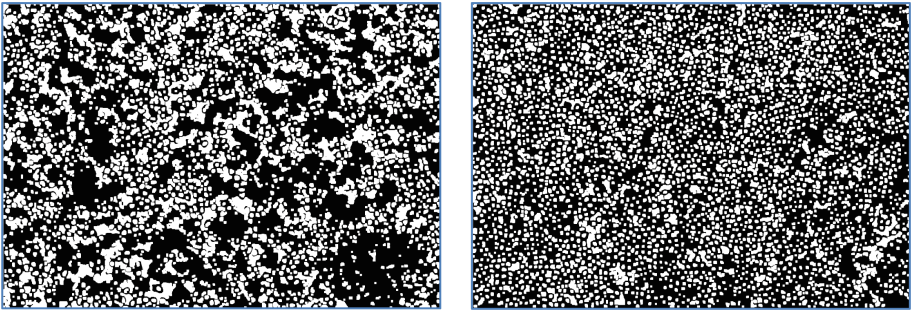


Fig. 8. Foreground

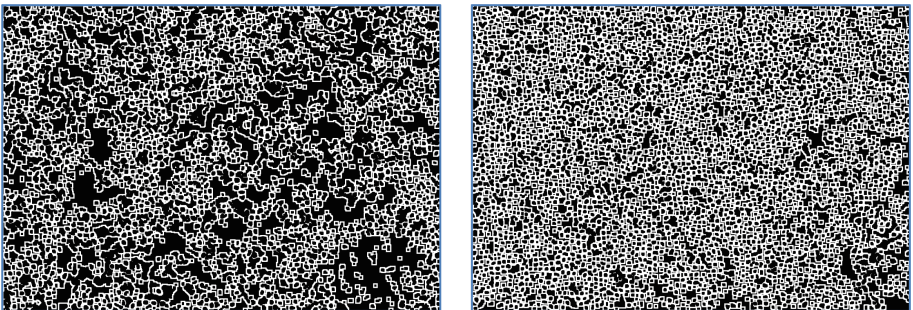


Fig. 9. Unknown pixels

The results of the segmentation procedure are depicted in Fig. 11, in which the contours are overlapped on the input image. As it can be seen, not all the detected objects correspond to nanotubes. Thus, some geometric criteria are applied in order to accept or reject them. The first idea is to check if the shape of each contour is close to a circle by evaluating the value of the ratio between the area and the perimeter.

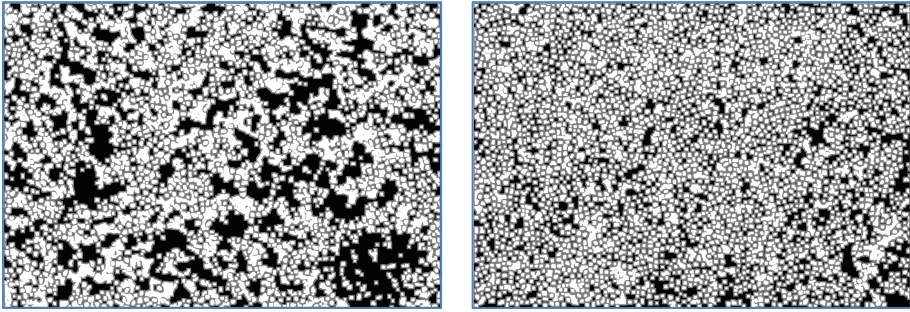


Fig. 10. Marker images

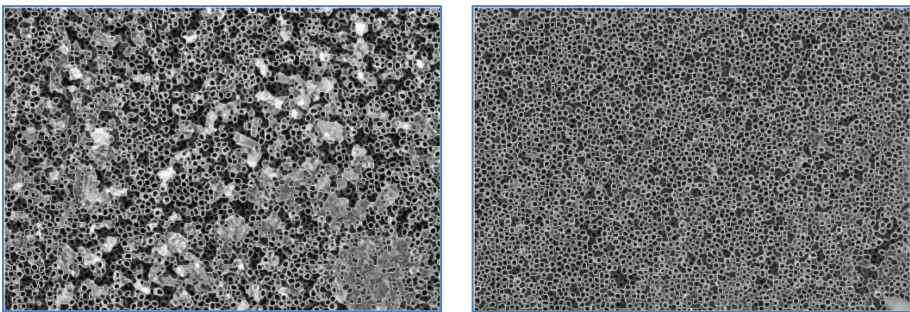


Fig. 11. Segmentation results. Contour of the detected areas is overlapped over the input image

Unfortunately this criteria is not relevant because either the size of objects is too reduced, or there are other large objects for which the condition is met.

The adopted solution was to use two simpler conditions:

- Ratio of bounding box dimensions must be in range [0.6; 1.5]
- Area must be less than an established threshold which depends on the image type.

The results obtained for the two images are presented in table below and in Fig. 12.

Thus, we observe that the preprocessing step of the image is essential and we manage to count the spurious structures (background) and the nanotubes surfaces on a probe (Table 1).

2.2 Texture and Support Vector Machine for Nanotubes Identification

Another possible approach on this kind of nanostructure images is to consider them as a mixed composition of different patches of textures [12], similar to classical textures from the Brodatz album [13] and to use a Support Vector Machine (SVM) [14] to classify their texture features. This classifier provides also, besides the best match class texture, the posterior probabilities that the tested texture belongs to each of the classes from the training set (Fig. 13).

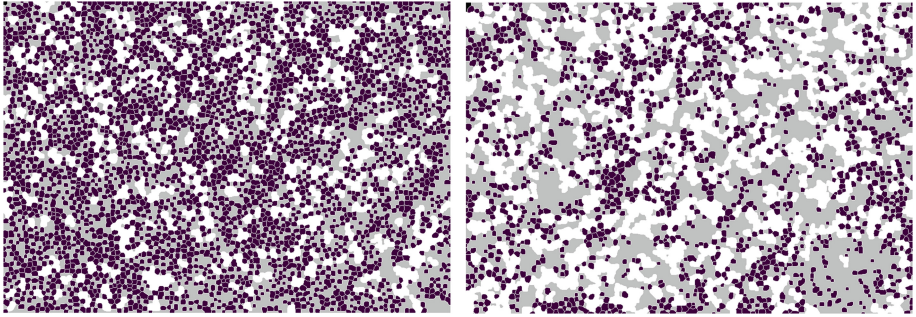


Fig. 12. Final segmentation results: white - background, gray - rejected items, black - accepted items. The images correspond also to the two selected samples shown in Fig. 2.

Table 1. Evaluation of the surface (all values are in pixels)

Total pixels	728064		Total pixels	729088	
Background	252627	(34.7%)	Background	186036	(25.5%)
Rejected	243653	(33.5%)	Rejected	127467	(17.5%)
Tubes	231575	(31.8%)	Tubes	415332	(57.0%)

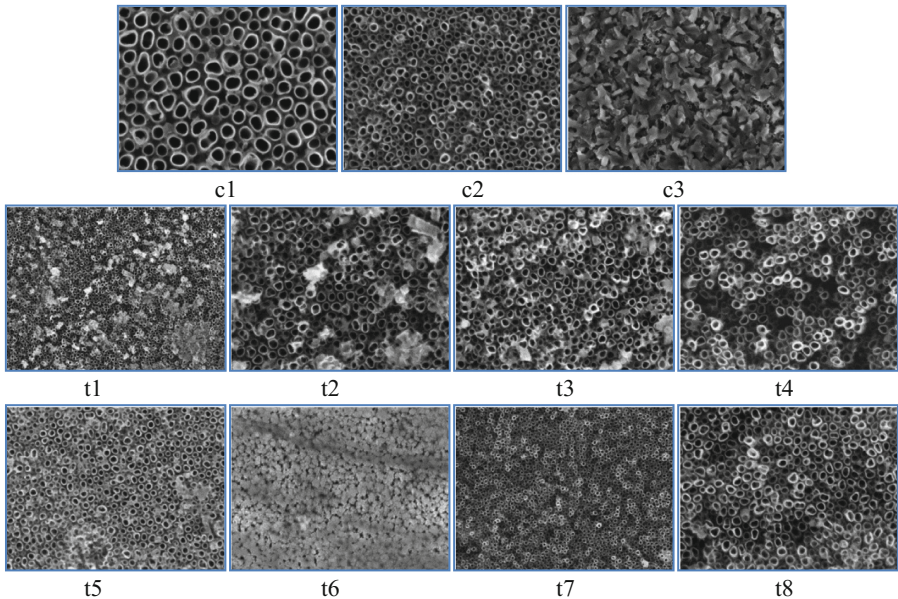


Fig. 13. Training texture samples c1, c2, c3 and the set of nanostructure images to be classified

The texture features were computed with Local Binary Patterns [15]. We have selected three different classes of textures, c1, c2, c3 (c1 and c2 are nanotubes while c3 are spurious surface structures). We computed texture features using training samples

c1, c2, c3 and then on all the images which we characterize, denoted t1 ÷ t8. The results (presented in Table 2) give the proportions of each texture on the chosen samples. In order to form classes from these images, we divided them in blocks of size 256×256 . The tested images were also divided in subimages and the average value for the class membership probabilities was computed.

Table 2. Evaluation of nanosurface structures using SVM on texture features

	c1	c2	c3
t1	22.5838%	31.1687%	46.2475%
t2	24.0894%	45.6697%	30.2409%
t3	29.9821%	56.4385%	13.5794%
t4	26.7677%	62.5379%	10.6944%
t5	2.2692%	92.9440%	4.7868%
t6	0.0000%	0.0998%	99.9002%
t7	13.0332%	59.2060%	27.7608%
t8	35.3091%	55.1788%	9.5121%

3 Conclusions

Using two image processing approaches, we quantitatively evaluate the TNA structures in terms of spatial (morphological) ordering, alleviating the computing burden related to the characterization of large area samples.

The first approach uses the watershed transform based evaluation method, with adequate (usual) image processing procedures and low requirements for complexity and computing resources. Its parameters are automatically tuned and so the operator intervention is minimal. It is implemented in C++ as a Windows application. The processing time is less than one second on a core I3, 2.4 GHz, 6 GB RAM based computer, while 10 images that contain the partial processing results are displayed by the user-friendly interface. A quick visual inspection of its results reveals that the contours of low height nanostructures are not properly detected. Even if they were detected as foreground objects, due to incorrectly detected contours, these regions are rejected by the classifier. A more precise assessment can be made by applying a two level evaluation, in which the rejected regions in the first evaluation are analyzed by a second classifier.

The second approach is based on texture analysis and SVM classification of regions in the nanostructure images. The texture computations were performed with MATLAB on a computer with a core i7, 2.5 GHz processor, 8 GB RAM. Computing the features for the images in the training set and the SVM model took on average 4 s (CPU time). The classification process was done in approximately 3 s per image.

The work presented in this paper is still in progress. The proposed evaluation methods can be improved and their hybridization is also considered in order to maximize the precision of the results. These methods are mainly useful to automatically detect the best method of nanosurface structuring according to the variations of

different parameters; it is useful for quality control assessment of novel materials and optimizing the technology of their production. The two procedures are dedicated to this type of images, yet they might be adapted for other textures, also.

References

1. Schneider, J., Matsuoka, M., Takeuchi, M., Zhang, J., Horiuchi, Y., Anpo, M., Bannemann, D.W.: Understanding TiO₂ photocatalysis: mechanisms and materials. *Chem. Rev.* **14**(19), 9919–9986 (2014)
2. Chen, X., Mao, S.S.: Titanium dioxide nanomaterials: synthesis, properties, modifications, and applications. *Chem. Rev.* **107**(7), 2891–2959 (2007)
3. Thompson, T.L., Yates, J.T.: Surface science studies of the photo-activation of TiO₂ . new photochemical process. *Chem. Rev.* **106**, 4428–4453 (2006)
4. Huang, J.-Y., Zhang, K.-Q., Lai, Y.-K.: Fabrication, modification, and emerging applications of TiO₂ nanotube arrays by electrochemical synthesis: a review, *Int. J. Photoenergy*, Article ID 761971, pp. 1–19 (2013)
5. Teodorescu Soare, C.T., Catrinescu, C., Stoian, G., Luca, D.: Growth of TiO₂ nanotube arrays under dynamic anodization, Photocatalytic activity (2017, submitted)
6. Roerdink, J.B.T.M., Meijster, A.: The watershed transform: definitions, algorithms and parallelization strategies. *Fundamenta Informaticae* **41**, 187–228 (2001)
7. Gonzales, M.A., Cuadrado, T.R., Ballarin, V.L.: Comparing marker definition algorithms for Watershed segmentation in microscopy images. *J. Comput. Sci. Technol.* **8**(3), 151–157 (2008)
8. Bejinariu, S.-I.: Spatial Decision Support Systems. *Memoirs Sci. Sections Rom. Acad.* **XXXVIII**, 67–82 (2015)
9. Felzenszwalb, P.F., Huttenlocher, D.P.: Distance transforms of sampled functions. *Theor. Comput.* **8**, 415–428 (2012)
10. Otsu, N.: A threshold selection method from gray-level histograms. *IEEE Trans. Syst. Man Cybern.* **9**(1), 62–66 (1979)
11. Beucher, S., Meyer, F.: The morphological approach of segmentation: the watershed transformation, in mathematical morphology. In: Dougherty, E. (ed.) *Image Processing*, pp. 433–481. Marcel Dekker, New York (1992)
12. Varma, M., Zisserman, A.: A statistical approach to material classification using image patch exemplars, *IEEE Trans. Pattern Anal. Mach. Intell.* **31**(11) (2009)
13. Brodatz, P.: *Textures: A Photographic Album for Artists and Designers*. Dover Publications Inc., New York (1966)
14. Ben-Hur, A., Horn, D., Siegelmann, H., Vapnik, V.: Support vector clustering. *J. Mach. Learn. Res.* **2**, 125–137 (2001)
15. Ojala, T., Pietikainen, M., Maenpaa, T.: Multiresolution gray-scale and rotation invariant texture classification with local binary patterns. *IEEE Trans. Pattern Anal. Mach. Intell.* **24**(7), 971–987 (2002)

Friction and Adhesion Forces at a Nanoscopic Contact Between Titanium Dioxide Thin Film Surfaces

Lucel Sirghi^(✉)

Faculty of Physics, Iasi Plasma Advanced Research Center (IPARC),
Alexandru Ioan Cuza University of Iasi, Blvd. Carol I Nr. 11,
Iasi 700506, Romania
lsirghi@uaic.ro

Abstract. Magnetron sputtering deposition of titanium dioxide (TiO₂) thin films on commercial AFM probes (silicon nitride) and silicon wafer substrates was employed to fabricate surfaces with controlled wettability. The wettability of the TiO₂ covered AFM probe and sample surfaces was improved by UV light irradiation, as indicated by macroscopic measurements of the water contact angle. Then, the friction and adhesion forces at a single-asperity contact between TiO₂ surfaces were measured in air at constant humidity before and after UV light irradiation. An important increase of adhesive and friction forces was observed when the wettability of the AFM tip and sample surfaces was increased. The increase of the friction force cannot be explained solely by the increase of the adhesive force. A friction force associated to the energy dissipation in formation and destruction of an ice-like structure of water at the sliding tip-sample contact is considered in order to explain the increased friction force observed at the contact of the hydrophilic TiO₂ surfaces. Infrared adsorption spectra of a thin water layer captured between two superhydrophilic TiO₂ surfaces suggested a solid-like hydrogen bonding structure of the water adsorbed on the superhydrophilic surfaces. Formation of such water structure increases the shear stress of the water at nanoscopic contacts and causes a corresponding increase of the contact friction force.

Keywords: Nanoscopic contact · Nanoscopic friction · Adhesion · Titanium dioxide · Superhydrophilic surfaces

1 Introduction

The development of atomic force microscope with its unique ability to measure tiny normal and lateral forces allowed a multitude of experiments on friction at a scale that can go down to the atomic resolution [1, 2]. The atomic force microscopy (AFM) experiments performed in the ambient air showed that the humidity and wettability of the solid surfaces in contact are decisive factors for the microscopic friction [3–5]. However, the underlying physics of the absorbed water effect on the friction and adhesion forces is not well understood. The experiments revealed a complex dependence of the adhesive [6] and friction forces [7] at microscopic contacts on the air humidity. While

the effect of the humidity on the adhesive force can be explained by the capillary and superficial tension forces of the water neck formed at the microscopic contacts by capillary condensation of water vapor [8], the explanation of the effect of humidity on the microscopic friction force is not straightforward. In an attempt to explain this effect, Fogden and White [5] proposed a simple model that accounts for enhancement of the solid-solid friction force caused by the adhesion force generated by the capillary condensed water at the microscopic contacts. Recent investigations of the adsorbed water effect on the microscopic friction pointed to the role that the solid-like structure of thin water layers on the solid surfaces may have on the friction force [9]. Therefore, the ice-like hydrogen bonding in the capillary neck of water formed around a nano contact may increase the contact friction force.

The present work reports the results of an AFM study of the friction force dependence on the surface wettability at constant air RH. Commercial AFM probes and silicon substrates covered by ultra thin films of amorphous titanium dioxide (TiO_2) were used in this study. The wettability of the AFM probe and sample surfaces was changed by UV irradiation [10]. The load dependence of the average friction force is determined by processing friction loops acquired at different external loading force values before and after UV irradiation of the AFM sample and probe surfaces. It is shown that the increase of the friction force with the improvement of the surface wettability cannot be explained solely by the increase of adhesion force. Fourier transform infra red (FTIR) absorption spectra is used to prove the solid-like hydrogen bonding in a thin water layer caught between surfaces of UV light-irradiated TiO_2 thin films.

2 Experimental Results and Discussion

The samples used in the friction experiments consisted of ultra thin films of amorphous TiO_2 deposited on silicon wafers [Si(100)] by radio frequency magnetron sputtering deposition in argon-oxygen gas at a pressure of 10 mTorr at a discharge power of 200 W. Details on the deposition process, film characterization and film UV light induced hydrophilicity were published elsewhere [10]. The AFM probes (Olympus, OMCL-TR800PSA-1) were also covered by an ultra thin layer of TiO_2 . In order to decrease the damages generated by positive ion bombardment of the cantilever, the film deposition on silicon nitride AFM probes was performed at low discharge power (20 W). The thickness of the deposited films was measured by ellipsometry and found to be around 10 nm. Measurements of cantilever resonant frequency before and after deposition showed that there was no noticeable change of the force constant of the cantilever (0.57 N/m) as a result of TiO_2 deposition. Investigations by X-ray diffraction (XRD) and reflection high-energy electron diffraction showed that the deposited TiO_2 films were amorphous [10]. UV irradiation of the TiO_2 film surfaces for 10 min improved their hydrophilicity, fact indicated by a decrease of water contact angle from 60° for the surfaces before UV irradiation to about 40° for the surfaces after UV irradiation. Figure 1 shows the topography (left) and friction (right) images of the TiO_2 thin film deposited on silicon substrate.

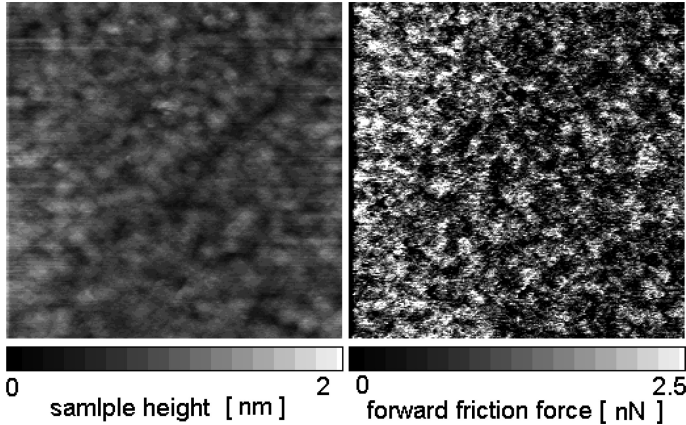


Fig. 1. Typical topography (left) and lateral force (right) images of TiO_2 sample surface. The scanned area is $2 \mu\text{m} \times 2 \mu\text{m}$.

Because of the smoothness (rms roughness was evaluated to less than 0.25 nm) and homogeneity of the TiO_2 thin film surface, the topography-induced variations in the AFM lateral force were negligible small. The average and standard deviation values of the friction force were determined by processing lateral force loops (lateral force versus the forward and backward displacements of the AFM tip at a constant value of the external normal loading force). The typical lateral force loop acquired in these experiments is presented in Fig. 2. Because of the friction, the lateral force jumped between forward and backward values when the moving direction of the tip changed. On average the forward/backward values of the lateral force are with the average friction force value above/below the zero lateral force line. The average value of the friction force was computed by the ratio between the area of the friction loop and the total (forward and backward) displacement of the tip. The fluctuations of the lateral force around the average forward or average backward values were processed to give the standard deviation value of the lateral force. The friction-load dependence was obtained by processing the friction loops acquired at different values of the externally applied normal force (external load, L).

Pull-off experiments were also conducted in order to determine the contribution of the adhesive force, L_0 , to the normal loading force. The friction and pull-off experiments were conducted in atmospheric air at constant temperature (26°C) and relative humidity ($\text{RH} = 32 \pm 2\%$), parameters monitored with a precision hygrometer (HM34C, Vaisala Oyj, Finland). Figure 3 shows the histograms of the pull-off force values determined for 100 points randomly placed on the sample surface. The histograms show that the adhesive force increased by the increase of the wettability of the AFM tip and sample surfaces. Also, it has been noticed a widening of the pull-off force value distribution by the increase of the wettability of the interaction surfaces. The increase of the adhesive force by the increased hydrophilicity may be attributed to the increase of the size of the water neck formed by capillary condensation at the tip-sample contact.

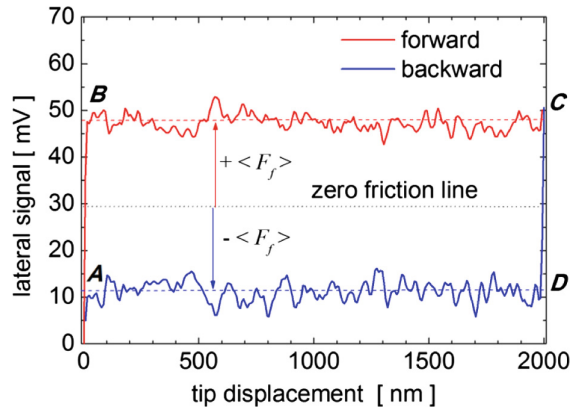


Fig. 2. Typical friction loop.

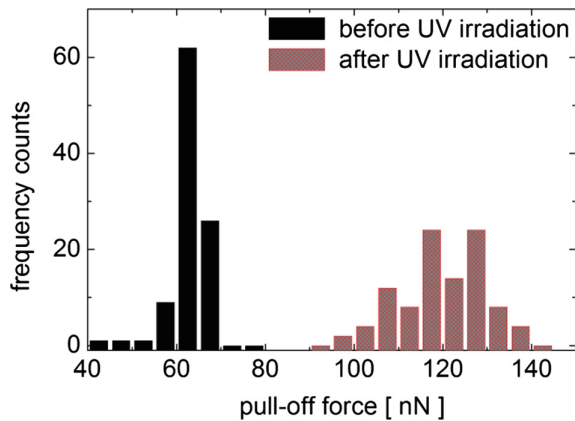


Fig. 3. Histograms of pull-off force values measured for one hundred points placed randomly on the scanned surface for different water contact angle values of the tip and sample surfaces before and after UV irradiation.

Widening of the adhesive force value distribution can be attributed to the heterogeneity of the water film adsorbed on the surfaces. For the UV light-irradiated surfaces, water menisci of a relatively large variety of shapes and sizes may form at the contact of these surfaces with the effect of widening of the pull-off force value distribution. The effect of the surface wettability on friction is illustrated by Fig. 4, which presents the average and standard deviation (error bars) values of the friction force versus the loading force, before and after UV light irradiation of the AFM tip and sample surfaces. To account for the contribution of the adhesive force to the friction force, the total normal loading force, which is the sum of externally applied normal force and the contact adhesive force, was used for the friction-load plots. The adhesive force was taken as the most probable value of the pull-off force values determined in tip-sample

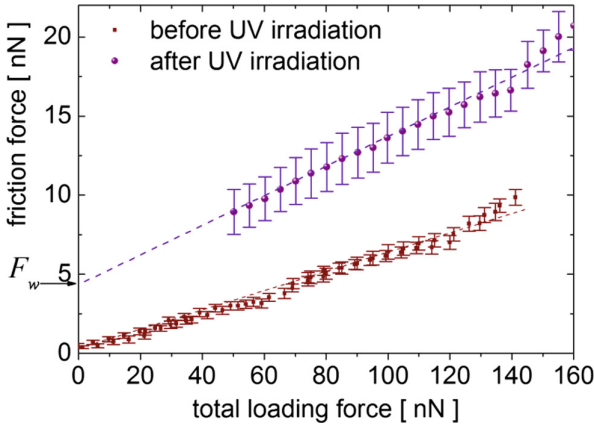


Fig. 4. Friction force versus total loading force (external and adhesion forces) measured before and after UV light irradiation of tip and sample TiO_2 surfaces.

pull-off measurements (Fig. 3). The friction load dependence was linear, fact that may indicate a multiple-asperity tip-sample contact [11]. The friction coefficient increased slightly with the increase of the surface wettability from 0.08 (at tip and sample water contact angles of 60°) to 0.09 (at tip and sample contact angles of 40°). The larger friction force observed for contacts of surfaces with increased hydrophilicity can be explained if one assigns a friction force, F_w , to account for the shear stress in the water neck that surrounds the tip-sample contact [7]. The occurrence of the friction force F_w is indicated by the finite value of the friction force (Fig. 4) obtained by extrapolation of the friction-load curve to zero (when L is negative and equal in absolute value to L_0). The friction-load dependence represented in Fig. 4 can be expressed by:

$$F = \mu \cdot (L + L_0) + F_w \quad (1)$$

where F_w and L_0 increase by the increase of the hydrophilicity of the tip and sample surfaces and μ does not suffer noticeable changes. The increase of L_0 can be justified by the increase of the amount of water condensed at the contact of the surfaces with increased hydrophilicity.

Just before breaking of the tip-sample contact the total loading force is zero and the friction force is generated only by shear stress in the water neck that surrounds the contact:

$$F_w = \tau_w \cdot A_w \quad (2)$$

where τ_w is the shear modulus of the adsorbed water. The shear stress in the adsorbed water may be attributed to ice-like coordination of the hydrogen bonds in a water layer in the vicinity of a solid surface [12]. Figure 5 shows a sketch of the water neck formed by capillary condensation at the tip-sample contact. Let us assume that the hydrophilic surfaces of the tip and sample modify the bulk properties of the water within a layer of thickness h in their vicinity (dark gray area on the sketch). Then the area A_w can be

regarded as the contact area of the two layers of “modified” water on the tip and sample surfaces, respectively. For $h \ll R_t$ (tip radius) simple geometrical considerations (see the inset in Fig. 5) lead to formula $r_2' = (2R_t \cdot 2h)^{1/2}$. Therefore, A_w can be regarded as the area of a circle with the radius r_2' .

$$A_w = 4\pi R_t \cdot h \quad (3)$$

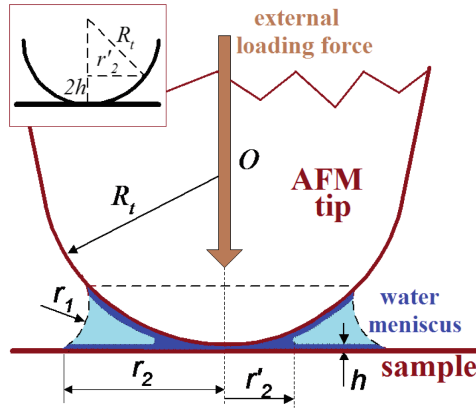


Fig. 5. Sketch of the water neck formed by capillary condensation at the tip-sample contact. The solid-like layers of water on the tip and sample surfaces are shown in dark gray. The inset is showing a sketch of the geometry used for estimation of solid-like water contact area, which is the area of a circle with the radius r_2'

Considering $F_w = 4$ N (for the surfaces with the increased hydrophilicity), $h = 0.5$ nm [12] and $R_t = 40$ nm, a value of 17 MPa is computed for τ_w . This is much smaller than the bulk ice shear modulus, but enough large to be attributed to a solid-like behavior. The friction force F_w for less hydrophilic surfaces is smaller because a decrease of the thickness of “modified” water layer on the solid surfaces and a possible decrease in the water shear modulus. For surfaces with water contact angle of 60° the shear modulus of the adsorbed water can be estimated to a much smaller value (around 1 MPa). The solid-like hydrogen bonding coordination in the water layers on the UV irradiated TiO_2 is proved by FTIR absorption spectroscopy measurements. Figure 6 shows a comparison between infrared adsorption spectra obtained for thin water layers captured between silicon, Si(100), wafers and UV light-irradiated TiO_2 thin films, respectively. The water contact angle for the silicon wafers (with a native silicon oxide surface) was 70° . The FTIR absorption spectrum of water on Si/SiO₂ surface shows a relative broad peak corresponding to the OH adsorption in liquid water (3390 cm^{-1}). The FTIR spectrum for water on the UV light-irradiated TiO_2 thin films shows a convolution of peaks corresponding to OH stretch vibrations in vapor (3754 cm^{-1} , 3657 cm^{-1}), liquid and solid water (3250 cm^{-1}), respectively [13].

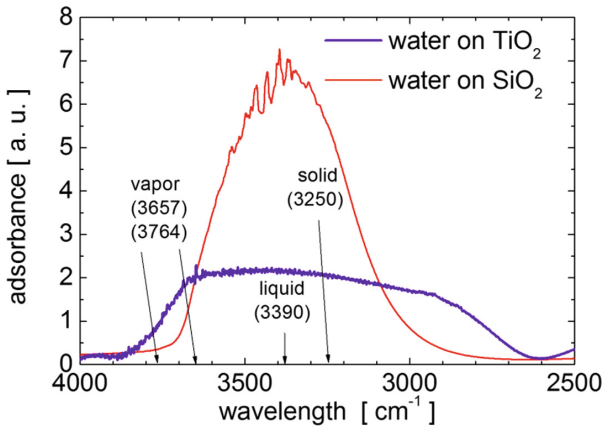


Fig. 6. Adsorption Fourier transform infrared (FTIR) spectra obtained for thin water layers on silicon/silicon oxide and on UV light irradiated TiO_2 thin films.

The large broadness of the OH adsorption peaks observed in this case can be understood if the structure of the water is regarded as one of an amorphous solid (glass) where a short-range coordination of hydrogen bonds causes ice-like adsorption and the occurrence of many OH dangling bonds causes vapor-like adsorption. Such an amorphous solid-like water structure modifies the viscosity and shear stress in the adsorbed water layers on the UV irradiated TiO_2 surface.

3 Conclusion

The dependence of nanoscopic friction on the surface hydrophilicity was investigated by AFM measurements of the friction force between TiO_2 covered AFM tips and samples. The hydrophilicity of the tip and sample surfaces was improved by UV irradiation. The AFM measurements of the friction and pull-off forces have shown an increase of friction force caused by the increase of the hydrophilicity of the interacting surfaces. The dependence of the friction force on the total (external plus internal) loading force was linear and showed a finite friction force value, F_w , for zero total loading force. The force F_w was attributed to the shear stress in the water neck that surrounds the nanoscopic tip-sample contact. Because of the increase of the amount of water condensed at the tip-sample contact and solid-like induced structure of the condensed water, F_w increased by improving of the hydrophilicity of tip and/or sample surfaces. Considering that the solid-like water on the hydrophilic solid surfaces is formed by about two molecular layers, a shear modulus about 17 MPa of solid-like water was estimated. This large value for liquid water is showing the solid-like behavior of the water condensed at the contact between good hydrophilic surfaces. The solid-like behavior of water films on the UV light irradiated TiO_2 surface was confirmed by FTIR adsorption spectra, which showed a convolution of peaks corresponding to OH stretch vibrations in vapor, liquid and solid water, respectively.

References

1. Mayer, E., Overney, R.M., Dransfeld, K., Gyalog, T.: *Nanoscience: Friction and Rheology on the Nanometer Scale*. World Scientific, Singapore (1998)
2. Gnecco, E., Mayer, E.: *Fundamentals of Friction and Wear on the Nanoscale*. 2nd edn. Springer, London (2015)
3. Xu, L., Bluhm, H., Salmeron, M.: An AFM study of the tribological properties of NaCl (100) surfaces under moist air. *Surf. Sci.* **407**, 251 (1998)
4. Rhee, T.H., Shin, M.W., Jang, H.: Effects of humidity and substrate hydrophilicity on nanoscale friction. *Tribol. Int.* **94**, 234–239 (2016)
5. Fogden, A., White, L.R.: Contact elasticity in presence of capillary condensation: I. The non adhesive Hertz problem. *J. Colloid Interface Sci.* **138**, 414–420 (1990)
6. Sirghi, L.: Transport mechanisms in capillary condensation of water at a single-asperity nanoscopic contact. *Langmuir* **28**, 2558–2566 (2012)
7. Sirghi, L.: Effect of capillary-condensed water on the dynamic friction force at nanoasperity contacts. *Appl. Phys. Lett.* **82**, 3755–3757 (2003)
8. Sirghi, L., Nakamura, M., Hatanaka, Y., Takai, O.: Atomic force microscopy study of the hydrophilicity of TiO₂ thin films obtained by radio frequency magnetron sputtering and plasma enhanced chemical vapor depositions. *Langmuir* **17**, 8199–8203 (2001)
9. Tocci, G., Joly, L., Michaelidis, A.: Friction of water on graphene and hexagonal boron nitride from *Ab Initio* methods: very different slippage despite very similar interface structures. *Nano Lett.* **14**(12), 6872–6877 (2014)
10. Sirghi, L.: Plasma synthesis of photocatalytic TiO₂ thin films. *Plasma Sources Sci. Technol.* **25**, 033003 (2016)
11. Gao, J., Luedtke, W.D., Gourdon, D., Ruths, M., Israelachvili, J.N., Landman, U.: Frictional forces and Amontons' law: from the molecular to the macroscopic scale. *J. Phys. Chem. B* **108**, 3410 (2004)
12. Wensink, E.J.W., Hoffmann, A.C., Apol, M.E.F., Berendsen, H.J.C.: Properties of adsorbed water layers and the effect of adsorbed layers on interparticle forces by liquid bridging. *Langmuir* **16**(19), 7392–7400 (2000)
13. Foster, M., Ewing, G.E.: An infrared spectroscopic study of water thin films on NaCl (100). *Surf. Sci.* **427–428**, 102–106 (1999)

Photoluminescence Properties of the Nanocomposites $PEPC/Eu(o-MBA)_3Phen$ and $PEPC/Eu(TTA)_3(Ph_3PO)_2$

O.T. Bordian 

Institute of Applied Physics of the Academy of Sciences of Moldova,
5 Academy Str., MD-2028 Chisinau, Republic of Moldova
bordiano1ea@gmail.com

Abstract. The nanocomposites (NC) tri (o-methylbenzoic acid) 1,10-phenanthroline Europium(III) $PEPC/Eu(o-MBA)_3Phen$ and tris (thenoyl-trifluoroacetone) bis (triphenylphosphine oxide) Europium(III) $PEPC/Eu(TTA)_3(Ph_3PO)_2$ have been studied. ($PEPC$ stands for poly-N-epoxy propylcarbazol, TTA – 4,4,4-trifluoro-1-(2-thienyl)-1,3-butanedione, Ph_3PO – triphenylphosphine oxide and $o-MBA$ – 2-methylbenzoic acid, $Phen$ – 1, 10-Phenanthroline). Experimental results on technology, optical transmission and photoluminescence (PL) spectroscopy are presented. The absorption spectra of thin layers of NCs $PEPC/Eu(o-MBA)_3Phen$ and $PEPC/Eu(TTA)_3(Ph_3PO)_2$ revealed an intensive absorption bands with the absorption threshold at 3.40 and 3.34 eV respectively. The PL spectra of both NCs are similar and show an intense red luminescence with the main maximum at 611–615 nm, as well as other 4 less intensive maxima, situated in the domain 578–750 nm, which are assigned to the transitions of excited electrons ${}^5D_0 \rightarrow {}^7F_i$ ($i = 0, 1, 2, 3, 4$) on energy levels within the $4f$ -shell of the Eu^{3+} ion.

Keywords: Rare-earth · Nanocomposite · Eu^{3+} · Photoluminescence

1 Introduction

The basic properties of lanthanide elements are determined by the optically active electrons $4f$ which form a compressed electronic shell, being protected from the outside with two complete $5s$ and $5p$ shells, which typically are screened of any interaction of the electrons $4f$ and external environment [1]. Therefore, the optical transitions in the $4f$ shell are characterized by narrow absorption and laser-like emission lines. But the spherical symmetry of the Eu^{3+} ion prohibits the optical transitions of electrons in the energetical levels of $4f$ shell [2, 3].

Formation of organic compounds of Europium with different ligands and polymeric nanocomposites causes the distortion of spherical symmetry and removal of the forbidding Laport's rule for energy transitions of the electrons in the $4f$ shell. This idea can be used in the development of optical amplifiers, lasers, light emitting diodes, etc. [4, 5]. Europium compound complexes appear to be attractive in view of the high photoluminescent efficiency and the high monochromatic red emission [1].

Coordination of Eu^{3+} ion with different ligands allows the distortion of its spherical symmetry, the transfer of external excitation energy to the Eu^{3+} ion and, consequently, the increase in luminescence efficacy. In addition, coordination adds protection to the radiation transitions in the 4f electronic shell, to the compatibility of the coordination compound with the various solvents and polymers required for various applications. The maximal number for coordination with Eu^{3+} ion is 12.

Physical properties of the organic compound (efficacy of photoluminescence and volatility) depend on the ligands that are part of the new coordination compounds [1]. From the point view of practical application, it is interesting to investigate the $\text{Eu}(o\text{-MBA})_3\text{Phen}$ and $\text{Eu}(\text{TTA})_3(\text{Ph}_3\text{PO})_2$ coordination compounds and polymeric nanocomposites based on them. Hereafter *o*-MBA and TTA - are anionic ligands and form the first Eu^{3+} ion coordination sphere, and Phen and Ph_3PO - neutral ligands that form the subsequent coordination sphere [6].

2 Experiment and Results

2.1 Thin films preparation

All used reagents had analytical grade and were used without further purification. Synthesis of $\text{Eu}(\text{TTA})_3(\text{Ph}_3\text{PO})_2$ 0.66 g (3 mmol) of thenoyltrifluoroacetone and 0.56 g (2 mmol) of triphenylphosphine oxide were dissolved in 10 ml of warm 96% ethanol and 3 ml of 1 N solution of sodium hydroxide was added. The mixture was stirred, while 1 mmol of Europium chloride in 5 ml of water was added dropwise. A type of light pink precipitate formed immediately. The precipitate was filtered off, washed with small portions of ethanol and diethyl ether, dried thoroughly in air, and the solid of the complex was obtained. Yield was 0.68 g. For $\text{C}_{60}\text{H}_{42}\text{F}_9\text{EuO}_8\text{P}_2\text{S}_3$ calcd, %: $C = 52.53$; $H = 3.09$. Found, %: $C = 52.37$; 52.28 ; $H = 3.18$; 2.98 .

Synthesis of $\text{Eu}(o\text{-MBA})_3\text{Phen}$. A warmed ethanol solution (96%) containing 0.4 g (3 mmol) of *o*-methylbenzoic acid and 0.2 g (1 mmol) of 1,10-phenanthroline was adjusted to pH 6.0–7.0 with 1M NaOH solution. Further, Europium chloride (1 mmol) dissolved in 5 ml of water was added dropwise to the organic mixture and stirred. A light pink precipitate was formed immediately. The precipitate was filtered, washed with small portions of ethanol, dried thoroughly in air. The synthesis yield was 0.56 g (37.6%). For $\text{C}_{36}\text{H}_{29}\text{O}_6\text{N}_2$ it was calculated, %: $\text{Eu} - 20.61$; $C - 58.63$; $H - 3.97$; $N - 3.80$. Found, %: $\text{Eu} - 20.88$; $C - 59.23$; $H - 4.17$; $N - 3.75$.

Molecular structures of coordinative compounds of tris (thenoyltrifluoroacetone) bis (triphenylphosphine oxide) Europium(III) ($\text{Eu}(\text{TTA})_3(\text{Ph}_3\text{PO})_2$), tri *o*-methylbenzoic acid 1,10-phenanthroline Europium(III) ($\text{Eu}(o\text{-MBA})_3\text{Phen}$) and poly-N-epoxypropyl carbazole ($\text{Eu}(o\text{-MBA})_3\text{Phen}$) are represented in Fig. 1.

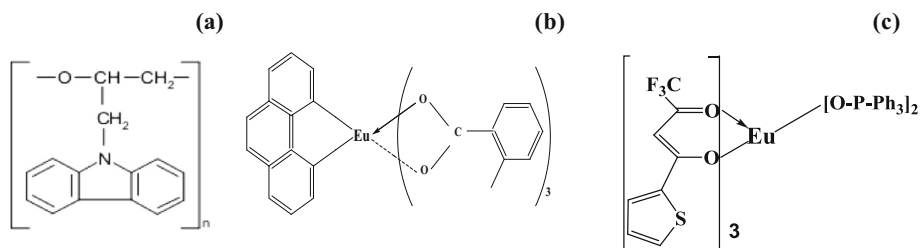


Fig. 1. The schema of chemical structures: (a) PEPC; (b) $Eu(o-MBA)_3Phen$, (c) $Eu(TTA)_3(Ph_3PO)_2$.

Thin layers of the NCs PEPC/ $Eu(o-MBA)_3Phen$ and PEPC/ $Eu(TTA)_3(Ph_3PO)_2$ with various concentrations of $Eu(o-MBA)_3Phen$ and $Eu(TTA)_3(Ph_3PO)_2$ in PEPC were obtained from colloidal solutions on the quartz substrate by the spin-coating method. The layers of NCs PEPC/ $Eu(o-MBA)_3Phen$ were dried at the temperature of 50–60 °C for 24 h, and PEPC/ $Eu(TTA)_3(Ph_3PO)_2$ were dried at room temperature for 24 h [6, 8].

The NCs layers of PEPC/ $Eu(o-MBA)_3Phen$ and PEPC/ $Eu(TTA)_3(Ph_3PO)_2$ after drying are transparent and homogeneous (Fig. 2). For optical transmission investigations a Specord UV/V is (300–800 nm) CARL ZEISS Jena unit was used. All measurements were performed at room temperature.

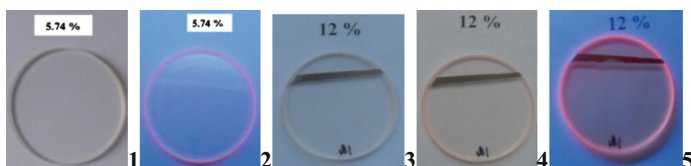


Fig. 2. The images of the NCs (1, 2) $Eu(o-MBA)_3Phen$, (3, 4, 5) $Eu(TTA)_3(Ph_3PO)_2$ deposited on quartz substrates: (1, 3) thin film illuminated with white light, (4) half dark (2) and (2, 5) illuminated with UV light.

PL spectra were measured under excitation of a laser beam 337 or 405 nm using a MDR-23 monochromator and a photon counting module H9319-12 connected to a PC.

2.2 Results

The photoluminescence spectra of the nanocomposite PEPC/ $Eu(o-MBA)_3Phen$ are similar to PL spectra of corresponding $Eu(o-MBA)_3Phen$ powder. The photoluminescence spectra of PEPC/ $Eu(o-MBA)_3Phen$ show strong emission bands centered at 579, 590, 619, 650, 687 nm (Fig. 2a) and 578, 590, 609, 613 and 699 nm (Fig. 2b) [6]. The nanocomposite PEPC/ $Eu(TTA)_3(Ph_3PO)_2$ exhibits a photoluminescence emission in

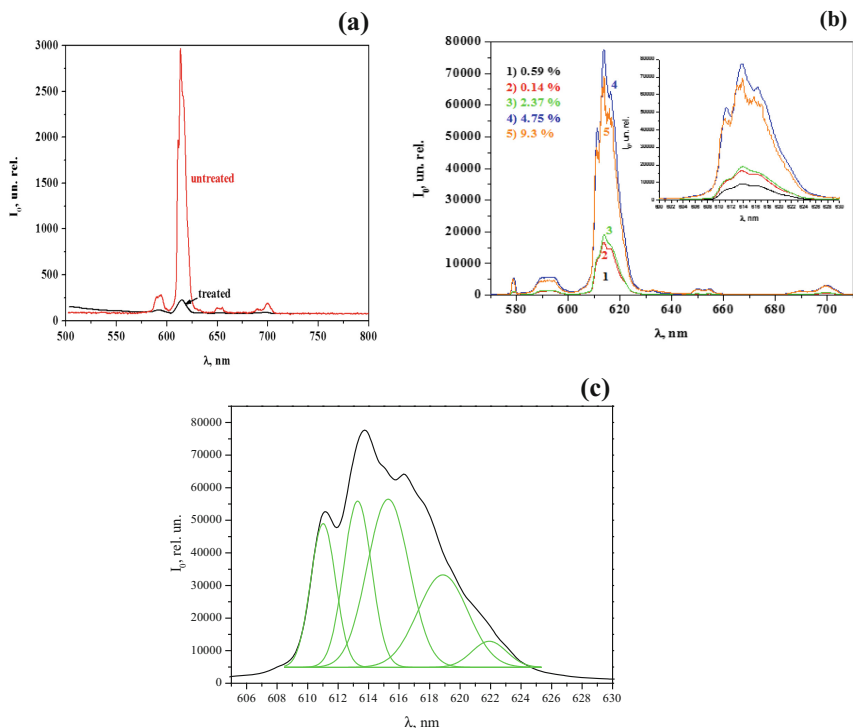


Fig. 3. The photoluminescence of the nanocomposite: (a) PEPC/Eu(*o*-MBA)₃Phen –with UV treatment and without; (b) PEPC/Eu(TTA)₃(Ph₃PO)₂. (c) The deconvolution of the main maximum of PL of PEPC/Eu(TTA)₃(Ph₃PO)₂ (9.3%).

the range 560–750 nm, with the main photoluminescence band at 613 nm, and PEPC/Eu(*o*-MBA)₃Phen–613 nm (Fig. 3).

The splitting of each maximum of luminescence in the fine structure is caused by the influence of the molecular-crystalline electric field of the Eu³⁺ coordination compound. According to the Judd-Ofelt theory [1], the splitting of energy levels is in accordance with the symmetry of the crystalline structure. Otherwise, from the analysis of the luminescence spectrum displacement we can conclude about the type of symmetry that persists in the given material. An indication of the number of crystallographic non-equivalent sites in a Europium(III) β-diketonate complex can be obtained from the number of lines observed for the ⁵D₀ → ⁷F_{*i*} (*i* = 0, 1, 2, 3, 4) transitions [1] based on the splitting numbers of the PL spectrum and the theoretical data for such compounds in NC materials.

According to [1] and the data presented in (Fig. 4c), the coordination compounds Eu(TTA)₃(Ph₃PO)₂ and Eu(*o*-MBA)₃Phen incorporated in the polymer matrices of the NCs PEPC/Eu(TTA)₃(Ph₃PO)₂ and PEPC/Eu(*o*-MBA)₃Phen have a triclinic symmetry. The threshold of optical absorption was determined from the Tauc plot (αhν)^{1/2} vs hν (Fig. 4). The energy values, determined from the absorption data of the polymer and NCs are presented in Table 1.

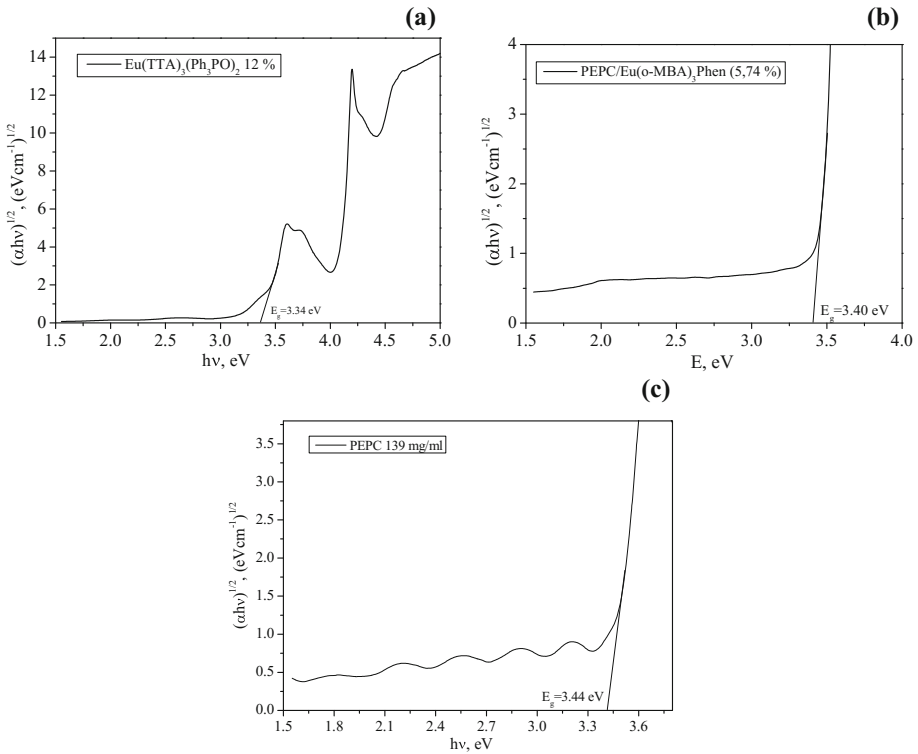


Fig. 4. The threshold of optical absorption in the Tauc's coordinates $(\alpha h\nu)^{1/2}$ vs $h\nu$ for: (a) $\text{PEPC}/\text{Eu}(\text{TTA})_3(\text{Ph}_3\text{PO})_2$ (b) $\text{PEPC}/\text{Eu}(\text{o-MBA})_3\text{Phen}$ and (c) PEPC .

Table 1. The energy threshold in the absorption spectrum

Materials	E_g , eV
PEPC	3.44
$\text{PEPC}/\text{Eu}(\text{TTA})_3(\text{Ph}_3\text{PO})_2$	3.34
$\text{PEPC}/\text{Eu}(\text{o-MBA})_3\text{Phen}$	3.40

The NCs and polymer layers have a thickness of $\sim 1 \mu\text{m}$, from the absorption spectrum of NCs $\text{PEPC}/\text{Eu}(\text{TTA})_3(\text{Ph}_3\text{PO})_2$ and $\text{PEPC}/\text{Eu}(\text{o-MBA})_3\text{Phen}$ are observed an additional bands which allow the transitions in NC to upper bands to excite electrons from HOMO. The energy threshold in the absorption spectrum of the polymer and the NC is shown in Table 1.

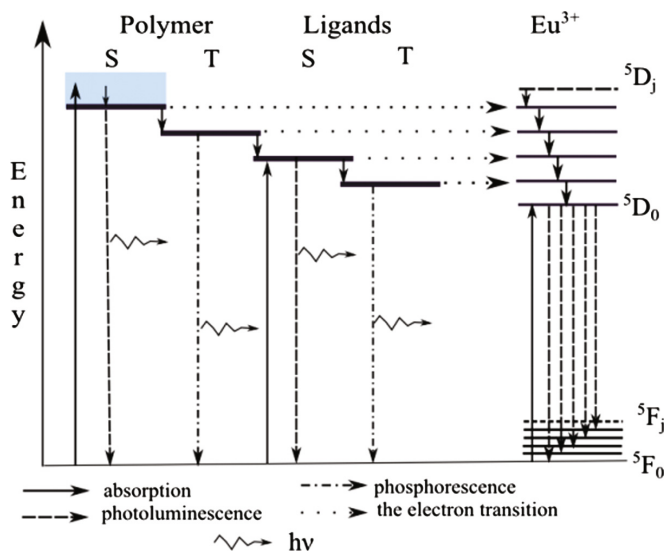


Fig. 5. Illustration of the possible energy transfer to the Eu^{3+} after external UV excitation and photoluminescence in the NCs.

3 Conclusions

Luminescent $Eu(TTA)_3(Ph_3PO)_2$ and $Eu(o-MBA)_3Phen$ and polymer nanocomposites based on them were synthesized.

The FWHM of the main maximums of luminescence of NCs was found to be less than 10 nm for $PEPC/Eu(TTA)_3(Ph_3PO)_2$ and 15 nm for $PEPC/Eu(o-MBA)_3Phen$. All emission bands of the PL spectrum have a specific shape, splitted on five levels.

PL emission of the nanocomposites is due to the so-called “antenna” effect, defined as a light conversion process via an absorption UV energy transfer-emission sequence involving distinct absorption of energy by a polymer and ligands and subsequent energy transfer to Eu^{3+} ions and their final emission. The intensity of the transitions of ${}^5D_0 \rightarrow {}^7F_i$ ($i = 0, 1, 2, 3$ and 4) increases with increasing the concentration of $Eu(TTA)_3(Ph_3PO)_2$ in NC.

The energy differences LUMO– HOMO (Fig. 5) for the ligand and for the $PEPC$ corresponds to the UV absorption domain and are higher than ${}^5D_0 \rightarrow {}^7F_i$ energy transitions ($i = 0, 1, \dots, 4$).

Acknowledgement. This work was supported by the Supreme Council for Science and Technological Development of the Academy of Sciences of Moldova (Project No. 11.817.05.03A and No. 11.836.05.04A), as well as by the Science and Technology Center in Ukraine (Project No. 6117).

References

1. Binnemans, K.: *Handb. Phys. Chem. Rare Earths* **35**, 111–247 (2005)
2. Sanchez, C., Lebeau, B., Chaput, F., Boilot, J.-P.: Optical properties of functional hybrid organic-inorganic nanocomposites. *Adv. Mater.* **15**, 1969–1994 (2003)
3. Carlos, L.D., Ferreira, R.A.S., Bermudez, V., Julian-Lopez, B., Escibano, P.: Progress on lanthanide-based organic-inorganic hybrid phosphors. *Chem. Soc. Rev.* **40**, 536–549 (2011)
4. Liu, H.G., Feng, X.S., Jang, K., Kim, S., Won, T.J., Cui, S., Lee, Y.I.: Influences of compositions and ligands on photoluminescent properties of Eu(III) ions in composite europium complex/PMMA systems. *J. Lumin.* **127**, 307 (2007)
5. Dwivedi, Y., Singh, A., Prakash, R., Rai, S.B.: Preparation and characterization of Tb³⁺ and Tb(sal)₃·nH₂O doped PC:PMMA blend. *J. Lumin.* **131**, 2451 (2011)
6. Bordian, O., Verlan, V., Culeac, I., Iovu, M., Zubareva, V.: Photoluminescence properties of *Eu(o-MBA)₃Phen* organic compound embedded in PEPC polymer matrix. *JOAM* **19**(3–4), 223–227 (2017)

Surface Forces Between Hydrophobic Surfaces Obtained by Self-assembled Monolayers Deposition of Octadecyltrichlorosilane

Alexandra Besleaga, Florentina Samoila, and Lucel Sirghi^(✉)

Faculty of Physics, Iasi Plasma Advanced Research Center (IPARC),
Alexandru Ioan Cuza University of Iasi,
Blvd. Carol I Nr. 11, Iasi 700506, Romania
lsirghi@uaic.ro

Abstract. Hydrophobic surfaces of silicon nitride atomic force microscopy (AFM) probes and silicon wafers (used as AFM samples) were prepared by silanization with octadecyltrichlorosilane (OTS, $C_{18}H_{37}SiCl_3$) molecules. The silanization process included plasma cleaning and hydroxylation of silicon nitride or silicon surfaces and self assembled monolayer deposition of OTS molecules. The surface forces between OTS functionalized AFM tip and sample surfaces in deionized water were determined by AFM force spectroscopy measurements. The measurements indicated a repulsive double layers force caused by electrical charging of OTS surface in water at neutral pH and an attractive hydrophobic force. The distance range and magnitude of attractive hydrophobic force showed a large variability due to presence of conglomerates of polymerized OTS molecules on the OTS modified surface of silicon wafers.

Keywords: OTS functionalized surface · SAM deposition · Atomic force spectroscopy · Double layer force · Hydrophobic force

1 Introduction

Recent improvements in preparation techniques of hydrophobic surfaces [1] combined with ability of atomic force microscope for measuring tiny interaction forces in water for very small interface separation distance values [2] allowed for important advancement in the experimental study of hydrophobic interaction at molecular level [3]. Hydrophobic interaction is the driving force for self assembling of molecules in large supramolecular aggregates in aqueous media, as micelles, vesicles and bilayers [4], and also plays an important role in protein folding [5]. The hydrophobic interaction manifests as an important attraction force between hydrophobic surfaces placed at microscopic separation distance in water. The interpretation of this attraction force emerged from results of molecular dynamic simulations as an entropic force caused by reorganization (and depletion) of hydrogen bonding between water molecules in the water layer caught between the hydrophobic surfaces [5].

Organosilane self-assembled monolayers (SAM) deposition technique has been used to prepare surfaces with various functionalities on glass, quartz or Si substrates.

Particularly, SAM deposition of octadecyltrichlorosilane (OTS, $C_{18}H_{37}SiCl_3$) molecules on silica is used to generate hydrophobic surfaces with high density of hydrophobic CH_3 surface groups. Such modified surfaces have found important applications in the fields of electronics, adhesion, corrosion inhibition, microelectromechanical systems (MEMS), etc. [6]. Particularly, because miniaturization in the MEMS, the surface forces such as capillary force become dominant over gravity and inertia and can cause device failure by stiction. Stiction is a serious problem in applicability of silicon microstructures in MEMS and occurs when the internal restoring forces of microstructures cannot overcome the large attractive capillary forces [7]. Strong capillary forces occur usually at microscopic contacts between hydrophilic silicon surfaces in humid environment [8]. Therefore, the modification of silicon surfaces by silanization to generate surface hydrophobic functional groups may eliminate the effect of humidity on the performances of MEMS.

In the present work, surfaces of silicon nitride atomic force microscopy (AFM) probes and silicon wafers were functionalized by SAM deposition of OTS to obtain AFM probes and samples with hydrophobic surfaces. The hydrophobicity of the functionalized surfaces is investigated by water contact angle measurements, while the compactness and homogeneity of the deposited SAM of OTS are assessed based on topography AFM images of the surfaces. The surface interaction forces between thus functionalized AFM sample and probe surfaces in deionized water are investigated by atomic force spectroscopy measurements.

2 Fabrication of OTS Functionalized Surfaces

2.1 Materials and Methods

Octadecyltrichlorosilane ($CH_3(CH_2)_{17}SiCl_3$, OTS, >90%), toluene (anhydrous 99.8%) and ethanol (>99.8%) were purchased from Sigma-Aldrich and used as received. Distilled water was freshly purified and deionized (electric resistivity > 2 $M\Omega$ cm, pH = 5.6) using an Ultrapure Academic Milli-Q system. The silicon Si (100) wafers (1.5 cm \times 1.5 cm) with a surface roughness of less than 0.05 nm were used as substrate for OTS deposition. Before OTS deposition, the silicon surfaces were cleaned with ethanol in an ultrasonic bath (3 \times 15 min) and then dried. The AFM topography images of OTS modified surfaces was obtained in air and then in water by an atomic force microscope (XE70 from Park Systems, South Korea) with a liquid cell. The AFM measurements in air were performed in tapping mode using a silicon probe (HQ: NSC35/No Al from Micromasch) with the nominal resonance frequency and tip curvature radius of 150 kHz and 8 nm, respectively. The AFM measurements in deionized water were performed in contact mode using OTS modified silicon nitride probes (MLCT from Bruker) with nominal values for resonance frequency of 10–20 kHz and for the spring constant of 0.02 N/m. The surface force measurements in deionized water were performed with the same OTS modified AFM probe on a sample consisting of a silicon substrate with OTS modified surface. The force versus AFM probe

displacement curves were acquired during approach and retraction movements (total displacement of 800 nm with a speed of 1 $\mu\text{m/s}$) of the AFM tip against the sample surface. The cantilever deflection signal was calibrated to the force signal considering a null deformation of the sample surface during force loading of the AFM tip-sample contact.

2.2 Preparation of Hydrophobic Surfaces of AFM Tips and Samples by SAM Deposition of OTS

Prior to SAM deposition of OTS, the silica surfaces were activated (cleaned and hydroxylated) using a dc glow discharge plasma (discharge voltage and current intensity of 380 V and 5 mA, respectively) in water vapor and air mixture at pressure values ranged between 0.2 and 0.5 Torr. Plasma treatment for 10 min resulted in efficient decontamination and hydroxylation of surface, as proved by water contact angle [9] and X-ray photoelectron spectroscopy [10] measurements. The freshly activated surfaces of silicon wafers and silicon nitride AFM probes were then transferred into a Teflon vessel in a 3 mM solution of OTS in anhydrous toluene. The solution was prepared in a glove box to minimize exposure of OTS solution to atmospheric water vapor, which reacts with OTS to form an organo-silicon polymer. The substrates were immersed in the solution for 24 h at 60° to enhance de SAMs deposition, and then washed with toluene to remove residual OTS molecules. The silanized substrates were baked in an oven at 120° for 4 h to complete formation of a Si-O bond, and then stored in low vacuum until use in the AFM measurements. The entire process of silanization is presented schematically in Fig. 1.

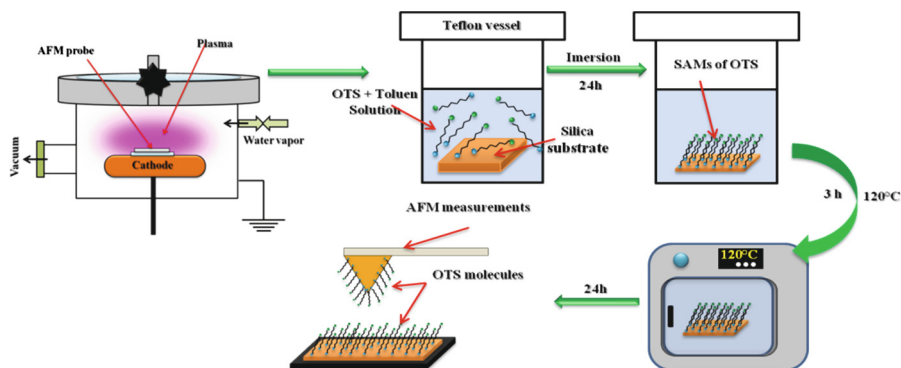


Fig. 1. Schematic representation of the preparation steps used in SAM deposition of OTS on silicon wafers and silicon nitride AFM probes. The steps are: surface activation in plasma, SAM deposition in OTS solution, baking in oven at 120 °C. Finally, the silanized silicon wafers and AFM probes were used for surface force measurements in deionized water.

3 Experimental Results

3.1 OTS Surface Morphology and Hydrophobicity

The surface morphology of OTS modified surface of silicon wafers was characterized by AFM measurements performed in tapping mode in ambient air. The topography image [panel (a) in Fig. 2] shows a relatively heterogeneous surface due to formation on surface of small conglomerates of polymerized OTS molecules. Apart of numerous very small OTS conglomerates (2 nm in height 20 nm in diameter), there are rare larger conglomerates (about 10 nm in height and 100 nm in width). The AFM image taken in contact mode in water [panel (b) in Fig. 2] showed a slightly modified topography because surface hydration and deformation during scanning.

The large OTS conglomerates are clearly visible while the small OTS conglomerates are not well defined on the topography image taken in water. This indicates that

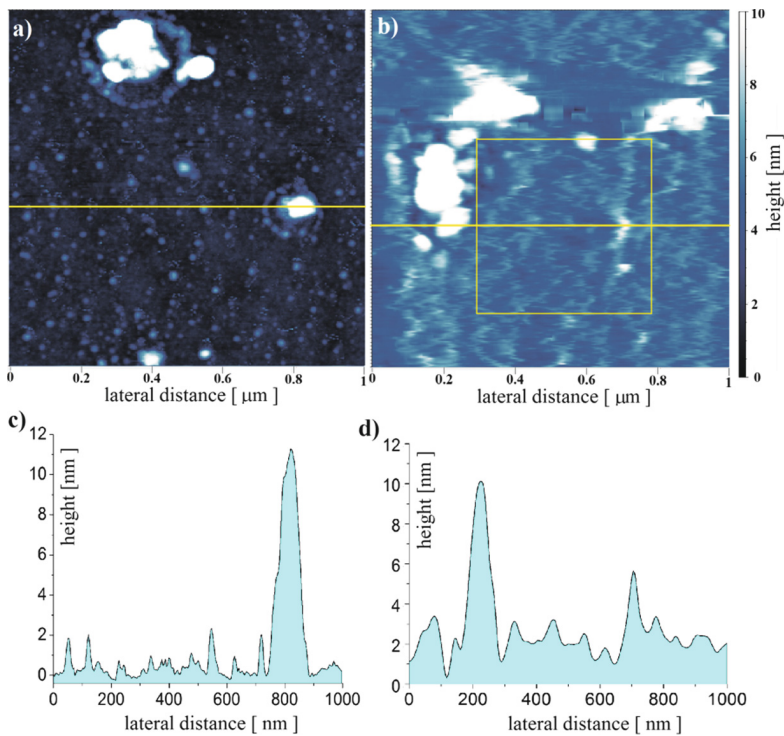


Fig. 2. (a) AFM topography image of OTS modified surface of silicon taken in tapping mode in air. (b) AFM topography image of OTS modified surface of silicon taken in contact mode in deionized water before force curve measurements. The force-displacement curves were taken on an array of 8×8 equidistant points placed in the rectangle ($0.5 \mu\text{m} \times 0.5 \mu\text{m}$) shown by the yellow square on the topography image. (c) Height profile of the OTS surface along the scanning line showed in panel (a). (d) Height profile of the OTS surface along the scanning line showed in panel (b).

the hydrated OTS surface suffer deformation during AFM scanning in contact mode. The characteristic dimensions (height and diameter) of the OTS conglomerates in air and water can be easily determined from the height profiles of the OTS surfaces along scanning lines as those shown in Fig. 2.

The hydrophobicity of the OTS modified surfaces of silicon wafers were characterized by water contact angle (WCA) measurements based on analysis the height profiles of small sessile droplets (1 μl) of deionized water deposited on the silanized surfaces. The OTS depositions on the silicon surfaces increased the surface hydrophobicity, which was evidenced by an important increase of the water contact angle value. However, without the post deposition baking step in the surface preparation, the OTS modified surfaces showed WCA values around 30° . This is an indicator of a poor uniformity and homogeneity of surface coverage with OTS molecules. Backing of substrates with OTS modified surfaces promoted formation of covalent bonds of OTS molecules with the substrate and improved the homogeneity of the OTS modified surfaces, processes that improved substantially the surface hydrophobicity, the WCA reaching a value around 100° . Improving of surface hydrophobicity reached saturation in about 4 h of baking treatment. Figure 3 shows profile images of water droplets on the OTS modified silicon wafers before and after the baking treatment.

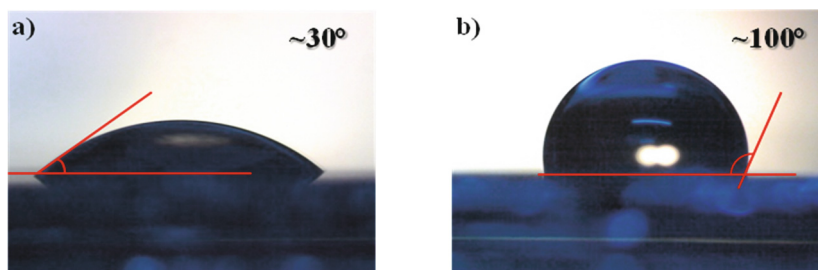


Fig. 3. Profile images of sessile water droplets on OTS modified surfaces of silicon wafers (a) before and (b) after baking treatment.

3.2 Surface Forces Between Hydrophobic OTS Surfaces in Deionized Water

The surface force measurements were performed in deionized water (electric resistivity $> 17 \text{ M}\Omega \text{ cm}$ and $\text{pH} = 5.6$). The AFM sample and probe used in measurements were a silicon wafer and a silicon nitride tip with OTS modified surfaces. The AFM sample was loaded on the liquid cell of the AFM apparatus that was then filled with deionized water. The measurements were done after 20 min, time required for temperature and surface charge stabilization. Three sets of force-distance curves were recorded on an array of 8×8 equidistant points placed on a square ($0.5 \mu\text{m} \times 0.5 \mu\text{m}$) on the OTS sample surface, which is shown by the yellow square on the topography image in Fig. 2(b). The analysis of the total number of 192 force-distance curves showed three main types of curves, i.e. curves showing: (1) no adhesion (hydrophobic) force; (2) small adhesion (hydrophobic) force, and (3) large adhesion (hydrophobic)

force. All types of force-distance curves showed a weak repulsive double layers force, which proved that the OTS surface in water at neutral pH charged negatively [11]. The double layer force can be easily analyzed on force curves that presented no adhesion. Figure 4 shows the typical force-distance curves measured for the approach and retract movements of the tip in the case of negligible tip-sample adhesion forces (no hydrophobic interaction). In this case, the approach and retract curves were practical identical with no visible hysteresis effect. Except separation distance values smaller than 1 nm, the force curves show the typical exponential decay dependence on the separation distance of the double layer repulsive force. This dependence is expressed by the following relationship:

$$F(d) = F_0 \cdot \exp(-d/\Lambda), \quad (1)$$

where F_0 is the double layers electrostatic force at zero separation of surfaces, d , the separation distance between surfaces and Λ , the Debye length. The semi logarithmic plot of the interaction force versus surface separation distance [shown in Fig. 4(b)] determines $\Lambda = 5.4$ nm and $F_0 = 200$ pN.

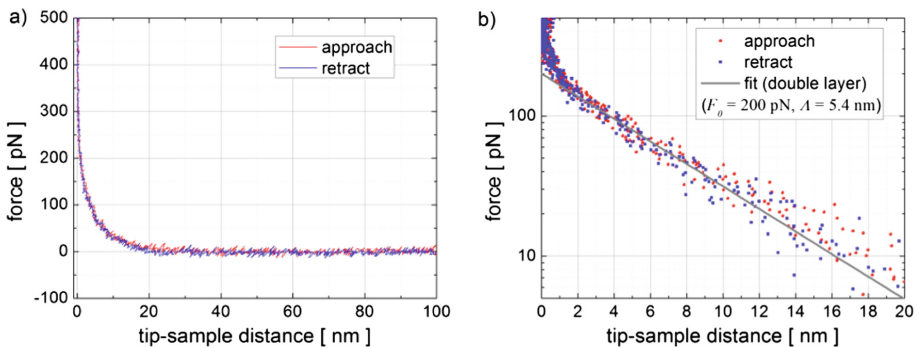


Fig. 4. (a) Force-distance curve showing repulsive double layer force and no adhesion force recorded during the approach (red) and retraction (blue) of a OTS modified AFM tip to and from the OTS surface of a sample. (b) Semi logarithmic plot of force-distance curve showing typical exponential decay of double layer force with the tip-sample separation distance.

Force versus distance curves showing adhesion between OTS modified surfaces of AFM tip and sample exhibit an important hysteresis. This hysteresis is caused by the mechanical work of adhesion between OTS modified surfaces in water. Figure 5 presents typical force versus distance curves showing relatively small [panel (a)] and large [panel (b)] adhesion forces. Typical values of small adhesion forces are in the range of one hundred pN, while typical values of large adhesion forces are in the range of few hundreds pN. The range of the action distance of adhesive forces is not well resolved in these measurements due to the mechanical instability of the AFM cantilever during the retraction movement (indicated by arrows on the plots in Fig. 5).

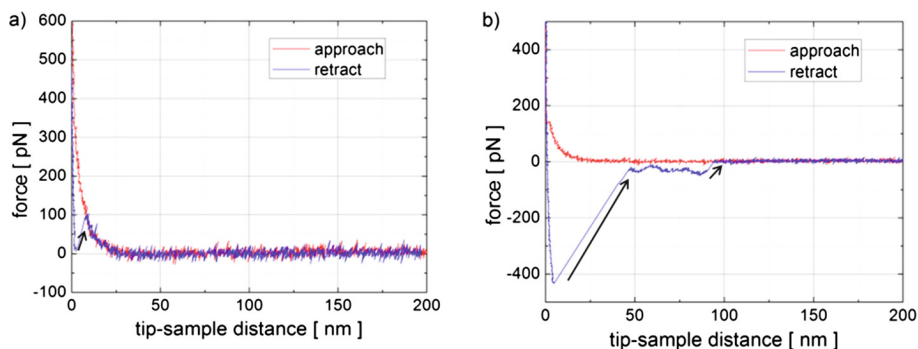


Fig. 5. (a) Typical force-distance curve showing repulsive double layer force during approach (red) and a small adhesion force during the retraction (blue) of a OTS modified AFM tip to and from the OTS surface of the sample. (b) Typical force-distance curve showing repulsive double layer force during approach (red) and a large adhesion force during the retraction (blue) of a OTS modified AFM tip to and from the OTS surface of the sample.

This instability occurs at few nanometers of the tip-sample separation distance. However, for the case of large adhesion forces, multiple instabilities can occur on the same retraction force-distance curve Fig. 5(b). The large dispersion of adhesive force values is own to the presence of conglomerates of polymerized OTS molecules on the sample surface. Because these conglomerates are easily deformable in water, the contact area of the AFM tip-sample contact may change very much as subject of position on the sample surface. Therefore, there are positions on sample surface with no adhesion interaction because the OTS molecules are well packed and bound to substrate, at these positions the OTS surfaces being less deformable and corresponding to a smaller AFM tip-sample contact area. On the other hand, there are places on sample surface where the deformable conglomerates of polymerized OTS molecules determines a large tip-sample contact area with enhanced probability of attractive hydrophobic interaction between OTS molecules. On these places, the adhesive force values recorded during AFM tip retraction movement have large values. Also, as a characteristic of the AFM tip-sample interaction in these positions, is the long distance range of the adhesive force, in some cases significant adhesion force with detachment instability being noticed at AFM tip-sample separation distance values of few hundred nanometers. A tentative explanation for this behavior of the attractive hydrophobic interaction between OTS surfaces in water is illustrated by the sketch in Fig. 6. Thus, long range of action and variable magnitude of the attractive interaction force between OTS surfaces is attributed to hydrophobic interaction during pulling and peeling of OTS molecules in the relatively large packs of molecules caught in the gap between the AFM tip and sample surface. During the AFM tip retraction the configuration of the conglomerate of OTS molecules changes continuously causing change in value of the attraction force with final rupture of the molecular bridge formed between the AFM tip and sample surface.

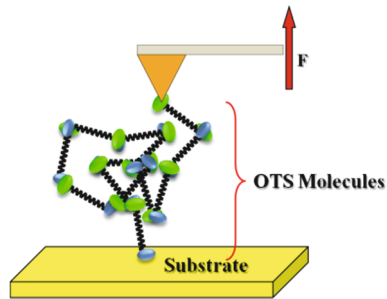


Fig. 6. Schematic representation of molecular OTS bridges formed between OTS functionalized surfaces of AFM tip and sample. The bridges are pulled by the AFM tip during AFM probe retraction movement.

4 Conclusions

Hydrophobic surfaces of AFM probes and silicon wafers (used as AFM samples) were prepared by silanization with OTS molecules. The silanization process included plasma activation of silicon nitride or silicon surfaces, self assembled monolayer deposition of OTS molecules and baking at 120° for 4 h. The OTS modified surfaces of silicon showed good hydrophobicity, the water contact angle being around 100°. The AFM topography images of OTS modified surface of silicon wafers showed presence of numerous small (2 nm in height and 20 nm in diameter) conglomerates of polymerized OTS molecules and rare large (10 nm in height and 100 nm in diameter) conglomerates. Occurrence of these conglomerates had a strong effect on the adhesion forces measured between OTS modified surfaces of AFM probe and samples in deionized water. All the force versus tip-sample separation distance showed a double layer repulsive force due to negative charging of OTS surfaces in deionized water. The force curves showed a large variability in adhesion force measurements. Typically, three types of force curves were recorded on the sample surface: force curves with no adhesion, force curves with weak adhesion (one hundred pN), and force curves with large adhesion (few hundreds pN). This wide dispersion of adhesive force values is own to presence of conglomerates of polymerized OTS molecules on the sample surface. Presence of such conglomerates determines large adhesive forces due to relatively large packs of OTS molecules caught between the AFM tip and sample surface. During the retraction the configuration of these molecular packs changed with noticeable changes in the adhesive force.

Acknowledgement. This work was supported by CNCISIS, IDEI Research Program of Romanian Research, Development and Integration National Plan II, Grant no. 267/2011.

References

1. Knapp, H.F., Stemmer, A.: Preparation, comparison and performance of hydrophobic AFM tips. *Surf. Interface Anal.* **27**, 324–331 (1999)

2. Azadi, M., Nguyen, A.V., Yakubov, G.E.: Attractive forces between hydrophobic solid surfaces measured by AFM on the first approach in salt solutions and in the presence of dissolved gases. *Langmuir* **31**(6), 1941–1949 (2015)
3. Derek, C.M., Acevedo-Vélez, C., Wang, C., Gellman, H.S., Abbott, L.N.: Interaction of the hydrophobic tip of an atomic force microscope with oligopeptides immobilized using short and long tethers. *Langmuir* **32**, 2985–2995 (2016)
4. Israelachvili, J.N.: *Intermolecular and Surface Forces*. Academic, New York (1992)
5. Spolar, R.S., Ha, J.H., Record, M.T.: Hydrophobic effect in protein folding and other noncovalent processes involving proteins. *Proc. Nat. Acad. Sci.* **86**(21), 8382–8385 (1989)
6. DiBenedetto, S.A., Facchetti, A., Ratner, M.A., Marks, T.J.: Molecular self-assembled monolayers and multilayers for organic and unconventional inorganic thin-film transistor applications. *Adv. Mater.* **21**, 1407–1433 (2009)
7. Zhuang, Y.X., et al.: Vapor-phase self-assembled monolayers for anti-stiction applications in MEMS. *J. Microelectromech. Syst.* **16**(6), 1451–1460 (2007)
8. Sirghi, L., Szoszkiewicz, R., Riedo, E.: Volume of a nanoscale water bridge. *Langmuir* **22**, 1093–1098 (2006)
9. Sirghi, L.: *Rom. J. Phys.* **56**, 144–148 (2011)
10. Apetrei, A., Sirghi, L.: *Langmuir* **29**(52), 16098–16104 (2013)
11. Tian, C.S., Shen, Y.R.: Structure and charging of hydrophobic material/water interfaces studied by phase-sensitive sum-frequency vibrational spectroscopy. *PNAS* **106**(36), 15148–15153 (2009)

Nanostructure and Ferroelectric Properties of Sol-Gel SBTN-Films for Electronic Devices

Sergei A. Khakhomov¹, Alina V. Semchenko¹✉, Vitaliy V. Sidsky¹,
Vladimir E. Gaishun¹, Dumitru Luca², Vladimir V. Kolos³,
Vitaliy A. Solodukha³, Alyaxandr N. Pyatlitski³,
and Natalya S. Kovalchuk³

¹ Francisk Scorina Gomel State University,
Sovetskaya Str., 104, Gomel, Belarus

{khakh, semchenko, sidsky, vgaishun}@gsu.by

² Alexandru Ioan Cuza University of Iasi, 11 Carol I Blvd, Iași, Romania
dumitru.luca@uaic.ro

³ JSC “INTEGRAL”, Korjenevsky Str., 12, Minsk, Belarus
{VVKolos, vsolodukha, nkovalchuk}@integral.by,
petan@tut.by

Abstract. The great problem for ferroelectric capacitors is the physico-chemical and mechanical interaction of ferroelectric films with surrounding materials, which leads to degrading of the characteristics of the ferroelectric element, increasing of current leakage and degradation of the transistor structures. Nanostructured ferroelectric films with the general formula $\text{SrBi}_2(\text{TaxNb1-x})_2\text{O}_9$ (SBTN-films) were obtained by sol-gel method and their properties were investigated. We demonstrated that the above-mentioned interaction depends not only on the external parameters, but also on the nanostructural properties of the ferroelectric. A content of niobium of 10 wt.% has the best suited for improving the structure and ferroelectric properties. In such case, grains of a quasispherical shape ($95 (\pm 3) \text{ nm}$) were detected, with a maximum residual polarization ($7.9 \mu\text{C}/\text{cm}^2$), a maximum perovskite phase content (86%), and small sub-roughness (11 nm). Most probably, using materials with 10 wt.% Nb are a good candidate for elements of nonvolatile memory, more effectively than the SBT films. obtain coatings by electron-beam sputtering have been developed and synthesized by a sol-gel method based on a target of SiO_2 , TiO_2 , ZrO_2 .

Keywords: SBTN-films · Ferroelectrics · Nanoparameters · Sol-gel method · Electronic devices

1 Introduction

One of the urgent problems of modern engineering is to obtain a ferroelectric capacitor with various structures. A promising material in the class of ferroelectrics with perovskite structure is strontium bismuth tantalate-niobate $\text{Sr}_x\text{Bi}_y\text{NbzTa}_{2-z}\text{O}_9$ (SBTN). Synthesized layers of this material should be homogeneous in structure and thickness, have good fatigue characteristics (i.e. keep constant under remanent polarization after

repeated inclusion/de-energizing cycles) and to possess small leakage current. The great problem for ferroelectric capacitors is the physico-chemical and mechanical interaction of ferroelectric films with surrounding materials, which leads to decreasing of the performance characteristics of the ferroelectric element, thus increasing of current leakage, and the degradation of the transistor structures [1]. This interaction depends not only on the external parameters, but also on the nanostructural properties of the ferroelectric. It is possible to reduce the annealing temperature to 600 °C, improve the ferroelectric properties, and achieve a higher residual polarization by partially replacing Ta by Nb in the tantalate-niobate bismuth-strontium films (SBTN). The surface characteristics of a nanostructured ferroelectric film are also very important factors affecting the current leakage of capacitors.

In this paper, we report on our investigation of the influence of the niobium contents, synthesis conditions and nature of substances on the nanostructure and ferroelectric properties of sol-gel SBTN-films for FRAM.nuclei of matrix structure.

2 Materials and Methods

Nanostructured ferroelectric films with the general formula $\text{SrBi}_2(\text{Ta}_x\text{Nb}_{1-x})_2\text{O}_9$ (SBTN-films) were obtained by sol-gel method. Gelation took place under the effect of centrifugal force. The films were deposited on Pt/TiO₂/BPSG/SiO₂/Si sublayers by spin-coating at different substrate speeds (500–1000 r/min) or by dip-coating. To achieve the desired thickness (200–300 nm), the sol was applied 2–3 times, followed by heat treatment of each layer at the temperature of 800–1000 °C. Annealing of SBTN-films in order to form perovskite structure was made at 800 °C for 40 min.

3 Results and Discussion

Figure 1 shows the X-ray diffraction patterns of the SBTN films with different niobium contents in the material annealed at 800 °C. For comparison, the X-ray diffraction pattern of the SBT film is also shown. As follows from the intensity and position of the peaks, SBTN film with Nb content of 10 and 20 wt.% is as close as possible to the perovskite structure. As can be seen from Table 1 and Fig. 1, the shape and size of the grain affect the ferroelectric properties of the SBTN films samples.

As it can be seen from Fig. 2 and Table 1, an increase above 20 wt.% in the Nb concentration leads to a decrease in the content of the perovskite phase, as is evidenced by the expansion of the line (115) and a decrease in its intensity at the angle $2\theta \sim 28.9^\circ$. The change in the content of the perovskite phase with the introduction of the niobium ion into the $\text{SrBi}_{2+x}\text{Ta}_2\text{O}_9$ matrix can be explained by the change in the parameters of the crystal lattice, its bond strength and rigidity, and the surface energy of the material. The authors in ref. [2] carried out the corresponding calculations for the $\text{SrBi}_2(\text{Ta}_{1-x}\text{Nb}_x)_2\text{O}_9$ layered system and showed that in the case of doping with niobium or Bi_2SiO_5 , the angle of inclination of TaO_6 octahedrons to the c axis changes, the size of the octahedron decreases along the a and b axes and increases along the axis c , i.e. the parameters of the covalent bond change anisotropically.

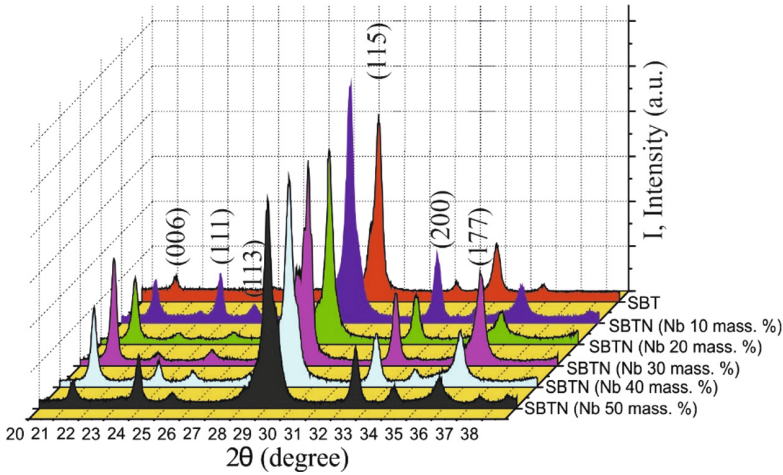


Fig. 1. Transmission spectra of the obtained coatings

Table 1. Nanoparameters of SBT-, SBTN-films

Parameters	SBT						SBTN					
	0	10	20	30	40	50	0	10	20	30	40	50
Nb contents, mass%	0	10	20	30	40	50	0	10	20	30	40	50
Perovskite structure contents, %	65.2	86.3	85.2	77.3	76.4	70.0	65.2	86.3	85.2	77.3	76.4	70.0
Grain size, nm (AFM)	98	95	85	83	96	h = 105 L = 200	98	95	85	83	96	h = 105 L = 200
Crystalline size, nm	22	24	18	19	22	21	22	24	18	19	22	21
Residual polarization, P_r , $\mu\text{K}/\text{cm}^2$	5.9	7.9	7.0	5.1	5.8	2.1	5.9	7.9	7.0	5.1	5.8	2.1

The appearance of anisotropy of the crystal structure leads to a decrease in the content of the perovskite phase in the SBTN film, with an increase above 20% in the niobium impurity content. An increase to 50 wt.% in the content of niobium in the SBTN film leads to the formation of cylindrical grains with an average size of $H = 105 \pm 3$ nm, $L = 200 \pm 3$ nm, which leads to the deterioration of the ferroelectric properties ($P_r = 2.1 \mu\text{C}/\text{cm}^2$).

As it can be seen from Table 1 and Fig. 3, the shape and size of the grain affect the ferroelectric properties of the obtained samples. As it can be seen from the AFM images (Fig. 4) and Table 1, the average grain size increases with the increase of Nb concentration above 30 wt.% and it is about 100–120 nm (the crystallite size in this case is 23 nm). With the content of niobium of 50 wt.% (Fig. 4), the SEM images confirms the formation of cylindrical grains. With the decrease in the Nb concentration to 10–20 wt.%, the surface of the film has a finer grain structure (average grain size about 83–86 nm).

With partial replacement of tantalum with niobium in the SBT film, the crystallite growth rate increases, as evidenced by the increase in their sizes. As it is known, the rate of growth of crystallites, as well as the process of their nucleation, is significantly influenced by the physico-chemical properties of the initial substances. The final size of the crystallites depends on the ratio of the rates of nucleation and subsequent growth.

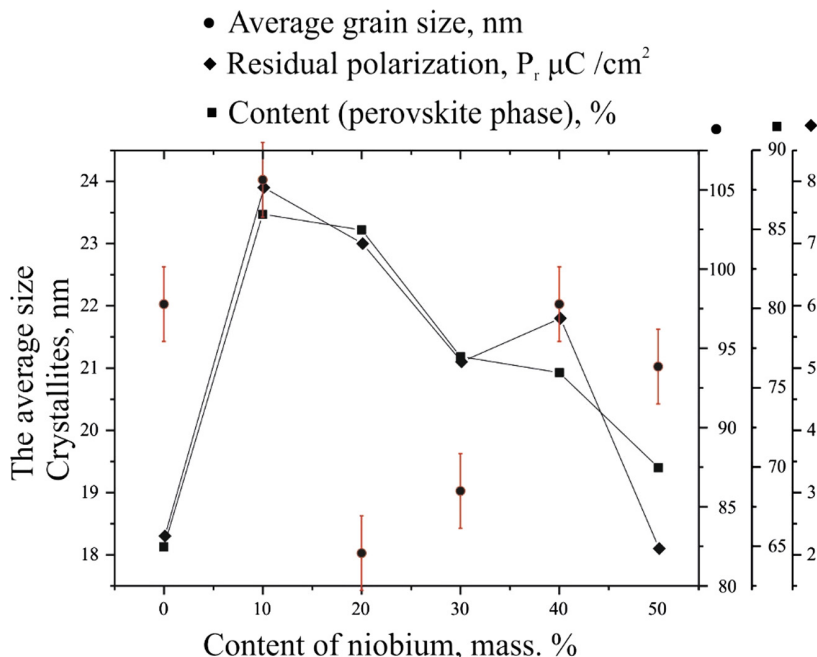


Fig. 2. The dependence of the average size of crystallites, residual polarization, SBTN-film phase content on the niobium content

In the SBT film, the rate of occurrence of the crystallization centers exceeds their growth rate, as a result, the crystallite size is 22 nm (± 1). With partial (10 mass%) replacement of tantalum with niobium, the crystallite growth rate increases, and as a result, crystallites are coarsened to 26 nm, which leads to an improvement in the ferroelectric properties (Table 1).

The increase in the content of the perovskite phase and, as a consequence, the growth of residual polarization in samples with a 10% tantalum impurity content, can also be explained by the expansion of the concentration range of the initial elements at which the perovskite phase is formed. For the SBT system, this region is extremely small in size and is actually shrinking to a point in the Gibbs triangle (Fig. 5).

With partial replacement of tantalum with niobium in the SBT film, the crystallite growth rate increases, as evidenced by the increase in their size. As it is known, the rate of growth of crystallites, as well as the process of their nucleation, is significantly influenced by the physico-chemical properties of the initial substances. The final size of the crystallites depends on the ratio of the rates of nucleation and subsequent growth. In the SBT film, the rate of occurrence of the crystallization centers exceeds their growth rate, as a result, the crystallite size is 22 nm (± 1). With partial (10 mass%) replacement of tantalum with niobium, the crystallite growth rate increases, and as a result, crystallites are coarsened to 26 nm, which leads to an improvement in the ferroelectric properties (Table 1). The increase in the content of the perovskite phase and, as a consequence, the growth of residual polarization in samples with a 10% tantalum impurity content, can also be explained by the expansion of the concentration range of the initial elements at which

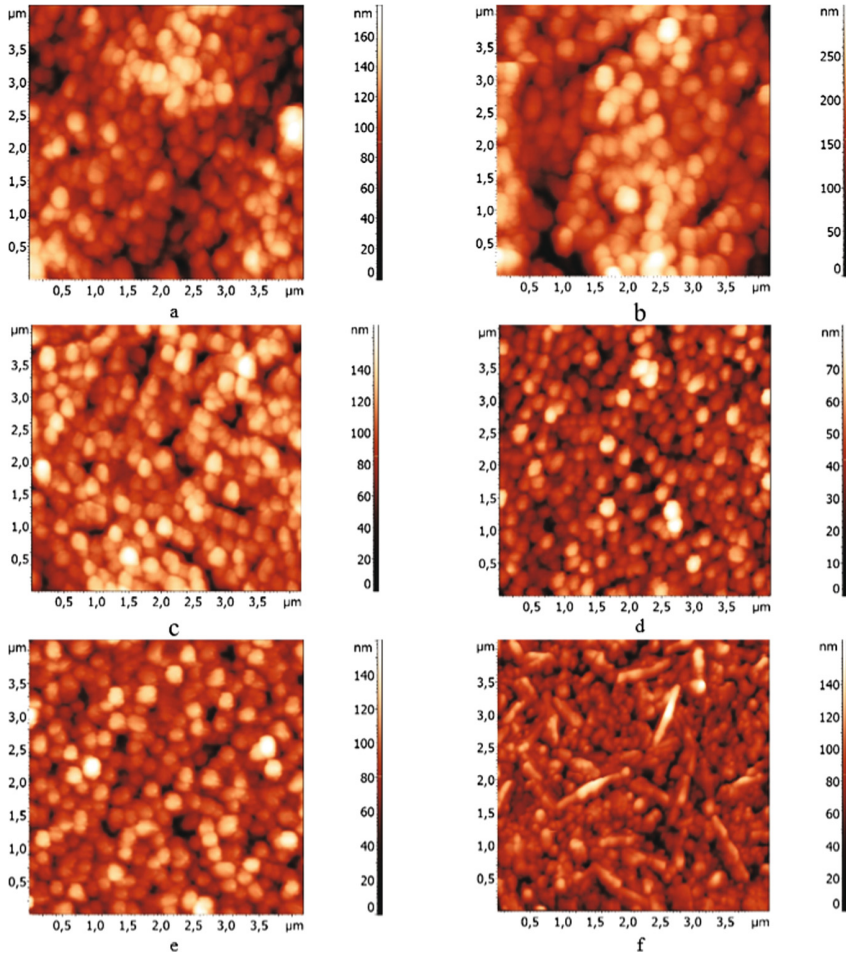


Fig. 3. The AFM-images of the SBT and SBTN-films surface: a – SBT-film, SBTN-films with content of Nb: b – 10%, c – 20%, d – 30%, e – 40%, f – 50%

the perovskite phase is formed. For the SBT system, this region is extremely small in size and is actually shrinking to a point in the Gibbs triangle (Fig. 4).

Compliance with the stoichiometry of the composition is an important factor, since the required properties of the ferroelectric correspond to the formation of the perovskite phase, which occurs only in an extremely narrow range of concentrations of the elements that make up the ferroelectric film. However, it has been established that even when the concentration of elements in the original ash is strictly observed, when the ferroelectric film is formed, the stoichiometry of the composition is disrupted for several reasons [3]. These include the high volatility of bismuth oxide during heat treatment, the dependence of the limiting solubility of metal chlorides on the temperature of the solution, the moisture sensitivity of metal chlorides. These factors are essential for the production of films with a thickness of 300–400 nm.

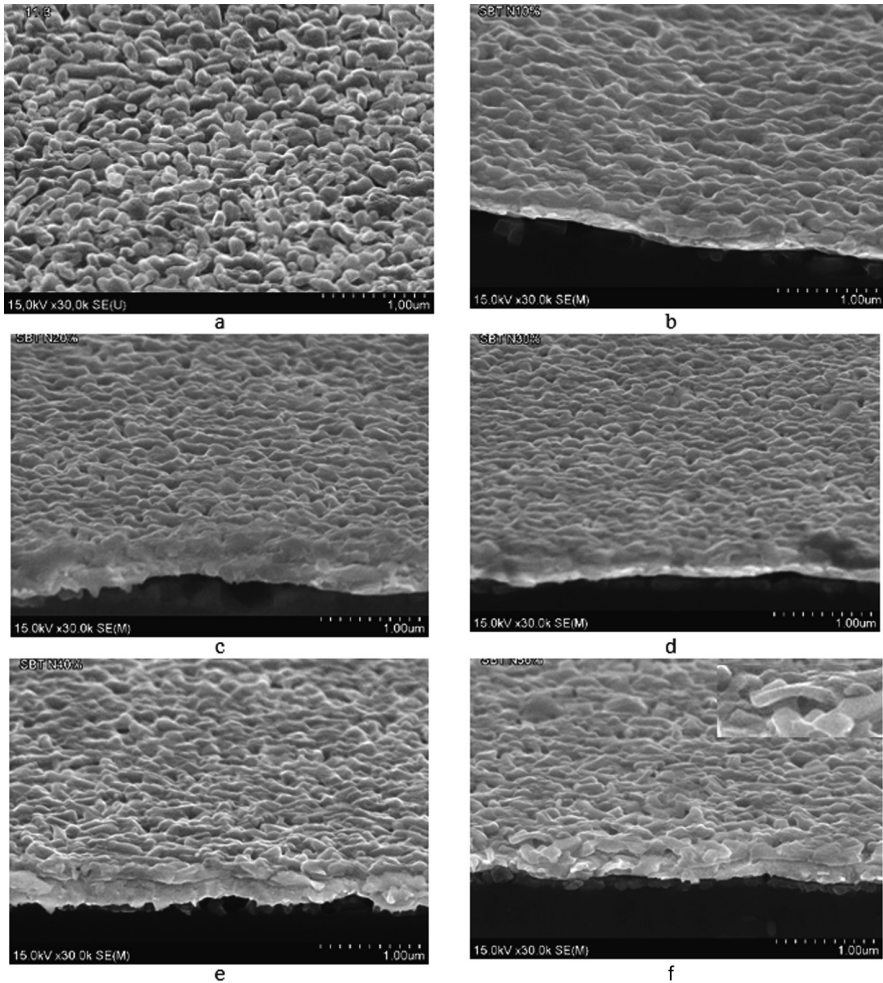


Fig. 4. SEM-images of SBT and SBTN-films: A – SBT-film, SBTN-films with Nb content: b – 10%, c – 20%, d – 30%, e – 40%, f – 50%

In addition, the process of repolarization in individual grains in the SBT (SBTN) film with a crystallite size of 12–20 nm occurs independently [4], which is an additional positive factor in case of the use of ferroelectric in devices with nonvolatile memory. However, a further increase in the concentration of the niobium impurity does not have a significant effect on the crystallite size, due to the different covalent bond strengths of O-Ta-O and O-Nb-O. An increase in the concentration of niobium leads to a decrease in the content of the perovskite phase and a change in the shape of the grains from spherical to cylindrical (Fig. 3e). Therefore, it is likely that the reason for the change in shape is the relative weakening of bonds in the plane of the $\{\text{Bi}_2\text{O}_2\}^{2-}$ layers and their amplification in the perpendicular direction containing the polar groups

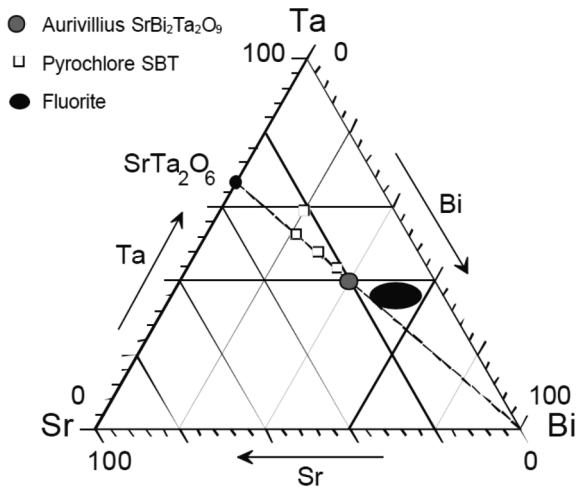


Fig. 5. Triangular phase stability Gibbs diagram in the SBT system

$\{\text{Sr}(\text{Ta}_x(\text{Nb})_{1-x})_2\text{O}_7\}^{2+}$. This anisotropy leads to the growth of predominantly elongated particles in the sample with a 50% niobium content and a decrease in the residual polarization for this sample.

4 Conclusion

The sample with a content of niobium of 10 mass% has the best structure and ferroelectric properties, in comparison with the rest of the samples (Fig. 3). This sample consists of grains of a quasispherical shape ($95 (\pm 3 \text{ nm})$), has a maximum residual polarization ($7.9 \mu\text{C}/\text{cm}^2$), a maximum perovskite phase content (86%), a small sub-roughness (11 nm). Taking into account the SBT- and SBTN-films studied, the use of a sample with a niobium content of 10 wt.% as an element of nonvolatile memory is more effective than SBT-films.

Acknowledgments. The work was supported by Belarusian Foundation for Fundamental Research (Project № T16-RA005) and by the Romanian Academy.

References

1. Tagantsev, A.K., Gerra, G.: Interface-induced phenomena in polarization response of ferroelectric thin films. *J. Appl. Phys.* **100**, 051607–051615 (2006)
2. Eliseev, E.A., et al.: Surface and finite size effects impact of the phase diagrams, polar and dielectric properties of $(\text{Sr}, \text{Bi})\text{Ta}_2\text{O}_9$ ferroelectric nanoparticles. *J. Appl. Phys.* **119**, 204104–204111 (2016)
3. Yan, Y., Al-Jassim, M.M., Xu, Z., Lu, X., Viehland, D., Payne, M., Pennycook, S.J.: Structure determination of a planar defect in $\text{SrBi}_2\text{Ta}_2\text{O}_9$. *Appl. Phys. Lett.* **75**(13), 1961–1963 (1999)
4. Akira, O., Masanori, F., Masaki, T.: Ferroelectric instability and dimensionality in bi-layered perovskites and thin films. *Adv. Condens. Matter Phys.* **2012**, 2–9 (2012)

Sol-Gel Synthesis of ZnO Nanorods for MEMS

Alexandr V. Rogachev¹, Alina V. Semchenko¹(✉),
Dmitry L. Kovalenko¹, Vitaliy V. Sidsky¹, Olga I. Tyulenkova¹,
Nina I. Tyulenkova¹, Dumitru Luca², Vitaliy A. Solodukha³,
Alyaxandr N. Pyatlitski³, and Natalya S. Kovalchuk³

¹ Francisk Scorina Gomel State University,
Sovetskaya Str., 104, Gomel, Belarus
{rogachevav, semchenko, dkov, sidsky, tyulenkova}@gsu.by,
ninaOmaita@gmail.com

² Alexandru Ioan Cuza University of Iasi,
11, Carol I Blvd., 700506 Iași, Romania
dumitru.luca@uaic.ro

³ JSC “INTEGRAL”, Korjenevsky Str., 12, Minsk, Belarus
{vsolodukha, nkovalchuk}@integral.by, petan@tut.by

Abstract. A liquid-phase method to grow strictly ordered arrays of ZnO nanorods is introduced. Silicon substrates with a sol-gel pre-deposited seed layer of ZnO were used to grow nanostructures of zinc oxide. The types, the content of precursors and the technological parameters of sol-gel synthesis have been determined and their effects on the morphology and crystallinity of the investigated materials were evaluated. We demonstrated that an appropriate choice of parameters of the hydrothermal synthesis is necessary to ensure a directional change in the properties and morphology of the resulting materials. This is a pre-requisite for the fabrication of MEMS.

Keywords: Zinc oxide · Sol-gel method · Seed underlayer coating · Hydrothermal synthesis · Columnar nanostructures

1 Introduction

Zinc oxide (ZnO) materials are of great interest for use in many fields of science, engineering and medicine as functional materials. Zinc oxide (ZnO) is a semiconductor material featuring a wide direct band gap (3.37 eV), high exciton energy (60 meV), and excellent physical and chemical stability [1]. Currently, a number of semiconductor devices are intensively being developed using nanostructures of zinc oxide in the form of nanowires, nanorods, nano-rolls etc. Such structures can find application as the components of microelectromechanical systems (MEMS) [2, 3]. Zinc oxide materials with different morphology characteristics were obtained in various ways. Such high-quality crystal structures can be synthesized by molecular beam epitaxy, like deposition from the gas phase during thermal or laser evaporation, magnetron sputtering, or by hydrothermal synthesis [4].

The requirements for industrial fabrication always include low-cost manufacturing of identical products in large quantities. From this point of view, the methods of sol-gel synthesis are highly convenient, due to manufacturing simplicity, use of low temperatures and cheap reagents. Therefore, there has been great flexibility, by appropriate choosing of the initial components and synthesis methods [5]. By varying the nature of precursors and modifying and process conditions, one can synthesize dispersed forms of ZnO nanostructures with different morphology and size. The hydrothermal method allows for creating uniform layers of ZnO nanorods for gas sensors, optoelectronic and piezoelectric nanodevices [6].

In this paper, we investigated the influence of the seed underlayer, the synthesis conditions and the nature of substances and the corresponding effects on the morphology and structure of the columnar ZnO nanostructures are presented.

2 Methodology of the Experiments

Polished single crystal silicon plates were used as substrates. All the substrates were previously thoroughly sonicated in acetone, then in ethanol for 10 min. ZnO thin films were prepared using a sol obtained by dissolving 1.5 g of zinc acetate $\text{Zn}(\text{CH}_3\text{COO})_2$ in 8 ml of isopropyl alcohol. Maturation of the sol lasted 2–3 days at room temperature (22 ± 2) °C. Isopropyl alcohol was used as liquid medium to maintain the stability of the solution and to create the necessary viscosity. ZnO films were deposited on the substrates by spin coating: the sol was applied to the substrate by a dispenser and spread over the surface by centrifugation at rotation frequency of 2000 rpm.

The substrates were then placed in a muffle furnace and held at 250 °C for 5 min. The final annealing, which was carried out at 350 °C on the air for 60 min in a muffle furnace resulted in the formation of a uniform ZnO layer on top of the substrate. The typical thickness of a layer, as measured by SEM ranged between 30 and 40 nm. For some samples, the seed layer was applied twice and even three times. To synthesize columnar ZnO nanostructures, chemical precipitation from solutions of zinc salts was used. In the first case, 1 ml of ethylenediamine was placed in a reaction beaker in 200 ml of distilled water. Further on, a 0.2 molar aqueous solution of zinc acetate ($\text{Zn}(\text{CH}_3\text{COOH})_2$) was dropwise added to the ethylene-diamine solution under constant stirring, until the pH was adjusted to 8.5. The samples were incubated with a seeded ZnO layer in the resulting mixture. The reaction vessel was placed in a closed state for 2 h in a drying cabinet at a temperature of 85–110 °C. At the end of the synthesis experiments, the samples were gently rinsed with distilled water and dried in air. The second synthesis solution was prepared by mixing 0.01 M zinc nitrate solutions $\text{Zn}(\text{NO}_3)_2 \cdot 6\text{H}_2\text{O}$ and hexamethylene-tetramine $(\text{CH}_2)_6\text{N}_4$ in distilled water. The solutions were mixed in the ratio 1:1. The substrates were arranged vertically in the reaction vessels. Time and temperature of exposure were similar to the first case.

At the end of the growth, the samples were removed from solution, then washed with distilled water and dried in air.

3 Results and Discussion

The possibility of synthesizing one-dimensional nanostructures of zinc oxide on the seed underlayer deposited by a sol-gel method was demonstrated. Figure 1 shows the SEM image of ZnO nanostructures grown using Si substrates, on top of the previously applied seed underlayer.

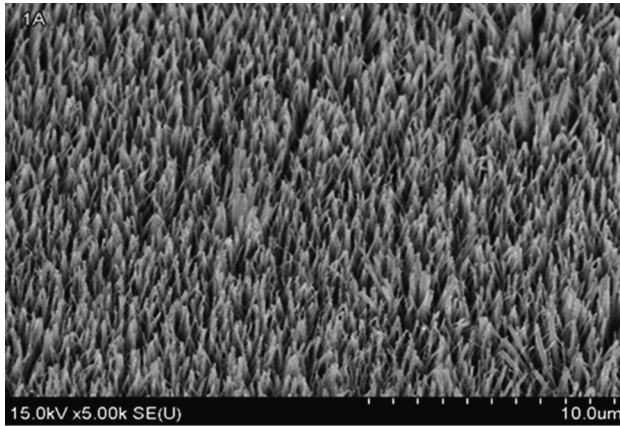


Fig. 1. A SEM image of ZnO nanorods grown on the substrate with ZnO seed layer.

As can be seen from the Fig. 1, the utilization of the seed layer allows one to obtain uniformly distributed arrays of nanorods. We found that the uniformity of the morphology of the columnar nanostructures depends on the thickness of this seed underlayer. The best results were obtained for the seed layer thickness of 60 nm. In addition, we noticed that good crystallinity of the seed layer is necessary for growing dense arrays of high-quality columnar nanostructures, oriented perpendicularly to the substrate. As a proof, Fig. 2 shows images of ZnO columnar nanostructures grown on seed layers 60 and 150 nm thick. The thickness of the seed layer was measured with an ellipsometer LEF-757. It is evident that an increase in the thickness of the seed underlayer causes a decreasing of the uniformity of the columnar structures.

Such phenomena are well studied in the physics of epitaxial layers and reflect the transition from the pseudomorphic structure of the seed layer to the layer with the formation of the crystalline phase. This is due to the energetically favorable process of restructuring with the relaxation of strain-stresses [7].

We noticed that the temperature of hydrothermal synthesis influences the growth of columnar nanostructures of zinc oxide. Higher temperature leads to densification of the nanorods. Figure 3 shows the SEM image of the ZnO nanorods synthesized at a temperature of 90 °C.

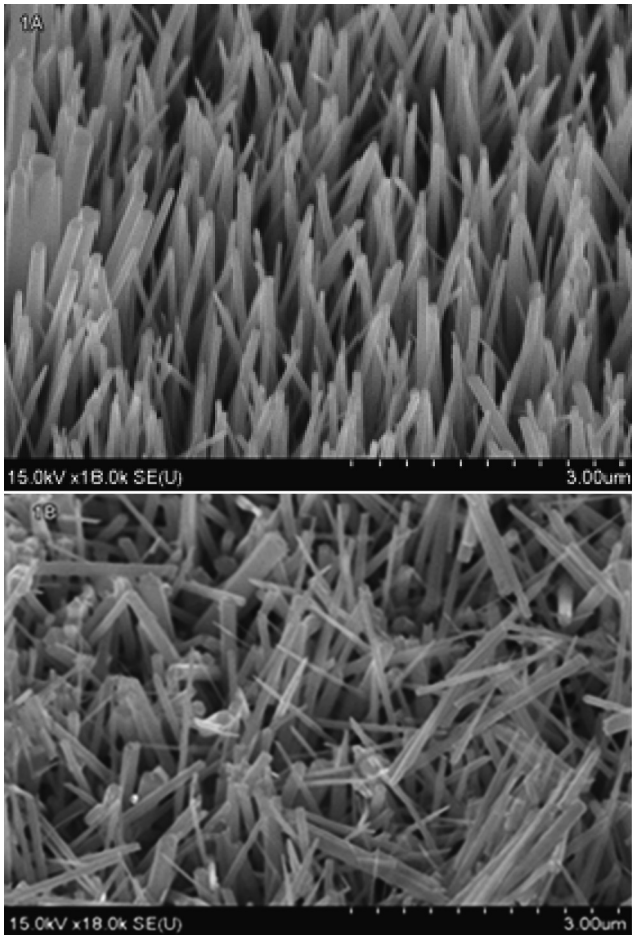


Fig. 2. SEM images of zinc oxide columnar nanostructures grown on substrates with ZnO seed layers: (a) 60 nm, (b) 150 nm thick.

A significant improving of the properties of the investigated ZnO nanostructures can be achieved by a preliminar annealing of the seed layer. The quality of nanorods is significantly improved upon annealing the seed layer in an oxygen atmosphere.

Table 1 shows the data of the chemical composition of seed layers deposited on silicon substrates by the sol-gel method, as well as the chemical composition of the solutions for the subsequent formation of columnar zinc oxide structures by the hydrothermal method. The chemical composition of the seed layer was determined by X-ray phase analysis. The obtained data concerning the height and average diameter (at apex and base, respectively) of columnar structures are inserted in Fig. 3. The histograms in Fig. 4 show the average heights and diameters of the investigated zinc oxide nanorods grown on seed layers with several chemical composition, and with different

composition of the working solutions. Based on Fig. 4, we can see that the largest value of the average height of ZnO structures is observed for sample No. 1 (Fig. 3). This sample was grown on the seed layer of pure zinc oxide, without adding polyethyleneglycol to the working solution. The lowest height was observed for sample No. 6, which was synthesized on a seed layer with an aluminum oxide content of 3.5%.

Table 1. Chemical composition of substrates and of working solutions

Sample number	Seed layer composition	Working solution composition
1	ZnO	Ethylenediamine and zinc acetate
2	ZnO	Ethylenediamine, zinc acetate and polyethylene glycol (PEG)
3	ZnO and Al ₂ O ₃ (2%)	Ethylenediamine and zinc acetate
4	ZnO and Al ₂ O ₃ (3%)	Ethylenediamine and zinc acetate
5	ZnO and Al ₂ O ₃ (3%)	Ethylenediamine, zinc acetate and polyethylene glycol (PEG)
6	ZnO and Al ₂ O ₃ (3.5%)	Ethylenediamine and zinc acetate

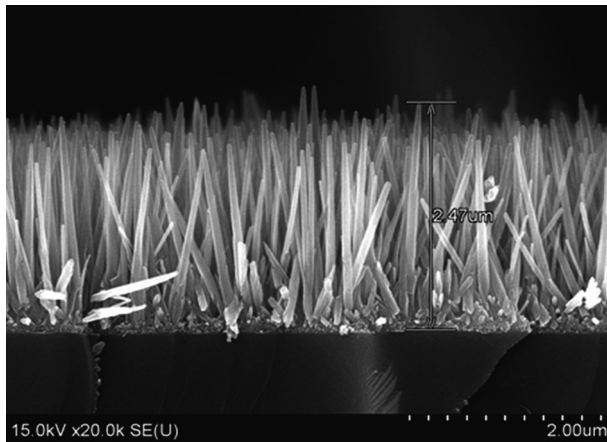


Fig. 3. A SEM image of the ZnO nanorods synthesized at a temperature of 90 °C.

Figure 4 shows that the largest average diameter of the zinc oxide nanorods is observed for sample No. 5. This sample was grown on the seed layer with an aluminum oxide content of 3% and with the addition of polyethylene glycol to the working solution. The smallest average diameter at apex was observed for the sample No. 1, which was synthesized on a seed layer of zinc oxide without aluminum content.

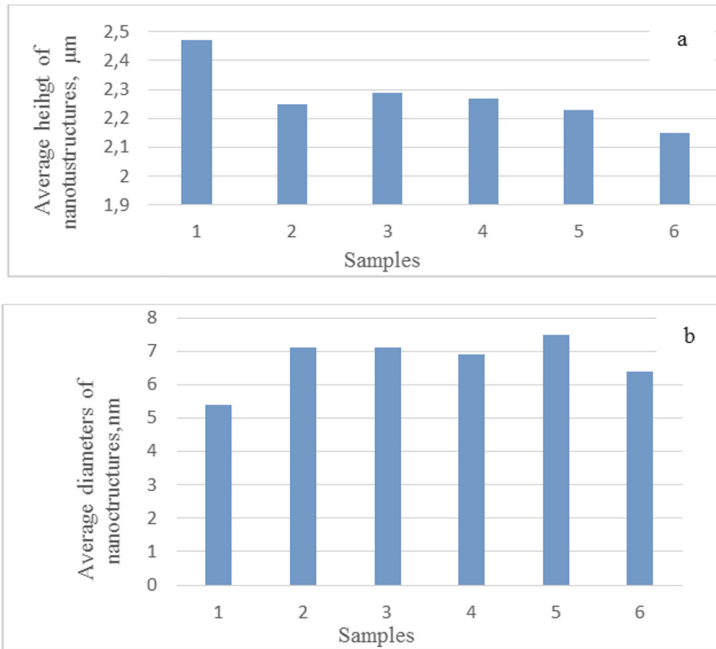


Fig. 4. Histograms of average heights (a) and diameters (b) of the zinc oxide nanorods.

4 Conclusion

Zinc oxide nanorods were synthesized on silicon and amorphous glass substrates with a seed underlayer. The nature and the content of precursors, as well as the technological parameters of sol-gel synthesis were determined. Vertically oriented, strictly ordered arrays of ZnO nanorods can be obtained via hydrothermal synthesis only by creating appropriate single-crystal seed nanolayer, able to ensuring the matching of the nanorods to the substrate.

The optimum temperature for the hydrothermal synthesis of highly ordered columnar arrays of ZnO nanorods and the necessary thickness of the seed layer were, additionally established. Doping the seed underlayer with aluminum ions resulted in decreasing the height and a gradual approaching to cylindrical shape of the nanorods.

The effect of polyethylene glycol on the shape and height of columnar nanostructures is not fully established. By choosing the parameters of the hydrothermal synthesis, a directional change in the properties and morphology of the resulting material is possible. This is a pre-requisite for the fabrication of MEMS.

Acknowledgments. The work was supported by Belarusian Foundation for Fundamental Research (Project T16-RA005) and by Academy of Sciences of Romania.

References

1. Asthana, A., et al.: In situ observation of size-scale effects on the mechanical properties of ZnO nanowires. *Nanotechnology* **22**(26) (2011)
2. Klingshirn, C.F., Meyer, B.K., Waag, A., et al.: *Zinc Oxide from Fundamental Properties Towards Novel Applications*. Springer, Heidelberg (2010)
3. Jing, L.: The preparation and characterization of ZnO ultrafine particles. *Mat. Sci. Eng.* **332**, 356–361 (2002)
4. Yao, B.D.: Formation of ZnO nanostructures by a simple way of thermal evaporation. *Appl. Phys. Lett.* **81**, 757–759 (2002)
5. Zhabrev, V.A., et al.: *Sol-Gel Technology*. LETI, St. Petersburg (2004)
6. Maksimov, A.I., Moshnikov, V.A., Tairov, Y., Shilova, O.A.: *Fundamentals of Sol-Gel Nanocomposite Technology*, 2nd edn. LETI, St. Petersburg (2007)
7. Baruah, S.: pH-dependent growth of zinc oxide nanorods. *J. Cryst. Growth* **311**, 2549–2554 (2009)

Plasma Physics

Pharmacokinetics of Cyclosporine A of Transdermal Delivery Using Microplasma and Oral Administration

Jaroslav Kristof¹(✉), Hideto Miyamoto², Marius Blajan³,
and Kazuo Shimizu^{1,2,3}

¹ Graduate School of Science and Technology,
Department of Optoelectronics and Nanostructure Science, Shizuoka University,
Johoku, Hamamatsu, Shizuoka 432 8561, Japan
kristof.jaroslav.15@shizuoka.ac.jp,
shimizu@cjr.shizuoka.ac.jp

² Graduate School of Engineering, Shizuoka University, Johoku, Hamamatsu,
Shizuoka 432 8561, Japan

³ Organization for Innovation and Social Collaboration,
Shizuoka University, Johoku, Hamamatsu, Shizuoka 432 8561, Japan

Abstract. Oral drug delivery is a very convenient way of drug administration because no special assistance or instructions are usually needed. But difficulty swallowing or side effect because of first-pass metabolism can appear and also high doses have to be administrated to maintain concentration in blood at a therapeutically level for a longer time. Transdermal drug delivery seems to be very promising because current patches can deliver a stable flow of drugs, so the possibility of over dosage is reduced and as well metabolic effect. In this study, we investigated transdermal method using microplasma discharge to modify upper layer of skin to allow to penetrate the drug. After treatment, drug solution applied on skin can penetrate through the skin into bloodstream. Cyclosporine A was used as model drug with a weight 1203 Da (g mol^{-1}). Cyclosporine A prevents rejection of organs after transplantation. This drug suppresses immunity of body and any infection can be fatal. Two-compartment model was used for monitoring of drug level in the bloodstream. We compared plasma drug delivery with oral administration during several hours. Combination of oral administration with plasma drug delivery could be feasible to decrease initial dosage of Cyclosporine A.

Keywords: Microplasma · Pharmacokinetics · Cyclosporine A · Microplasma drug delivery

1 Introduction

If seriously damaged organs are not possible to heal and restore them their function, they must be transplanted. But immune reaction of the recipient can cause rejection of the organ by the body followed by death. Finding of immunosuppressive drugs helped

to prevent rejection response. The immunosuppressive drugs reduce rejection and the action of the immune system but it can expose body to risk of an infection. Acute rejection can occur up to 3 months and chronic rejection occurs after this time. It means that the recipient has to take the immunosuppressive drugs during rest of his life with the transplanted organ. When Cyclosporine A was first used, the survival rate and number of transplantations increased [1]. Number of transplantation has increasing tendency also in Japan but not as dramatic as in other western countries. In 2015, 1661 kidney transplantations were realized, while 14 years ago (2001) it was only 705 [2]. The therapeutic level of Cyclosporine A in a bloodstream is between 100–400 $\mu\text{g/l}$ [3].

Cyclosporine A is the main immunosuppressant for all kinds of organ transplantation but its use is associated with risk of nephrotoxicity, hypertension, hepatotoxicity and neurotoxicity [4]. The main pathway of the administration of Cyclosporine A is intravenous or oral. But transdermal delivery was also investigated several times, using iontophoresis, chemical enhancers or ultrasound [5–7].

Oral administration represents a very simple way but the bioavailability is low because of the metabolic effect of gastrointestinal tract. Two thirds of metabolic reactions of the drug are realized in gut and one third in liver [8]. Administration of the other drugs can increase or decrease metabolism of Cyclosporine A [8]. This complication always has to be kept in mind. Too high concentration of Cyclosporine can be followed by some side effects and in the extreme cases leads to death. On the other hand, lower concentration leads to the risk of rejection of the organ. During intravenous delivery, special assistant is needed. However, microneedles represent hope for the future. If microneedles are shorter than 0.5 mm, they are not painful. But redness of the skin can cause increased sensitivity to the sun in the place of administration [9]. In our study, we used drug delivery by dielectric barrier plasma on electrode of micrometer dimensions (microplasma drug delivery). Before, this kind of technique was also investigated for delivery of Galantamine Hydrobromide [10] and Cyclosporine A [11].

In this paper, we studied transdermal delivery of Cyclosporin A and the concentration of the drug in the bloodstream after oral delivery, microplasma drug delivery and their combination. This study was realized by two-compartment model using data published in a previous publication [11].

2 Experiment

2.1 Microplasma Dielectric Barrier Discharge

Dielectric barrier discharge is generated by a thin-film electrode described before in ref. [11]. Atmospheric argon plasma was maintained by a relatively low voltage of 950 V and a frequency of 25 kHz by a Neon transformer (ALPHA Neon M-5). Flow of argon was set to 5 L/min by a flow meter (Yamato). The skin treatment lasted 5 min. The distance between electrode and skin was 0.5–1 mm (Fig. 1).

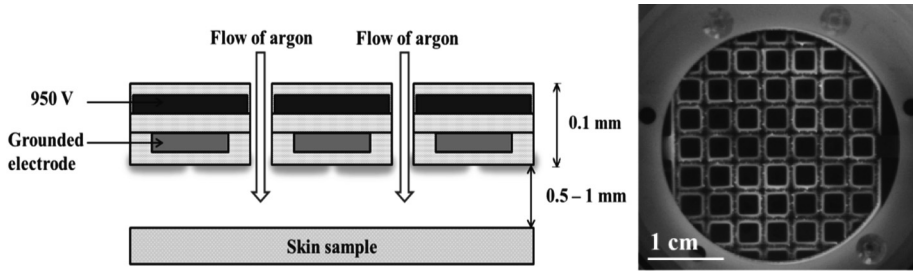


Fig. 1. Left: Experimental set-up of skin treatment by microplasma dielectric barrier discharge – white arrows indicate flow of argon. Right: Surface discharge on electrode. Argon gas is flowing through the openings (space inside of dark squares).

2.2 Two-Compartment Model

Pharmacokinetic models are usually used for suitable setting of drug dose and repetition of administration. Comparison of various methods of delivery will show the best way of delivery or the best combination of more methods. A two-compartment model is suitable for describing Cyclosporine A in bloodstream and it was used in this study [3, 11]. X_1 (in μg) represents the amount of Cyclosporine A in bloodstream (first compartment). Cyclosporine A is delivered to bloodstream with flux k_0 and it is eliminated of body by rate constant k_e . The second, peripheral compartment X_2 consists from amount of drug in tissues, bones, skin, etc. and is represented by amount X_2 (second compartment) (in μg). Exchange of drug between compartments X_1 and X_2 is defined by rate constant k_{12} and k_{21} . The whole process can be described by differential equations as shown in (1) and (2):

$$\frac{dX_1}{dt} = k_0 - k_e X_1 - k_{12} X_1 + k_{21} X_2 \quad (1)$$

$$\frac{dX_2}{dt} = k_{12} X_1 - k_{21} X_2 \quad (2)$$

Concentration of Cyclosporine A in bloodstream is expressed by relation

$$C_b = \frac{X_1}{V_1} \quad (3)$$

where V_1 (in liters) is the volume of the first compartment. The volume of the first compartment depends very often on the weight of the patient. Also in the literature the volume is usually introduced normalized to the weight (see Table 1). Equations (1) and (2) were calculated by Runge-Kutta method of 4th order with initial conditions $X_1(t=0) = 0$ and $X_2(t=0) = 0$. Variables X_1 and X_2 are calculated using linear variation.

In the case of oral delivery, k_0 was replaced by $F \cdot \text{Dose} \cdot k_a \cdot e^{-k_a t}$. F is the bioavailability of drug and k_a is absorption constant of gastro-intestine tract. We used data of Cremers et al. [12] for calculation of Cyclosporine A in bloodstream (Table 1).

Table 1. Constants for two-compartment model of Cyclosporine A in bloodstream [12].

k_a (h^{-1})	0.741
F	0.3*
V_1 (L/kg)	0.491
k_e (h^{-1})	0.559
k_{12} (h^{-1})	0.567
k_{21} (h^{-1})	0.149

*taken from [3]

3 Results

Drug delivery can have influence on quality of life. When the drug has to be applied too often, there is a risk of failure of the patient. Also, application can be avoided because actual situation in the life. On the other hand, if administration method is too complicated, there is a risk of any mistake. This mistake can be fatal in the case of

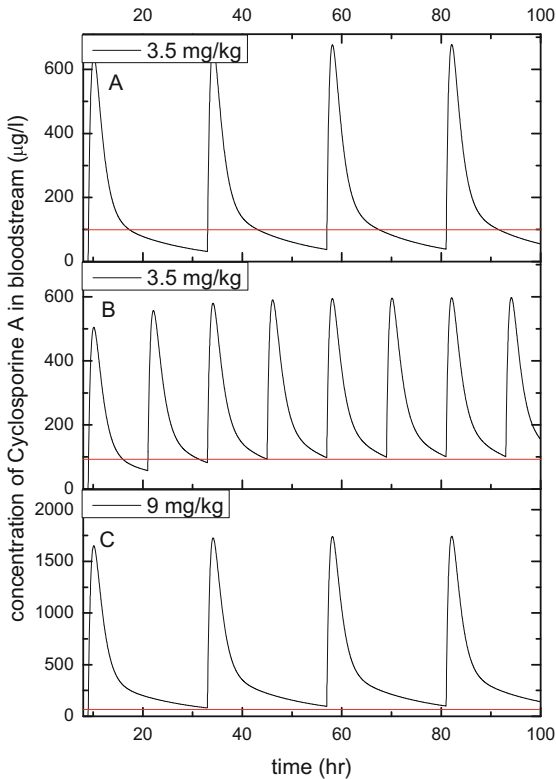


Fig. 2. A. Oral delivery of 3.5 mg/kg of Cyclosporine A every 24 h. B. Oral delivery of 3.5 mg/kg of Cyclosporine A every 12 h C. Oral delivery of 9 mg/kg of Cyclosporine A every 24 h. The weight of the patient was 55 kg in the model. The red line indicates the lowest therapeutic concentration.

Cyclosporine A, if it is followed by the dramatic change of the concentration in the bloodstream. Our model in Fig. 2A illustrates oral administration of 3.5 mg/kg every 24 h. 10 h after the drug application, the concentration in the bloodstream decreased below the therapeutic level of 100 $\mu\text{g/l}$. To achieve the level above therapeutic level, it is needed take 9 mg/kg of the drug every 24 h (Fig. 2C). This amount resulted in a high peak of 1744 $\mu\text{g/l}$ 1 h after application, what is a toxic level according Ragab et al. [13]. They claimed that the toxic level of the peak concentration achieves value above 1000 $\mu\text{g/l}$ and the therapeutic peak level is between 800–1000 $\mu\text{g/l}$. Oral delivery of Cyclosporine A is usually administered 2 times a day every 12 h. In our model, 3.5 mg/kg given every 12 h could maintain a level of the drug above 100 $\mu\text{g/l}$ (Fig. 2B).

Amount of the drug delivered by transdermal pathway depends on the concentration of the drug in applied solution and the size of the treated area by microplasma, where the drug is applied. We used a concentration of 400 mg/ml in propylene glycol and the size of the area was 225 cm^2 in our model. Flow of the drug through the skin was taken from Kristof et al. [11] and the delivery was applied for 9 h. The concentration of the drug in

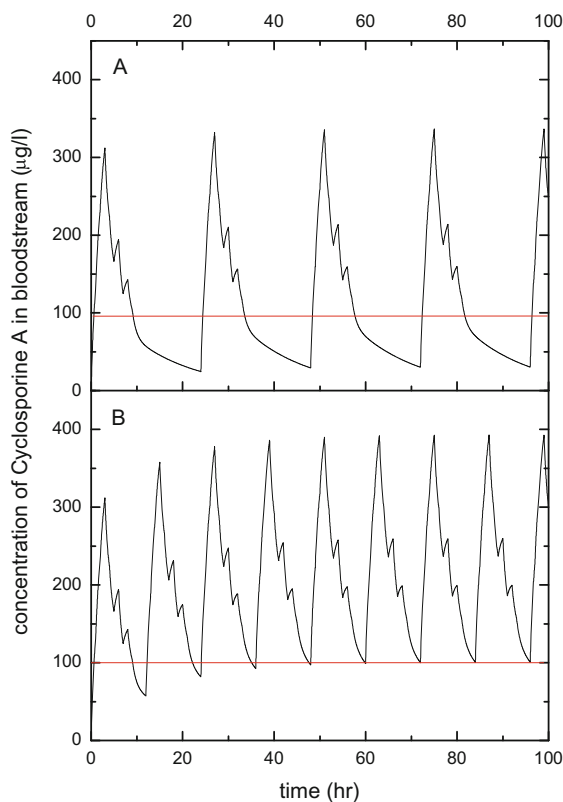


Fig. 3. A. Transdermal drug delivery of Cyclosporine A every 24 h. B. Transdermal drug delivery of Cyclosporine A every 12 h. The weight of the patient was 55 kg in the model. The red line indicates the lowest therapeutic concentration.

the bloodstream depended on the volume of the first compartment and the volume of the first compartment was proportional to the weight of the patient. The average weight of a Japanese man was less than 70 kg and the average weight of Japanese woman was less than 55 kg. In the calculations of our model, we used the weight of an average Japanese woman (55 kg). Results for men were very similar. The application of plasma drug delivery every 24 h did not allow holding of Cyclosporine A concentration in the therapeutic range and the concentration decreased below 100 $\mu\text{g/l}$ 9.5 h after the application (Fig. 3A). But the plasma drug delivery applied every 12 h allowed maintaining of the therapeutic level (Fig. 3B).

Oral drug delivery represents a simple method of the administration, but because of the influence of other drugs or even drinks on the metabolism of Cyclosporine A, it is needed to be very careful. Investigation of the influence, for example, of grapefruit juice on Cyclosporine A metabolism was demonstrated in Murray et al. [14]. After oral administration of Cyclosporine A and drinking of 250 ml of grapefruit juice, the bioavailability of the drug increased about 62%. But they did not observe any influence of the grapefruit juice if the drug was administered intravenously. We also did not expect any influence of grapefruit juice on microplasma drug delivery and we can avoid the metabolic effect. Changes of the bioavailability following other drugs and substances can sometimes have fatal results [15].

Combination of microplasma transdermal delivery and oral delivery is demonstrated in Fig. 4. 3.5 mg/kg was administered every 24 h, 9 h after transdermal delivery. The peak values appeared every 24 h for approximately 3 h (value above 400 $\mu\text{g/l}$). Oral delivery was reduced to half and also the risk of side effects (caused by gastrointestinal tract) as Cyclosporine A was administered every 24 h instead of every 12 h. The time

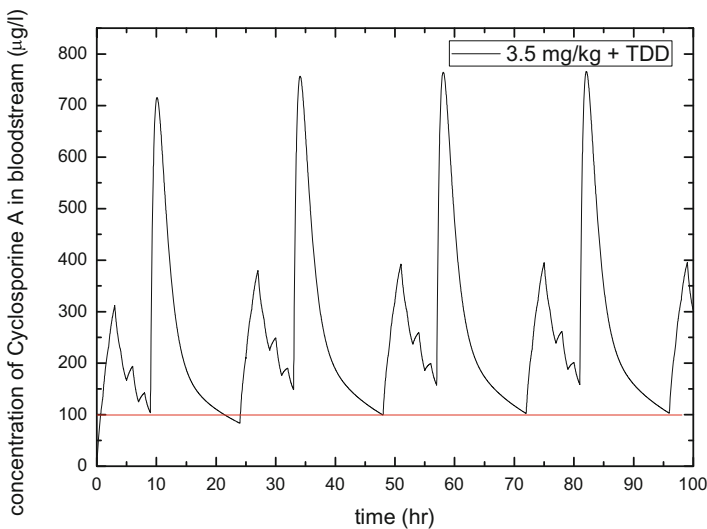


Fig. 4. Oral delivery of 3.5 mg/kg of Cyclosporine A with combination of transdermal drug delivery (TDD) of Cyclosporine A every 24 h. Delay between transdermal drug delivery and oral delivery is 9 h and patient weight was 55 kg in the model. The red line indicates the lowest therapeutic concentration.

shift between the both administrations can be adjusted to microplasma transdermal delivery in the evening and to oral administration in the morning. This setting can improve the quality of life of the patient and partially decrease the effect of the interaction of Cyclosporine A with other substances because of oral administration.

4 Conclusion

A Two-compartment model for the description of Cyclosporine A evolution in the bloodstream was developed. This model compared oral drug delivery and microplasma delivery. As Cyclosporine A metabolism can be influenced by other substances, we decreased the amount of drug administered orally thus, lowering of the interaction. The remaining amount of the drug was delivered by transdermal pathway. Both administrations were realized daily, every 24 h with a time shift of 9 h (microplasma delivery was used 9 h before oral delivery). This setting allows application of transdermal patch during the night and it can improve quality of life in comparison with the cases when the drug has to be delivered by infusion/injection or orally several times during day.

References

1. Mehrabi, A., Wiesel, M., Zeier, M., Kashfi, A., Schemmer, P., Kraus, T., Buchler, M.W., Schmidt, J.: Results of renal transplantation using kidneys harvested from living donors at the university of Heidelberg. *Nephrol. Dial. Transplant.* **19**(Suppl 4), iv48–iv54 (2004)
2. Yagisawa, T., Mieno, M., Yoshimura, N., Yuzawa, K., Takahara, S.: Current status of kidney transplantation in Japan in 2015: the data of the kidney transplant registry committee, Japanese society for clinical renal transplantation and the Japan society for transplantation. *Renal Replace. Ther.* **2**, 68 (2016)
3. Bauer, L.A.: *Applied Clinical Pharmacokinetics*. McGraw-Hill Professional, New York/Columbus (2008)
4. Christians, U., Sewing, K.-F.: Alternative cyclosporine metabolic pathways and toxicity. *Clin. Biochem.* **28**(6), 547 (1995)
5. Liu, H., Li, S., Pan, W., Wang, Y., Han, F., Yao, H.: Investigation into the potential of low-frequency ultrasound facilitated topical delivery of Cyclosporin A. *Int. J. Pharm.* **326**, 32 (2006)
6. Liu, H., Li, S., Wang, Y., Yao, H., Zhang, Y.: Effect of vehicles and enhancers on the topical delivery of cyclosporin A. *Int. J. Pharm.* **311**, 182 (2006)
7. Wang, D.-P., Lin, C.-Y., Chu, D.-L., Chang, L.-Ch.: Effect of various physical/chemical properties on the transdermal delivery of cyclosporin through topical application. *Drug Dev. Ind. Pharm.* **23**, 99 (1997)
8. Gavhane, Y.N., Yadav, A.V.: Loss of orally administered drugs in GI tract. *Saudi Pharm. J.* **20**(4), 331 (2012)
9. Koch, B., Rubino, I., Quan, F.-S., Yoo, B., Choi, H.-J.: *Materials* **9**, 646 (2016)
10. Shimizu, K., Tran, A.N., Kristof, J., Blajan, M.: Investigation of atmospheric microplasma for improving skin permeability. In: *Proceedings of the 2016 Electrostatics Joint Conference, Lafayette, 13–18 June*, p. 14 (2016)
11. Kristof, J., Miyamoto, H., Tran, A.N., Blajan, M., Shimizu, K.: Feasibility of transdermal delivery of cyclosporine a using plasma discharges. *Biointerphases* **12**, 02B402 (2017)

12. Cremers, S.C.L.M., Scholten, E.M., Schoemaker, R.C., Lentjes, E.G.W.M., Vermeij, P., Paul, L.C., den Hartigh, J., de Fijter, J.W.: A compartmental pharmacokinetic model of cyclosporin and its predictive performance after Bayesian estimation in kidney and simultaneous pancreas–kidney transplant recipients. *Nephrol. Dial. Transplant.* **18**, 1201 (2003)
13. Ragab, A.R., Al-Mazroua, M.K., Al-Dakrory, S.A.-E.: Cyclosporine toxicity and toxicokinetics profiles in renal transplant recipients. *J. Clin. Toxicol.* **3**, 154 (2013)
14. Ducharme, M.P., Warbasse, L., Edwards, D.J.: Disposition of intravenous and oral cyclosporine after administration with grapefruit juice. *Clin. Pharmacol. Ther.* **57**(5), 485 (1995)
15. Tafazoli, A.: Accidental overdose of oral cyclosporine in haematopoietic stem cell transplantation: a case report and literature review. *Drug Saf. - Case Rep.* **2**, 20 (2015)

Flow Control by Dielectric Barrier Discharge Microplasma

Marius Blajan¹, Akihiko Ito², Jaroslav Kristof³,
and Kazuo Shimizu^{1,2,3(✉)}

¹ Organization for Innovation and Social Collaboration,
Shizuoka University, Johoku, Hamamatsu 432-8561, Japan
blajanmarius@yahoo.com, shimizu@cjr.shizuoka.ac.jp

² Graduate School of Engineering, Shizuoka University,
Johoku, Hamamatsu 432-8561, Japan
ailvhs.46@gmail.com

³ Department of Optoelectronics and Nanostructure Science,
Graduate School of Science and Technology, Shizuoka University,
Johoku, Hamamatsu 432-8561, Japan
jaroslav.kristof@gmail.com

Abstract. Dielectric barrier discharge (DBD) plasma actuators are a technology which could replace conventional actuators due to their simple construction, lack of moving parts and fast response. Our study was carried out to investigate experimentally and by numerical simulations a micro scale plasma actuator energized at 1.4 kV. A multi-electrode plasma actuator was used which allowed the electrodes to be energized at different potentials or waveforms, thus changing the direction of the flow. The movement of incense particles was tracked by the high speed camera. The observation with the high speed camera showed at various time intervals the modification of the flow by the microplasma. The numerical simulation of the flow was carried out using Suzen-Huang modela and Navier-Stokes equations.

Keywords: Microplasma actuator · Dielectric barrier discharge · Flow control · Numerical simulation

1 Introduction

The conventional actuators used on aircraft could be replaced with plasma actuators which are a safe and efficient alternative due to their lack of moving parts, simple construction and fast response due to the electric field. Dielectric barrier discharge (DBD) plasma actuators developed by various researchers are conventionally energized at voltages of tens of kilovolts [1–3]. Such high voltages are difficult to insulate and require a large sized power supply. For flow control applications we have developed a microplasma actuator which can be energized at only 1 kV.

Microplasma is a type of dielectric barrier discharge non-thermal plasma that proved to be a more economical and ecological replacement of conventional technologies for surface treatment of various materials, indoor air treatment, biomedical applications or flow control [4–6].

In this study, numerical simulations were carried out in order to investigate the flow velocity near the electrode surface where the experimental measurements were difficult to carry out.

The numerical simulation of the flow modification was carried out using the Suzen & Huang model [7–9]. The Suzen & Huang model is close to the physical phenomena of the plasma actuator and was also used by other researchers [10, 11].

Our first approach in modeling the microplasma actuator consisted in a simulation code based on Suzen-Huang model [4].

2 Experimental Setup

A multi-electrode microplasma actuator was used which allowed the electrodes to be energized at different potentials or waveforms, thus changing the direction of the flow. The microplasma actuator schematic image is shown in Fig. 1. The top-side electrode is composed from 20 strip-like electrodes and placed above a plate electrode with a dielectric layer of 25 μm thicknesses in between. The strips have a width of 200 μm and thickness of 16 μm . Resin film was used for the dielectric layer and copper for electrodes.

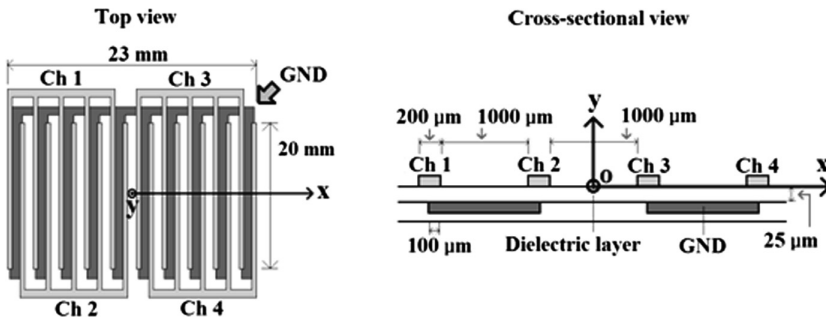


Fig. 1. Multi-electrode microplasma actuator. (a) Top view showing strip-like electrodes; (b) Schematic cross-sectional view.

Due to the four channels type microplasma actuator, each channel can be driven independently as shown in Fig. 1. AC voltage with 1.4 kV and 20 kHz was applied to channels Ch1 and Ch4. The applied voltage was pulse modulated at 50% duty ratio with a burst frequency of 4 kHz. Channels Ch1 and Ch4 were energized by the AC voltage for 100 ms. Flow was visualized by using the particle tracking velocimetry (PTV) [12]. Approximately 0.3 μm tracer particles were used as incense smoke. Nd YVO₄ 532 nm laser was utilized to visualize the flow. The phenomena induced by the microplasma actuator were measured with a high-speed camera. The PTV results were obtained manually using two consecutive images taken at each state.

3 Results

3.1 Experimental Results

Pulse modulated AC voltage with 1.4 kV and 20 kHz was applied to channels Ch1 and Ch4 with a duty ratio of 50%.

After turning on the voltage to energize the electrodes in the first 2 ms vortexes appeared near the strip-like energized electrodes having a counter clockwise direction for the Ch1 channel and clockwise direction for the Ch4 channel as shown in Fig. 2 at time $t = 2$ ms. The microplasma is generated near the active strip-like electrodes and the Electrohydrodynamic (EHD) force is the result of the electric field acting on the charged particles thus the apparition of vortexes near the electrodes. With the lapse of time the vortexes on each side unite and form above Ch1 channel a flow directed to the right and above Ch4 channel a flow directed to the left. These flows collide at the center part of the actuator and upward flow is obtained as shown in Fig. 2 at $t = 10$ ms. The maximum flow velocity was measured above the electrodes and was about 0.3 m/s at $t = 2$ ms and 0.5 m/s at $t = 10$ ms. The upward flow maximum value was about 0.4 m/s. The flow at 20 ms shows no vortexes just upward flow and after 100 ms the flow could be considered in a steady state. The channels of the multi-electrode microplasma actuator could be energized separately thus by choosing Ch1 and Ch4 channels to be energized, an upward flow could be obtained.

3.2 Simulation Results

Numerical simulations could give more information about the phenomena near the active electrodes. Suzen & Huang model [7, 8] was used for developing the simulation code. The model is described in [4, 7, 8]. According to the model because of the atmospheric pressure microplasma and consequently weakly ionized gas particles, the potential V was considered as being composed from the potential ϕ of the external electric field, and the potential φ of the net charge density. Based on these potentials the body force was calculated.

Harmonic mean of the permittivity of the dielectric material which covers the grounded electrodes with $\epsilon_{rd} = 4$ and air with $\epsilon_{rair} = 1$ was calculated for the conservation of the electric field [7]. The charge distribution over electrodes covered with dielectric material was calculated by considering these electrodes as source charge. The value of the source charge in our calculations was $\rho_c = 0.00751 \text{ C/m}^3$. Also the Debye length was considered $\lambda_D = 0.00017 \text{ m}$ for the air, and $\lambda_D = \infty$ for the dielectric [8]. The obtained body force F_x and F_y on x - and y - axes respectively were introduced in the Navier-Stokes equations in order to obtain the flow.

The boundary conditions were considered open. The computational geometry is shown in Fig. 3.

The flow velocity has the components u , v and w on x -, y - and z -axes respectively. We calculated the dynamic viscosity μ by taking the value of air density $\rho = 1.177 \text{ kg/m}^3$ and kinematic viscosity $\nu = 1.57 * 10^{-5} \text{ m}^2/\text{s}$, thus dynamic viscosity is $\mu = 1.8 * 10^{-5} \text{ kg/m s}$. The dimensions of the grid were $14 \times 14 \text{ mm}$ with 561×561 grid nodes. The “push-push” theory was considered in the numerical simulations, thus

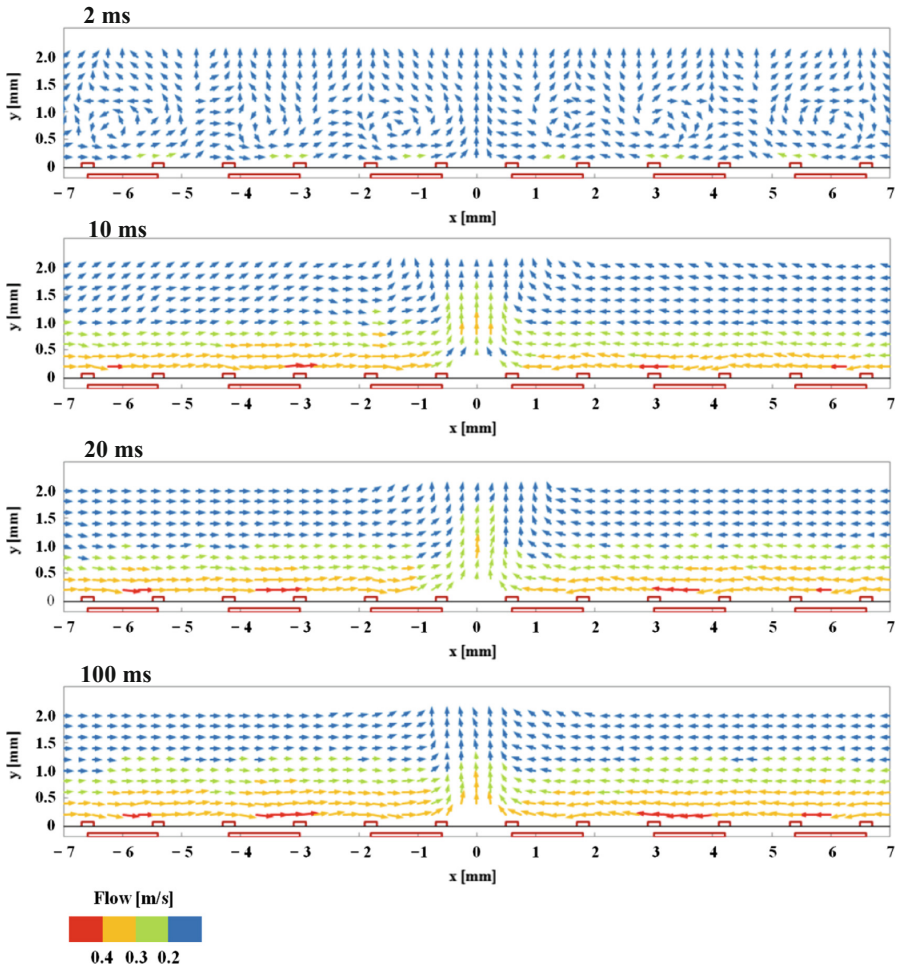


Fig. 2. PTV results of generated flow by microplasma actuator. The maximum flow velocity was measured above the active electrodes.

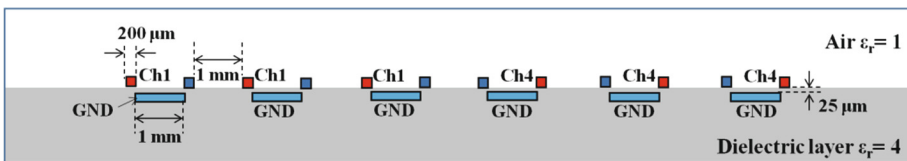


Fig. 3. Computational geometry. Ch1 and Ch4 channels were energized.

the body force magnitude and direction obtained in the positive and negative half-cycle were very similar [9]. Thus we have considered for the simulation positive pulse signal with peak value of 1 kV and duty ratio 50% since the effective value of 1.4 kV peak

AC voltage is about 1 kV as shown in Fig. 4. The finite difference method was used for the discretization of the equations, which were computed before solving the Navier-Stokes equations. Julia programming language was used to write the simulation code [13]. The Navier-Stokes equations were solved using the projection method in primitive variables on a collocated mesh. The time step was 1 μ s.

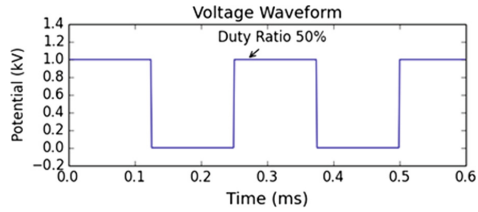


Fig. 4. Voltage waveform. A pulse with amplitude 1 kV and duty ratio 50% energized the electrodes.

In Fig. 5 are shown the simulation results for the flow. The results are similar with the experimental results. At the initial stages of discharge vortexes appeared near the energized electrodes. The body force that acts on air molecules was calculated

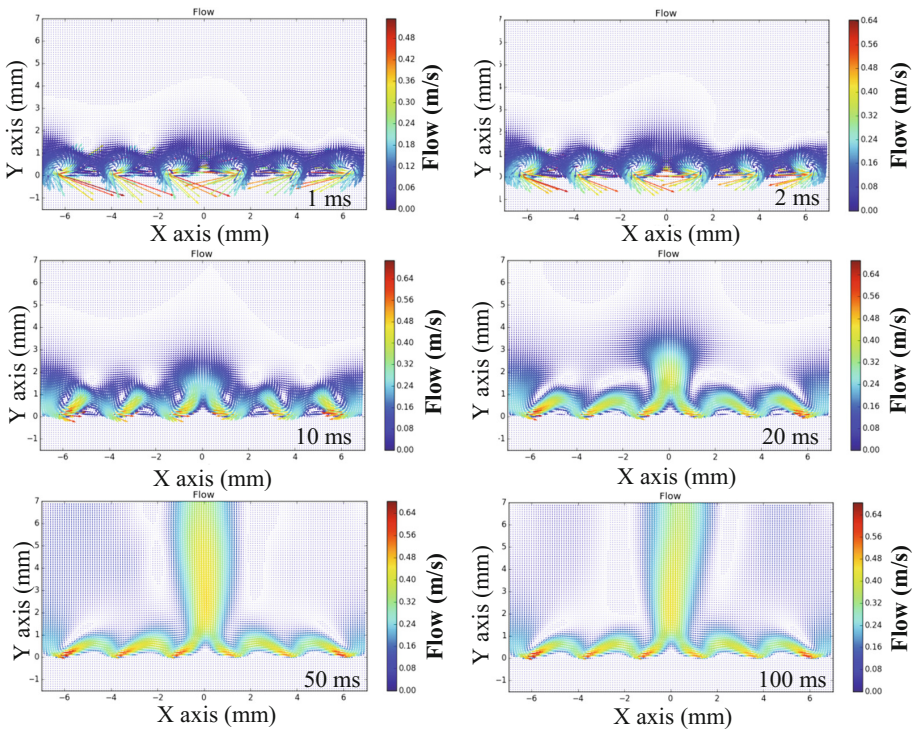


Fig. 5. Flow: electrodes Ch1 and Ch4 are energized at a duty ratio of 50%. Up to 10 ms vortexes appeared above active electrodes. Upward flow is generated after 10 ms.

according with [8] and its distribution for slightly different setup can be found in our previous publication [4]. The values of body force are high near the strip-like active electrodes thus also the flow has higher velocity in these regions as shown in Fig. 5. For the Ch1 electrodes the vortexes were rotating counter clockwise and for the Ch4 electrodes the vortexes were rotating clockwise. These results were obtained up to 10 ms. After 10 ms the vortexes unite and in the left side of the actuator over the Ch1 electrodes the resultant flow was right ward flow. In the right part of the actuator the resultant flow was left ward flow. These 2 flows collide at the center of the actuator and the resultant flow is upward flow which was obtained after 10 ms. The calculated values of the flow were about 0.5 m/s near the active electrodes at 1 ms and with the lapse of time the maximum value increased up to about 0.7 m/s. The upward flow maximum value was about 0.45 m/s. Due to the microplasma light emission the flow was difficult to measure above the active electrodes up to 0.2 mm height thus the experimental data obtained for that region are lower than the numerical simulation data but a better fit was obtained for the upward flow. In all the stages of the flow development including also the steady state the same phenomena was observed in the experiments and in the simulations from the apparition of vortexes to the upward flow. This confirms the validity of the developed numerical simulation software.

4 Conclusion

Upward flow was obtained by dielectric barrier discharge microplasma. The experimental results showed the apparition of vortexes in the initial stages of the discharge and with the lapse of time the formation of upward flow. The flow maximum value was 0.5 m/s near the active electrodes. The upward flow value was 0.4 m/s. The flow maximum value near the active electrodes was 0.7 m/s and the upward flow was 0.45 m/s. The numerical simulation matched the experimental results.

References

1. Roth, J.R., Sherman, D.M., Wilkinson, S.P.: Boundary layer flow control with a one atmosphere uniform glow discharge surface plasma. In: AIAA 98-0328, 36th Aerospace Sciences Meeting, Reno, NV, 12–15 January 1998 (1998)
2. Roth, J.R., Din, X.: Optimization of the aerodynamic plasma actuator as an electrohydrodynamic (EHD) electrical device. In: 44th AIAA Aerospace Sciences Meeting and Exhibit. AIAA, 9–12 January 2006
3. Benard, N., Moreau, E.: Electrical and mechanical characteristics of surface AC dielectric barrier discharge plasma actuators applied to airflow control. *Exp. Fluids* **55**, 1846 (2014). doi:10.1007/s00348-014-1846-x
4. Shimizu, K., Mizuno, Y., Ito, A., Blajan, M.: Microplasma actuator for active flow control. In: Proceedings of the 14th International Conference on Global Research and Education, Inter-Academia 2015. JJAP Conference Proceedings, p. 011202 (2016)
5. Shimizu, K., Kuwabara, T., Blajan, M.: Study on decomposition of indoor air contaminants by pulsed atmospheric microplasma. *Sensors* **12**(11), 14525–14536 (2012)

6. Blajan, M., Umeda, A., Muramatsu, S., Shimizu, K.: Emission spectroscopy of pulsed powered microplasma for surface treatment of pen film. *IEEE Trans. Ind. Appl.* **47**, 1100–1108 (2011)
7. Suzen, Y.B., Huang, P.G., Jacob, J.D., Ashpis, D.E.: Numerical simulations of plasma based flow control applications. In: 35th Fluid Dynamics Conference and Exhibit, Toronto, Ontario, 6–9 June 2005. AIAA 2005-4633 (2005)
8. Suzen, Y.B., Huang, P.G., Ashpis, D.E.: Numerical simulations of flow separation control in low-pressure turbines using plasma actuators. In: 45th AIAA Aerospace Sciences Meeting and Exhibit, Reno, Nevada, 8–11 January 2007. AIAA 2007-937 (2007)
9. Orlov, D.M.: Modelling and simulation of single dielectric barrier discharge plasma actuator. Ph.D. thesis, University of Notre Dame (2006)
10. Abdollahzadeh, M., Pascoa, J.C., Oliveira, P.J.: Modified split-potential model for modeling the effect of DBD plasma actuators in high altitude flow control. *Curr. Appl. Phys.* **14**, 1160–1170 (2014)
11. Brauner, T., Laizet, S., Benard, N., Moreau, E.: Modelling of dielectric barrier discharge plasma actuators for direct numerical simulations. AIAA Aviation, 8th AIAA Flow Control Conference, 13–17 June 2016, Washington, D.C. AIAA 2016-3774 (2016)
12. Fu, S., Biwole, P.H., Mathis, C.: Particle tracking velocimetry for indoor airflow field: a review. *Build. Environ.* **87**, 34–44 (2015)
13. <http://julialang.org/>

Investigations on Crystallinity and Surface Oxidation States of Nb:TiO₂ DC-Sputtered Films

Marius Dobromir¹(✉), Radu Paul Apetrei¹,
Claudia Teodora Teodorescu-Soare¹, Alina Semchenko²,
Dmitry Kovalenko², and Dumitru Luca¹

¹ Department of Research, Faculty of Physics,
Alexandru Ioan Cuza University of Iasi, 11 Carol I Blvd., 700506 Iasi, Romania
{marius.dobromir, rapetrei, dumitru.luca}@uaic.ro,
claudia_teodora89@yahoo.com

² Francisk Skorina Gomel State University, Sovetskaya 104, Gomel, Belarus
{semchenko, dkov}@gsu.by

Abstract. Pure anatase-ordered Nb:TiO₂ thin films were prepared using a pulsed-DC sputtering source with a composite (TiO₂)_{0.94}Nb_{0.06} cathode. A mixture of Ar and O₂ was used as discharge environment, under the total pressures of 1.0×10^{-2} and 5.0×10^{-2} mbar. The related effects of these parameters on film properties, associated with different deposition rates were monitored. The DC discharge was supplied by a pulsed voltage supply with a repetition rate of max. 350 kHz working in constant power mode, for two values of the injected power into discharge, 100 W and 200 W. Polycrystalline Nb-doped TiO₂ thin films with the thickness in the range of 300 and 1100 nm and Nb content ranging between 2.1 and 2.8 at.% were deposited on heated (100)Si and glass substrates. Their optical transmittance measurements were used to derive the optical band gap using the Tauc plots spectra. Data processing showed band gap energy, E_g , values ranging between 3.21 and 3.31 eV. Upon increasing the dopant content, a decrease in surface roughness and film crystallinity were observed. The results were used to design conductive electrodes in dye-sensitized solar cells with improved performances.

Keywords: Nb-doped titania · Thin films · Crystallinity · Oxidation state · DC magnetron sputtering

1 Introduction

Nb-doped titania materials feature peculiar physical and chemical properties, such as wide band gap, high transmittance and – for a narrow concentration of the dopant – high electrical conductivity [1–3]. In the later case, some authors consider them as “transparent metals” [4]. Various fabrication means of such films have been reported in the literature, based on plasma- or chemically-assisted techniques. The materials’ characteristics significantly vary, even for small variation in the synthesis parameters [5–7]. Therefore, investigations are still necessary to further explore the properties of these transparent conductive oxide (TCO) materials.

In this contribution, pure anatase-ordered thin films Nb:TiO₂ were prepared using a pulsed-DC discharge. Samples, with different thicknesses were prepared in a discharge mixture of Ar and O (10 vol.%). As proven by X-ray photoelectron spectroscopy, the oxidation states of the niobium and titanium are Nb⁵⁺ and Ti³⁺/Ti⁴⁺. By increasing the dopant concentration, the band gap energy increase, while RMS surface roughness decreases.

2 Experimental Details

The investigated films were prepared using a pulsed - DC magnetron sputtering facility, which ensured a base pressure of 1.5×10^{-5} mbar, described in more detail in ref. [6]. A sintered (TiO₂)_{0.94}Nb_{0.06} target was used as discharge cathode. The samples were deposited during 240 min. on (100)Si and glass substrates. A mixture of Ar and small amount of O₂ (10 vol.%) was used as discharge environment, under total pressures of 1.0×10^{-2} and 5.0×10^{-2} mbar. The partial pressure ratios in the discharge were ensured using adequate mass flow controllers. In separate deposition experiments, the total pressure of the gas mixture was adjusted to the desired values by modifying the vacuum pump throughput. The related effects on film properties, associated with different deposition rates were monitored. The pulsed DC discharge was supplied by a power supply with a repetition rate of max. 350 kHz, operated in constant power conditions, for two values of the injected power, 100 W and 200 W (see Table 1).

Table 1. The deposition parameters and the thickness of the samples

Sample	p ($\times 10^{-2}$ mbar)	P (W)	T (°C)	d (nm)
TNO_DC_1	1.0	200	250	1100
TNO_DC_2	5.0	200	250	380
TNO_DC_3	1.0	100	350	300

The surface elemental composition of the samples and the oxidation states were derived from X-ray Photoelectron Spectroscopy (XPS) measurements, performed on a Physical Electronics PHI 5000 VersaProbe instrument, equipped with a mono-chromated AlK _{α} X-ray source ($h\nu = 1486.6$ eV).

The surface topography and surface root mean square (RMS) were recorded and, respectively, measured using an atomic force microscope (AFM) NT-MDT SolverPro7. The films structure was derived from the X-ray diffraction (XRD) patterns (Bruker D8-Advance diffractometer using the monochromated CuK _{α} radiation, $\lambda = 1.54182$ Å).

The Tauc plots [8] were calculated from the optical transmittance spectra recorded using a Evolution 300 UV-Vis Thermo Scientific spectrophotometer. Also, from the transmittance spectra, the sample thickness was derived according to the procedure by Sreemany and Sen [9].

3 Results and Discussion

The XPS measurements show that at the investigated surface's samples are composed of Ti, O and Nb and that the dopant concentration is ranging between 2.1 and 2.8 at.% (see Table 2).

Table 2. Atomic concentration of the elements

Sample	Ti (at.%)	O (at.%)	Nb (at.%)
TNO_DC_1	37.9	60.0	2.1
TNO_DC_2	38.1	59.6	2.3
TNO_DC_3	38.5	58.7	2.8

Since the dopant concentration varies only within 0.7%, no significant differences occur in the high-resolution XPS spectra of the investigated samples, therefore we will indicate and discuss here only one case of the XPS spectra, namely the samples with the highest Nb content (TNO_DC_3). The high-resolution experimental XPS spectrum of the Ti 2*p* signals is shown in Fig. 1, along with its deconvolution in the BE range values of 455 through 468 eV.

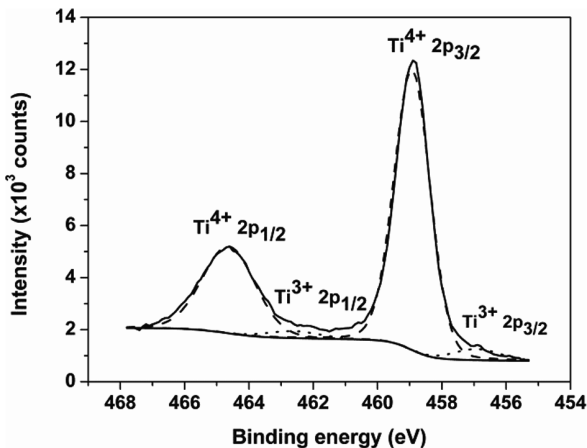


Fig. 1. The Ti 2*p* high-resolution spectra of the TNO_DC_3 samples.

The spectrum deconvolution shows the presence of both 2*p*_{3/2} and 2*p*_{1/2} signals due to Ti⁴⁺ and Ti³⁺. The binding energy (BE) values at 458.8 ± 0.2 eV and 464.3 ± 0.2 eV correspond to the Ti⁴⁺ oxidation state [10], while the peaks at BE = 456.7 ± 0.2 eV and 462.2 ± 0.2 eV correspond to Ti 2*p*_{3/2} and Ti 2*p*_{1/2} XPS signals of Ti³⁺ [11].

The presence of both oxidation states indicates that the samples contain a mixture of TiO_2 and Ti_2O_3 oxides (see Table 2). The $\text{Ti}^{3+}/\text{Ti}^{4+}$ ratio for the TNO_DC_3 samples is 0.05.

The deconvolution of the Nb $3d$ high resolution spectra showed a binding energy of the Nb $3d_{5/2}$ peak of 207.1 ± 0.2 eV, specific to Nb^{5+} oxidation state [5], exclusively. The Nb $3d_{3/2}$ peak has a higher binding energy 209.8 ± 0.2 eV with a separation of about 2.7 eV (Fig. 2).

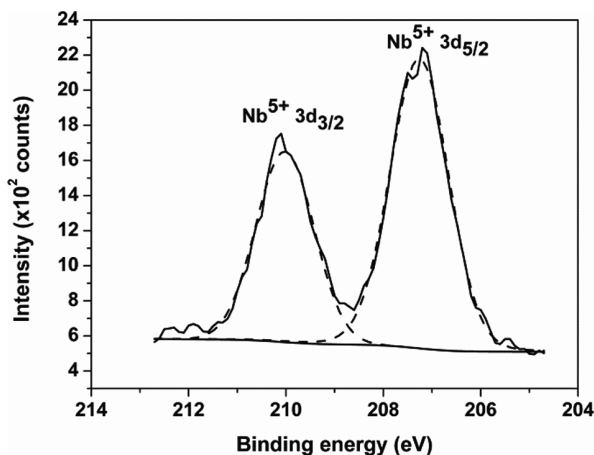


Fig. 2. The Nb $3d$ high resolution spectra of the TNO_DC_3 samples.

The O $1s$ high resolution spectrum (Fig. 3) feature two peaks at BE of 531 ± 0.2 eV and 531.5 ± 0.2 eV, corresponding to the Ti-O bond [10] and -OH groups adsorbed at surface [12], respectively.

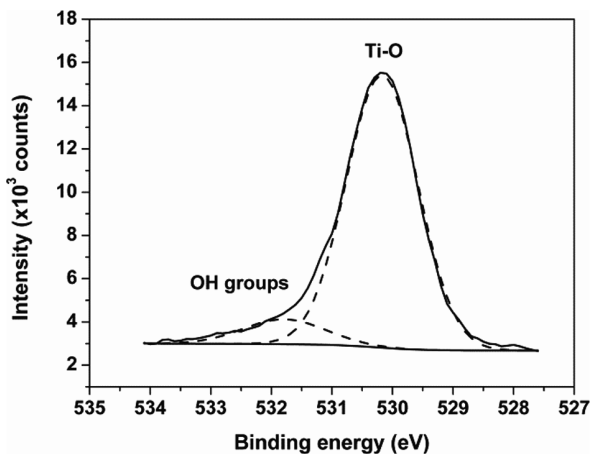


Fig. 3. The O $1s$ high resolution spectra of the TNO_DC_3 samples.

The XRD patterns of the as-prepared samples, with the thickness in the range of 300–1100 nm, are shown in Fig. 4. The diffraction peaks were assigned to corresponding pure anatase (101), (004), (112), (200), (105) and (211) of the dominant polycrystalline phases of TiO_2 .

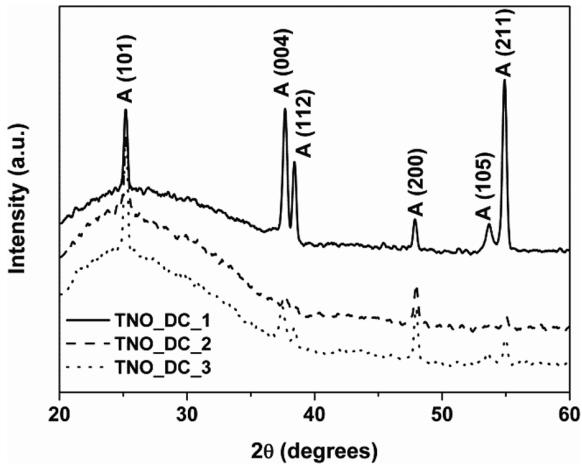


Fig. 4. The XRD plots of the samples.

The analysis of the differences in the diffraction patterns reveals the diminishing of film crystallinity, due to the decrease in film thickness, a result which is in agreement with published results [13]. As it can be observed in the plots, there are no peaks corresponding to impurity phases such as rutile TiO_2 and Nb_2O_5 .

Figure 5 depicts the surface topography (as shown by AFM imaging data) of the TNO_DC_1 and TNO_DC_3 samples. The morphology statistics of the images revealed changes with the increase of the niobium dopant concentration. The root mean square (RMS) surface roughness decrease from 36.2 nm for the samples with 2.1 at.% Nb to 11.5 nm for the samples with 2.8 at.% Nb.

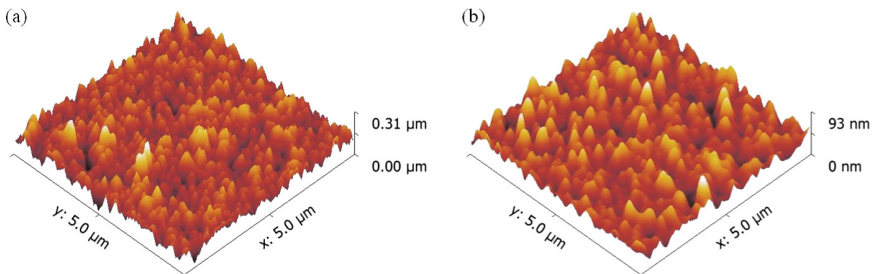


Fig. 5. AFM images of (a) TNO_DC_1 and (b) TNO_DC_3 samples.

The transmittance measurements of the three samples within the spectral range 300–1100 nm are shown in Fig. 6. The characteristic minima and maxima are due to interference associated with multiple light reflections at the film interfaces with air and substrates, and are different for the two samples, in correspondence with their thickness. The transmittance data were used to derive the optical band gap of the materials, using the Tauc plots [8], where $(\alpha h\nu)^{1/2} = f(h\nu)$ are plotted. The extrapolation of the high-energy wing of the plots towards the abscissa (Fig. 7) allowed us to derive the optical band gap of the three investigated samples.

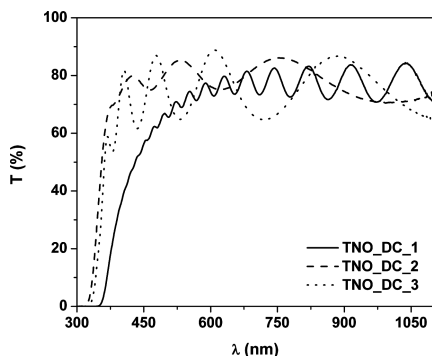


Fig. 6. The transmittance spectra of the samples.

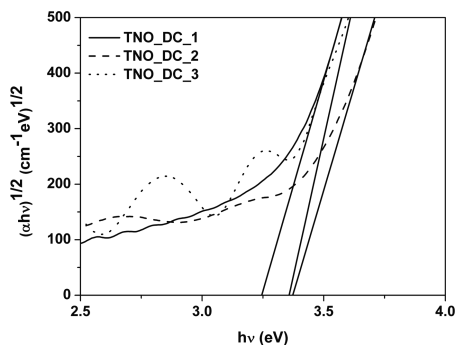


Fig. 7. The Tauc plots corresponding to the three investigated samples.

The data processing showed band gap energy, E_g , of 3.31 eV for the sample with 2.8 at.% Nb and 3.21 eV for the sample with 2.1 at.% Nb, in agreement with findings in literature concerning the increase of the optical band gap values with increasing dopant concentration [5, 14].

4 Conclusions

Anatase-ordered Nb:TiO₂ polycrystalline thin films, with thickness ranging between 300 and 1100 nm were deposited onto treated (100) Si and glass substrates using a pulsed-DC sputtering source with composite (TiO₂)_{0.94}Nb_{0.06} cathode. A mixture of Ar and small amounts of O₂ (10 vol.%) gases was used as discharge environment, under the total pressure of 1.0×10^{-2} and 5.0×10^{-2} mbar. The DC discharge was supplied by a pulsed voltage supply with a repetition rate of max. 350 kHz, working in constant power mode, for two values of the injected power, 100 W and 200 W. Under these conditions, the Nb content ranged between 2.1 and 2.8 at.%. The Tauc diagrams showed band gap energy, E_g , values ranging between 3.21 and 3.31 eV.

Changes in film morphology, as a function of dopant concentration were observed, i.e. with increasing the dopant content, a decrease in surface roughness and crystallinity were observed. The results were used to design conductive electrodes in dye-sensitized solar cells with improved performances.

Acknowledgments. This research was supported by the Bilateral Romania - Belarus grant AR-FRBCF-2016.

References

1. Yamada, N., Hitosugi, T., Kasai, J., Hoang, N.L.H., Nakao, S., Hirose, Y., Shimada, T., Hasegawa, T.: Direct growth of transparent conducting Nb-doped anatase TiO₂ polycrystalline films on glass. *J. Appl. Phys.* **105**, 123702 (2009)
2. Hitosugi, T., Ueda, A., Furubayashi, Y., Hirose, Y., Konuma, S., Shimada, T., Hasegawa, T.: Fabrication of TiO₂-based transparent conducting oxide films on glass by pulsed laser deposition. *Jpn. J. Appl. Phys.* **46**, L86 (2007)
3. Yamada, N., Hitosugi, T., Hoang, N.L.H., Furubayashi, Y., Hirose, Y., Konuma, S., Shimada, T., Hasegawa, T.: Structural, electrical and optical properties of sputter-deposited Nb-doped TiO₂ (TNO) polycrystalline films. *Thin Solid Films* **516**, 5754–5757 (2008)
4. Furubayashi, Y., Hitosugi, T., Yamamoto, Y., Inaba, K., Kinoda, G., Hirose, Y., Shimada, T., Hasegawa, T.: A transparent metal: Nb doped anatase TiO₂. *Appl. Phys. Lett.* **86**, 252101 (2005)
5. Sato, Y., Akizuki, H., Kamiyama, T., Shigesato, Y.: Transparent conductive Nb-doped TiO₂ films deposited by direct-current magnetron sputtering using a TiO_{2-x} target. *Thin Solid Films* **516**, 5758–5762 (2008)
6. Potlog, T., Dumitriu, P., Dobromir, M., Manole, A., Luca, D.: Nb-doped TiO₂ thin films for photovoltaic applications. *Mater. Des.* **85**, 558–563 (2015)
7. Wang, G.Q., Lan, W., Han, G.J., Wang, Y., Su, Q., Liu, X.Q.: Effect of Nb doping on the phase transition and optical properties of sol-gel TiO₂ thin films. *J. Alloy. Compd.* **509**, 4150–4153 (2011)
8. Tauc, J.: *Optical Properties of Solids*. Academic Press, New York (1966)
9. Sreemany, M., Sen, S.: A simple spectrophotometric method for determination of the optical constants and band gap energy of multiple layer TiO₂ thin films. *Mater. Chem. Phys.* **83**, 169–177 (2004)
10. Moulder, J.F., Stickle, W.F., Sobol, P.E., Bomben, K.D.: *Handbook of X-ray Photoelectron Spectroscopy*. ULVAC-PHI/Physical Electronics, Chigasaki/Chanhasen (1995)
11. Fu, Y., Du, H., Zhang, S., Huang, W.: XPS characterization of surface and interfacial structure of sputtered TiNi films on Si substrate. *Mater. Sci. Eng. A* **403**, 25–31 (2005)
12. Fujishima, A., Zhang, X., Tryk, D.A.: TiO₂ photocatalysis and related surface phenomena. *Surf. Sci. Rep.* **63**, 515–528 (2008)
13. Zhang, W., Zhu, S., Li, Y., Wang, F.: Photocatalytic property of TiO₂ films deposited by pulse DC magnetron sputtering. *J. Mater. Sci. Technol.* **20**, 31–34 (2004)
14. Maghanga, C.M., Niklasson, G.A., Granqvist, C.G.: Optical properties of sputter deposited transparent and conducting TiO₂: Nb films. *Thin Solid Films* **518**, 1254–1258 (2009)

Pulsed Magnetron Sputtering: The Role of the Applied Power on W Coatings Properties

Ioana-Laura Velicu¹(✉), Vasile Tiron², Ilarion Mihaila³,
and Claudiu Costin¹

¹ Iasi Plasma Advanced Research Center (IPARC),
Faculty of Physics, Alexandru Ioan Cuza University of Iasi,
700506 Iasi, Romania

laura.velicu@uaic.ro

² Research Department, Faculty of Physics,
Alexandru Ioan Cuza University of Iasi, 700506 Iasi, Romania

³ Integrated Center of Environmental Science Studies in the North-Eastern
Development Region (CERNESIM), Alexandru Ioan Cuza University of Iasi,
700506 Iasi, Romania

Abstract. The interaction of low/high density transient plasma with tungsten (W) target was investigated *via* the sputtered material: in the gas phase, measuring the ion energy distribution function, and as deposited coatings, analyzing the compositional, structural, morphological, mechanical and tribological properties. The W target was sputtered in Ar atmosphere, at two different target power densities (instantaneous peak values of 0.2 and 3 kW/cm²), using a pulsed magnetron discharge. All obtained coatings were polycrystalline. A porous columnar structure was observed for the films deposited at low target power density, while denser-than-bulk films were obtained at high target power density. Comparing the high and low power modes, the W⁺ ion flux is seven times higher in the first case, while the deposition rate is three times higher in the second one.

Keywords: Tungsten coatings · Pulsed magnetron sputtering · Mass spectrometry · Tribological properties

1 Introduction

Magnetron sputtering is a well-known deposition technique designed to produce coatings, from a large variety of materials, both for basic research and industrial purpose. In the last two decades, the magnetron sputtering was extensively operated in high power pulsed mode, being generally known in the literature as High Power Impulse Magnetron Sputtering (HiPIMS) [1]. In HiPIMS, a high power density (several kW/cm²) applied to the magnetron target in unipolar pulses, at low duty cycle and low repetition frequency, facilitates the generation of high density plasma, with high ionization degree (>70%) [2] and broad energy distribution function of the sputtered species [3]. The high ion-to-neutral ratio and intense energetic particle bombardment have been shown to enable the deposition of ultra-dense and smooth metallic and

compound films, allowing to tailor the phase composition, microstructure and morphology, the elemental composition and, subsequently, the properties and functionality of deposited coatings [4].

Beside the well-known application in thin films deposition, the magnetron discharge, operated in high power pulse mode, is suitable to simulate critical aspects of the plasma-wall interaction under fusion devices relevant conditions, the power density applied on the magnetron cathode [5, 6] being comparable with the one expected to be delivered to the ITER divertor (10 MW/m^2) [7]. In such experiments, the selection of the plasma facing material is of great importance. Due to its low erosion yield and high melting temperature, tungsten (W) is one of the most promising plasma-facing material for fusion devices, used in both bulk and thin film (deposited on carbon tiles) form. Hence, the present work reports on the use of the magnetron discharge for fusion related experiments, both as deposition device and as plasma-wall interaction model system. Regarding the deposition device, we studied the role of the applied power on the properties of the deposited W coatings. Such coatings are proposed to cover the carbon fiber composite (CFC) tiles of the wall and/or divertor of future tokamaks [7]. As plasma-wall interaction model, we studied W erosion under low/high density plasma bombardment, by measuring the ionized sputtered material flux. Details of the experiment, analysis techniques and results follow in the next sections.

2 Experimental Set-up

The W coatings were deposited in a high vacuum deposition system using the pulsed magnetron sputtering technique. The magnetron was housed in a vacuum chamber (40 cm in length and 40 cm in diameter) which was pumped to a base pressure of 10^{-5} Pa, using a turbomolecular pump backed by a dry scroll pump. The W planar target (99.995% purity, disk-shape, 5 cm in diameter and 3 mm thickness) was sputtered in pure argon atmosphere, at 1 Pa pressure, by applying low (500 V) and high (1000 V) discharge voltage, in pulses of 10 μs . The short-pulse regime was obtained using a fast pre-ionized high-power pulsed-magnetron sputtering system [8]. For each mode, the pulsing frequency was varied in order to maintain a constant average power of 100 W, which corresponds to a frequency of 3 kHz for low voltage and 500 Hz for high voltage, respectively. Tungsten coatings were deposited on grounded and unintentionally heated molybdenum (Mo) substrates, by setting the deposition time to 100 min. The substrate (disk-shape, surface area of 5 cm^2) was placed at 10 cm in front of the target, axially aligned to it. During the deposition process, time-averaged ion energy distribution functions (IEDFs) of both gas and sputtered material were recorded with an energy resolving mass spectrometer (EQP 1000 Hiden Analytical), facing directly the target surface from the substrate position. Simultaneously, the deposition rate was monitored by a quartz crystal microbalance mounted in the vicinity of the substrate. The analysis of the deposited coatings was made by Atomic Force Microscopy (AFM) and Scanning Electron Microscopy (SEM) for topological and morphological characterization and by X-Ray Diffraction (XRD) and Rutherford Backscattering Spectrometry (RBS) for structural characterization. For mechanical and tribological properties, nanoindentation and nanoscratch tests were performed using a

Nanoindentation Tester (NHT2) equipped with a three-sided diamond pyramidal Berkovich indenter tip with an average radius of curvature of about 100 nm and a Micro-Scratch Tester (MST) equipped with a Rockwell type indenter (100 Cr6, 100 μm radius), both from CSM Instruments. The nanoindentation data were analyzed with the Oliver-Pharr method.

3 Results and Discussion

The temporal evolution of the instantaneous discharge power delivered to the magnetron target, during one pulse at low and high target voltage, is illustrated in Fig. 1a. A peak current of about 4 A was reached during the low voltage pulse, while 36 A was the maximum current value for the high voltage pulse, the corresponding peak power density on the target surface being 0.2 and 3 kW/cm^2 , respectively. The two working regimes will be further referred as low and, respectively, high power mode, even if the average power is the same for both of them. In order to investigate the influence of the applied power on the metal ion flux towards the substrate, the energy distribution function of the sputtered material (W) resulted in ionized state was measured with the energy resolved mass spectrometer. The twofold purpose of this diagnostic was: the correlation of the metal ion flux with the deposited coatings properties (surface morphology, microstructure, density, adhesion, hardness, Young's modulus, and coefficient of friction) and the knowledge of W^+ ion energy distribution function, when W^+ ion is seen as impurity in the discharge. The W^+ IEDF (Fig. 1b) recorded for the high power mode (HiPIMS) is much broader, with a significantly more energetic tail, and contains a larger fraction of both low and high energy ions as compared to that recorded in the low power mode. The W^+ ion flux (proportional to the integral of the IEDF) obtained in HiPIMS mode is seven times higher as compared to the ion flux recorded in low discharge power mode.

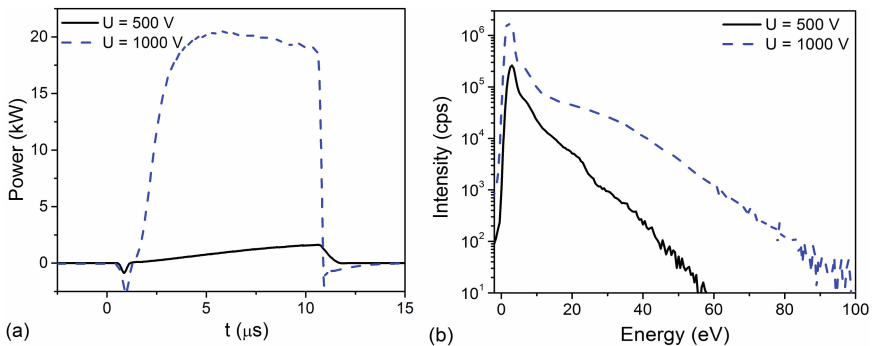


Fig. 1. (a) Temporal evolution of the discharge power and (b) time-averaged ion energy distribution function of W^+ , in low and high power pulsed magnetron sputtering.

The low metal ion flux at the substrate, registered in low power mode, shows that this operation mode behaves more like direct current magnetron sputtering (DCMS) than HiPIMS mode. This aspect is well illustrated in Fig. 2 which shows the W deposition rate as a function of discharge voltage.

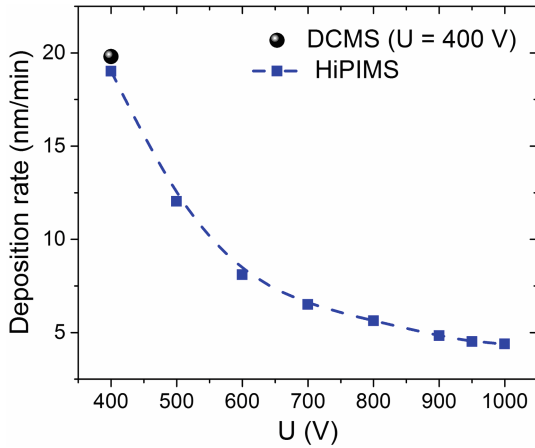


Fig. 2. Deposition rate as a function of the discharge voltage, measured at the same average power of 100 W.

By reducing the discharge voltage from 1000 V to 400 V, the deposition rate gradually increases from 4.5 to 19 nm/min, its maximum value being very close to that obtained in DCMS regime, for the same average power. The main cause for the loss in deposition rate in HiPIMS is the fact that the ionization degree of the sputtered atoms is very high and a large fraction of metallic ions is back-attracted to the target, resulting also in a self-sputtering process. In addition, the metal ion fraction returning to the target contributes to the peak current, a very important parameter included in the power normalized deposition rate. Therefore, the loss deposition rate in HiPIMS is strongly related to the target peak current.

We demonstrated in a previous work [9] that the power normalized deposition rate decreases as the peak current increases. The peak target current was controlled by certain magnetron operation parameters such as: target voltage, pulse duration, magnetic field, target erosion depth, and HiPIMS operation mode. Recently, Greczynski *et al.* have found that the power normalized deposition rates in HiPIMS decays exponentially with the peak target current increasing [10]. In our experiments, the peak current showed a linear increase with the increase of the target voltage (not shown here).

Despite a lower deposition rate as compared to DCMS, HiPIMS technique still represents a powerful deposition technique due to its high metal ion flux directed towards the growing film. It is expected that the intense and energetic metal ion bombardment during magnetron sputtering, in high power mode, to improve the properties of the coatings due to a higher surface activation energy delivered at the growing film surface and increased adatoms mobility. The influence of the applied power (and thus metal ion flux) on the coatings properties (crystallinity, microstructure, packing density, adhesion, hardness, Young's modulus, coefficient of friction) is discussed below.

The crystallinity and crystal orientation of W deposited coatings were investigated by X-ray diffraction. The diffraction patterns (Fig. 3) indicate, in both cases, polycrystalline structure with a preferential growth of W (200) phase ($2\theta \approx 58^\circ$). HiPIMS mode leads to

a higher crystalline structure, revealed by the higher intensity of the diffraction peaks. The crystallite size was estimated from dominant W (200) peak, using the Debye–Scherrer formula. The HiPIMS deposition technique tends to produce films with larger nanocrystallites as compared to the low power pulsed deposition technique. The size of nanocrystallites increased when the applied power was also increased, from 40 to 54 nm.

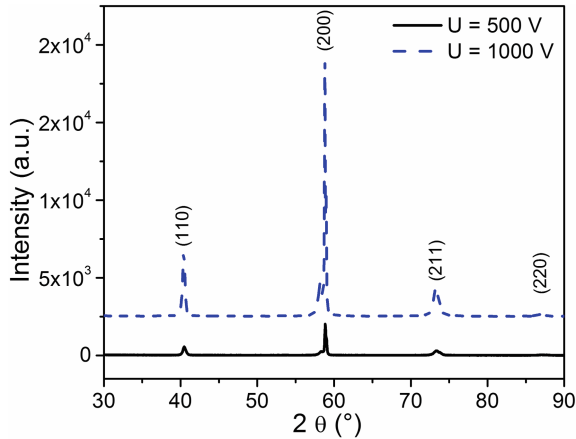


Fig. 3. XRD patterns of W coatings deposited by low/high power pulsed magnetron sputtering.

SEM and AFM images of W deposited coatings are shown in Fig. 4. The cross-sectional SEM image of the coating deposited at low power reveals a porous columnar structure, while the coating deposited at high power shows a very dense structure and smooth surface. Although the deposition time and the average power were the same in both cases, the thickness of the W coating deposited in HiPIMS regime (≈ 400 nm) is three times lower as compared to that of the coating deposited in low power magnetron sputtering regime (≈ 1270 nm). This difference has two main reasons: (i) the higher coating density and (ii) the lower deposition rate in HiPIMS mode as compared to low power pulsed magnetron sputtering. The density of the deposited W coatings was estimated by measuring the areal atomic density using Rutherford backscattering spectrometry and the coating thickness from cross-sectional SEM images [11]. The measurements showed that the mass-density of W coatings deposited in low power magnetron sputtering regime is approximately 8% lower than the mass-density of the bulk W (19.25 g/cm^3), while the W coatings deposited by HiPIMS is about 5% denser than the reported bulk value. The enhanced mass-density of W coatings deposited by HiPIMS may be attributed to the intense and energetic bombardment of the growing film, as well as to the increased fraction of ionized metal flux [12]. Compared to low power pulsed magnetron sputtering, in HiPIMS the sputtered metal flux is highly ionized and it is subjected to strong back-attraction effect caused by the high negative voltage applied to the target. Self-sputtering, gas rarefaction, a less than linear increase in sputtering yields with target voltage and side-wall

loss of metal ions, all these processes represent other important factors decreasing the deposition rate in HiPIMS [13]. The back-attraction effect is strongly reduced when operating with very short pulses [14].

In order to analyze and compare the surface roughness of the deposited coatings, three random areas of $3 \times 3 \mu\text{m}^2$ were scanned over the surface for each deposited sample. The root mean square (RMS) roughness values were calculated using image processing software. For the W coatings deposited by low power pulse magnetron sputtering, the mean value of the RMS roughness is about 14.4 nm, while the RMS roughness of the coating deposited in HiPIMS mode is 1.2 nm (very smooth surface, with very fine grain sizes). The lower roughness obtained using HiPIMS may be attributed to the high mobility of the adatoms induced by the growing film bombardment with highly energetic ions (see Fig. 1b). Increasing the target voltage, the RMS roughness of the surface decreases and the grains have smaller sizes, being more homogeneously distributed on the coating's surface. Therefore, during film growth process in HiPIMS regime, the intense ion bombardment improves the surface mobility, leading to enhanced packing density and smoother surface by removing asperities, voids and defects in the material.

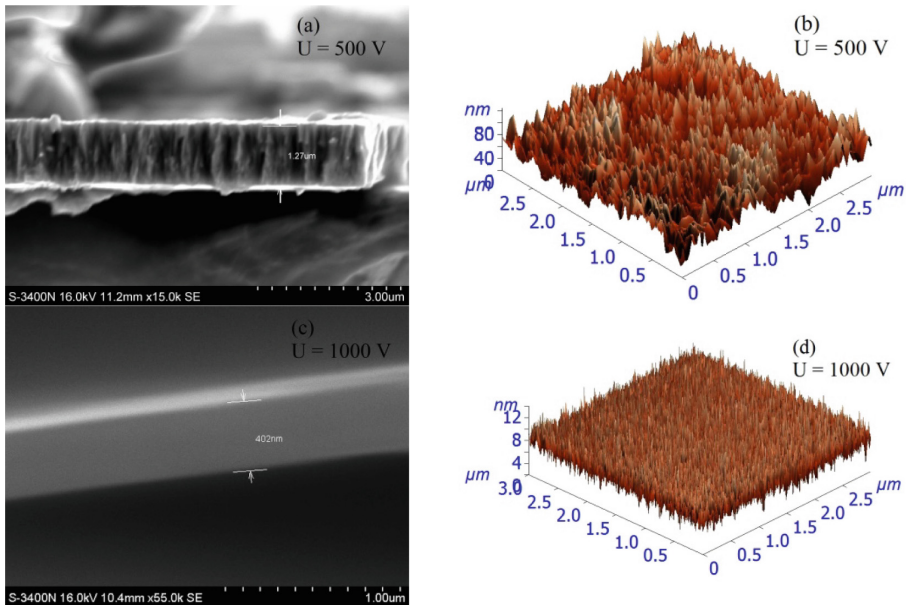


Fig. 4. Cross-sectional SEM (a, c) and 3D AFM (b, d) images for W coatings deposited by low (a, b) and high (c, d) power pulsed magnetron sputtering.

Load-controlled indentation tests were performed at room temperature, on each sample, to determine hardness and absolute Young's modulus values. In order to minimize the Mo substrate influence on the indentation data, the indentation depth was

limited to less than 15% of the coating thickness. It was found that the coatings deposited in high discharge power mode have higher hardness and Young's modulus values as compared to those of the coatings deposited in low power mode. Hardness and absolute Young's modulus values are listed in Table 1. The improvements in hardness may be correlated with the observed densification of the coatings deposited in HiPIMS mode. Coatings with columnar structures contain voids which allow deformation and movement of dislocations in the material when a load is applied [15]. Due to reduced voids, coatings with denser structure exhibit a good resistance to deformation and limit the propagation of dislocations.

In order to study the critical loads (L_{c1} – cohesive failure, L_{c2} – adhesive failure) of the W coatings, linear and progressive-load scratches were performed on each sample, on different surface location, by linearly increasing the load applied on the indenter from 0 to 20 N (0.5 N/min loading rate). L_{c1} and L_{c2} values increase from approximately 5 N and 10 N for coatings deposited by low power pulsed magnetron to 15 N and 17 N, respectively, for the W coatings deposited by HiPIMS.

The coefficient of friction was measured as friction force divided by the applied normal load. The coefficient of friction is generally known to decrease with an increase in hardness and decrease in the roughness [16]. In our case, the coatings deposited in HIPIMS mode show significant improvement in friction resistance (see Table 1) as compared to W coatings deposited in low power pulse mode due to higher hardness and much lower RMS roughness value.

Table 1. Values of deposition rate (S), RMS surface roughness (R_{RMS}), hardness (H), absolute Young's modulus (E), coefficient of friction (μ) and critical loads (L_{c1} and L_{c2}) for W coatings deposited by low (500 V) and high (1000 V) power pulsed magnetron sputtering.

U (V)	S (nm/min)	R_{RMS} (nm)	H (GPa)	E (GPa)	μ	L_{c1} (N)	L_{c2} (N)
500	19.2	14.4	20.5	348	0.05	5	10
1000	4.2	1.2	25.2	392	0.03	15	17

4 Conclusion

The sputtering process of a W target by high and low power pulsed magnetron discharge was analyzed from two perspectives: the deposited coatings and the energy distribution function of the ionized sputtered material. The deposited films were characterized, in term of morphology and structure, by Atomic Force Microscopy, Scanning Electron Microscopy, X-Ray Diffraction and Rutherford Backscattering Spectrometry. W sputtered material was investigated in the gas phase by Mass Spectrometry. The deposited coatings have polycrystalline structure, with a preferential growth of W (200) phase, having a higher crystalline structure when is deposited in HiPIMS mode. The coatings deposited at low instantaneous power reveal a porous columnar structure, with a RMS surface roughness of about 14.4 nm and lower mass-density than bulk, while the coatings deposited at high instantaneous power show a very dense structure, with a RMS surface roughness of about 1.2 nm and higher mass

density than the bulk. The W^+ ion flux, measured at the substrate position, in high power mode, is seven times higher than the ion flux recorded in low power mode, while the deposition rate is three times lower. The observed changes in texture, surface morphology and coatings density with the applied power are a result of the increased ion flux and increased mobility on the surface which caused an evolution from rough surface and columnar structure to a very smooth surface and fully dense structure, with high hardness and elastic modulus, good adhesion to the substrate and low coefficient of friction.

Acknowledgment. This work has been carried out within the framework of the EUROfusion Consortium and has received funding from the Euratom research and training programme 2014–2018 under grant agreement No 633053. The views and opinions expressed herein do not necessarily reflect those of the European Commission. The project has also received funding from the Romanian National Education Minister/Institute of Atomic Physics under contract 1EU-1/2/2016.

References

1. Gudmundsson, J.T., Brenning, N., Lundin, D., Helmersson, U.: *J. Vac. Sci. Technol., A* **30**, 030801 (2012)
2. Helmersson, U., Lattemann, M., Bohlmark, J., Ehiasarian, A.P., Gudmundsson, J.T.: *Thin Solid Films* **513**, 1–24 (2006)
3. Greczynski, G., Hultman, L.: *Vacuum* **84**, 1159–1170 (2010)
4. Samuelsson, M., Lundin, D., Jensen, J., Raadu, M.A., Gudmundsson, J.T., Helmersson, U.: *Surf. Coat. Technol.* **205**, 591–596 (2010)
5. Tiron, V., Velicu, I.-L., Porosnicu, C., Burducea, I., Dinca, P., Malinský, P.: *Appl. Surf. Sci.* **416**, 878–884 (2017)
6. Dinca, P., Porosnicu, C., Butoi, B., Jepu, I., Tiron, V., Pompilian, O.G., Burducea, I., Lungu, C.P., Velicu, I.-L.: *Surf. Coat. Technol.* **321**, 397–402 (2017)
7. Federici, G., et al.: *Nucl. Fusion* **41**, 1967–2137 (2001)
8. Konstantinidis, S., Dauchot, J.P., Ganciu, M., Ricard, A., Hecq, M.: *J. Appl. Phys.* **99**, 013307 (2006)
9. Tiron, V., Velicu, I.-L., Vasilovici, O., Popa, G.: *J. Phys. D Appl. Phys.* **48**, 495204 (2015)
10. Greczynski, G., Hultman, L.: *Vacuum* **124**, 1–4 (2016)
11. Velicu, I.-L., Tiron, V., Rusu, B.G., Popa, G.: *Surf. Coat. Technol.* (2016) doi:[10.1016/j.surfcoat.2016.11.001](https://doi.org/10.1016/j.surfcoat.2016.11.001)
12. Velicu, I.-L., Tiron, V., Porosnicu, C., Burducea, I., Lupu, N., Stoian, G., Popa, G., Munteanu, D.: *Appl. Surf. Sci.* (2017) doi:[10.1016/j.apsusc.2017.01.067](https://doi.org/10.1016/j.apsusc.2017.01.067)
13. Anders, A.: *J. Vac. Sci. Technol., A* **28**, 783 (2010)
14. Antonin, O., Tiron, V., Costin, C., Popa, G., Minea, T.M.: *J. Phys. D Appl. Phys.* **48**, 015202 (2015)
15. Ehiasarian, A.P., Vetushka, A., Aranda Gonzalvo, Y., Sáfrán, G., Székely, L., Barna, P.B.: *J. Appl. Phys.* **109**, 104314 (2011)
16. Bhushan, B.: *Introduction to tribology*, 2nd edn. Wiley, NewYork (2013)

Preparation of Nb-Doped TiO₂ Nanotubes Using Magnetron Sputtering

Claudia Teodora Teodorescu-Soare¹, Marius Dobromir¹,
George Stoian², and Dumitru Luca¹✉

¹ Faculty of Physics, Alexandru Ioan Cuza University of Iasi, 11 Carol I Blvd.,
700506 Iași, Romania

dumitru.luca@uaic.ro

² National Institute of Research and Development for Technical Physics,
47 Dimitrie Mangeron Blvd., 700050 Iași, Romania

Abstract. Niobium-doped TiO₂ nanotubes were obtained by electrochemical anodization in a 0.5 wt.% NH₄F glycerol electrolyte of previously-deposited Nb-doped Ti/TiO₂ layers on Si(100) substrates. For film deposition, a DC magnetron sputtering setup was used, with a mosaic target made of metallic Ti and variable numbers of Nb₂O₅ pellets, placed on the intense sputtering area. By adjusting the number of pellets, we adjusted the dopant concentration in the films. After deposition, both Nb and Ti species were identified in the samples, while after anodization, an increase in the Nb concentration was found, mainly at layer surface.

The nanotube arrays were thermally annealed in air by gradually increasing the temperature between 250 °C and 450 °C, for 45 min. Scanning-electron microscopy images revealed well-formed columnar structures for the three dopant concentrations. While the nanotube diameters varied around 40 nm, the length diminished upon increasing the dopant concentration. Before anodization the samples contained a mixture of metal Ti, titanium dioxide and suboxides (Ti₂O₃ and TiO) in different concentrations. After anodization and thermal treatment, the Ti⁴⁺ oxidation state occurs in the XPS high resolution spectra, corresponding to the presence of the TiO₂ anatase polymorph, exclusively.

No detectable differences exist in the Nb valence state, before and after anodization. The former OH⁻ groups, whose presence was detected in the XPS spectra of the films, are no longer present in the anodized samples.

Keywords: Nb doping · Titania nanotube array · Magnetron sputtering

1 Introduction

Doping titania with niobium results in an increase in electrical conductivity of the materials, due to the introduction of new occupied states in the semiconductor band gap [1] and widening of the host lattice [2]. Titanium is one of the valve metals [1, 2], which, through electrochemical anodization, can be self-organized in nanoporous or nanotubular structures. Similar behavior is specific for Nb [1, 3–7], Zr [8], Al [9], W [10], and Ta [11]. The possibility of nanotube formation through electrochemical

anodization of such a metallic material is strongly dependent on its capacity to form (in the early growth stages) a flat barrier-type anodic oxide layer under an electric field. Further on, an equilibrium state between the oxide formation and metal dissolution processes must be reached, in order to cause the transition to nanotubular or nanoporous growth [12].

It has been demonstrated since long that anatase TiO_2 is a highly functional, non-toxic, thermally and mechanically stable semiconductor photocatalyst [4]. It features a wide band gap ($E_g = 3.2$ eV) and high electrical resistivity. Introduction of Nb impurities into the lattice of TiO_2 increases the electrical conductivity, due to the effects of the extra electrons provided by Nb [3–7] and the occurrence of new occupied states in the band gap [13]. Due to rather comparable atomic radii of Ti (146 pm) and Nb (215 pm), the dopant easily enters into the TiO_2 lattice.

Nb-doped TiO_2 materials have been synthesized mostly by the sol-gel method [4, 5] and magnetron sputtering using composite or mosaic targets. For the synthesis of nanotube arrays of the same material, direct anodization of TiNb thin films, previously grown by magnetron sputtering on non-conducting substrates was reported in refs. [3, 7]. This procedure is a low-cost and highly efficient way of Nb-doped TiO_2 layers synthesis, magnetron sputtering allowing for the possibility to easily control and adjust the Nb concentration and layer thickness. Additionally, magnetron sputtering allows for a high degree of control over purity, shape and quality of the layer.

The focus of this work is to analyze the effects of Nb doping of the TiO_2 nanotube lattice and to investigate the morphologic and functional changes that appear.

2 Materials and Methods

2.1 Deposition of Nb-Doped Ti Through Magnetron Sputtering

Thin films of Nb-doped Ti/ TiO_2 were prepared by means of magnetron sputtering, under three different deposition conditions. A metallic Ti cathode and variable numbers of (5 mm diameter) Nb_2O_5 pellets were sputtered by ion bombardment. The sputtered material was collected on precut and prewashed Si substrates placed in front of the target, at 4 cm distance. The deposition was carried out in a vacuum chamber having $p_{limit} = 1 \times 10^{-5}$ mbar, under $p_{work} = 5 \times 10^{-3}$ mbar of Ar, for a deposition time of 10 min. By adjusting the gas flow rate of the Ar gas, Q_{Ar} , the number of the niobium oxide pellets placed on the high-rate sputtering area of the target, and keeping the residual O_2 pressure to a minimum value, we could adjust the dopant (Nb) concentration and ensure sufficient amount of metallic Ti in the layer. Keeping the oxygen content as low as possible during the deposition is favorable for Nb incorporation into the TiO_2 lattice by avoiding Ti vacancies [7]. This made possible to grow, in a second step, oxide nanotube arrays. We report here the results of a study involving three samples, labeled as S_1 , S_2 and S_3 (see Table 1).

Table 1. Atomic concentration for the deposited samples

Sample	Ti	- of which Ti ⁰	O	Nb
S1	38.8%	15.8%	61.2%	0.0%
S2	39.9%	18.3%	60.0%	0.2%
S3	37.6%	11.3%	61.2%	1.1%

2.2 Anodization of As-Deposited Nb-Doped Ti Thin Films

The second step of synthesizing Nb-doped TiO₂ arrays was the electrochemical anodization of the as-prepared Nb-doped Ti/TiO₂ layers. For this, an electrochemical cylindrical Teflon® chamber was manufactured, which had a volume of 50 ml. The as-prepared Nb-doped Ti/TiO₂ layers were anodized in an organic electrolyte solution of glycerol containing 0.5 wt.% NH₄F. A programmable power supply (Hameg HM8142) was employed to bias this anode with respect to a Pt-foil electrode with a voltage $V = 30$ V for a $t = 45$ min in all experiments.

2.3 Film Characterization

Scanning-electron microscopy SEM was used (Fig. 1) for detailed inspection of sample surface morphology in both top-view and cross-section modes. The length and the diameter of the tubes were obtained from the SEM imaging cross-sections. Chemical composition of the as-prepared Nb-doped Ti/TiO₂ layers was investigated by X-ray Photoelectron Spectroscopy (XPS), before and after anodization. The nanotube arrays were subsequently annealed in air by gradually increasing the temperature from 250 °C to 450 °C and then left for 45 min. X-ray Diffraction (XRD) was employed to establish the crystalline structure of the samples.

3 Experimental Results and Discussion

3.1 Scanning Electron Microscopy Imaging Post Anodization

SEM images shown in Fig. 1 depict top- and side-views of the samples S₁, S₂ and S₃. Well-formed columnar structures are revealed.

While the average diameter remained constant (40 nm), the length of the nanotubes shortens with increasing the Nb concentration. The nanotube length diminished from 650 nm (S₁) to 380 nm (S₂) and 470 nm (S₃). The pore diameter of an as-formed nanotube layer depends on the applied voltage under which it is grown. In our case it is constant, while the tube length decreases by increasing the Nb concentration (see Table 1). The growth of nanotube arrays depends on the constant formation and migration of O²⁻, OH⁻, F⁻ and metallic ions Ti⁴⁺, Nb⁵⁺ on the anode-electrolyte interface. Thus, equilibrium must be established between chemical dissolution and electrochemical etching for the smooth growth of such nanostructures. For obtaining pore formation on a metallic valve layer, chemical dissolution of the formed oxides is necessary. F⁻ ions act as a dissolution agent on the metallic oxide, resulting in soluble metal-fluoride complexes [8].

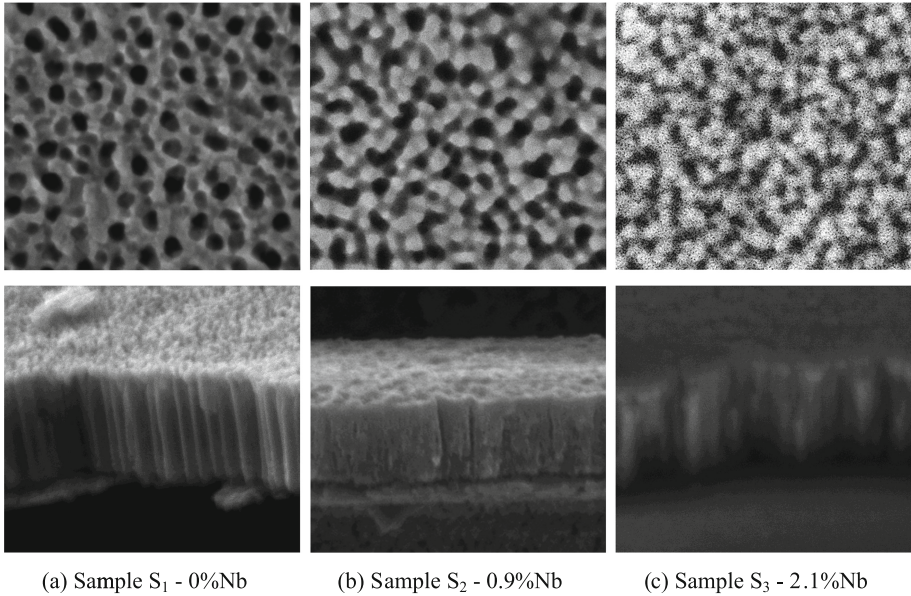


Fig. 1. Field-emission scanning-electron microscope images of top and cross-section views of samples (a) S_1 , (b) S_2 and (c) S_3 post-anodization.

3.2 High-Resolution X-Ray Photoelectron Spectroscopy

The surface atomic concentrations of the investigated samples were derived from the XPS data, before and after anodization, to better understand the evolution of the chemical oxidation state. The XPS spectra are shown in Figs. 2, 3 and 4. We obtained the chemical elements on the sample's surface after deposition and after anodization, which can be viewed in Tables 1 and 2, respectively.

It can be observed that both metallic Ti and bonded Ti exist post-deposition, while after anodization the entire quantity of metallic Ti^0 transforms into a bonded state Ti^{4+} . An increase in the Nb concentration at the surface occurs through the anodization of the thin films.

Due to small variation in Nb concentration, we only present and discuss here the XPS spectra of the sample having higher Nb content (S_3). The deconvolutions of the Ti $2p$ high resolution spectra of the as-deposited and anodized samples S_3 samples are presented in the Fig. 2.

For the Nb:TiO₂ films (before anodization), the deconvolution showed binding energy (BE) values of the peaks Ti $2p_{3/2}$ of 454.0 ± 0.2 eV, 455.0 ± 0.2 eV, 456.7 ± 0.2 eV and 458.8 ± 0.2 eV (Fig. 2a), which are signatures of Ti^0 and Ti^{2+} [14], respectively Ti^{3+} [15] and Ti^{4+} [14]. The Ti $2p_{1/2}$ signals present the same oxidation states, with a separation of about 5.7 eV. After anodization, only the Ti^{4+} oxidation state appears in the deconvolution of the Ti $2p$ high resolution spectra (Fig. 2b).

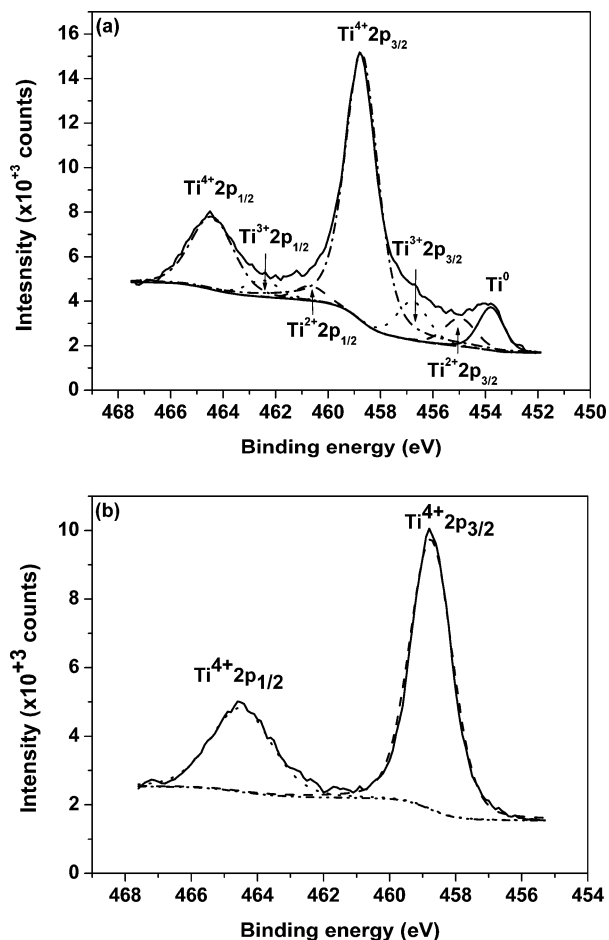


Fig. 2. The Ti 2p high resolution spectra of the as-deposited (a) and anodized (b) S3 sample.

The deconvolution of the Nb 3d high resolution spectra, for the as-deposited and anodized samples (Fig. 3), showed Nb 3d_{5/2} peak with BE = 207.1 ± 0.2 eV, specific to Nb⁵⁺ oxidation state [16]. The Nb 3d_{3/2} peak has a higher binding energy 209.8 ± 0.2 eV, with a separation of about 2.7 eV (Fig. 3a). After anodization, the oxidation state of the Nb is the same, as presented in Fig. 3b.

The O 1s high resolution spectra for the as-deposited and anodized samples (Fig. 4), show two peaks at BE of 530.3 ± 0.2 eV and 531.5 ± 0.2 eV, corresponding to O in TiO₂ bond [17] and adsorbed OH⁻ groups [18] (Fig. 4a). After anodization, a new peak occurs, located at 532.7 ± 0.2 eV corresponding to H₂O [19], instead the OH⁻ groups peak (Fig. 4b).

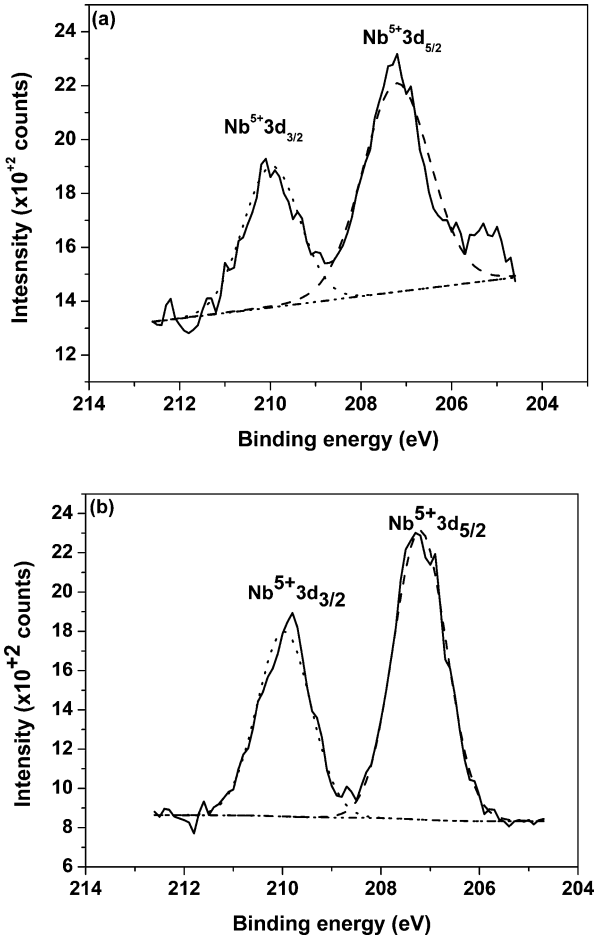


Fig. 3. The Nb 3d high resolution spectra of the as-deposited (a) and anodized (b) S3 sample.

3.3 Thermal Treatment

The nanotube arrays were annealed in air from 250 °C to 450 °C for 45 min. The annealed TiO₂ layers were then left to cool off at room temperature overnight.

3.4 Electric Resistivity Measurements

Electrical resistivity was measured using the the van der Pauw four-point probe configuration. By passing a current $I = 1 \mu A$ through the outer pins a voltage was measured between the inner ones. We noticed a decrease in layer resistivity with the increase in Nb concentration from 1.0 to 0.45 to 0.25 Ω cm for the samples in the order S1 - S2 - S3.

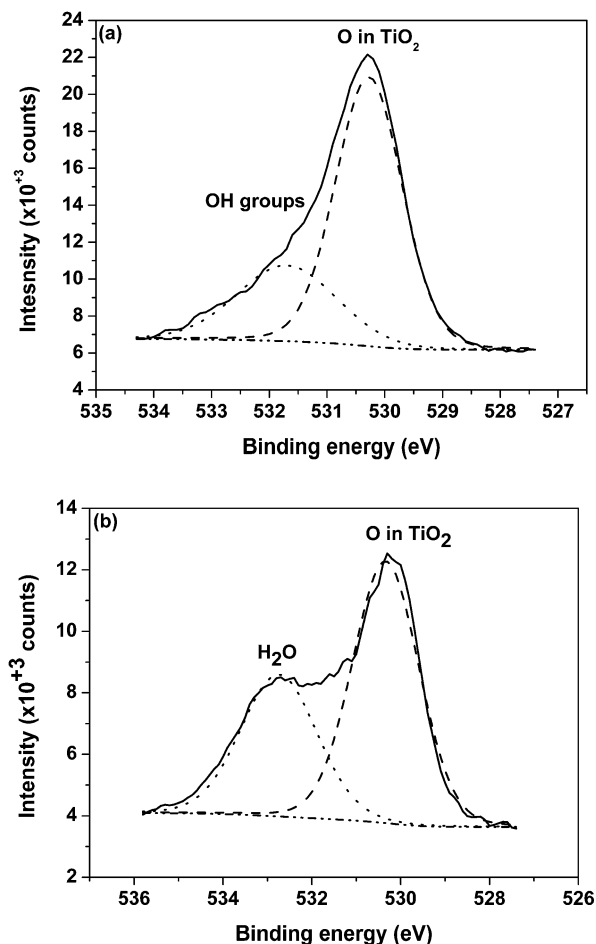


Fig. 4. The O 1s high resolution spectra of the as-deposited (a) and anodized (b) S3 sample.

Table 2. Atomic concentration for the anodized samples

Sample	Ti	- of which Ti ⁰ -	O	Nb
S1	23.0%	0.0%	77.0%	0.0%
S2	21.6%	0.0%	77.5%	0.9%
S3	26.3%	0.0%	71.6%	2.1%

4 Conclusions

Nb-doped TiO₂ nanotube arrays were successfully prepared in the outlined two-step process on Si substrates. The chemical composition of the as-prepared layers was investigated by XPS, before and after anodization. After deposition, both Nb and metallic Ti were identified in the samples. After anodization, an increase in Nb

concentration was found at layer surfaces. The nanotube arrays were annealed in air from 250 °C to 450 °C for 45 min. SEM images revealed well-formed columnar structures for three Nb doping concentrations. The length of the nanotubes was found to diminish with increasing Nb concentration, from 650 nm to 380 nm while, the diameters remained predominantly unaffected.

While before anodization, the sample was a mixture of metal Ti and suboxides (TiO₂, Ti₂O₃ and TiO) in different concentration, after anodization and thermal treatment, only the Ti⁴⁺ oxidation state appears in the XPS high resolution spectra, corresponding to the presence of the TiO₂ anatase polymorph, exclusively. No detectable differences exist in the Nb valence state, before and after anodization, while the former OH⁻ groups detected by the XPS spectra in the films, are no longer present in the anodized samples, at the expense of the H₂O molecules adsorbed at the nanotube surfaces.

Finally, the resistivity measurements showed a decrease in the electrical resistivity with increasing dopant concentration.

Acknowledgements. This research was supported by the Bilateral Romania – Belarus grant AR-FRBCF-2016.

References

1. Ghicov, A., Yamamoto, M., Schmuki, P.: Lattice widening in niobium-doped TiO₂ nanotubes: efficient ion intercalation and swift electrochromic contrast. *Angew. Chem. Int. Ed.* **47**, 7934–7937 (2008)
2. Duța, M., Predoana, L., Calderon-Moreno, J.M., Preda, S., Anastasescu, M., Marin, A., Dascalu, I., Chesler, P., Hornoiu, C., Zaharescu, M., Osiceanu, P., Gartner, M.: Nb-doped TiO₂ sol-gel films for CO sensing applications *Mat. Sci. Semicon. Proc.* **42**, 397–404 (2016)
3. Wu, J.-M., Chen, C.-J.: Dielectric properties of (Ba, Nb) doped TiO₂ ceramics: Migration mechanism and roles of (Ba, Nb). *J. Mater. Sci.* **23**, 4157–4164 (1988)
4. Hsu, L.-S., Luca, D.: Substrate and annealing effects on the pulsed-laser deposited TiO₂ thin films. *J. Optoelectron. Adv. Mater.* **5**(4), 841–848 (2003)
5. Lim, H.-D., Seong, W.M., Kim, J., Lee, B., Kim, D.H., Kang, K.: Nb-doped TiO₂ air-electrode for advanced Li-air batteries. *J. Asian Ceram. Soc.* **3**(1), 77–81 (2015)
6. Lu, Y., Khan, S., Song, C.L., Wang, K.K., Yuan, G.Z., Li, W., Han, G.R., Liu, Y.: Doping concentration effects upon column-structured Nb: TiO₂ for transparent conductive thin films prepared by sol-gel method. *J. Alloy. Compd.* **663**, 413–418 (2016)
7. Lu, L., Guo, M., Thornley, S., Han, X., Hu, J., Thwaites, M.J.: Remote plasma sputtering deposited Nb-doped TiO₂ with remarkable transparent conductivity. *Sol. Energy Mater. Sol. C.* **149**, 310–319 (2016)
8. Tsuchiya, H., Macak, J.M., Ghicov, A., Taveira, L., Schmuki, P.: Self-organized porous TiO₂ and ZrO₂ produced by anodization. *Corros. Sci.* **47**, 3324–3335 (2005)
9. Lv, X., Deng, J., Sun, X.: Cumulative effect of Fe₂O₃ on TiO₂ nanotubes via atomic layer deposition with enhanced lithium ion storage performance. *Appl. Surf. Sci.* **369**, 314–319 (2016)
10. Tsuchiya, H., Macak, J.M., Sieber, I., Taveira, L., Ghicov, A., Sirotna, K., Schmuki, P.: Self-organized porous WO₃ formed in NaF electrolytes. *Electrochem. Commun.* **7**, 295–298 (2005)

11. Minagar, S., Berndt, C.C., Wen, C.: Fabrication and characterization of nanoporous niobia and nanotubular tantalum, titania and zirconia via anodization. *J. Funct. Biomater.* **6**, 153–170 (2015)
12. Kowalski, D., Kim, D., Schmuki, P.: TiO₂ nanotubes, nanochannels and mesosponge: self-organized formation and applications. *Nano Today* **8**, 235–264 (2013)
13. Yu, C.-F., Sun, S.-J., Chen, J.-M.: Magnetic and electrical properties of TiO₂: Nb thin films. *Appl. Surf. Sci.* **292**, 773–776 (2014)
14. Moulder, J.F., Stickle, W.F., Sobol, P.E., Bomben, K.D.: *Handbook of X-ray Photoelectron Spectroscopy*, ULVAC-PHI Japan, Physical Electronics, USA (1995)
15. Fu, Y., Du, H., Zhang, S., Huang, W.: XPS characterization of surface and interfacial structure of sputtered TiNb films on Si substrate. *Mater. Sci. Eng., A* **403**, 25–31 (2005)
16. Sato, Y., Akizuki, H., Kamiyama, T., Shigesato, Y.: Transparent conductive Nb-doped TiO₂ films deposited by direct-current magnetron sputtering using a TiO_{2-x} target. *Thin Solid Films* **516**, 5758–5762 (2008)
17. Ingo, G.M., Dire, S., Babonneau, F.: XPS studies of SiO₂-TiO₂ powders prepared by sol-gel process. *Appl. Surf. Sci.* **70**, 230–234 (1993)
18. Fujishima, A., Zhang, X., Tryk, D.A.: TiO₂ photocatalysis and related surface phenomena. *Surf. Sci. Reports* **63**, 515–528 (2008)
19. Mårtensson, N., Malmquist, P.-Å., Svensson, S., Basilier, E., Pireaux, J.J., Gelius, U., Siegbahn, K.: Molecular and solid water - a comparative ESCA study. *Nouveau J. de Chimie* **1**, 191–196 (1977)

**Electric and Electronic Engineering.
Manufacturing Technology**

Generation and Evaluation of Surrogate to Design Fuel Supply System

Keisuke Fujii^(✉), Shun Egawa, and Kazuhiro Takeda

Department of Engineering, Graduate School of Integrated Science
and Technology, Shizuoka University, Shizuoka, Japan
fujii.keisuke.17@shizuoka.ac.jp

Abstract. To design a fuel supply system, some properties of real gasoline as fuel are needed. However, real gasoline is a mixture which has more than two hundreds of components. It is not rational to identify all the components. In this study, a surrogate is generated to be available in a simulator. It was made by limiting to the ingredients frequently used for real gasoline. The composition of the surrogate was decided by the characteristics evaporation of real gasoline using the process simulator HYSYS. The evaporation characteristics, the Reid vapor pressure, density and kinetic viscosity are target properties in this study. The target properties of the surrogate were estimated and evaluated. The evaporation characteristics were estimated by the flow diagram of multi-stage flash distillation in the HYSYS. The generated surrogate consisted of five components. The surrogate include dangerous, volatile, environment-tally hazardous and flammable components. Therefore, the surrogate will be used by computer simulation and not be used by experiments. The evaporation characteristics of the surrogate were compared with those of real gasoline. The characteristics were well represented up to 120 °C. The target fuel system of this study will not become more than 100 °C, so the estimation results have enough accuracy. Furthermore, density and kinetic viscosity of the surrogate were close to those of real gasoline.

Keywords: Real gasoline · Surrogate · Thermodynamic properties · Reid vapor pressure · Evaporation characteristic

1 Introduction

In a fuel supply system, fuel goes through various equipment such as intermediate tank. Finally, it flows to the injector and is injected to the engine. Figure 1 shows the outline of the target fuel supply system.

In the system that supplies fuel to the engine of the outboard motor, as there is no pressurizing mechanism. It is supplied by decompressing with a pump. Since the fuel is decompressed, the fuel is evaporated and the gas-liquid ratio is changed. It affects the operation of the engine and the injector. As a solution, a gas-liquid separator is installed in the fuel path to stabilize the gas-liquid ratio. However, there are problems with this fuel path. When the engine is in operating, enough gasoline is supplied to the engine. However, when the engine stops, the fuel supply from the fuel tank to the gas-liquid

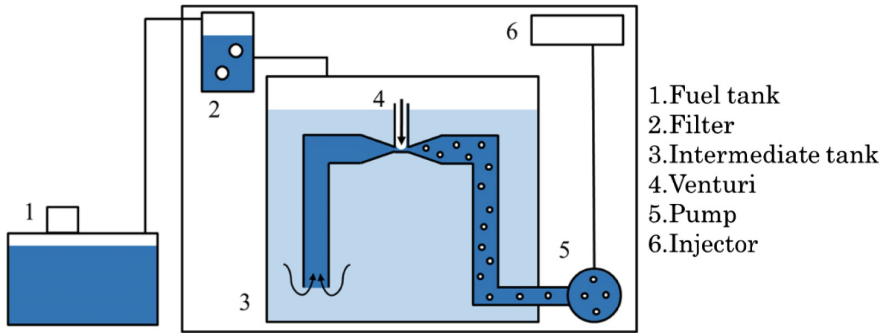


Fig. 1. Schematic view of the apparatus.

separation tank is stopped. Furthermore, the engine and the fuel supply system inside of the cowl may exceed 50 °C. After stopping the operation, part of the gasoline may evaporates in the fuel path. As the internal pressure rises with evaporation, the fuel gasoline in the system flows backward to the fuel tank. At engine restart, the system cannot supply enough gasoline to the injector.

In order to solve the problem, it is preferable to design the capacity of the gas-liquid separation tank to a sufficient size. However, the tank cannot be enlarged by the space limitation of the cowl. Then, it is examined by using the process simulator HYSYS whether or not the necessary amount of liquid remains in the gas-liquid separation tank. To design a fuel supply system, we need to simulate for the fuel supply system. To simulate the system, some thermodynamic properties of real gasoline are needed. However, real gasoline is a mixture which has more than two hundreds of components. The simulation using all components has a large calculation load. The surrogate was made by limiting to the ingredients frequently used for real gasoline. The composition of the surrogate was formulated by the evaporation characteristics of real gasoline. Thus, the properties of the surrogate emulate the properties of real gasoline. Many studies have been proposed each types of the surrogate. However, the surrogate for a fuel supply system have not been proposed. The proposed surrogate in this study is decided to use a simulator of the fuel supply system. We estimate for properties using the surrogate.

2 Methodologies

2.1 Generation of the Surrogate

In this study, the surrogate is generated from evaporation characteristics of real gasoline. For the generation of the surrogate, the component and composition of the surrogate is determined according to the procedure of Japanese Industrial Standards (JIS) K 2254 [1] using the process simulator HYSYS. JIS K 2254 is distillation test method of petroleum in Japan.

The estimating step is as follows,

1. Supply components and compositions as initial settings with many components in real gasoline.
2. Supply as a boiling point liquid, and separate gas and liquid.
3. Define the dew point of the separated gas as the initial boiling point.
4. Specify the temperature of the heater at the evaporation data of real gasoline.
5. Change the component and compositions and go to step 1 until the estimation accuracy will be sufficient.

2.2 Estimation of Evaporation Curve

The steps to estimate the evaporation curve according to the procedure of JIS K 2254 using the HYSYS is as follows. The flow diagram is Fig. 2.

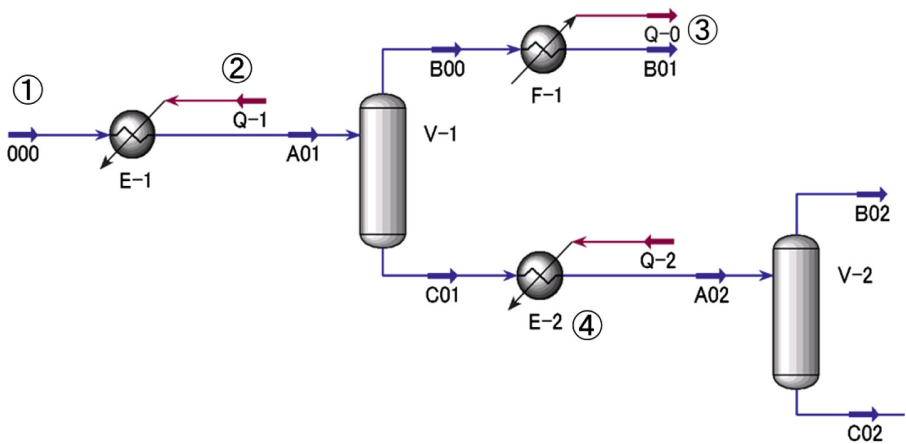


Fig. 2. Part of the HYSYS flow diagram for estimating evaporation component ratio of surrogate.

1. Supply fuel as boiling point liquid.
2. Separate it into gas and liquid.
3. Let the initial boiling point be the dew point of the separated steam.
4. Increase the temperature of the separated liquid and separate it into gas and liquid.
5. The evaporation rate and the temperature of the separated steam are measured as the distillation temperature.
6. Go to step 4 until the end point.

2.3 Estimation of Reid Vapor Pressure

To validate the calculated accuracy of the Reid vapor pressure, we used n-Pentane as a test substance in this study. Table 1 compares the experimental values, the default estimated value of the HYSYS, and the estimated value using the flow diagram of the HYSYS.

From the results in Table 1, the proposed method can estimate more accurately estimated than default in the HYSYS. Furthermore, we obtained estimation results closer to experimental values when mixing N_2 and O_2 than using the pseudo component air. The pseudo component air had O_2 of 99% [2].

Table 1. Result of estimation of Reid vapor pressure.

	n-Pentane air	n-Pentane $N_2 + O_2$
Experiment		15.5 psia
Default		11.1 psia
Proposed	13.8 psia	14.2 psia

Therefore, the estimation of the Reid vapor pressure is considered better to use a mixed component of N_2 and O_2 than using pseudo component air in the HYSYS has improved accuracy.

A method to estimate the Reid vapor pressure according to the procedure of JIS K 2258 was simulated using the HYSYS. JIS K 2258 is vapor pressure test method of oil in Japan (Fig. 3).

The estimating step is as follows,

1. Feed the fuel at 0 °C, 101.3 kPa.
2. Extract liquid using a gas-liquid separator.
3. Mix the air at 37.8 °C corresponding to 4 times the volume of the fuel.
4. Heat to 100 °F (37.8 °C).
5. Pressurize until the gas:liquid ratio becomes 4:1.
6. Get the gauge pressure as the estimated Reid vapor pressure.

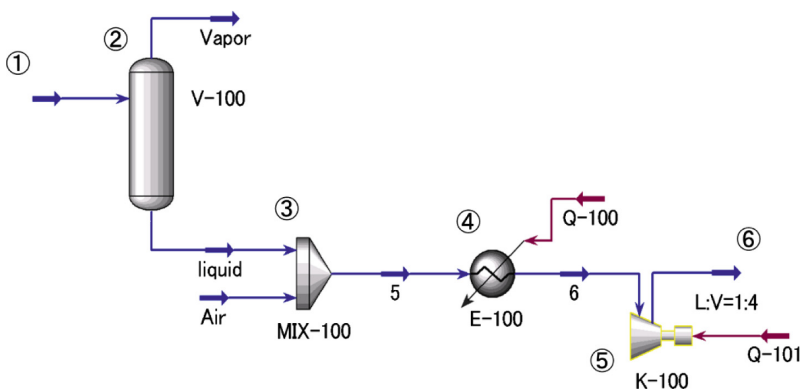


Fig. 3. HYSYS flow diagram for estimating the Reid vapor pressure of surrogate.

3 Results

3.1 Generation of Surrogate

Based on of the evaporation curve of real gasoline, the surrogate was determined. Table 2 shows the component and composition of the generated surrogate.

Table 2. Composition of surrogate.

Component	Mass fraction	Mole fraction
n-Butane	0.008	0.012
i-Pentane	0.235	0.292
2-Mpentane	0.249	0.259
Toluene	0.255	0.248
124-Mbenzene	0.253	0.189

The components of surrogate are composed of 5 components. i-Pentane, 2-Mpentane and Toluene are main components of real gasoline. In addition, they were composed using n-Butane as a low-boiling point component and 124-Mbenzene (1, 2, 4-trimethyl benzene) as a high-boiling point component to emulate the evaporation curve. The surrogate include dangerous, volatile, environment-tally hazardous and flammable components. Therefore, the surrogate will be used by computer simulation and not be used by experiments.

Figure 4 shows the evaporation characteristics of the surrogate and the real gasoline.

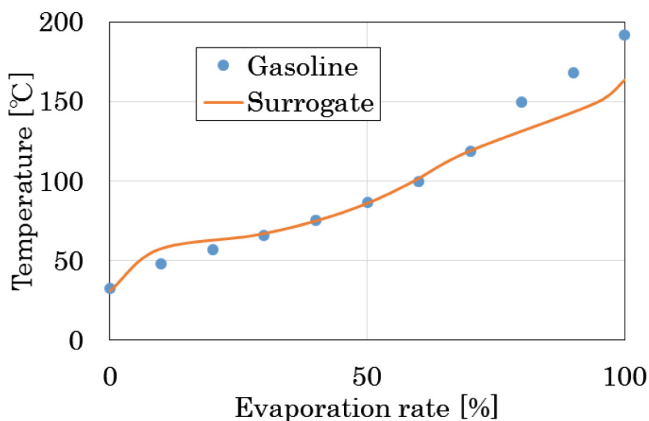


Fig. 4. Estimated evaporation characteristic.

From the results in Fig. 4, the evaporation characteristics of surrogate can accurately emulate the evaporation characteristics of real gasoline to 120 °C or less. The target fuel system of this study will not become more than 100 °C, so the estimation results have enough accuracy. In order to improve the accuracy in the high temperature range, it is necessary to add a component with a higher boiling point.

From the results of Table 3, the Reid vapor pressure of the surrogate was 15 kPa lower than that of real gasoline. The vapor pressure has a very large influence on n-Butane, and generated surrogate has a small amount of n-Butane. Therefore, the estimated Reid vapor pressure of the surrogate is thought to be lower than the experimental value.

Table 3. Estimated Reid vapor pressure.

	Gasoline	Surrogate
Reid vapor pressure	72 kPa	57 kPa

The estimated density and kinetic viscosity were shown in Table 4. The density and kinetic viscosity of the proposed surrogate were in those of JIS. Therefore, the surrogate have sufficient properties for the fuel supply system simulation.

Table 4. Estimated density and kinetic viscosity.

	Gasoline (JIS)	Surrogate
Density	0.72–0.76 g/cm ³	0.738 g/cm ³
Kinetic viscosity	0.5–0.6 cSt	0.506 cSt

4 Conclusions

Generating and evaluation method for the surrogate for a fuel supply system simulation is proposed. The proposed five-component surrogate can accurately emulate the evaporation characteristics of real gasoline consisting of 200 or more components. The Reid vapor pressure of the surrogate was 15 kPa lower than that of real gasoline. The density and kinetic viscosity of the proposed surrogate were in those of JIS. Therefore, the surrogate have sufficient properties for the fuel supply system simulation.

References

1. Japanese Industrial Standards Committee. <http://www.jisc.go.jp/>
2. ChemicalBook. http://www.chemicalbook.com/ChemicalProductProperty_EN_CB9159242.htm

Optimal Design of Electrical Machines: State of the Art Survey

Marcell Baranyai¹, Amir Mosavi¹(✉), Istvan Vajda¹,
and Annamária R. Varkonyi-Koczy^{1,2}

¹ Kando Kalman Faculty of Electrical Engineering, Institute of Automation,
Obuda University, Budapest, Hungary

{baranyai.marcell, amir.mosavi, vajda.istvan,
koczy.annamaria}@kvk.uni-obuda.hu

² Department of Mathematics and Informatics,
J. Selye University, Komarno, Slovakia

Abstract. Scientific optimization has become a popular term in the modern design of electrical machines. Due to the current competitive and dynamic market, and the increasing importance of energy efficiency and energy conservation, the design optimization of electrical machines has become an essential strategy for research and development. Yet the multi-disciplinary, multiobjective, high-dimensional, nonlinear, and coupled nature of the electrical machines' design optimization poses a great challenge to the research communities. Nevertheless, the recent advanced algorithms for multiobjective optimization and multiple-criteria decision analysis have been empowering designers to push the existing boundaries of electrical machines design in dealing with the complexity for the novel concepts and innovative designs. This paper presents a state of the art survey on the advancements of the novel optimization tools and applications, and further demonstrates the progress of the academic research in this realm.

Keywords: Electrical machines · Design optimization · Optimal design

1 Introduction

The task of solving optimal engineering design problems of electrical machines is considered as a demanding decision-making process where the real-life design problems have to be considered simultaneously from very different perspectives [1, 2]. In fact the design objectives of the electrical machines are often in contradiction as described in literature [3]. In addition, due to the large number of design parameters and constraints of the machines' performance, finding an optimal solution which can simultaneously satisfy the design objectives can be an overwhelming task [4]. Even though there exists a number of case studies utilizing classical optimization algorithms, e.g. [5], their applicability is heavily constrained. For instance the objective function needs to be continuous and derivable.

Many electrical machines models are based on finite element models, without analytical expressions for the optimization model itself. Thus, various intelligent

optimization algorithms using non-analytical machine models have been employed, particularly in multiobjective optimization problems, such as those based on the popular genetic algorithms (GAs) [6], and particle swarm optimization (PSO) algorithms [7].

2 Optimization of Electrical Machines

A general workflow for finite element analysis (FEA) for electrical machines optimization was presented by Stipetic et al. [8]. According to their proposed workflow the process of optimization starts with the description of the problem i.e., identifying the boundary conditions, objectives and a set of constant model parameters e.g., topology of the motor, number of slots on the rotor and stator, number of poles, and type of winding. After setting the optimization algorithm, the following steps are performed iteratively in a loop: (1) the optimization algorithm generates variables (e.g. vectors of design variables), (2) the variables are converted to model parameters, (3) the model is converted into a FEA environment, (4) the FEA model is solved, (5) the performance of the model is extracted, (6) constraint functions and objective functions values are calculated, (7) the values of these constraint and objective functions are given back to the optimization algorithm. After the termination of the algorithm a set of optimal solutions or so called Pareto optimal front is created. According to Lei et al. [6], differential evolution algorithm (DEA), nondominated sorting genetic algorithm (NSGA) [9], Kriging-model based optimization [10], and PSO [7], follow the similar principle design optimization workflow with the widest usage in electrical machines design.

2.1 Genetic Algorithms

Lei et al. [6] well describe the potential and drawbacks of using GAs in optimal design of the electrical machines. The algorithm starts with a set of population represented by chromosomes. Solutions from one population (known as parent population) are taken and used to form a new population (known as offspring or children population) by three genetic operations of crossover, mutation and selection. The solutions which are used to generate new solutions are selected in terms of their fitness. This means that the more suitable the solutions are, the more opportunities they have to reproduce in the evolution process. This strategy of optimization is repeated until the design objectives are satisfied [11]. GAs are popular and are widely used due to their capabilities to find global optimum and not get trapped in the local minima [8]. However they are not considered the most computationally efficient [11]. In a recent study [9] the reluctance network of a synchronous reluctance motor (SynRM) was successfully optimized by means of a GA. With some modifications the GAs can be well adapted for solving multiobjective optimization problems of electrical machines [12]. Multiobjective genetic algorithm (MOGA) [10], the nondominated sorting algorithm (NSGA/NSGA-II) [11–13], and the strength Pareto evolutionary algorithms (SPEA/SPEA2) [14], are a number of real-life case studies.

2.2 Differential Evolution

Differential evolution (DE) algorithms [15] are among the widely used algorithms in designing the electric machines [16]. Like the genetic algorithms, the DE method works on a population which is a set of individuals, where each individual presents one machine design configuration [17]. Initial population is randomly initialized within the constraints of the design boundary. The candidate population is obtained by crossover and mutation processes from the existing population. As Zhang [16] describes in a case study the next generation of the design solutions is obtained by comparing the existing and candidate population by choosing members that satisfy boundary functions and as well as objective functions. Mutluer and Bilgin [17] utilize an effective DE algorithm in solving a number of real-life problems in electric machines design optimization where the effectiveness of the DE algorithm is compared with the stochastic methods.

2.3 Particle Swarm Optimization

The standard particle swarm optimization (PSO) is an evolutionary population-based optimization technique inspired by the behavior of bird flocks searching for food, widely used in designing of the electric machines [18]. As Sankardoss and Geethanjali [7] describe a PSO algorithm begins with the population of individuals called particles. Each particle constitutes a number of parameters to be optimized known as a candidate solution in a multidimensional space. The population of particles is called the swarm. The PSO then starts with the random initialization of swarm size and particle of the swarm. The swarm starts searching for the optimal solution in a multidimensional parameter space with random position and zero velocity. The swarm then moves in the search space depending on the fitness value estimated from the defined objective function [2]. The particles in the swarm drive toward the best solution by adjusting the velocity based on own experience and other particles' experience known as neighborhood solutions at every time step in the parameter search solution. The velocity and hence the position of each particle are updated over a time in a number of iterations by evaluating the fitness function and comparing current solution with the personal best position of the particle and the group's best solution [11]. Along with its multiobjective version (MOPSO) the algorithm's many variants, e.g. the dynamic particle swarm optimization (DPSO) [18], and distance-based intelligent particle swarm optimization (DiPSO) [19], were utilized widely in numerous electrical machines design optimization.

2.4 Comparisons

In a study conducted by Mutluer and Bilgin [17], the design optimization of 16-poles/18-slots concentrated winding surface-mounted PMSM was investigated by using GA, simulated annealing (SA), and DE. The results showed that DE was more reliable than the other two methods. In two recent articles by Rebahi [20, 21], PSO, GA, and DE was compared in the optimization of a doubly salient 8/6 switched reluctance machine (SRM) aiming at the best results for the chosen objective functions. Computation cost or running time of algorithms was not considered. They concluded

that GA and DE gave almost equally sufficient values, better than the results found by PSO. Though, ranking attempts between the different algorithms are not truly appropriate out of the framework of an optimization problem, their performance is therefore strongly case-dependent [22]. Furthermore it has been reported that the integration of PSO algorithms with GAs would result robust and efficient algorithms [21].

A brushless DC motor benchmark problem was presented in [23] and the MATLAB source code created for computing the objective function of a single objective optimization. A multiobjective problem definition for the same motor utilizing SPEA2, NSGA-II and sequential quadratic programming (SQP) algorithms are presented in [24]. The optimization problem was characterized by five continuous design variables subjected to six inequality constraints which are related to technological, and operational considerations regarding the wheel motor. The brushless DC motor benchmark problem was further used to test advanced algorithms suitable for electrical machine optimization e.g. modified social spider optimization (MSSO) algorithms [25], multiobjective symbiotic organism search (MOSOS) and improved multiobjective symbiotic organism search algorithms [26], the multiobjective krill herd algorithm (MOKH) [27], improved teaching-learning-based-optimization (ITLBO) technique [28], multiobjective firefly optimization (MOFO) and modified multiobjective firefly optimization (MOBFO) in [29].

2.5 Surrogate Models, Multi-level and Hybrid Methods

Because of the high computational cost of FEM, methods based on approximate models can present an effective way to solve optimization problems [30]. By using design of experiments (DoE) techniques [11, 31], and statistical analysis methods [32], approximate models [33] can be established as surrogate models for FEM or circuit models, to reduce the high computation cost of the iterative optimization process [34]. Though in problems with high number of design variables the number of FEM samples required for the DoE techniques is comparable to those required for a direct optimization with an evolutionary algorithm [35]. The two popular surrogate models in electrical machine design are the response surface (RS) [36], and the Kriging model [37]. Abbaszadeh [28] combined DoE and the RS method in a single-objective optimization problem to reduce cogging torque in a surface mounted permanent magnet motor. Similar methodology was used in a study by Zhu [29] for multiobjective optimization of magnetic planetary geared permanent magnet brushless machines. A recent example for application of a Kriging model based optimization can be found in [38], where the waveform of air-gap flux density was optimized in a flywheel motor. To do so Bu [9] combines DoE, surrogate model and a multiobjective evolutionary optimization algorithm (NSGA-II). A similar Kriging model was adopted by Tan [10] where the output power of a doubly-fed induction generator (DFIG) was optimized by means of DoE, Kriging-model construction and a PSO algorithm.

As an alternative to the above surrogate models, multi-level optimization methodologies can be utilized to address the demanding and complexity of machines design optimization for a robust design [3]. According to Lei [39] a multi-level optimization is done via initially subdividing the design variables set in many subsets in such a way that the first part of the optimization is driven by the more sensitive

variables for a better search. This subdivision is conducted in order to quickly approach the region of Pareto-optimal solutions, and then switching to the full set of variables, in order to focus on the details of the search region [40].

Although, one may find the multi-level optimization not time-efficient, a thorough case study by Bramerdorfer [41], investigates the possibilities of speeding-up the process. They clarify that combining surrogate modeling and evolutionary algorithms, generally would lead to a reduction of the required number of FE simulations needed to achieve high-quality Pareto fronts [42]. This would lead to the sophisticated optimization techniques of hybrid optimization algorithms [43]. Applications include the FE model simplification based on geometrical symmetry and the symmetry of the time course of machine parameters [12, 31]. A great number of such hybrid optimization methods have been developed and applied in electrical machine design [44–47]. Thorough investigation of these methods exceeds the framework of the recent survey and it is going to be the matter of further research. Figure 1 illustrates the annual progress of the number of academic publications considering the well-known algorithms/methods used in the context of design optimization of electric machines.

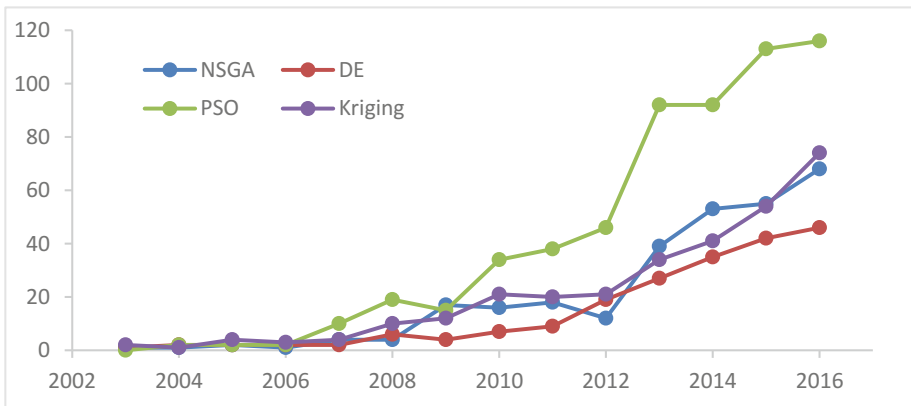


Fig. 1. Growth of the major optimization algorithms used for electric machines design presented in the literature (2003–2016) (source: village database www.engineeringvillage.com)

NSGA, DE, PSO, and Kriging, are considered as the major optimization algorithms widely used in the design optimization of the electric machines. These algorithms are seen as the essential but not sufficient tools to enhance creating the efficient global optimization approaches in dealing with dimensionality [12, 48, 49]. The dimensions of the real-life optimization problems due to the increasing number of variables, objectives, constraints and decision criteria are ever expanding. Yet, presenting a decision-maker with numerous representative solutions on a multidimensional Pareto-optimal set strongly reported to be impractical [13, 36, 50]. In fact dealing with the ever increasing dimensionality a supplementary decision-support system to enhance the existing optimization algorithms would be essential [51]. On the other hand in a number of studies e.g. [52, 53], it has been reported that performing the process of

optimal design within the integrated design environment of a commercial optimization package [54], would be highly desirable. Via commercial optimization packages e.g. [55] the coupling and integration requirements are well customized, and it further fill the gap between optimization approaches and electric machines optimal design. Furthermore the true potential of machine learning [56, 57], and intelligent optimization [49], has still not been explored in the realm of electric machines design.

3 Conclusions

The design of the electrical machines has been dramatically revolutionized by utilizing the advanced optimization algorithms. A great number of methods have been introduced to solve the electrical machines optimization problems, and the research in this field has become a booming topic in recent years. The multiobjective and hybrid algorithms provide a solid platform for designers to explore the design space for a robust design and the global optimum options. In this article we surveyed the latest advancements in this realm and visualized the ever increasing progress of the applications of the novel optimization algorithms.

Acknowledgement. This work has partially been sponsored by the Research & Development Operational Program for the project “Modernization and Improvement of Technical Infrastructure for Research and Development of J. Selye University in the Fields of Nanotechnology and Intelligent Space”, ITMS 26210120042, co-funded by the European Regional Development Fund.

References

1. Pyrhonen, J., Jokinen, T., Hrabovcova, V.: Design of Rotating Electrical Machines, 2nd edn. Wiley, Hoboken (2013)
2. Mosavi, A.: Decision-making models for optimal engineering design and their applications. Doctoral Dissertation, University of Debrecen, Hungary (2013)
3. Khelifa, M., Mordjaoui, M., Medoued, A.: An inverse problem methodology for design and optimization of an interior permanent magnetic motor. *Hydrog. Energy* **3**, 345–367 (2017)
4. Wang, W.: Rotor shape investigation and optimization of double stator switched reluctance machine. *IEEE Trans. Magn.* **51**, 1–4 (2015)
5. Nguyen, T.D., Lanfranchi, V., Doc, C., Vilain, J.P.: Comparison of optimization algorithms for the design of a brushless DC machine. *Electric Drives* **78**, 1–6 (2009)
6. Lei, G., Zhu, J.G., Guo, Y.: *Multidisciplinary Design Optimization Methods for Electrical Machines and Drive Systems*, pp. 73–159. Springer, Heidelberg (2016)
7. Sankardoss, V., Geethanjali, P.: PMDC motor parameter estimation using bio-inspired optimization algorithms. In: *IEEE Access*, pp. 1–11 (2017)
8. Stipetic, S., Werner M., Damir, Z.: Optimization in design of electric machines: methodology and workflow. In: *Electrical Machines & Power Electronics*, pp. 441–448 (2015)
9. Bu, J.: Optimization for airgap flux density waveform of flywheel motor using NSGA-2 and Kriging model based on MaxPro design. *IEEE Trans. Magn.* **14**, 1–7 (2017)

10. Tan, Z.: DFIG machine design for maximizing power output based on surrogate optimization algorithm. *IEEE Trans. Energy Convers.* **30**(3), 1154–1162 (2015)
11. Mosavi, A.: Optimal engineering design. Technical report, University of Debrecen (2013)
12. Khaliq, S.: Rotor pole optimization of novel axial-flux brushless doubly fed reluctance machine for torque enhancement. *IEEE Trans. Magn.* **52**(7), 1–4 (2016)
13. Kuznetsov, V.: Technique of evolutionary optimization permanent-magnet synchronous motors. *Procedia Comput. Sci.* **103**, 198–204 (2017)
14. Beniakar, M.: Strength pareto evolutionary optimization of an in-wheel PM motor with unequal teeth for electric traction. *IEEE Trans. Magn.* **51**(3), 1–4 (2015)
15. Zhang, P.: Saliency ratio and power factor of IPM motors optimally designed for high efficiency and low cost objectives. In: *ECCE*, pp. 3541–3547 (2014)
16. Zhang, P.: Establishing the relative merits of interior and spoke-type permanent magnet machines with ferrite. *IEEE Trans. Ind. Appl.* **9**, 2940–2948 (2015)
17. Mutluer, M., Bilgin, O.: Comparison of stochastic methods for design optimization of permanent magnet synchronous motor. *Neural Comput. Appl.* **21**, 2049–2056 (2012)
18. Lee, J.H.: Distance-based intelligent particle swarm optimization for optimal design of permanent magnet synchronous machine. *IEEE Trans. Magn.* **53**(6), 1–4 (2017)
19. Mosavi, A., Vaezipour, A.: Reactive search optimization; application to multiobjective optimization problems. *Appl. Math.* **3**, 1572–1582 (2012)
20. Rebahi, F.: Optimization design of a doubly salient 8/6 SRM based on three computational intelligence methods. *Turk. J. Electr. Eng. Comput. Sci.* **24**, 4454–4464 (2016)
21. Rebahi, F.: Multi-objective optimization design of 8/6 switched reluctance motor using GA and PSO algorithms. *Electr. Eng.* **15**, 86–99 (2015)
22. Brisset, S., Brochet, P.: Analytical model for the optimal design of a brushless DC wheel motor. *Int. J. Comput. Math. Electr. Electron. Eng.* **20**(3), 829–848 (2005)
23. Moussouni, F., Brisset, S.: A benchmark for a mono and multi objective optimization of the brushless DC wheel motor (2008)
24. Klein, C.: Modified social-spider optimization algorithm applied to electromagnetic optimization. *IEEE Trans. Magn.* **52**(3), 1–4 (2016)
25. Ayala, H.: Multiobjective krill herd algorithm for electromagnetic optimization. *IEEE Trans. Magn.* **52**(3), 1–4 (2016)
26. Ayala, H., Klein, C., Mariani, V., Coelho, L.: Multi-objective symbiotic search algorithm approaches for electromagnetic optimization. *IEEE Trans.* **53**(6), 1–4 (2017)
27. Boucekara, H.R.E.H., Nahas, M.: Optimization of electromagnetics problems. *Appl. Comput. Electromagn.* **30**(12), 1341–1347 (2015)
28. Abbaszadeh, K.: Torque optimization in surface-mounted permanent-magnet motors by using design of experiment. *Convers. Manag.* **52**(10), 3075–3082 (2011)
29. Zhu, X.: Multiobjective optimization design of a magnetic planetary geared permanent magnet brushless machine. *IEEE Trans. Magn.* **50**(11), 1–4 (2014)
30. Mosavi, A.: A multicriteria decision making environment for engineering design and production decision-making. *Int. J. Comput. Appl.* **69**, 26–38 (2013)
31. Mosavi, A.: Decision-making in complicated geometrical problems. *Int. J. Comput. Appl.* **87** (19), 22–25 (2014)
32. Mosavi, A.: Application of multi-objective optimization packages in design of an evaporator coil. *World Acad. Sci.* **4**, 145–167 (2010)
33. Mosavi, A.: Decision-making software architecture; the visualization and data mining assisted approach. *Int. J. Inform. Comput. Sci.* **3**, 12–26 (2014)
34. Mosavi, A.: The large scale system of multiple criteria decision making; pre-processing. *Large Scale Complex Syst. Theory Appl.* **9**, 354–359 (2010)

35. Mosavi, A.: Data mining for decision making in engineering optimal design. *J. AI Data Min.* **2**(1), 7–14 (2014)
36. Esmacili, M., Mosavi, A.: Variable reduction for multiobjective optimization using data mining techniques. *Comput. Eng. Technol.* **5**, 325–333 (2010)
37. Han, Z.: Surrogate-based optimization. In: *Real-World Applications of Genetic Algorithms*, pp. 343–362 (2012)
38. Silva, R.: Visualization and analysis of tradeoffs in many-objective optimization. *IEEE Trans. Magn.* **52**(3), 1–4 (2016)
39. Lei, G.: Techniques for multi-level design optimization of permanent magnet motors. *IEEE Trans. Energy Convers.* **30**(4), 1574–1584 (2015)
40. Di, B.: Magnetic design optimization approach using design of experiments with evolutionary computing. *IEEE Trans. Magn.* **52**(3), 1–4 (2016)
41. Bramerdorfer, G.: Possibilities for speeding up the fe-based optimization of electrical machines. *IEEE Trans.* **52**(6), 4668–4677 (2016)
42. Ma, C., Qu, L.: Multiobjective optimization of switched reluctance motors based on design of experiments and particle swarm. *Energy Convers.* **30**, 1144–1153 (2015)
43. Xia, B.: A novel subregion-based multi-dimensional optimization of electromagnetic devices assisted by kriging surrogate model. *IEEE Trans. Magn.* **53**(6), 1–4 (2017)
44. Mohammadi, M.: A computationally efficient algorithm for rotor design optimization of synchronous reluctance machines. *IEEE Trans. Magn.* **52**(3), 1–4 (2016)
45. Mosavi, A., Varkonyi-Koczy, A.R., Füllsack, M.: Combination of machine learning and optimization for automated decision-making. In: *MCDM* (2015)
46. Mosavi, A., Rabczuk, T.: Learning and intelligent optimization for material design innovation. In: *Theoretical Computer Science and General Issues, LION11* (2017)
47. Zhang, B.: Multi-objective optimization of a transverse flux machine with claw-pole and flux-concentrating structure. *IEEE Trans. Magn.* **52**(8), 1–10 (2016)
48. Mosavi, A.: Application of data mining in multiobjective optimization problems. *Int. J. Simul. Multi. Design Optim.* **5**, A15 (2014)
49. Mosavi, A., Vaezipour, A.: Developing effective tools for predictive analytics and informed decisions. Technical report, University of Tallinn (2013)
50. Mosavi, A.: Multiple criteria decision-making preprocessing using data mining tools. *Int. J. Comput. Sci. Issues* **7**, 26–34 (2010)
51. Santos, C.: A multiobjective firefly approach using beta probability distribution for electromagnetic optimization problems. *IEEE Trans. Magn.* **49**(5), 2085–2088 (2003)
52. Lopez, T.: Rotor of Synchronous Reluctance Motor optimization (2016)
53. Mosavi, A.: On engineering optimization the splined profiles. In: *Proceedings of International modeFRONTIER* (2010)
54. Bramerdorfer, G., Zavoianu, C.: Surrogate-based multi-objective optimization of electrical machine designs facilitating tolerance analysis. *IEEE Trans.* **8**, 1–11 (2017)
55. Mosavi, A.: Predictive decision model (2015). <https://doi.org/10.13140/RG.2.2.21094.63047>
56. Mosavi, A., Varkonyi-Koczy, A.R.: Integration of machine learning and optimization for robot learning. In: *Advances in Intelligent Systems and Computing*, vol. 519, pp. 349–355 (2017)
57. Mosavi, A.: Multiple criteria decision making integrated with mechanical modeling of draping for material selection of textile composites. In: *Composite Materials* (2012)

Review on the Usage of the Multiobjective Optimization Package of modeFrontier in the Energy Sector

Amir Mosavi¹(✉), Rituraj Rituraj¹,
and Annamária R. Varkonyi-Koczy^{1,2}

¹ Kalman Kando Faculty of Electrical Engineering, Institute of Automation,
Obuda University, Budapest 1034, Hungary

{amir.mosavi, R.Rituraj,
koczy.annamaria}@kvk.uni-obuda.hu

² Department of Mathematics and Informatics, J. Selye University,
945 01 Komarno, Slovakia

Abstract. The multiobjective optimization (MOO) software package of modeFrontier has recently become popular within industries, academics and research communities. Today, universities as well as research institutes are using modeFrontier optimization toolboxes for teaching and research proposes around the world. One of the reason behind the popularity of the package, is the way it utilizes the available resources in an efficient and integrated manner and providing multidimensional post-processing tools. The user-friendly design optimization environment of modeFrontier integrates various optimization methods with the major computer aided engineering codes and commercial numerical analysis tools. Among the wide range of applications of modeFrontier, the energy sector, particularly, has been highly benefiting from the advancements in design optimization. This article presents the state of the art survey of the novel applications of modeFrontier in this realm.

Keywords: Multiobjective optimization · Optimization packages · modeFrontier

1 Introduction

The multiobjective optimization (MOO) software package of *modeFrontier* is a commercial software package which provides a user-friendly environment for innovative design optimization. The package was developed by ESTECO, which is an independent technology provider software solutions located in Italy [1]. The package provides an advanced simulation-driven design process with powerful workflows, innovative algorithms and user-friendly post-processing for advanced statistical analysis, data visualization and decision making [2]. The optimization is performed with modular and profile based access, enabling the automation of the design simulation process and, further through facilitating the advanced analytical decision. The *modeFrontier* includes two modules of *modeSpace* and *modeProcess* for managing the data space, process, and optimization aspects and further dependent functions and

interfaces [3]. The data space aspect of the package consists of four different sectors i.e. data viewer, data inspector, data intelligence and data explorer [4]. The process and optimization aspects further consists of four sectors i.e. automation designer, single discipline design, multi discipline design and the *optimeazy*. The function of the data viewer is to make analytical charts used for the purpose of post-processing. The function of data inspector is to make analytical charts for review and edit mode. The data intelligence is also used for analytical purposes. In addition the data explorer functions as the essential analytical tools and the design space exploration [5]. In the sector of process and optimization, the function of automation designer is to create, edit and run the workflow, as well as providing medium for integration of the computer aided design codes [6].

The analytics charts consist of statistical and response surface charts. The analytical tools consist of statistical charts, such as minimum vectoring altitude, clustering and self-organizing maps. Design of experiment (DOE) further deals design space exploration (DSE) to systematically analysis and pruning of unwanted design points. In order to couple the *modeFrontier* with the computation tools in different size of projects, the integration packages are of three types of small, medium and large. The small package includes only one node for commercial computational codes, the medium package has three, and the large has seven. For conducting a robust design at the presence of numerous objective functions and design criteria, the package includes multi-objective robust design optimization (MORDO), and multiple criteria decision making (MCDM) algorithms [7].

2 Survey

The modeFrontier couples with reduced basis methods [8], which allows a fast and reliable approximation of certain scalar quantities. Such ability, which is derived from partial differential equation solutions, along with response surface methods would lead to the improvement of a four-joint leverage amplifier [9]. Through implementation of a response surface algorithm within modeFrontier, a dual acoustic gravitational wave detector is highly advanced. The improvements made would help to measure the mechanical transfer function and improve the apparatus to perform a first thermal noise measurement [9].

Manzan [10] uses the modeFrontier for optimization for night ventilation. Through an implementation of genetic algorithms within the modeFrontier an energy saving system for night ventilation is optimized for better performance. An advanced genetic algorithm analyzes the conflicting objectives and result a graph for Pareto Frontier solutions. The design objectives are to save energy for the plant system and to minimize the fan energy.

For providing design novelties in an old industry power products a hybrid multi-objective optimization approach is used through an implementation of *modeFrontier* [11]. The project includes two procedures i.e. filed analysis and optimization. In this case the package transmits a set of parameters from the hybrid optimization algorithm to the filed solver. The result obtained from the simulation are necessary for the objective function evolution. Further, the results are sent back to the optimizer for

producing a multidimensional visualization for the post-processing. In another industrial project, a sophisticated multidisciplinary optimization strategy is implemented for improving the shape of a rotor for railway traction system [12]. The objective is to maximize the reluctance torque of the rotor. The response surface and DOE algorithms for the advanced statistical analysis are performed through *modeFrontier*. Here the multidimensional visualization tools provide the ability to analyze the Pareto Frontier solutions more deeply. The in depth analysis, however, requires multivariate data analytics of clustering. In a commercial project, an innovative domestic refrigerator is optimized using the *modeFrontier* software package [13]. The thickness of the insulator panel of the refrigerator is parameterized, and further the Pareto Frontier solutions are generated using the genetic algorithms. In a similar approach, a fuel consumption minimization procedure of self-assisted motor vessel is presented in [14]. A multi-objective genetic algorithm (MOGA) algorithm is used as optimization procedure combined with a systematic meshing to explore the design space.

In 2010, the energy transfer of the bounce tubes for optimizing the acceleration on Adidas bounce shoes is done using *modeFrontier* [15]. Today the high performance shoes use tube with an angle shaped cross section incorporated into the shoe sole. The *modeFrontier* optimization strategy through the use of response surface and coupled numerical analysis showed a very promising results. The improved design provides permissible performances which increases the runner's acceleration. In another energy transfer project, a hybrid optimization model of design optimization is created for vehicle realization [16]. In this case MOGA enables the optimal configuration of the braking system. It maximizes the structural rigidity and minimizes the weight of the drive. For the advancement of the renewable micro generation technologies, *modeFrontier* plays a vital role in designing an optimal generative system for the off-grid community energy demand [17]. In this case an optimal energy system with 100% renewable micro-generation technology is advanced. The novel design satisfies the electrical and thermal energy demand.

For the energy harvesting in micro-electromechanical-systems (MEMS), *modeFrontier* has numerous applications to report. In a number of applications e.g. [18], the MEMS's design process, through an automated optimization process, reduces the time and cost of the design procedure. The optimization strategy integrates computational fluid dynamics (CFD) with a genetic algorithm to numerically analyze and optimize the harvesting patterns [19]. In fact, coupling the optimization algorithms and commercial CFD codes brings numerous advantage to the engineering community and therefore the applications are vast. In a number of cases e.g. [20, 21], a multiobjective shape optimization approach is used for the optimization and automation design of CFD systems for the aerospace and automotive structures. The *modeFrontier* provides an efficient platform for design, so called "*CFD automatic design toolbox*", facilitating CFD engineers to benefit from the high-end solution-techniques. This is indeed done without detailed diving into the intricacies of modern optimization theory and complications of the mathematical implementation and expensive computation as described in e.g. [21].

In 2013, the composite structural optimization is advanced through an integration of ANSYS Composite PrepPost (ACP) and genetic algorithms [22, 23]. The work fellow focuses on composites structures used in power plants and energy harvesting applications. In these two cases the optimization is performed using a parametric

geometry and CFD simulations. Integration of the computer aided engineering tool of ACP and the advanced optimization algorithms provides an effective design environment for composites structural design and analysis. The design tool reported effective in reducing the weight and minimizing the risk of structural failure.

In the oil and gas industry, for the production and exploration in the deep water, *modeFrontier* is utilized to improve the design of a Riser connected to a vessel [24, 25]. In this project the high offsets and vertical motions imposed by the vessel at the top of the Riser is optimized. To do so, the steel lazy-wave Riser (SLWR) finds an adequate solution for this particular structural dynamic behavior. In this case, a response surface model defines the design verification phases in an effective manner. The proposed model can further be utilized for the optimization procedure of the similar SLWR cases. In the oil and gas industry, the pipe-laying task is an expensive, demanding, and highly time-consuming process. An optimized process, in this case, can dramatically save money and time.

In 2012 a structural modeling of pipe-laying vessel is dedicated to the laying of long and deep-water submarine pipelines [26]. The proposed methodology adopted to convert the structural drawings in finite element model coupled with advanced optimization algorithms through *modeFrontier*. The static loads of weights and tank pressures, along with the hydrostatic and hydrodynamic loads are optimized. The methodology provides the ability to calculate the inertia loads associated to the vessel motion. It further provides the ability to use global and more detailed local models.

In 2013, a decision support system for the large-scale problems of energy supply is designed using *modeFrontier* optimal design platform [27]. Due to the increasing demand for sustainable energy supply accessing a combined multiobjective optimization system for multi attribute analysis of energy systems would be essential. In this particular case the functioning of the design support system is done in three steps: (1) estimating the total emissions; (2) utilizing MCDM methodology; (3) focusing on the sustainability benefits of combined heating and power plants. In this case, *modeFrontier* provides an interactive Pareto Frontier solution graph and, further improves the efficiency of the energy plant [28]. Worth mentioning that the earlier case presented in [11], the decision support system works on the similar principal for the simulation and optimization of zero energy industrial halls. In practice the net-zero energy building (NZEB) requires a sophisticated tool for optimization over the investment cost. Therefore, it is very important to optimally design and implement the amount of the additional capital investment. In the considered cases of Attia [11], and Subudhi [27], in an integrated design approach, the decision support system provides maximized energy production capability and minimized additional capital investment.

Zhang [28] uses the *modeFrontier* as a simulation-optimization platform for the advancement of laminated lithium-ion batteries. He performs the simultaneous estimation of multiple thermal parameters of large-format laminated lithium-ion batteries. These batteries are having multiple thermal parameters to be optimized and estimated for achieving the longer life cycles and higher energy density. This is done by identifying the minimum residuals and temperature rise using genetic algorithms. In the materials design realm, the Uranium enrichment cascades model is a demanding design optimization which has been considered using *modeFrontier* strategy [29, 30]. The design optimization workflow is performed by mixing parameters for non-proliferation

analysis. The hybrid optimization algorithms are used to manage the numerical analysis of the U isotopes separation process. Here a coherent dataset for analysis and simulation demonstrates the possibility to use the simulation as a valid additional tool when some information on the real plant performance is missing or is inaccurate. The grid geometry effects on pressure drops and heat transfer for an EMbaffle heat exchanger is optimized in [31]. The DOE and response surface are used to investigate the influence of different electron microscopy grids on heat transfer. In this case the development and propagation of turbulence in the shell-side fluid is investigated to improve the performance of the heat exchanger.

The convenience of the coupling of the finite element method (FEM) with optimization algorithms provides numerous advantage to the design optimization community as well as energy systems designers. The applicability and the efficiency of the method have been reported in e.g. designing of the hybrid energy storage systems [32], building energy [33, 34], insulation [35], oil and gas [36], robotics energy [37], motor drive systems [38], acoustics energy [39], and power supply optimization [27]. In the particular optimization case for motor drive systems [38], a large turbo generator is optimized through an integrated multiple criteria optimization workflow at the presence of CFD and FEM analysis. The induced currents in the rotor components, the damper windings configuration, and the temperature of the rotor are analyzed and optimized. In a similar case reported in [23], the current pulsation calculation of an induction machine driving reciprocating compressor is optimized. The model of induction motor has enhanced by adding the effects of the air-gap torque. The method is validated by simulation of the system through the integration of *LMS Imagine Lab Amesim* software [40] which is an advanced computation platform for simulation and prediction of the multidisciplinary performance of intelligent systems. In this case *modeFrontier* provides accurate design environment to analyzes and simulate the torsional natural behavior of the system. Coupling the CFD and FEM commercial codes is also utilized for annular distributors of heat exchangers [16, 19], where ANSYS workbench is integrated with response surface use. In [21], a couple model of ANSYS and response surface, the geometry of the heat exchanger has been improved. To run the optimization model the CFD model of the flow in the distributor is investigated within different configurations.

3 Survey Results

As surveyed above, the *modeFrontier* is used in numerous design applications and levels in firms around the world. These levels can be component, system and sub-system. From the review analysis presented in section two along with the analysis presented on *engineering village* database, it is observed that only 52% of all the companies deals with the service level as it is depicted in Fig. 1a. The percentage of the major algorithms used by companies is illustrated in Fig. 1b. In addition, Fig. 2 illustrates the total number of projects in energy sectors using *modeFrontier*.

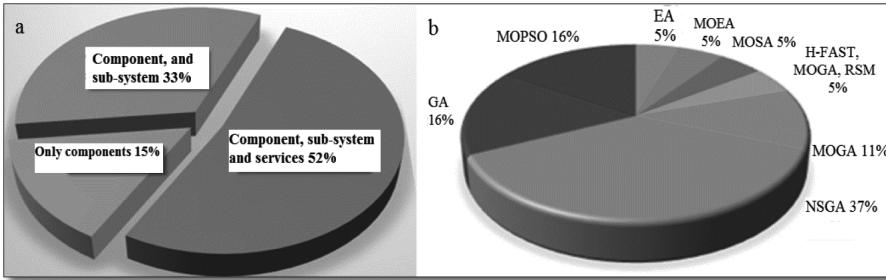


Fig. 1. a: Percentage of companies using *modeFrontier* at different configuration levels, b: Percentage of the major algorithms used by companies (source: www.engineeringvillage.com)

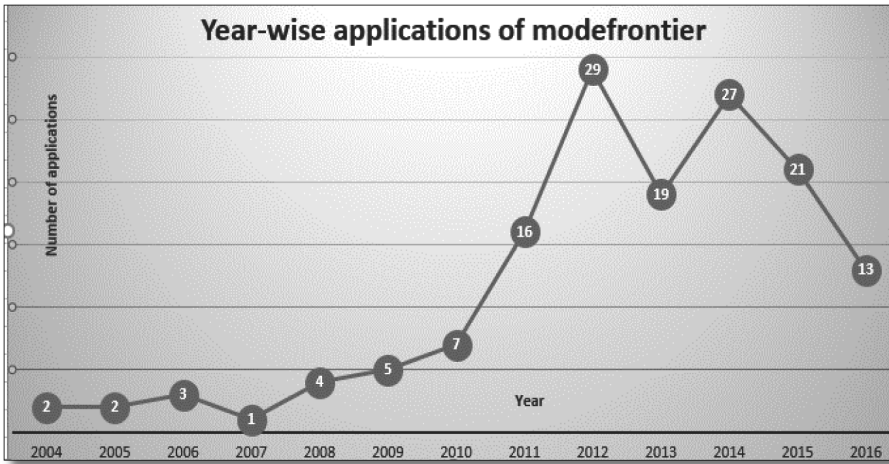


Fig. 2. Number of projects in energy sectors using *modeFrontier* (source: village database www.engineeringvillage.com)

4 Conclusions

This article surveys the novel applications of the multiobjective optimization software package of *modeFrontier* in the energy sector around the world. In the realm of energy sector the design environment of *modeFrontier* provides an effective workflow of linking different design and engineering modules. This would assist engineers to save their time and well progress with an automated design workflow. The popularity of this software package has been reported to be due its simplicity and fact integration with major computer engineering application. Furthermore due to the importance and beneficial of the CFD and FEM integrated simulations design environment, particularly in the energy sector, brought by *modeFrontier* the usage of this package has been increasing within the engineering community. In fact the survey indicates that the usage of the *modeFrontier* has been dramatically increased during past decade.

Acknowledgement. This work has partially been sponsored by the Research & Development Operational Program for the project “Modernization and Improvement of Technical Infrastructure for Research and Development of J. Selye University in the Fields of Nanotechnology and Intelligent Space”, ITMS 26210120042, co-funded by the European Regional Development Fund.

References

1. Stephenson, P.: Multi-objective optimization of a charge air cooler using modeFRONTIER. SAE Technical Paper 886 (2008)
2. Mosavi, A.: Multiobjective optimization of spline curves using modefrontier. In: Proceedings of International modeFrontier Users' Meeting (2010)
3. Arrichiello, V.: System models simulation process management and collaborative multidisciplinary optimization. *Syst. Eng.* **14**, 1–5 (2014)
4. Mosavi, A.: Hydrodynamic design and optimization: application to design a general case for extra equipment on the submarine's hull. *Comput. Technol.* **2**, 139–143 (2009)
5. Mosavi, A.: Computer design and simulation of built environment; application to forest. *IEEE Environ. Comput. Sci.* **9**, 81–85 (2009)
6. Mosavi, A.: Decision-making software architecture; the visualization and data mining assisted approach. *Inf. Comput. Sci.* **3**, 12–26 (2014)
7. Mosavi, A.: Multiple criteria decision-making preprocessing. *IJCSI Int. J. Comput. Sci. Issues* **7**, 26–36 (2010)
8. Maday, Y.: A reduced-basis element method. *C. R.* **2**, 195–200 (2002)
9. Attia, S.: Assessing gaps and needs for integrating building performance optimization tools in net zero energy buildings design. *J. Energy Build.* **60**, 105–113 (2013)
10. Manzan, M.: Optimization of night ventilation for energy savings in an HVAC systems for summer climatization. In: International CAE Conference, vol. 21, pp. 11–19 (2014)
11. Costa, M.: Increasing energy efficiency of a gasoline direct injection engine through optimal synchronization. *Energy Convers. Manag.* **60**, 24–31 (2012)
12. Luise, F.: Use of time-harmonic FE analysis to compute rotor eddy-current losses in synchronous machines. *Electr. Mach.* **61**, 1503–1509 (2012)
13. Silvano, C.: Multi-objective design space exploration of multi-core architectures. In: VLSI Annual Symposium, vol. 105, pp. 47–63 (2011)
14. Dlamini, M.: Detecting faults in inverter-fed induction motors during startup transient conditions. In: Energy Conversion Congress and Exposition IEEE, vol. 104, pp. 3131–3138 (2014)
15. Dickson, M.: Directional energy transfer in Adidas bounce tubes. In: 8th Conference of the International Sports Engineering Association, vol. 2, pp. 2795–2800 (2010)
16. Liao, L.: Numerical and experimental study of heat transfer in a BIPV-thermal system. *J. Sol. Energy Eng.* **4**, 423–430 (2007)
17. Tassarolo, A.: Multiobjective design optimization of an alternator for small power wind generation. In: CAE International Conference on Clean Electrical Power, vol. 11, pp. 1–6 (2014)
18. Benkhelifa, E.: Evolutionary multi-objective design optimization of energy harvesting MEMS: the case of a Piezoelectric. *Evol. Comput.* **34**, 1856–1863 (2011)
19. Bhutta, M.: CFD applications in various heat exchangers design; a review. *J. Appl. Therm. Eng.* **32**, 118–123 (2012)

20. Mosavi, A.: Decision-making in complicated geometrical problems. *Int. J. Comput. Appl.* **87** (19), 22–25 (2014)
21. Mosavi, A.: Application of multiobjective optimization packages in design of an evaporator coil. *World Acad. Sci. Eng. Technol.* **37**, 25–29 (2010)
22. Mosavi, A.: Decision-making models for optimal engineering design and their applications. Doctoral Dissertation, University of Debrecen, Hungary (2013)
23. Mosavi, A.: Optimal engineering design. Technical report of University of Debrecen (2013)
24. Clarich, A.: Connecting rod optimization integrating modefrontier with FEMFAT. In: *CAE International Conference* (2016)
25. Esmaeili, M., Mosavi, A.: Variable reduction for multiobjective optimization using data mining techniques. *Comput. Eng. Technol.* **5**, 325–333 (2010)
26. Westgate, Z.: Modelling the embedment process during offshore pipe-laying on fine-grained soils. *Can. Geotech. J.* **50**, 15–27 (2012)
27. Subudhi, B.: Neuro-evolutionary approaches to power system harmonics estimation. *Int. J. Electr. Power Energy Syst.* **64**, 212–220 (2015)
28. Zhang, J.: Simultaneous estimation of multiple thermal parameters of large-format laminated lithium-ion batteries. In: *IEEE Conference on Vehicle Power and Propulsion*, vol. 36, pp. 1–5 (2013)
29. Glaser, A.: Characteristics of the gas centrifuge for uranium enrichment and their relevance for nuclear weapon proliferation. *Sci. Global Secur.* **16**, 1–8 (2008)
30. Kumar, A.: A review of multi criteria decision making (MCDM) towards sustainable renewable energy development. *Renew. Sustain. Energy Rev.* **69**, 596–609 (2017)
31. Nguyen, A.: A review on simulation-based optimization methods applied to building performance analysis. *J. Appl. Energy* **113**, 33–42 (2014)
32. Nielson, G., Emadi, A.: Hybrid energy storage systems for high-performance hybrid electric vehicles. In: *Vehicle Power and Propulsion Conference*, vol. 4, pp. 1–6 (2011)
33. Lee, B.: Building energy simulation and optimization. In: *Proceeding of International Conference*, vol. 7, pp. 229–236 (2014)
34. Flager, F.: Multidisciplinary process integration and design optimization of a classroom building. *J. Inf. Technol. Constr.* **38**, 595–612 (2009)
35. Shi, X.: Design optimization of insulation usage and space conditioning load using energy simulation and genetic algorithm. *J. Sci. Dir.* **36**, 30–34 (2011)
36. Mosavi, A.: Multiple criteria decision-making preprocessing using data mining tools. *Int. J. Comput. Sci. Issues* **7**, 26–34 (2010)
37. Mosavi, A., Varkonyi-Koczy, A.R.: Integration of machine learning and optimization for robot learning. *Adv. Intell. Syst. Comput.* **519**, 349–355 (2017)
38. Tang, Y.: Simplified common-mode equivalent circuit for inverter-fed motor drive systems. *Trans. Electr. Electron. Eng.* **11**, 243–249 (2016)
39. Bignotto, M.: Dual acoustic gravitational wave detector. In: *CAE International Conference*, vol. 24, pp. 24–33 (2015)
40. Yongling, F.: *LMS Imagine. Lab AMESim System Modeling and Simulation*. Beihang University Press, Beijing (2011)

Industrial Applications of Big Data: State of the Art Survey

Amir Mosavi^{1(✉)}, Alvaro Lopez¹,
and Annamária R. Varkonyi-Koczy^{1,2}

¹ Institute of Automation, Óbuda University, Bécsi Way 94-96,
Budapest 1034, Hungary

{amir.mosavi, Alvaro.Lopez,
koczy.annamaria}@kvk.uni-obuda.hu

² Department of Mathematics and Informatics,
J. Selye University, Komarno, Slovakia

Abstract. Big data analytics has become an important tool for the progress and success of a wide range of businesses and industries. Its diversity and flexibility offer a steady increasing scope for the several applications to stay competitive in the market. For that, big data approach provides several advantages such as advanced analytics, intelligent optimization, informed decision making, large-scale modeling, and accurate predictions. Due to the numerous advantages, it has been particularly possible to find more accurate and feasible solutions for the current engineering problems. Hence, the impact of big-data analytics in the engineering realm and applications is increasing more than ever. This article presents a survey to investigate how engineering community has adopted big data technologies to stay competitive. To conduct the investigation a state of the art survey of the academic literature on the big data applications to engineering is presented.

Keywords: Big data · Data science · Big data analytics

1 Introduction

Over the last years, data has been growing in a large scale. Due to different activities, every day society is generating data in several fields. Nowadays there is a dramatic increase in data generation. It brings new challenges for data storing, data processing and the way to get useful information from big datasets. The challenge is to analyze big datasets and the aim is to find patterns within them. Hence, performing big data analysis is a suitable solution for current problems in industry [1].

Big data is mainly used to describe a huge dataset generated with a high rate. Compared to the traditional datasets, big data includes a significant amount of structured and unstructured data which demands more time and complex resources to analyze it. Big data analysis devolves upon the introduction of new process and new technologies to find the potential value in data. Furthermore, people are looking for trends in enormous quantities of data and they are performing analytics on it to discover what is happening. By applying big data, it is possible to simplify data analysis and understand some features from big datasets [2].

Social human activities can be analyzed by algorithms. After an algorithm is performed, a set of attributions will appear [3]. These attributions will help to create new models for services, launching a new product or even create a new technology. Previously, this procedure was based on guesswork or not appropriate procedures; but now it can be created based on the data itself. Furthermore, big data analysis will bring a new lifestyle for people, and companies can improve their processes [4]. Consequently, companies are able to better understand their business, customers, manufacturing products and market; which will enhance efficiency related to sales, production costs, customer service and other aspects.

Big Data is present everywhere in numerous applications. Several fields in industry are demanding to analyze their data in order to better understand their environment. Furthermore, big data is becoming a main part of the IT department in companies. Regarding decision making, big data analysis will be the next challenge for the innovation, competition, and productivity. In addition, many solutions will be generated to support all the issues involved in this context.

2 Big Data

In the present day, big data has become an important topic which is discussed by several researchers. Before defining what big data is, it is necessary to define information and the difference between dataset types. Data can be defined as structured and unstructured elements which in a suitable manner can be processed by intelligence systems and computers. Yet datasets may not necessarily have a particular meaning before processing. Data becomes information only when it communicates a meaning [5].

Big Data is a concept about digital information in a big scale. Hence, having a suitable definition for big data is necessary. According to [3, 6] big data is a larger collection of heterogeneous datasets which traditional databases or software are not able to process. In order to process big datasets, clusters sets of super computers are needed working toward the same aim.

Understanding the nature of big data and its features, open the possibility for new technology development, architecture model, and algorithms. Regarding dataset features and properties, there is other definition about big data. As described in [7], big data is high-volume, high-velocity and high-variety information assets that demand cost-effective, innovative forms of information processing for enhanced insight and decision making". Hence, volume, velocity, variety, and complexity of big data continue to be an important challenge for computer systems.

According to [8], there are three important big data features: velocity, volume, and variety. Velocity refers to how fast data is generated or transmitted. Volume feature refers to the amount of data that has been generated in a period of time. Variety refers to the heterogeneity embracing different types of the data diversity, regarding data sources. Within big data framework, there are three important levels: Data Acquisition, Data Processing, and Data Services. These levels should be characterized by efficiency, processing time, flexibility and scalability [9].

3 Big Data in Industry

Nowadays, several applications, services, and products are offered by different sectors and people are demanding access to these services or try to obtain new products according to their preference and tendency. Regarding people's culture, age, gender, education, and other aspects; their preferences for a certain service or product change. An industry responsibility is to find better solutions for a specific problem taking into account the aspects mentioned above, achieve a fault-free and a cost efficient process within the companies. Solving problems in engineering fields is a demanding decision making process and should be considered from different perspectives [10].

Although for enterprises finding a solution for a given problem is important, they are also identifying how to increase their revenue and processes optimization. Therefore, decreasing costs during the manufacturing process is imperative. Therefore, big data analysis plays an important role during the fourth industrial revolution as it helps to find a low cost strategy for companies to be more competitive [11].

4 Big Data in Mobile Networks

Applying big data in mobile networks is possible in two scenarios. One of them is for business support, business modeling and marketing [11]. The second scenario is to apply big data analysis for optimizing the mobile network design. Big data analysis provides three capabilities for fifth generation (5G) design [7]. The first is full intelligence of the current network status, the second is predicting user's behavior, and the third is related to the dynamic response association to the network parameters [12]. The 5G technology will allow users to have high speed Internet access consequently new applications and services will emerge.

For launching 5G, researchers have to investigate big data sets and find information to enhance technical parameters such as bandwidth, mobile network distribution, mobile network architecture, and others. With the advances of big data analysis in mobile networks, operators can have a deep insight when different events occur in the network. Thus, correlations can be determined to be within these events, and they will help in resources optimization and operational costs. Considering Quality of Experience (QoE) [7], there are important challenges regarding 5G standardization, the way to enhance the services and make the network more efficient than 4G networks. Mobile network operators are looking for the best way to adjust traffic requirements and optimize resources allocations. All these activities are performed by big data analysis intelligent usage. The data is collated from different layers of 4G networks. The data collated from these networks is very complex; it has features such as multisource data, high volume, unstructured, and real time data [13].

In a mobile network there are a variety of parameters which can be analyzed by a big data platform. These parameters are divided within four groups: Subscriber level, Cell level, Network core level, and others sources [14]. In the subscriber level, parameters such as call success rate, call drop ratio, speech quality, and hand over success are analyzed. In the same level, IP traffic flow, IP throughput and data streaming quality are also collated. Radio measurements are collected on cell level such

as: received interference power, thermal noise power, channel baseband power, etc. Additionally, the number of user per cell, received random access, preamble per cell are collected Regarding Network core level, historical alarms logs devices configuration, network performance, call data records are collected [15]. In other sources, customer retention manager, costumer complaint center and spectrum utility maps are collated as well. The analysis of all parameters enumerated above will help to determine a proper decision. Thus, big data visualization plays an important role after the big data analysis/ Good visualization techniques should be applied in order to avoid information lost. Finally, a suitable big data optimization helps managers to take the best decision for a certain problem [16].

Figure 1 illustrates the number of literature on big data analysis in mobile networks publications from different publishers from 2013-2016. It shows that in 2016, there has been a major increase in the number of publications in this field, this trend continues in 2017. Figure 1 well represents the evolution of big data applications throughout the past few years and, how this technology is used for optimizing processes in mobile networks.

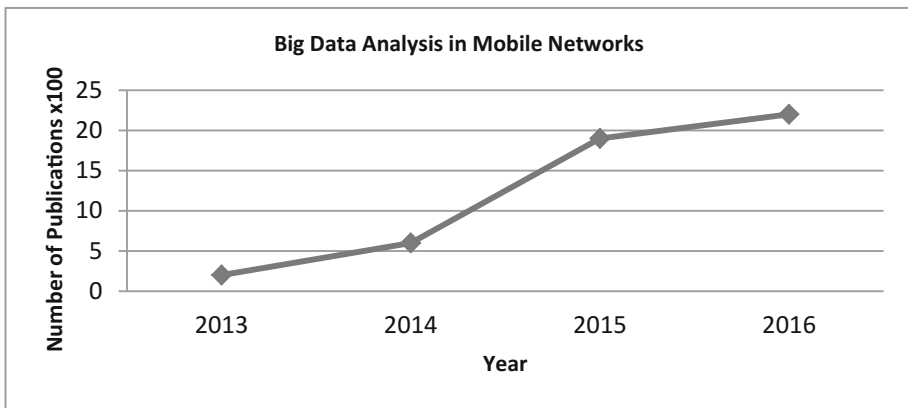


Fig. 1. Number of publications on big data analysis in mobile networks application. (source: village database www.engineeringvillage.com)

4.1 Big Data in Industry 4.0

According to [17], in 2050 about 70% of the world population will live in cities. Consequently, new challenges will appear for different sectors. Companies, who provide water supply, electricity, transportation, and health, should deal with the city overcrowding population. Furthermore, governments want to have a better control of natural resources and also they are looking for better life conditions for their citizens. All these areas can be addressed by an important technology which will help to optimize all the processes within a city; this technology is called the Internet of Things (IoT) [18]. It allows connecting multiple devices within a common network. Devices like sensors, actuators, and others, can be installed in different elements or other

electronics devices [19]. Consequently, it is possible to have an integral management of them, but the most fascinating advantage is that all this management can be possible through the Internet. Authors in [20] describes how big data analysis in IoT works beside an intelligent traffic controllers system and the big advantages this technology can bring into a smart city. People can decide the suitable route depending on the current traffic status. Likewise, traffic optimization network and traffic forecast can be accomplished and it will help in decision making. On the other hand, there are advantages related to air pollution. By big data analysis it is possible to create a suitable traffic model which helps to reduce the fuel consumption in vehicles.

The IoT is also related to Industry 4.0 [21], where it supports factories with a rapid product developing, flexible production and complex environment. The age of smart factories is coming, and intelligent and customized products can be manufactured in a shorter period of time with real-time considering the customer's preferences [21]. Such automation process is generating big datasets. It is worth to analyze these datasets in order to find new strategies for the supply chain processes to increase profitability. The big amount of data generated by all these devices connecting to the Internet will generate a big amount of structured and unstructured data. This sharp increase converges once again in a big data analysis [20]. Nevertheless, the data gathered by IoT have different features comparing to traditional big data because of data generation, data interoperability, and data quality [4]. Interpretation of big datasets from IoT is a challenge because the data sources are ubiquitous; the transmitted data is noisy, heterogeneous, and spatiotemporal dependent [18]. Figure 2 illustrates the progress in number of publications on big data in IoT over the past four years.

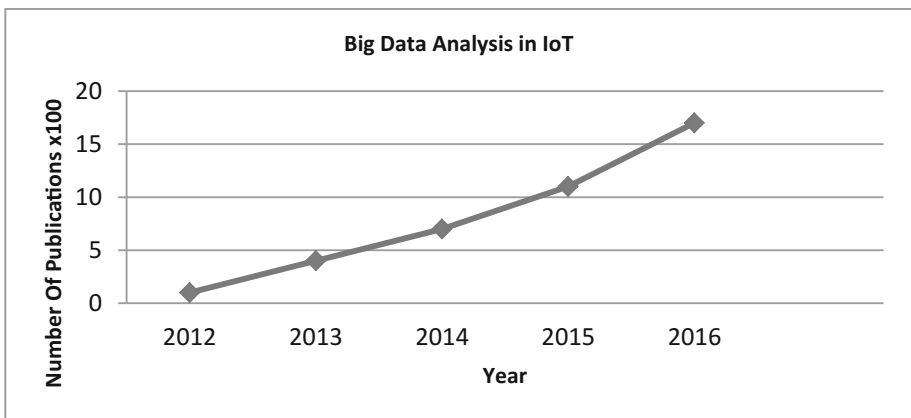


Fig. 2. Number of publications about big data analysis in IoT (source: village database www.engineeringvillage.com)

4.2 Big Data in Mechanical Engineering

Over the last decade, the automobile industry has developed important solutions for car driving, and all the mechanical and electronic systems within Electronic Vehicles (EV) [19, 22]. These developments allowed manufacturing autonomous vehicles,

which are equipped with advanced sensing, navigation devices, communication capabilities and computer vision. Thus, these entire new characteristic in vehicles are a potential support for all the user and transportation systems since it can avoid crashes, reduce the travel time, assisting traffic flows, among other benefits [17]. There are several sensors installed in vehicles, which help in different vehicle functions and, at the same time, provide large amount of data for research purposes. By the analysis of data collected from vehicles, it is possible to improve all the systems inside. Using Big Data techniques, all the function in the vehicle can be substantially improved [22, 23].

Regarding the range estimation for EV in [23], there are several parameters to analyze and this big amount of data has different levels of accuracy, relevance, and unstructured ways. Big Data analysis provides much better estimation for vehicle driving range [24]. In order to give an optimum solution for this particular problem, the data acquisition, from e.g., state of charge of the battery, battery manufactures model, driving history, the model of the vehicle, GPS location, weather conditions, traffic report etc. are collected and categorized according to their properties within three groups. The first is standard data, this category includes data such as GPS position, weather conditions, and estimation of the driving time to the destination. The second is historical data, within this group there are parameters like mile per gallon, and the data from other people who did the same trip are collected. The third is the real time data, which includes data collected when an event occurs unexpectedly, for instance a traffic jam due to an accident [24]. Figure 3 illustrates the progress in number of publications from different publishers for big data analysis over the past 8 years in mechanical engineering.

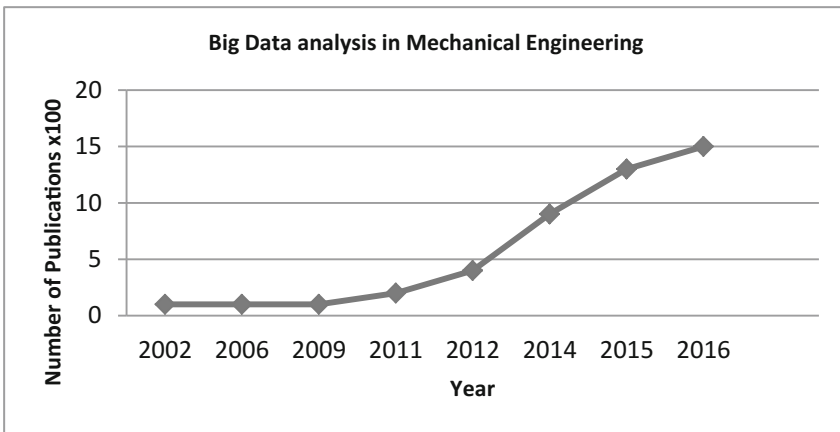


Fig. 3. Number of publications about big data analysis in mechanical engineering. (Source: village database www.engineeringvillage.com)

4.3 Big Data Future Challenges

Big Data analysis involves several challenges and nowadays the research at the industry and laboratories are in the beginning phase. There is much work to do and big efforts are needed to improve different features in big data analysis. Moreover, there

will be new fields in which a big data analysis will be the solution to tackle the problem. According to [20, 21] there are several problems to be solved as it is addressed below.

4.4 Standardization

The need of an evaluation standard for data computing efficiency and a system which can evaluate the quality of data to enhance big data features is an important issue now and in the future [25]. Although there are several big data solutions, there is no capacity to measure the big data performance by mathematical algorithms. This performance is evaluated by the implemented system and it shows the results, however it is not possible to evaluate and compare them before and after the big data analysis.

4.5 Big Data Computing Modes

Regarding computing modes, transferring data is a challenging aspect as there are several features that a network should offer for this type of applications. There are many features to analyze and transfer data within a network such as channels features, security, reliability, high network availability, and others. All these features should be ensured in order to avoid a bottleneck in this process. Nasser et al. [15] states that, the big data processes involve multiple phases of data acquisition, extraction of information and filtering, data integration, aggregation and visualization, query processing, data modelling, data analysis, and data interpretation and presentation. The disadvantage is that every phase has its own challenges and many difficulties to face [26].

5 Conclusions

In this article it is discussed that, how engineering community is adopting the big data technologies within their processes to stay competitive. In particular this article presents a state of the art survey of the academic literature on the big data applications in the engineering realm. It was well illustrated that, the big data technologies has become an important tool to manage big datasets generated in engineering applications. As it is addressed, the availability of a large number of scientific papers, reports and proceedings confirms the progress of big data analysis in a wide range of industrial applications and a diverse number engineering fields. It is concluded that, the world is adopting big data tendency because it is an efficient option to perform analysis of large the databases and conduct decision support analysis in an effective manner.

Acknowledgement. This work has been sponsored J. Selye University, ITMS 26210120042, and co-funded by the European Regional Development Fund. Authors would like to thank PhD candidate Lourdes Ruiz for her supports during the preparation of the manuscripts.

References

1. Chen, C.: Data-intensive applications, challenges, techniques and technologies: a survey on big data. *Inf. Sci.* **275**, 314–347 (2014)
2. Mosavi, A., Varkonyi, A.: Learning in Robotics. *Learning* **157**, 8–11 (2017)
3. Elarabi, T.: Big data analytics concepts and management techniques. *IEEE Invenive Comput. Technol.* **2**, 183–202 (2016)
4. Gubbi, J.: Internet of Things (IoT): A vision, architectural elements, and future directions. *Future Gener. Comput. Syst.* **29**, 1645–1660 (2013)
5. Demchenko, Y.: Defining architecture components of the big data ecosystem. *Collab. Technol. Syst. IEEE* **15**, 345–378 (2014)
6. He, T.: Big data analytics in mobile cellular networks. *IEEE Access* **4**, 1985–1996 (2016)
7. Imran, A.: Challenges in 5G: how to empower SON with big data for enabling 5G. *IEEE Netw.* **28**, 27–33 (2014)
8. Jati, G.: Big data compression using spihit in Hadoop. *Big Data Inf.* **34**, 64–73 (2016)
9. Rahimi-Eichi, H.: Big-data framework for electric vehicle range estimation. *Ind. Electron. Soc., IEEE* (2014)
10. Mosavi, A.: Optimal Engineering Design. Technical report University of Debrecen (2013)
11. Mosavi, A., Vaezipour, A.: Developing Effective Tools for Predictive Analytics and Informed Decisions. Technical report (2013). <https://doi.org/10.13140/RG.2.2.23902.84800>
12. Latinovic, T.: Big Data in industry. *Mater. Sci. Eng.* **144**, 36–59 (2016)
13. Mosavi, A.: Predictive decision model (2015). <https://doi.org/10.13140/RG.2.2.21094.63047>
14. Mosavi, A.: Predictive Decision Making, Predictive Decision Model, Tech. Report. (2015). <https://doi.org/10.13140/RG.2.2.21094.63047>
15. Nasser, T., Tariq, R.: Big data challenges. *J. Comput. Eng. Inf. Technol.* **4**, 122–143 (2015)
16. Prasath, R.R., Ozturk, P.: An Approach to Content Extraction from Scientific Articles using Case-Based Reasoning. *Res. Comput. Sci.* **117**, 85–96 (2016)
17. Jin, J.: An information framework for creating a smart city through internet of things. *IEEE Internet Things J.* **2**, 112–121 (2014)
18. Lelwala, N.: Ensemble inference based framework for creating knowledge from big data in IoT. *Adv. ICT Emerg. Reg.* **4**, 84–94 (2016)
19. Mosavi, A., Varkonyi-Koczy, A.R.: Integration of machine learning and optimization for robot learning. *Adv. Intell. Syst. Comput.* **519**, 349–355 (2017)
20. Mosavi, A., Rabczuk, T.: Learning and intelligent optimization for material design innovation, Theoretical Computer Science and General Issues, LION11 (2017)
21. Kagermann, H.: Recommendations for Implementing the strategic initiative INDUSTRIE 4.0: securing the future of German manufacturing industry; Technical report of the Industrie 4.0 working group. *Forschungsunion* (2013)
22. Mosavi, A.: Decision-Making Models for Optimal Engineering Design and their Applications. Doctoral Dissertation, University of Debrecen, Hungary (2013)
23. Petit, J., Shladover, E.: Potential cyberattacks on automated vehicles. *IEEE Trans. Intell. Transp. Syst.* **16**, 546–556 (2015)
24. Mosavi, A.: Multiple criteria decision making integrated with mechanical modeling of draping for material selection of textile composites. *Compos. Mater.* **12**, 73–81 (2012)
25. Sowmya, R., Suneetha, K.: Data mining with big data. *IEEE Intell. Syst. Control* **11**, 342–360 (2017)
26. Yin, S.: Big data for modern industry. *Challenges Trends IEEE* **103**, 143–146 (2015)

Robotics, Measurement, Identification and Control

Calculation Method of Chemical Kinetics to Search the Optimal Experimental Conditions in a Micro Flow Reactor

Keisuke Nonaka^(✉), Masato Abe, and Kazuhiro Takeda

Graduate School of Integrated Science and Technology, Shizuoka University,
Shizuoka, Japan

{nonaka.keisuke.17, takeda.kazuhiro}@shizuoka.ac.jp,
abechan312@yahoo.co.jp

Abstract. In recent years, the micro flow reactor, which takes the place of a batch reactor, is remarkable. The flow reactor is used to synthesize products heated by microwaves in a micro tube. The yield of products is increased by providing the micro flow reactor with the suitable experimental conditions. However, it is hard to set the optimal experimental conditions. A small difference in the experimental conditions can significantly change the result because the channel has a micro size. Therefore, it requires a lot of experimental time and cost to determine the adequate conditions. The purpose of this study is estimation of kinetic parameters to find out the optimum condition. The parameters were determined from experimental results under a variable temperature condition. The model of the variable temperature experiment was created using the following three kinetic relations: the reactor design equation, the rate equation and the Arrhenius equation. The model results were fitted with the real experimental data to estimate the kinetic parameters. Consequently, the kinetic parameters were calculated by curve fitting using the experimental data obtained at different flow rates (Fig. 1). It requires a lower cost to calculate the proper kinetic parameters than the traditional method using the Arrhenius plot (Table 1). The more experiments we examined at various flow rates, better results were obtained.

Keywords: Micro flow reactor · Variable temperature · Kinetic parameter

1 Introduction

A batch reactor is used for many organic syntheses but it requires a lot of time and cost to analyze the products. In recent years, a micro flow reactor, which takes the place of a batch reactor, is remarkable since measurements can be done on-line. The flow reactor is used to synthesize products heated by microwaves in a micro tube. Also, the experimental conditions such as the output of microwaves and flow rate can be gradually changed. Figure 1 shows a schematic of a micro flow reactor.

A micro flow reactor enables rapid heating of solvents and generates a more uniform profile, which significantly reduces the reaction times, and in many cases, increases the yields and saves energy. Junichi Yoshida reported that the micro flow

reactor is able to safely and effectively synthesize products [1]. Minjing Shanga reported that the yield of the objective products increases by providing the micro flow reactor with suitable experimental conditions [2]. However, it is hard to strictly set the optimal experimental conditions. A small difference in the experimental condition can significantly change the result because the channel has a micro size. Therefore, it requires a lot of experimental time and cost to determine the adequate conditions. The purpose of this study is estimation of the kinetic parameters to find out the optimum conditions.

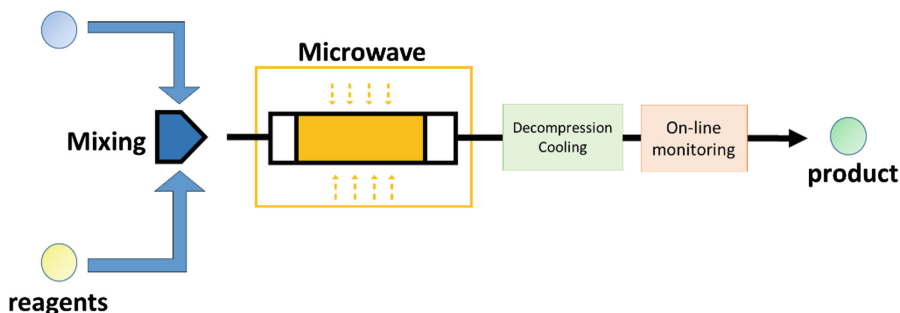


Fig. 1. Schematic of micro flow reactor

Table 1. Calculated results

Flow rate [mL/min]	Set	n + m	A	E_a [kJ/mol]	Residuals
1.0, 2.0, 3.0	1	0.79	$7.2E + 06$	77.2	0.1054
	2	0.85	$1.5E + 07$	79.7	0.1064
	3	0.88	$2.4E + 07$	81.5	0.1083
	4	1.16	$7.7E + 08$	93.7	0.1405

2 Method

To determine the optimal conditions, the kinetic parameters (reaction order, frequency factor and activation energy) need to be estimated. The conventional method by the Arrhenius plot takes a lot of time to estimate these parameters. This study proposes a variable temperature kinetics (VTK) analysis.

2.1 VTK Analysis

The VTK analysis was performed on an unsteady state reaction system. The Variable reaction temperature T and conversion X of the substance were measured. Calculating the kinetic parameters can be performed by curve fitting of the profile and kinetic model representing the state of the reaction.

Creating the Kinetic Model. Three relations are necessary to describe the reaction kinetics during the variable temperature kinetics experiment, i.e. the reactor design equation (Eq. (1)), the rate equation (Eq. (2)), and the Arrhenius equation (Eq. (3)).

$$-r_a = C_{a,0}v_0 \frac{dX}{dV} \quad (1)$$

$$-r_a = k [C_{a,0}(1-X)]^n \prod_i^j \left[C_{a,0} \left(\Theta_i - X \frac{b_i}{a} \right) \right]^{m_i} \quad (2)$$

$$k = A \exp\left(-\frac{E_a}{RT}\right) \quad (3)$$

They are combined to form Eq. (4).

$$-r_a = C_{a,0}v_0 \frac{dX}{dV} = A \exp\left(-\frac{E_a}{RT}\right) [C_{a,0}(1-X)]^n \prod_i^j \left[C_{a,0} \left(\Theta_i - X \frac{b_i}{a} \right) \right]^{m_i} \quad (4)$$

V is the reactant volume; $C_{a,0}$ is the inlet concentration of the limiting reactant; v_0 is the inlet volumetric flow; a and b_i are the stoichiometric coefficients of the limiting reactant a and each non-limiting reacting species i , respectively; and Θ_i is the molar ratio of species i and a . The reaction orders with respect to species a and i are designated n and m_i , respectively.

In favorite cases, Eq. (4) can be integrated and solved for X . For example, when the rate law depends on just two reactants, and the ratio of their inlet concentration (Θ_b) is chosen to be equal to the ratio of the stoichiometric coefficients b/a . The results are Eqs. (5) and (6).

$$X = 1 - \left[1 + (n+m-1) \left(\frac{b}{a} \right)^m C_{a,0}^{n+m-1} \tau A \exp\left(-\frac{E_a}{RT}\right) \right]^{\frac{1}{1-n-m}} \quad (n+m \neq 1) \quad (5)$$

$$X = 1 - \exp\left(-\tau \Theta_b^m A \exp\left(-\frac{E_a}{RT}\right)\right) \quad (n+m = 1) \quad (6)$$

If the second reactant is present in large excess over the limiting reactant, such that ($\Theta_b - Xb/a \approx \Theta_b$), Eqs. (7) and (8) are obtained instead.

$$X = 1 - \left[1 + (n-1) C_{a,0}^{n+m-1} \tau A \exp\left(-\frac{E_a}{RT}\right) \right]^{\frac{1}{1-n}} \quad (n \neq 1) \quad (7)$$

$$X = 1 - \exp\left(-\tau C_{a,0}^m \Theta_b^m A \exp\left(-\frac{E_a}{RT}\right)\right) \quad (n = 1) \quad (8)$$

Calculating the Kinetic Parameters. The parameters to be determined are the overall reaction order $n+m$, frequency factor A and activation energy E_a . The parameters are

calculated by curve fitting. The combination of the optimum parameters for reducing the residual are determined so that the result of the estimation is the closest curve to the measured data.

The calculations are performed using the function “lsqcurvefit” of the numerical analysis software MATLAB. The function solves nonlinear curve-fitting (data-fitting) problems in a least-squares sense. The solver is shown below.

$$\min_x \|F(x, xdata) - ydata\|_2^2 = \min_x \sum_i (f(x, xdata_i) - ydata_i)^2$$

Given input data, $xdata$, and the observed output, $ydata$.

The estimated parameters are different for each set of calculated starting points. In order to determine the suitable kinetic parameters, it is necessary to set appropriate starting points. The procedure for optimization is shown below.

1. Set the start points to $(n + m, A, E_a) = (0, 0, 0)$ and calculate each kinetic parameters
2. Confirm the calculated residuals
3. Change only the start point of A one digit and calculate the parameter
4. Similarly, change the starting point of A to $1.0E + 20$ and calculate each parameter
5. The estimated result that minimizes the residual within the searched range is set as the next starting point
6. Change A again and confirm the calculation result.

Using the above procedure, the suitable combination of kinetic parameters is searched so that the profile of the estimation result almost agrees with that of the measured data.

2.2 Experiment

In this study, the Fischer indole synthesis was evaluated. Indole was synthesized by the reaction of equivalent amounts of cyclohexanone and phenyl-hydrazine. This scheme is shown in Fig. 2.

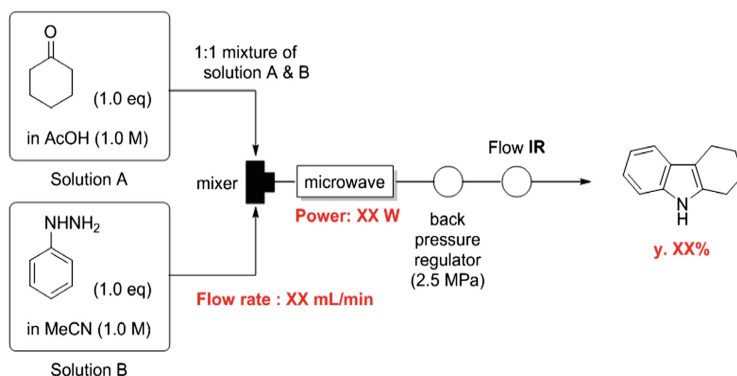


Fig. 2. Scheme of fisher indole synthesis by micro flow reactor

In this reaction, measurements are taken under variable temperature conditions. The output of the microwaves is gradually increased (30 steps in 10 min) from 10 W to 50 W. After 10 min from the start of the reaction, the output remained constant at 50 W.

Based on the above conditions, the measurement and analysis are performed at the flow rate 1.0, 2.0 and 3.0 mL/min.

3 Results and Discussion

3.1 Estimation of Kinetic Parameters by the VTK Analysis

For the experimental conditions shown in 2.2, the reaction temperature and conversion were measured. The data were analyzed by curve fitting with the kinetic model.

When the number of flow rate option was less than three, there were many sets of kinetic parameters in which the estimation result almost agreed with the experimental data. However, the kinetic parameters cannot be unique. By increasing the number of flow rate options used for the analysis up to three, the estimation result was refined, and it was possible to determine a suitable set of kinetic parameters. When there are several sets of appropriate kinetic parameters, the parameter is expressed as a range of kinetic parameters. The results of the curve fitting using three flow rate options are shown in Table 1 and Figs. 3, 4, 5 and 6.

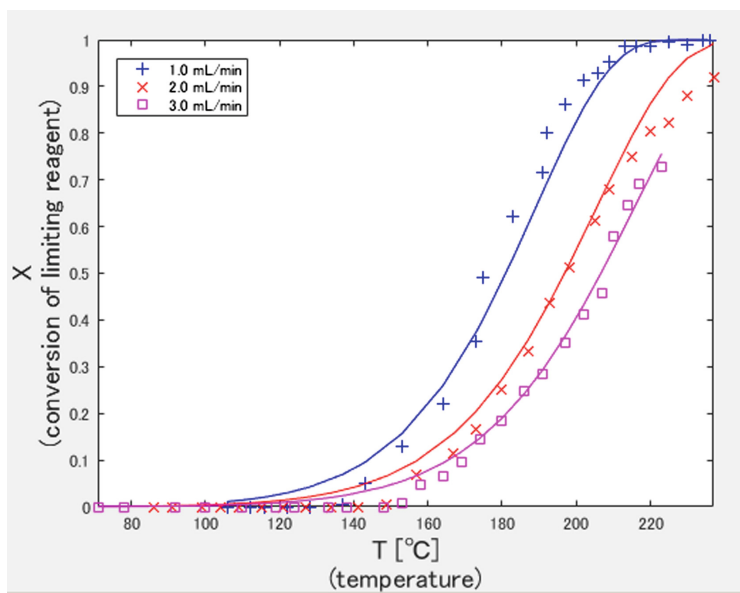
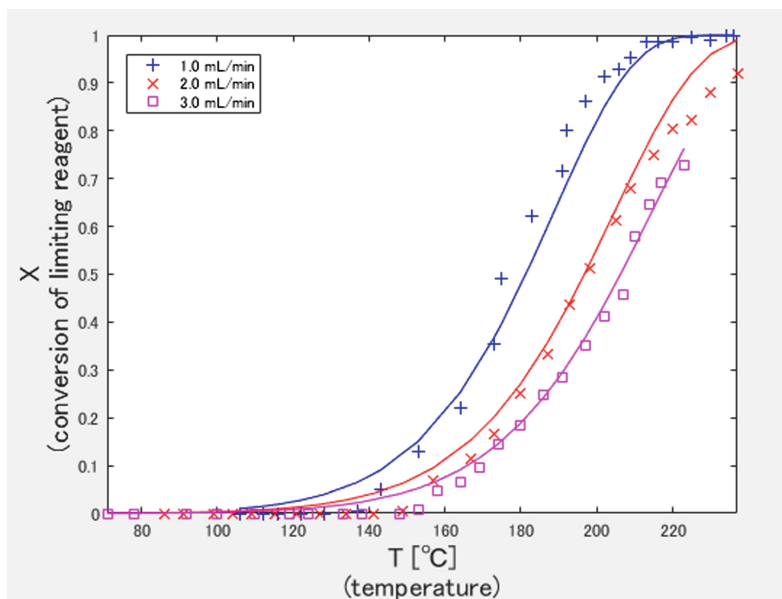
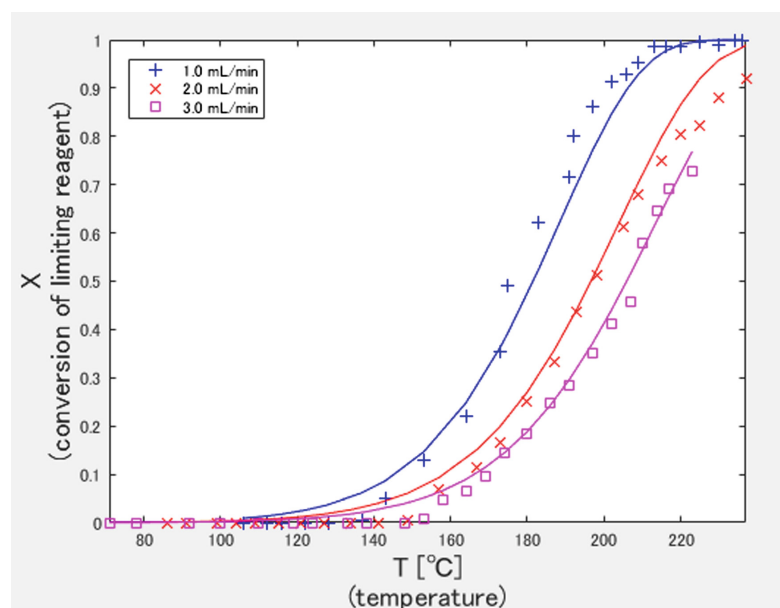


Fig. 3. Reaction profile (set 1)

**Fig. 4.** Reaction profile (set 2)**Fig. 5.** Reaction profile (set 3)

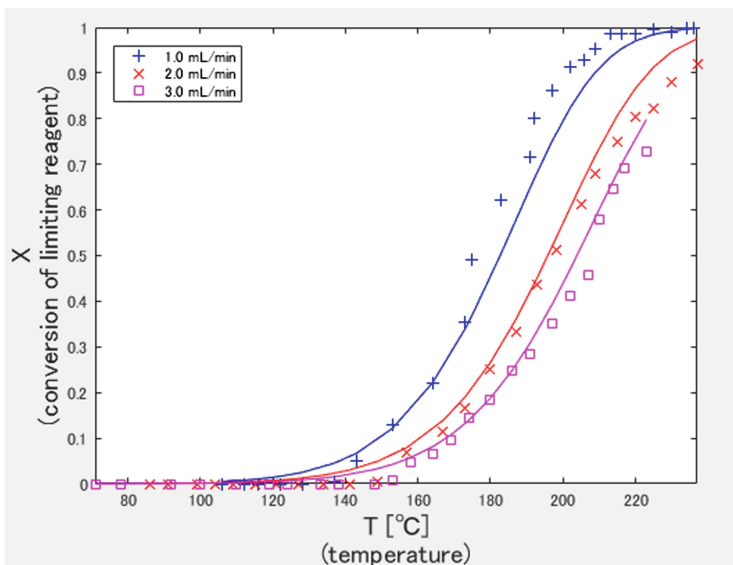


Fig. 6. Reaction profile (set 4)

The estimated profile of set 4 did not agreed well with the measurement data and the estimation results as compared to each profile of sets 1, 2 and 3. Therefore, the range of the kinetic parameters at which the residuals were 0.1083 or less was determined as the estimation result of the appropriate kinetic parameters (Table 2).

Table 2. Calculated result of kinetic parameters

n + m	A	E_a [kJ/mol]
0.85 ± 0.05	$(1.6 \pm 0.8)E + 07$	(80 ± 2)

3.2 Comparison with Steady State Analysis

The kinetic parameters and the experimental cost (the time required for the experiment) were estimated by a steady state analysis using the Arrhenius plot. The cost of the VTK analysis was compared to the cost of the steady state analysis.

It takes about 12 min to measure one flow set of the flow data for the VTK analysis. The twelve minutes was multiplied by the number of flow rate options to be evaluated, and the total experimental time was 36 min. For the steady state analysis, it takes about 10 min of experimentation time to measure one data point. When the measurement of four points to identify the reaction order and the measurement of three points to make the Arrhenius plot were carried out, the total experimentation time was 70 min. As a result, the cost of the VTK analysis decreased to about half that of the steady state analysis. The results are summarized in Table 3.

Table 3. Results of analysis

	n + m	A	E _a [kJ/mol]	Cost [min]
VTK analysis	0.85 ± 0.05	(1.6 ± 0.8)E + 07	(80 ± 2)	36 (12 min × 3)
Steady state analysis	1	4.0E + 06	75	70 (10 min × 7)

Comparing the two results, it was found that the VTK analysis can estimate the same value as the steady state analysis in a shorter experiment time.

4 Conclusion

In this study, in order to determine the optimum experimental conditions for a micro flow reactor, estimation of the kinetic parameters using the VTK analysis was proposed. The reaction profiles of the variable temperature and conversion were fitted to a kinetic model. As a result, the kinetic parameters were well estimated. Moreover, when comparing the VTK analysis with the result of the estimation by the steady state analysis, which is a conventional analysis method, the VTK analysis could estimate almost the same value as the estimation result of the steady state analysis at a lower cost. In a future study, the optimal experimental conditions (temperature and flow rate) will be determined using the estimated kinetic parameters. More complex reactions (reversible reaction, side reaction) will also be considered.

References

1. Yoshida, J., Nagaki, A., Yamada, D.: Continuous flow synthesis. *Drug Discov. Today Technol. Spring* **2013**(10), 53–59 (2013)
2. Shanga, M., Noela, T., Wanga, Q., Sua, Y., Miyabayashi, K., Hessela, V., Hasebe, S.: 2-and 3-stage temperature ramping for the direct synthesis of adipic acid in micro-flow packed-bed reactors. *Chem. Eng. J.* **260**, 454–462 (2015)

Robot Control in iSpace by Applying Weighted Likelihood Function

Adrienn Dineva^{1,2(✉)}, Balázs Tumor², Péter Csiba²,
and Annamária Várkonyi-Kóczy²

¹ Kálmán Kandó Faculty of Electrical Engineering, Institute of Automation,
Óbuda University, Budapest, Hungary

dineva.adrienn@kvk.uni-obuda.hu

² Department of Mathematics and Informatics, J. Selye University,
Komárno, Slovakia

{tumorb, csibap, koczya}@ujs.sk

Abstract. Recently the intelligent space applications have become increasingly beneficial considering robot control. In this paper the visual controlling concept is presented in the iSpace framework. The positions of the end-effector of the robot manipulator are presented by the 3D spatial coordinates extracted from image pairs. The exact image Jacobian matrix of the mapping from Cartesian space to image space is given, the task space controllers can be directly extended to image-space controllers. The Jacobian matrix poses uncertainty if modeling and calibration errors are present. Despite the fact that much progress has been presented in the literature of visual servoing, there are only a few results obtained for the stability analysis in presence of the uncertain camera parameters. This research aims developing a new method for the control of the manipulator in Cartesian space, using the vision information of the environment obtained by cameras using the OptiTrack framework. The robotic manipulator is mounted on a mobile tank. The control scheme allows the end effector to transit smoothly from Cartesian-space feedback to vision-space feedback when the target is inside the vicinity of the camera. Key points on the manipulator are marked which are detected by the camera system. The framework calculates the coordinates of the markers, and thus estimate the state of each joint of the manipulator within a margin of error. In order to achieve the most precise estimation each camera image is weighted during the evaluation. The weights are determined using data set of images. After, a likelihood function is assigned for each joint that is used for defining the position and designing the motion. During the experiments the proposed control concept has proven to be reliable.

Keywords: Robot control · Visual-based control · Likelihood function · iSpace · Mechatronics · Intelligent systems

1 Introduction

During the last decade intelligent space applications have become the focus of many researches [1]. The iSpace concept incorporates the effective application of various sensors, robots, actuators through communication network. The iSpace can be

considered as a large scale mechatronics system which integrates the actuators, sensors, intelligent algorithms [2, 3]. iSpace applications have many advantages, for instance remote accessibility, the elimination of unnecessary wiring, efficient data distribution, scalability, etc. Recently an ample number of iSpace applications have been proposed. In its study, Leung et al. [4] describe an intelligent space with the purpose of localization and control of robotic wheelchairs to help people. Especially vision-based robot control (generally called visual servoing) is discussed widely in the literature [5, 6]. The purpose of the visual-based concept is to control a robot using the information provided by a camera system. These vision systems are generally classified depending on the number of cameras and on their positions. The camera can be mounted on the robot, mainly on the end effector, or over the robot. Two main categories of visual based robot control are exists. The first one is referred to as direct visual servoing. In this case the input of the system is computed directly by the vision system. The second main approach is indirect visual servoing, where the vision-based control compute a reference control law which is sent to the low-level controller of the dynamic system [7, 8]. This paper introduces a visual based control method using OptiTrack camera system consisting of 24 cameras. Many concepts have already been published in the literature highlighting advanced image processing, for instance [9–11]. In our concept, the image analysis method is based on a weighted likelihood function. The system processes the individual camera images in order to extract the straight line segments. The 3D spatial positions of these lines are determined by combining the results from pairs of neighboring cameras, of which the most likely results are chosen. The system controls a mobile robot by sending commands to execute predefined tasks. The mobile robot has two main parts; a mobile tank and a robot arm which is mounted on a tank. The mobile robot can autonomously execute different tasks controlled by the iSpace. The iSpace is developed at the Robotic Center of the J. Selye University. The proposed method ensures satisfactory performance.

2 Robot Control by Visual Information Applying Weighted Likelihood Function

The positions of the end-effector of the robot manipulator are presented by the 3D spatial coordinates extracted from image pairs. The exact image Jacobian matrix of the mapping from Cartesian space to image space is given, the task space controllers can be directly extended to image-space controllers. The Jacobian matrix poses uncertainty if modeling and calibration errors are present. In the presence of the uncertain camera parameters the result may be degraded. In order to overcome this limitation a weighted likelihood function has been introduced. Based on the image analysis the position of the robot and its distance from the object is calculated. After, an appropriate motion is selected from a motion library in order to execute the desired task.

2.1 The Image Analysis

The first and main step of this method is the image analysis. An improved edge detection (Canny [12]) technique is performed on the original images (see, Fig. 1). The

result can be seen in Fig. 2. The steps of the image analysis process are displayed in Fig. 3. In presence of the uncertain camera parameters, etc., the evaluated coordinates of the joints can be biased. In order to overcome this limitation the following weighted likelihood function is introduced in the pose recognition [13] step of the method.



Fig. 1. Original camera image

Based on the obtained edges the d distance is calculated. Let $x = (x_1, \dots, x_n)$ ($n = 24$, the number of cameras) be the vector of the calculated distances between two arbitrary points A and B (for e.g., the end effector middle point and the target object middle point) obtained on each camera image. Its unknown probability function is $(m \mid \theta)$ that is an element of the parametric $M = \{(x|\theta), \theta \in \Theta \subset \mathbb{R}\}$. After that, we can apply the following weighted likelihood function [14]:

$$L^w(\theta) = L^w(x|\theta) = \prod_{i=1}^n m(x_i|\theta)w(x_i) \tag{1}$$

According to theorem presented in [15] Eq. (1) leads to a weighted score function:

$$s^w(\theta) = s^w(x|\theta) = \sum_{i=1}^n w(x_i)s(x_i|\theta), \tag{2}$$

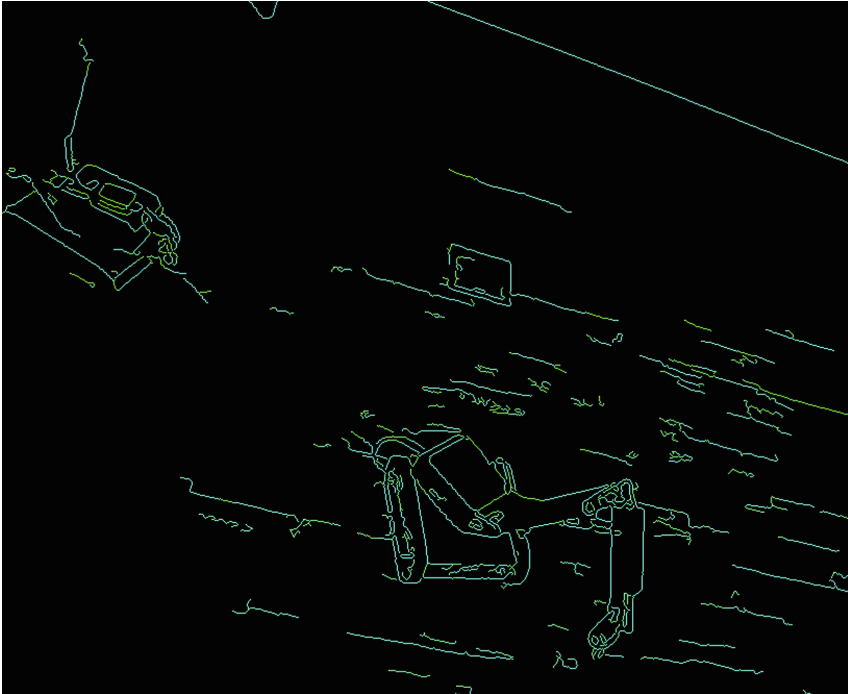


Fig. 2. Sketch of the robot (obtained from camera image displayed in Fig. 1.)

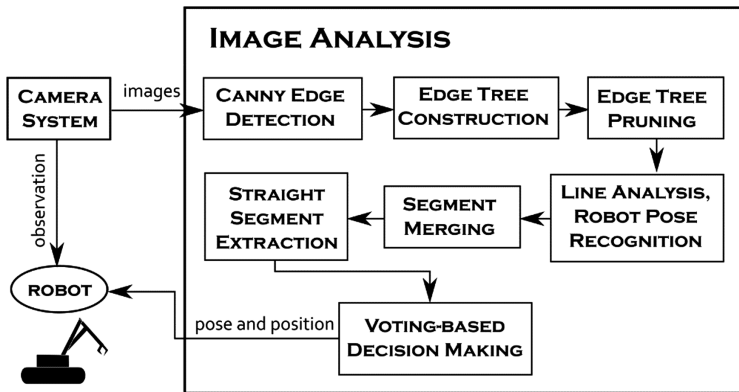


Fig. 3. Image analysis process

that can be used to precisely define the value of d distance. After that, from image pairs using also the above described weights the joint coordinates are calculated. Thus, the actual pose of the manipulator can be correctly determined. This strategy is used both for calculating the distance between the mobile robot and the target object and for defining the actual position of each joint on the 6 DoF (Degree of Freedom) manipulator.

2.2 Motion Planning

The motion planning is based on a predefined library of primitive motions. According to the evaluated distances the next step is selecting the appropriate primitives in order to execute the task. For each primitive motion the distance of movement is assigned. The motion planning is based on selecting the primitives by minimizing the overall distance. However, further corrections above the predefined motions are necessary in order to complete the tasks that are calculated also on the evaluated distances by the image analysis.

3 Conclusions

In this paper a new visual-based robot control method using the vision information of the environment obtained by cameras using the OptiTrack framework has been presented. The proposed strategy at first analyzes the camera images and defines the actual position of each joint using the edge map. In order to precisely define the distances by taking into account the uncertainties, calibrations errors, etc., a weighted likelihood function has been introduced in the distance evaluation. The task execution is carried out by using a predefined primitive motion and pose library. During the experiments the proposed control concept has proven to be reliable and serves as a basis for further investigations.

Acknowledgement. This work has been sponsored by the Hungarian National Scientific Fund (OTKA 105846). This publication is also the partial result of the Research & Development Operational Programme for the project “Modernisation and Improvement of Technical Infrastructure for Research and Development of J. Selye University in the Fields of Nanotechnology and Intelligent Space”, ITMS 26210120042, co-funded by the European Regional Development Fund.

References

1. Hashimoto, H.: Intelligent space - how to make spaces intelligent by using DIND? In: 2002 IEEE International Conference on Systems, Man and Cybernetics, 6–9 October 2002, Yasmine Hammamet, Tunisia (2002)
2. Cheah, C.C., Liu, C., Slotine, J.J.E.: Adaptive vision-based tracking control of robots with uncertainty in depth information. In: Proceedings of the IEEE International Conference on Robotics and Automation, Rome, Italy, pp. 2817–2822 (2007)
3. Espiau, B.: Effect of camera calibration errors on visual servoing in robotics. In: Proceedings of the International Symposium on Experimental Robotics, Kyoto, Japan, pp. 182–192 (1993)
4. Leung, W.-L.D., et al.: Intelligent space with time sensitive applications, advanced intelligent mechatronics. In: Proceedings of the 2005 IEEE/ASME International Conference on, 24–28 July 2005, Monterey, CA, USA (2007). <http://aim2005.mtu.edu/>. ISBN: 0-7803-9047-4
5. Rampinelli, M., et al.: An intelligent space for mobile robot localization using multi-camera systems. *Sens. (Basel)* **14**(8), 15039–15064 (2014)

6. Kelly, R.: Robust asymptotically stable visual servoing of planar robots. *IEEE Trans. Robot. Autom.* **12**(5), 759–766 (1996)
7. Reyes, F., Kelly, R.: Experimental evaluation of fixed-camera direct visual controllers on a direct-drive robot. In: *IEEE International Conference on Robotics and Automation*, Leuven, Belgium, vol. 2, pp. 2327–2332, May 1998
8. Vakanski, A., Janabi-Sharifi, F.: *Robot Learning by Visual Observation*. Wiley, Hoboken (2017). ISBN 9781119091806
9. Mosavi, A.: On developing a decision-making tool for general applications to computer vision. *Int. J. Comput. Appl. RTPRIA*(1), 10–17 (2013). doi:[10.5120/11797-1003](https://doi.org/10.5120/11797-1003). Special Issue on Recent Trends in Pattern Recognition and Image Analysis
10. Mosavi, A.: Decision-making software architecture; the visualization and data mining assisted approach. *Int. J. Inf. Comput. Sci.* **3**(1), 12–26 (2014). doi:[10.14355/ijics.2014.0301.03](https://doi.org/10.14355/ijics.2014.0301.03)
11. Mosavi, A., Sevtsenko, E.: Application of visual and predictive analytics in engineering design and production. In: *Conference of DAAAM Baltic, Industrial Engineering*, 24–26 April 2014, Tallinn, Estonia, ISSN 2346-612X (print), ISSN 2346-6138 (online) (2014)
12. Canny, J.: A computational approach to edge detection. *IEEE Trans. Pattern Anal. Mach. Intell.* **8**(6), 679–698 (1986)
13. Narayanan, K.K.: *Learning vision-based mobile robot behaviors from demonstration*. Robotik und Automation. DrHut Verlag (2015). ISBN 978-3-8439-2481-8
14. Agostinelli, C., Markatou, M.: Test of hypothesis based on the weighted likelihood methodology. *St. Sinica* **1**, 499–514 (2001)
15. Huber, P., Ronchetti, E.: *Robust Statistics*, 2nd edn. Wiley, Hoboken (2009)

Dissipation and Thermal Time Constants in Graphite of an Ultra-Small Bead Thermistor

Daniel Radu^(✉), Iordana Astefanoaei, and Catalin Agheorghiesei

Faculty of Physics, Alexandru Ioan Cuza University of Iasi,
Carol I Blvd., no. 11, 700506 Iasi, Romania
{dradu, iordana, catalin.agheorghiesei}@uaic.ro

Abstract. The thermistors are indispensable devices in experimental arrangements for electrical calibration of graphite calorimeters. The present experiments determine the two basic thermal constants in graphite – the thermal time constant, τ_g and dissipation constant, δ_g – of commercially-available VECO ultra-small bead thermistors; these constants are essential parameters in thermal modeling of graphite calorimeters. For the above-mentioned kind of thermistors, the dissipation constant in graphite is found to be approximately ten times larger than that in still air, whereas the thermal time constant in graphite is approximately one hundred times smaller than that corresponding to a thermistor placed in still air.

Keywords: Graphite calorimetry · Thermal time constant · Dissipation constant

1 Introduction

The modeling of a graphite calorimeter implies, in principle, to know as precisely as possible the main characteristics of all the components and materials involved in the construction of such a device. Although this situation might appear to be natural/normal, often in practice it is not so. For instance, the aluminized Mylar is a material used in any vacuum graphite calorimeter, and different bibliographic sources (books, journals, network sites) report different values for Mylar's emissivity. That is why direct measurements are always preferable; for the above-mentioned example, the investigation was performed by Domen [1].

The purpose of the present paper is to present two simple experimental methods to measure the dissipation constant, δ , and the thermal time constant, τ , of a NTC thermistor (a thermistor having negative temperature coefficient of resistance). This kind of thermistor is an indispensable component in experimental arrangements for electrical calibration of graphite calorimeters [2–5].

No matter which mode of operation is used to run a graphite calorimeter that is electrically calibrated, the same space-time temperature distributions in all the bodies of the calorimeter must be ensured during both the calibration runs and the corresponding irradiation runs. Because of the appearance of thermal gradients in the point-like electrically heated calorimeter bodies, the two temperature distributions are different,

especially in the first part of the heating period, when the transient regime is present. This situation requires a careful analysis on the effects of thermal gradients that appear especially in the core, which is the main body of a graphite calorimeter. Thus, for understanding the performance of the calorimeter, extensive modeling of the heat transfer within the calorimeter should be done. Usually, the finite-element packages are used to model various setups. Any serious analysis that must be carried out to obtain the space-time distribution of the temperature in the calorimeter bodies should start with the following question: what really happens when a certain amount of power is dissipated in a point-like heating thermistor? To give a satisfactory answer to this question requires the knowledge of two basic constants of a thermistor: the dissipation constant, δ [W/K] and thermal time constant, τ [s].

The reported nominal values of dissipation and thermal time constants in still air @ 25 °C of VECO ultra-small bead 41A14 thermistors are given in Sect. 3. Unfortunately, all the NTC thermistor manufacturers give in their Product Bulletins [6] the nominal values for δ and τ in still air, and only occasionally in other media (often in moving air and, at most, in still and/or moving water). Because in graphite calorimetry the medium in which the thermistor is embedded is the graphite, the knowledge of both the dissipation constant in graphite, δ_g , and the thermal time constant in graphite, τ_g , of a NTC thermistor are required.

2 Heat Transfer and the Definition of the Constants

For a thermistor, the instantaneous heat transfer equation writes [7]:

$$dQ/dt = P = EI = \delta(T - T_0) + mc dT/dt = \delta(T - T_0) + C dT/dt, \quad (1)$$

where $P = dQ/dt$ is the rate of thermal energy supplied to the thermistor, E and I are the instantaneous thermistor voltage and current, C is the heat capacity of the thermistor, t is the instantaneous time and δ is the dissipation constant of the thermistor, defined as the ratio, at a specified ambient temperature, T_0 , of a change in power dissipation in a thermistor to the resultant temperature change of the body, T ; m and c are the mass of the thermistor bead and the specific heat of the thermistor material, respectively. Since the term $\delta(T - T_0)$ in Eq. (1) is the rate at which heat is transferred away from the thermistor, it is seen that the dissipation constant must be dependent upon the thermal conductivity and the relative rate of motion of the medium surrounding the thermistor, the heat loss due to free convection in a still medium, the rate of heat conduction through the leads of the thermistor to its mount and the heat loss due to radiation (radiation losses are significant only when the medium is a gas at low pressure). Hence the dissipation constant δ is not a true constant, but varies slightly with both T_0 and $(T - T_0)$; it is typically measured under equilibrium conditions. When solving the Eq. (1) care must be taken when large integrating time intervals are considered, because both δ and C vary with temperature; obviously, the larger time intervals, the larger temperature variations. If only small temperature intervals are

considered, δ and C can be taken as true constants and the integration can be performed without any special caution. When $P = const.$, the solution of Eq. (1) is

$$T = T_0 + (P/\delta)(1 - e^{-(\delta/C)t}). \quad (2)$$

The relation (2) shows that when a significant amount of power is dissipated in a thermistor, its body temperature will rise above the ambient temperature as a function of time. The transient conditions at “turn on”, and all the applications that are based upon the current-time characteristics, are governed by relation (2). When the power is reduced in a thermistor to an amount where the self-heating is considered negligible, then the heat transfer equation can be re-written as follows: $dT/dt = -(\delta/C)(T - T_0)$ and has the following solution: $T(t) = T_0 + (T_i - T_0)e^{-t\delta/C} = T_0 + (T_i - T_0)e^{-t/\tau}$, where T_i is the initial body temperature (at $t = t_0 = 0$, $T_i \equiv T_0$), T_0 is the ambient temperature and $\tau = C/\delta$ is the thermal time constant of the thermistor. The thermal time constant is the amount of time required for a thermistor to reach 63.2% of the temperature difference when subjected to a step function change in temperature under negligible power dissipation conditions. The thermal time constant is dependent upon the same environmental factors as the dissipation constant, namely, the thermal conductivity and the motion of the medium, the conduction through the leads, the free convection in the medium and the radiation losses. The thermal time constant and dissipation constant data which is given in thermistor product literature must indicate the test methods and mounting methods employed if it is to be valuable to the designer. The thermal properties are somewhat difficult to predict by mathematical modeling and manufacturing variances will introduce enough uncertainty so that testing of the finished thermistor is usually required to obtain data on the response time and dissipation constant.

3 NTC Thermistors

Figure 1 illustrates a VECO ultra-small bead NTC thermistor. The bead surface approximately has the shape of a prolate spheroid, which is a spheroid that is “pointy” instead of “squashed”, *i.e.*, one for which the polar radius c is greater than the equatorial radius a , so $c > a$ (it is called “spindle-shaped ellipsoid” by Tietze [8]). A prolate spheroid is a surface of revolution obtained by rotating an ellipse about its major axis. The main characteristics of VECO ultra-small bead 41A14 thermistor are as follows: the lower “diameter” of the thermistor bead is $D_b^s = 2a = 2b = 2.8 \times 10^{-4}$ m, the upper “diameter” of the thermistor bead is $D_b^b = 2c = 3.9 \times 10^{-4}$ m, the volume of the thermistor bead is $V_b = 16 \times 10^{-12}$ m³, the mass of the thermistor bead is $M_b = (0.6 \div 0.8) \times 10^{-7}$ kg, the length, diameter and mass of the Pt-Ir (10% Ir) leads are $L_{Pt-Ir} = 1.419 \times 10^{-2}$ m, $D_w^{Pt-Ir} = 2.54 \times 10^{-5}$ m and $M_l = (0.29 \div 0.31) \times 10^{-6}$ kg, respectively, the mass of the thermistor is $M_T = 0.37 \times 10^{-6}$ kg, the specific heat capacity in still air @ 25 °C is $c_T^{air} = 712$ J kg⁻¹ K⁻¹, the zero-power resistance @ 25 °C is $R_0(T_0) \equiv R_{25} = 10683 \Omega$, the dissipation constant in still air @ 25 °C is $\delta = 9 \times 10^{-5}$ W/°C, the thermal time constant in still air @ 25 °C is $\tau = 0.5$ s, the

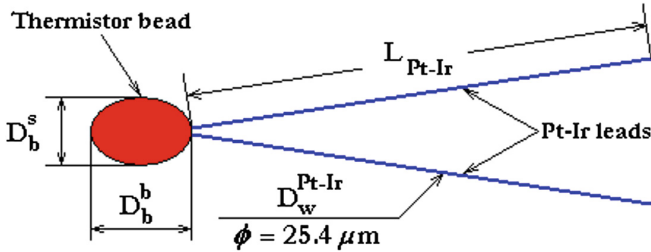


Fig. 1. Schematic representation of VECO ultra-small bead 41A14 thermistor (not at scale).

material constant of the thermistor is $\beta_{0^{\circ}\text{C}-50^{\circ}\text{C}} = 3460.29 \text{ K}$ and the temperature coefficient @ 25°C is $\alpha = -3.9\%/^{\circ}\text{C}$ (the last four quantities are provided by the manufacturer).

4 Arrangements for Experimental Measurements

There is a major difference between considering a thermistor in still air or in graphite; whereas in the former case (it can be stated that) the two constants (δ and τ) of a thermistor belong to the thermistor itself (i.e., they characterize the thermistor itself), in the latter case the two constants describe the ensemble ‘thermistor plus its surrounding medium’; in other words, this ensemble (known as a “thermistor structure”) must be regarded as a whole.

This situation appears every time when a thermistor is mounted in a solid medium; to ensure a good thermal contact between the two elements (the thermistor bead and the solid medium) they are soldered together in one way or another. Whereas from a fluid medium (a gas or a liquid) the thermistor can be extracted in a very short time (for instance, to determine the thermal time constant of the thermistor), to dismount a thermistor from its solid surrounding medium is quite impossible. In such cases, the heat capacity of the entire structure is significantly different from the enclosed thermistor element and special care must be taken when the experimental measurement techniques are established to determine the two constants of the thermistor structure. The thermistor under consideration in this paper (the VECO ultra-small bead 41A14 thermistor) was mounted in graphite as shown in Fig. 2.

A good thermal contact between the thermistor bead and the graphite sample was ensured using (as glue) an epoxy resin having the thermal conductivity [9] $k_g \cong 0.43 \text{ W m}^{-1} \text{ K}^{-1}$. An exact evaluation of the heat transfer between the two bodies based on the Newton law written for the geometry implied by this system leads to the conclusion that, even if the thermal conductivity of the glue seems to be small, in fact it is sufficient to ensure that essentially all the heat that flows into the epoxy resin from the thermistor bead, subsequently flows into the graphite sample (apart of a very small quantity which is absorbed by the glue itself and which can be neglected). The volume of the graphite sample, V_g , was chosen such that $V_g/V_b > 5 \cdot 10^3$, where V_b is the volume of the thermistor bead; consequently, the boundary effects on the thermal transfer can be completely neglected.

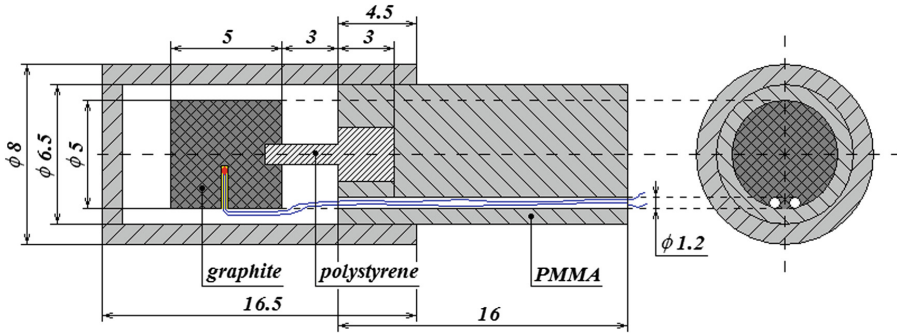


Fig. 2. Mounting assembly in graphite of VECO ultra-small bead 41A14 thermistor (not at scale). All the dimensions are in mm.

Both the dissipation constant and the thermal time constant of the thermistor were determined following the instructions given in *Technical Bulletin MCT181*, REV A 11-68 “Techniques for Testing Thermistors” of VECO manufacturing company [6]. These instructions are as follows.

4.1 Dissipation Constant Measurement

The dissipation constant in graphite of the VECO ultra-small bead NTC 41A14 thermistor can be determined by measuring the power required to rise the body temperature of the thermistor by 50 °C (from 25 °C to 75 °C) and then dividing this value by 50. First, the zero-power resistance of the thermistor under test at 75 °C was determined. Then the thermistor was connected as shown in Fig. 3(a), being mounted in graphite controlled at 25 °C.

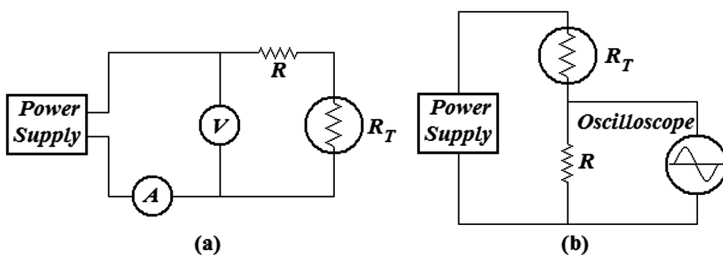


Fig. 3. Test circuits: (a) for thermistor dissipation constant measurement and (b) for the measurement of very short thermal time constants.

The power supply was increased slowly to heat the thermistor structure to 75 °C, the “point” when the resistance value calculated from the voltage and current readings, $R = E/I$, is equal to the R_0 value measured at 75 °C. The dissipation constant in graphite was then determined by dividing the computed power, $P = EI$, by the rise in temperature (50 °C).

4.2 Thermal Time Constant Measurement

Usually, the test conditions for measuring the thermal time constant of a thermistor are the same as those used for determining its dissipation constant.

For this reason, the two tests are usually performed sequentially. As described in [6], after the thermistor has stabilized at 75 °C, the power is switched to its “zero-power” level and the time required for the thermistor to cool to 43.4 °C (63.2% of the difference between the initial 75 °C and final 25 °C temperatures) is its thermal time constant.

First, the thermistor is preheated to the higher reference temperature (75 °C) in a controlled temperature bath. Then, the thermistor is removed to the low ambient of 25 °C. Of course, caution is taken in the choice of bath fluid, since the evaporation of the fluid on the surface of the thermistor can accelerate its true cooling rate.

For convenience, the zero-power resistance values of the thermistor under test are first measured at the initial, final and 63.2% body temperature points. The constant temperature bath is set at the initial 75 °C temperature and the temperature of the air in the enclosed area above the bath is checked for the low temperature point (25 °C). Using an electrical bridge and a precise clock the thermal time constant of the thermistor under test can be then simply determined; it is given by the time elapsed from the instant when the thermistor is withdrawn from the bath (more precisely, from the instant when the unit leaves the surface of the bath) and the instant when the thermistor reaches the previously determined resistance value at 43.4 °C (this instant can be established using the bridge).

This is the common/ordinary procedure, which can be only used when both the thermistor can be removed/extracted from the controlled temperature bath and the time constant of the thermistor is significantly greater than the reaction time of the operator. When the time constant of the thermistor structure is relatively small, the elapsed time should be measured automatically. Because this is the case for the VECO ultra-small bead NTC 41A14 thermistor, the elapsed time was measured automatically using the circuit shown in Fig. 3(b), the thermistor being inside the assembly.

The vertical sensitivity of the oscilloscope was adjusted to correspond to the high and low temperature points and its sweep rate was calibrated so that only one complete output curve of the thermistor can be obtained as it was subjected to the step change in temperature. No auxiliary devices have been used to obtain the record of the trace, because the oscilloscope used in the circuit in Fig. 3(b) automatically ensured this function.

5 Procedures

5.1 Procedure for Measurements in Still Air

First, to verify if the experimental measuring methods presented in the previous section are correct and accurate, the nominal values of dissipation and thermal time constants in still air of a VECO ultra-small bead 41A14 thermistor were determined and compared with those reported by the manufacturer.

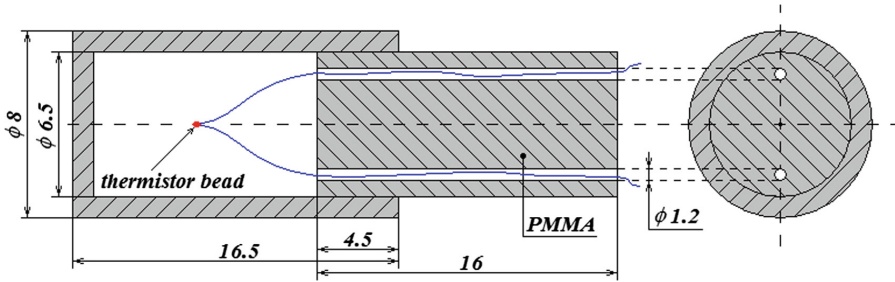


Fig. 4. Mounting assembly in still air of VECO 0.010'' ultra-small bead 41A14 thermistor (not at scale).

The thermistor was mounted as shown in Fig. 4, the resulting assembly being then sealed in “Univolt 35” transformer oil that has filled a big enough test tube which, in its turn, was sealed in a water bath. The water’s temperature was precisely controlled through a thermostatic device. The liquid volume of the water bath was approximately one hundred times greater than the volume of the oil bath, which in its turn was three hundred times greater than the volume of the air, V_a , in which the thermistor bead was placed; in addition, $V_a/V_b > 2 \cdot 10^4$. Since the baths were to be used at temperatures remote from room temperature, entire ensemble was thermally insulated. For the ohmic resistor R (introduced in the test circuit to limit the current through thermistor) the value $R_{sa} = 10.64 \text{ k}\Omega$ was chosen for the measurements related to the thermistor placed in still air, and $R_g = 10.56 \text{ k}\Omega$ for the measurements related to the thermistor mounted in graphite. In a circuit lacking a current-limiting resistor the thermistor resistance may drop down to a value low enough to allow the large resulting current to destroy it. A simple calculation of current-limiting resistor R based on a maximum voltage across the two resistors in series ($R + R_T$) of $U = 64.4 \text{ V}$, when the thermistor structure is operated at the higher reference temperature, gives for R a value of about $10^4 \Omega$ in order for the thermistor not to be destroyed.

The temperature of the water was increased very slowly to the room controlled temperature ($25 \text{ }^\circ\text{C}$) and then it was kept constant for a long enough period to determine as accurately as possible the zero-power resistance of the thermistor under test at this temperature; it was found $R_{sa} + R_{25} = 21.323 \text{ k}\Omega$. Then, the temperature of the water was increased in the same way (to ensure, at every moment, the thermal equilibrium between the water and oil – on the one hand – and between the oil and the air surrounding the thermistor bead – on the other) to $75 \text{ }^\circ\text{C}$, when, again it was kept constant for a long enough period to guarantee accurate measurements at this temperature too. For the zero-power resistance of the thermistor in still air at $75 \text{ }^\circ\text{C}$ it was found $R_{sa} + R_{75} = 12.47 \text{ k}\Omega$. Following the procedure presented in Sect. 4 (adapted for measurements related to the thermistor placed in still air) the following data were obtained: $U = 2 \text{ V}$ (the maximum voltage across the circuit @ $25 \text{ }^\circ\text{C}$), $T_0 = 25 \text{ }^\circ\text{C}$ (the room controlled temperature), $R_{25} = 10.683 \text{ k}\Omega$ and $R_{75} = 1.83 \text{ k}\Omega$ (the zero-power resistance of the thermistor under test @ $25 \text{ }^\circ\text{C}$ and @ $75 \text{ }^\circ\text{C}$, respectively), $U_T = 2.877 \text{ V}$ (the voltage across the thermistor under test @ $75 \text{ }^\circ\text{C}$), $I_T = 1.567 \text{ mA}$ (the dc through the thermistor under test @ $75 \text{ }^\circ\text{C}$). Therefore, the dissipation constant in still

air is $\delta_{sa} = P_T/50 = U_T I_T/50 = 0.0902 \text{ mW}/^\circ\text{C} \pm 0.35\%$, *i.e.*, it has a value which is very close to that provided by the manufacturer and thus, it can be concluded that the experimental method used for dissipation constant measurements is correct and accurate; the difference between the value determined from direct measurements and the value that was provided by the manufacturer is of only 0.18%.

5.2 Procedure for Measurements in Graphite

For determining the dissipation constant in graphite of the thermistor structure under test, the cap of the device shown in Fig. 2 was removed and the graphite sample (in which the thermistor bead was embedded) was directly sealed (like in Fig. 5) in the oil bath containing the “Univolt 35” transformer oil, which is an electrical insulating material. Then, following the instructions presented in Sect. 4, the measurements were taken again and the following data were obtained: $R_{25} = 8.838 \text{ k}\Omega$ and $R_{75} = 1.52 \text{ k}\Omega$ (the zero-power resistance of the thermistor under test @ 25 °C and @ 75 °C, respectively), $U_T = 8.115 \text{ V}$ (the voltage across the thermistor structure under test that is heated to 75 °C), $I_T = 5.33 \text{ mA}$ (the direct current through the thermistor structure under test in the same conditions) and $P_T = U_T I_T = 43.253 \text{ mW}$.

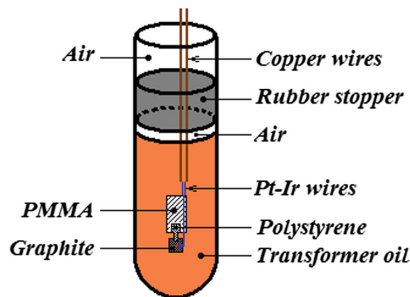


Fig. 5. Test tube containing the thermistor test mounted in graphite (not at scale).

Thus, for the dissipation constant in graphite of the VECO ultra-small bead 41A14 thermistor it was obtained the value $\delta_g = P_T/50 = 0.8651 \text{ mW}/^\circ\text{C} \pm 0.35\%$, which is approximately ten times greater than that corresponding to the thermistor placed in still air. All the data reported above concerning the voltage and current readings (U_T and I_T) were obtained as average values of ten corresponding experimental results; the measurements were repeated ten times in both cases: thermistor placed in still air and thermistor mounted in graphite, respectively. Between each two successive sets of measurements, a long enough waiting period was ensured, so that at the beginning of each new set of measurements all the components (the air surrounding the thermistor bead, the graphite, the transformer oil, the water etc.) can reach the thermal equilibrium between them and with the room controlled atmosphere, whose temperature was kept quasi constant at about 25 °C Throughout the paper the indicated uncertainties (determined as the relative combined standard uncertainties) were calculated using the standard procedure explained in [10].

The thermal time constant of the thermistors under test was determined directly from the output curves of the thermistors subjected to the step change in temperature. The oscilloscope (having a standard capture time up to 2 ms at full sample rate on all four channels and a minimum precision of 0.01 ms for time measurements) was adjusted so that only one complete output curve can be obtained and maintained on the screen. Considering the settings on the time basis of the oscilloscope, for the two cases – thermistor in still air and graphite, respectively – the following data were obtained: $\tau_{sa} = 0.4989 \text{ s} \pm 0.32\%$ and $\tau_g = 0.0048 \text{ s} \pm 0.32\%$.

The measurements were repeated ten times for each case, like in the previous situation when the dissipation constant was determined; hence the above two figures (τ_{sa} and τ_g) are in fact average values of two corresponding sets of ten results, each of them obtained from ten experimental determinations.

6 Results and Discussion

The result of the experimental measurements related to the dissipation constant in graphite of a VECO ultra-small bead 41A14 thermistor is $\delta_g = 0.8651 \text{ mW}/^\circ\text{C}$, the corresponding relative combined standard uncertainty being $u_{c,r}(\delta_g) = 0.35\%$, while the result related to the thermal time constant in graphite of the same thermistor is $\tau_g = 0.0048 \text{ s}$, with a relative combined standard uncertainty $u_{c,r}(\tau_g) = 0.32\%$. The $u_{c,r}(\delta_g)$ and $u_{c,r}(\tau_g)$ were calculated according to the Guide to the Expression of Uncertainty in Measurement [10]. The evaluation of the sources of uncertainty associated with the measurement of physical quantities involved in the electrical measurement equations does not present significant problems, as the influences are known for decades. Relative uncertainties of measurement of the resistance R , direct current I_T and voltage U_T are negligible for good equipment. Very small relative uncertainties can be achieved if stability and temperature effects are considered. With such a low instrumental uncertainty, other factors normally limit the achievable uncertainty, mainly those connected to (i) the maximum power applied (at high powers both the electrical and structural properties of a NTC thermistor can be irreversibly affected); (ii) the rate of heat conduction through the leads of the thermistor to its mount; (iii) the quality of the thermal contact between the thermistor bead and the graphite sample and (iv) the quality of room controlled atmosphere.

It's important to mention that some doubts regarding the correctness of the method used to determine the thermal time constant have arisen. This fact is due to the impossibility of withdrawing of the thermistor from the graphite heated at the 75°C , as well as to the inexactness of the condition of being a true constant for both the dissipation and thermal time constants of the thermistor. However, the result obtained from the first set of measurements on the thermal time constant (i.e. in still air) has been encouraging in solving this problem, because the value found there ($\tau_{sa} = 0.4989 \text{ s}$) differs from that provided by the manufacturer by only 0.18%.

Another proof for the correctness of the method used to determine the thermal time constant comes from the comparison of the graphs representing the change in temperature at the sensor thermistor vs time dependence, for two cases: (i) by considering the exact geometry of the thermistor bead and the explicit time dependence of the

temperature on the surface of the heating thermistor bead – which is given by the Eq. (2), where the “constant” C is calculated using the experimentally obtained values for δ_g and τ_g , and (ii) by considering the model of a point-like thermistor which plays the role of a heating source that furnishes a constant power of $P = 98 \mu W$.

Both graphs were obtained by numerical (thermal) modelling, using the finite element method for describing a Domen type calorimeter [3] (a three-body graphite calorimeter). The essence of the above-mentioned comparison relies in that the results obtained in the second case are certainly correct, as demonstrated in many studies (see for example [11–13]). Indeed, as already have been shown in [11–13], the numerical modelling done by means of the finite element method gives results that are in very good agreement with the experimentally obtained results, provided that the model of a point-like thermistor – which plays the role of a heating source that furnishes a constant power – is considered in numerical modelling of the problem. These results refer to the change in temperature at the sensor thermistor vs time dependence.

Because the graphs obtained in the above mentioned two cases – (i) and (ii) – are very close to each other (they even overlap in the first part of the heating process – as can be easily seen from the Fig. 6) it follows that the experimentally obtained values for both δ_g and τ_g are correct.

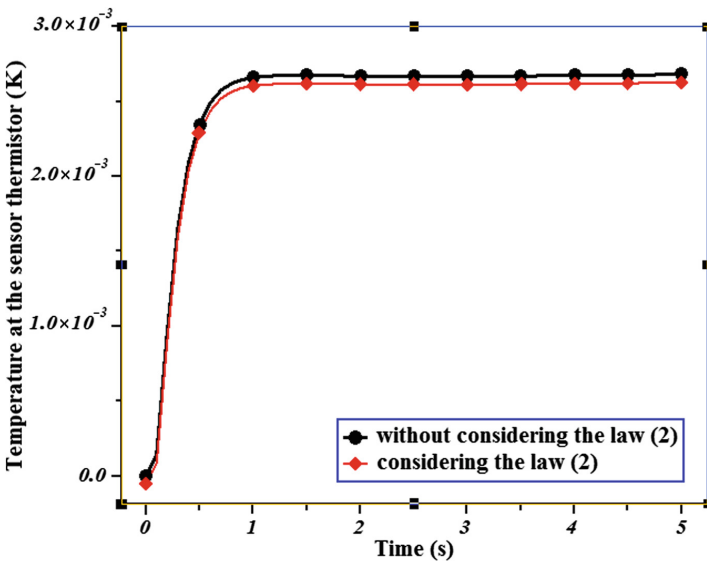


Fig. 6. The time-dependence of temperature measured by the sensor thermistor in the core of a Domen type calorimeter. The black curve (the dotted line) corresponds to the case when the point-like thermistor plays the simple role of a heating source of constant power, while the red curve (the “squared” line) corresponds to the case when the Eq. (2) is considered.

7 Conclusions

The two basic thermal constants – the thermal time constant, τ_g and dissipation constant, δ_g – of commercially-available VECO ultra-small bead 41A14 thermistors were determined for the case when the thermistors are mounted in graphite. Customarily, the manufacturer gives the values of these two constants only in still air, or, at most in still water, but in the important field of nuclear calorimetry these constants turn out to be essential parameters in thermal modeling of graphite calorimeters and thus, the determination of the values for these two constants in graphite proves to be quasi-compulsory.

The two constants were defined in Sect. 2, while the Sect. 3 presents the main characteristics of VECO ultra-small bead 41A14 NTC thermistors. The arrangements for experimental measurements were exposed in Sect. 4, while the concrete procedures for measurements in still air and graphite were presented in Sect. 5. Both the dissipation constant and the thermal time constant of the analyzed thermistor were determined following the instructions given in *Technical Bulletin MCT181*, REV A 11-68 “Techniques for Testing Thermistors” of VECO manufacturing company [6], while the corresponding uncertainties (determined as the relative combined standard uncertainties) $u_{c,r}(\delta_g)$ and $u_{c,r}(\tau_g)$ were calculated according to the Guide to the Expression of Uncertainty in Measurement [10].

For the above-mentioned kind of thermistors, the dissipation constant in graphite is found to be approximately ten times larger than that in still air, whereas the thermal time constant in graphite is approximately one hundred times smaller than that corresponding to a thermistor placed in still air.

The validation of both the used measuring methods and measured values in graphite for δ_g and τ_g was done by the help of the numerical thermal modelling of a Domen-type graphite calorimeter through the finite element method. The argumentation is based on some previously obtained results which are described in refs. [11–13], as well as on the graphs showed in Fig. 6.

References

1. Domen, S.R.: Emissivity of aluminized Mylar. *Radiat. Phys. Chem.* **37**, 199–201 (1991)
2. Laughlin, J.S., Genna, S.: Calorimetry. In: Attix, F.H., Roesch, W.C. (eds.) *Radiation Dosimetry*, vol. 2, 2nd edn. Academic Press, New York (1966)
3. Domen, S.R., Lamperti, P.J.: A heat-loss-compensated calorimeter: theory, design and performance. *J. Res. NBS – A Phys. Chem.* **78A**(5), 596 (1974)
4. Janssens, A., et al.: Equilibration of a graphite absorbed-dose calorimeter and the quasi-isothermal mode of operation. *Metrologia* **22**, 265–270 (1986)
5. Dares, J., Ostrowsky, A.: New constant-temperature operating mode for graphite calorimeter at LNE-LNHB. *Phys. Med. Biol.* **50**, 4035–4052 (2005)
6. VECO Technical Bulletin MCT181 – Techniques for Testing Thermistors, Rev A 11-68, Printed in U.S.A., Victory Engineering Corporation, 1964, P.O. Box 559, Victory Road, Springfield, New Jersey 07081, TWX: 710-983-4430, Tel.: (Area 201) 379-5900
7. Sapoff, M., Oppenheim, R.M.: Theory and application of self-heated thermistors. In: *Proceedings of the IEEE*, pp. 1292–1305 (1963)

8. Tietze, H.: Famous Problems of Mathematics: Solved and Unsolved Mathematics Problems from Antiquity to Modern Times, p. 27. Graylock Press, New-York (1965)
9. Giaretto, V., Torchio, M.F.: Estimation of the thermal conductivity of an epoxy resin by the use of an internal parallelepiped heat source. II. Exp. Anal. High Temp. – High Pressures **31**, 643–651 (1999)
10. ISO Guide to the Expression of Uncertainty in Measurement, 1st ed. ISBN 92-67-10188-9 (Geneva, Switzerland: International Organization for Standardization)
11. McEwen, M.R., Duane, S.: Development of a portable graphite calorimeter for photons and electrons. CIRM **42**, 52–64 (1999)
12. Duane, S.: The NPL Primary Standard of Photon Absorbed Dose, CCRI(I)05–35, 3 p. (2005)
13. Ionita, C., Radu, D., Astefanoaei, I.: 3D-modeling of temperature gradients induced by electrical power dissipation in a 3-body Domen-type calorimeter for absorbed dose measurements. Mater. Sci. Eng., B **178**(19), 1275–1284 (2013)

Monitoring Hand Gesture and Effort Using a Low-Cost Open-Source Microcontroller System Coupled with Force Sensitive Resistors and Electromyography Sensors

Andrei Vasile Nastuta¹(✉) and Catalin Agheorghiesei²

¹ Faculty of Medical Bioengineering,
'Grigore T. Popa' University of Medicine and Pharmacy Iasi,
M. Kogalniceanu Str., no. 9-13, 700454 Iasi, Romania
andrei.nastuta@gmail.com

² Faculty of Physics, 'Alexandru Ioan Cuza' University of Iasi,
Carol I Blvd., no. 11, 700506 Iasi, Romania

Abstract. In this study, we consider a low-cost open-source environment, where users interact with several computing devices and platforms. Thus, the specific usage of any tool requires a specific configuration process in order to meet the end user's needs. The aim is to compare the effectiveness of hand gesture recognition using electromyography (EMG) electrodes when using sensors located on the forearm in comparison to force-sensitive resistor (FSR) array located over the fingers of the hand. Our study involves monitoring the movement of the fingers in a single (angular) direction corresponding to gestures of gripping and releasing objects (a single degree of freedom). Our interest is in how the relocation of sensors would affect the classification rates of finger gestures. Our study confirmed that by including EMG along the FSR sensors the classification rate for different kinds of gesture (including all fingers and wrist) increased, providing a better understanding of the complex hand dynamics. These findings can be used in machine learning systems for developing versatile hand prosthesis or in rehabilitation.

Keywords: Hand gestures · Biomedical-based sensors

1 Introduction

In the last several years, the increased use of wearable devices has generated interest in novel gesture input techniques for many applications, including novel rehabilitation techniques [1–7], interactions with mobile devices and social media [8]. Of particular importance is real-time biosignals monitoring [9] and integration of various biomedical-based sensors into devices that are already user-friendly [10–12]. However, current techniques can be sometimes unsuitable due to signal interference of different wearable devices, requirement for additional sensors mounted independently of the wearable, and inability to sense different types of gestures. Hand disability limits a human's activities of daily life, leading to reductions in self-sufficiency and deterioration of life quality. This

condition can have different origins, such as injuries, surgery or diseases. Its oncoming can be immediate or progressive, demanding different therapeutic approaches. Recovering hand function usually requires pharmacological treatment together with a rehabilitation protocol including therapeutic exercises tailored to the patient's particular needs.

In this study we consider a low-cost open-source environment, where users interact with several computing devices and platforms. Thus, the specific usage of any tool requires a specific configuration process in order to meet the end user's needs. The aim is to compare the effectiveness of hand gesture recognition using electromyography (EMG) electrodes when using sensors located on the forearm in comparison to force-sensitive resistor (FSR) array located over the fingers of the hand. This study involves monitoring the movement of the fingers in a single (angular) direction corresponding to gestures of gripping and releasing objects (a single degree of freedom). Our interest is in how the relocation of sensors would affect the classification rates of finger gestures. These sensors (EMG and FSR) are connected, through circuit boards, to an Arduino Uno microcontroller. The Arduino is programmed to read analogue data from the sensors, which are then sent to the computer via serial communication for data collection and processing. We used Python environment in order to acquire these signals and process them.

Our study confirmed that by including EMG along the FSR sensors the classification rate for different kinds of gesture (including all fingers and wrist) increased, providing a better understanding of the complex hand dynamics. These findings can be used in machine learning systems for developing versatile hand prosthesis or in rehabilitation.

2 Materials and Methods

In order to accomplish the proposed experiment, an adjustable angle measuring device (tracking angular displacement from 0° to 90° , 1° accuracy) was used, simulating finger engagement of the experiment's hand. Although it allows a simple hand movement monitoring (e.g. grip, release, adduction, flexing, extending), and not a dynamic one with different types of movements, the data are specific and as precise as possible. Bending sensors (force-sensitive resistor FSR) are attached to a glove worn by participants in the experiment, so that their spatial dynamics will be identical to that of their fingers.

An equivalent, simplified and flexible finger model is shown in Fig. 1, segments A, B, C and D being experimentally tracked. In addition to the device used for biomechanical signals, a second device for recording bioelectric data from the heart and upper limb muscles was also used.

The following materials were used in the project: five FSR (Spectra Symbol), two Arduino Uno microcontrollers (Arduino), an EKG-EMG Shield (Olimex LTD), two types of EKG/EMG passive electrodes (bracelet type dry electrode and cable with snap connector for gel ECG electrodes), a computer for data acquisition and representation, a glove of textile material, angle measuring device.

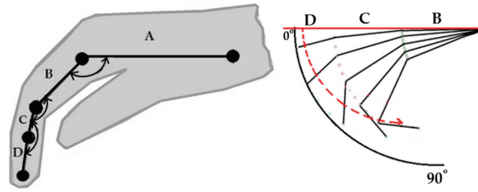


Fig. 1. Sketch of the proposed equivalent finger-motion model. Segments A, B, C and D are experimentally tracked through bending sensors system.

Functional parameters of FSR: 11 cm length, resistance varies depending on the degree of bending ($10 - 130 * 10^3 \Omega$). For measurements of the ECG/EMG biosignals two types of electrodes were used: disposable circular electrodes with conductive self-adhesive gel (Ag/AgCl solid hydrogel, $\Phi_{\text{activ}} = 1 \text{ cm}$, PRIMA) and metallic bracelet type dry electrodes (Shield-Ekg-Emg-PA, Olimex).

The FSR array fixed to the glove is connected to the Arduino board analog pins (A0–A4) (as shown in Fig. 2). Further on, we connect the microcontroller to the computer following the acquisition of signals from sensors for the established angles. For each analog pin the acquired signal will be noted as follows: pin A0 – signal S-a0, pin A1 – signal S-a1, pin A2 – signal S-a2, pin A3 – signal S-a3, pin A4 – signal S-a4. This is done through the implementation of control and acquisition programs in Matlab and Python environment of the data obtained with the microcontroller.

The system architecture is achieved by connecting in series of five FSR, each associated with a finger. Each participant in the study (user) will wear the glove on the surface of which the FSR are attached (Fig. 2) and will place his hand in a relaxed position on the holder which has attached a measuring system for the angles of flexion of each phalange (segments ‘B’ ‘C’, ‘D’) of the fingers (as in Fig. 1).

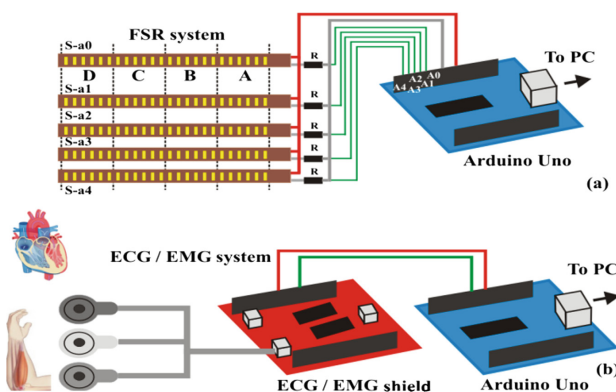


Fig. 2. Sketches of the FSR system (a) for hand kinematics and ECG/EMG system (b).

The experiment was performed on 6 users (2 male and 4 female participants, average age of 21 years), following the hand dynamic in the 0–90° angular range, to simulate the grip/release movement. At the same time, the ECG/EMG electrodes were positioned on the wrist/arm of the volunteers. To record the ECG signal the electrodes were positioned as follows: right hand - left hand - left foot. To test the ECG system, the electrodes were positioned at the chest level above and below the heart, respectively under the chest in the liver area. EMG signal recording electrodes were positioned on the skin surface in the muscles of the forearm or the wrist.

For acquisition of ECG/EMG biosignals, a second Arduino microcontroller was used together with an additional acquisition shield (Olimex EKG/EMG, Fig. 2). These biosignals recording was made while the user controls the FSR system for monitoring the hand movements (gestures). As a protocol, the user attaches his glove and then places his hand in a relaxed position on the angle measuring support at the 0° angle. Simultaneously attaches the ECG/EMG electrodes, so it can start the data acquisition. In real time, a graphical representation of the data is obtained using a program created in Python environment to control the data acquired from the microcontroller. The ECG/EMG representation was done in two steps: first, the ECG/EMG system was tested through the open source ElectricGuru [13] and FreeHC [14] programs; subsequently, the acquisition of the signals, statistical processing as well as their visualization was accomplished through a Python environment acquisition and representation program [15, 16].

3 Results and Discussion

3.1 Hand Kinematics and Gesture Through Open-Source FSR System

Data recording is from 0° to 90°, so for each flexed segment ('B', 'C' or 'D') 10 sets of measurements were performed. For each angle of acquisition (from 0 to 90°, with a 10° step), 100 measurements were acquired, thus acquiring over 1000 electrical signals from a single FSR, and a specific segment ('B', 'C' or 'D'). For all 5 sensors, these signals were acquired. Figure 3 shows the angular distributions of the voltage readings at the terminals of a FSR sensor for different segments, corresponding to phalanges, which are gradually flexed.

The 'B', 'C' and 'D' segments of the sensors were fixed at a length of 2.5 cm. The sensor recovers the initial resistance in the horizontal position (0°) after the bending operation. Each point on the chart represents the average value of more 1,000 records. In Fig. 3 the curves **S-a0** corresponds to the signals acquired from the **thumb finger**, the curves **S-a1** corresponds to the signals acquired from the **index finger**, **S-a2** to the **middle finger**, **S-a3** to **ring finger**, and **S-a4** to the **pinky finger**.

We also monitored the gestures that are not focused only on single finger movement, consisting of whole-hand gesture that uses multiple fingers simultaneously. In this sense, we have been monitoring the movement of gripping objects of different dimensions (as seen in Fig. 4).

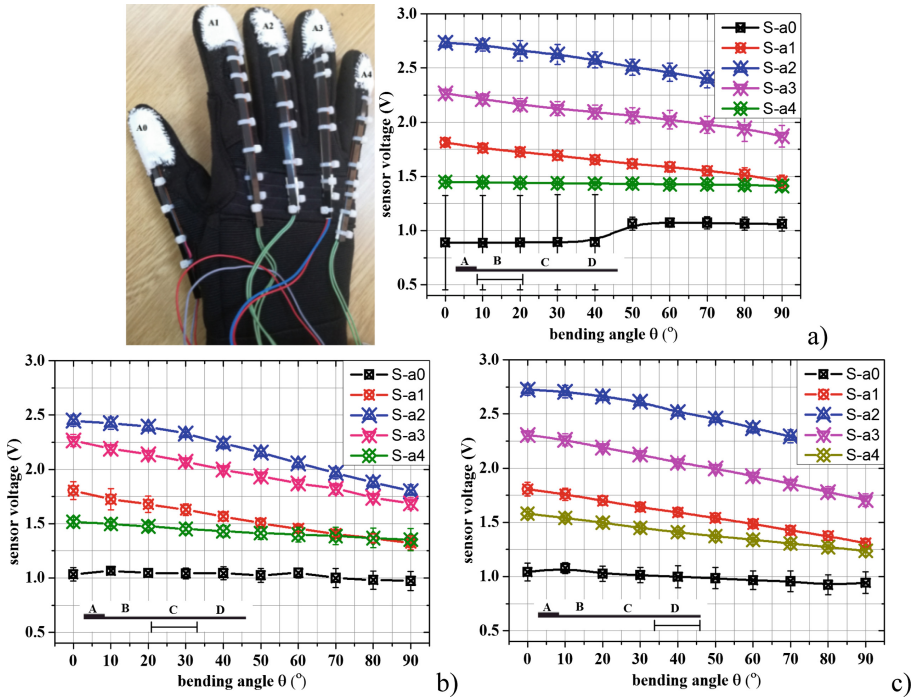


Fig. 3. The angular dependence of the voltage measured at the terminals of the 5 FSR at the same time, in the case of the flexion of B (a), C (b) and D (c) segment.

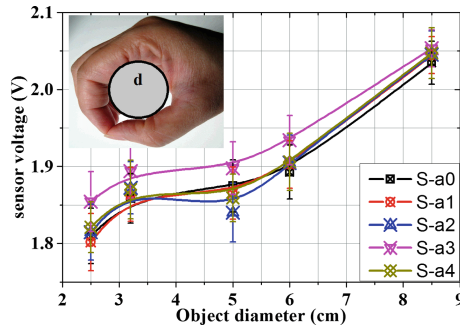


Fig. 4. Angular voltage dependence measured simultaneously at the 5 FSR terminals when gripping objects of various sizes.

3.2 Hand Gesture and Biosignals Monitoring Through Open-Source ECG – EMG Systems

Simultaneously with the FSR measurement, acquisition of the bioelectric signals was made. The ECG/EMG system being tested using the freeware programs ElectricGuru and FreeHC. The software interface for acquiring and visualizing the ECG/EMG was

done in Python environment. During the acquisition of hand dynamics, the ECG signals showed no significant variation compared to when the person was in a relaxing position (seating in the chair, elbow at the level of the chest leaning against the table, hand in relaxed position - semi-open, normal breathing). Figure 5 shows the acquired ECG biosignals (in arbitrary units) by positioning the passive electrodes at the forearm or wrist respectively. There is a difference in the signals acquired due to both the anatomical positioning of the electrodes and because of biodiversity (different electrical properties of the user's skin). Furthermore, experimental data should be verified and validated using complementary ECG measurement devices such as pulse-oximeters, medical ECGs, etc.

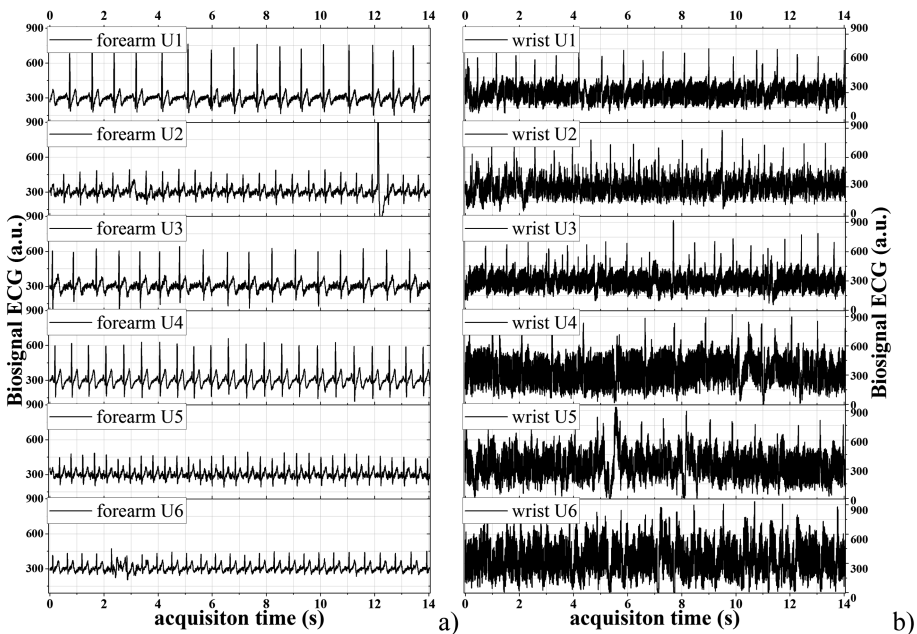


Fig. 5. ECG signals acquired by placing the electrodes on the forearm (a) or wrists (b) for different users (U1-6). Even though the wrist ECG signals are noisy they can be used for heart rate determination.

Figure 6 shows EMG signals (in arbitrary units) taken from the user's forearm. There is a change in the amplitude of the electric signal, but also in the form of the signal for cases where the user's hand is in a relaxed position, or by performing the gripping movement of some objects of different sizes (diameters): 2.5–8.5 cm. Moreover, a relative simple hand gesture (e.g. gripping/releasing an antistress ball) can have different EMG response on different users. These results underscore the need to create a database of multiple signals corresponding to simple and complex hand movements. This can only be achieved by acquiring a large amount of data, so for a certain type of hand gesture we know the response of the monitoring system (FSR or EMG).

Furthermore, the experimental data show the need to optimize these monitoring systems so that they can be used by a larger number of users (increasing the versatility of the system).

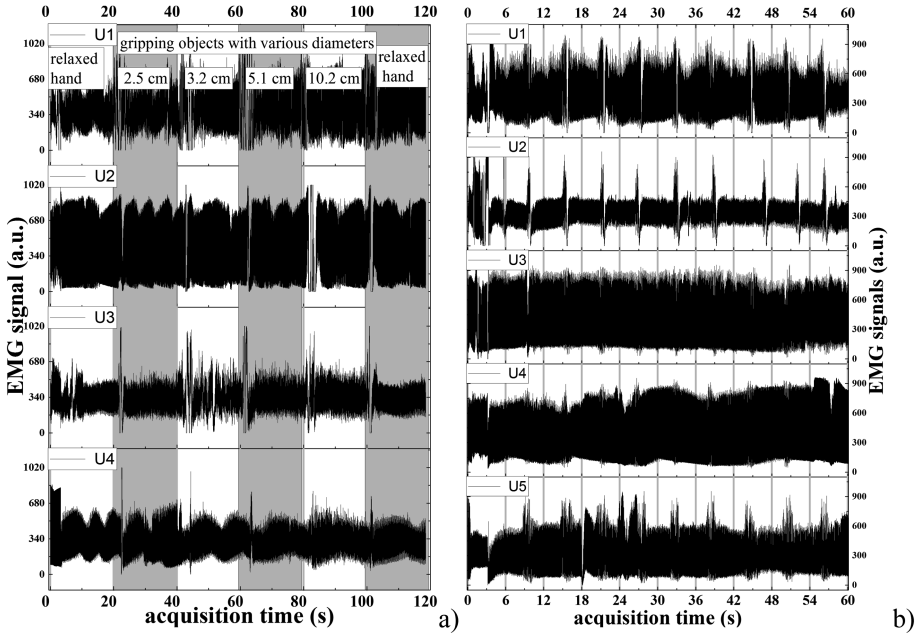


Fig. 6. EMG signals acquired by positioning the electrodes on the wrists for different users and monitoring the grip/release action of (a) objects with various diameters or (b) antistress ball.

Future experiments, including validation of complex hand gestures using accelerometer and gyroscope systems [17, 18], as well as galvanic skin response devices, can provide additional information about the anatomical and physiological state of the user.

4 Conclusions

In this study we followed the principle of operation of a force-sensitive sensor array system attached to a glove in order to improve methods of monitoring fingers and wrist movements, while monitoring the ECG EMG biosignals through a second recording system.

Our study confirmed that by including EMG along the FSR sensors the classification rate for different kinds of gesture (including all fingers and wrist) increased, providing a better understanding of the complex hand dynamics. These findings can be used in machine learning systems for developing versatile hand prosthesis or in rehabilitation.

The need to implement a simple system of rapid monitoring, during recovery processes, of hand mobility through repeated exercises, after a prescribed therapeutic program, remains a perpetual challenge. The use of microcontroller-based ‘open-source’ platforms allows rapid development at relatively low cost of solutions for such needs.

References

1. Halabi, N.E., Achkar, R., Daou, R.A.Z., Hayek, A., Börcsök, J.: Design and testing tool for a safe monitoring system for neurodegenerative disorder patients. In: 3rd International Conference on Advances in Computational Tools for Engineering Applications, pp. 172–177 (2016)
2. McIntosh, J., McNeill, C., Fraser, M.C., Kerber, F., Löchtfeld, M., Krüger, A.: EMPress: practical hand gesture classification with wrist-mounted EMG and pressure sensing. In: 34th Annual ACM Conference on Human Factors in Computing Systems, pp. 2332–2342 (2016)
3. Pani, D., Brabino, G., Dessi, A., Tradori, I., Piga, M., Mathieu, A., Raffo, L.: A device for local or remote monitoring of hand rehabilitation sessions for rheumatic patients. *IEEE J. Transl. Eng. Health Med.* **2**, 2100111 (2014)
4. Majumder, S., Mondal, T., Jamal, D.M.: Wearable sensors for remote health monitoring. *Sensors* **17**, 130 (2017)
5. Haghi, M., Thurow, K., Stoll, R.: Wearable devices in medical internet of things: scientific research and commercially available devices. *Healthcare Inform. Res.* **23**(1), 1–15 (2017)
6. Risto, S., Kallergi, M.: Modelling and simulation of the knee joint with a depth sensor camera for prosthetics and movement rehabilitation. *J. Phys: Conf. Ser.* **637**(1), 012043 (2015)
7. Guerrero, F.N., Spinelli, E.: Surface EMG multichannel measurements using active, dry branched electrodes. In: Braidot, A., Hadad, A. (eds.) VI Latin American Congress on Biomedical Engineering CLAIB 2014. IFMBE Proceedings, vol. 49. Springer, Cham (2015). doi:[10.1007/978-3-319-13117-7_1](https://doi.org/10.1007/978-3-319-13117-7_1)
8. Kinnunen, M., Mian, S.Q., Oinas-Kukkonen, H., Riekkö, J., Jutila, M., Ervasti, M., Ahokangas, P., Alasaarela, E.: Wearable and mobile sensors connected to social media in human well-being applications. *Telematics Inform.* **33**, 92–101 (2016)
9. Satiya, U., Ramkumar, B., Sabarimalai Manikandan, M.: Real-time signal quality-aware ECG telemetry system for IoT-based health care monitoring. *IEEE Internet Things J.* **PP**(99), 1–9 (2017)
10. Guerreiro, J., Lourenco, A., Silva, H., Fred, A.: Performance comparison of low-cost hardware platforms targeting physiological computing applications. *Procedia Technol.* **17**, 399–406 (2014)
11. da Silva, H.P., Fred, A., Martins, R.: Biosignals for everyone. *IEEE Pervasive Comput.* **13**(4), 64–71 (2014)
12. Muhlbacher-Karrer, S., Mosa, A.H., Faller, L.M., Ali, M., Hamid, R., Zangl, H., Kyamakya, K.: A drive state detection system-combining a capacitive hand detection sensor with physiological sensors. *IEEE Trans. Instrum. Meas.* **66**(4), 624–635 (2017)
13. ElectricGuru. http://realization.org/page/topics/electric_guru.htm
14. FreeHC. <https://github.com/jamesrdelaney/Arduino/tree/master/ECG%20Monitoring%20Software>

15. Python. <https://www.python.org/>
16. pyEKGduino. <https://github.com/TDeagan/pyEKGduino>
17. Luczak, S., Grepl, R., Bodnicki, M.: Selection of MEMS accelerometers for tilt measurements. *J. Sens.* Article ID 9796146, 13 (2017)
18. Luczak, S.: Guidelines for tilt measurements realized by MEMS accelerometers. *Int. J. Precision Eng. Manufact.* **3**(15), 489–496 (2014)

Soft Computing Techniques and Modeling

Firmware Enhancements for BYOD-Aware Network Security

Massimiliano Pedone¹(✉), Kamen Kanev², Paolo Bottoni¹,
Domenico Vitali¹, and Alessandro Mei¹

¹ Sapienza University of Rome, Piazzale Aldo Moro 5, 00185 Rome, Italy
massimiliano.pedone@uniroma1.it

² Shizuoka University, 3-5-1 Johoku, Naka-Ku, Hamamatsu 432-8011, Japan

Abstract. In today's connected world, users migrate within a complex set of networks, including, but not limited to, 3G and 4G (LTE) services provided by mobile operators, Wi-Fi hotspots in private and public places, as well as wireless and/or wired LAN access in business and home environments. Following the widely expanding Bring Your Own Device (BYOD) approach, many public and educational institutions have begun to encourage customers and students to use their own devices at all times. While this may be cost-effective in terms of decreased investments in hardware and consequently lower maintenance fees on a long-term basis, it may also involve some security risks. In particular, many users are often connected to more than one network and/or communication service provider at the same time, for example to a 3G/4G mobile network and to a Wi-Fi. In a BYOD setting, an infected device or a rogue one can turn into an unwanted gateway, causing a security breach by leaking information across networks. Aiming at investigating in greater detail the implications of BYOD on network security in private and business settings we are building a framework for experiments with mobile routers both in home and business networks. This is a continuation of our earlier work on communications and services with enhanced security for network appliances.

Keywords: Network security · Modeling · Diagnostics · Learning techniques

1 Introduction

In our current study, we shift the focus to BYOD and mobile Wi-Fi routers, which require more advanced functionality and interfacing. In particular, we explore extensions of existing community firmware necessary for BYOD-aware, secure, seamless integration of the mobile communication appliances in private, public, and business networks, as carried on by their owners. The multiplatform firmware will also allow a carefully designed single GUI to be made available to users of communication appliances from different producers, irrespectively of their make and model.

While this is still work in progress, we are considering the possible applicability of our approach to the LM-28225 Master's Programme in Computer Science at Sapienza [1]. The specialized BYOD-based framework, for example, could be instrumental in a Networks and Security course [2], while the advanced BYOD-aware communication model would be more relevant to a Software Engineering course [3].

The paper follows with Sect. 2 which provides an overview of typical security problems in a university network used by thousands of people every day. Section 3 considers opportunities for securing personal devices when their use is intended in third party networks, while Sect. 4 concludes the paper and discusses future work.

2 Large Networks and Security

Network access has never been considered entirely secure. As a large number of devices share the same network, one has to be vigilant against many security threats. In fact, any neighboring device can get infected by malicious software and perpetrate all kinds of attack unbeknownst to its owner.

As all devices share the same radiofrequency, all data, sent and received, is potentially accessible by others. Indeed, as wireless transmissions are inherently broadcast, any device can monitor and record them. Although access to the information embedded in such communications is protected by encryption and various user authentication mechanisms, its security cannot be guaranteed [4]. Security threats are much higher though, in public network environments and open access community networks.

Every day, students, faculty members, and other personnel use university networks both to exchange sensitive information and to access cloud resources and external websites [5]. In this work we consider the Sapienza University campus wireless network as a reference and test bed environment. Our university domain consists of over 3,000 wired PCs, workstations, and laboratory computers and services over 10,000 of Wi-Fi based mobile connections daily. In Figs. 1 and 2 we show summaries of the detected security threats and virus infection incidents in a recent 7-day period (dates withheld on security grounds).

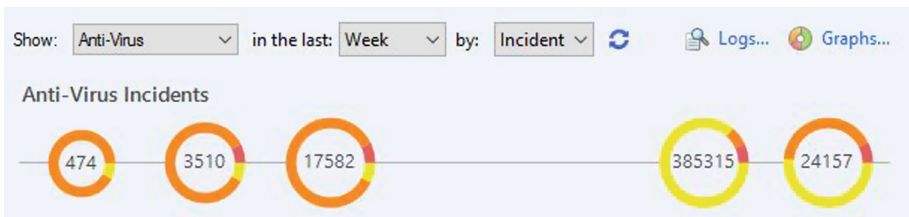


Fig. 1. Number of security incidents over a 7-day period. Risk levels ranging from yellow to red indicate Low, Medium, and Critical values as defined in the Common Vulnerability Scoring System (CVSS) database.

Any virus protection software, however, impacts the performance of the firewall core on which it is installed [6]. The potential slowdown depends on the complexity of the protection and the nature of the traffic blend. HTTP server access, for example, generates a lot of traffic in contrast to the FTP and Telnet traffic which is more limited while all those protocols require different levels of inspection.

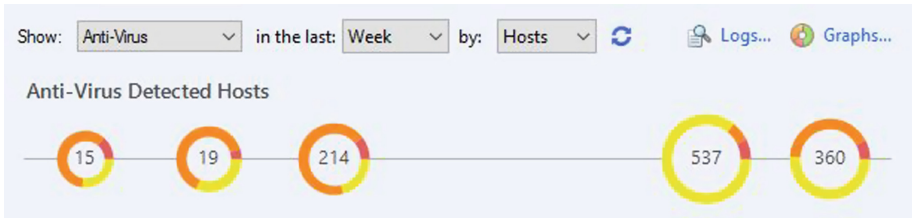


Fig. 2. Number of infected hosts over a 7-day period. Virus infections are classified as adware (low severity) and malware (medium or high severity) as per the severity levels of antivirus and antibot protections given in Table 1.

The relationships between the threat severity levels and their relevant protective measures with respect to performance are outlined in Table 1.

Table 1. Severity levels of antivirus and antibot protections [7]

Severity levels	Case
Very low	<ul style="list-style-type: none"> • All protections which do not cause any performance degradation • New protections are not added to this category without performance tests
Low	<ul style="list-style-type: none"> • All simple signatures over any protocol, which have very unique traffic patterns
Medium	<ul style="list-style-type: none"> • All HTTP Client protections, which use complex detection logic • All protocol parsers, which perform protocol anomaly over PSL • All signatures executed on HTTP responses
High	<ul style="list-style-type: none"> • Protections which are executed on all ports • Performs extremely heavy and complex detection logic. For example, decoding of RC4 encryption
Critical	<ul style="list-style-type: none"> • Requires deep inspection of a significant portion of the traffic

2.1 Network Security Threats

From a technical point of view, users sharing the same network segment are also sharing one and the same broadcast domain. While various security policies may be implemented by network operators within the domain, establishing and managing a security perimeter is usually conducted at the inter-domain communication level, where firewalls and other specialized network access control equipment is employed.

The security mechanisms that are generally available in advanced network switches, routers, and other communication equipment are usually not applicable or are simply missing within the broadcast domain itself. Such intra-domain communications are indeed rarely moderated and, in most cases, the responsibility is left to individual users to install and properly maintain the necessary security tools. Unfortunately, given the complexity of the current network threats, only a small portion of the connected users are in a position to properly install and maintain such tools on the large diversity

of communication devices they use [8]. To address this situation we propose the use of inexpensive, privately owned Mobile Network Appliances (MNAs) that establish a security perimeter for each individual network user in a unified way.

2.2 Security and Communication Protocols

In business environments, various attempts to improve the security of private devices have been made through the selection of more appropriate network protocols, advanced packet routing and firewalling, and other responsive network solutions [6]. Unfortunately, for a more complete coverage of existing users and their devices, many network security features have to be excluded or kept off, in particular when legacy devices are used. For example, the IEEE 802.1x standard provides a secure, per port authentication protocol, but legacy hardware and even recent devices based on certain chipsets do not support it, so network operators often opt to implement other less secure network access mechanisms.

In many cases, users are admitted to the Wi-Fi network without authentication, e.g. via captive portals. With this technology users are authenticated at a later stage through a dedicated Web page, just before granting them access to the Internet. This implies insecure communication between the mobile device and the access point at the initial stages of the communication, which may allow eavesdropping and collection of login information by bystanders. Employing Wi-Fi Protected Access (WPA) or another secure Wi-Fi access protocol since the very beginning of the session would certainly be a much better solution which, unfortunately, may be difficult to enforce [4].

In our security model, we address this problem by employing private MNAs serving as security gateways and providing encrypted access to the AP for all user devices despite the existing inherent limitations. In our model, the secure channel between the MNA and the AP is established by the MNA itself based on its own credentials.

2.3 Man in the Middle Attacks

The Man-in-the-Middle (MITM) attack is a complex technique allowing a malicious user to eavesdrop on communications between other customers. Such an attack may lead to severe consequences in terms of privacy and confidentiality when user information is stolen and used for malicious purposes. MITM attacks are widespread in large networks and have in fact been often detected in the Sapienza network. While mounting a MITM attack, the malicious agent impersonates a trustworthy authority or a third party that may be a gateway or an authentication host. Since this remains undetected by the attacked device, its user will believe to have been prompted for authentication credentials by the legitimate authority. In reality, however, every communication the attacked device sends or receives will be intercepted and altered by the malicious agent employing it for breaking the security settings of the user.

Secure protocols like Secure Socket Layer and Transport Layer Security are often ineffective with respect to MITM attacks. Indeed, advanced MITM techniques allow attackers to divert encrypted traffic (e.g. `https`) to clear text traffic (e.g. `http`).

While such attacks can only be mounted on Web servers that support both clear text and encrypted traffic, this remains one of the most common configurations on the net.

2.4 Malware Threats

While a network scan could be benign in its nature, it is often recognized as the first step in a chain of attacks on a network. Users can employ publicly available net scan application and host maintenance script for both discovering the hosts connected to the network and identifying the services exposed by those hosts [9]. Such software allows malicious users to discover the programs installed on the scanned hosts and to proceed with identifying the specific versions that may be vulnerable. Through this technique, malicious users can find exploits allowing them unauthorized privileged access to just one host on the attacked network which may jeopardize the safety of all computers in the security perimeter domain.

The recent incidents of virus attacks and consequent security breaches affecting entire domains clearly indicate that users are confronting increasing dangers in their daily networking. In business oriented network environments this problem is usually addressed through timely virus protection patches and more advanced packet filtering. For better understanding of the threat identification and consequent data exclusion at the time of a network attack, we have provided in Fig. 3 the graph of all virus related connections and respective dropped packets over a 24 h period.

The “wanna cry” virus (WCv) is a malware which infects a storage device on an unpatched system and asks for a ransom to decrypt the contents of the stored files. It exploits the `EternalBlue` vulnerability to install a backdoor called `DoublePulsar` (DPb), both supposedly developed by the U.S. National Security Agency. The WCv first attempts to load the infection through the public key infrastructure (`.pki`). If `.pki` is not found, WCv creates a key pair by “`CriptGenKey`”, saves the public part of the key, and uses the master key to encrypt the private part stored in a file with `.eki` extension. Then “`CriptGenRandom`” is used to generate separate Advanced Encryption Standard

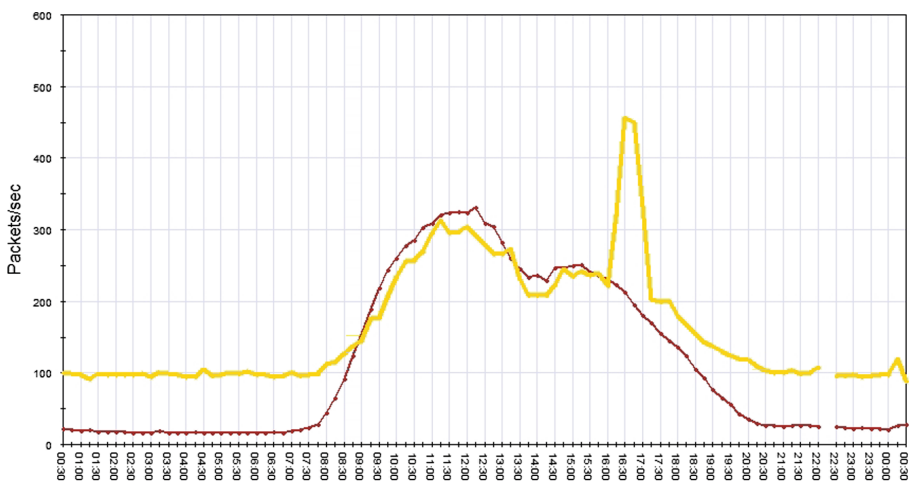


Fig. 3. The activity of the “wanna cry” virus: the yellow curve represents the dropped packets while the red one indicates the number of related connections during the attack. The peak of the dropping indicates the adequate reaction of the updated and properly patched firewall system.

(AES) keys for every file that is encrypted. Each AES key is encrypted using the previously generated public key and is merged into its corresponding file. To decrypt the resulting files, the unlucky owner needs the private part of the master key, for which a ransom is requested. In the course of the above and afterwards, the DPb keeps sending out scans and mounts attacks to propagate the worm. The yellow peak in Fig. 3 indicates that the Sapienza firewall has successfully detected and dropped the large number of connections initiated by the DPb.

3 Securing Your Own Device

In the context of all the network threats discussed so far, securing your own device appears to be far from trivial task. With respect to this, however, a dedicated MNA, hosting an embedded system configured with network security in mind, can incorporate a number of essential network control and security applications and tools. This will ensure a centralized deep packet inspection and monitoring of related network activities as a basis for timely feedback and support of the MNA owner by alerts and flagging of suspicious traffic [1].

While such network control and security applications can be directly installed on the user devices, in such a case they will consume computing resources on each device and will need separate maintenance and updates on a per device basis. Furthermore, in case of infection, the malicious software can alter the security settings of the applications directly installed on the device, creating serious security breaches. As MNA-based security applications and tools are installed in the read-only flash memory of the embedded device, they cannot be altered by any malicious software.

Moreover, the MNA approach allows users to establish and maintain secure VPN channels between the MNA device and the owner's home or business network. Thus, user communications are secure at all times, regardless possible differences in the setups and corresponding security levels supported by the employed devices [10].

The MNA approach extends our earlier work with augmented embedded systems for communication appliances. In this approach, as sketched in Fig. 4, we are considering mobile routers, with community DD-WRT firmware as MNAs, which are not confined to a home or laboratory environment. As such MNAs are constantly with the user, they can help enforcing a consistent security policy across several network environments, thus ensuring better protection of users in the context of the BYOD model.

First of all, DD-WRT features a fully fledged State Packet Inspection (SPI) firewall with additional filters for cookies, Java applets, and ActiveX content. It can keep track of all incoming and outgoing traffic locally up to a certain extent along with a full record on a remote log server. A special single click options for impeding Wide Area Network (WAN) Denial of Service (DoS) and brute force attacks is also included. Even if these firewall features are turned off, the DD-WRT will isolate the user from the WAN by acting as a Network Address Translations gateway [11]. In such a scenario, the MNA equipment is directly exposed to the network, while the mobile devices of the user are masqueraded. The DD-WRT router mediates each outgoing connection and inhibits unrelated and undesired ingoing connections. Implicitly, the mobile devices of

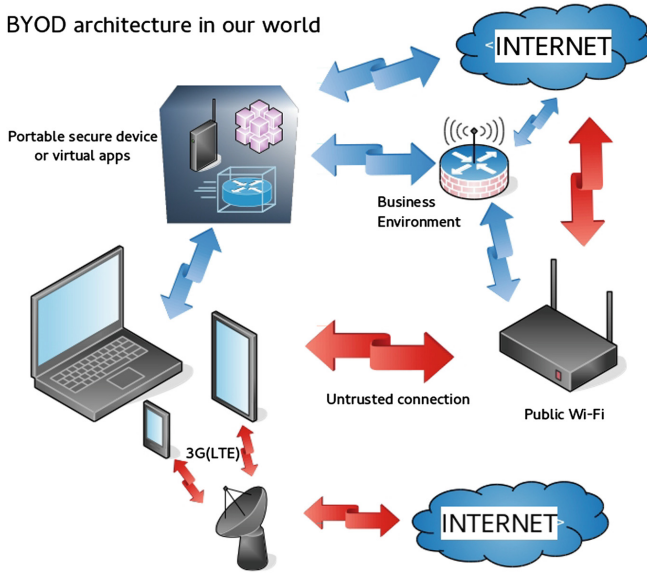


Fig. 4. MNA access for secure BYOD communications. The red arrows represent unsecure communications while the blue arrows correspond to connections secured through MNA.

the user connected to the Internet through the MNA remain protected and no direct connections to them from the outside world can be established.

The Wi-Fi component of the DD-WRT software supports multiple physical and virtual wireless interfaces. This makes it possible to create a number of transparently connected and/or fully isolated network segments as dictated by the security requirements of any specific application. As discussed earlier, suggested way to avoid clear text credential exchanges is to employ WPA or WPA2 with AES cryptography. While the WPA/WPA2-Personal version is more appropriate for individual use, the WPA/WPA2-Enterprise version is also supported through a RADIUS server. In addition to this, MAC based control employing black/white lists is also available.

With respect to VPN connectivity, DD-WRT can act as both Point-to-Point Tunneling Protocol (PPTP) and/or OpenVPN server and client simultaneously [10]. The OpenVPN communications are considered more secure as they are enhanced by verification of server and client certificates. Last, but not least, mobile routers with SD memory slots can be turned into Network Attached Storage (NAS) servers accessible by all mobile devices of the MNA owner.

4 Conclusions and Future Work

We have considered BYOD and mobile Wi-Fi routers, which require advanced functionality and interfacing. In particular we are exploring the extensions of the existing community firmware that are necessary for BYOD-aware secure seamless integration

of the mobile communication appliances in private, public, and business networks as they are carried by their owners. A multiplatform firmware will also allow a carefully designed single GUI to be made available to users of communication appliances from different producers, irrespectively of their make and model.

While this is still work in progress, we are considering the possible applicability of our approach to the LM-28225 Master's Program in Computer Science at Sapienza. The specialized BYOD-based framework, for example, could be instrumental in a Networks and Security course, while the advanced BYOD-aware communication model would be more relevant to a Software Engineering course.

Acknowledgements. Part of the work reported in this article is supported by the 2017 Cooperative Research Project at Research Center of Biomedical Engineering and Research Institute of Electronics, Shizuoka University.

References

1. Kanev, K., Mei, A., Bottoni, P.: Home communications and services with enhanced security: augmented embedded systems for communication appliances as an educational platform. *JAP J. Appl. Phys. Conf. Proc.* **4**, 011615(1–5) (2016)
2. Heldenbrand, D., Carey, C.: The linux router - an inexpensive alternative to commercial routers in the lab. *J. Comput. Sci. Coll.* **23**(1), 127–133 (2007)
3. Jasani, H.: Vendor neutral hands-on labs using open-source products for wireless networks courses. In: *Proceedings of FIE*, pp. S3F1–6 (2010)
4. Antoniewicz, B.: 802.11 Attacks. http://download.aircrack-ng.org/wiki-files/doc/wireless_basics_and_tutorials/802.11%20Attacks.pdf
5. Villa, A., Varki, E.: Characterization of a campus internet workload. In: *Proceedings of CATA*, pp. 140–148 (2012)
6. Athanasiades, N., Abler, R., Levine, J., Owen, H., Riley, G.: Intrusion detection testing and benchmarking methodologies. In: *Proceedings of the IWIA 2003*, Darmstadt, Germany, 24 March 2003
7. Check Point Software Technologies: Official Web Site, IPS, Anti-Bot, and Anti-Virus Protections Severity, Performance, and Confidence Levels. https://supportcenter.checkpoint.com/supportcenter/portal?eventSubmit_doGoviewdetails=&solutionid=sk116254
8. Meurisch, C., Seeliger, A., Schmidt, B., Schweizer, I., Kaup, F., Mühlhäuser, M.: Upgrading wireless home routers for enabling large-scale deployment of cloudlets. In: *Mobile Computing, Applications, and Services, LNICST*, vol. 162, pp. 12–32. Springer (2015)
9. Heffner, C.: Remote Attacks Against SOHO Routers. <https://defcon.org/images/defcon-18/dc-18-presentations/Heffner/DEFCON-18-Heffner-Routers-WP.pdf>
10. Hall, M.: Performance Analysis of OpenVPN on a Consumer Grade Router. <http://www.cse.wustl.edu/~jain/cse567-08/ftp/ovpn/index.html>
11. Mortier, R., Rodden, T., Tolmie, P., Lodge, T., Spencer, R., Crabtree, A., Sventek, J., Kolioussis, A.: Homework: putting interaction into the infrastructure. In: *Proceedings of UIST*, Cambridge, pp. 197–206 (2012)

Ontology Extension for Personalized Accessible Indoor Navigation

Gabriella Simon-Nagy^(✉) and Rita Fleiner

John von Neumann Faculty of Informatics, Obuda University,
96/b Bécsi St., Budapest, Hungary
{nagy.gabriella, fleiner.rita}@nik.uni-obuda.hu

Abstract. In this paper an accessibility extension is described for an ontology supporting indoor navigation called iLOC. In iLOC, a basic support for accessible route planning can be found, but the accessibility description of objects like doors, floors, restrooms etc. were based on measurements and accessibility criteria included in the Hungarian government regulations. This regulation is designed to ensure a safe and unobstructed environment for every motion disabled person with every kind of wheelchair, but it can be unnecessarily restrictive for some users. Our accessibility extension adds classes and properties that can be connected to the classes of the original iLOC, and allows of a detailed description of the objects in the building in terms of attributes such as width, height or quantity.

Keywords: Accessibility · Indoor navigation · Linked Open Data

1 Introduction

Accessible construction of public places and equal opportunities for disabled persons are important topics in these days. In most developed countries, there are laws to enforce an appropriate design of new buildings to be usable for people with motion disabilities. However, older buildings may not be accessible, or not all paths in the building are, and poorer countries may not have the financial means to correct these accessibility problems in the near future. This situation presents a challenge to wheelchair users and (to a lesser extent) persons with motion disabilities in general, especially when they need to find their way in occasionally visited, unknown buildings e.g. in hospitals or public office buildings.

In our previous works [1], we used Linked Open Data (LOD) [2] to describe building parts. We created a data model in the form of ontology which included the indoor location description of buildings, the indoor navigation features and the accessibility attributes for people with motion disabilities. However, the legal criteria of accessibility, which we based our accessibility labels on [3], can be unnecessarily restrictive for some users when it comes to navigation.

Therefore, in this paper we extend our indoor navigation ontology to accommodate specific situations and allow for a personalized route search for motion disabled persons. We demonstrate the usability of the ontology in a NOSQL-type database with queries that perform the route search based on personalized parameters.

2 Related Work

Several ontologies have been developed to provide data storage structures for indoor navigation applications [4–7]. Most of these are designed to describe the structure of buildings, the position of rooms and floors in connection to each other, in a way that makes navigation queries easily executable. Some of them provide some degree of support for accessible route planning, however this support is based on government accessibility requirements at best.

2.1 The iLOC Ontology [1]

We created iLOC ontology to support indoor navigation in a simple, inexpensive way, without the need for special hardware, and also to provide a method for finding accessible routes for motion disabled users. The ontology describes the various parts of a building, some of their properties, and the relationships between the parts. (see Fig. 1)

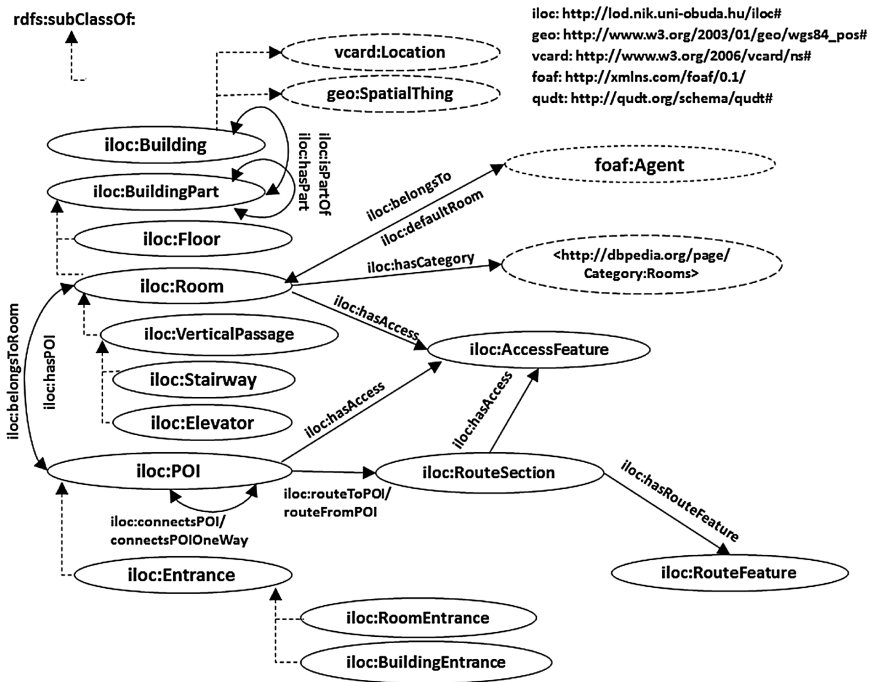


Fig. 1. iLOC ontology

In the iLOC ontology, there are classes for building parts in the form of subclasses of BuildingPart class (Floor, Room, Point of Interest - POI). POIs are set to places in the building that are important in navigation: entrances of rooms, floor junctions and frequently visited service points (vending machine, internet access terminal, etc.). The

RouteSection class describes an available route from a POI or to a POI. Wayfinding is based on POI connections, all the way to the destination POI.

The Rooms, POIs and the RouteSections can have accessibility features as an AccessFeature instance. The AccessFeature class can represent different accessibility needs for motion disabled users: Wheelchair, EWheelchair (for electronic wheelchair), WheelchairWHelp (for wheelchair with help), Stretcher and Stroller.

Detailed accessibility data are attributed only to RouteSections using RouteFeature class. For example, the length, incline and floor covering type of a route section, the number of steps in a staircase, or the restricted access of a building part can be stored.

2.2 Accessibility in Law and in Practice

The accessibility features of objects were based on measurements and accessibility criteria included in the Hungarian government regulation about national settlements planning and building requirements (OTÉK) [3]. For example, based on this law, a door can be regarded as accessible if it has an inner width of at least 90 cm. This criterion guarantees that all kinds of wheelchairs can pass through the doorway safely. Therefore in iLOC, we labeled a room wheelchair accessible if its door has an inner width of at least 90 cm. In our navigation method, a doorway was included in the accessible route search if it had the label “wheelchair accessible”.

However, the accessibility regulations only apply to new public buildings, or during renovations of a public building. Several older public buildings in Hungary are only partially accessible. To make our indoor navigation ontology useful for motion disabled people in everyday situations, the ontology has to be extended with detailed descriptions of accessibility properties of rooms, floors and POIs.

3 Description of the Ontology Extension

The legal criteria of accessibility can be unnecessarily restrictive for some users when it comes to navigation. There are wheelchair users who can walk one or two steps if absolutely necessary. There are so-called “sports wheelchairs” that are not obstructed by a few cm-s high thresholds, and an experienced and athletic user can even drive the wheelchair down a staircase if it consists of only a few steps (or many steps if a handrail is available). Most importantly, wheelchair widths are personalized: there are wheelchairs that can pass through a 70 cm wide doorway easily.

We can see that in reality, the partially (or not at all) accessible building parts can be accessible for some motion disabled users, or the users can organize the appropriate help for their visit in the building. Therefore in our ontology extension, instead of basic, yes-or-no type labeling of accessibility, we store the measurements of different objects in the buildings: e.g. the width of doors and passageways, the height of thresholds and stairs, and so on.

On Fig. 2, the iACC¹ extension and its connection to iLOC is represented: the *iloc:Room* class is connected to the *iacc:RoomEquipment* by the *iacc:hasEquipment* property. *iacc:hasEquipment* shows, which equipments belong to a given room.

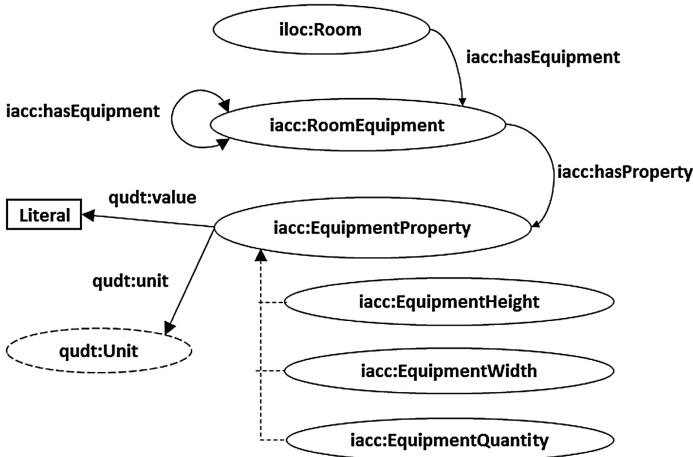


Fig. 2. The iACC extension

The *RoomEquipment* class describes a built-in part (e.g. door, threshold, stairs) or an equipment (e.g. mirror, handrails, emergency button) of an *iloc:Room* instance. *RoomEquipment* instances can also be connected with other *RoomEquipment* instances by *hasEquipment*. This type of connection describes a containing relationship between the objects, for example: a restroom (*Room* instance) has multiple toilet stalls (*RoomEquipment* instances), and the stalls have toilets in them (*RoomEquipment* instances).

Equipment can be connected to multiple *EquipmentProperty* instances by *hasProperty*. *EquipmentProperty* class has three subclasses: *EquipmentHeight*, *EquipmentWidth* and *EquipmentQuantity*. *EquipmentHeight* is used to describe the height of objects like door and window handles, light switches, mirrors in a restroom, or thresholds. *EquipmentWidth* is used to store the widths of doorways, toilet stalls, staircases, etc. *EquipmentQuantity* plays a dual role: it can store e.g. the number of stairs, but it can also describe binary situations: is there an emergency button near the toilet or not (value equals 1 or 0). *EquipmentProperty* instances have a value and a unit, for example the *EquipmentWidth* instance of a door can have the value of 80 and a unit of centimeters.

4 Usage Examples

In this section data excerpts and SPARQL queries are presented to demonstrate the possibilities of the developed ontology extension.

¹ <http://lod.nik.uni-obuda.hu/iacc/>.

The following excerpt describes RoomEquipment instances of a Room, and their properties. On the third floor, there is a restroom that has three pieces of equipment stored: a door, a stall and a mirror. The door is 80 cm wide; the mirror is 110 cm high on the wall. The stall is 300 cm wide and has a 48 cm high toilet in it.

```
@prefix iloc: <http://lod.nik.uni-obuda.hu/iloc/iloc#>
@prefix iacc: <http://lod.nik.uni-obuda.hu/iacc/iacc#>
@prefix rdfs: <http://www.w3.org/2000/01/rdf-schema#>
```

```
:Restroom302 a iloc:Room;
rdfs:label "Restroom"@en;
iacc:hasEquipment :Restroom302Door,
:Restroom302Stall,
:Restroom302Mirror.

:Restroom302Door a iacc:RoomEquipment;
rdfs:label "Door"@en;
iacc:hasProperty [
a iacc:EquipmentWidth;
qudt:value 80;
qudt:unit qudt:centimeter].

:Restroom302Stall a iacc:RoomEquipment;
rdfs:label "Stall"@en;
iacc:hasEquipment :Restroom302StallToilet;
iacc:hasProperty [
a iacc:EquipmentWidth;
qudt:value 300;
qudt:unit qudt:centimeter].

:Restroom302StallToilet a iacc:RoomEquipment;
rdfs:label "Toilet"@en;
iacc:hasProperty [
a iacc:EquipmentHeight;
qudt:value 48;
qudt:unit qudt:centimeter].

:Restroom302Mirror a iacc:RoomEquipment;
rdfs:label "Mirror"@en;
iacc:hasProperty [
a iacc:EquipmentHeight;
qudt:value 110;
qudt:unit qudt:centimeter].
```

The following query is an example on finding restrooms with a door at least 70 cm wide, and a mirror not higher than 120 cm. 70 cm wide doors are not regarded as accessible, according to neither Hungarian, nor USA laws. However, some narrower kinds of wheelchairs can pass through a 70 cm wide doorway.

```
prefix iloc: <http://lod.nik.uni-obuda.hu/iloc/iloc#>
prefix iacc: <http://lod.nik.uni-obuda.hu/iacc/iacc#>
prefix rdfs: <http://www.w3.org/2000/01/rdf-schema#>
```

```
SELECT ?fl ?rnum
WHERE {
  ?rr a iloc:Room;
      rdfs:label "Restroom".
  OPTIONAL {?ffloor rdfs:label ?fl.}
  OPTIONAL {?rr rdfs:label ?rnum.}
  ?rr iloc:isPartOf ?ffloor.
  ?rr iacc:hasEquipment ?door.
  ?rr iacc:hasEquipment ?mirror.
  ?door rdfs:label "Door";
      iacc:hasProperty ?w.
  ?w a iacc:EquipmentWidth;
      qudt:value ?ewidth.
  ?mirror rdfs:label "Mirror";
      iacc:hasProperty ?h.
  ?h a iacc:EquipmentHeight;
      qudt:value ?eheight.
  FILTER ( ?ewidth > 69 && ?eheight < 121 )
}
```

The following query is an example on finding the nearest restroom with a stall at least 250 cm wide, starting from the main entrance. (Because of the capabilities of SPARQL 1.1, a given number of intermediate POIs have to be defined – 3 in this example – which is the maximum length of the route.)

```
prefix iloc: <http://lod.nik.uni-obuda.hu/iloc/iloc#>
prefix iacc: <http://lod.nik.uni-obuda.hu/iacc/iacc#>
prefix rdfs: <http://www.w3.org/2000/01/rdf-schema#>
prefix ex: <http://example.org/>
```

```

SELECT ?poi1 ?poi2 ?poi3 ?endl
WHERE {
  BIND (ex:MainEntrance AS ?start ).
  ?end a iloc:Room;
    rdfs:label "Restroom".
  OPTIONAL {?p1 rdfs:label ?poi1.}
  OPTIONAL {?p2 rdfs:label ?poi2.}
  OPTIONAL {?p3 rdfs:label ?poi3.}
  OPTIONAL {?end rdfs:label ?endl.}
  ?start iloc:connectsPOI ?p1.
  ?p1 iloc:connectsPOI ?p2.
  ?p2 iloc:connectsPOI ?p3.
  ?plast iloc:belongsToRoom ?end.
  ?end iacc:hasEquipment ?stall.
  ?stall rdfs:label "Stall";
    iacc:hasProperty ?w.
  ?w a iacc:EquipmentWidth;
    qudt:value ?ewidth.
  FILTER ((?p3 = ?plast || ?p2 = ?plast || ?p1 = ?plast) &&
ewidth > 249 )
  BIND ((if( ?p3 = ?plast , 3, if( ?p2 = ?plast , 2, if( ?p1 = ?plast
, 1, -1)))) AS ?distance)
} ORDER BY ?distance LIMIT 1

```

5 Conclusion

In this paper we presented the ontology extension iACC for the iLOC ontology. Using this extension, the ontology is able to support personalized, accessible free-text type indoor navigation in public buildings like schools, hospitals and government buildings. iACC allows of a detailed description and data storage of important parameters of objects in the rooms, which can be used to execute parameterized searches and wayfinding queries, according to the personal preferences of motion disabled users. The possible use of the ontologies was demonstrated by presenting data excerpts and SPARQL queries that future mobile and web applications can build on to provide these navigation features.

References

1. Fleiner, R., Szász, B., Simon-Nagy, G., Micsik, A.: Indoor navigation for motion disabled persons in medical facilities. *Acta Polytech. Hung.* **14**(1), 111–128 (2017)
2. Bizer, C., Heath, T., Berners-Lee, T.: Linked data—the story so far. *Int. J. Semant. Web Inf. Syst.* **5**(3), 1–22 (2009)

3. 253/1997. (XII. 20.) Government regulation about national settlements planning and building requirements (Korm. rendelet az országos településrendezési és építési követelményekről). http://net.jogtar.hu/jr/gen/hjegy_doc.cgi?docid=99700253.KOR. Accessed 07 Jun 2017
4. Anagnostopoulos, C., et al.: OntoNav: a semantic indoor navigation system. In: 1st Workshop on Semantics in Mobile Environments, SME 2005, Ayia (2005)
5. Dudas, P. M., Ghafourian, M., Karimi, H.: ONALIN: Ontology and algorithm for indoor routing. In: Mobile Data Management: Systems, Services and Middleware, MDM 2009, pp. 720–725. IEEE, Taipei, Taiwan (2009)
6. Scholz J., Schabus S.: An indoor navigation ontology for production assets in a production environment. In: Duckham, M., Pebesma, E., Stewart, K., Frank, A.U. (eds) Geographic Information Science. GIScience 2014. Lecture Notes in Computer Science, vol. 8728, pp. 204–220. Springer, Cham (2014)
7. Matuszka, T., Gombos G., Kiss A.: A new approach for indoor navigation using semantic webtechnologies and augmented reality. In: Shumaker, R. (eds) Virtual Augmented and Mixed Reality, VAMR 2013. Designing and Developing Augmented and Virtual Environments. Lecture Notes in Computer Science, vol. 8021, pp. 202–210. Springer, Berlin, Heidelberg (2013)

A Load Balancing Algorithm for Resource Allocation in Cloud Computing

Syedmajid Mousavi¹(✉), Amir Mosavi²,
and Annamária R. Varkonyi-Koczy³

¹ Faculty of Informatics, University of Debrecen,
Kassai Str. 26, Debrecen 4028, Hungary
majid.mousavi@inf.unideb.hu

² Kando Kalman Faculty of Electrical Engineering, Institute of Automation,
Obuda University, Becsí Str. 94-96, Budapest 1431, Hungary
amir.mosavi@kvk.obuda-uni.hu

³ Department of Mathematics and Informatics, J. Selye University,
Elektrarenska cesta 2, 945 01 Komarno, Slovakia
koczy.annamaria@kvk.obuda-uni.hu

Abstract. Utilizing dynamic resource allocation for load balancing is considered as an important optimization process of task scheduling in cloud computing. A poor scheduling policy may overload certain virtual machines while remaining virtual machines are idle. Accordingly, this paper proposes a hybrid load balancing algorithm with combination of Teaching-Learning-Based Optimization (TLBO) and Grey Wolves Optimization algorithms (GWO), which can well contribute in maximizing the throughput using well balanced load across virtual machines and overcome the problem of trap into local optimum. The hybrid algorithm is benchmarked on eleven test functions and a comparative study is conducted to verify the results with particle swarm optimization (PSO), Biogeography-based optimization (BBO), and GWO. To evaluate the performance of the proposed algorithm for load balancing, the hybrid algorithm is simulated and the experimental results are presented.

Keywords: Cloud computing · Resource allocation · Optimization

1 Introduction

Cloud computing is an emerging technology and new trend for computing based on virtualization of resources [1]. In cloud environment the physical machines run multiple virtual machines (VM) which are presented to the clients as the computing resources. The architecture of a VM is based on a physical computer with similar functionality [2]. In fact VM is a guest program with software resources functioning similar to a physical computer. Resource allocation technique is an important process to allocate resources based on user's application demands to achieve an optimal number of servers in use [3]. This process is done dynamically for the purpose of load balancing of non-preemptive tasks. Load balancing is an *NP*-hard optimization problem in cloud computing. This technique strives to balance the workload across VMs, which

aims to minimize response time in order to keep promises and quality of service in accordance with service level agreements (SLA) between the clients and the provider. Furthermore, this process has to be carried out regularly due to the time-variant nature of the loads of Application Environments (AE). In fact cloud's clients are interested to have their jobs completed in the shortest possible time and at the minimum cost [4]. On the other hand, the cloud providers are interested to maximize the use of their resources with a lower overall cost to increase their profit. Obviously these two objectives are in conflict and often they are not satisfied with the traditional methods of resource allocation and load balancing techniques [5]. The classical methods are very time consuming [6]. Traditional approximate methods are reported inconclusive and inaccurate and often trapped in local optimum [7]. Further algorithms proposed in literature for multi-objective scheduling e.g. FIFO [8] and Round-Robin [8] are in fact not effective in allocating the resources.

Therefore, In order to achieve maximum resource efficiency and scalability, exploring new meta-heuristic algorithms as well as development of novel algorithms are highly desired. Meta-heuristic optimization techniques have had an exceptional growth over the last two decades [9]. The remarkable ability of meta-heuristic techniques is motivated scientists from different fields to solve *NP*-hard problems. Furthermore, such techniques can often find optimal solutions with less computational effort than optimization algorithms, iterative methods, or simple heuristics. The question that arises is why this technique is remarkably common. The answer will be easily found in four main properties that characterize most meta-heuristics: simplicity, flexibility, derivation-free mechanism, and avoidance of entrapment in local optima.

Accordingly, this paper proposes a hybrid meta-heuristic load balancing algorithm with combination of two relatively new optimization algorithms, which can well contribute in maximizing the throughput using well balanced load across virtual machines and overcome the problem of trap into local optimum. The proposed algorithm is a hybrid of Grey Wolves Optimization (GWO) algorithm [10] and Teaching-Learning-Based Optimization (TLBO) algorithm [11]. The main idea is to integrate the ability of exploitation and exploration in GWO with the ability of the convergence in TLBO to provide a new population-base algorithm for dynamic allocation of virtual resources in cloud environment. Furthermore, the proposed algorithm well balances the priorities of tasks and effectively considers load balancing based on time, cost which consequently leads to minimal amount of waiting time of the tasks in the queue.

2 Related Works

Selecting and developing an appropriate algorithm to solve multi-objective problems is of utmost importance [12]. Therefore, meta-heuristic algorithms which have a global overview, as they ensure convergence to the solution and do not fall into the trap in local optimum, are of importance. Salimi et al. [13] introduce a multi-objective optimization algorithm for scheduling using fuzzy systems for load balancing in the distributed system. The authors aim at minimizing implementation time and costs while increasing the productivity of resources.

Cheng [14] provides an optimized hierarchical resource allocation algorithm using a general meta-heuristic algorithm. His model accomplishes workflow tasks scheduling aiming at load balancing with dividing the tasks into different levels. Gomathi and Karthikeyan [15] introduce a method for assigning tasks in a distributed environment using hybrid swarm optimization algorithm. The aim is to minimize the longest completion of task time among processors and creating load balancing. Pandey et al. [16] introduced a meta-heuristic method based on particle swarm optimization algorithm for scheduling on distributed environment resources. This optimization method is composed of two components, one of them is tasks scheduling operations and the other one is, using particle swarm algorithm (PSA) to obtain an optimal mix of the tasks to resource mapping. In this method, each particle represents a mapping of tasks to available resources. Traditional resource allocation methods [17] due to the multiple objectives and the dynamic nature of the problem and also difficulties in dealing with local optimum need advancement and major improvement. Consequently, the purpose of this paper is to address this research gap.

3 Proposed Method

The proposed methodology is based on bonding the algorithms of TLBO and GW. These two algorithms are currently used as approximation algorithm for establishing load balancing based on time and cost between resources and efficiency. With such hybridization it is aimed at speeding up the process while maintaining the improvement of local optimization and increasing the accuracy [18–20]. The TLBO and GWO algorithms are later introduced as the primary solutions to the described problem.

The optimization problem is described as a distributed network in a cloud environment with resource systems $S1, S2, S3, \dots, Sn$. The resources are ready to service in the distributed network for various nodes. Different jobs are sent for the source systems by nodes. Here the scheduler is responsible to allocate one or more jobs to VM in a distributed system [21]. Scheduler provides a scheduling for resource allocation [22]. Several jobs are allocated and processed in parallel with each other at time t in the distributed system. The number of variables T_k is permutation between jobs and resources, this variable is called P , and its value is calculated as follows:

$$P = n^m \quad (n \text{ is number of tasks and } m \text{ is the number of sources}) \quad (1)$$

As it is described each node includes several jobs j_1, j_2, \dots, j_n . Each job requires a series of specific resources R_1, R_2, \dots, R_m . If in the particular example, the resources R_1, R_2, \dots, R_m have the same capacity and processing power and jobs j_1, j_2, \dots, j_n all need 1% of the processor processing, the professional model can be defined in the form of what jobs use which resources to achieve maximum load balancing, average response time, and minimum cost. For the exact solution of the problem, all possible allocation modes must be calculated and the best mode chosen. Due to the large number of exponential modes, the problem is an example of set packing problems which is of NP -complete type.

Optimization function is defined for resource i and job j . y_i is the number of resources. x_{ij} represents that job j is assigned to resource i . C is the maximum capacity for each resource. w_i represents the amount of job i that is covered by the resource. The objective function and mathematical programming model that should be optimized are as follows:

$$Min B = a * (1 - L_{(y_j)}) + b * C_{(y_j)} + c * T_{(y_j)} \tag{2}$$

$$\begin{aligned} \sum_{i=1}^n w_i x_{ij} &\leq Ky_j, \forall j \\ \sum_{j=1}^n x_{ij} &\leq b_j, \forall j \end{aligned} \quad x_{ij}, y_i = 0, 1 \forall i, j \tag{3}$$

where $x_j = \begin{cases} 1 & \text{job } j \text{ is used} \\ 0 & \text{job } j \text{ is not used} \end{cases}$, $y_j = \begin{cases} 1 & \text{resource } j \text{ is used} \\ 0 & \text{resource } j \text{ is not used} \end{cases}$

The aim is to find the minimum number of virtual machines y_j that minimize the objective functions. The values of L , C , and T (load balancing, cost, and response time) are considered based on the number of virtual resources y_j , where a , b , c are variable based on cloud system. The variable of x_{ij} demonstrates that the i^{th} job is in j^{th} virtual machines, and if its value is equal to 0, it means that there is no any resource in j^{th} virtual machine and if its value is equal to 1, it means that there is enough resource to allocate in the j^{th} virtual machine. Every job has capacity of w_i . The first limitation shows that total capacity of jobs can be placed at the maximum K available resources. The second limitation shows the maximum capacity of each virtual resource. b_j is the capacity of each virtual resource.

3.1 Grey Wolf Algorithm

Mirjalili et al. [10] introduced GW for solving engineering problems. GW is a new optimization algorithm inspired by behaviour of grey wolves' hunting and their rule hierarchies. The hierarchical structure and social behaviour of wolves is modelled during hunting process in the form of mathematical models and is used for design of optimization algorithm.

3.2 Teaching-Learning-Based Optimization Algorithm

Rao et al. [11] introduced a novel approach to explore a problem space to find the optimal settings and parameters to satisfy the problem's objectives. This algorithm is inspired from modelling the teaching and learning problem mathematically and presents a new model for solving optimization problems. The algorithm operates in two phases, the first phase is the teacher share to develop class knowledge level and the second phase is the review of courses by students in the same class.

3.3 The Proposed Hybrid Algorithm

Given more convergence power in the global optimality, the GWO algorithm is used as base algorithm in the proposed algorithm. This algorithm can also perform multi-objective optimization [23]. The proposed algorithm is:

```

Initialize the grey wolf population  $X_i=(i=1,2,\dots,n)$ 
Initialize  $a, A$  and  $C$ 
Calculate the fitness of each search agent
 $X1$ =the best Search agent
 $X2$ =the second best Search agent
 $X3$ =the third best Search agent
While  $t < \text{Max number of iterations}$ )
  For each search agent
    Update the position of the current search agent by equation
  End for
Calculate the fitness of all search agents
Update  $X1, X2, X3$ 
 $t=t+1$ 
If not improve solution
  Begin
   $\text{sol\_wolf} = \text{Solution grey wolf}$ 
  Initialize  $\text{sol\_wolf}$  for initialize_solution for TLBO
  Sol TLBO=Do TLBO with Initialize Population with  $\text{sol\_wolf}$ 
  Initialize the grey wolf population  $X_i = \text{Sol\_TLBO}$ , Initialize  $a, A$  and  $C$ 
  Calculate the fitness of each search agent
   $X1$ =the best Search agent,  $X2$ =the second best Search agent,  $X3$ =the third best Search agent
  end
end while
return  $X1$ 

```

The Steps are as Follows: In the initial state, a series of random numbers as the initial population are considered with uniform distribution and a basic solution is considered for the problem. Coefficients a, b, c are initialized. Each wolf is considered as a solution to the problem. In other words, each wolf is considered as a solution to the problem. These solutions or wolves have an answer. Wolves are divided into three categories; alpha, beta, and gamma. Yet on the basis of the fitness function (objective), one of them gives a better answer to the fitness function. Further, the solution enters the main loop where after a few iterations best solution for the fitness function is discovered. Based on the equations in the GWO algorithm, the wolves' position is updated. According to the wolves of first class, the new positions are fitted. Later on more values for the probability of solution are considered. Correspondingly, the values of beta and gamma classes, and new positions of wolves' and their classifications can be obtained. In addition, a new fitness function for the wolves and division of three new wolves groups is calculated. If a suitable solution is found in the new classification, the algorithm is to be improved further. The best solution between the wolves is considered as the initial solution (initial population) for teaching and learning algorithm. Further the problem using teaching and learning algorithm is solved and the solution is considered as initial population to start again. In this stage the GWO algorithm is implemented.

4 Computational Experiments

Here the main purpose is comparison on the performance of hybrid algorithm with three algorithms of GWO, particle swarm optimization (PSO) [24] and Biogeography-based optimization (BBO) [25]. At the first experiment, the mathematical models of algorithms are implemented using MATLAB (2014) and then it is run for 11 benchmark functions [26]. At the second experiment, the algorithms are simulated for resource allocation using CloudSim tool and the results are compared. Each algorithm has been investigated on a number of generations 200 and a constant population size of 50. It is noteworthy that the algorithms have been run 20 times on a benchmark function, and the final result has been obtained from the average of 20 times of running so that the rate of error decreases. Benchmark functions are divided into two groups: unimodal and multimodal.

Table 1. Results of benchmark functions for 200 generations and population size of 50.

	Function	Hybrid method	GWO	PSO	BBO
Unimodal	Sphere	0.007653	0.052347	0.064355	0.045546
	Chung reynolds	0.004355	0.062645	0.052134	0.063455
	Schwefel 2/22	0.008455	0.049545	0.035231	0.024245
	Schwefel 2/21	0.005634	0.015366	0.104434	0.223567
	Cube	0.002347	0.094653	0.073244	0.083556
	Dixon & price	0.064556	0.034444	0.042324	0.075743
Multimodal	Griewank	0.034567	0.043433	0.047651	0.124456
	Rosenbrock	0.022345	0.022655	0.107431	0.144677
	Ackley	0.014238	0.072762	0.052764	0.034357
	Rastrigin	0.013251	0.094749	0.074321	0.073534
	Brown	0.025231	0.030769	0.060328	0.053567

According to the results presented in Table 1, the hybrid algorithm outperforms in comparison with all other algorithms in unimodal and multimodal functions. Computational results showed that concerning unimodal functions like sphere and Chang Reynolds, which are simple functions with no local optima, if we have many or few iterations or large or small population, hybrid algorithm outperforms other algorithms. This rule also applies to Schwefel 2/21 function because not only is it a simple function, but it also does not have any local optima. In conclusion, hybrid algorithm is the best algorithm to solve a problem for the simple functions that do not have any local optima. Regarding Schwefel 2/22 function, hybrid algorithm delivered better results than other algorithms. This function is a bit more complex than Sphere function. Therefore, hybrid algorithm could be used to solve a bit complex and problems that contain local optima. Hybrid algorithm outperforms in Restrigin and Ackley functions. These two functions also have many local optima same as Schwefel 2/22. In Griewank function, which is a rather complex function, hybrid algorithm still delivers the best results. Figure 1 shows an example of proposed algorithm using bin packing problem.

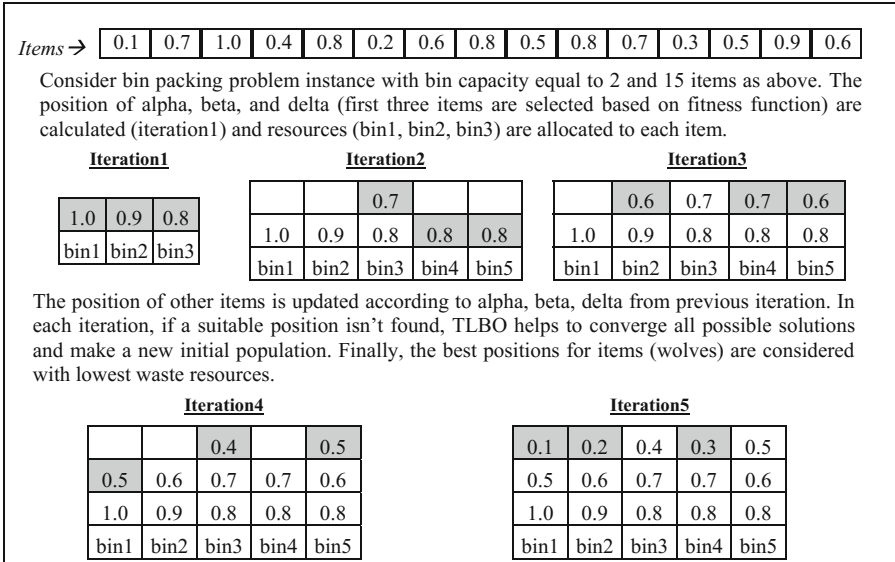


Fig. 1. An example of the execution process of proposed algorithm using bin packing problem

In addition to the following example the novel algorithm has been recently used in a number of industrial applications e.g. creating predictive decision models [27], and materials design innovation [28].

5 Conclusion

For an effective dynamic resource allocation in cloud computing a novel algorithm is proposed. The evaluation of experimental results indicates the novel hybrid approach has better performance comparing to the existing algorithms, in particular, in high-volume data of cloud scheduler. It is concluded that the main problem in the resource allocation of cloud scheduler is the lack of convergence in the optimal solution.

Acknowledgement. This work has partially been sponsored by the Research & Development Operational Program for the project “Modernization and Improvement of Technical Infrastructure for Research and Development of J. Selye University in the Fields of Nanotechnology and Intelligent Space”, ITMS 26210120042, co-funded by the European Regional Development Fund.

References

1. Mousavi, S.M., Gabor, F.: A novel algorithm for Load Balancing using HBA and ACO in Cloud Computing environment. *Int. J. Comput. Sci. Inf. Secur.* **14**, 48–55 (2016)
2. Bertsimas, D., Gupta, S., Lulli, G.: Dynamic resource allocation: a flexible and tractable modeling framework. *Eur. J. Oper. Res.* **236**, 14–26 (2014)

3. Ayesta, U., Erasquin, M., Ferreira, E., et al.: Optimal dynamic resource allocation to prevent defaults. *Oper. Res. Lett.* **44**(4), 451–456 (2016)
4. Chen, Q., Zhang, X.: The local optimum in topology optimization of compliant mechanisms. *Mech. Mach. Sci.* **12**, 621–632 (2016)
5. Dhinesh, B., Venkata, K.: Honey bee behavior inspired load balancing of tasks in cloud computing environments. *Appl. Soft Comput.* **13**, 2292–2303 (2013)
6. Mosavi, A.: The large scale system of multiple criteria decision making. *IFAC Proc.* **43**, 354–359 (2010)
7. Selvaraj, C.: A survey on application of bio-inspired algorithms. *Int. J. Comput. Sci. Inf. Technol.* **67**, 366–370 (2014)
8. Mosavi, A., Varkonyi, A.: Learning in robotics. *Int. J. Comput. Appl.* **157**, 8–11 (2017)
9. Izakian, H., et al.: A discrete particle swarm optimization approach for Grid job scheduling. *Int. J. Innov. Comput. Inf. Control* **55**, 4219–4252 (2014)
10. Mirjalili, S., et al.: Multi-objective grey wolf optimizer: a novel algorithm for multi-criterion optimization. *Expert Syst. Appl.* **47**, 106–119 (2016)
11. Rao, R.V.: *Teaching-Learning-Based Optimization Algorithm*, vol. 45, pp. 9–39. Springer (2016)
12. Mousavi, S., et al.: Dynamic resource allocation in cloud computing. *Acta Polytech. Hung.* **14**, 38–59 (2017)
13. Salimi, R., et al.: Task scheduling using NSGA II with fuzzy adaptive operators for computational grids. *Parallel Distrib. Comput.* **74**, 23–50 (2014)
14. Cheng, B.: Hierarchical cloud service workflow scheduling optimization schema using heuristic generic algorithm. *Prz. Elektrotech.* **88**, 92–105 (2012)
15. Gomathi, B., Karthikeyan, K.: Task scheduling algorithm based on hybrid particle swarm optimization in cloud computing. *Appl. Inf. Technol.* **55**, 33–38 (2013)
16. Pandey, S.: A particle swarm optimization-based heuristic for scheduling workflow applications in Cloud Computing. *Inf. Netw.* **76**, 400–407 (2010)
17. Mousavi, S., Mosavi, A.: A novel algorithm for cloud computing resource allocation. *Open J. Cloud Comput.* **5**, 123–144 (2017)
18. Mosavi, A., Vaezipour, A.: Developing effective tools for predictive analytics and informed decisions. University of Tallinn, Technical report (2014)
19. Mosavi, A.: Application of data mining in multiobjective optimization problems. *Int. J. Simul. Multisci. Des. Optim.* **5**, 15–28 (2014)
20. Mosavi, A., et al.: Combination of machine learning and optimization for automated decision-making. In: *Multiple Criteria Decision Making MCDM*, vol. 7 (2015)
21. Suleiman, M.H., Mustafa, Z., Mohmed, M.R.: Grey Wolf optimizer for solving economic dispatch problem. *APRN Appl. Sci.* **65**, 1619–1628 (2015)
22. Yagoubi, B., Slimani, Y.: Task load balancing strategy for grid computing. *J. Comput. Sci.* **8**, 186–194 (2007)
23. Malarvizhi, M., Uthariaraj, V.R.: Hierarchical load balancing scheme for computational intensive jobs in Grid computing. *Adv. Comput.* **14**, 97–104 (2009)
24. Kennedy, J.: Particle swarm optimization. *Mach. Learn.* **87**, 760–766 (2011). Springer
25. Simon, D.: Biogeography-based optimization. *Evol. Comput.* **12**, 70–79 (2008)
26. Jamil, M., Yang, S.: A literature survey of benchmark functions for global optimisation problems. *J. Math. Model. Optim.* **4**, 150–194 (2013)
27. Mosavi, A.: Predictive decision model (2015). <https://doi.org/10.13140/RG.2.2.21094.63047>
28. Mosavi, A., Rabczuk, T.: Learning and Intelligent Optimization for Material Design Innovation. *Theoretical Computer Science and General Issues. LION11* (2017)

A Fuzzy Data Structure for Variable Length Data and Missing Value Classification

Balazs Tusor^(✉), Annamária R. Várkonyi-Kóczy, and János T. Tóth

Department of Mathematics and Informatics, J. Selye University,
Bratislavská Str. 3322, P.O. BOX 54, 945 01 Komárno, Slovakia
{tusorb,koczya}@ujss.sk, tothj@selyeuni.sk

Abstract. Variable length data classification is an important field of machine learning. However, while there are plenty of classifiers in literature that can efficiently handle fixed length data, not many can also handle data with varying length samples. In this paper, a structure is proposed for quick and robust classification of such data, as well as data sets with occasionally missing values. It builds on the principle of look-up table classifiers, realizing a direct assignment between the attribute values of the given data samples and their corresponding classes. The proposed data structure solves this problem by decomposing the problem space into a sequence of integer value combinations, thus creating and maintaining a layered structure in the combined form of 1D and 2D arrays. Furthermore, a simple analysis regarding the data structure can reveal functional dependencies considering the attributes of the data set, offering an option to simplify the structure thus reduce its complexity.

Keywords: Classification · Data mining · Missing data · Machine learning · Data structure · Pattern recognition

1 Introduction

Variable length data classification is an important field of machine learning. Among its applications are the processing of time series, speech recognition, shape recognition, motion analysis, robotics, etc.

The generally applied method to handle variable length data is to extend the individual data samples with zeros to convert the data set to uniform length, while the typical way to handle missing data is to substitute a zero value in its place. After that, the resulting data set is processed using a fixed-length classifier, e.g. Artificial Neural Networks [1].

In this paper, a data structure is proposed for quick and robust classification of data with varying length samples, as well as data sets with occasionally missing values. It builds on the principle of look-up table classifiers [2], which realize a direct assignment between the attribute values of the given data samples and the corresponding classes or a likelihood function based on the observed attribute value – class occurrences. The advantage of applying this method is that the classification phase is reduced to a single step. The main disadvantage is that the whole problem space is needed to be accounted for, which causes very high memory usage for problems with a high number of attributes.

This problem can be solved by only accounting for interesting or important parts of the problem space (i.e. where the known training data points are located). The data structure proposed in this paper implements it through problem space decomposition.

The rest of the paper is as follows. In Sect. 2, the data structure is described. First, in Subsect. 2.1 the architecture of the proposed fuzzy structure is described, along with its usage for classification problems. In Subsect. 2.2 a graph representation is presented that improves the interpretability of the structure. In Subsect. 2.3 a structure simplification method is given, while Subsect. 2.4 presents two ways to use the structure for missing data value handling. The performance of the network is shown in Subsect. 2.5. Finally, in Sect. 3 the conclusions are given.

2 Extended Sequential Fuzzy Indexing Tables

The proposed data structure is an *extended* version of *Sequential Fuzzy Indexing Tables* (SFIT, [3–5]) which solve the problem of multi-dimensional problem spaces by decomposing the problem space into a sequence of attribute value combinations, thus creating and maintaining N layers (where N is the number of dimensions in the given problem), each layer L_i consisting of a Λ^{L_i} index matrix and an M^{L_i} fuzzy matrix. The index matrices manage the combinations of the attribute values, assigning an index number (so-called marker) to each known $A_0 A_1 \dots A_i$ attribute combination, which is used to further combine it with another attribute in the next layer (thus increasing the complexity of the combinations by one attribute per layer).

Remark: since the structure applies the given attribute values of the data set as matrix coordinates, the data needs to be in positive integer format. Thus, floating-point type data is needed to be scaled and rounded using a simple mapping function before it can be used.

The fuzzy matrices assign fuzzy membership function values to each element of the index matrices. Their role is to maintain a certain level of generalization ability of the system: the classifier can detect not only the trained value combinations, but any combinations that are similar to them (within a given margin).

Furthermore, in each layer there is a G^{L_i} matrix and a v^{L_i} 1D array for additional statistical data. The former stores the number of occurrences of each class in each row (of the index matrix), while the latter stores the most occurring class for each row. This makes the classification process even more robust, because even if the evaluation step does not find a result (when the input data is not similar enough to any of the input data), then the system can still provide with an answer (the appropriate element of v^{L_i}). For a more detailed description of SFIT, please see [5].

2.1 Extended Sequential Fuzzy Indexing Tables

Although the SFIT structure can be efficiently used for pattern recognition and storage (considering supervised learning), it only works for cases where the number of input variables is constant. In case of varying input lengths, the structure is needed to be extended in each layer with K^{L_i} class matrices that assign a class ID to each known

combination and an additional \widehat{M}^{L_i} fuzzy matrix that appoints fuzzy membership values to each cell of the corresponding class matrices (similarly to the index and fuzzy matrices in SFIT).

The training of *Extended Sequential Fuzzy Indexing Tables* (ESFIT) is illustrated by Fig. 1. First, the training data set is analyzed and the coefficients of the linear mapping function (which can be skipped if the data is already made of positive integers), as well as the size of each domain and the order of layers (considering the attributes, the structure can be optimized by manipulating this order) in the topology. Using the obtained parameters, the structure is created next and a training sample is taken. For each layer L_i (where i is the corresponding attribute), if i is not the last unprocessed attribute in the sample, then examine the $M_{\eta, \tilde{x}_i}^{L_i}$ fuzzy matrix value (where η is an index number ($\eta = 1$ for the first layer), and \tilde{x}_i is the scaled and rounded value of input attribute value x_i). If the fuzzy value is 1, then there is already an index value

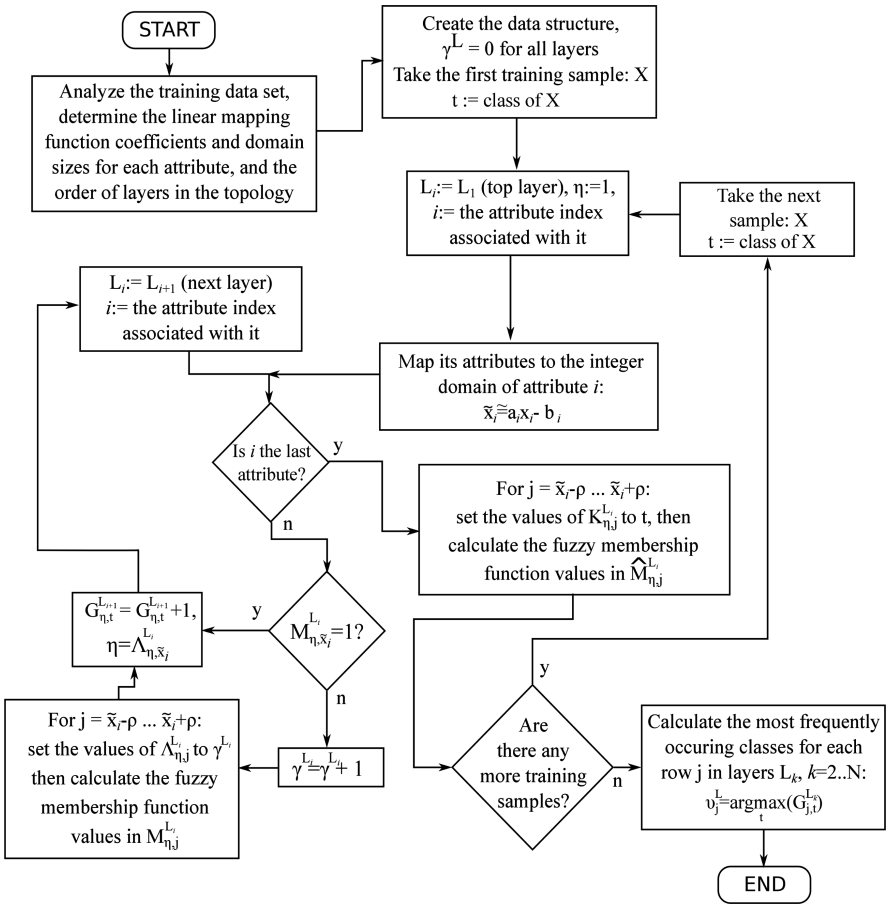


Fig. 1. The training process of the ESFIT classifier.

(so-called *marker*) in the index matrix, so set the index variable to that value ($\eta = \Lambda_{\eta, \tilde{x}_i}^{L_i}$), update the appropriate element of G^{L_i} and proceed to the next layer. If the fuzzy value is not 1, then add a new marker to $\Lambda_{\eta, \tilde{x}_i}^{L_i}$ and its vicinity in the same row in a δ -wide range, then update M^{L_i} in the modified area, set index variable η and update G^{L_i} before proceeding to the next layer. In Fig. 1, γ^{L_i} denotes the current number of markers in L_i .

If i is the last attribute, then instead of Λ^{L_i} index and M^{L_i} fuzzy matrices, the class matrix K^{L_i} and fuzzy matrix \hat{M}^{L_i} are updated in a δ -range area around (η, \tilde{x}_i) . After that, the next training sample is taken for processing.

After the last training sample is processed, the values of v^L are calculated for each row in each layer.

An example for a trained structure can be seen on Fig. 2. The problem consists of 3 attributes and 3 classes ($\alpha_1, \alpha_2, \alpha_3$). The trained 7 samples are shown in the bottom left corner in each column of the matrix.

Furthermore, the path of evaluation of input sample [2 5 4] (marked by dashed lines) can be followed in the figure. The evaluation procedure first sets the value of the index variable to the marker value in the index matrix at $\tilde{x}_1 = 2$: $\eta = \Lambda_2^{L_1} = 2$. Then, for the second layer, $\eta = \Lambda_{\eta, \tilde{x}_2}^{L_2} = \Lambda_{2,5}^{L_2} = 3$. In the last layer, the class matrix $K_{\eta, \tilde{x}_3}^{L_3} = K_{3,4}^{L_3}$ is examined. Since there is no known value in $K_{3,4}^{L_3}$ (due to the lack of training samples that are similar to the input value combination), the value of $v_{\eta=3}^{L_3} = \alpha_2$ is returned, as the most likely answer.

Remark: The start of indexing depends on the development framework. For example, in Matlab indexing starts with 1, while in other frameworks (e.g. C/C++) it starts with 0. This should be considered when using ESFIT structures.

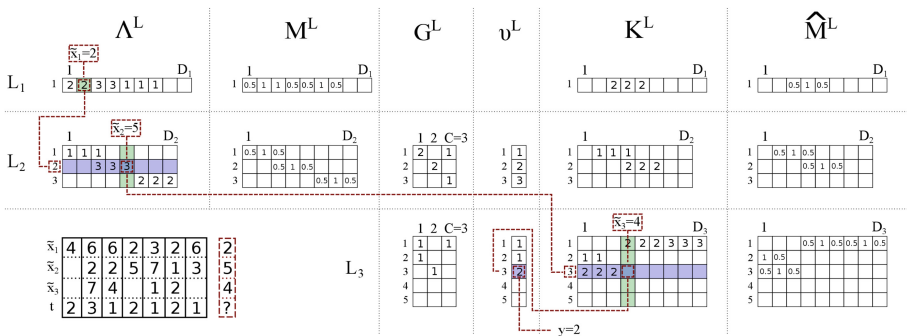


Fig. 2. The training process of the ESFIT structure (for supervised classification problems).

2.2 Graph Representation

The visual interpretation of the data structure used for classification can be improved by using a suitable directed graph (or more precisely, a directed tree) representation. Let a

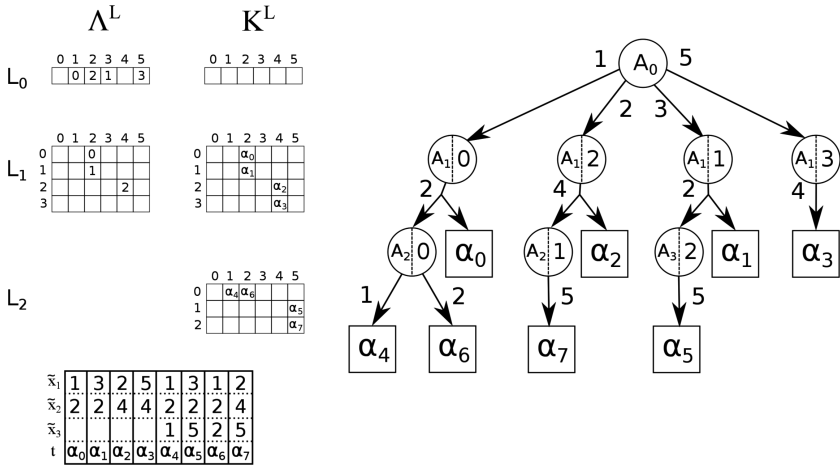


Fig. 3. Graph representation of an ESFIT structure.

node represent a given row in each vector or matrix, and the edges between them the scaled value of the given input attributes, while the leaves are the corresponding class labels. An illustration can be seen in Fig. 3, where the structure on the left side is taught with samples on the bottom left corner. On the right side the graph representation is shown. In order to improve visibility, only the index and class matrices are shown.

The root node represents the row vector of the first layer (linked to attribute A_0). It has markers in columns 1, 2, 3 and 5, thus the edges originating from it gain these labels. Under column 1 of L_0 , the marker stands for index number 0, therefore in the next layer (that is linked to attribute A_1) the 0th row needs to be examined. Thus, the child node here is $(A_1 | 0)$. In row 0 of layer L_1 , there is a marker at column 2 (marker 0) in the index table and one class marker α_0 in the class matrix, so there are two directed edges to node $(A_2 | 0)$ and leaf $[\alpha_0]$. The tree ends in leaves $[\alpha_i]$, where i marks the class of the given training samples.

This demonstrates the close relationship between the ESFIT structures and decision trees, especially considering readability: both can be easily evaluated manually by going through the tree, starting from the root node and using the (scaled) values of the input attributes to choose branches until a leaf is reached.

Remark: the main goal of this representation is visualization for human users, it does not implicitly use the generalization ability of the system (with the data stored in the fuzzy matrices). It can be mended if the user chooses the paths closest to the input values (e.g. if the closest stored value to 15 is 12, then take that path).

2.3 Functional Dependency Detection

The ESFIT structure can be used to detect functional dependencies [6] among the attributes of the data set, from the training samples. Functional dependency is present in any database where the values of one attribute (or more attributes combined) uniquely determine the values of one (or multiple) other attributes. In such case, the problem can

be simplified by excluding the latter attribute(s) from the classification, because it does not contribute into the classification, making the process needlessly longer.

The presence of such relationship can be easily detected by observing the number of markers (γ^{L_i}) in each layer i . If it is the same as in the previous layer ($\gamma^{L_{i-1}}$), and there are no classes stored in the class matrix of layer i , then using attribute i is not necessary for the classification, it can be deleted and the markers in layer L_{i-1} be set to reference the appropriate rows in layer L_{i+1} .

2.4 Missing Value Data Analysis

The ESFIT structure can also be used for classification even if there are missing values among the input data, with a slightly modification to the evaluation procedure. There are two ways to achieve this. The first method processes known values in the way described in Subsect. 2.1, and when it reaches an unknown valued variable then the evaluation process is continued through all markers in the given row (referenced by the marker in the previous layer). Thus, for n markers in the given row there will be n branches of evaluation till the last attribute is processed. The fuzzy matrix values have an important role here as well, as the fuzzy membership function values of each branch are examined. The branches that cannot be continued (there are no known markers around the path it should take considering the input values) are discarded. At the end, the resulting class with the highest fuzzy value (the product of all fuzzy membership function values of the given path) is chosen as the output of the system.

Another method is using a so-called *meet in the middle* approach: the evaluation is started at both the beginning (L_1) and the end (L_N , where N is the attribute number of the given sample). The first search is propagating forwards and the second backwards. The former one is trivial, using the evaluation process already described. However, to make the latter one work, for each row of each layer L_i , the row number in L_{i-1} that contains the marker referencing the given row must be stored so the evaluation can work backwards. This can be done simply with an additional column vector in each layer. Both searches continue until they both reach the layer with the missing value variable. If they meet in the same row, then there is a match, the evaluation returns with the class of the endpoint where the second search started. If the second search started from multiple endpoints (if the last attribute value matches multiple rows in the last layer) then the fuzzy membership function values are used to choose the most likely answer.

2.5 Experiments

To investigate the performance of the classifier, experiments have been conducted in Matlab™ R2012a, on a PC (Intel® Core™ i5-4590 CPU @ 3.30 GHz, 16 GB RAM).

An image processing problem has been considered: 36 shape pictures have been selected from the MPEG-7 database [7] and processed using a shape extractor framework [8] that generated a shape descriptor array of each shapes. Each array consists of a series of numbers between 0 and 149. The length of the vectors is not constant, ranging from 5 to 21. The shapes can be seen in Fig. 4, the data set is divided into 6 classes (shown with dotted lines). The data was used to train an Artificial Neural



Fig. 4. Shape images from the MPEG-7 data set.

Table 1. A performance comparison between ANNs and ESFIT classifiers.

Testing data	Correct/wrong answer ratio	
	Artificial neural network	ESFIT
Added noise, $\delta = 1$	75.3%	98.74%
Added noise, $\delta = 2$	73.7%	97.88%
Added noise, $\delta = 3$	72.2%	97.7%
Shortened pattern	0%	100%
Elongated pattern	25.5%	100%

Network (with 100 neurons) and an ESFIT classifier. The former took 1.76 s on average to learn the problem, while the latter only took a fraction of that time, 0.03 s.

For testing purposes, new sets of data vectors (1000 samples each) have been generated from the training data, by randomly choosing a sample and modifying it. The first 3 sets have been generated by adding a certain amount of noise (adding a random integer number $\beta \in [-\delta, \delta]$ to a random attribute, where δ is an arbitrary integer) to the samples. The fourth set has been made by erasing an attribute (and thus *shortening* the sample), and the fifth set was created by adding an additional attribute with a random value to the samples.

The average performance of both classifiers on the testing data sets can be seen in Table 1. While the ANN is generally faster (taking 0.0075 s for each set) than the ESFIT (which takes 0.117 s for each set of 1000 samples), the latter provides a much more reliable pattern recognition rate on the noisy data sets. Furthermore, the ANN has achieved a very weak (0–25.5%) performance rate where the length of the samples has been manipulated, while the ESFIT has classified them perfectly (due to the additional statistical data it stores in form of arrays G and v).

Remark: These experiments have also been conducted using Non-Linear AutoRegressive Neural Network (NARX, [9]) and Recurrent Neural Network (RNN, [10]) classifiers (that are both part of the Machine Learning toolbox of Matlab 2012b). However, neither of them could provide a performance higher than 38%.

3 Conclusions

In this paper, a fuzzy data structure is proposed that makes the classification of variable length data quick and reliable, at the cost of memory usage. It uses 1D and 2D arrays to map the known areas of the problem space based on the training data. The readability of the structure can be increased by constructing a graph representation. Furthermore, the structure can be used to process input data with missing values, for this problem two methods are proposed.

The performance of the network is shown through an image processing problem, where the system is shown to be slower than ANNs during the evaluation phase, but also much more reliable and robust.

The structure is also useful to indicate the presence of functional dependencies in the data set. However, the exact relationship (which attributes are involved exactly) cannot be determined simply in the current format of the system, in future work this will be explored further, as well as the acceleration potentials of the training and evaluation phases by applying parallelization.

Acknowledgements. This work has partially been sponsored by the Hungarian National Scientific Fund under contract OTKA 105846 and the Research & Development Operational Program for the project “Modernization and Improvement of Technical Infrastructure for Research and Development of J. Selye University in the Fields of Nanotechnology and Intelligent Space”, ITMS 26210120042, co-funded by the European Regional Development Fund.

References

1. Rumelhart, D.E., McClelland, J.: *Parallel Distributed Processing: Explorations in the Microstructure of Cognition*. MIT Press, Cambridge (1986)
2. Campbell-Kelly, M., Croarken, M., Robson, E.: *The History of Mathematical Tables from Sumer to Spreadsheets*, 1st edn. Oxford University Press, New York (2003)
3. Várkonyi-Kóczy, A.R., Tusor, B., Tóth, J.T.: Multi-attribute classification method to solve the problem of dimensionality. In: *Proceedings of the 15th International Conference on Global Research and Education in International System, Inter-academia 2016*, pp. PS39-1–PS39-6. Warsaw, Poland (2016)
4. Várkonyi-Kóczy, A.R., Tusor, B., Tóth, J.T.: Active problem workspace reduction with a fast fuzzy classifier for real-time applications. In: *Proceedings of the 2016 IEEE International Conference on Systems, Man, and Cybernetics, Budapest, Hungary*, pp. 4423–4428. IEEE (2016)
5. Várkonyi-Kóczy, A.R., Tusor, B., Tóth, J.T.: Robust variable length data classification with extended sequential fuzzy indexing tables. In: *2017 IEEE International Instrumentation and Measurement Technology Conference (I2MTC), Torino, Italy*, pp. 1881–1886. IEEE(2017)
6. Date, C.: *Database Design and Relational Theory: Normal Forms and All That Jazz*, p. 21. O’Reilly Media Inc, Newton (2012)
7. Latecki, L.J., Lakamper, R., Eckhardt, T.: Shape descriptors for nonrigid shapes with a single closed contour. In: *Proceedings IEEE Conference on Computer Vision and Pattern Recognition, Hilton Head Island, SC*, pp. 424–429 (2000)
8. Várkonyi-Kóczy, A.R., Tusor, B., Tóth, J.T.: A fuzzy shape extraction method. In: *6th World Conference on Soft Computing, Berkeley, CA, USA* (2016)
9. Billings, S.A.: *Nonlinear System Identification: NARMAX Methods in the Time, Frequency, and Spatio-Temporal Domains*, p. 574. Wiley, Hoboken (2013)
10. Graves, A., Liwicki, M., Fernandez, S., Bertolami, R., Bunke, H., Schmidhuber, J.: A novel connectionist system for improved unconstrained handwriting recognition. *IEEE Trans. Pattern Anal. Mach. Intell.* **31**(5), 855–868 (2009)

Multimedia, Internet-Based Education and e-Learning

A Multifaceted Approach Towards Education in Data Analytics

Reneta P. Barneva^{1(✉)}, Isabelle Bichindaritz², Valentin E. Brimkov³,
Joaquin Carbonara³, Sanjeena Dang⁴, Federico Gelsomini⁵,
Kamen Kanev⁶, Jeanette Sperhac⁷, and Lisa Walters¹

¹ SUNY Fredonia, 280 Central Ave., Fredonia, NY 14063, USA
Reneta.Barneva@fredonia.edu

² SUNY Oswego, 7060 New York 104, Oswego, NY 13126, USA

³ SUNY Buffalo State, 1300 Elmwood Ave., Buffalo, NY 14222, USA

⁴ Binghamton University - SUNY, 4400 Vestal Parkway East, Binghamton
NY 13902, USA

⁵ Università degli Studi di Roma “La Sapienza”, Piazzale Aldo Moro 5,
00185 Rome, Italy

federico.gelsomini@gmail.com

⁶ Shizuoka University, 3-5-1 Johoku, Naka-ku, Hamamatsu,
Shizuoka 432-8011, Japan

⁷ Center for Computational Research, SUNY Buffalo, 701 Ellicott St.,
Buffalo, NY 14203, USA

Abstract. This work presents a novel multifaceted approach for facilitating education in data analytics. This novel approach is necessary as this new and growing discipline warrants understanding within diverse organizational arenas while recognizing that students are likely non-traditional, usually already employed in various fields and having different level of preparation. Elements of the approach are applied at the State University of New York (SUNY) – one of the largest university systems in the world.

Keywords: Data science · Online education · Multi-campus programs · Collaborative learning · Tangible interactions

1 Introduction

Data science is a rapidly developing discipline with practical applications in virtually every field of human activities. Projections indicate a need of one million data scientists in the USA alone [16]. Thus, a pressing need exists to educate data scientists and establish a foundation to support transdisciplinary research and training in data science.

According to IBM, “[a] data scientist will most likely explore and examine data from multiple disparate sources. The data scientist will sift through all incoming data with the goal of discovering a previously hidden insight, which in turn can provide a competitive advantage or address a pressing business problem. A data scientist does not simply collect and report on data, but also looks at it from many angles, determines what it means, then recommends ways to apply the data” [10]. As the professional

work of a data scientist is to examine the data and discover useful information in the subject field, the best approach to become a data scientist is to gain expertise in some specific area and develop skills to work with data. Thus, workforce professionals within various existing disciplines must be trained to effectively use data science methods and tools. An ideal approach in this case is through synchronous and asynchronous distance education and internships, which allow for both conceptual understanding as well as facilitating practical experience within disciplines. Distance education would not only allow non-traditional students to continue their full-time work while taking courses at their convenience, but it would also allow for the inclusion of program courses offered by diverse instructors from different institutions and industries, thereby tailoring the program to specific needs while disseminating the most recent advances in this dynamic field.

2 Multifaceted Approach

Teaching data science differs from teaching other disciplines: it not only requires building theoretical foundations in statistics, mathematics, and computer science, but also needs specific knowledge in various applied fields from which the data originates. Thus, a multifaceted approach was adopted, promoting data science across disciplines at undergraduate and graduate levels in the form of courses, minors, certificates, as well as complete degree programs. As a result, we arm students entering various disciplines with the power of data analytics, while additionally providing the existing workforce with online data analytics education in the form of short courses on specific topics.

2.1 Applying Asynchronous Distance Education

As noted, preparing professionals in various fields to use the methods and tools for data analytics is one aspect of our approach. Distance education readily facilitates this approach. Such a tactic could be either synchronous in the form of participation in a virtual classroom, or asynchronous, in the form of distance education courses. In the latter category, of particular interest are the Massive Open Online Courses (MOOCs). For example, the course “Big Data, Genes, and Medicine” is taught by one of the authors, in the form of a MOOC offered through Coursera. It attracts thousands of students already employed full-time (53%), part-time (10%), self-employed (5.4%), and unemployed looking or not looking for work (24.7%). Students take the course from all over the world with a balanced distribution between mainly three continents (about 1/3 from America, Asia, and Europe). The course has been designed to take diverse learners where they are in terms of technical skills and distill in them expert knowledge and skills in Health Big Data Science and Bioinformatics by synergistically providing background domain knowledge in biology, chemistry, and genomic as well as Big Data Science analytics concepts, methods, and tools [4]. Open Educational Resources (OERs) in R programming, biomedical research methods, and biostatistics are in preparation to complement the course and offer to learners the background concepts in which they may be interested. Figure 1 illustrates the concept.

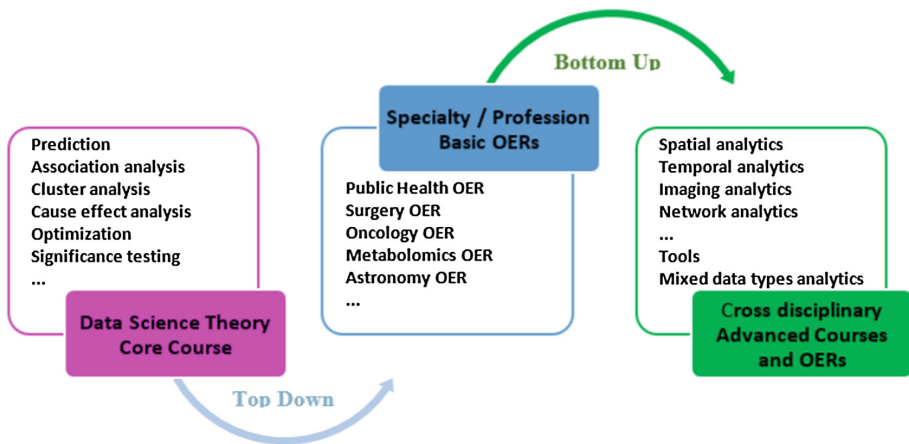


Fig. 1. Educational framework guided by a transdisciplinary theoretical foundation, infused and augmented by cross-disciplinary courses and OERs.

2.2 Applying Synchronous Distance Education

As data science is a dynamically developing discipline and MOOC preparation is time-consuming, at times it may be inappropriate to develop online courses for asynchronous learning. As students who may wish to participate in synchronous data analytic courses are often employed, it makes it impractical for them to attend face-to-face courses and programs. Another obstacle to synchronous learning may be that qualified instructors are geographically disperse, coming from different universities and/or industry. Thus, a distance learning synchronous solution is necessary. Different platforms might be used to connect learners with instructors in a synchronous format; a useful survey is provided in [21].

The authors of SUNY Buffalo State and SUNY Fredonia – two campuses of the State University of New York (SUNY) located at about 90 km (60 mi) from each other are launching a joint multidisciplinary multi-campus master’s program on data science called *Data Analytics across Disciplines* based on synchronous distance learning using the instructional resources of the two universities as well as combining students from the two institutions into the program so that the courses could have sufficient enrollment to be fiscally viable. More about this model is given in [2].

2.3 Resource Sharing

Serious constraints for offering data science courses include the software and storage requirements. Thus, a computational gateway, called VIDIA – Virtual Infrastructure for Data Intensive Analysis – is used for this purpose [13]. It enables users to build, launch, and access advanced software tools and computations with a web browser, without having to download, compile, or install code on local systems. As of February 2017, VIDIA has supported data analytics coursework for 17 unique courses, among which:

- POLS-200 – *Approaches to Political Science* – introduces research methods and techniques with extensive computation. (SUNY Oneonta)
- POLS-284 – *U.S. Foreign Policy* – uses data analytics to explore the influence of social media on foreign policy. (SUNY Oneonta)
- SOCL-294 – *Animals and Society* – uses social media data to study controversies in issues of wilderness, animal research, and animal rights. (SUNY Oneonta)
- PHIL-230 – *Environmental Ethics* – analyzes large social media datasets to study the ethics of environmental issues, such as hydraulic fracturing and dam construction. (SUNY Oneonta)
- BIO-4/595– *Introduction to Bioinformatics* – assigns bioinformatics exercises and problems in Perl and Python. (SUNY Brockport)
- PHY-410– *Computational Physics I* – examines numerical solutions of problems in physics, and examines root-finding, numerical differentiation, quadrature, matrix inversion, and ordinary differential equations. Programming assignments in C++ and Python. (SUNY Buffalo—planned Fall 2017)

VIDIA server not only provides faculty with a maintenance-free shared environment for teaching courses; it also allows conducting research. At least 25 users can simultaneously run VIDIA tool sessions in their local browsers. Each virtual container that runs a tool session is pre-configured with software tools and memory, and the individual users are provided an allocated disk quota, which could be extended upon request. Table 1 lists the software tools currently provided by VIDIA.

Table 1. Software tools provided by VIDIA.

Software tool	Description
RapidMiner [17]	Workflow-based environment for data and text mining and machine learning
RStudio [18]	Interactive development environment (IDE) for the R language offers statistical analysis libraries
PSPPP [15]	GNU version of IBM’s SPSS software enables analysis of sampled data
Orange [14]	Workflow-based data visualization, exploration, and analysis environment
Spyder [19]	Numerical computing and interactive development environment for Python
Workspace [13]	Linux desktop with compilers, scripting languages, and access to user’s home directory on VIDIA

VIDIA, housed at SUNY Buffalo’s Center for Computational Research (CCR), was started in 2013 with a grant from New York State [5, 20, 22]. It is built on the HUBzero® Platform for Scientific Collaboration [13], which combines a Linux, Apache, MySQL, PHP (LAMP) stack with unique middleware that enables users to run advanced computational tools and coordinate job submission to CCR’s high-performance computing (HPC) cluster. In addition to using deployed tools and available HPC codes, VIDIA users can develop and deploy their own interactive software tools on the platform, for sharing with the community. VIDIA has over 375 users; interested parties may request an initial registration on the platform with their academic credentials and institution name.

2.4 Collaboration and Tangible Interactions Support

Distance learning and resource sharing discussed in the previous sections could be further enhanced through interactivity and collaborative support. Many studies have confirmed that a more interactive learning style stimulates better retention and faster development of targeted skills [1]. Learning objectives are further reinforced in set outs that provoke and stimulate true collaborative efforts [23]. The distance learning model that we employ allows for certain level of interactivity and access to various shared resources. It is therefore possible to apply various methods, approaches and algorithms through of Computer Supported Collaborative Learning (CSCL) [12]. As a study by Cho et al. suggests, a high degree of interaction through social platforms between students is a key element to obtain good results in a distributed learning environment. Students can then maintain individual and joint communication channels for messaging, data sharing and joint works [7].

In a broader perspective, Cook et al. have used Internet-based learning to facilitate collaborative learning, by bringing together a community of learners irrespective of physical location [8]. In such a learning setting, group formation is a very important factor to realize meaningful collaborative activities. Correct assignment of a student to a particular group allows for substantial interactions, factual cognitive improvement, and the maintenance of a high level of motivation [9]. In our earlier work [11] we have addressed the problems of collaborative work in dynamic groups considering assignment-based formation, maintenance, and disbanding of groups. While in a traditional group-work setup, participants could use a “collaborative surface” such as a table or a blackboard for information sharing, our distance learning approach would obviously require different collaborative means.

In [3] we have conducted a classification of different technology-enhanced collaborative surfaces (TECS), some of which could be enhanced for online and distance learning. While we have described TECS-I and TECS-II surfaces as whiteboards enhanced with digitizing capabilities and digital ink, in distance education set outs these surfaces can be replaced by touch sensitive displays and tablets, which would help facilitate learning communities and contribute to better educational experiences. This concept is conceivable, either at home or in distance collaboration classrooms, due to the growth of the Bring Your Own Device (BYOD) educational approach [6]. The devices owned by the students are equipped with the technological hardware features and software apps to access a ubiquitous learning experience. As a result, new instructional methods could be crafted applying Tangible Augmented Reality (T-AR) technologies. In this way, the possibility exists to develop and share innovative and interactive learning spaces, integrating and merging the computer-generated learning materials with the real world experiential data and stimuli.

3 Data Institute

A new academic discipline is usually fostered in a department in which faculty gradually begin pursuing research and offering courses in the new field. Data science, however, is rooted in at least three disciplines—computer science, mathematics, and

statistics—with applications in virtually every other academic discipline. As a result, establishing a cross-functional foundation to support transdisciplinary research and training in data science is critical, requiring a unique approach. Such an approach will eliminate barriers created by the different terminology and formalisms created in the fields that use data science; give algorithms developed for theoretical purposes a sound context to account for the peculiarities of data science; provide a bridge among scientists and stakeholders in this arena, an already existing reality in terms of industry and scientific enterprises; and effectively support the training of graduating data science experts with solid foundations, practical experience, and communication skills across the involved disciplines.

Data science requires strong links among education, the sciences and the businesses that need data analytics. To operationalize such links, we propose to establish an institute of data science within the SUNY system—one of the largest university systems in the USA. The SUNY-Data Science Institute would combine faculty and members from different institutions, disciplines, and roles (researchers, teachers, consultants, and others) to advance the transdisciplinary research and training in data science, with a focus on infusing practical applications with data science theory. The institute is aimed at promoting the development of foundational knowledge, the implementation of novel, effective classroom training techniques, and the incorporation of experiential learning. The structure of the institute is illustrated in Fig. 2.

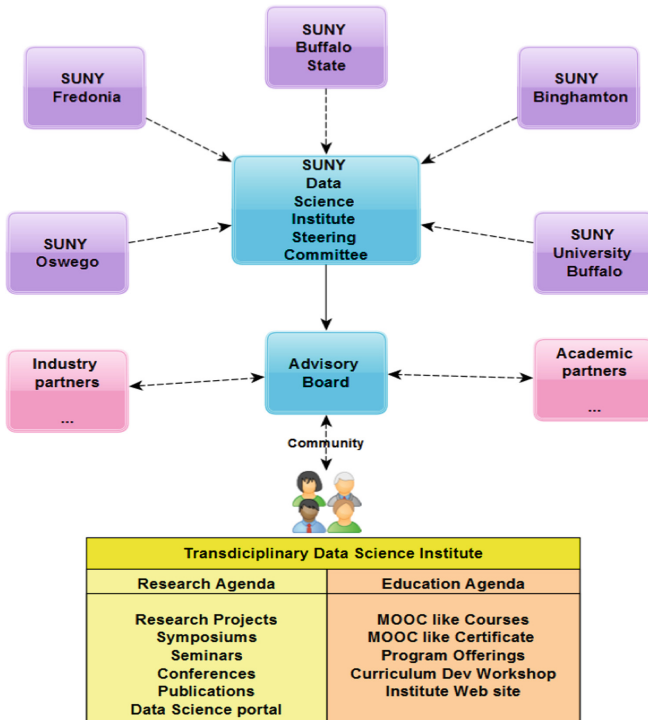


Fig. 2. SUNY data science institute structure.

The consortium of SUNY institutes included has applied for a National Science Foundation grant with the following goals:

1. **Create a SUNY-Data Science Institute** to serve as a catalyst for defining the scientific infrastructure necessary to enable the science of data.
2. **Define and launch the research agenda of the Institute** to foster the mapping of the theoretical realms of data science to the practical realms of applied science and industry.
3. **Define and launch the educational agenda of the Institute** through innovative instructional methods and technology.
4. **Define and launch the community sharing and dissemination** of methods, tools, and processes to benefit local partners, the local community, NY state, the country, and the world.
5. **Evaluate and improve the Institute's performance** at enabling the enrichment and transfer between theory and practice in data science.
6. **Share the unique infrastructure** as a model for other parts of the country and the world.

Most of the Institute's activities will be managed and documented online. The five Principal Investigators (PIs), from five different institutions constitute the Steering and Oversight Committee and will manage all aspects of the Institute. An Advisory Board will be established, comprised of the Institute's administration as well as members of organizations served by the Institute. These members will represent a broad range of stakeholders, including academics from diverse STEM and applied disciplines, commercial enterprises, government, and non-governmental organizations. The PI's, Co-PI's, Senior Personnel, and Advisory Board members from industry and academia constitute the Board of Directors. This group will oversee the assignment of specialized tasks to subgroups from the Board.

4 Conclusion

The paper considers a versatile approach towards education in data analytics, describing synchronous and asynchronous distance education; sharing of resources; and tangible interfaces. Examples of various tactics at SUNY are given. Particularly, it is proposed to create a SUNY Data Science Institute, which will facilitate the education and scholarship in the field of data analytics among faculty.

Acknowledgments. Part of the work reported in this article is supported by the 2017 Cooperative Research Project at Research Center of Biomedical Engineering and Research Institute of Electronics, Shizuoka University.

The pilot VIDIA project was funded by a SUNY Innovative Instruction Technology Grant (IITG), 2012, renewed 2013 [5, 20, 22].

V. Brimkov is on leave from the Institute of Mathematics and Informatics, Bulgarian Academy of Sciences.

References

1. Argote, L., Insko, C.A., Yovetich, N., Romero, A.A.: Group learning curves: the effects of turnover and task complexity on group performance. *J. Appl. Soc. Psychol.* **25**, 512–529 (1995)
2. Barneva, R., et al.: Japanese Journal of Applied Physics Conference Proceedings 4, ID 011617 (2016)
3. Barneva, R., et al.: Integrating technology-enhanced collaborative surfaces and gamification for the next generation classroom. *J. Educ. Technol. Syst.* **45**(3), 309–325 (2017)
4. Bichindaritz, I.: <https://www.coursera.org/learn/data-genes-medicine>
5. Big Data on a Small(er) Campus: use of large-scale text analysis by a comprehensive primarily undergraduate institution. <http://commons.suny.edu/iitg/big-data-on-a-smaller-campus-use-of-large-scale-text-analysis-by-a-comprehensive-primarily-undergraduate-institution/>
6. Chen, R., Wang, X.: Conceptualizing tangible augmented reality systems for design learning. In: *Design Computing and Cognition '08*, pp. 697–712 (2008)
7. Cho, H., et al.: Social networks, communication styles, and learning performance in a CSCL community. *Comput. Educ.* **49**, 309–329 (2007)
8. Cook, D.A., et al.: Internet-based learning in the health professions: a metaanalysis. *J. Am. Med. Assoc.* **300**, 1181–1196 (2007)
9. Cruz, W.M., Isotani, S.: Group formation algorithms in collaborative learning contexts: a systematic mapping of the literature. *Lecture Notes in Computer Science. Collaboration and Technology*, pp. 199–214 (2014)
10. IBM: What is a Data Scientist? <https://blog.ibm.jobs/2014/01/29/what-is-a-data-scientist/>. Accessed 29 Jan 2014
11. Kanev, K., Kimura, S.: Collaborative learning in dynamic group environments. In: Jin, Q. (ed.) *Distance Education Environments and Emerging Software Systems: New Technologies*, pp. 1–14. IGI Global (2011)
12. Kirschner, P.A., Erkens, G.: Toward a framework for CSCL research. *Educ. Psychol.* **48**, 1–8 (2013)
13. McLennan, M., Kennell, R.: *Comput. Sci. Eng.* **12**(2), 48–52 (2010)
14. Orange. <https://orange.biolab.si/>
15. PSPP. <https://www.gnu.org/software/pspp>
16. Rajpurohit, A.: Businesses Will Need One Million Data Scientists by 2018. <http://www.kdnuggets.com/2016/01/businesses-need-one-million-data-scientists-2018.html>
17. Rapidminer. <http://www.rapidminer.com>
18. Rstudio. <http://www.rstudio.com>
19. Spyder. <https://pythonhosted.org/spyder/>
20. SUNY Innovative Instruction Technology Grants (IITG). <http://commons.suny.edu/iitg/>
21. Top 5 free video chat software for groups up to 12 people. <http://www.freemake.com/blog/top-video-chat-software-for-video-calls-with-up-to-25-people/>
22. VIDIA: Virtual Infrastructure for Data Intensive Analysis. <http://commons.suny.edu/iitg/virtualinfrastructure-for-data-intensive-analysis-vidia-2/>
23. Weingart, L.R.: Impact of group goals, task component complexity, effort, and planning on group-performance. *J. Appl. Psychol.* **77**, 682–693 (1995)

BYOD Collaborative Kanji Learning in Tangible Augmented Reality Settings

Federico Gelsomini^{1,2(✉)}, Kamen Kanev^{2,3}, Patrick Hung³,
Bill Kapralos^{2,3}, Michael Jenkin^{2,4}, Reneta P. Barneva⁵,
and Mariagioia Vienna¹

¹ Sapienza University of Rome, P. le Aldo Moro 5, 00185 Rome, Italy
federico.gelsomini@uniroma1.it

² Shizuoka University, 3-5-1 Johoku, Naka-ku, Hamamatsu 432-8011, Japan

³ UOIT, 2000 Simcoe St N, Oshawa, ON L1H 7K4, Canada

⁴ York University, 4700 Keele St, Toronto, ON M3J 1P3, Canada

⁵ SUNY Fredonia, 280 Central Ave., Fredonia, NY 14063, USA

Abstract. In this work, we consider the challenges of studying Japanese, both as a mother tongue and as a second language, stemming from the complexity of its writing system employing over 2000 ideograms (kanji) and two different alphabets. We discuss a novel educational approach based on computer assisted collaborative learning incorporating direct interactions with digitally encoded physical artifacts acting as tangible interfaces components. The learning experiences are further enhanced by the BYOD based Virtual and Augmented Reality support engaging the tangible interface objects as physical attractors for focused discussions and collaboration.

Keywords: BYOD · Collaborative learning · M-CSCL · Tangible Augmented Reality T-AR · Laser marking

1 Introduction

Students of Japanese as a second language (JSL), either in school or in college, often experience difficulties learning over 2000 different Chinese characters. These Chinese derived ideograms are called *kanji*, and most of these kanji characters have multiple readings. Together with them, the *hiragana* and *katakana* syllabic alphabets are also used to form the Japanese modern writing system. The exposure to kanji characters happens to be the most challenging phase of both teaching and learning of the Japanese language. In an effort to stimulate faster development of kanji character deciphering, reading, and writing skills, many educational approaches resort to retention enforcement and rote memorization. This is particularly true when a learner of JSL comes from an alphabetical linguistic system [1].

Among the various implications of teaching and learning kanji in the course of developing generic Japanese reading skills, different models have been proposed and analyzed by a number of authors [2], who are trying to clarify issues in JSL kanji learning and instruction. In our earlier work [3] we considered different approaches for enhanced learning of kanji characters exploring the employment of tangible, Virtual

Reality (VR), and Augmented Reality (AR) toys as teaching aids and discussing their limitations. Other authors have conducted similar studies with respect to the employment of augmented tabletop applications [3, 4] for developing better kanji understanding and study approaches.

In this paper, we focus on extending the AR application approach with ad-hoc designed scaffolds of collaborative kanji learning settings employing Tangible Augmented Reality (T-AR). In this context, we introduce the notion of digitally-enhanced tangible interface components as attractors and building blocks for collaborative learning activities. As most of the modern kanji characters are decomposable in recurring components (*radicals*), in our approach those components can serve as starting points of different T-AR interactions for focused learning. This can be considered as a functionally enhanced T-AR based version of kanji learning stemming from the traditional printed (2D) kanji training sets widely available off the shelf. The proposed T-AR approach extends such training sets to 2.5D and even 3D where the radicals are redesigned as physical artifacts that are created with a 3D printer or manufactured. To enable AR capabilities, such artifacts are digitally encoded either at the time of printing or afterwards by laser marking [5] and used as building blocks for collaborative learning activities involving both construction and decomposition of kanji and compound words (*jukugo*).

In the course of the collaborative learning process, learners use AR-enabled devices, to point at and interact with the digitally enhanced physical objects thus obtaining suggestions with respect to meaning, pronunciation, usage, composition, and so on. We are currently evaluating the potential of the Bring Your Own Device (BYOD) model and its possible use in the construction of our novel Mobile Computer Supported Collaborative Learning (M-CSCL) environment with embedded T-AR support. Such a learning setting will support students in their choices and learning tasks through their own mobile devices, enabling them to interact in a novel and enhanced manner with the kanji characters while developing their collaborative skills.

2 Kanji Learning

Most of the difficulties in the process of learning the Japanese language stem from the complexity of its writing system, which has been deemed by many educators to be particularly difficult to convey to new learners, given the large number and the multiple readings of the kanji characters on top of the hiragana and katakana alphabets [6] (Fig. 1). Such excessive difficulties in learning to read and write Japanese often lead to discouragement, lack of motivation, and ultimately study abandonment, especially for students coming from a non-kanji background [7].

2.1 Difficulties and Importance of Kanji Learning

Acquiring proper kanji knowledge for reaching a particular level of proficiency is a complex, and difficult to complete task. It entails, the student acquiring a range of different strategies to interpret and learn the different orthographic elements, patterns



Fig. 1. Example of using kanji, hiragana, and katakana in the same sentence.

and rules, which are also generally related to the learning of new lexical elements. This is a fundamental process that takes place in the acquisition of Japanese both as a native tongue and as a second language [8].

At the same time, Japan has one of the highest literacy rates in the world. However, such a high proficiency rate does come with a price, and more specifically, a minimum of 12 years of schooling are required for a native Japanese person to reach the required level of proficiency with respect to the fundamental *Jouyou Kanji* (Regular Use Kanji). While kanji reading proficiency appears to be stable, with less and less handwriting practice in our computerized world, many native Japanese people are currently experiencing difficulties recalling how to write rarely used kanji characters. While this may be considered a minor problem for native Japanese speakers, for a JSL learner with an alphabet-based mother tongue just maintaining the global amount of kanji needed in everyday life situations may be intimidating and perceived as too hard to sustain.

2.2 Existing Technological Solutions and Possible Extensions

Various approaches involving software applications, specialized hardware, and tools have been employed to address the problem of kanji learning, many of them relying on novel technologies, devices, and methods. Among the multimedia assisted kanji learning tools, for example, the most widely used are various types of flashcard programs [9].

Other scholars have explored the use of collaborative AR in teaching kanji to software users. The approach presented in [10] is representative. Their approach is positioned as a computer game between two players in an Augmented Reality setting and uses mobile computing devices (e.g. PDAs) enabled with optical marker-based tracking to augment these real-world targets. In another approach employing a story-based kanji learning method [4], experiments were conducted with a system involving physical assembly of kanji components, creation of descriptive mnemonics to remember part-to-whole relationships, and projection of video as procedural guidance. The authors report a higher engagement and better student results with the addition of AR media to the mnemonics.

In our earlier work, while focusing on the application of AR to kanji learning, we have also addressed the use of augmented toys [3]. Our ideas stem from the observation that symbol and object resemblance can support, to a certain degree, the acquisition of kanji shape and meaning through object transformations similar to the Bandai's *Mojibakeru* physical toys [11] (Fig. 2).

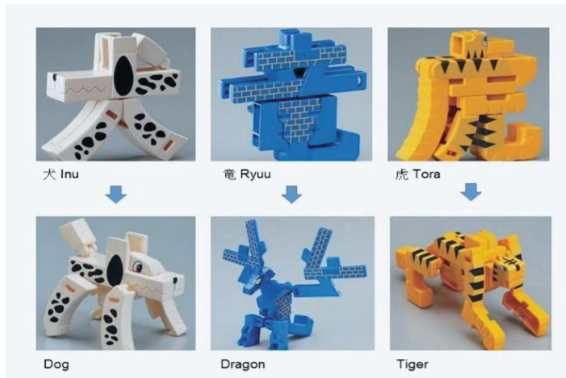


Fig. 2. Mojibakeru transformable toys.

Given the large number of kanji characters and the need to implement a specific transformation for every meaning the physical toy approach becomes impractical. Therefore, instead of physical toys, we use in our system AR toys, that greatly reduce the implementation cost and allow for higher levels of abstraction in the transmutation process and the explanation of abstract notions and difficult to convey concepts. Another more tangible assistive kanji learning environment is discussed in [12] where the interactive kanji composition is supported by a dedicated AR infrastructure. Our system is based on augmented physical card targets, whose content is enhanced with virtual layers. Such AR kanji learning links the virtual representation of a character to its physical one, thus allowing students to explore different possible combinations. A revised version of this approach employs 3D printing for experimental manufacturing of various 2.5D and 3D kanji components.

In this work, we continue to build upon the AR approach that we have discussed so far, aiming at expansions beyond the employment of toys and fixed game settings. More specifically we are focusing on designing a framework for kanji learning activities in collaborative settings employing T-AR environment interactions and adhering to the BYOD model. The framework relies on 3D printing technologies for fast prototyping and test production of augmented physical object as building blocks in the construction of kanji knowledge. Through advanced digital encoding implemented as surface or undersurface information layers associated with the objects we create durable and practically undetectable marking for direct tracking and interactions [13] (Fig. 3).



Fig. 3. Kanji composition. Each differently colored and numbered radical represents a T-AR interactive object.

3 The Novel T-AR Kanji Learning Approach

In 2011, the Japan Foundation released a report identifying and discussing a range of language education related problems, the most serious of which appeared to stem from the inadequateness of some widely employed teaching methods [14]. Indeed the kanji teaching methodologies for native Japanese speakers and for JSL students seem to be almost equivalent, despite that non-native learners have to deal with the written and spoken elements of the language simultaneously while facing serious restrictions on the time allocated for learning the characters [15]. In this work we attempt to address and tackle the above problem by proposing a novel, more flexible strategy for kanji learning. It stems from the derivative and summative usage of the learning involving the interventional sub-strategies discussed in [16], namely: morphological analysis, rote memorization, context-based strategies, association methods, meta-cognitive strategies, helplessness, and mnemonic, contextual, and rote learning.

We believe that a T-AR setting together with a collaborative learning methodology supporting BYOD modalities will be in a position to properly address many of the problems associated with the previously discussed strategies by significantly expanding the scope of kanji learning through novel technologies, presentation media, digitally enhanced artifacts, and tangible interactions. As pointed out in previous research, classroom learning mediators comprise of tasks, teacher and peer resources, subject content, and semiotic artifacts. From a Vygotskian perspective, the mediation by artifact concept [17] stipulates that knowledge building itself can assume as starting points physical artifacts. Such artifacts are used either as a medium or as a production and represent by themselves knowledge building artifacts [18]. In this context we introduce AR capabilities and augmented interactions that are supported by digital encoding of the said artifacts. This is done either at the time of printing or afterwards by laser marking [5] and the artifacts are consequently used as physical building blocks for collaborative learning activities. This methodology confronts students with both construction and decomposition of kanji and compound words (*jukugo*) in a tangible set out that is designed to render as memorable and meaningful as possible the formation of the character.

In the course of the collaborative learning process students would be able to use AR-enabled devices, such as smartphones or tablets, to point at and interact with the digitally enhanced physical objects thus obtaining suggestions with respect to meaning, pronunciation, reading, composition, contextual usage and useful mnemonics, all in a multimedia format. The interactions are regulated by a series of tasks, prepared by the

teacher before the activity and presented to the students once they point at an augmented object. As each student can be recognized by the system through an ID associated with his/her device, the entire process can be tracked and guided so that the AR based suggestions and aids follow and support the learning path of each particular student.

We are currently evaluating the potential of the Bring Your Own Device (BYOD) model and its implications on the construction of our novel Mobile Computer Supported Collaborative Learning (M-CSCL) environment with embedded T-AR support. Through BYOD, such a model can take advantage of the ubiquitous possession of mobile and connected devices [19] greatly reducing the deployment time and cost. Similar approaches have already been employed by some of the leading educational software producers and universities to create innovative and interactive learning environments with BYOD Learning Management Systems (LMS) like *Top Hat* [20] and *SmartClass+* [21].

Such a learning setting provides support for both teachers with their educational activities, and students with their studies and practical exercises. Learning objects and learning tasks can be made accessible through student mobile devices not only on campus but also at home and in other public places, e.g. during commuting. This will allow students to interact in a novel and enhanced way with Japanese characters while developing their collaborative skills in ubiquitous communication environments.

3.1 Data Encoding and AR Image Processing

The tangible artifacts employed in our methodology can be implemented as plastic objects with digitally encoded information layers for recognition and tracking. This type of marking allows constructing different patterns of machine-readable patches not only on the surface but also in the subsurface region of the objects through laser induced damage. This way, subsurface encoding layers with greatly improved durability can be created in contrast to other methods such as printing and laser ablation which are limited to surface modifications.

A range of plastic materials that are opaque in the visible light spectrum become semitransparent when irradiated with infrared light. This opens possibilities to induce damage in the subsurface layers and in the bulk of such materials by tightly focused pulses of an infrared laser beam. Such pulses penetrate with ease into the bulk of the plastic objects and cause nonlinear alteration of the plastic material in the highly localized area at the focal point [22]. The laser beam motion and pulsing is further programmed for controlled alteration of selected regions of the object to construct layers with digitally encoded information. Such digital encoding is well protected from environmental and manipulative damage since it is enclosed in the bulk of the object.

Alternatively, a single digital encoding layer can be situated in the subsurface region of the object (at tens of μm depth) where the information is again well protected and cannot be easily modified or erased [5]. As indicated by the experiments that we have conducted, this process is applicable to a wide range of plastic materials and can be carried out with a fairly low-cost laser with limited power. While practically invisible for the naked human eye, the encoded data can be reliably extracted by a computer-based vision system with proper magnification and lighting. Therefore, once

an object is encoded with machine-readable information as described above, it can be used for building augmented interfaces and tangible Human-Computer Interactions (HCI).

3.2 The BYOD Concept and Its Use in Education

The advances in mobile computing and the ubiquity of mobile devices have reshaped our world allowing us to interact in different and unconventional manners with the surrounding environment. Employing the BYOD concept in educational environments opens a wide range of new opportunities for innovating and optimizing the teaching and learning. Students, for example, become easily identifiable with a possibility to track their involvement in the educational process based on the sensors built in their own devices. Any privacy concerns related to information gathering are easily resolved in this case since all information is confined to the devices that students own. The processing of the gathered information can also be carried out on the owner's device then a selected subset along with some aggregate information can be communicated to the educational institution on a need-to-know basis. Another distinct advantage of the BYOD concept is that it shields the institutional computing facilities such as servers and high-performance computer clusters from their end users. Instead of direct access, students will employ their own devices which are well known to them and can thus serve as a convenient easy to use interface to the institutional computing facilities.

In mobile settings, real-time vision technologies such as tracking, object and scene recognition, localization, and scene model construction are essential for overlaying the virtual and the real worlds and creating AR educational environments. In contrast to static computer environments, however, mobile set outs face a range of limitations with respect to battery life, processing power for applications, and memory capacity that are essential for building robust AR and other interactive applications [23]. To support mobility, current portable devices will typically incorporate various detectors and sensors such as gyroscopes, accelerometers, and magnetometers that help determine the position and orientation of the device with respect to the environment. Some portable devices are designed for specific tasks, e.g. game controllers, audio and video players, and may thus have limited interfaces and functionality. Most of the modern mobile computing devices, however, are touch screen based and equipped with digital cameras, biometric sensor, Radio-Frequency Identification (RFID), Global Positioning System (GPS), and other technologies that render them suitable for surface interaction, image processing, motion tracking, biometric, and other applications [13].

Our M-CSCL framework takes into account the above outlined benefits of the BYOD concept and attempts to build upon the mobility and AR related advantages that can be employed in the development of more advanced T-AR educational approaches.

3.3 The BYOD Aware M-CSCL with AR as a Language Learning Framework

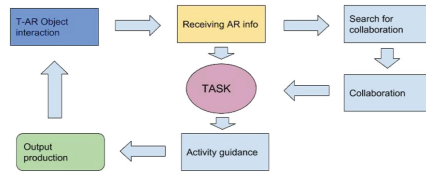
The BYOD concept that we adopt requires universal support of a variety of mobile devices owned by the student so adequate software engineering, design, and development technologies must be employed. Based on our preliminary research and

experiments of different platforms for development of iOS, Android, and Window mobile applications, we have identified the Unity platform [24] as one of the most suitable for BYOD compliant software development. It provides direct support for imaging, VR, and AR applications that can be developed and extensively tested within the Unity environment through embedded simulators for different target platforms. A final application can then be generated for any of the supported target platforms without any platform specific development and coding. So far, we have used this Unity-based approach to create AR-based educational applications for instruction and training of medical students and practitioners [25].

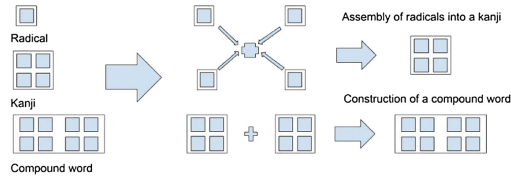
Language acquisition and training require much broader coverage including practically all concepts, notions, and artifacts we face in our daily activities. A comprehensive implementation of this for any language will obviously require an enormous amount of work incurring high costs. With respect to Japanese language learning that we use as a test bed platform, we minimize the amount of work and related cost by focusing on the writing aspect of the language and in particular on the composition of the kanji. This however, does not restrict the generality of our coverage, since many kanji characters are derived from real artifacts and actions, etc. representing notions and concepts that can be mapped back to the real world and presented to the language learners in a more tangible way for better understanding and remembrance.

As shown in Fig. 4a, our educational framework incorporates T-AR objects implemented as digitally enhanced physical artifacts. These artifacts are then recognized and tracked based on the information encoded and permanently embedded in them. The identification and tracking information is then used for synchronizing the views of the related physical objects with their VR counterparts and thus presenting an enhanced AR view to the student. Enhanced AR views can contain additional explanations, instructions and study guidance to facilitate the learning process. Our study framework is specifically designed to support and enhance collaborative activities between students which are considered an important component of the learning process, essential for the proper acquisition of the language. With respect to collaboration, the digitally enhanced artifacts play the role of physical attractors or objects marking points of interest. In this way, based on the content of their assignments, their study progress, and the guidance provided by their mobile devices with respect to the physical attractors, students engage in group work and collaborative activities. In Fig. 4b, we present a specific example of collaborative activities when kanji character components (radicals) are used as physical attractors. The language learning goals in this example are confined to the meaning of the kanji components and how to assemble them into valid kanji character followed by learning the meanings, multiple readings, and the general usage of the constructed kanji. This concept is further extended with the creation of compound words incorporating more than one kanji and possibly hiragana characters.

The employed BYOD aware M-CSCL method extended with AR capabilities and tangible interface support creates a solid foundation for building different types of educational frameworks to support the studies on novel learning design theories and their practical implementations. In a more general perspective our results could be linked to other educational areas not directly related to language learning [26].



(a) Educational Framework



(b) Kanji composition

Fig. 4. The study framework (a) and an example of its use for kanji learning (b).

4 Conclusion and Future Work

In this work, we have discussed various approaches for supporting and augmenting the learning experiences in the course of Japanese language acquisition both as a mother tongue and as a second language. We have identified a range of fundamental problems and challenges with respect to the development of graphemic, phonetic, and semantic kanji processing skills needed for approaching and successfully deciphering Japanese texts. To assist this process, we have introduced a novel T-AR learning approach employing physical objects as interface components and attractors for focused discussions and collaboration. To ensure more extended BYOD coverage we are planning to conduct more experimental work and implementations in a platform independent way under Unity [24].

Acknowledgements. Part of the work reported in this article is supported by the 2017 Cooperative Research Project at Research Center of Biomedical Engineering and Research Institute of Electronics, Shizuoka University.

References

1. Matsunaga, S.: Teaching and learning to read kanji as L2: why are they difficult? In: Xing, J., Ng, P.-S. (eds.) *Indigenous Culture, Education and Globalization*, pp. 245–262. Springer, Berlin Heidelberg (2016)
2. Mori, Y.: Review of recent research on kanji processing, learning, and instruction. *Jpn. Lang. Lit.* **48**, 403–430 (2014)

3. Kanev, K., Oido, I., Hung, P.C.K., Kapralos, B., Jenkin, M.: Case study: approaching the learning of kanji through augmented toys in Japan. In: Hung, P.C.K. (ed.) *Mobile Services for Toy Computing*, pp. 175–192. Springer Int. Publishing, Cham (2015)
4. Lin, N., Kajita, S., Mase, K.: Collaborative story-based kanji learning using an augmented tabletop system. *JALT CALL J.* **2009**(5), 21–44 (2009)
5. Mizeikis, V., Kanev, K.: Sub-surface laser encoding of physical objects for enhanced privacy and digital security. *Jap. J. Appl. Phys. Conf. Proc.* **4**, 011602(1–6) (2016)
6. Gamage, G.H.: Perceptions of kanji learning strategies. *Aust. Rev. Appl. Linguist.* **26**, 17–30 (2003)
7. Grainger, P.: Second language learning strategies and Japanese: does orthography make a difference. *Syst.: Int. J. Educ. Technol. Appl. Linguist.* **33**, 327–339 (2006)
8. Mori, Y.: Five myths about “Kanji” and “Kanji” learning. *Jpn. Lang. Lit.* **46**, 143–169 (2012)
9. Librenjak, S., Vučković, K., Dovedan, Z.: Multimedia assisted learning of Japanese kanji characters. In: *2012 Proceedings of the 35th International Convention MIPRO*, pp. 1284–1289 (2012)
10. Wagner, D., Barakonyi, I.: Augmented reality kanji learning. In: *Proceedings of the Second IEEE and ACM International Symposium on Mixed and Augmented Reality*, pp. 335–336. IEEE Computer Society (2003)
11. Mojibakeru. <http://www.dannychoo.com/en/post/25596/Mojibakeru.html>
12. Kanev, K., Oido, I., Yoshioka, R., Mirenkov, N.: Employment of 3D printing for enhanced kanji learning. In: *Proceedings of the Joint International Conference on Human-Centered Computer Environments HCCE 2012, Aizu-Wakamatsu, Japan, 8–13 March*, pp. 165–170 (2012)
13. Kanev, K.: Augmented tangible interface components and image based interactions. In: *Proceedings of the 13th International Conference on Computer Systems and Technologies*, pp. 23–29. ACM, New York (2012)
14. Paxton, S., Svetanant, C.: Tackling the kanji hurdle: investigation of kanji learning in non-kanji background learners. *Int. J. Res. Stud. Lang. Learn.* **3**, 89–104 (2013)
15. Tollini, A.: The importance of form in the teaching of kanji. *世界の日本語教育 (Sekai no Nihongo Kyooiku)*, **4**, 107–116 (1994)
16. Mori, Y., Shimizu, H.: Japanese language students’ attitudes toward kanji and their perceptions on kanji learning strategies. *Foreign Lang. Ann.* **40**, 472–490 (2007)
17. Stahl, G.: Contributions to a theoretical framework for CSCL. In: *Proceedings of the Conference on Computer Support for Collaborative Learning: Foundations for a CSCL Community*, pp. 62–71. Int. Society of the Learning Sciences, Boulder (2002)
18. Wong, L.-H.H., Chen, W., Jan, M.: How artefacts mediate small-group co-creation activities in a mobile-assisted seamless language learning environment? How artefacts mediate small-group co-creation activities. *J. Comput. Assist. Learn.* **28**, 411–424 (2012)
19. Burston, J.: The future of foreign language instructional technology: BYOD MALL. *EuroCALL Rev.* **24**, 3–9 (2016)
20. Homepage - Top Hat. <https://tophat.com/>
21. Robotel Language Laboratory. <https://www.robotel.com/>
22. Juodkakis, S., Mizeikis, V., Misawa, H.: Three-dimensional microfabrication of materials by femtosecond lasers for photonics applications. *J. Appl. Phys.* **106**, 051101 (2009)
23. Turk, M., Fragoso, V.: Computer vision for mobile augmented reality. In: Hua, G., Hua, X.-S. (eds.) *Mobile Cloud Visual Media Computing*, pp. 3–42. Springer Int. Publishing, Cham (2015)
24. Unity- Game Engine. <http://unity3d.com>

25. Nguyen, M., Uribe-Quevedo, A., Jenkin, M., Kapralos, B., Kanev, K., Jaimes, N.: An interactive virtual reality environment for image based fundus examination training, abstracts and short communications. In: Fifth International Symposium CompIMAGE'16 - Computational Modeling of Objects Presented in Images: Fundamentals, Methods, and Applications, Niagara Falls, USA, 21–23 September 2016
26. Chen, R., Wang, X.: Tangible augmented reality for design learning: an implementation framework. In: International Conference on the Association for Computer-Aided Architectural Design Research in Asia (2008), pp. 350–356 (2008)

Flipping Out in Japan: Engineering the Academic English Classroom for Innovation

Valerie Anne Wilkinson¹(✉) and Damon Michael Chandler²

¹ Faculty of Informatics, Shizuoka University,
Hamamatsu, Shizuoka 432-8011, Japan
vwilk@inf.shizuoka.ac.jp

² Faculty of Engineering, Shizuoka University,
Hamamatsu, Shizuoka 432-8011, Japan
chandler.damon.michael@shizuoka.ac.jp

Abstract. Inspired by Simon Sinek’s TED Talk, “How Great Leaders Inspire Action” (2009) and Carol Dweck’s *Mindset* (2006), George Couros’s book, *The Innovator’s Mindset* (2015) builds idea of a “flipped classroom”. Couros’s thinking resonated with an American engineer, partnering with a seasoned language teacher. The routine class, Academic English, required for all third year Electrical/Electronic Engineering students presents a context for creative improvisation. We are “flipping” the classroom. Standard Academic English is simple. Right? The true case is that is not a simple matter at all. Too much vocabulary for too long a time period is stultifying and hypnotic. A 90-minute class once each week is not the best setting, either. The problem is how to teach a substantial amount of technical vocabulary to a large number of Japanese “false beginners,” who have studied English since age twelve, yet who evidently do not wish to speak or be seen to understand spoken English. This situation led to the experimental “flipped” classroom, in which homework is done outside of the class while class time is devoted to laboratory/workshop activities in teams. The investigator roles are Professor and Language Facilitator (Principle Investigator). In this work, we set up the experiment of a new vocabulary learning strategy (VLS), “flipped classroom” combined with Middle-Up-Down2 management style and the SECI3 model of dynamic knowledge creation. Via an intensive 15-week course, students are being immersed in an international-style conference setting, where they must regularly participate in mini-poster presentations on various technical topics. Our research shows that the topic of vocabulary learning strategies (VLSs4) focused on evaluating the efficacies of existing techniques rather than creating new techniques. Furthermore, previous VLS studies largely aimed at word recall rather than on context mastery. In this study, we specifically ask if the use of e-VLS comprised of mini-poster sessions and centered on a core set of engineering vocabulary can have a significant impact on English listening and speaking skills.

Keywords: Experiential learning · Innovation mind-set · English vocabulary learning strategy (e-VLS) Mini-Poster-Presentation · Middle-Up-Down management · Socialization-Externalization-Combination-Internalization (SECI) · Task-Based-Language-Learning (TBLL) · English for academic purposes (EAP) · English for specific purposes (ESP)

1 Introduction

1.1 Motivation

Despite decades of strategic planning, reform, and input from scholars, spoken English remains a largely elusive goal for many Japanese university students. Japanese students memorize endless lists of often irrelevant words, numerous sets of confusing grammar rules, and tricks for succeeding on entrance exams given only a very shallow understanding of what is written or spoken. Not surprisingly, 6–8 years of such intensive study makes the vast majority of university students in Japan “false beginners” who cannot hold even a basic conversation in English.

The class entitled “Academic English for Electrical Engineers” is a standard language class for Shizuoka Faculty of Engineering, required for third year majors. The American Electrical and Electronic Engineer was recruited from the University of Oklahoma, came to Japan, and was specifically asked to teach Academic English as part of his course load. Like many foreigners who come to Japan and are asked to teach English, this teacher was plainly hired for his engineering qualifications and not for his English language teaching. The English teacher obtained the honor of a position on the Faculty of Informatics with the requisite PhD (It happens to be Comparative Literature). She teaches the class titled “Communication Skills One” required of all Informatics freshmen for graduation. For the scientist and the scholar at Shizuoka University, one aspect of the problem is whether to teach English or to teach in English. We have to come to terms with the demands of the class and hiring institution.

1.2 The Task: What Is ACADEMIC ENGLISH?

When undertaking the task of preparing for a new class, it is a good idea to make a survey of the field. Three examples from a random global search for classification found: (1) University of Delaware has an English Language Institute (ELI) which has the following copy for English for Academic Purposes (EAP): “The ELI has developed a strong reputation for its university preparation programs. We specialize in providing **comprehensive preparation** for international students who plan to pursue their undergraduate (i.e., bachelor’s) or graduate (master’s or doctoral) degrees in the United States. **This means that some of our programs not only focus on Academic English development, but also developing the social skills, leadership skills, and academic skills that are necessary for a successful and well-rounded university experience.**” In other words, ELI provides EAP for acculturation and socialization as well as the vocabulary, grammar, and composition of the English language itself.

(2) The British Association of Lecturers in English for Academic Purposes (BALEAP) gives another summary in the 2015 Proceedings of their conference: “This volume gives an insight into the current state of EAP through the prescribed and emergent themes. It is divided into four sections: Globalisation, acculturation, socialisation; Knowledge of ourselves and of our learners; Approaches to genre and discourse; and Achieving specificity.” The academic register of this conference is clearly aimed at practitioners, for the phrase “Knowledge of ourselves and of our learners” includes the lecturers themselves, while the phrase “Approaches to genre and

discourse” appeals to the higher order classification of language by holders of advanced degrees in language teaching. This summary provides a terse outline of the field, including the specificity which an Electrical/Electronic engineer majoring in image processing could bring to two large classes of twenty year old students

Finally (3) in Romania, Violate Negrea made comprehensive summary with her *English for Specific Purposes (ESP): Curriculum Development* [10]. The link to the pdf is included in the references, below. One striking addition to her thoroughly researched book is the reference (pages 3 and 4) to David Carter’s 1983 ground breaking schema:

3 Types of ESP		
(1) English as restricted language. Language for ex. Aviation, medical procedures, etc.	(2) English for Academic and Occupational. Broad range language for master and doctoral candidates.	(3) English with restricted topics. “Academic English for Engineers” falls into this category.
Only used for specific contexts. This type of English may not help to communicate effectively outside of the specific context.	(a) EAP Academic English for general and specific capabilities. (b) EOP English for technicians.	This English is uniquely concerned with anticipated future needs, for a graduate class, conference, or job interview.

David Carver’s (David Carter *sic.*) schema is the most widely cited of the general references one could locate in the discovery portion of background references because he created an easily disseminated chart. Received from:

(<https://image.slidesharecdn.com/esp-englishforspecificpurposes>). This review situates Academic English as a class for English for Special Purposes. Our approach is to focus on Presentation.

1.3 Background and Motivation

One of the most important objectives of college education is to provide the requisite variety that students need in order to develop themselves and learn how to identify their own strengths and weaknesses while developing their own learning strategies. Japanese students are quite adept at self-regulated learning (SRL), particularly when it comes to topics in science, technology, education, and math (STEM), topics on which students from other nations often struggle. In fact, the traditional Japanese university teaching framework seems to have evolved to rely heavily on students’ SRL skills. Most university classes meet only once a week for 90 min, where the material is traditionally delivered in a one-way, lecture-type setting. The impetus is placed on the students’ discipline and SRL skills to learn via homework assignments. This symbiosis between teaching framework and SRL is quite effective for all of the subjects that a typical Japanese undergraduate student will encounter—with one exception: English. When it comes to learning English as a foreign language (EFL), the situation is completely reversed.

Much research in second language (L2) learning still fails to substantiate the common-sense view that perhaps the root causes of the general lapse of English

language achievement nationally, lack of commitment and poor listening skills are two predominant explanations. L2 scholars are highly refined linguists whose elegant work provides insight into “natural learning”, for example. But I am not a linguist *per se*. Vocabulary learning strategies (VLSs) can assist in the first regard, but they largely fail to leverage the capability of vocabulary imprinting attained from repeated speaking experiences. Prior research on the topic of vocabulary learning strategies (VLSs) has focused on evaluating the efficacies of existing techniques rather than creating new techniques. Furthermore, previous VLS studies have largely aimed at word recall rather than on context mastery.

1.4 The Problem

The situation in at the Academy in Japan is that that most beginners are “false beginners.” Teaching false beginners and absolute beginners require different approaches.” [3]. We know we have “false beginners.” They have graduated from high school and took the English achievement test. We’ve tried conventional approaches with notable lack of success. Now we want to “kick-start” processes for building self-confidence, activating latent English, and creating a dynamic classroom. We want to go from “bored to death” to “amazing.”

Shy, woefully embarrassed Japanese students at conferences stand head-bowed, hiding behind a script clutched in trembling hands. We’ve seen this scene often enough and know it for what it is, i.e. a poor “mind-set.” We want our students to stand in front of their posters, ready to explain them to an inquirer. For this we need techniques, strategy, and improvisation. We looked at Carol Dweck’s 2006 book *Mindset* and then found George Couros’ *The Innovator’s Mindset* (2015) with the idea of the “flipped classroom.”

A good explanation of “flipped classrooms” is available at Educause (2012), but also elsewhere, even Wikipedia, because the methodology is not specific. Rather it is blended learning and a strategic structuring of the educational environment which is utilized by practitioners idiosyncratically in each their own situation. It requires trial and error as well as recurring sessions so to as to establish the practice as a routine in the mind of the students and the teachers. Our class room looks like an engineering or programming workshop; the teachers and TA wander around seeing the students work on their assignments and make themselves available for discussion. Meanwhile the Professor posts videos and reading assignments on MOODLE to be done as homework.

2 Research Framework

In this work, we describe and present the initial results of a new vocabulary learning strategy (VLS) that we have designed for third-year Engineering students at Shizuoka University. Utilizing a framework derived from recent popular applications of “flipped classroom” we put experiential, applied learning right into the classroom. Via an intensive 15-week course, students are being immersed in an international-style conference setting, where they must regularly participate in mini-poster presentations on various technical topics. The core training entails a strategy that we call an experiential

VLS (e-VLS) in which words are learned in context and ingrained through a series of regular presentations. Specifically, with mentoring, team-building, and peer-learning, students themselves serve as interpreters using a sufficient mixture of English and Japanese—first with mostly Japanese and a little English, but gradually progressing to all English. Active, simultaneous use of both languages is encouraged. In their team work, the students speak in Japanese among themselves, but in preparing the slides for the poster presentation, with the labels and scripts in English, the students prepare to give their presentations entirely in English.

2.1 Methods

Subjects

The proposed research is currently being conducted with third-year university students enrolled in a course offered each year called Academic English for Electrical Engineers. The course consists of approximately 100 students, split into two approximately 50-student groups based on their specialization in electrical engineering. The two groups take the course on two separate days, thus providing natural control and test subject pools.

Procedures

On the first day of class, all students were asked to create a writing sample as a “self-introduction.” The principle investigator (PI) rapidly sorted all the samples and noted the English test scores on each. The best scoring students were appointed as team leaders. At the next class, students were given to believe that team leaders and teams were assigned on the basis of what was written. This exact procedure was the same for both classes. The idea and schedule of Mini-Poster Presentations was also introduced. The syllabus, including one practice sequence of three weeks, and three three-week cycles, leading up to three mini-poster presentations to be done in class, was in place at the end of the second class meeting. At this writing, we have completed two of the three series.

Assignments

For each assignment, students are given an assignment for their poster presentation. The practice round was an introduction to SKYPE technology for a friend. What equipment and procedures in English can get your friend to use SKYPE. The first round was a presentation about circuits, including a stuffed animal equipped with led lights and sound with the circuit diagrams for the sound and lights. For the “flipped” part of the class, the students were given a writing assignment relevant to the project to translate. The tasks of making the slides, posting the translation, and composing the script for the presentation were divided among the students. The second Mini-Poster presentation involved the use of Arduino technology to design a piece of equipment to enhance the safety of a bike or car. For both the test and control groups, the weekly in-class lessons cycle between (a) training for mini-poster sessions, and (b) the mini-poster sessions themselves.

“Control” vs. “Experimental” Groups

The Control class was divided into 12 teams of 4–5 members. The team leaders were chosen for their tested English level. Neither the teams nor the leaders were told how the team leaders were selected. The Control class is taught by both of the foreigners. Professor Damon spoke about the experiment and PI translated into Japanese as best she could, to confirm understanding. We also gave specific instructions about Poster Design.

The Experimental class was divided into 13 teams. The division was not random, but aimed and conscious. For example, the high TOEIC- scoring international students were put into teams together with high TOEIC scoring Japanese leaders; some teams had no high TOEIC scoring member, but all members had scored well on the listening test; some leaders were chosen at random by the wish of the group, while most leaders were appointed. The Experimental class had idiosyncratic teams formed with various core ideas known to the Investigators.

The Experiment class has a coach/mentor, i.e. a Japanese student of a higher grade level, who can support and guide the team leader in weekly short meetings and function as a TA available to the whole class, speaking in Japanese if required. He also confers with the Professor and the Language Facilitator in English. The coach/mentor who is present in the Experiment class is not present in the Control class, where the Professor and PI manage the class themselves without a mediator.

A few retired Japanese business men have been invited to the three scheduled Mini-Poster-Presentations for the experimental class. No such invitation has been issued for attendance to the three events of the Control class. Their comments and advice have been extremely valuable and supportive.

3 Considerations

Although we’ve discussed the improvements in language, performance, and motivation that we’d like to see, we are operating in a quasi-experimental situation. The Experimental and Control group, doing the 15-week experiment have no specific parameters and we cannot ensure that we are not vitiating our own results with subjective perceptions. The boundary between the two groups is permeable.

While there are clear differences in the make-up, structure, and handling of the two groups, the two teachers learn from the problems encountered in the Wednesday class (Experimental) and make improvements in the Friday class. Thus, the boundary between the two groups is entirely permeable.

Nevertheless, once the teams were established, the classes as a whole immediately settled into functioning teams. Team spirit and group dynamics are activated, with a certain amount of pride of accomplishment and healthy competition developing. Admittedly, this is wishful thinking. The maneuver of assigning teams with leaders is based on the Japanese educational practice from elementary school and kindergarten. It is also the most efficient way to deal with large numbers of people. The basic division into units (“han”) is the bedrock of Informatics “group work” as well.

Of course, in the beginning we hoped the presence of retired executives would have a positive effect on the performance of the Experimental team. It is proving to have a

positive effect on the instructors. We will administer a final questionnaire to students regarding their attitudes about the visitors and one to the seniors regarding their perceptions of the three poster presentations and interactions with the students. After two sequences with the invited retired business men, I would say that they have exceeded our hopes. At the end of each poster session, they give some final words of encouragement and advice.

2017 is the second year of the partnership between Engineer and PI. In 2016 the management of the two classes involved word lists, spelling, “Pictionary” and short dictations. PI used the first 20 min of the class for a brief language exercise that also functioned as attendance. The program was piecemeal and lacking in cohesion. It did give professor and PI regular opportunities to talk. Our discussion centered on engaged, active learning and Middle-Up-Down management for Knowledge Creation. In 2017, we are focusing on presentation skills, eye contact, hearing, and the creation of Poster Presentations. We used the 2016 experiences to come to a new understanding and new framework.

We have little control the of experimental environment available to us, the givens of which will be basically the same for the next two years as well. A number of features remain constant; two electrical/electronic engineering classes with a similar number of students on two days and the same CALL classroom. We are getting more efficient with the Moodle as a tool for “flipping” the classroom and providing material such as videos or Japanese texts to translate into English for homework.

Of course, it is wishful thinking. We want quantifiable results, such as improved scores on standardized language tests, more students becoming interested in graduate school and research, and positive reviews from hiring bodies in the industry. We may get unexpected results, but still find it valuable to run the class as a mini-poster session. We may be able to establish a protocol that we can transmit to others in an article such as this. The negative feed-back which might urge us to abandon this format and methodology has not yet appeared.

4 Conclusions

This is a report of a work in process. I believe that I have established that our educational environment does not present us with a true controlled experiment. However, in the next couple of years we will be able to establish a methodology and practice, with substantial records. We are just beginning and will make changes in recording and verifying results in the future. The positive results in the ease of organizing and the engagement of the students indicate that we can try this scenario again.

References

1. The principle of change. <http://georgecouros.ca/blog/archives/3603>, 16 January 2013. The “Flipped” Classroom and Transforming Education
2. Little, A., Kobayashi, K.: Vocabulary learning strategies of Japanese life science students. *TESOL J* 6, 81–111 (2015). doi:[10.1002/tesj.141](https://doi.org/10.1002/tesj.141)

3. Beare, K.: Teaching English to Absolute and False Beginners, 28 March 2017. <https://www.thoughtco.com/> (2(5), 99–110 (2016))
4. de Cassia Veiga Marriott, R., Lupin Torres, P.: Handbook of Research on E-Learning Methodologies for Language Acquisition (2008)
5. Dweck, C.S., Chiu, Y.H., Hong, Y.: Implicit theories and their role in judgments and reactions: a word from two perspectives. *Psychol. Inquiry* **6**(4), 267–285 (1995)
6. Hazenberg, S., Hulstijn, J.H.: Defining a minimal receptive second-language vocabulary for non-native university students: an empirical investigation. *Appl. Linguist.* **7**, 145–163 (1996)
7. Hulstijn, J.H.: Intentional and incidental second language vocabulary learning: a reappraisal of elaboration, rehearsal and automaticity. In: Robinson, P. (ed.) *Cognition and Second Language Instruction*, pp. 258–286. Cambridge UP, Cambridge (2001)
8. Nation, I.S.P.: *Teaching and Learning Vocabulary*. Newbury House, New York (1990)
9. Kemp, J. (ed.): EAP in a rapidly changing landscape: Issues, challenges and solutions. In: *Proceedings of the 2015 BALEAP Conference* (2017). <http://www.garneteducation.com/Book/28/812/EAP>
10. Negrea, V.: *English for Specific Purposes (ESP): Curriculum Development* (2010)
11. PDF: http://euromentor.ucdc.ro/en/nr1_vol3/engleza_articole/violeta_negrea.pdf. (3–4) http://euromentor.ucdc.ro/en/nr1_v0I3/
12. Nonaka, I., Takeuchi, H.: Middle-up-down management process for knowledge creation, Chapt. 5, pp. 124–159, *The Knowledge-Creating Company*, Oxford UP (1995)
13. University of Delaware. <http://sites.udel.edu/eli/programs/up/>
14. University of Trento, Italy. *Technical and Scientific English for Engineers (Academic writing for the sciences)* (2017). <http://web.unitn.it/en/dricam/40272/technical-and-scientific-english-for-engineers-academic-writing-for-the-sciences>

An Exercise in First and Second-Order Cybernetics: The 18th Year of General Systems Theory (GST) Communication Project

Valerie Anne Wilkinson^(✉)

Faculty of Informatics, Shizuoka University,
Hamamatsu, Shizuoka 432-8561, Japan
vwilk@inf.shizuoka.ac.jp

Abstract. The Faculty of Informatics (1995~) is a natural consequence of the emergence cybernetics [1] ala Norbert Wiener. The context of my long term communication project of 18 years requires the mention of GST (von Bertalanffy), Game Theory (von Neumann), Information Theory (Shannon), and Second-Order Cybernetics (SOC) [2]. The framework of the GST Communication Project is both cybernetic and informatic. This inquiry involves a tangle of **experiential learning**, **educational environment** and **professional development**. The project, an event, or community simulation, in a living system, has been enacted twice each year for 18 years in connection with the elective class, Communication Skills 2. The GST practitioner is a participant/observer, functioning as interface engineer in the real time learning organization of the “system of the event.” The conclusion: the university ought to offer “requisite variety” to the community to develop four bottom lines: People, Planet, Profit, and Presence.

Keywords: GST · Complexity · Cybernetics · Interface engineer · Participant/observer · Living system · Learning organization · Real time learning · Requisite variety · Four bottom lines

1 Introduction

The Faculty of Informatics (1995~) came into existence as natural consequence of the emergence of cybernetics [1] ala Norbert Wiener. It was inevitable that Computer Science which directly applies the concepts of Cybernetics to the control of devices and the analysis of information would become a college major, but this is a gnarly and complicated story. To untangle the context of the long term communication project of 18 years which began on June 26, 2000, requires the mention of GST (von Bertalanffy) [2], but if we go strictly in order, Gregory Bateson came first for me. I had published an article in 1989 doing a close reading of his “The Logical Categories of Learning and Communication” [3, 4]. I had been reading Bateson for years. His writing persona came into my ken by way of Co-Evolution Quarterly and The Whole Earth Catalogue. The hiring institution made it plain to me up front that my job at the Faculty was to teach “Communication Skills One,” a required class for all Informatics students. How was a class with that name to be defined? I had been teaching Communication subjects

in Japan for several years under the aegis of English, so I preferred to hear “Communication” as the dominant word and “Skills” as plural, as in several and various. I also learned that my colleagues called that class “英会話” which is translated as “English conversation.” It was one of the “katakana classes” which are neither English nor Japanese, but a blend.

My praxis of teaching English as a foreigner in Japan since 1980, involves task-based language learning (TBLL), person-to-person conversation practice, and English writing assignments based on experiences we share and activities we do. It is not easy to keep up with developments (which were huge and various) in my “area” while teaching a full-time load of freshman and sophomore English classes each term. I organized freshers and sophomores, promote and execute a mid-sized event connected to Communication Skills 2 class twice each year. I called that exercise “The GST Communication Project.” and set the year 2000 as the start point. In that year the Faculty completed the move from the Oya Campus to the Hamamatsu Campus. This paper explores the rationale and methodology of the semiannual real time educational event.

In what follows, I layout first the main intellectual entanglements of the event: Cybernetics, second-order cybernetics, GST, and Game Theory. It is a story full of paradox and a transdisciplinary field in which I teach freshers of all three Faculty majors in Informatics. Fortunately, the interaction of the human intellectual communities in the 1940s was the fertile ground of discussions going toward synthesis. Here I hit some of the core notions.

2 Cybernetics

Nobert Weiner gets the credit for defining Cybernetics in 1948 with the publication of his book. The subtitle is Control and Communication in the Animal and the Machine. He is central to associating the term cybernetics with machines, and the circular causal relationship which is called feedback. 1948 is not the beginning of “cybernetics,” not historically, nor semantically, nor even technologically. We give the credit to Weiner because he published the book with the keyword of the moment. Princeton was as thick with genius polymath scientists as MIT. The publication date, however, seals Weiner’s name to Cybernetics. Any simplification of the history of those times can only hit some selected high points.

[The concrete **application** of cybernetics in the case of the GST community simulation is to plan and execute a real event, setting date and time, promoting, planning, recruiting and establishing teams, inviting guests, seeking sponsors. It is a goal directed activity, with a management team, top director, and team leaders, and an event to produce by a certain time on a certain date with mentoring and coaching support from former leaders and the professor. Evaluation and due diligence is important to the event, leaving a record for the next project.]

2.1 Digital

Weiner's best selling book was *The Human Use of Humans* (1950), where his trans-disciplinary humanitarian concerns came to the fore, but the meme CYBER soon overshadowed the humanitarian side, becoming synonymous with computers and computer networks in the popular and academic mind. In a 1971 British book called *Cybernetics*, Professor George says:

“Cybernetics has a reasonably well-defined pure and applied side to its activities. The pure theory is mainly abstract – mathematical, statistical and logical – whereas the applied side is relevant to everything human beings do, especially how they learn, how they make decisions, how they plan and how they solve problems. Cybernetics also applies to the contexts in which they perform...” [5] [**Application** to GST event: the work of IT/ICT specialists, i.e. networking, ordering, reservations, etc.]

2.2 The Cybernetics of Society [6]

A concise history of the term “cybernetics” can be found in D. Barnabas Johnson's article, giving the credit for the first use of the term in English to Wiener, but showing that André-Marie Ampère (1775–1836) coined the French term “*cybernétique*” in 1834. He points out, “The distinction between science and cybernetics becomes ever more crucial as the “found-in-nature” and the “made-by-culture” become ever more intertwined. This intertwining must not be haphazard, yet it is irreducibly complex and therefore unpredictable.” [**Application** to GST event: nested system levels, the self, the teams, inner (student) communities, outer (guest) communities, the multi-purpose venue.]

2.3 The Semantic and the Philosophical

Johnson's article goes on to show that Cybernetics and Governance have the same semantic root, he cites Plato's *Alcibiades* (c410 BCE):

SOCRATES: “Or again, in a ship, if a man having the power to do what he likes, has no intelligence or skill in navigation [αρετης κυβερνητικης, aretes kybernetikes], do you see what will happen to him and to his fellow-sailors?”

Plato, *Alcibiades I*; Benjamin Jowett, translator

The learned author proceeded with a derivation of the word governance as the true meaning behind the original Greek word. “These and related words in other languages are rooted in the ancient Greek word *κυβερνητικός* or *kybernetikos*, meaning (*good at steering*). *The precise concept was* αρετης κυβερνητικης, aretes kybernetikes.” The one who steers the ship with a rudder is a human using technology, whether it is the concrete boat in a real ocean with wind and waves, or a ruling metaphor of a governor guiding the ship of state. The abstract sense of cybernetics includes all concrete applications and therefore encompasses all majors in informatics. [**Application** to the GST event: PMBOK text [7], Fifth Discipline text [8], mapping of the whole system, review of former records, regular meetings, general security, waste disposal, gate monitoring, etc. The vision of the whole system, with shared vision and responsibility of stakeholders.]

3 Second-Order Cybernetics

A 2003 article by Glanville [9], written under the auspices of UNESCO, says that “Second-order cybernetics (also known as the cybernetics of cybernetics, and the New cybernetics) was developed between 1968 and 1975 in recognition of the power and consequences of cybernetic examinations of circularity. It is Cybernetics, when Cybernetics is subjected to the critique and the understandings of cybernetics. It is the cybernetics in which the role of the observer is appreciated and acknowledged rather than disguised, as had become traditional in western science: and is thus the cybernetics that considers observing, rather than observed systems.”

Comment. A paradigm shift should have eventually come after Max Planck described *quanta* in 1900, essentially founding Quantum Theory. Quantum Theory, Einstein’s General Theory of Relativity (1906) and Heisenberg’s Uncertainty Principle (1927) all assume the position of an observer. We have not yet seen this paradigm shift in the world of conventional science, which does not admit the subjective point of view. The term “paradigm shift” entered popular discourse with Thomas A. Kuhn’s work *The Structure of Scientific Revolutions* (1962). Kant had used the phrase first (albeit in German) in *The Critique of Pure Reason* (1781).

The paper explaining 2nd Order Cybernetics goes on: “To claim predictability, science looks for mechanism, the embodiment of regularity and repeatability. If there is mechanism, predictability results. There are circumstances where mechanism is obscured. When this occurs, we may invoke the Black Box concept originated by James Clerk Maxwell. This concept, trivialized by later behaviourist psychologists, allows us to operate while remaining essentially ignorant.”

In 1968, at the meeting of The American Association for the Advancement of Science, Margaret Mead read a paper entitled “The cybernetics of cybernetics,” In certain respects, the symposium reflected the earlier Macy Conferences organized by Heinz von Foerster. Foerster gave the title to Mead while Warren McCulloch who had also convened the Macy Conferences chaired the symposium. Thus Margaret Mead became the face of the behavioral sciences, such as sociology, anthropology, psychology, communication, economics and political science. Many hard scientists do not think of these as “science” at all and insist that they produce results in scientific form as if buying into that paradigm. Insofar as those scientists accept the demand for provable, replicable results, the work has continued with scientific accuracy. But when results appear mysteriously, the explanatory principle is called “Black Box.”

It is perhaps fair to call the author “ignorant” because I cannot prove the mathematics of the quadratic equation or the algorithm for relativity ($E = MC^2$) or indeed anything about the flow of photons, atoms, or quanta. I can look anything up on Wikipedia, to see how term I selected has been summarized, with what concrete research to substantiate it. I can seek out those articles, then read and discuss them from my ignorance, while attempting to teach freshers from all three programs in Informatics. The majors cover the whole spectrum of Informatics. At the same time, all of the majors are cybernetic. Establishing the proposal in this essay with word and history study does not mean I can do the experimental research, write the equations, or confirm

the validity. Nevertheless, I have been teaching freshers in all majors, both in Informatics and Engineering since I came to Shizuoka University. I am part of all of this. [Application to GST event: develop Personal Mastery, daily inventory, Double Loop learning (Argyris [10]), discuss, question, give feedback, repeatedly confirm work and individual assignments, coordinate, facilitate.]

3.1 Black Boxes and Ruling Metaphors

“The Star Festival” is a ruling metaphor, one name for the Tanabata Party GST Communication Project event. That name trades on the image of a popular local festival in Japan. Students and guests who “buy into” the image have no difficulty participating in it. The main difficulty is to persuade them that this is, in fact, a field research project as part of the research. To conduct it “as research” would be to take the fun out of it for many of the participants. The framing of an event so that the guests are glad participants, not ritual sacrifices, or conscripted unpaid labor is the whole job of creating a shared vision for the organization. Santa Claus shows up at The Christmas Party, and we usually have Live Jazz provided by the university club, an OB group and a city-based amateur group of professional quality musicians.

Norbert Weiner and Ross Ashby worked with Black Boxes in imaginary circuits, where the term “Black Box” stands for unobserved, undocumented, and unknown processes, an imaginal realm which prepares for Second Order Cybernetics. It is sort of like a carrot on a stick to keep the donkey moving forward.

4 GST

I mentioned that I have been working with Gregory Bateson, and that is how I came to Bertalanffy’s GST. In A Brief Review of Systems Theories [11], I found a systematic review of the work done, the background, and the managerial applications of Systems Theory. The contributors and their contributions are in place. Finding and reviewing such articles is Second-Order Cybernetics, Double Loop Learning or Learning Two. The practitioner adapts to the changing context and real time players in the unique context of “this event” by reviewing, reflecting, and evaluating.

Basic tenets of GST come into play as we establish the environment in which we set up the “community simulation.” Somehow the group will self-organize and self-correct, to enact the preparations, invite participants, execute the event, and clean up after. The supervisor does not tell the students what to do so much as tell them the date, facilitate the selection of a leader, and support the emerging team in its discovery of what has to be done to make the event happen.

The students create the necessary conditions for observing organizational behavior as a participant/observer, but they are not observing yet. Students can work cooperatively, but they are accustomed to doing group work. Can they understand team building, leadership, and roles as they do so? The leader, whether chosen or appointed, assigns roles and conducts meetings. Blocks and filters between the students and the teacher in a supervising role cause impediments. As we repeat the process again and again, some of us do learn something.

4.1 Community Simulation in Open System with Constraints

The group that comprises the class is the activity system of the event. The whole map of the “system of the event” includes the stages where we hold meetings and interactions occur, i.e. the classroom and the hall and grounds. All participants, be they management, clubs members providing entertainment, logistic assistance, or cooking, as well as the guests are part of the system.

The mandate is to arrange an enjoyable event on a Saturday for some hours in the afternoon, promote, get sponsors, sell tickets, and purchase ingredients for food. There are tons of things to do. It is quite astounding that everyone pitches in to do it gladly on the day. It is not always smooth sailing. There are quarrels in upper management for control or comprehension. We have experienced the fierceness of the team that sets its eye on the goal, becoming impervious to futile reminders that the class is about English, inclusiveness, and management. They go the way they want to.

The whole sequence of unique events over 18 years has proven to be impossible to control or predict. Something persists, and twice each year, we produce this event. The semiannual event, routinely held in the alumni building, Sanaru Kaikan, gives a few students a chance to build a team, make decisions, and co-operate with each other while experiencing intrinsic learning. The supervisor gets ample opportunity to test the truth of Korzybski’s dictum, “The map is not the territory.” Room for personal spiritual growth and development is unlimited. First, we talk about first-order Cybernetics and managing the event with input, planning, and evaluation. We talk about how this organizational experience might provide applicable insights into future personal and institutional settings. Evaluate, evaluate, and evaluate.

5 Game Theory

“Equilibrium is as central to the study of social systems as it is to the analysis of physical phenomena. In the physical world equilibrium results from a balancing of forces. In societies, it results from a balancing of intentions. In a physical system, particles are in equilibrium when they do not deviate from a given position or stable trajectory. In a social system, individuals’ intentions are in equilibrium when no one wants to deviate from his intended behavior given the intentions of others.” [12].

The second-order cybernetics of the researcher: In this context, it means observing the effect of the whole event on the team, class, Faculty, communities and the self. I note preparations that failed, things that worked perfectly, times when things went well, or when the energy sagged. We talk about what we hoped to happen, what is happening, and what might happen so that one can adapt oneself to the givens of a new order, which happens every year. The challenge is to keep the event afloat against falling popularity. Somehow families with kids are onto it. They will come. We’ve had classes of thirty and forty students and classes of one, two or four students. One learns to carry on. One may finally learn patience. Someday everything will work!

6 Conclusion

Every event has a beginning and an end. Each student attending the first day of class is a Black Box of personal history and experience. What do we bring to the table, what do we want to do, hope to accomplish, what makes a satisfactory memory? Each event needs an evaluation, to applaud fixes that worked, lessons learned to move forward, and a chance to ventilate and “debrief” as we reflect on the process.

“What we call the beginning is often the end.
And to make an end is to make a beginning.
The end is where we start from.
T.S. Eliot *The Four Quartets*.

References

1. Weiner, N.: *Cybernetics, or Control and Communication in the Animal and the Machine*. MIT Press, Cambridge (1948)
2. von Bertalanffy, L.: *General System Theory: Foundations, Development, Applications*. George Braziller, Inc., New York (1968)
3. Bateson, G.: The logical categories of learning and communication. *Steps Ecol. Mind*, 279–308 (1972)
4. Wilkinson, V.A.: A critical commentary of Bateson’s “the logical categories of learning and communication.” *Bull. Natl. Inst. Multimedia Educ.* **2** (1989)
5. George, F.H.: *Cybernetics*. Teach Yourself Books, London (1971)
6. Johnson, B.D.: *The Cybernetics of Society: The Governance of Self and Civilization* (2012). <http://www.jurlandia.org/cybsoc.htm#Conclusion>
7. PMBOK, Project Management Institute (2000)
8. Senge, P.: *Fifth Discipline*. Doubleday/Currency, New York (1990)
9. Glanville, R.: Second-order cybernetics. In: Parra-Luna, F. (ed.) *Systems Science and Cybernetics, Encyclopedia of Life Support Systems, Developed Under the Auspices of the UNESCO*. EoLSS Publishers, Oxford (2003). <http://cepa.info/2326>
10. Argyris, C.: *Integrating the Individual and the Organization*. Wiley, New York (1964)
11. Mele, C., Pels, J., Polese, F.: A brief review of systems theories and their managerial applications. *Serv. Sci.* **2**(1/2), 126–135 (2010)
12. Young, H.P.: *Strategic Learning and Its Limits*. OUP, Oxford (2004)

Predicting the Future Using Web Knowledge: State of the Art Survey

Amir Mosavi¹(✉), Yatish Bathla¹, and Annamária Varkonyi-Koczy^{1,2}

¹ Kando Kalman Faculty of Electrical Engineering, Institute of Automation,
Obuda University, Budapest 1431, Hungary
{amir.mosavi,yatish.bathla,
koczy.annamaria}@kvk.uni-obuda.hu

² Department of Mathematics and Informatics, J. Selye University,
945 01 Komarno, Slovakia

Abstract. Accurate prediction models can potentially transform businesses, organizations, governments, and industries. Data-driven prediction methods and applications have recently become very popular. One of the novel method of building prediction models is to use data-driven methods and knowledge discovery on the web contents. This includes the news and media as well as social networks contents. This method uses advanced technologies of big data, machine learning, deep learning and intelligent optimization for finding patterns in big data to build prediction models. This article presents a state of the art survey on the latest technological advancements, novel methods, and applications in developing prediction models.

Keywords: Predictive analytics · Predictive decision models · Web dynamics

1 Introduction

An intelligent agent in a complex environment of numerous intelligent agents is often concerned with the future changes to its environment [1]. As Radinsky [2] describes, the potential changes may partly be the consequences of its own actions, and partly due to the various chains of the events caused by the actions of other agents situated in the same environment. Scientific prediction would be the way to study and analyze the future events [3]. Due to the limited perceptive capabilities of intelligent agents building the prediction models in the complex environments is considered as a highly demanding task. However the rapid reproduction of the World Wide Web and, internet of things (IoT) [3, 4] is changing all that. Today people as the intelligent agents in the virtual world of the Web are changing the current state of the world [4, 5]. Consequently, today the perceptive capabilities of intelligent agents have been highly improved by the expansion of the IoT, e.g. Web pages, increasing the sources of textual information, news reports, Wikipedia pages, tweets, search inquiries, organizing, and generating information. This would lead to build better predictive models for providing knowledge on likelihoods of future events and actionable forecasts [5]. This paper is concerned with the novel concept used for the predictions of an event using web technologies. The goal is to identify the novel applications and the potentials of the concept.

2 Prediction Models

Prediction brings insight into unknown. Accurate prediction models can transform businesses, industries, and almost any organization. Marketing, financial services, insurance, retail, election forecasting and healthcare are just a few industries seeking for accurate predictions to enhance their decisions. Predictive analytics, emerged from data science, identifies patterns in big data to build predictive models. Building accurate prediction models is a challenging task [5]. Due to uncertainties, complexity of the prediction functions and high computation costs, the conventional mathematical modeling approach cannot provide any reliable prediction model. Instead predictive analytics, emerged from data science, identifies patterns in big data to build predictive model for organizations. However the true purpose of prediction is about taking an action with more knowledge about the consequences of it. Today, humanity more than ever seeks accurate predictions to better react to the climate changes [6]. For instance, Mosavi [7], coins the term *predictive decision model* for the accurate disaster prediction.

Prediction is statement about the future and defined as an uncertain event that is more likely to be occurred based on the past knowledge. It has wide area of application in politics, entertainment industries, government and private organization and many more. Today organizations highly invest for predicting the future. The obtained information can be used in many ways: increase the profit, avoid disasters, cure diseases, minimize the destruction etc. According to Asur and Huberman [4], and Radinsky [5], the World Wide Web (WWW) is considered as a giant information system where numerous intelligent agents are involved to achieve their goals. Some of these are human agents while others are computerized ones. Yet the Web content presents a dynamic characteristics with constantly changing its contents. In addition the Web content includes a big database of user behaviors, queries, and interactions with the capability to convey current trends in the future. Web based predictions shown to have the potential to transform the reality into virtual state and provide best possible solution by assuming the future events in the virtual environment [3]. There are several prediction models, algorithms and methods introduced to predict the future events based on web contents. Examples include predicting the economic growth [4], sales prediction [5], political predictions [6] entertainment industry [7], health industry [8–10], stock market [11, 12], traffic management system [13, 14], robotics [15–17], engineering [18–21], decision support systems [22–24], business modeling [25] etc. Accordingly, Web contents database has already found its place as a novel resource of prediction [26]. According to Radinsky [27, 28], the ever-changing Web content and user Web behavior are the main resources to create prediction models. To build prediction models decades of news reports can be mined for extracting the knowledge, and learn to predict the future by generalizing sets of concrete transitions in sequences of reported news events. In fact the Web dynamics can be used for future real-world event prediction [29].

There are various prediction mediums available in the market to make predictions about the future events to make prediction based on their experience. The process of searching prediction medium is explained in Fig. 1, where a human agent decides the

areas for the prediction of future events. Based on the selected areas, human agent interacts with the computerized agent to search for the best prediction medium. The Prediction medium can be implemented as a prediction model. Case studies of this workflow include predicting automobile sales [30], predicting the popular movies [31–33], and politics [34, 35].

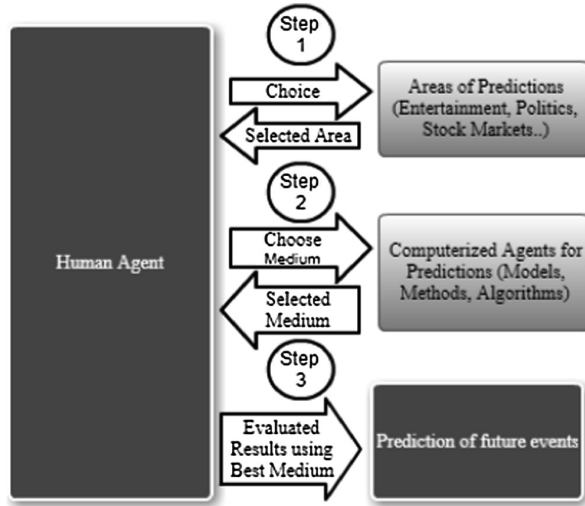


Fig. 1. Communication between agents for the prediction of future events from Web contents

The state of the art of artificial intelligence and computing technologies which are reported efficient to create prediction models, through the Web content, may include Big data [36], Web mining [29], data mining [14, 18, 37], machine learning [10, 17], deep learning [23, 37, 38], deep networks [36, 39], intelligent optimization [18], and neural networks [11, 40]. In these cases the authors extracted valuable information to build prediction models to anticipate the future events using the Web contents. Consequently prediction models that are associated with the human agents in the virtual world are created. To do so one approach has been predicting the user behavior based on historical dynamics and interactions on the Web [3]. The examples include predicting search query popularity, predicting URL clicks, and also predicting when an agent is likely to modify the content of a Web page. Such behaviors which utilize the time-series provide significant beneficial over existing prediction methods [3]. The second approach include predicting the real-life future events based on the dynamics of the virtual world of the Web which uses Web dynamics. In this approach the prediction algorithm provide the ability to learn and generalize from past events as well described in [5]. In the next section the concept and a case study is presented.

3 Concept and Case Study

Building prediction models based on the internet contents is considered as a novel approach to prediction. After introducing the concept by Radinsky [3], the applicability and beneficial of the general concept and the novel idea have been increasing and we have been witnessing a great progress in the number of publications during past few years. The concept can be employed to explore the temporal dynamics of Web behavior for investigating the changes in the Web queries [5]. For that matter one can model and predict the informational goals corresponding to the queries, and the search results they click on during Web search sessions. The concept therefore provides the ability to predict how the search behavior of users changes over time and use these prediction models to enhance retrieval [26]. In fact the frequency of a query and the number of clicks for that query which change over time can be carefully investigated for an accurate prediction model. To better demonstrate the concept here we present a case study on predicting the disasters.

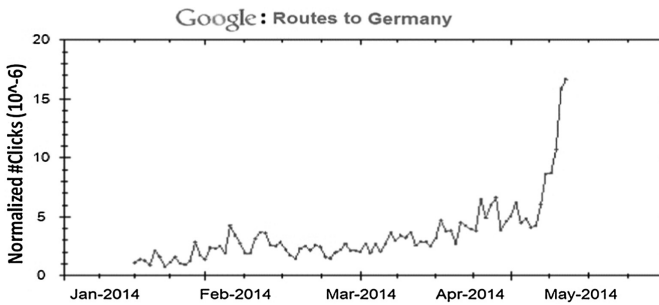


Fig. 2. A time-series for the query *routes to Germany*



Fig. 3. A time-series for sample Facebook clicked URLs for query *prosperity life in Germany*

In this case study we propose the predictive modeling from the Web to build insights about the likelihood of transitions and influencing the real-life events. We demonstrate this predictive model of mining the Web contents to create classifiers for

the forthcoming disasters in this case Europe refugee crisis. Figure 2 illustrates the total clicks for the query routes to Germany. We can see a dramatic change in behavior associated with this query in May 2014. Likewise, in the Fig. 3, the Facebook URLs that people choose to click surges in Feb 2014 for the query prosperity life in Germany for a period of time, and then slowly decays indicating a change in what people consider relevant for that query. According to the case study, by observing the queries of prosperity life in Germany & Query routes to Germany the predictive model alerts about high likelihood of refugee crisis in an accurate date (Fig. 4).

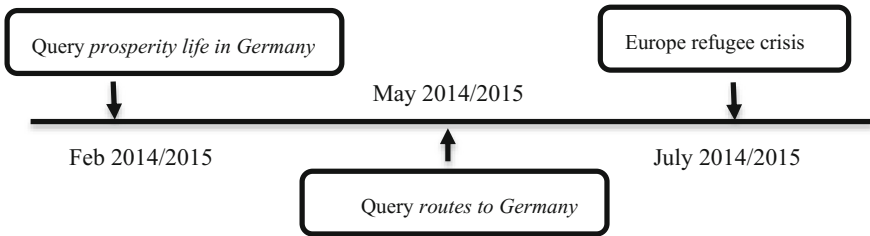


Fig. 4. Predicting the refugee crisis in Europe using dynamics of the Web contents: the system alerts about high likelihood of refugee crisis in July of 2014/2015 by observing the queries.

4 State of the Art Survey

Currently there exists various prediction models for predicting the future events using Web technologies [5]. The concept and a number of case studies briefly presented in [26]. Prediction of future dynamics of websites is performed using models may be obtained from the changing patterns of Web contents, numerical fitting techniques, and auto regressive moving average (ARMA) Models [1, 5]. Such models form the basis of the revolutionized forecasting. One of the early methodologies was proposed in [14, 29, 30] for modeling and predicting the future news events using machine learning and data mining techniques [17]. The work of Radinsky [27], propose an algorithm for generalized examples of causality pairs to infer a causality predictor. For generalization, the model uses a vast amount of world knowledge ontologies mined from LinkedData. Prediction of events like disease out-breaks, riots has been taken by building predictive models [28]. Such models are created using automated abstraction techniques and generalization of sequences of events from decades of news report as well as multiple Web resources, including e.g., Wikipedia, FreeBase, OpenCyc, GeoNames and, LinkedData platform [37]. In addition the social media is widely used as a medium to make prediction for instance about box office revenue of a movie [4, 33, 34]. Predictive models are created using Web technologies based on the information scent [41]. This is done by outlining the computational methods for modeling user needs. The area of application of this algorithm are personalizing Web environments, designing Web site and identifying parts of a Web as bad designs [11]. Prediction model of unlabeled video [39] was constructed by using Deep networks [39]. This network is trained to predict the visual representation of images in the future.

Furthermore, the Selective Markov Models [42], were used for Predicting the Web-Page Access. In [37], a number of innovative techniques are proposed for selecting different order of Markov Models so that resulting model has a reduced state complexity and improved prediction accuracy. In the work of Amodeo [43], the hybrid models was obtained using New York Times corpus for the future event prediction. For this purpose he used a modeling technique so called ARMA modeling analysis. Furthermore, a competitive prediction model was obtained by intertwining Hybrid models with the SARIMA model.

In another case study the Portfolio optimization model [40], was created for predicting the short-term investment opportunities in stock market. In this case study, the autoregressive moving reference neural network (AR-MRNN) method, is used to predict the stock returns. In the similar approach, the prediction of network traffic in production Web server has been done by using autoregressive (AR) models for forecasting [13], where the trend model is obtained using low pass filter, residual process and Gaussian distribution. In other related case study, a Takagi–Sugeno–Kang (TSK) type Fuzzy Rule Based System [44], was developed for stock price prediction. This model is used on the Electronic Shares from the Stock Exchange and forecasts the price variation for stocks with high accuracy.

Prediction of health issues has been done by exploring techno-social predictive analytics (TPA) [8, 29] and related methods for Web data mining. A visual artifact called Dynamic Time Warping Radar (DTWRadar) [6] was created to predict the behaviors of Web systems. It is a tool that used for data mining and evaluate the common interest of Internet users by comparing the time series of different Web systems.

There are plenty of algorithms and methods created and used as a medium for the predictions. For instance a series of novel algorithms e.g., [27, 45–47], were created for predicting content change on the Web. Such algorithms combine the information in an expert prediction framework for identifying related pages, including pages that are close in the Web graph, pages with similar content, and pages with correlated content across time. Hybrid Group Method of Data Handling (GMDH) algorithms [23, 43] were used to predict currency exchange rates. This algorithm is improved by using Genetic Algorithms (GA) and Particle Swarm Optimization (PSO) and provide more accurate predictions as compare to conventional GMDH in foreign exchange market. Dynamic Modeler Learner (DML) algorithm [3] used to determine predictive model use for predicting behavior based on large search logs of Web search behavior over time. This algorithm learns the correct model by query, URL or query-URL pair and incorporates multiple types of models for time aware search models. A model-based clustering algorithm [12] was designed for detecting future events based on information extracted from a text corpus. Deep-learning-based method was created for Traffic flow prediction [36]. Here, stacked auto-encoder model was used to learn generic traffic flow features. This method used the greedy layer-wise unsupervised learning algorithm to train the deep network and fine-tuning process to update the model's parameters to improve the prediction performance. The spatial and temporal correlations are inherently considered in the modeling. The PROFET method [2], was created for the prediction of future events using their patterns in past. This method aggregates history of user queries from Google Trends and Google Hot Trends [30]. The Web-log mining

method [14] is used for predicting the Web caching systems. They applied a segment of Web-log data to train a predictive model. This model is then integrated with an existing caching algorithm for predictive caching where n-gram-based prediction algorithm provides accurate prediction.

5 Conclusions

Internet content reflects the current state of the physical and social world. This paper presents the novel concept and the state of the art of the predictive models to predict the future events by using the internet contents. It is demonstrated that, how, businesses today learn to predict the future using the Web knowledge and the Web dynamics to stay competitive in the market. The goal of this article is to present all the latest sources of the methods and the advanced applications in this realm. This research covered the applications in health industries, entertainment, software development, traffic management, finance, economics, politics, and foreign exchange markets. It is observed that, today the major methodologies to predict include big data, Web mining, data mining, deep learning, intelligent optimization, deep networks and neural networks.

References

1. Maria, C.: Modeling and predicting. *Netw. Appl.* **56**, 115–123 (2015)
2. Radinsky, K.: Predicting the news of tomorrow using patterns in web search queries. In: *Web Intelligence and Intelligent Agent Technology*, vol. 1, pp. 363–367 (2008)
3. Radinsky, K.: Behavioral dynamics on the web: learning, modeling, and prediction. *J. Trans. Inf. Syst.* **31**, 363–367 (2013)
4. Asur, S., Huberman, A.: Predicting the future with social media. In: *Web Intelligence and Intelligent Agent Technology*, vol. 1, pp. 492–499 (2010)
5. Radinsky, K.: Learning to predict the future using Web knowledge and dynamics. In: *ACM SIGIR Forum*, vol. 46, pp. 114–115 (2012)
6. Adar, E.: Visualizing and predicting user behavior. In: *International Conference on World Wide Web*, vol. 6, pp. 161–170 (2007)
7. Mosavi, A.: Predictive decision model (2015). <https://doi.org/10.13140/RG.2.2.21094.630472>
8. Vaezipour, A., et al.: Visual analytics and informed decisions in health and life sciences. In: *Paper in Proceedings of International CAE Conference, Verona, Italy* (2013)
9. Vaezipour, A.: Visual analytics for informed-decisions. In: *CAE Conference, Italy* (2013)
10. Vaezipour, A.: Machine learning integrated optimization for decision making. In: *26th European Conference on Operational Research, Rome* (2013)
11. Vaezipour, A.: Visual analytics for multi-criteria decision analysis. In: *Proceedings of International CAE Conference, Verona, Italy* (2013)
12. Jatowt, A., Au Yeung, C.: Extracting collective expectations about the future from large text collections. In: *Information and Knowledge Management*, vol. 20, pp. 1259–1264 (2008)
13. Shen, D.: Predictive models for proactive network management. In: *Network Operations and Management Symposium*, vol. 1, pp. 833–846 (2002)
14. Yang, Q., Zhang, H.: Web-log mining for predictive web caching. *IEEE Trans. Knowl. Data Eng.* **15**, 1050–1053 (2003)

15. Mosavi, A., Vaezipour, A.: Developing effective tools for predictive analytics and informed decisions. Technical report (2013). <https://doi.org/10.13140/RG.2.2.23902.84800>
16. Mosavi, A., Varkonyi-Koczy, A.R.: Integration of machine learning and optimization for robot learning. In: *Advances in Intelligent Systems and Computing*, vol. 519, pp. 349–355 (2017)
17. Mosavi, A., Varkonyi, A.: Learning in robotics. *Learning* **157**, 8–11 (2017)
18. Mosavi, A.: Decision-making software architecture; the visualization and data mining assisted approach. *Int. J. Inf. Comput. Sci.* **3**, 12–26 (2014)
19. Mosavi, A.: The large scale system of multiple criteria decision making; pre-processing. *Large Scale Complex Syst. Theory Appl.* **9**, 354–359 (2010)
20. Esmaeili, M., Mosavi, A.: Variable reduction for multiobjective optimization using data mining techniques. *Comput. Eng. Technol.* **5**, 325–333 (2010)
21. Mosavi, A.: Data mining for decision making in engineering optimal design. *J. AI Data Min.* **2**, 7–14 (2014)
22. Mosavi, A., Vaezipour, A.: *Visual Analytics*. Obuda University, Budapest (2015)
23. Mosavi, A., Vaezipour, A.: Reactive search optimization; application to multiobjective optimization problems. *Appl. Math.* **3**, 1572–1582 (2012)
24. Mosavi, A., Varkonyi-Koczy, A.R., Fullsack, M.: Combination of machine learning and optimization for automated decision-making. In: *MCDM* (2015)
25. Mosavi, A., Delavar, A.: *Business Modeling*. Obuda University, Budapest (2016)
26. Radinsky, K.: Learning causality for news prediction. In: *WWW*, vol. 21, pp. 909–918 (2012)
27. Radinsky, K.: Predicting content change on web. In: *Web and Data Mining*, vol. 6, pp. 415–424 (2013)
28. Radinsky, K., Horvitz, E.: Mining the web to predict future events. In: *International Conference on Web Search and Data Mining*, vol. 6, pp. 255–264 (2013)
29. Maged, N.: Social web mining and exploitation for serious applications. *Comput. Methods Progr. Biomed.* **100**, 16–23 (2010)
30. Varian, H., Choi, H.: Predicting the present with Google Trends. *Economic* **88**, 2–9 (2012)
31. Leetaru, K.: Culturomics 2.0: forecasting large-scale human behavior using global news media tone in time and space. *First Monday* **15**, 92–103 (2011)
32. Asur, S., Huberman, B.: Predicting the future with social media. In: *Arxiv* (2010)
33. Joshi, D., Gimpel, K., Smith, N.: Movie reviews and revenues: an experiment in text regression. In: *Computational Linguistics - Human Language Technologies* (2010)
34. Mishne, G.: Predicting movie sales from blogger sentiment. In: *Advancement of Artificial Intelligence Spring Symposium*, vol. 23 (2006)
35. Passman, R.: Predicting the future. *Circulation* **125**, 3031–3037 (2012)
36. Lv, Y.: Traffic flow prediction with big data: a deep learning approach. *IEEE Trans. Intell. Transp. Syst.* **16**, 865–873 (2015)
37. Mosavi, A.: Application of data mining in multiobjective optimization problems. *Int. J. Simul. Multidisc. Des. Optim.* **5**, 15–25 (2014)
38. Mosavi, A., Rabczuk, T.: Learning and intelligent optimization for material design innovation. In: *Theoretical Computer Science and General Issues, LION11* (2017)
39. Carl, V.: Anticipating the future. In: *Computer Vision and Pattern Recognition*, vol. 1, pp. 98–106 (2016)
40. Freitas, F.D.: Prediction-based portfolio optimization model using neural networks. *Neurocomputing* **72**, 2155–2170 (2009)
41. Chi, E.H.: Using information scent to model user information needs and actions on the web. In: *SIGCHI Conference on Human Factors in Computing Systems*, vol. 1, pp. 490–497 (2001)

42. Deshpande, M., Karypis, G.: Selective Markov models for predicting web-page accesses. *J. Trans. Internet Technol.* **4**, 163–184 (2000)
43. Amodeo, G.: Hybrid models for future event prediction. In: *International Conference on Information and Knowledge Management*, vol. 20, pp. 1981–1984 (2011)
44. Chang, P.C., Liu, C.H.: A TSK type fuzzy rule based system for stock price prediction. *Expert Syst. Appl.* **34**, 135–144 (2008)
45. Mosavi, A.: *Visual Analytics*. Obuda University, Budapest (2016)
46. Abbod, M., Deshpande, K.: Using intelligent optimization methods to improve the group method prediction. In: *Knowledge Management*, vol. 20, pp. 1259–1264 (2008)
47. Mosavi, A.: Predictive decision making. Technical report (2015). doi:[10.13140/RG.2.2.16061.46561](https://doi.org/10.13140/RG.2.2.16061.46561)

Author Index

A

Abe, Masato, 235
Agheorghiesei, Catalin, 249, 261
Aoki, T., 87
Apetrei, Radu Paul, 176
Astefanoaei, Iordana, 249
Azuma, Keisuke, 41

B

Bakhmetyev, Vadim V., 3
Baranyai, Marcell, 209
Barneva, Reneta P., 307, 315
Bathla, Yatish, 341
Bejinariu, Silviu-Ioan, 110
Benkreif, Rami, 32
Besleaga, Alexandra, 135
Bichindaritz, Isabelle, 307
Blajan, Marius, 161, 169
Bogdanov, Sergey, 81
Bordian, O.T., 11, 128
Bottoni, Paolo, 273
Brimkov, Valentin E., 307
Buchenauer, Dean, 41

C

Carbonara, Joaquin, 307
Chandler, Damon Michael, 326
Ciobanu, Adrian, 110
Costin, Claudiu, 183
Csiba, Péter, 243
Culeac, I.P., 11

D

Dang, Sanjeena, 307
Dineva, Adrienn, 243
Dobromir, Marius, 176, 191
Dorokhina, Anastasiya M., 3
Dubov, V.L., 87

E

Egawa, Shun, 203

F

Fedosenko, Nikolay N., 18
Fleiner, Rita, 281
Fomin, D.V., 87
Fujii, Keisuke, 203

G

Gaishun, Vladimir, 59, 65, 144
Gelsomini, Federico, 307, 315
Gnatyuk, V.A., 87

H

Hatano, Yuji, 41
Hélie, David, 26
Hung, Patrick, 315

I

Ignat, Anca, 110
Iovu, M.S., 11
Ito, Akihiko, 169

J

Jenkin, Michael, 315
Jiang, Xiaohong, 18

K

Kanev, Kamen, 273, 307, 315
Kapralos, Bill, 315
Khakhomov, Sergei, 72, 144
Kolasinski, Robert, 41
Kolos, Vladimir V., 144
Kosenok, Yanina, 65
Kovalchuk, Natalya, 72, 144, 151
Kovalenko, Dmitry, 59, 65, 151, 176
Kristof, Jaroslav, 161, 169

L

Lopez, Alvaro, 225
 Luca, Dumitru, 59, 65, 110, 144, 151, 176, 191
 Luca, Mihaela, 110

M

Mei, Alessandro, 273
 Mihaila, Ilarion, 183
 Miyamoto, Hideto, 161
 Mosavi, Amir, 32, 50, 209, 217, 225, 289, 341
 Mousavi, Seyedmajid, 289

N

Nastuta, Andrei Vasile, 261
 Negrub, Maryana M., 26
 Nonaka, Keisuke, 235

O

Oya, Yasuhisa, 41

P

Pedone, Massimiliano, 273
 Piliptsov, Dmitry G., 18
 Podalov, Maksim, 72
 Poperenko, Leonid V., 26
 Pyatlitski, Alyaxandr, 72, 144, 151

R

Rabczuk, Timon, 50
 Radu, Daniel, 249
 Rakos, Balázs, 99
 Rituraj, Rituraj, 217
 Rogachev, Alexandr A., 104
 Rogachev, Alexandr V., 18, 65, 104, 151
 Rudenkov, Alexander S., 18
 Rusikin, Alexey, 59, 65

S

Samofalov, Andrey, 72
 Samoila, Florentina, 135
 Semchenko, Alina, 144, 151, 176
 Semchenko, Igor, 72
 Seteikin, A.Yu., 87

Shimada, Masashi, 41
 Shimizu, Kazuo, 161, 169
 Sidsky, Vitaliy V., 144, 151
 Simon-Nagy, Gabriella, 281
 Sirghi, Lucel, 120, 135
 Solodukha, Vitaliy, 72, 144, 151
 Sperhac, Jeanette, 307
 Stoian, George, 110, 191
 Sudnik, Larisa, 59, 65
 Sychov, Maxim, 3, 81

T

Takeda, Kazuhiro, 203, 235
 Teodorescu-Soare, Claudia Teodora, 110, 176, 191
 Tiron, Vasile, 183
 Togari, Akihiro, 41
 Tóth, János T., 297
 Tusor, Balázs, 243, 297
 Tyulenкова, Nina I., 151
 Tyulenкова, Olga I., 151

V

Vajda, Istvan, 209
 Várkonyi-Kóczy, Annamária, 32, 50, 209, 217, 225, 243, 289, 297, 341
 Vaskevich, Vasily, 59, 65
 Velicu, Ioana-Laura, 183
 Verlan, V.I., 11
 Vienna, Mariagioia, 315
 Vitali, Domenico, 273

W

Walters, Lisa, 307
 Wilkinson, Valerie Anne, 326, 334

Y

Yarmolenko, Maxim A., 104
 Yurgelevych, Iryna V., 26

Z

Zhou, Qilai, 41
 Zubareva, V.E., 11